DEVELOPMENT OF SCOUR IN COHESIVE SOILS BY NORMAL IMPINGEMENT OF A SUBMERGED CIRCULAR TURBULENT JET

A Thesis

Submitted to the College of Graduate Studies and Research

in Partial Fulfilment of the Requirements

for the

Degree of Master of Science

in the

Department of Civil and Geological Engineering

University of Saskatchewan

Saskatoon

By

MAHMUD RASHEDUL AMIN

PERMISSION TO USE

In presenting this thesis in partial fulfilment of the requirements for a Postgraduate degree from the University of Saskatchewan, I agree that the Libraries of this University may make it freely available for inspection. I further agree that permission for copying of this thesis in any manner, in whole or in part, for scholarly purposes may be granted by the professor or professors who supervised my thesis work or, in their absence, by the Head of the Department or the Dean of the College in which my thesis work was done. It is understood that any copying or publication or use of this thesis or parts thereof for financial gain shall not be allowed without my written permission. It is also understood that due recognition shall be given to me and to the University of Saskatchewan in any scholarly use which may be made of any material in my thesis.

Requests for permission to copy or to make other use of material in this thesis in whole or part should be addressed to:

Head of the Department of Civil and Geological Engineering
University of Saskatchewan
57 Campus Drive
Saskatoon, Saskatchewan
Canada, S7N 5A9

ABSTRACT

Scour is an important issue due to the potential great extent of loss and risks associated with scouring. The work described herein constitutes laboratory testing of the time development of scour holes in clayey soils produced by a submerged vertical circular impinging jet. Long term laboratory tests were performed on three types of manufactured pottery clays, Buffstone clay (50.3-51.7% clay), P300 clay (48.7-50.7% clay), and M370 clay (51.1-51.3% clay). Detailed measurements of the entire scour hole were performed on a 2 mm grid using a computer controlled laser optical profiler after scouring times of 5 min, 10 min, 15 min, 20 min, 30 min, 40 min, 50 min, 1 h, 1.5 h, 2 h, 4 h, 8 h, 16 h, 24 and then at every 24 h interval until the scour hole was considered to have reached equilibrium based on the criterion used by Mazurek *et al.* (2001). This resulted in long test durations ranging from 120 h to 384 h.

For the time development of the scour hole, a three-dimensional scour hole surface was produced using the data taken by an optical profiler. Thereafter, four cross-sections of the scour hole were extracted from the three-dimensional scour hole surface. Dimensions considered for analysis were taken from both the three-dimensional scour hole surface and the cross-sections of the scour hole. The volume of the scour hole, and the centreline and maximum scour hole depths were extracted from the scour hole surface. The section-wise maximum scour depth, radius of the scour hole, half-width about the jet centreline, and half-width about the section-wise maximum scour depth were extracted for each cross-sections. The growth of these dimensions were observed with time. For a significant portion of scouring, the centreline and maximum scour hole depths increased linearly with the logarithm of time. For the majority of the tests, the half-widths decreased with time. Temporary ceasing of the increment of the centreline and maximum scour hole depths was observed, called “plateaus”, in the time development plot. Scour hole dimensions for the cross-sections showed variability from the average scour hole dimensions. However, for most of the tests this variability decreased with time as the scour test proceeded.

To decide on whether the equilibrium state of the scour hole was achieved, all of the aforementioned scour hole dimensions were evaluated. The characteristic scour hole dimension to decide on the equilibrium condition was termed as the “critical equilibrium dimension”. Four of

the scour tests reached an overall equilibrium state, the section-wise maximum scour hole depth was the critical equilibrium dimension for three of those. The half-widths were the critical equilibrium dimension for one of the tests. However, previous studies did not consider the “side slope erosion” of the scour hole, hence neglected the section-wise maximum scour depth and half-widths for identifying equilibrium condition.

Dimensionless scour hole profiles were developed using the centreline scour depth as the scale for scour hole depth and the half-width about the centreline depth as the scale for radial distance from the jet centreline. A general equation of the dimensionless equilibrium scour hole profile was developed by fitting a sine function to the equilibrium scour test profiles using linear regression analysis. Dimensionless scour hole profiles with time during the scour test were compared to the dimensionless profile at equilibrium. It was observed that while for some scour tests the equilibrium scour hole shape formed quickly compared to the time to equilibrium, for some scour tests the equilibrium shapes did not form until the scour hole stopped growing.

ACKNOWLEDGMENTS

I would like to sincerely thank my supervisor Dr. Kerry Mazurek for her continuous support, guidance and supervision throughout this research. I am also thankful to the lab technicians, Dale Pavier, Brennan Pokoyoway, and Adam Hammerlindl for building and helping with the experimental setup. Gratitude is also extended to my colleagues at the Hydrotechnical Lab. Their sincere advice and inspirations helped me during the course of my graduate study.

I acknowledge the financial support provided by the Natural Sciences and Engineering Research Council of Canada (NSERC) to my supervisor in the form of a Discovery Grant. I am also thankful to the Department of Civil and Geological Engineering of the University of Saskatchewan for the Departmental Scholarship, and the Government of Saskatchewan for Saskatchewan Innovation and Opportunity Scholarship.

I appreciate the sacrifice and dedication of my parents, brother and sister towards achieving this milestone. Last, but certainly not least, I would like to thank my wife, Sharifunnesa Chowdhury, for continuous support and encouragement.

This thesis is dedicated to my father, Muhammad Golam Rasul
and my daughter, Fatima Mahmud.

TABLE OF CONTENTS

LIST OF TABLES

LIST OF FIGURES

LIST OF SYMBOLS

A_0 cross-sectional area of the nozzle (m^2)

A_1 cross-sectional area of the jet plenum at Point 1 (m^2)

b_{cl} half-width of a scour hole based on the centreline scour depth; which is the radius of the scour hole where the scour hole depth is half of the centreline scour hole depth (m)

$\bar{\bar{b}}_{cl}$ average half-width based on the centreline scour depth for all the cross-sections of a scour hole (m)

$b_{cl\infty}$ half-width of a scour hole based on the centerline scour depth at equilibrium (m)

b_j jet half-radius, which is the radial distance from the jet centreline where the axial velocity is half of the maximum axial velocity (m)

b_m half-width of a scour hole based on the maximum scour depth; which is the radius of the scour hole where the scour hole depth is half of the maximum scour hole depth (m)

$\bar{\bar{b}}_m$ average half-width based on the maximum scour depth for all the cross-sections of a scour hole (m)

$b_{m\infty}$ half-width of a scour hole based on the maximum scour depth at equilibrium (m)

b_p radial distance from the jet centreline where the static pressure is half of the maximum static pressure inside the impingement region (m)

B bulk density of the sediment (kg/m^3)

c a dimensionless constant in Walder (2015) definition for the time scale t_s

C a constant in Haehnel *et al.* (2008) equation for scour development (s^{-1})

C_d jet diffusion constant

C' a dimensionless constant in Haehnel *et al.* (2008) equation for scour development

d nozzle diameter (m)

d_a the apparent depth of water due to refraction error (m)

d_r real or actual depth of water after refraction correction (m)

E erosion rate (m/s)

E_c erosion parameter

F_0 dencimetric Froude number

g gravitational acceleration (m/s^2)

h vertical distance from jet origin to the scour hole surface (m)

h_e vertical distance from jet origin to the scour hole surface at equilibrium condition (m)

h_f pipe friction loss (m)

h_m minor loss in pipe (m)

h^* dimensionless scour term, h/H

H impingement height of the jet, height of the jet nozzle above the impingement surface (m)

H^* dimensionless scour term, H/h_e

i positive integer, where $n=i/2$

j vertical distance between points *b* and *a* in the manometer setup (m)

k vertical distance between points *1* and *b* in the manometer setup (m)

K pipe exit loss coefficient

K_d coefficient of erodibility (m^3/N-s)

l vertical distance between points *2* and *a* in the manometer setup (m)

m_c an exponent in Ansari *et al.* (2003) equation for maximum scour depth in cohesive sediments

m_s an exponent in Ansari *et al.* (2003) equation for maximum scour depth in cohesionless sediments

n erosion exponent in excess shear stress model

p static pressure inside the impingement region (N/m^2)

p_a pressure at point *a* in the manometer setup (N/m^2)

p_b pressure at point *b* in the manometer setup (N/m^2)

p_m maximum static pressure at jet centerline (N/m^2)

p_1 pressure at point *1* in the manometer setup (N/m^2)

p_2 pressure at point *2* in the manometer setup (N/m^2)

Q jet flow rate (m^3/s)

r radial distance of any point on the scour hole from the jet centerline (m)

r_j radial distance from the jet centerline (m)

r_0 radius of the scour hole measured from the jet centerline (m)

$\bar{\bar{r}}_0$ average radius of the scour hole for all the cross-sections (m)

$r_{0\infty}$ radius of the scour hole at equilibrium (m)

R radius of the potential core (m)

Re jet Reynolds number

Re_κ permeability Reynolds number

s_d bulk specific gravity of sediment

s_s specific gravity of sediment grains

S_g specific gravity of water

t time (s)

t_d duration of scour test (s)

t_s a time scale, $t_s = H^2Re^{1/4}/(c^{1/2}U_0d)$ (m)

t_{35} time to reach 35% of the equilibrium scour depth (s)

t_{50} time to reach 50% of the equilibrium scour depth (s)

t_{80} time to reach 80% of the equilibrium scour depth (s)

t^* dimensionless time, $t=t/t_s$

t_* the time at which the growth of scour hole dimensions starts to deviate from logarithmic behavior (s)

t_+ time at which the maximum depth of scour is half of the maximum depth scour at equilibrium condition (s)

t_∞ time to reach equilibrium scour condition (s)

t^*_∞ critical time to equilibrium shape of the scour hole (s)

T_r a reference time, $T_r= Bh_e/(K_d\tau_c)$ (s)

T^* dimensionless time, $T^*= t/T_r$

u time-averaged axial velocity of the flow (m/s)

u_m maximum time-averaged axial velocity at the centreline of the jet (m/s)

u_* the critical friction velocity corresponding to the critical shear stress (m/s)

U_o flow velocity at the nozzle (m/s)

U_s the surface velocity for circular jet (m/s)

V_1 velocity at point 1 in the manometer setup (m/s)

V_2 velocity at point 2 in the manometer setup (m/s)

w_f the average fall velocity of a single particles in a fluid at rest (m/s)

x axial distance along the jet centerline (m)

x_0 axial distance of virtual origin from jet nozzle (m)

X erosion parameter of cohesive soil, $X=\rho U_o^2(d/H)^2$ (N/m^2)

X_c the critical value of X, below which no mass erosion can occur (N/m^2)

z_1 vertical distance of point 1 from a fixed datum in the manometer setup (m)

z_2 vertical distance of point 2 from a fixed datum in the manometer setup (m)

α a coefficient in Walder (2015) equation for erosion rate

β a constant denoting the jet spreading rate, $\beta = db_j/dx$

β_1 an exponent in Haehnel *et al.* (2008) equation for scour development

$\Delta\rho$ difference between the bed material density and fluid density (kg/m^3)

ε scour depth (m)

ε_{cl} centreline scour depth (m)

$\varepsilon_{cl\infty}$ centreline scour depth at equilibrium condition (m)

ε_m maximum depth of scour (m)

$\varepsilon_{m\infty}$ maximum depth of scour at equilibrium condition (m)

ε_{ms} maximum depth of scour along a section of the scour hole (m)

γ unit weight of water (N/m^3)

κ the permeability of the eroding bed (m^2)

μ_w refractive index of water

ν the kinematic viscosity of the eroding fluid (m^2/s)

ρ density of water (kg/m^3)

ρ_b density of sand particle (kg/m^3)

τ_c critical shear stress on soil bed due to jet impingement (N/m^2)

τ_m maximum shear stress on the wall due to jet impingement (N/m^2)

τ_o shear stress on the wall due to jet impingement (N/m^2)

ξ volume of scour hole (m^3)

ζ a constant in Walder (2015) equation for erosion rate

$\sum h_L$ total headloss between points 1 and 2 in the manometer setup (m)

CHAPTER 1. INTRODUCTION

1.1 Background

Scour is the removal of soil particles from the soil surface by flowing water. Embankment breaching, bridge failures (e.g., piers, abutments), and failure of river banks are examples of the consequences of scour. Due to the great potential extent of loss of infrastructure and risks associated with scour, understanding scour is important to engineers.

As compared to cohesionless soils such as sand, erosion and scour of cohesive soils are much less understood. One of the reasons is that cohesive soils show different forms of erosion. Erosion can happen in the form of particle by particle removal, termed “surface erosion”; removal of flakes, termed “flake erosion”; and in the form of large chunk removal, termed “mass erosion” (Mazurek 2001). Also, there are a number of factors that influence cohesive soil erodibility. These include the physical properties of the soil (average particle size, particle size distribution, bulk density and water content, temperature), geochemical factors (clay mineralogy, dissolved ions, pH, organic content) and biological factors (disturbance of the sediment surface, integrated biofilms, extracellular polymeric substances) (Grabowski *et al.* 2011). Further, the appropriate method for determining the erodibility of cohesive soils is still under review.

One of the most commonly used erodibility tests is the jet erodibility test developed by Greg Hanson of the Agriculture Research Service of the USDA (Hanson 1990; Hanson 1991; Hanson and Cook 1997; Hanson and Cook 2004). The method was adopted as an ASTM Standard (ASTM D5852 2007). This test can be performed in the laboratory as well as in the field. The soil sample remains undisturbed in the field test and the in situ water can be used as the eroding water. This is a significant advantage as the eroding water chemistry affects the erodibility of the soil (Arulanandan *et al*. 1975).

In the jet erosion test, a submerged vertical circular jet is used to erode the surface of the soil and the time dependent development of the scour hole is measured in terms of the centerline depth progression. As the jet impinges on the soil, it develops shear stresses on the surface of the soil and if the shear stresses exceed a threshold value, known as the critical shear stress, the soil

erodes. Hanson and Cook (2004) related the shear stress of the soil to the jet velocity at the soil surface. They used the jet decay equation given by Rajaratnam (1976) for a free circular jet (one that is not impinging on a surface) to find the jet velocity at the jet centerline.

However, there are some issues with the reliability of the jet scour test (Annandale 2006). The accuracy of the test cannot be judged precisely because none of the available methods provide absolute erodibility coefficient values that can be compared against the test values (ASTM D5852 2007). Cossette *et al.* (2012) performed an analysis of the jet scour test using experimental data of three reconstituted soils and two natural soils, and used four different analysis techniques to assess the critical shear stress of the soils. Results of the analysis produced significantly different values for each soil type. They concluded that the theoretical framework and the underlying assumptions of the analysis techniques need careful review.

One of the issues is that the widely used analysis technique by Hanson and Cook (2004) is based on the theory given by Rajaratnam (1976) for the decay (decrease in jet velocity with distance from its origin) of an axisymmetric free jet. But in the case of the jet scour test, the jet is impinging and as the scour hole progresses with time, the jet becomes confined inside the concave scour hole. The decay of the confined jet is not similar to the decay of a free jet. Ghaneeizad *et al.* (2014) (and also Ghaneeizad *et al*. 2015) showed that for a confined jet the maximum wall shear stress resulting from the jet impingement is higher than for an unconfined system. However, the confinement of the jet inside the scour hole was not considered in their work. Mazurek and Gheisi (2009) also noted that there were likely problems with the prediction of jet diffusion within the scour hole. They applied a correction factor based on the work of Rajaratnam *et al.* (1993) for drop shafts for the confinement of a circular jet. However, this correction factor was not based on the decay values for confinement of the jet within a scour hole. Following Mazurek and Gheisi (2009), Weidner (2012) and Weidner *et al.* (2012) attributed the variability of the measured critical shear stress by the jet erosion test of the same soil to the scour hole shape. They developed a computational fluid dynamics (CFD) model using the ANSYS 13.0 (FLUENT) software to model the shear stress and pressure distribution for scour holes of different shapes and to compare with the flat plate impingement of Beltaos and Rajaratnam (1974). The simulation results for wide, shallow holes were in good agreement with the flat plate impingement results. However, for

narrow, deep holes, the results varied significantly. This indicated the shape of the scour hole has an influence on the jet inside of a scour hole. However, the simulations were limited and not verified by laboratory experiments and they assumed a fixed (equilibrium) shape for the scour holes.

For a detailed analysis of time development of scour for the jet erosion test, the computation of the decay of a jet inside the scour hole is an important factor. As the scour hole grows with time, the shape of the scour hole changes and ultimately takes an equilibrium scour hole shape (Mazurek 2001). However, this likely does not occur until later in the scour process. Several studies have been conducted to study the time development of a scour hole by a vertical circular impinging jet in cohesive sediments (Moore and Masch 1962; Hanson and Cook 1997; Mazurek 2001; Mazurek *et al.* 2001; Ansari *et al.* 2003; Mazurek *et al.* 2006). However, in all of these studies only the centerline or maximum scour depth was measured. The evolution of the scour hole shape to equilibrium scour hole needs to be studied to be able to model time development of scour by mass erosion in cohesive soils. Further, it is important information for proper analysis of the jet erodibility test.

This study focuses on the time development of the shape of scour hole in cohesive sediments caused by a submerged vertical circular turbulent impinging jet. The hypothesis of this study is that the dimensionless scour hole does not form the equilibrium shape until later in the test. Before that a scour hole formed by mass erosion can be quite irregular.

1.2 Objectives

The objectives of this study are the following:

1. To observe the time dependent development of the scour hole shape in clayey soils caused by a submerged vertical circular impinging jet;
2. To assess what characteristic dimension of the scour hole might best indicate the equilibrium condition; and
3. To compare the dimensionless scour hole profiles during scour to the dimensionless equilibrium scour hole profile, to find at what time in the scouring process any similarity in the scour hole shape starts to be present.

1.3 Scope

With respect to the scope of the research, the scour testing is experimental and is performed in manufactured clay soil samples because the selected manufactured clays were very uniform. Tests were performed in a laboratory setting. Natural clay soils are mostly non-uniform resulting in high variability of properties. Repeatability tests and numerical modelling of the flow within the scour hole was outside the scope of this research.

1.4 Organization of the Thesis

This thesis is organized into five chapters. Chapter 2 includes the review of previous studies regarding the time development of a scour hole. Both cohesionless and cohesive soil scouring researches have been compared and the shape of the equilibrium scour hole has been discussed. Chapter 3 describes the experimental setup, methodology of the experiment and programs used for data collection, processing and analysis. Chapter 4 provides the results of the experiments and detailed analysis of the experimental results. Finally, Chapter 5 includes the summary of the observations, conclusions developed from the study and recommendations for future research.

CHAPTER 2. LITERATURE REVIEW

2.1 Introduction

In this chapter, the behavior of a submerged circular impinging jet is first discussed. A review of the literature on scour by a circular impinging jet is presented, along with a discussion about equilibrium in the context of scour. The development of scour holes created by a submerged circular vertical impinging jet in cohesionless and cohesive soils are also compared.

2.2 Behavior of Submerged Circular Turbulent Impinging Jets

A jet is the flow of fluid generated by a continuous source of momentum (Lee and Chu 2003). A stream of fluid discharged forcefully from a narrow opening can create a jet. Consider a submerged circular jet originating from a circular nozzle supplied by a continuous source of momentum and moving through the stagnant surroundings of an ambient fluid that is the same fluid as the jet. The jet can be characterized by the flow velocity at the nozzle, U_o, nozzle diameter, d, and kinematic viscosity of the flowing fluid, ν. Hence, the jet Reynolds number is defined as, $Re = U_o d / \nu$. It is known from experiments that when $Re > 500$, the jet becomes turbulent after a certain laminar length and when $Re > 3000$, the jet becomes fully turbulent (Rajaratnam and Flint-Petersen 1989). When a submerged circular turbulent jet impinges against a wall or boundary, it termed a submerged circular turbulent impinging jet.

For normal impingement of a submerged jet on a smooth flat rigid plate, as shown in Figure 2.1, the dynamics of flow can be separated into three distinct regions (Beltaos and Rajaratnam 1974; Beltaos 1974). In Region I, the flow is unaffected by the flat plate and behaves as a circular free jet. Therefore, this region is termed the "Free Jet Region". In Region II, the flow undergoes considerable deflection due to impingement on the flat surface. The flow direction is altered from its initial direction and becomes parallel to the surface of the plate. Hence, this region is termed the "Impingement Region". In Region III, the flow resembles the characteristics of a wall jet. Therefore, this region is termed the "Wall Jet Region". However, transition zones may exist between these flow regions (Beltaos and Rajaratnam 1974; Beltaos 1974).

2.2.1 Free Jet Region

In the Free Jet Region of the impinging jet, as the jet leaves the nozzle, the turbulence generated on the edges of the jet penetrates into the jet and causes decay in the jet's axial and radial velocity. Up to a certain distance from the nozzle, the initial velocity U_o remains undiminished in the form of a core with radius R, which is referred to the jet's "potential core". However, the jet nozzle design affects the length of the potential core and for an "efficiently designed nozzle" (a nozzle designed to keep the energy loss very low; normally this is achieved by reducing the nozzle diameter smoothly) the potential core is longer than an inefficient one. For example, Beltaos and Rajaratnam (1977) recommended the length of potential core lies within the range 6.1d to 6.3d for a efficiently designed nozzle. In a recent study, Hashiehbaf *et al*. (2015) used a simple circular pipe as a nozzle without any mechanism to develop a smooth flow contraction and the potential core length was found to be 4d. Further, based on different estimation approaches the potential core length can vary up to 2.5d (Ashforth-Frost and Jambunathan 1996). For example, Ghaneeizad *et al*. (2014) estimated the potential core length to be 2.3d considering very little variation of centreline velocity from the jet velocity at nozzle, while they estimated the length to be 5d from the same experiment considering a 10% variation of the velocity. Lee and Chu (2003) proposed an average potential core length of 6.2d for general purposes.

The portion of the jet from the nozzle to the end of the potential core is termed the "Flow Development Region" and after the end of the potential core, the remaining portion of the jet is known as the "Fully Developed Flow Region" (Rajaratnam 1976). Phares *et al*. (2000) termed these regions as the "Near-Field Region" and "Far-Field Region" respectively. However, impingement of a submerged circular turbulent jet can occur either in developing jets (e.g., Beltaos and Rajaratnam 1977; Kristiawan *et al.* 2015) or in fully developed jets (e.g., Beltaos and Rajaratnam 1974; Bradshaw and Love 1961; Ghaneeizad *et al.* 2015). The standard jet erosion test (ASTM D5852 2007) proposed an impingement height of approximately 17d. Hence, the focus here will be on the impingement of fully developed jets ($H \geq 6.2d$).

In the fully developed flow zone, the axial velocity of the jet decays with increasing axial distance from the nozzle. Consequently, the time-averaged or "mean" axial velocity profiles of the jet also change, but the shape of the dimensionless axial velocity profiles remains constant and

independent of the Reynolds number. In experiments by many researchers (e.g., Corrsin 1943; Hinze and Zijnen 1949; Albertson *et al.* 1950; Wygnanski and Fiedler 1969; Rajaratnam 1976; Phares *et al.* 2000) this phenomenon known as self-similarity has been observed. Lee and Chu (2003) gave the following equations of flow for the axial velocity of a turbulent circular jet, which also shows that the velocity profiles are self-similar and the distribution of mean axial velocity is Gaussian. In the flow development zone ($x \leq 6.2\ d$):

$$u = U_0;\ r_j \leq R \qquad [2.1]$$

$$u = U_0 e^{-\left\{\left(r_j - R\right)^2 / b_j^{\,2}\right\}};\ r_j \geq R \qquad [2.2]$$

and in the fully developed flow zone ($x \geq 6.2\ d$):

$$u = u_m e^{-\left(r_j / b_j\right)^2} \qquad [2.3]$$

where u = time-averaged axial velocity of the flow; u_m = maximum time-averaged axial velocity at the centreline of the jet; r_j = radial distance from the jet centreline; and b_j = jet half-width, which is the radial distance, r_j, where the velocity is half of the maximum velocity at the axis of the jet, or at $r_j = b_j$, $u = ½\ u_m$. Experimental results showed that the turbulent circular jet spreads linearly:

$$b_j = \beta x \qquad [2.4]$$

where β is a constant denoting the jet spreading rate ($\beta = db_j/dx$), and x is the axial distance along the jet centreline. Values of β may vary depending on the nozzle design. For example, Xu and Antonia (2002) measured the value 0.085 and 0.095 for a pipe nozzle and contraction nozzle respectively for the same hydraulic conditions and same nozzle diameter. However, Rajaratnam (1976) and Lee and Chu (2003) recommended the values 0.100 and 0.114 respectively for practical purposes. Values of β from different studies are shown in Table 2.1.

In the fully developed region, the dimensionless axial velocity distribution shows self-similarity (Albertson *et al.* 1950; Wygnanski and Fiedler 1969; Hussein *et al.* 1994), which implies that the dimensionless time-averaged velocity versus axial distance curves collapse onto a single curve. For the decay in the maximum velocity of the jet along its centreline, it has been found that

$$\frac{u_m}{U_0} = C_d \left(\frac{x}{d} \right)^{-1} \qquad [2.5]$$

where C_d is the diffusion constant (Rajaratnam 1976). However, the similarity characteristic for axial velocity was observed for different ranges of relative axial distance (x/d) in different studies and different values of C_d were obtained from these studies (Table 2.2). Rajaratnam (1976) stated that C_d varies from 5.8 to 7.3 due to turbulence and a non-uniform velocity at the nozzle. Hanson and Cook (2004) used C_d =6.3 for the analysis of scour by a circular turbulent impinging jet.

The self-preservation of the jet in the fully developed region indicates that the flow apparently originates from a point source of momentum, known as the virtual origin. Axial distance measurements from the location of the virtual origin (x_o) instead of the nozzle improves the solution of the self-preservation equation (Uddin and Pollard 2007). However, there is uncertainty in the estimation of the precise location of the virtual origin and this estimate found by considering either the length scale or the velocity scale does not coincide (Rajaratnam 1976). Also, the virtual origin can be located either upstream of the nozzle (e.g., Hinze and Zijnen 1949) or downstream of the nozzle (e.g., Hussein *et al*. 1994). Though most of the studies agreed on one virtual origin, Wygnanski and Fiedler (1969) estimated two separate virtual origins in the developed jet corresponding to two ranges of axial distance. Further, George (1989) argued that, the self-preservation of the jet is governed by the initial conditions (e.g., nozzle Reynolds number, turbulence at nozzle, nozzle boundary layer thickness etc.), rather than originating from a point source of momentum (virtual origin). However, Rajaratnam (1976) suggested that the virtual origin could be located at the nozzle exit for practical purposes.

The mean radial velocity is very small compared to the mean axial centreline velocity (about 40 times less) and can be determined from the continuity equation given by the known axial velocity component. Near the edge of the jet, the ambient fluid flows into the jet due to turbulence and is entrained. Thus, the radial velocity is negative at the edge of the jet; otherwise it is positive (Pope 2000). From the experiments of Hussein *et al.* (1994), it is observed that the transition of radial velocity from positive to negative occurs approximately at $r_j = 1.5b_j$.

2.2.2 Impingement Region

As the jet approaches towards the impingement surface, the velocity profiles deviate from free jet behavior (Phares *et al.* 2000). From the axial velocity profiles for Regions I and II, researchers including Ghaneeizad *et al*. (2015), Ghaneeizad *et al*. (2014), Beltaos and Rajaratnam (1974) and Rajaratnam *et al*. (2010) found the impingement region begins at a distance of about 0.86*H* from the nozzle, in which *H* is the "impingement height" of the jet (height of the nozzle above the impingement surface). From wall pressure distribution, they found the impingement region ends about at a distance of 0.22*H* from the jet centreline in the radial direction.

From a separate study by Beltaos and Rajaratnam (1977), it was revealed that for an impingement height less than 5.5*d*, the length scale for the impingement region is the diameter of the nozzle, and for impingement height greater than 8.3*d*, the length scale of the impingement region is the impingement height. These heights are termed as a "small impingement height" ($H < 5.5d$) and "large impingement height" ($H > 8.3d$) respectively. The range of *H* from 5.5*d* to 8.3*d* is a transitional range from small to large impingement height. This study involves the scour of cohesive soil by a circular turbulent jet impinging vertically with a large impingement height. Therefore, the remaining discussion in this section focuses on the characteristics of the impingement region considering a large impingement height.

The parameters that contribute to the characteristics of the impingement region include the axial velocity, pressure distribution and shear stress on the wall. The axial velocity profiles inside the impingement region are similar up to $x = 0.96H$ (Ghaneeizad *et al.* 2014, 2015; Rajaratnam *et al.*, 2010). The equation for the axial velocity profile inside the impingement region up to 0.96*H* is given by:

$$u = u_m e^{-0.693\left(r_j / b_j\right)^2} \;;\; x \le 0.96H \qquad [2.6]$$

However, the static pressure inside the impingement region is greater than the ambient pressure. The maximum pressure lies along the jet centreline. The pressure profiles are similar and given by:

$$p = p_m e^{-0.693\left(r_j / b_p\right)^2} \;;\; x \le 0.96H \qquad [2.7]$$

where p = static pressure in the impingement region, p_m = maximum static pressure on the jet

centreline and b_p = radial distance r_j where p = ½p_m. Using the pressure distribution equation (Equation 2.7), Beltaos and Rajaratnam (1974) derived the shear stress τ_o on the wall:

$$\tau_\circ = 0.18\tau_m \left(\frac{1-e^{-114\left(r_j/H\right)^2}}{r_j/H} \right) - 9.43\left(\frac{r_j}{H}\right)e^{-114\left(r_j/H\right)^2} \qquad [2.8]$$

in which, the maximum wall shear stress τ_m is given by:

$$\tau_m = 0.16\frac{\rho U_o^{\,2}}{\left(H/d\right)^2} \qquad [2.9]$$

where ρ = density of the eroding fluid. This maximum shear stress occurs at a distance $r_j = 0.14H$. However, Phares *et al*. (2000) argued that the derivation of wall shear stress by Beltaos and Rajaratnam (1974) is not valid, because it was based on the equations of motion in the axial direction, rather than the boundary layer equations in the radial direction. Hence, the modified wall shear stress equations by Phares *et al*. (2000) are:

$$\frac{\tau_o}{\rho U_0^2} Re^{1/2}\left(\frac{H}{d}\right)^2 = f\left(\frac{r_j}{H}\right) \qquad [2.10]$$

and

$$\tau_m = 44.6\frac{\rho U_0^2}{Re^{1/2}\left(H/d\right)^2} \qquad [2.11]$$

where τ_m is located about at a distance of $0.09H$ from the jet centreline.

2.2.3 Wall Jet Region

Some distance after the jet impingement, the excess pressure diminishes to zero and the static pressure reverts to the ambient pressure (Ghaneeizad *et al*. 2014) and this indicates the beginning of the wall jet region. Beltaos (1974) found the wall jet region starts at a radial distance of $0.36H$. Because the impingement region ends at a distance of $0.22H$, he defined the range $0.22H \le r_j \le 0.36H$ as a transition zone.

Many researchers (Glauert 1956; Poreh *et al.* 1967; Abramovich 1963) found the velocity profiles of the wall jet region are self-similar. Experimental results of Bradshaw and Love (1961) and Poreh *et al*. (1967) showed that the dimensionless velocity profile in the wall jet region is linear. Rajaratnam (1976) used these results to find the equation for that velocity:

$$\frac{u_m}{U_o} = \frac{1.03}{\left(r_j / d\right)} \qquad [2.12]$$

In deriving this equation, Rajaratnam (1976) neglected the correction for the virtual origin. An important observation about this equation is that it is independent of the impingement height *H*. Therefore, the impingement height may not affect the scaling of velocity in the wall jet region. The half-radius b_j is typically used as the length scale of the wall jet region and is given by the following equation:

$$b_j = 0.087 r_j \qquad [2.13]$$

However, very little is known about the characteristics of wall jet region for an impinging jet on a scoured bed.

2.3 Scouring by Submerged Circular Turbulent Impinging Jets in Cohesionless Soils

The hydrodynamic action of an impinging jet can lead to scouring of the soil bed, though the scour mechanism is different in cohesionless and cohesive soils. Cohesionless soils are eroded as individual particles, which implies erosion of such a soil depends on the buoyant weight of those particles. Hence, particle density, mean grain size, and gravity are determining factors for cohesionless soil erosion. In contrast, electrochemical forces bind cohesive soil particles together, and for erosion to occur, this force must be exceeded by the erosive force. Early studies on scour by circular impinging jets were dedicated mostly to scour in cohesionless soils (e.g., Doddiah *et al.* 1953; Poreh and Hefez 1967; Sarma and Sivasankar 1967; Sarma 1967; Westrich and Kobus 1973; Rajaratnam and Beltaos 1977; Rajaratnam 1982; Aderibigbe and Rajaratnam 1996; Aderibigbe 1996), and as a result, features of cohesionless soil scour are well known compared to scour in cohesive soils. In spite of the differences in scour mechanisms, studies of cohesionless soil scour can enlighten us to the expected outcomes for cohesive soil scour.

The progress of scour depends on the erosive capacity of the jet, where the applied wall shear stress on the soil bed is a measure of the erosive capacity. The maximum applied shear stress occurs on the initial (unscoured) soil surface. As the soil erodes, the effective impingement height of the jet increases. As a result, the applied shear stress eventually is reduced as scouring progresses and reaches a limiting value below which no erosion can occur. This mechanism affects the progress of scour by a circular impinging jet. During the initial stages of scour, the scour rate is

higher. In scour testing of cohesionless soils with circular impinging jet, more than 70% of the total scour occurs in only the first 30 minutes (Ansari 1999; Rajaratnam 1982). With time, the scour rate reduces, and eventually the applied shear stress can no longer erode the soil surface. This phase is normally termed as the "equilibrium phase", where the erosive forces and resistive forces are in balance on the soil. Therefore, scour by an impinging jet can be discussed as two phases, the "unsteady phase" and the "equilibrium phase".

2.3.1 Unsteady Phase of Scour by Circular Impinging Jets in Cohesionless Soils

Beltaos (1974), Poreh and Hefez (1967), and others, including Rajaratnam and Beltaos (1977), observed that for the initial part of the scouring process, the maximum scour depth occurs at a small distance away from the point of jet impingement. This phenomenon is a result of the boundary shear variation on the soil surface by the impinging circular turbulent jet (Rajaratnam and Beltaos 1977). However, later in the scouring process, the maximum scour depth is found to occur at the point of jet impingement. A characteristic ridge is formed around the periphery of the scour hole.

Following an initial time of scouring, the characteristic dimensions of the scour hole (e.g., the maximum scour depth) are observed to grow linearly with the logarithm of time (Rouse 1939; Laursen 1952; Doddiah *et al.* 1953; Beltaos 1974; Rajaratnam and Beltaos 1977). However, after an appreciable amount of time, the depth approaches an asymptotic or equilibrium value. Rajaratnam and Beltaos (1977) referred to the time for the deviation from the linear relationship as t_* and reported that the practical equilibrium condition is reached long after this characteristic time, approximately after $30t_*$. Further, at time t_*, the maximum depth of scour ε_m is about only 0.75 times the maximum depth of scour at equilibrium $\varepsilon_{m\infty}$.

Rajaratnam and Beltaos (1977) showed that for sand-air experiments with submerged circular turbulent impinging jets, the dimensionless plots of the growth of the scour hole depth are similar. For a series of experiments, the dimensionless maximum scour depths $\varepsilon_m/\varepsilon_{m\infty}$, were plotted against the dimensionless characteristic times t/t_+, to find that the curves collapse into a single curve, where t_+ is the value of the time t, for which $\varepsilon_m = ½\ \varepsilon_{m\infty}$. This finding is consistent with the findings of Rajaratnam and Berry (1977) for loose bed scour experiments (sand-air, sand-water,

and polystyrene-air) for submerged turbulent wall jets. From the similarity observed in the evolution of the scour hole depths, Rajaratnam and Beltaos (1977) showed that the equilibrium condition was reached at $100t_+$. However, no equation was developed to assess the scour development with time.

Ansari *et al.* (2003) developed an empirical relationship for the time development of scour holes in cohesionless soil by a submerged circular turbulent impinging jet. They compiled data from the earlier studies conducted by Aderibigbe and Rajaratnam (1996), Rajaratnam (1982), Sarma (1967), and Westrich and Kobus (1973) and combined with their own experimental data to develop the equation:

$$\frac{\varepsilon_m}{\varepsilon_{m\infty}} = \left[\sin\left(\frac{\pi t}{2t_\infty} \right) \right]^{m_s} \qquad [2.14]$$

where t= time, t_∞ = time to reach equilibrium scour, and m_s is an exponent. However, Ansari *et al.*, (2003) could not provide any relationship for obtaining the values of t_∞ and m_s. Because the mostly accepted logarithmic relationship is invalid near the initial (t = 0) and asymptotic ($t = t_\infty$) phase of the scouring process, the use of the sine function is advantageous. In contrast, during the intermediate phase of scouring, the sine function may not represent the scouring process well compared to the logarithmic relationship.

Haehnel *et al*. (2008) associated the sediment properties (sand) and jet characteristics to develop an equation for the evolution of a scour hole:

$$\frac{d\varepsilon_m}{dt} = C \frac{\rho}{\rho_b} \frac{1}{g} \left\{ C' \frac{U_0 d}{(H+\varepsilon) Re_\kappa^{\beta_1}} - u_*^2 \right\} \qquad [2.15]$$

where ρ is the density of water, ρ_b is the density of the sediment, C is a constant with units s^{-1}, C' is a dimensionless constant, β_1 is an exponent, u_* is the critical friction velocity corresponding to the critical shear stress, Re_κ is the permeability Reynolds number represented by $Re_\kappa = U_s \sqrt{\kappa} / \nu$ in which U_s is the surface velocity estimated from the momentum considerations for circular jet, and κ is the permeability of the eroding bed (with units m^2/s). Equation 2.15 was derived from the sediment flux removal relationship $d\varepsilon/dt = C(\tau-\tau_c)/\rho_b g$, considering that the particles leave the bed surface due to excess shear stress under uniform flow parallel to the bed surface. To adapt the

sediment flux removal relationship for an impinging jet flow, the constant C' was used. However, Equation 2.15 underestimates the depth of erosion for sand in the intermediate stages of the erosion testing (Haehnel *et al*. 2008).

2.3.2 Equilibrium Phase of Scour by Circular Impinging Jets in Cohesionless Soils

From the work of Beltaos (1974) and Rajaratnam and Beltaos (1977) on air-sand scour and Rajaratnam (1982) on water-sand scour, it has been proven that for a jet at a large impingement height (H>8.3d), the dimensions of the scour hole, scaled by the impingement height H, are functions of $F_0/(H/d)$ where, F_0 is the densimetric Froude number, given by $U_0/\sqrt{gD\Delta\rho/\rho}$, and g is the gravitational acceleration, D is the mean diameter of the bed material, and $\Delta\rho$ is the difference between the bed material density and fluid density ρ. The term $F_0/(H/d)$ is normally called the erosion parameter E_c; it represents the ratio of the force acting on the sediment bed directly under the jet at the uneroded bed level to the corresponding resistive force due to the buoyant weight of the particle (Aderibigbe 1996; Aderibigbe and Rajaratnam 1996). For small impingement heights (H<5.5d), the dimensions of the scour hole, scaled by the diameter at nozzle d, are functions of F_0 only.

Aderibigbe and Rajaratnam (1996) used maximum scour depth data obtained from Rajaratnam (1982) and Westrich and Kobus (1973) to develop an empirical equation for the equilibrium scour depth:

$$\frac{\varepsilon_{m\infty}}{H} = 1.26E_c^{\,0.11} - 1 \qquad [2.16]$$

Though Equation 2.17 represents the relationship between $\varepsilon_{m\infty}$ and E_c fairly well, Ansari *et al.* (2003) compared this equation with a combined scour dataset obtained from Sarma (1967), Westrich and Kobus (1973), Rajaratnam (1982), Aderibigbe and Rajaratnam (1996), and their own experiments, and proposed a slight modification to Equation 2.16:

$$\frac{\varepsilon_{m\infty}}{H} = 1.3E_c^{\,0.15} - 1 \qquad [2.17]$$

Some earlier studies (e.g., Sarma, 1967; Westrich and Kobus, 1973) had expressed $\varepsilon_{m\infty}/H$ in terms of u_o/u_* or u_o/w_f, in which w_f is the average fall velocity of a single particle in a fluid at rest. While deriving Equation 2.17, Ansari *et al.* (2003) verified that $\varepsilon_{m\infty}/H$ can be better represented by E_c.

Although the maximum scour depth reaches equilibrium, the radius of the scour hole can continue to increase in size (Rajaratnam and Beltaos 1977). Rajaratnam and Beltaos (1977) explained that this occurs because of the continuous "random bursts of erosion" at the side of the scour hole. Even if the radius does not reach the equilibrium state, the quasi-equilibrium scour holes (considering only the scour depth reaches the equilibrium state) shows similarity with some dispersion near the ridge. This type of similarity in the equilibrium scour hole profile was also observed in tests of scouring with submerged circular turbulent wall jets for sand beds (Rajaratnam and Berry, 1977) and submerged plane turbulent wall jets and submerged plane impinging jets experiments in polystyrene and sand beds (Rajaratnam, 1981). The studies of Aderibigbe and Rajaratnam (1996), Aderibigbe (1996), Beltaos and Rajaratnam (1977), Beltaos (1974) and Rajaratnam (1982) in experiments with a submerged circular turbulent impinging jet with a sand bed showed that an exponential equation represents the shape of the equilibrium scour hole well:

$$\frac{\varepsilon}{\varepsilon_{m\infty}} = e^{-0.693\left(r/b_{m\infty}\right)^2} \qquad [2.18]$$

where r = radial distance measured from the jet centreline; ε = scour depth at radius r below the original bed level; $\varepsilon_{m\infty}$ = maximum scour depth at equilibrium condition; $b_{m\infty}$ = half-radius of the scour hole, which is the radial distance r where the scour hole depth is half of the maximum scour hole depth at equilibrium, or at $r = b_{m\infty}$, $\varepsilon = ½\ \varepsilon_{m\infty}$.

The shape of the scour hole essentially affects the flow pattern inside the scour hole and the flow pattern inside the equilibrium scour hole can be divided into two distinctive regimes. Based on the jet deflection inside the scour hole, Rouse (1939) defined the "Maximum Jet Deflection" flow regime where the flow turns back on itself inside the scour hole by about 180°. The "Minimum Jet Deflection" flow regime was where the jet flowed along the boundary of the scour hole along with the ridges (Rouse 1939). Westrich and Kobus (1973) and Kobus *et al*. (1979) termed the "Scour Form I" and "Scour Form II" flow regimes based on the flow interaction with the bed inside the equilibrium scour hole. When a non-dimensional flow parameter similar to E_c is close to the value corresponding to incipient motion, Scour Form I was seen, whereas Scour Form II was seen for higher values of the parameter. Following Rouse (1939), Aderibigbe (1996) and Aderibigbe and Rajaratnam (1996) classified the flow regimes for the equilibrium scour hole as the "Strongly Deflected Jet Regime" (SDJR) and "Weakly Deflected Jet Regime" (WDJR).

Figure 2.2 shows typical scour hole shapes for weakly deflected and strongly deflected flow regimes. For the SDJR, $E_c > 0.35$ and for the WDJR, $E_c < 0.35$. In the SDJR, the jet always penetrates the bed and is strongly deflected inside the scour hole. The deflected jet carries lots of sediment in suspension and as the flow recirculates inside the scour hole, the suspended sediments also recirculate with the flow. Near the periphery of the scour hole the flow is weak, resulting in deposition of some sediments in the form of a ridge. However, after the jet is stopped, the remaining suspended sediments inside the scour hole settle back into the scour hole. Thus the dynamic scour hole and static scour hole for the SDJR are different and the dynamic scour hole depth is greater than the static scour hole depth. In case of the WDJR, the jet weakly penetrates into the bed, resulting in less interaction with the bed. The flow follows the boundary of the scour hole and there is only a small amount of suspended sediment inside the scour hole. This means that the depth for dynamic and static scour is almost the same. Further, it takes more time for the WDJR scour holes than the SDJR scour holes to reach equilibrium state (Rajaratnam and Beltaos, 1977). Other researchers including Rajaratnam and Mazurek (2003) also observed the SDJR and WDJR flow regimes.

In more recent experiments, Haehnel *et al*. (2006) (also Haehnel *et al*., 2008) classified the flow regimes into the "Shallow-Crater" regime and the "Deep-Crater" regime based on the erosion potential of the impinging jet. For some cohesionless bed material (i.e., glass beads and natural beach sand) a transitional regime termed the "Transition Crater" was also seen, whereas Polypropylene and Ottawa sand did not exhibit a transitional crater.

2.4 Scouring by Submerged Circular Turbulent Impinging Jets in Cohesive Soils

Though there are some similarities in the development and regime behavior of cohesive and cohesionless soil scouring, some characteristics of cohesive soil scouring make it unique. Notably, the variability of erosion forms in cohesive soils is the defining factor for the shape and evolution of the scour hole in cohesive soils.

2.4.1 Unsteady Phase of Scour by Circular Impinging Jets in Cohesive Soils

Mazurek (2001) suggested there were three forms of erosion seen in her experiment in scouring of a cohesive soil, namely flake erosion, mass erosion and rapid surface erosion. In the

experiments of Mazurek *et al.* (2001), examining flake erosion, flakes of diameter 1-3 mm and thickness less than 0.5 mm were removed from the clay sample (pottery clays). The scoured shape resembled a circle centered about the centreline of the jet. Mass erosion occurred by the removal of small to large chunks of soil. The small chunks were about 3 mm in length, 2 mm in width and a few milimetres in thickness, while the big chunks were about 130 mm in length, 40 mm in width and 20 mm in thickness. The chunks were angular in shape. Rapid surface erosion was seen at higher shear stresses (greater than 200 Pa). During this type of erosion, soil was removed particle by particle and the resulting scour hole was very smooth and symmetrical. This symmetry of the scour hole was always disrupted by subsequent mass erosion. Among the observed erosion forms, Mazurek (2001) found that most of the erosion occurred by mass erosion. Mass erosion in the form of removal of individual chunks of soil is the most common type of erosion in cohesive soils as observed by many researchers (e.g., Moore and Masch 1962; Hanson 1990; Mazurek 2001; Mazurek *et al.* 2001; Ansari *et al.* 2003). Ansari *et al.* (2003) reported that the size of the chunks during mass erosion is influenced by the percentage of clay, moisture present in the soil, and the applied shear stress.

No matter the form of erosion, the initial scouring of the sample under a circular impinging jet takes place a distance away from the jet centreline (Dunn 1959; Moore and Masch 1962; Mazurek *et al.* 2001). This behavior is a result of the distribution of shear stress on the initial soil surface by a vertically impinging submerged circular jet, as the maximum shear stress occurs at small distance away from the jet centreline (Beltaos 1974; Beltaos and Rajaratnam 1974; Hanson *et al.* 1990; Phares *et al.* 2000). It appears that the location of the maximum shear stress and initial scour may coincide for an undisturbed soil sample (Mazurek 2001).

Except for the initial scouring period, the growth of the scour hole in cohesive soil exposed to a submerged circular vertical impinging jet follows an approximately linear relationship with the logarithm of time until it reaches an asymptotic state (Moore and Masch, 1962; Mazurek *et al.*, 2001; Mazurek, 2001). The approximate nature of this relationship can be attributed to mass erosion. During the scouring process, removal of a large chunk of soil may disrupt the logarithmic progress of scouring. Mazurek *et al*. (2001) checked the logarithmic relationship for the cubic root of scour volume, centreline scour depth and maximum scour depth and reported that this

relationship holds true for the entire scouring process except at the very early stage and near the equilibrium stage.

To represent the time development of scour, Blaisdell *et al.* (1981) produced a hyperbolic function for the temporal development of a scour hole, which is often used to model scour by circular jets in cohesive soils (Hanson and Cook, 2004). Regression analysis of scour data on log-log, semi-log and hyperbolic plots was done to find the best fit for the maximum scour depths with time. The hyperbolic function showed the best fit and the semi-log plot showed the poorest fit. However, one must determine the focal point of the hyperbolic curve by trial and error to use this hyperbolic function for predicting time development of scour (Stein, 1990), which is a limitation of this approach. Further, the Blaisdell method has been found to greatly overestimate the equilibrium scour depth (Mazurek, 2010; Cossette *et al.*, 2012).

Stein (1990) (also described in Stein *et al.* (1993)) and Stein and Julien (1994) proposed relationships for the time development of a scour hole in cohesive soils created by an obliquely impinging plane jet. They related the jet diffusion principal to the sediment detachment rate using the well-known excess shear stress model. This excess shear stress model is $E=K_d(\tau_o-\tau_c)^n$; in which E is the erosion rate, K_d is the coefficient of erodibility, τ_c is the critical shear stress on soil bed, and n is the erosion exponent. Stein (1990) derived a time development relationship for different values of n, and it was found that the relationship for n=1 resulted in the best fit for the cohesive soil he tested. Later, Hanson and Cook (1997, 2004) adapted the Stein (1990) time development relationship for vertical circular turbulent impinging jet assuming n=1. The relationship is given as:

$$T^* = \left[-h^* + 0.5 \ln\left(\frac{1+h^*}{1-h^*}\right) \right]_{H^*}^{h^*} \qquad [2.19]$$

where T^* = dimensionless time, with $T^*= t/T_r$; T_r = a reference time, with $T_r= Bh_e/(K_d\tau_c)$; B = bulk density of the sediment; h^* = dimensionless scour term, h/h_e; h = vertical distance from the jet origin to the scour hole surface; $h_e = h$ at equilibrium; H^* = dimensionless scour term, H/h_e. There is concern about using Equation 2.19, because the temporal development of scour hole is dependent on the accuracy of the prediction of the equilibrium scour depth. Hanson and Cook (1997, 2004) proposed the Blaisdell method to determine the equilibrium scour depth, which is

not accurate. Further, the assumption of a linear excess shear stress model is still under review. A recent study by Walder (2015) showed that the erosion exponent *n* is a soil specific parameter and different cohesive soils may show different values of *n*.

Mazurek (2001) (also described in Mazurek *et al.*, 2006) showed that the plot of the dimensionless centreline scour depths against dimensionless time collapses on to one single curve for the same soil under different hydraulic conditions. This observation is consistent with the observation of Rajaratnam and Beltaos (1977) in case of cohesionless soil. However, the accuracy of this dimensionless relationship depends on the selection of appropriate time scale. Mazurek *et al.* (2006) used three different time scales - t_{35}, t_{50} and t_{80} where, 35, 50 and 80 represent time to reach 35%, 50 % and 80% of the equilibrium scour depth respectively. The best result was obtained when the time scale was t_{80}. The following equation was developed for the time development of scour holes in the tested clay soils:

$$\frac{\varepsilon_{cl}}{\varepsilon_{cl\infty}} = 0.10\ln\left(\frac{t}{t_{80}}\right) + 0.79 \qquad [2.20]$$

where $\varepsilon_{cl\infty}$ = centreline scour depth at equilibrium condition. Though Equation 2.20 represents the best fit curve for the experimental data presented, at the beginning of the scour test when time t = 0, the equation gives a small amount of scour instead of zero scour. This amount can be significant for scour holes with a large scour depth at equilibrium condition ($\varepsilon_{cl\infty}$). Hence, the equation seems to over fit the data rather than representing a general relationship. Also at earlier stages, the lower time scales (t_{35} and t_{50}) seem to fit the data well. Mazurek *et al.* (2006) explained, this happened because for the same soils tested under different hydraulic conditions the large time scale (t_{80}) varied significantly (as long as 73 hours). However, this relationship was not tested for other scour hole dimensions, such as the cube root of the scour volume, the maximum scour depth or the radius of the scour hole.

Ansari *et al.* (2003) provided a functional relationship for the temporal variation of the maximum scour depth in cohesive sediments:

$$\frac{\varepsilon_m}{\varepsilon_{m\infty}} = \left[\sin\left(\frac{\pi t}{2t_\infty}\right)\right]^{m_C} \qquad [2.21]$$

where $\varepsilon_{m\infty}$ = maximum scour depth at equilibrium condition; t_∞ = time to reach equilibrium scour; m_c = exponent. Mazurek (2003) used the cube root of the scour hole volume to verify Equation 2.21, and found that the equation satisfied the experimental data of Mazurek (2001). But the equation slightly underestimated the average scour depth at the initial state of the test. For a test run up to the equilibrium state, one can measure $\varepsilon_{m\infty}$ and m_c from the time development of the scour hole plot. However, the accurate measurement of t_∞ is a matter of concern because very small amount of scour occurs for comparatively large amount of time near the equilibrium condition. Therefore, some researchers used different time scales instead of t_∞ (Rajaratnam and Beltaos, 1977; Mazurek *et al*., 2006).

Walder (2015) derived dimensionless erosion laws for scour in cohesive sediments by a circular tubulent impinging jet after carefully reviewing the assumptions of the Hanson and Cook (1997, 2004) model. The assumption of a linear excess shear stress model was relaxed. The general form of the equation can be written as:

$$\frac{dh^*}{dt^*} = \left(\frac{s_s}{s_d}\right)\left(\frac{1}{\xi}\right)\alpha\left(\frac{\xi^2}{h^{*2}} - 1\right)^n \qquad [2.22]$$

where h^* = dimensionless scour depth from jet nozzle, h/H; t^* = dimensionless time, t/t_s, in which the time scale $t_s = H^2Re^{1/4}/(c^{1/2}U_0d)$, c is a constant; ζ = a constant, h_e/H; α = a coefficient; s_s = specific gravity of sediment grains; and s_d = bulk specific gravity of sediment. For scour by a jet with a boundary at some finite radius (typically the jet tank), Walder (2015) gives c = 107. One of the advantages of Walder (2015) model is that unlike Stein (1990) and Hanson and Cook (1997, 2004), the initial jet height H is used instead of the equilibrium jet height h_e as the characteristic length scale to compute the dimensionless depth. Further, the time scale t_s in this model is not dependent on the equilibrium scour time. Walder (2015) noted that the solutions of Equation 2.22 are likely available for all $n=i/2$, where i is a positive integer. However, this statement was not verified and the solutions were given only for i=1 to 5.

2.4.2 Equilibrium Phase of Scour by Circular Impinging Jets in Cohesive Soils

The equilibrium phase of cohesive soil erosion with a submerged circular turbulent impinging jet is less understood, as only a few studies have been performed with cohesive soils and most of the studies were not undertaken up to equilibrium scour. In this context, Mazurek

(2001) conducted a series of laboratory tests on scour of cohesive soils by circular turbulent impinging jets. The test conditions were varied by changing the flow rates, nozzle diameter and impinging heights. Every test was run until the equilibrium state was reached or until the sample was washed out. The equilibrium condition was determined as when the volume of the scour hole did not change for a period of 24 hours. The volume of the scour hole was measured by filling the scour hole with water from a graduated cylinder. Centreline and maximum scour depths were also measured during the experiment. At equilibrium, the entire scour hole profile was measured at two perpendicular cross-sections. The depth and radial distance from the jet centreline on the scour hole profile are given with the variables ε and r respectively.

Mazurek (2001) showed that the dimensionless lengths of the equilibrium scour hole (i.e., $\varepsilon_{cl\infty}/H$, $\varepsilon_{m\infty}/H$, r_∞/H, $b_{cl\infty}/H$, $b_{m\infty}/H$) are functions of a dimensionless parameter $(X\text{-}X_c)/X_c$, in which X is the erosion parameter of the cohesive soil ($=\rho U_o^2(d/H)^2$); X_c is the critical value of X, below which no mass erosion occurs; r_∞ is the radius of the scour hole at the equilibrium condition; and $b_{m\infty}$ is the half-radius of the scour hole for the maximum scour depth (at $r=b_{m\infty}$, $\varepsilon=\varepsilon_m/2$). Essentially, the maximum shear stress on the soil surface, $\tau_m=0.16X$, because $\tau_m=0.16\rho U_o^2(d/H)^2$. The parameter $(X\text{-}X_c)/X_c$ can be considered as a dimensionless excess shear stress.

Mazurek (2001) observed that the dimensionless equilibrium scour hole shapes are similar. Gaussian curves and sine curves were developed to represent the equilibrium scour hole shape and the sine curve showed a better fit. The shape of the equilibrium scour hole was given using either the centreline or maximum scour depths as scales for the scour depth:

$$\frac{\varepsilon}{\varepsilon_{m\infty}} = \sin\left\{\frac{2\pi\left(r/b_{m\infty}\right)}{-6.30} - 1.54\right\} \qquad [2.23]$$

$$\frac{\varepsilon}{\varepsilon_{cl\infty}} = \sin\left\{\frac{2\pi\left(r/b_{cl\infty}\right)}{-6.26} - 1.54\right\} \qquad [2.24]$$

where ε and r represent the depth and radial distance at any point on the scour hole profile. However, these equations do not produce a symmetric scour hole about the jet centreline. Therefore, Weidner (2012) used the data of Mazurek (2001) to generate a general symmetrical form of equilibrium scour hole by an impinging circular jet:

$$\frac{\varepsilon}{\varepsilon_m} = -\sin\left(\frac{\pi}{2}\frac{r}{r_\infty} + \frac{\pi}{2}\right) \qquad [2.25]$$

Because Weidner (2012) considered a symmetrical scour hole, centreline and maximum scour depths were the same for equation 2.25. Also, the half-width of the scour hole was not considered because the model for the scour hole was used for developing a computational fluid dynamics model. However, using r_∞ to scale the radius measurement is perhaps not an appropriate methodology because it is very difficult to precisely define the radial boundary of the scour hole at equilibrium conditions.

Based on the scour hole shape, two different flow regimes were reported: the Strongly Deflected Jet Regime (SDJR), when the scour hole is narrow and deep; and the Weakly Deflected Jet Regime (WDJR) flow regime, when the scour hole is wide and shallow (Moore and Masch 1962; Mazurek 2001). Although dimensionless scour hole profiles are similar, Mazurek (2001) differentiated the shape of the scour holes based on the "aspect ratio"; which is the radius to depth ratio of the scour holes. Aspect ratios ranging from 0.55 to 5.7 were reported, while the majority of scour holes fell within the range 1 to 3. Scour holes with lower aspect ratios were deep and narrow, while higher aspect ratio scour holes were wide and shallow. In the SDJR flow regime, the jet becomes confined and almost completely reversed inside the scour hole, but for the WDJR flow regime it does not. Moore and Masch (1962) suggested that the relative impingement height is the determining factor for the two types of flow regimes. When $H/d < 7$, the scour hole is narrow and deep and when $H/d > 7$, the scour hole is wide and shallow. However, in a different study, Hollick (1976) also observed these two forms of scour hole with an additional intermediate type of scour hole. Unlike Moore and Masch (1962), he did not change the impingement height or diameter of the jet; rather he varied the jet velocity. Therefore, these flow regimes are functions of the experiment hydraulics rather than the relative impingement alone. Also, as the scour hole grows with time, one can observe different flow regimes at different times. This transition of flow regimes is not a sudden change, rather a continuous process. Mazurek (2001) suggested that the transition from the weakly to strongly deflected flow regimes occurs at $(X\text{-}X_c)/X_c \approx 5$. Because the flow regime in scour testing might transition during a test, all the previous studies identified the flow regime at the end of the experiment.

2.5 Assessing Equilibrium Scour

As noted previously, from early studies on scouring it is known that later in the scouring process the scour hole does not change significantly with time if the hydraulics of the process remain unchanged (e.g., Laursen 1952; Chabert and Engeldinger 1956; Gill 1972; Zaghloul 1983). This phase of scouring is termed as the equilibrium phase and the corresponding scour hole is termed the "equilibrium scour hole". However, the question is how to determine when equilibrium scour has occurred.

Different researchers have defined equilibrium scour differently. Chabert and Engeldinger (1956) reported at equilibrium condition the scour depth does not change "appreciably" with time. Ettema (1980) identified three phases of scour and indicated that the last phase is the equilibrium phase where the scour depth remains "practically" unchanged with time. Coleman *et al*. (2003) doubted the existence of ultimate scour depth and they opined that at equilibrium condition the scour depth may continue to increase at a "relatively slow rate". Though these researchers believed in the existence of an equilibrium condition, the interpretation is different by the selection of the words "appreciably", "practically" and "relatively slow rate" (Simarro *et al*. 2011).

However, some researchers have rejected the theory of the existence of equilibrium scour (e.g., Rouse 1965; Breusers 1967; Melville and Chiew 1999; Kohli and Hager 2001; Oliveto and Hager 2002). Rouse (1965) considered scouring as a continuous event and rejected the existence of equilibrium scour depth. Franzetti *et al*. (1982) and Melville and Chiew (1999) opined that it is impossible to reach the equilibrium scour in a finite time. From similar reasoning, Oliveto and Hager (2002) stated that the scour hole continues to develop with time.

Nonetheless, the concept of equilibrium condition of scouring has important implications in designing scour experiments and hence it is required to assess experimental time properly. Many scour tests reported in the literature were performed for an insufficient period of time and thus are not useful for further study (Jones and Sheppard 2000). Even in spite of the good fit of the available data to the scour models, sometimes it is not possible to predict equilibrium scour depth accurately because of the short duration of the experiments (Simarro and Martín 2004). In this context, Simarro *et al*. (2011) inquired, "Assuming that equilibrium scour exists but it is not

reached in finite time, the question is how long should experiments be until scouring rate becomes insignificant or practically null and scour depth is close enough to its ultimate value?"

It may be possible to define the equilibrium condition long before the ultimate scour based on the progress of scouring. Anderson (1975) stated that, due to the logarithmic nature of local scour, a "practical equilibrium" can be obtained in relatively short amount of time. In view of this, Lauchlan (1999) used a uniform period of only 24 hours for all his experiments regarding bridge pier scour. According to Coleman *et al*. (2003), when the rate of scour is reduced to 5% of the minimum dimension of the structure (i.e., pier diameter, abutment length etc.) in a 24 hour period, the elapsed time can be considered as the time to reach equilibrium. Sheppard *et al*. (2004) also followed this approach for local scour experiments with circular piles in cohesionless sediments. On a relatively conservative approach, Ahmed and Rajaratnam (1998) ran experiments with cylindrical piers in cohesionless sediments for 2-3 weeks until the increments in scour depths were less than 1 mm in 24 hours. Grimaldi (2005) identified the equilibrium condition when the scour rate is reduced to 1.7% of the the pier diameter in 24 hours, also for bridge pier scour. Fael *et al*. (2006) studied local scour at vertical-wall abutments and proposed to consider the reduction of scour rate in 24 hours to two times of the mean diameter of the cohesionless sediment. However, such quantifications of equilibrium scour were criticized by Simarro *et al*. (2011) and Chreties *et al*. (2011) as these values are arbitrary and any change in the adopted scour reduction (e.g., 1 mm, 5%) or time of reading interval (e.g., 24 hour) could produce significant change in measured equilibrium time.

Unlike the arbitrary criteria set in different studies, a graphical approach based on the time development of scouring has been adopted by many researchers for the identification of the equilibrium scour state. The scour depth versus the logarithm of time is plotted to observe the change of the gradient of the resulting curve. When the gradient approaches zero, the system is considered to be in equilibrium. Studies employed the graphical approach to identify equilibrium state include the submerged circular turbulent wall jet experiments by Rajaratnam and Berry (1977), submerged circular impinging jet experiments by Rajaratnam and Beltaos (1977) and Rajaratnam (1982), submerged plane turbulent wall jet experiments by Rajaratnam (1981). All of the experiments were performed to assess loose bed scour, filled with sand or polystyrene and

eroded by air or water jets. Further, Cardoso and Bettess (1999) used the graphical approach in experiments of local scour at bridge abutments in sand. As this graphical relationship of the scour depth against the logarithm of time holds true for both cohesive and cohesionless soils, there are good reasons to believe that this approach can be used in cohesive soil scouring experiments to assess equilibrium scour.

However, there is also concern about using the graphical approach to identify the equilibrium state. Radice *et al*. (2002) argued this approach may fail as scour can initiate again after an apparently horizontal long lasting gradient (plateau) in the scour depth versus logarithm of time plot. Pertinent to this argument, Lança *et al.* (2010) observed multiple horizontal plateaus in laboratory flume experiments of local scour around bridge piers in sand beds. However, among the total of five experiments, only one of the experimental results showed such multiple plateaus and this experiment was not repeated to produce verifiable outcomes.

Despite the fact that none of the aforesaid methods are free from criticisms, the graphical approach can be used to define the equilibrium scour more confidently as it shows the continuity of the scouring progress towards the equilibrium state. Hence, it is easier to differentiate an apparent or quasi horizontal plateau from an actual one. However, one must consider that an absolute horizontal plateau may not be seen in the equilibrium state as the measured scour depths may fluctuate within the margin of the measurement errors of the instrument used.

2.6 Summary

Some important observations can be noted based on the development of a scour hole in cohesionless and cohesive soil by submerged circular vertically impinging turbulent jets. First, three types of erosion were reported for cohesive soils, whereas the cohesionless soils only erode by individual particles. Except initial scouring, the maximum scour depth in cohesionless soils is found at the jet centreline, whereas most of the time the maximum scour depth in cohesive soils occurs at a random location due to mass erosion of larger chunks of soil. A ridge that forms on the perimeter of the scour hole is a significant characteristic of the scour hole in cohesionless soils, while it has not been observed in cohesive soils. Both cohesionless soils and cohesive soils scour holes exhibit the Weakly Deflected Jet Regime (WDJR) and the Strongly Deflected Jet Regime

(SDJR) behavior. For SDJR scour holes in cohesionless soils, the static and dynamic dimensions of the scour hole are different. In cohesive soils, the static and dynamic scour hole dimensions are the same irrespective of the flow regime.

Table 2.1: Jet spreading rate constant for circular turbulent jet with smooth contraction nozzle.

Researchers	β
Hinze and Zijnen (1949)	0.094
Albertson *et al*. (1950)	0.097
Wygnanski and Fiedler (1969)	0.120
Hussein *et al*. (1994)	0.094
Xu and Antonia (2002)	0.095
Fellouah and Pollard (2009)	0.097

Table 2.2: Jet diffusion constant and location of virtual origin for circular turbulent jet with axial distance considered for estimation.

Researchers	C_d	x/d	x_o/d
Hinze and Zijnen (1949)	6.4	>8	-0.6
Wygnanski and Fiedler (1969)	5.7	≤ 50	3
	5.0	> 50	7
Hussein *et al*. (1994)	5.8	30-100	4
Xu and Antonia (2002)	5.6	20-75	3.7
Fellouah *et al*. (2009)	5.6	15-29	2.5

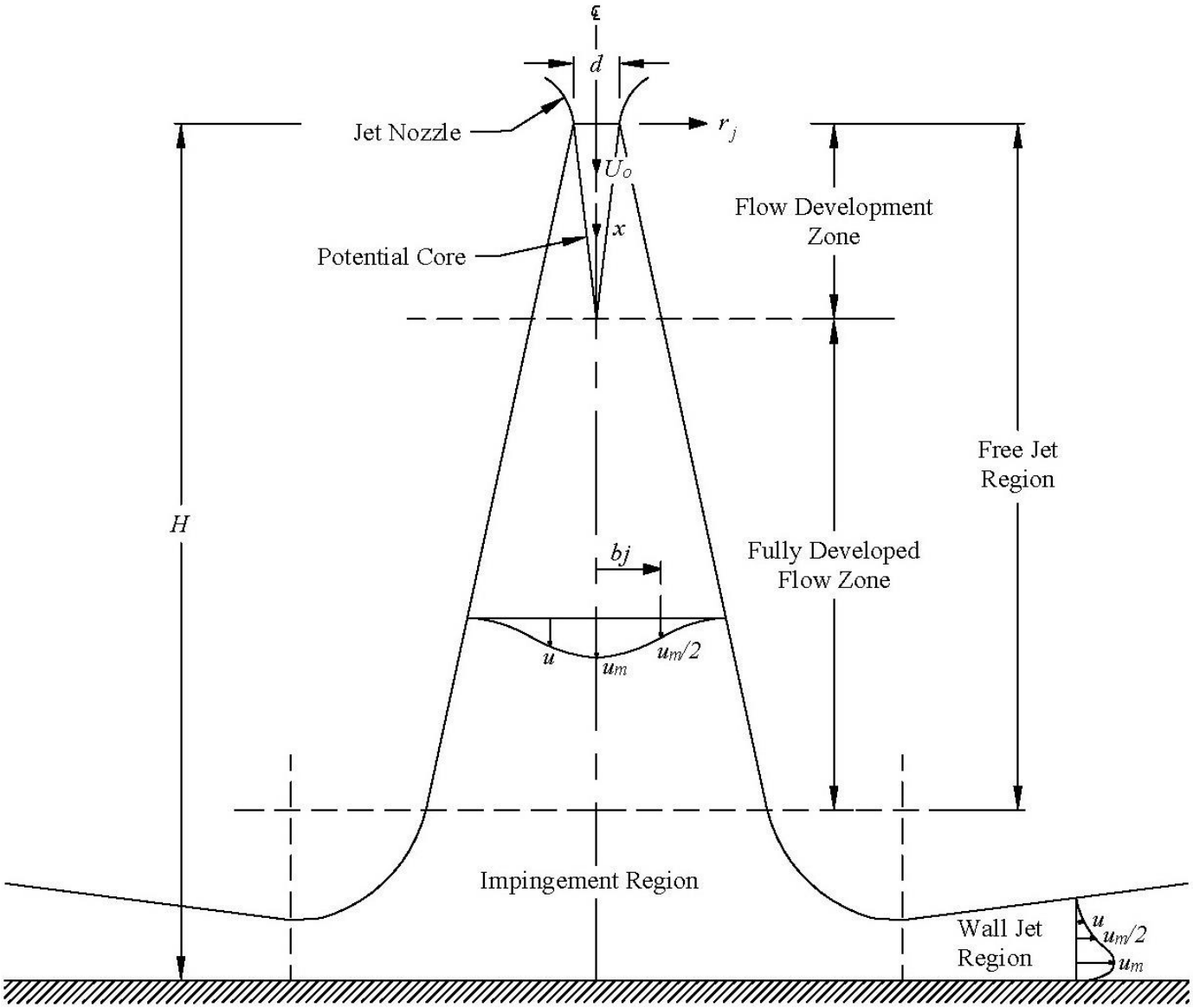

Figure 2.1: Definition sketch of a circular turbulent jet impinging on a flat plate with three distinctive flow regions.

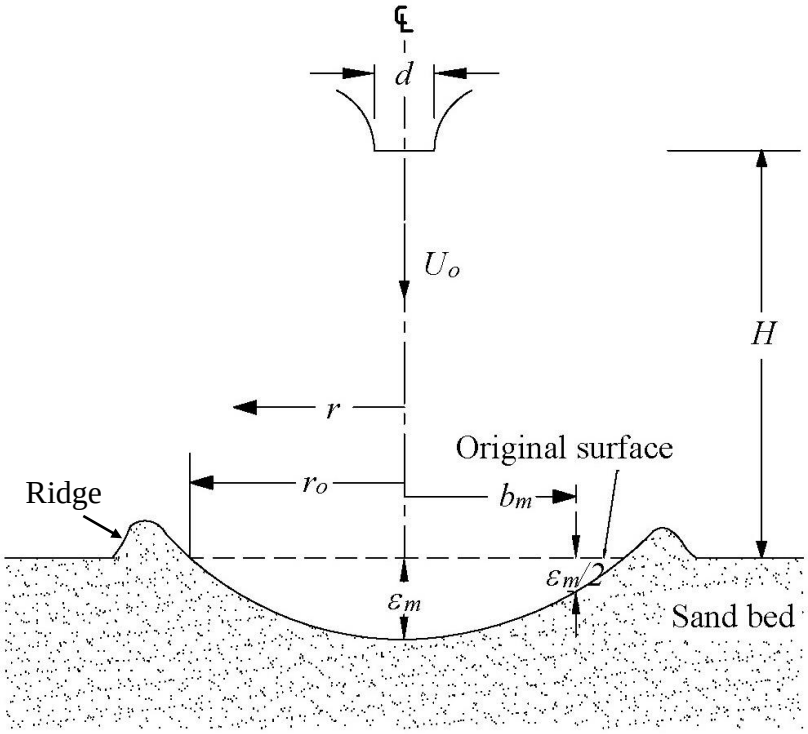

(a)

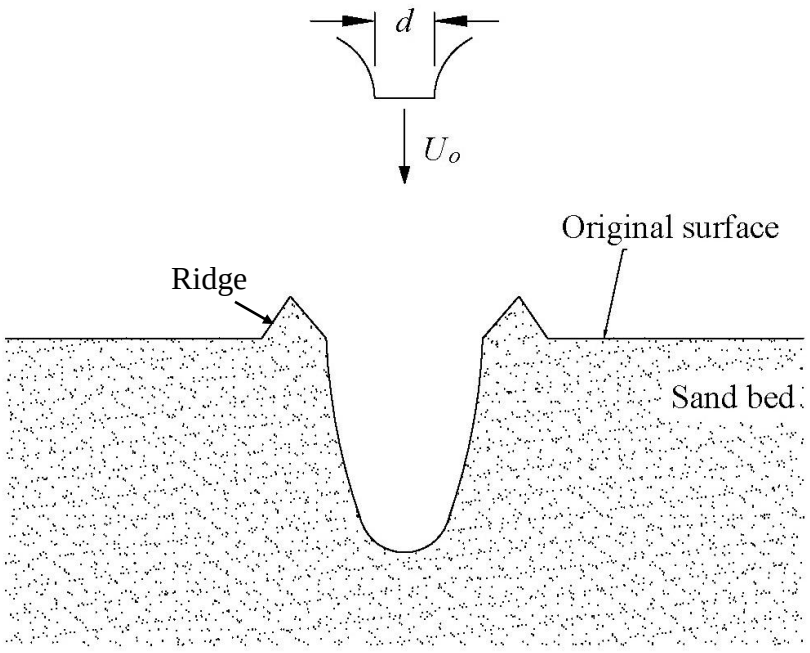

(b)

Figure 2.2: Typical Scour hole shapes in cohesionless soil scoured by circular impinging jets (a) weakly deflected jet type scour hole, and (b) strongly deflected jet type scour hole (adapted from Aderibigbe and Rajaratnam (1996))

CHAPTER 3. EXPERIMENTAL SETUP AND EXPERIMENTS

3.1 Introduction

This chapter describes the experimental setup and experiments for the present study of scour by submerged circular vertical turbulent jets in cohesive soil. First, a description of the experimental setup is provided. This is followed by the experimental procedures, data acquisition techniques, and a description of the properties of the tested clay soil samples. All of the experiments were performed in the Hydrotechnical Laboratory of the University of Saskatchewan.

3.2 Experimental Setup

The experiments were performed inside an octagonal Plexiglas tank of 1.2 m width and 1.1 m depth, referred to as the jet tank. An octagonal Plexiglas sheet of area equal to the cross-sectional area of the tank was placed inside the jet tank on four PVC (PolyVinyl Chloride) pipe supports to act as a table under the testing sample. The jet tank sits within a rectangular wooden box of 0.30 m height that is used to catch the overflow from the jet tank. Essentially, the walls of the jet tank act as a weir and the tank overflows inside a rectangular basin so that the submergence of the jet remains constant throughout the test. For all the tests, the jet was submerged 15 cm below the surface. A 0.95 m long plenum is hung vertically to a steel frame with hinges, centered above the jet tank. The plenum could be moved up and down using a hand winch attached to the steel frame. Also, the plenum can be moved sideways with the advantage of the hinged connection. However, a PVC guide is attached to the iron frame so that the plenum can be fixed at a constant position inside the jet tank during scour testing. A circular nozzle of 7.76 mm diameter was attached in the plenum to create the water jet. The nozzle is designed such that the flow contraction occurs smoothly without any significant head loss and the velocity across the nozzle is uniform following the standards laid out in ASME (1990). The major components of the experimental setup can be seen in Figure 3.1. Figure 3.2 gives a sketch of the entire experimental setup.

The soil sample was placed below the jet plenum on a plexiglass table inside the jet tank and aligned such that the jet impinges vertically on the centre of the sample surface. To centre and align the sample and to ensure the sample did not move during a test, a seat, a sample holder and

a jet normalizer were designed. The seat was made of a 32 cm long, 20 cm wide, and 5 mm thick aluminum plate. There were four leveling screws on the four corners of the seat to level it. Another four screws were attached on the sides of the seat to connect with the sample holder. The sample holder was made of a 2 mm thick aluminum sheet had overall dimensions of 25 cm long, 17.6 cm wide and 10.5 cm high. It was open to both sides and the sample could be pressed inside from either of these sides. Once the sample holder and the seat were connected together, Assembly-1 was made. This assembly was used during the scour testing. However, it was necessary to centre and align Assembly-1 vertically beneath the jet. Hence, a simple apparatus, the jet normalizer was designed.

The jet normalizer consisted of four PVC plates. Two plates were vertical and two plates were horizontal. The horizontal plates had holes at the centre. The upper plate hole was 9 mm in diameter and the lower plate hole was 10 mm in diameter. The plates were 30 mm apart. Assembly-1 fitted perfectly inside the space between the vertical plates of the normalizer. This new assembly was called Assembly-2. Assembly-2 was used before the scour test for positioning of Assembly-1. Centreing and alignment of Assembly-2 was corrected by moving it on the plexiglass table and aligning it with leveling screws. While the jet passes through both of the holes of the jet normalizer, then Assembly-2 was perfectly positioned (see Figure 3.4).

The flow control system for the apparatus consisted of a constant head tank, a centrifugal pump and three valves. Figure 3.5 gives schematic of the flow control system. City of Saskatoon tap water was pumped to the jet plenum from the constant head tank of dimensions 1.2 m by 1.2 m by 0.69 m. The water depth inside the tank was 0.22 m. The constant head tank was used to help maintain a constant flow rate through the system. The centrifugal pump was driven by a ½ HP motor and could deliver up to 68.10 L/min. The flow from the pump is controlled by Valve-1 connected into the line just downstream of the pump. An ultrasonic flow meter (Omega FMG-3000 series) was located 1.6 m downstream of Valve-1 to measure the flow rate. The flow meter could measure flow rate as low as 0.01 L/min. The accuracy of the flow meter was ±1% of the reading + 0.01 m/s. The flow through the flowmeter to the jet plenum was controlled by Valve-2. Valve-3 controlled the flow in the diversion line from the flow meter to the constant head tank. During flow to the jet plenum, Valve-3 remained closed and Valve-2 remained open. Alternatively,

for recirculating the flow between the constant head tank and the pump, Valve-2 remained closed and Valve-3 remained open.

The jet tank was typically full of water and overflowed into the rectangular box, which then discharged water into the laboratory sump using three outlets. Two of them were floor outlets (Floor Outlet- 1 and 2) and located in the floor of the rectangular spill box. The other one was the wall outlet and located in the mid-height of a wall of the spill box. The floor outlets discharged water during scour testing up to a flow rate of 35 L/min. For flow rates larger than 35 L/min, the wall outlet discharged water together with the floor outlets. Further, a central outlet was located at the bottom of the jet tank and used to empty the jet tank. All of the outlets discharge water into the sump under the Hydrotechnical Laboratory.

As an additional check on the flow through the system, a mercury U-Tube manometer was used (Figure 3.6). One end of the manometer was attached with a pressure tap installed on the jet plenum (Point-1) at 320 mm above the jet nozzle so that this point was not within the contraction section of the jet. The other end of the manometer was open in a stagnant water zone inside the jet tank (Point-2). Hence, the manometer could measure the differential pressure between Points 1 and 2. This differential pressure can be converted to the velocity of the jet at the nozzle as follows.

First, the pressure at Points *a* and *b* can be written using the manometer principle:

$$p_a = p_1 + \rho_w g\left(j + k\right) \quad [3.1]$$

$$p_b = p_a - S_g \rho_w g j \quad [3.2]$$

$$p_2 = p_b + \rho_w g\left(j - l\right) \quad [3.3]$$

where p_a, p_b, p_1 and p_2 are the pressure at points *a*, *b* ,*1* and *2* respectively; ρ_w is the density of water at the test temperature, g is gravity; S_g is the specific gravity of mercury at the test temperature; and j, k, and l are vertical distances shown in Figure 3.6. Rearranging Equation 3.1, 3.2 and 3.3, it is found:

$$p_b = p_1 + \rho_w g\left(j + k\right) - S_g \rho_w g j \quad [3.4]$$

$$p_2 = p_1 + \rho_w g\left(j + k\right) - S_g \rho_w g j + \rho_w g\left(j - l\right) \quad [3.5]$$

$$p_2 - p_1 = \rho_w g\left(j + k - l\right) - S_g \rho_w g j + \rho_w g j \quad [3.6]$$

Now, the energy equation can be written between Points 1 and 2:

$$\frac{V_1^2}{2g} + z_1 + \frac{p_1}{\gamma} = \frac{V_2^2}{2g} + z_2 + \frac{p_2}{\gamma} + \Sigma h_L \quad [3.7]$$

$$\Sigma h_L = h_f + h_m \quad [3.8]$$

$$h_m = \frac{K U_0^2}{2g} \quad [3.9]$$

where V_1, and V_2 are velocity of water in sections at Points 1 and 2 respectively; z_1, and z_2 are vertical distance of points *1* and *2* respectively from a fixed datum; γ is the unit weight of water at test temperature, Σh_L is the total head loss between Points 1 and 2; h_f is the pipe friction loss and h_m is the minor loss at the nozzle due to exit of the flow; K is the exit loss coefficient and U_0 is the jet velocity at the nozzle. At Point 2, the water is at rest (i.e., V_2=0), therefore K = 1. Also, because the flow is in a smooth contraction towards the nozzle and the flow length is short, it is assumed there is negligible friction losses within the pipe approaching the nozzle (i.e., $h_f \approx 0$).

$$p_2 - p_1 = \rho_w g\left(\frac{V_1^2}{2g} - \frac{U_0^2}{2g} + z_1 - z_2\right) \quad [3.10]$$

Combining Eq. 3.6 and 3.10, it is found:

$$\rho_w g\left(j + k - l\right) - S_g \rho_w g j + \rho_w g j = \rho_w g\left(\frac{V_1^2}{2g} - \frac{U_0^2}{2g} + z_1 - z_2\right) \quad [3.11]$$

From geometry, $$z_1 - z_2 = j + k - l \quad [3.12]$$

Hence, $$j - S_g j = \frac{V_1^2}{2g} - \frac{U_0^2}{2g} \quad [3.13]$$

$$j\left(S_g - 1\right) = \frac{1}{2g}\left(U_0^2 - V_1^2\right) \quad [3.14]$$

$$2gj\left(S_g - 1\right) = U_0^2 - V_1^2 \quad [3.15]$$

Considering the jet flow rate is Q and the cross-sectional area at the nozzle and at Point 1 are A_0 and A_1 respectively:

$$2gj\left(S_g - 1\right) = \left(\frac{Q}{A_0}\right)^2 - \left(\frac{Q}{A_1}\right)^2 \quad [3.16]$$

$$Q^2 = \frac{2gj\left(S_g - 1\right)}{\left(1/A_0^{\,2} - 1/A_1^{\,2}\right)} \qquad [3.17]$$

Because $A_1 >> A_0$, $1/A_1^2$ in Eq. 3.17 can be neglected.

Therefore, $$Q = A_0\sqrt{2gj\left(S_g - 1\right)} \qquad [3.18]$$

and $$U_0 = \sqrt{2gj\left(S_g - 1\right)} \qquad [3.19]$$

The operating range of the U-Tube manometer was from 47 to 800 mm of mercury pressure, which correspond to flows from 10 to 40 L/min through the 7.76 mm nozzle. Flow rates lower than 10 L/min were not sufficient to fill the jet plenum, hence the differential pressure readings during low flow are not the actual representation of corresponding flow rates. Also at higher flow rates more than 40 L/min, the mercury of the manometer would be pushed into the jet tank. The manometer could be read to about 1 mm for the differential pressure measurement.

There was concern for air entrapped inside manometer. To remove the entrapped air, two extra rubber tubes were connected to the ends of the manometer. The rubber tubes were kept closed with clamps during manometer operation. Whenever needed, entrapped air was removed by opening the tubes by removing the clamps.

3.3 Experimental Procedures

Before initiating the scour test, the soil sample was prepared. The sample holder was pressed against the manufactured clay block so that the clay block was cut according to the inner dimension of the sample holder. Then the sample holder with sample inside was placed on the seat and connected with screws. Hence, Assembly-1 was constructed. Assembly-1 with the sample was soaked 24 hours before testing. This was done to ensure that some swelling would occur before the test, before the sample was used for testing. The open surfaces of the sample were cut flush with the sample holder with a thin wire just before a test.

At the first step of scour testing, Assembly-1 with the soil sample inside was centreed and aligned with the jet. To do this, the jet plenum was placed in inclined position inside the jet tank with a rope attached to the rectangular box (see Figure 3.7a). Assembly-1 was placed

approximately at the centre of the tank on a plexiglass table. Then, Assembly-1 was covered with the PVC plate and the jet normalizer was placed on Assembly-1. Thus the setup of Assembly-2 was achieved. After that, the jet plenum was moved to the vertical position and the pump was switched on. The flow rate at this stage was not important because this flow was used only to centre and align the soil sample. Normally a lower flow rate of 15~20 LPM was used for this purpose. The level and position of Assembly-2 was adjusted until the jet went through both of the holes of the jet normalizer. At this position, Assembly-2 was centred and aligned. Then the jet plenum was moved to the inclined position again, and the jet normalizer and the PVC plate on top of the soil surface were removed.

Once the soil sample was in the "perfect" position, the desired flow rate for the scour test was adjusted using Valve-1. For the initial flow rate adjustment, the ultrasonic flow meter was used. Once the desired flow rate was achieved, the jet tank was refilled with water. Then the jet plenum was moved carefully to its vertical position over the soil sample (see Figure 3.7b). A deflector plate was used to deflect the jet until the jet plenum was properly placed inside the PVC guide. Once the jet was in the testing position, the deflector plate was removed and a stop watch was started to measure the time of scouring. During the scour testing, the manometer was used for precise recording of the flow.

When a data measurement time was reached, the flow was diverted to the constant head tank using the diversion line, the plenum was moved up by the hand winch and placed inclined by tying it to the side of the jet tank (see Figure 3.7c). Then the water of the jet tank was drained using the central outlet until the sample was free from water. A photo of the scoured sample was taken and then the tank was filled up to a predetermined level so that the scour profiling of the sample could be done in a submerged condition. After the scour profiling was done, flow was diverted to the jet plenum again, the jet tank was filled up to the top, and the plenum was moved to the vertical position. During movement of the plenum, again the jet deflector was used to deflect the jet to prevent scouring of the sample during this movement. When the jet was in its vertical position, the deflector was taken out and the stop watch was started again to measure the scouring time. This step was repeated for each measurement interval until the equilibrium condition was achieved.

Although a total of ten tests were performed in the laboratory, two of them were abandoned due to failure of the samples at the sides of the sample prior to the equilibrium condition. The hydraulic condition of the experiments, such as the jet diameter, the height of the jet impingement, and the submergence of the samples were kept the same except for the jet flow rates. Details of the experiments are given in Table 3.1.

3.4 Measurements

The scour hole profile of the sample was measured by using a laser optical profiler mounted on a two-dimensional computer controlled traverse system on a horizontal plane above the jet tank. The laser optical profiler used an optoNCDT 1700-500 model displacement and position sensor and the accuracy of the sensor was 0.0245 mm. The traverse system was operated using a custom program designed in LabVIEW 5.5 from National Instruments. The operating range of the profiler was 200 mm to 700 mm, hence the sample was always placed inside this range. During the measurements, the jet plenum was moved upward and set in an inclined position away from the sample (Figure 3.7c). Then the profiler was operated. Two motors were used in the traverse system to move the profiler in the *x* and *y* direction respectively in the horizontal plane to collect the data using a 2 mm by 2 mm grid. However, the motor movement from one point on the grid to another point was controlled by an electrical pulse and due to small variation of the pulse and inertia of the motors, very small errors were induced in each 2 mm movement. These errors were additive and caused relatively large errors (up to few millimeters depending on the span of the surface covered by the grid) as the profiler moved to the end portion of the grid. To overcome these errors, each of the motors were equipped with an encoder to record the exact distance the motor was moved. The custom program used in this study was designed to record the encoder value of the *x*, *y* position along with the profiler data. This program was developed by technician Brennan Pokoyoway. Thus the error in collected data was small. Also, the profiler measured to as small as 0.001 mm. It recorded the depths of the eroded sample with respect to the bottom of the laser optical profiler. Thus a high resolution three-dimensional profile of the eroded sample surface could be created by combining both the encoder and profiler data.

For each scour test, measurements of the scour hole were taken after scouring times of 5 min, 10 min, 15 min, 20 min, 30 min, 40 min, 50 min, 1 h, 1.5 h, 2 h, 4 h, 8 h, 16 h, 24 h, and

then after every 24 h until the equilibrium condition was achieved. During the test, the eroded volume was plotted against the logarithm of time to assess whether the resulting curve started to become parallel to the time axis to help decide if equilibrium had been reached. However, part of the analysis of the current work is to help decide on equilibrium criteria.

The measurements of the scour hole with the laser profiler were subjected to a "refraction error" as the optical properties of light is used for the laser profiler for depth measurements. The profiler has a laser-optical sensor and a signal conditioning electronics. The sensor uses the principle of optical triangulation. A visible point of light is projected onto the target. The reflection of the light spot is imaged by a receiver optical element. From the output signal, the sensor calculates the distance between the target and the sensor. During the measurements, the sample was kept under water so that it would not crack due to shrinkage during drying. Therefore, the light spot imaged by the receiver optical element was subjected to refraction error. For the refraction correction, the elevation of a specific point on the sample holder was measured without and with the water over the soil sample for each measurement to calculate the water level relative to the laser position. Later this water level was used for the refraction correction. Although for all the measurements, the water level was kept roughly at the same position, small variations of the water level were detected in calculated water levels. Hence, the calculated water levels were used for refraction correction.

Further, the measurements have an "inclination error" because the sample surface was not exactly parallel to the traversing plane of the laser. To find out the inclination of the sample surface, elevation of the four corner points of the sample holder were measured with the laser profiler. This gives the angles of the sample plane to the laser plane. These angles were used in AutoCAD to rotate the sample surface as discussed in the later section.

3.5 Data Processing

The custom program written in LabVIEW software stored data in text file format. For each scouring measurement, a single text file was created. The text files contain elevations against the *x, y* positions of the grid points on the scour hole surface. However, the data stored in the text files were still "raw" and needed to be processed "spatially". ArcGIS 10.2.2 and AutoCAD 2015

software were used for the spatial processing of the collected data. Later, the scour hole cross-sections were exported to MS Excel 2013 software. To obtain the dimensionless cross-sectional profiles, the half-widths of the cross-sections were calculated using a code written in the Visual Basic. The code was adapted from Excelfoum.com (2005). Figure 3.8 shows the schematic representation of the processing of laser profiling data.

First, the text files obtained from laser profiling were imported into ArcGIS. The text files were then converted to "Shapefiles", a native file format in ArcGIS for analyzing spatial data. The shapefiles represented each data point as a geometric point containing spatial information (i.e., *x, y* and *z* value). However, the elevation or *z* value was measured from the base of the laser profiler to the soil surface points.

For refraction correction a Python code was written. Appendix A provides the Python code for ArcGIS and the Visual Basic code for MS Excel. The Python code used the elevation of a fixed corner (say corner 1) and water level as input variables to calculate the actual elevations of the surface points. From Snell's Law, it is known that:

$$\mu_w = \frac{d_r}{d_a} \qquad [3.20]$$

in which μ_w is the refractive index of water, d_r is the real or actual depth of water, and d_a is the apparent depth of water. Since the water temperature was varied during the span of the scour testing, the value of μ_w used for refraction correction was 1.33. As a check of the accuracy of this correction, the scour contours under dry and wet conditions were checked during Scour Test 1. Figure 3.9a shows the effect of submergence during laser profiling of the scour hole of Scour Test 1 produced after 144 hours of scouring. Due to the refraction error, large variations in the dry and submerged contours are seen. Figure 3.9b shows the similarity of the dry and submerged contours after the refraction correction was applied. The small variations after the correction might partially be attributed to the shrinkage of the dried specimen, as the profiling took about 5 hours to complete. However, along with the refraction correction, the Python code also recalculated the elevation data of the surface points relative to the sample base, as initially the elevation was given relative to the laser profiler base.

Following the refraction correction, the corner 1 point shapefile was appended individually to other point shapefiles and then the shapefiles were converted to three-dimensional point shapefiles using the recalculated elevation data from the previous step. Corner 1 was appended to use as a reference point for the inclination correction. The three-dimensional point shapefiles were then exported to CAD file. In AutoCAD environment, the surface points were rotated twice with respect to the corner 1, one rotation around *x*-axis and another rotation around the *y*-axis. The amount of required rotation angles was determined from the elevations of the four corners of the sample holder. After the rotation was done, the corrected CAD files were imported again into ArcGIS as the final point shapefiles. Afterwards the Triangular Irregular Network (TIN) files were created using each point shapefiles. A TIN file is essentially a digital representation of surface morphology, and each vertex of the TIN represents the actual point from which the TIN is created. Therefore, the actual elevation data of the measured points are kept in TIN vertexes. Figure 3.10a shows the final three-dimensional point shape file, and Figure 3.10b shows corresponding TIN for Scour Test 3, produced after 96 hours of scouring.

The final outputs of the scouring data, i.e., the scoured volume and cross-sections of the scour hole were extracted from the TIN file. Four cross-sections for each measurement, spaced apart at a 45º angle were considered for the analysis of scour testing. All the cross-sections passed through the centreline of the jet. Figure 3.11 shows the plan view of the cross-sections. The cross-section data were exported into Excel file. For each cross-section, half-widths for the centreline and maximum scour depth were determined, then these dimensions were used to obtain dimensionless scour hole profiles.

3.6 Soil Samples

Manufactured soil samples were used for scour testing. Natural soil samples were not used as a large amount of variability can be seen in test results of the natural samples due to the non-uniformity present in those kind of samples. Therefore, Plainsman pottery clay was selected. Three types of pottery clay were used in the experiments, i.e., Buffstone clay (School clay), P300 (Porcelain), and M370 (Semi-Vitreous Porcelain). Although clay content in these samples were similar, the critical shear stress varied in previous scour tests performed in the Hydrotechnical Lab

of the University of Saskatchewan. Therefore, these samples were selected because in spite of similar clay content, they allowed wide range of eroding jet velocity.

The samples were obtained in wet form. Water contents (w_c) of the soil samples were measured before soaking (w_o), after soaking (w_p) and after the scour test (w_f) as per ASTM standard D2216-10 (2010). The specific gravity of the soil samples (G_s) were measured following ASTM standard D854-14 (2014). Bulk density (ρ_b) and dry density (ρ_d) of each sample was measured just after the test according to ASTM standard D7263-09 (2009). The grain size distribution of each sample was measured using mechanical sieving and the hydrometer test according to ASTM standard D421-85 (2007) and ASTM standard D422-63 (2007). The liquid limit (*LL*) and plastic limit (*PL*) were determined following the ASTM standard D4318-10 (2010). Further, the degree of saturation of the soil samples (S_w) was calculated using the measured bulk and dry density and water content of the samples calculated after a test. Table 3.2 gives a summary of tested soil properties.

Table 3.1: Hydraulic conditions of the scour testing experiments by submerged circular turbulent impinging jet.

Test No.	Flow Rate, Q (L/min)	Impinging Height, H (mm)	Nozzle Diameter, d (mm)	Jet Velocity at Nozzle, U_o (m/s)	Reynolds Number, R	Applied Stress, $\rho U_o^2 (d/H)^2$ (Pa)	Scouring Duration, t_d (h)	Remarks
1	24.4	85	7.76	8.6	38576	616	144	-
2	32.3	85	7.76	11.4	56248	1079	-	Test abandoned
3	28.5	85	7.76	10.0	48093	840	96	-
4	28.7	85	7.76	10.1	46978	852	120	-
5	23.6	85	7.76	8.3	38661	577	168	-
6	18.8	85	7.76	6.6	33030	367	168	-
7	13.2	85	7.76	4.4	21688	158	-	Test abandoned
8	28.0	85	7.76	9.9	61830	813	336	-
9	23.7	85	7.76	8.4	57923	581	336	-
10	18.5	85	7.76	6.5	46346	353	384	-

Table 3.2: Properties of the clay samples used in scour testing experiments.

Test No.	Type of Clay	Grain Size Distribution (%)			Specific Gravity (G_s)	Average Water Content, w_c (%)	Liquid Limit (*LL*) (%)	Plastic Limit, *PL* (%)	Bulk Density, ρ_b (Kg/m^3)	Dry Density, ρ_d (Kg/m^3)	Degree of Saturation, S_w (%)	Remarks
		Clay <0.005 mm	Silt 0.005 to 0.075 mm	Fine Sand 0.075 to 0.425 mm								
1	Buffstone	51.7	42.2	6.1	2.73	25.9	36.7	20.4	1963	1904	96.2	-
2	Buffstone	-	-	-	-	-	-	-	-	-	-	Test abandoned
3	Buffstone	51.7	42.8	5.5	2.71	26.7	34.5	18.8	1959	1924	96.6	-
4	P300	48.7	48.7	2.6	2.69	30.7	35.4	19.7	1902	1768	96.0	-
5	P300	50.7	46.6	2.7	2.70	31.3	34.0	18.5	1916	1686	98.3	-
6	Buffstone	50.3	42.1	7.6	2.75	26.1	37.3	19.6	1977	1942	96.9	-
7	P300	-	-	-		-	-	-	-	-	-	Test abandoned
8	M370	51.3	45.4	3.3	2.69	28.9	43.3	15.1	1951	1788	100.0	-
9	M370	51.1	46.6	2.3	2.70	29.4	40.0	14.6	1955	1839	97.2	-
10	M370	51.2	46.8	2.0	2.71	27.4	42.4	14.9	1952	1778	98.3	-

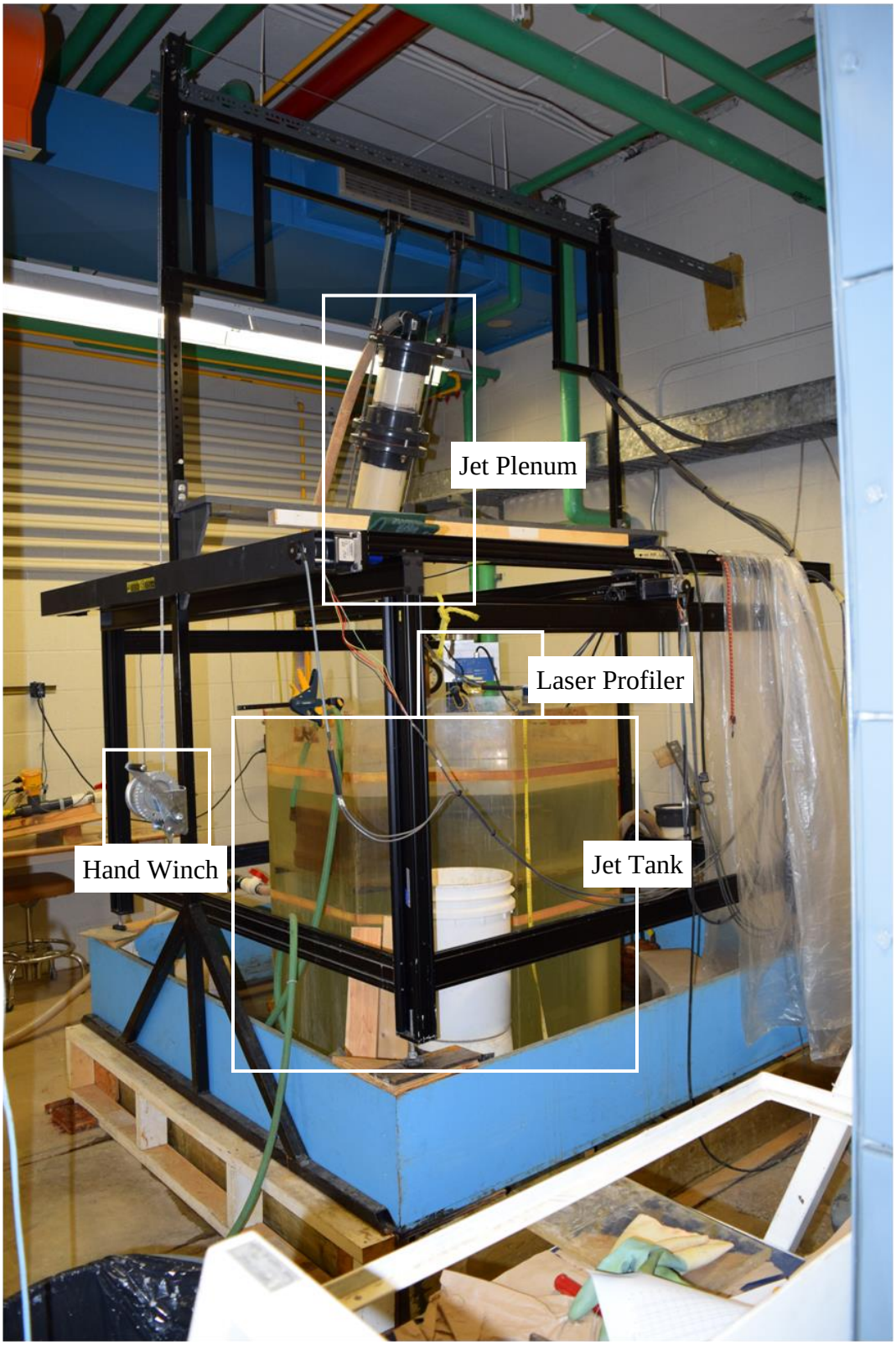

Figure 3.1: Major components of the experimental setup.

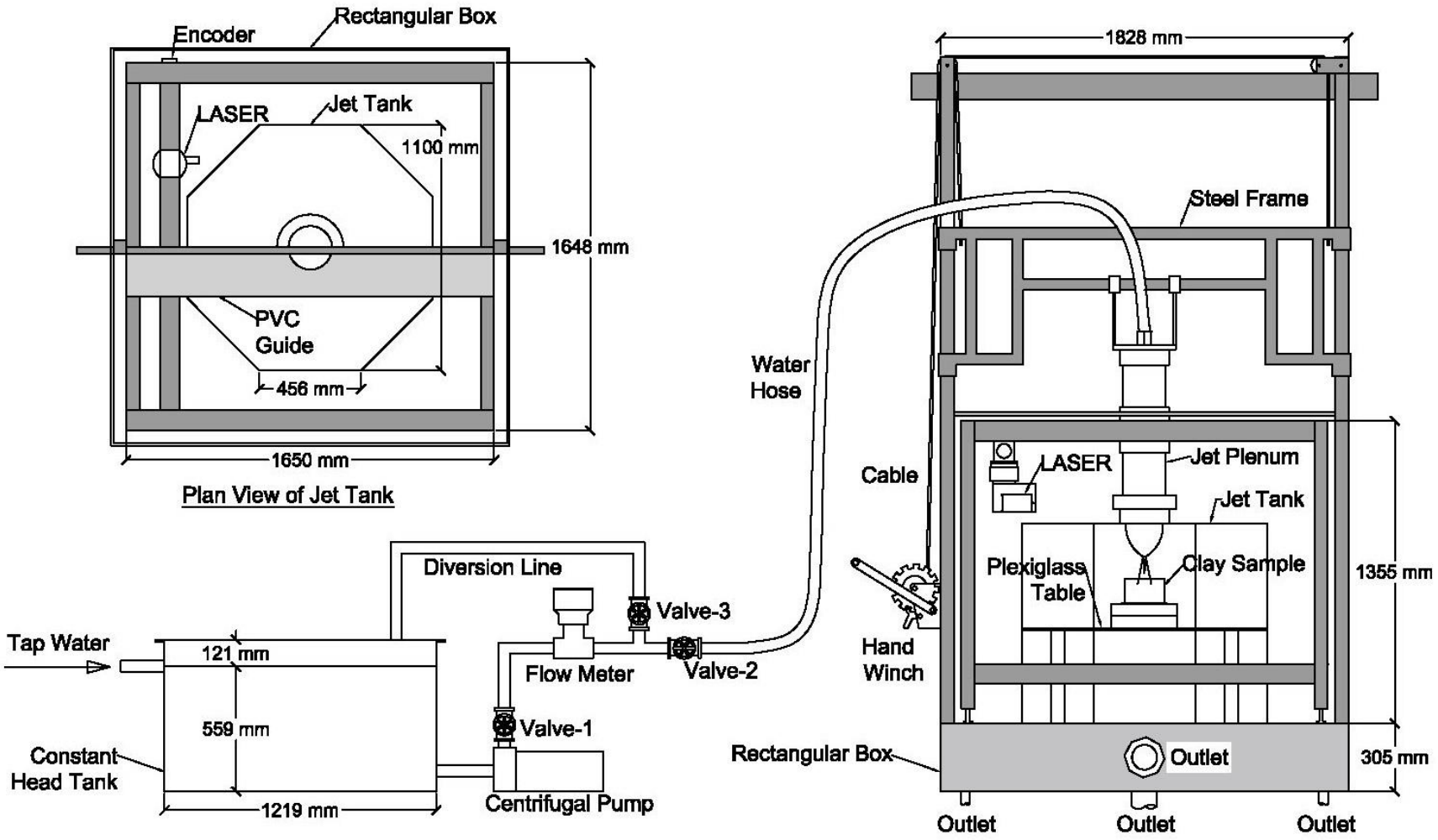

Figure 3.2: Sketch of the experimental setup for scour testing.

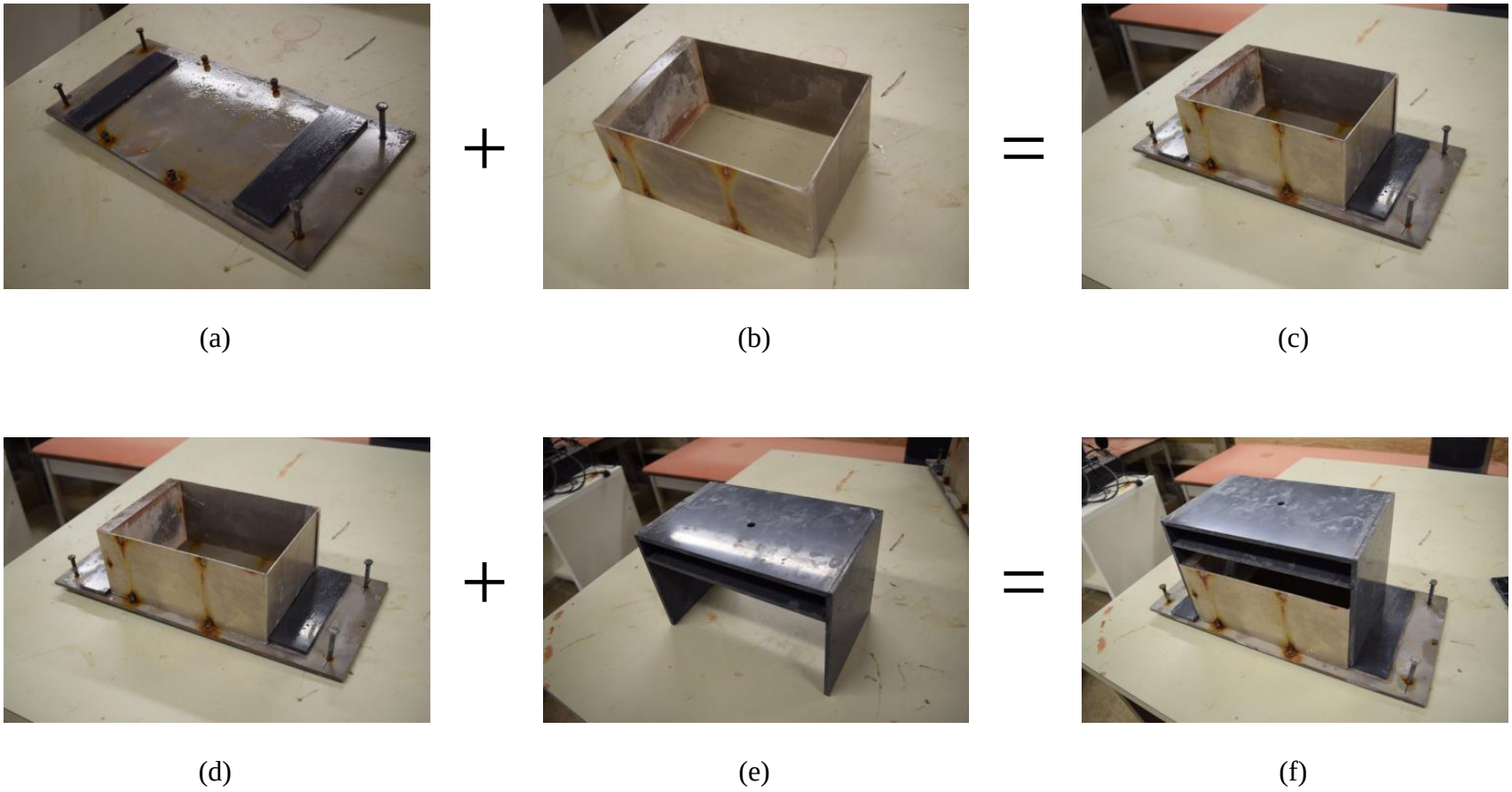

(a) (b) (c)

(d) (e) (f)

Figure 3.3: Sample positioning using sample holder, seat and jet normalizer: (a) Seat, (b) Sample Holder, (c) Assembly-1, (d) Assembly-1, (e) Jet Normalizer, and (f) Assembly-2.

Figure 3.4: Application of the jet normalizer for vertical alignment of the jet to the eroding surface.

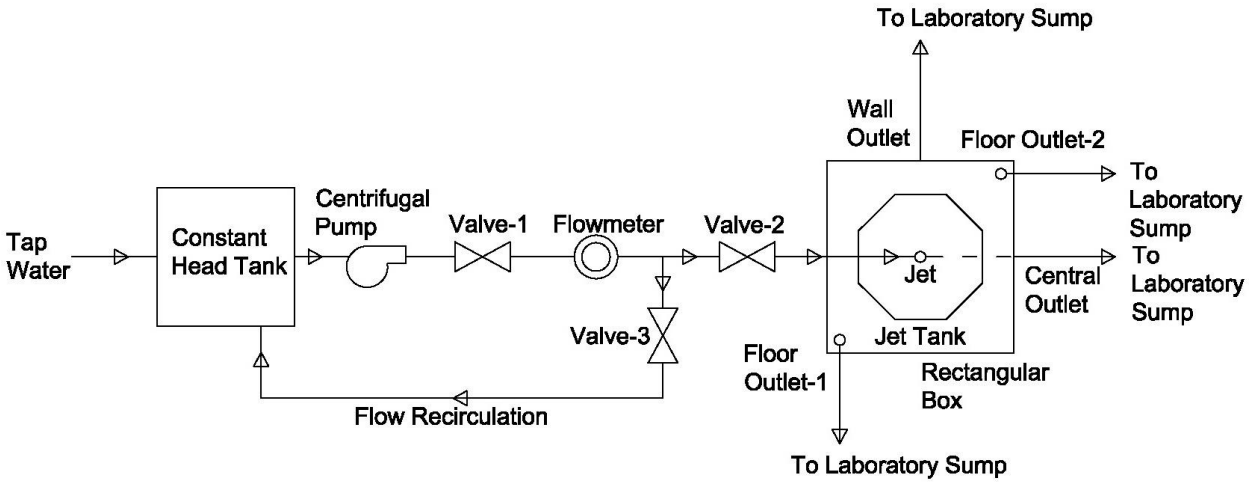

Figure 3.5: Schematic diagram of flow control system in scour testing.

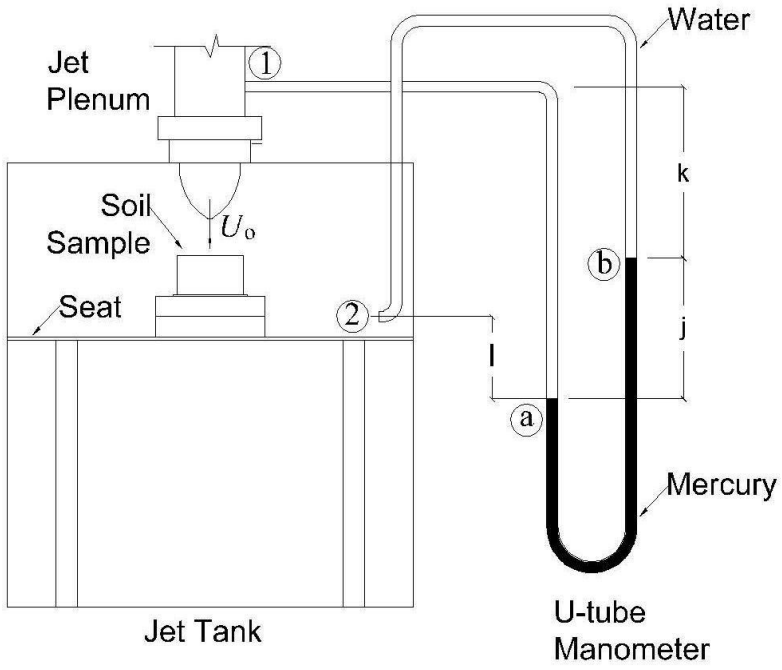

Figure 3.6: Setup for flow measurements using manometer.

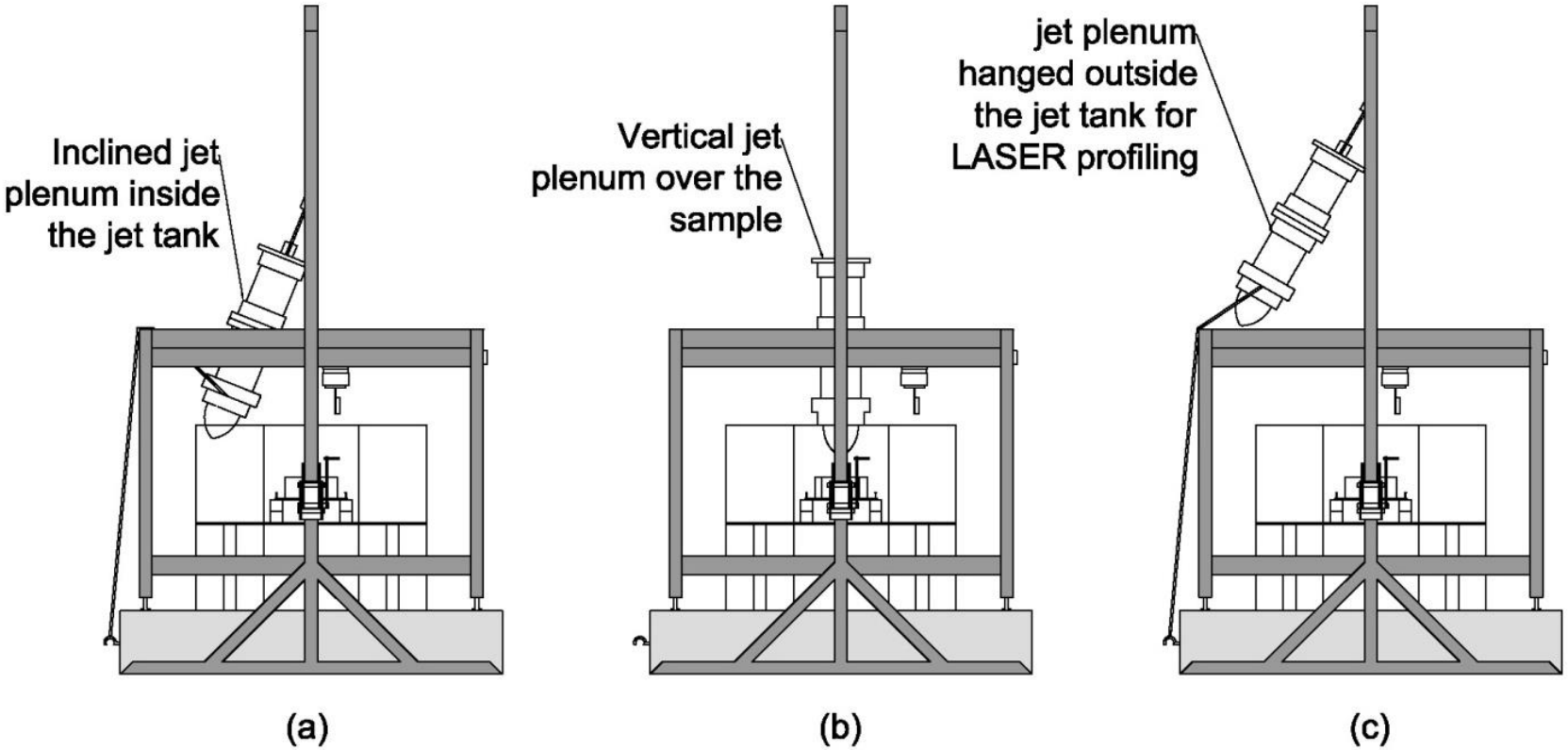

Figure 3.7: Different positioning of the jet plenum during (a) filling the jet tank, (b) scouring of the soil sample, and (c) laser profiling.

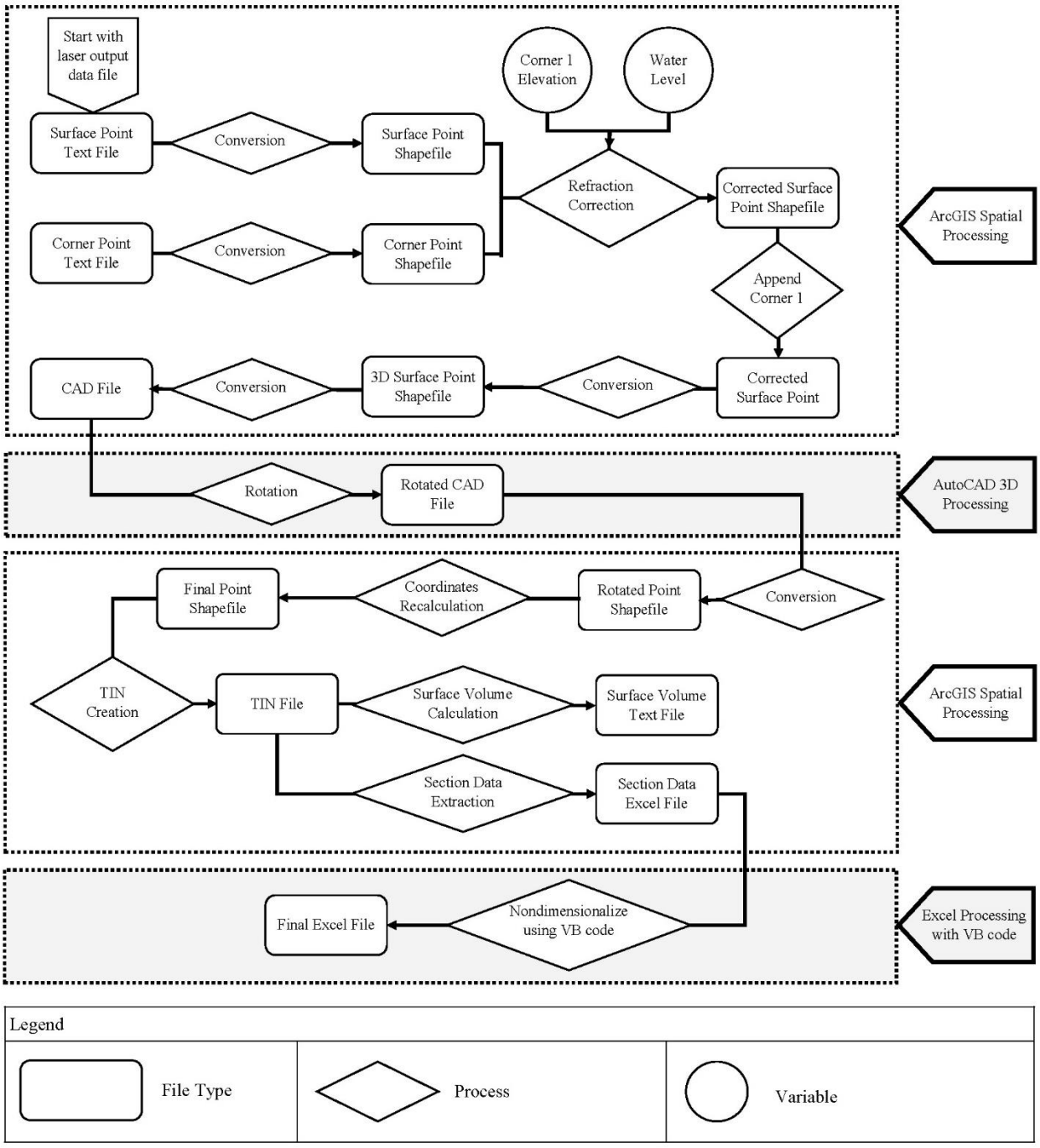

Figure 3.8: Schematic representation of the processing of scour testing data obtained by laser profiling.

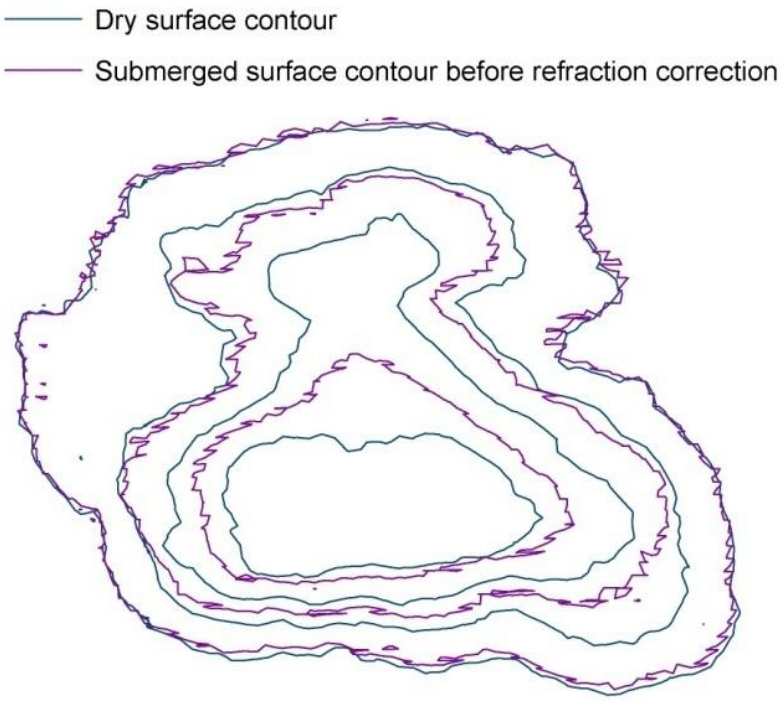

(a)

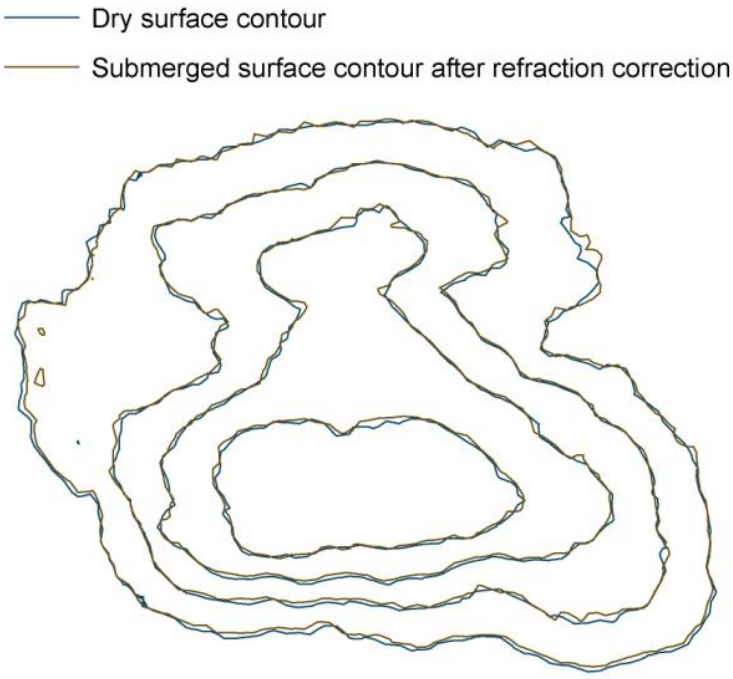

(b)

Figure 3.9: Dry versus submerged surface contours of the scour hole (a) before refraction correction, and (b) after refraction correction.

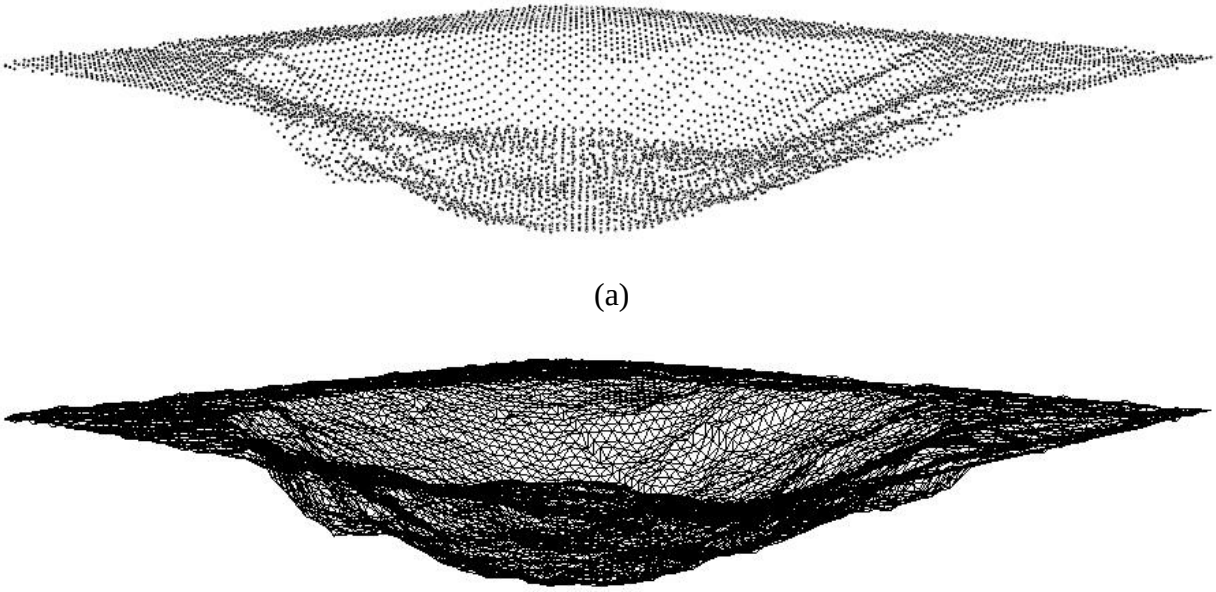

(a)

(b)

Figure 3.10: Final three-dimensional files in ArcGIS after refraction correction and inclination correction for Scour Test 3, produced after 96 hours: (a) point shape file, and (b) Triangular Irregular Network.

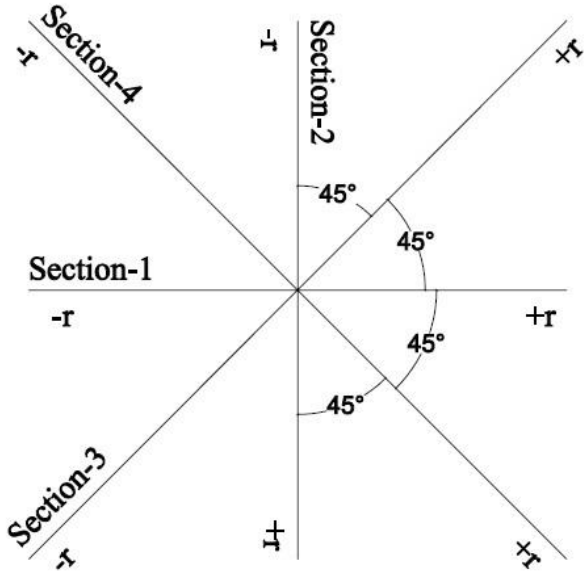

Figure 3.11: Orientations and the radial directions of the cross-sections of the scour hole considered for scour testing analysis.

CHAPTER 4. RESULTS AND ANALYSIS

4.1 Background

As found from the review of previous studies, in scour testing of clays with submerged circular impinging jets, the shape of the scour hole after different scouring times was not measured. Typically, only the maximum or centreline scour depths, and scour hole volumes have been reported. Mazurek (2001) studied the shape of the scour hole along two perpendicular cross-sections. However, the study was limited to equilibrium scour holes. This chapter first discusses the results and observations of the scour hole shape with time in cohesive soils. Then, the analysis of the scour hole shape is given. An analysis of what dimension should be used to assess equilibrium is presented. Uncertainty in the measurements is also discussed at the end of this chapter.

4.2 Results and Analysis of Scour Tests

4.2.1 Forms of Erosion Observed

For all scour tests in this study, mass erosion was the predominant form of erosion observed (erosion of chunks or lumps of soil). Surface erosion, in the form of individual particle removal, was also perceived on the surface of the soil sample around the scour hole. Early in a test, the chunks removed were bigger in size and more irregular in shape. However, as the scour hole approached equilibrium, the size of the chunks removed became smaller. The smaller chunks were between 1-3 mm, while the bigger chunks were as large as 1-2 cm. The typical eroded soil chunks for Scour Test 8 after 5 minutes of scouring are shown in Figure 4.1. There did not seem to be a variation in chunk sizes for the different soils tested.

4.2.2 Time Development of Scour

Observations of the evolution of the scour hole for two scour tests are presented in Figures 4.2 and 4.3. Appendix B contain similar plots for all the scour tests. Scour Test 1 (Buffstone clay, U_0=8.6 m/s, d=7.76 mm, H=85 mm, and t_d=144 h) and Scour Test 5 (P300 clay, U_0=8.3 m/s, d=7.76 mm, H=85 mm, and t_d=168 h) have been chosen as representative tests for time development of scour. Scour Test 1 is representative of the tests for which the scour hole shape

abruptly changed during the evolution of the scour hole, while Scour Test 5 represents the tests for which a regular scour hole shape gradually formed during the course of a test. In Figures 4.2 and 4.3, the scales of the axes *x* and *y* were not kept constant in order to observe the irregularity in the scour holes more clearly at earlier times in the scouring process.

For Scour Test 1, the initial scour depths after 5 minutes of the test due to the removal of the first soil chunks from the sample surface were only few millimeters (Figure 4.2a). The scour hole shape was irregular with multiple depressions on the surface instead of one distinct scour hole. After 10 minutes of scouring, the formation of a distinct hole had started (Figure 4.2b). After 15 minutes, the distinct scour hole had begun to widen (Figure 4.2c), although remnants of the multiple depressions were still seen. After 30 minutes, a more regular scour hole was forming (Figure 4.2e). A big soil chunk approximately 2 cm by 1 cm by 0.25 cm was removed between 30 to 40 minutes of scouring (Figure 4.2f). Another big soil chunk was removed (perhaps multiple big chunks) between 2 to 4 hours of scouring and abruptly resulted in a much bigger scour hole (Figure 4.2k). Some small to big soil chunks were removed after 4 hours of scouring and the scour hole began to obtain a more regular shape towards the end of the test (Figure 4.2 l-s). During the later part of the test, the scour hole mostly deepened but grew little in width.

Unlike Scour Test 1, in Scour Test 5 a distinct scour hole formed more quickly though there were still local minimums present, as seen after 5 minutes of scouring (Figure 4.3a). After 10 and 15 minutes of scouring, the scour hole became more regular (Figure 4.3b-c). This shape was disrupted again by the removal of multiple big chunks after 15 to 40 minutes of scouring (Figure 4.3d-f). After 40 minutes, the scour hole continued to grow in size without any significant abrupt change until the end of the test (see Figure 4.3f-t). The scour hole at 16 hours was very similar to that at 168 hours when the test was ended (see Figure 4.3m-t).

For both the tests, the initial scour occurred at locations other than the centreline of the jet similar to observation of early researchers (Dunn 1959; Moore and Masch 1962; Mazurek *et al.* 2001). However, the first measurements of the scour hole were taken after 5 minutes of scouring; therefore, the exact location of initial scour could not be determined. Significant changes of the scour hole shape occurred during the initial phases of the experiments, because the erosion rate

tended to be higher and larger chunks of soil were removed during this phase. As scouring progressed with time, the scour hole was observed to take a more regular shape; notably it was more symmetrical than the initial scour hole. No large soil chunks were removed after 4 hours of testing for Scour Test 1, and after 40 minutes of testing for Scour Test 5.

The time development of different characteristic dimensions of the scour hole for the scour tests (except for two abandoned tests) are plotted in Figures 4.4 to 4.9. The dimensions plotted are the cube root of the scour hole volume, $\xi^{1/3}$ (where ξ denotes the volume of scour hole); the depth of scour hole along the jet centreline, ε_{cl}; the maximum depth of scour hole, ε_m; the average radius of the scour hole, $\bar{\bar{r}}_o$; the average half-width of scour hole for the scour depth on the jet centreline, $\bar{\bar{b}}_{cl}$; and the average half-width of the scour hole for the section-wise maximum scour depth, $\bar{\bar{b}}_m$. Because four cross-sections of each scour hole were extracted from the measurements of the total scour hole, there were four section-wise maximum scour depths, ε_{ms}. The half-width of the scour hole based on the centreline depth, b_{cl}, is the radial distance from jet centreline to the location where the scour depth ε=½ ε_{cl}. Similarly, the half-width of the scour hole based on the section-wise maximum scour depth, b_m, is the radial distance from the section-wise maximum scour depth to the location where the scour depth ε=½ ε_{ms}. Therefore, there should be two values of b_m and b_{cl} for each section. The average values of scour hole radii and half-widths were determined by averaging these dimensions from the four perpendicular cross-sections of the scour hole that were used to evaluate the scour hole shape. The plots of these characteristic dimensions of the scour hole with time on an arithmetic scale clearly show how the dimensions were developing with time. Assessment of whether the scour hole has reached equilibrium is often carried out using plots with time given on a logarithmic axis and thus these plots are also included in Figures 4.4 to 4.9.

It was observed that for a significant portion of the plots, the scour hole depths increased linearly with the logarithm of time (Figures 4.4b, 4.5b, and 4.6b) as might be expected from previous studies (Moore and Masch 1962; Mazurek *et al* 2001; Mazurek 2001). However, this relationship was not identifiable in the case of the average scour hole radii and half-widths (Figures 4.7b, 4.8b, and 4.9b). Particularly $\bar{\bar{b}}_{cl}$ and $\bar{\bar{b}}_m$ (Figures 4.8b and 4.9b) did not show a linear growth with the logarithm of time. For example, in Figure 4.8b for Scour Test 8, $\bar{\bar{b}}_{cl}$ was larger at the initial stage of scouring and later decreased as the scour was progressing towards its last stage.

Initially the scour hole was wide and shallow and later changed into a narrow and deep scour hole. In Figure 4.9b for Scour Test 6, $\bar{\bar{b}}_m$ increased first and then decreased during the development of the scour hole. The reason for such behavior was the removal of large soil chunks, which resulted in an asymmetric scour hole with ε_{ms} located far from the centreline of the scour hole. Thus $\bar{\bar{b}}_m$ for this type of scour hole was larger than for the more symmetric scour hole that formed later in the scouring process. However, the scour hole radii and half-widths were averaged for four sections of the scour hole. Therefore, the aforesaid explanation for the growth of half-widths may not be applicable for all individual sections of a scour hole. For example, out of a total of eight numbers of $\bar{\bar{b}}_{cl}$ measured in Scour Test 8, five of them were larger initially and later decreased. For Scour Test 6, all the eight measured $\bar{\bar{b}}_m$ increased first and then decreased.

All the dimensions of the scour hole tend to stop growing or grow very slowly near the equilibrium state. However, it can be seen that the scour hole dimensions may even tend to remain constant earlier in a test. This temporary ceasing of the growth of the scour hole dimensions is seen as a plateau in the time development plots. For example, plateaus can be seen for ε_{cl} in Scour Test 8 and 10 (Figure 4.5b); for ε_m in Scour Test 4 and 1 (Figure 4.6b); for $\bar{\bar{r}}_o$ in Scour Test 5, 6, 8, and 10 (Figure 4.7b). However, no distinct plateaus can be seen for $\bar{\bar{b}}_{cl}$ and $\bar{\bar{b}}_m$ (Figures 4.8b and 4.9b). The temporary ceasing of the growth of these scour hole characteristic dimensions was associated with large chunks of soil removal by mass erosion. When a large chunk was removed, some parts of the scour hole stopped growing for some time. This resulted a plateau in the time development plots of some of the scour hole characteristic dimensions (such as the maximum depth of scour).

4.2.3 Scour Hole Profiles

4.2.3.1 Time Development of the Scour Hole Profiles

The time development of the scour hole profiles has been discussed here for two representative scour tests: Scour Test 1 and Scour Test 5. Appendix C contains the same information for the remaining experiments. The profiles of Scour Test 1 showed large variations between different sections of the scour hole compared to the profiles of Scour Test 5 for different sections. Figure 4.10a shows the scour hole profiles for Section 1 of Scour Test 1. The profiles are

roughly symmetric with the maximum scour hole depth near the centreline of the scour hole. Initially, up to 10 minutes of scouring, the scour hole was centred slightly to the positive side of the jet centreline. Later it shifted to the negative side of the jet centreline and stayed this way until about 40 minutes into the test. During the period from 5 to 40 minutes of testing, no large soil chunks were removed from Section 1 of the scour hole; thus the corresponding profiles through this period show no large changes. However, after 40 minutes of testing, larger chunks of soil were removed from Section 1, which can be seen in a much larger scour hole size at 50 minutes of testing. There is an associated change of the cross-sectional profile and after this the scour hole seemed to form its final shape. No significant change of the shape in the profile was observed after 50 minutes of testing. Hence, the removal of large soil chunks was the determining factor for the final shape for Section 1 for this particular scour hole. However, although the shape remains similar, the scour hole continued to deepen. The radii for this section also continued to grow with the scour hole depths from the beginning until the end of the test.

For Section 2 (see Figure 4.10b), the scour hole profiles did not show symmetry at any time of scouring about the centreline or maximum depth of scour. After 40 minutes of testing, the scour hole formed a distinct shape with the maximum scour depth located away from the jet centreline. After 50 minutes of testing, the maximum scour depth moved along the jet centreline. During 50 minutes to 2 hours of testing, no significant changes in the profiles were observed except erosion on the sides of the scour hole. Big soil chunks were removed between 2 hours to 4 hours of testing and produced a second depression to the right side of the jet centreline. Scouring along this side continued and took a final shape after 96 hours. For this section the growth of the radius along the negative side and positive side of the centreline ceased after 50 minutes and 4 hours of testing respectively. Big chunk removals from the sides of the scour hole ceased the growth of the radii earlier than the scour hole depths.

Similar to Section 2, Section 3 (Figure 4.10c) also started with a single depression scour hole, but eventually a secondary depression developed. No symmetry was observed with respect to the centreline scour hole depth with time. However, the profile kept an approximately symmetric scour hole shape about the maximum scour hole depth until 40 minutes of scouring. After 50 minutes of testing, scour depths on the positive side of the jet centreline apparently reached the

final depth. After 8 hours, big soil chunks removed from the negative side of the jet centreline and a second depression started to grow. This second depression continued to grow until the end of the scour test at 144 hours. Although the side slopes of the scour hole did not change after 50 minutes of scouring, the radii continued to grow until the end of the test.

Section 4 also showed formation of secondary depression due to big soil chunk removal (Figure 4.10d). But instead of a sudden secondary peak formation, big chunk removal continued on the positive side of the centreline until the end of the scour test. The initial peak and left side slope of the scour hole stabilized after 50 minutes of scouring. The radii and depth continued to grow with time.

Figure 4.11a shows the development of the scour hole profile with time for Section 1 of Scour Test 5. From the beginning to the end of the test, this scour hole was shifted away from the jet centreline. From 5 minutes to 4 hours during the scour test, the scour hole continued to grow with time without any removal of large soil chunks. From 4 to 8 hours of scouring, the scour hole seemed to take the final scour hole shape and no significant scouring was seen during this period. However, after 8 hours this section eroded again and took the final scour hole shape at 16 hours. This shape remained unchanged with very little change of scour depths until the end of the test at 168 hours. The radii for this section took the final size quite quickly compared to the scour hole depths. The radius of the positive side of the jet centreline obtained the final size within only 10 minutes, while the radius of the negative side of the jet centreline obtained the final size within 40 minutes of scouring.

Section 2 of Scour Test 5 (see Figure 4.11b) initially shows apparent symmetry about the jet centreline between 5 to 20 minutes of testing. Until 30 minutes of testing, the section-wise maximum scour depth ε_{ms}, stayed very close to the jet centreline. However, after 40 minutes of testing, big soil chunk removal made ε_{ms} shifted towards the negative side of the jet centreline. After then, the scour hole continued to grow until 16 hours of testing and took the final shape. After 16 hours, only a small amount of erosion was seen on the side slope of the profiles.

Scouring of Section 3 of Scour Test 5 (see Figure 4.11c) was very similar to scouring of Section 2. Apparent symmetry of the scour hole about the jet centreline was seen between 5 to 20 minutes of testing. After 30 minutes of testing, ε_{ms} shifted to the positive side of the jet centreline due to large soil chunk removal. After then, the scour hole continued to grow and obtained the final shape after 16 hours of testing. ε_{cl} was still growing in very small increments.

Section 4 of Scour Test 5 (see Figure 4.11d) continued to grow gradually between 5 minutes to 1 hours of testing with a tendency of ε_{ms} located near jet centreline. However, after 1 hour of testing, large soil chunks were removed and ε_{ms} shifted towards the negative side of the jet centreline. The scour hole continued to grow and take the final shape after 48 hours of testing.

4.2.3.2 Variability in Scour Hole Profiles for Different Sections

Because the scour holes were rarely symmetric about the jet centreline throughout the tests, there were variations in the scour hole profiles for different cross-sections at any measurement time. These variations in the scour hole profiles were investigated for different section-wise dimensions, namely the section-wise maximum scour depth ε_{ms}, the radius of the scour hole r_o, the half-width about the jet centreline b_{cl}, and the half-width about the section-wise maximum scour depth b_m. A series of tables (Tables 4.1 to 4.8) have been produced for all the scour tests (except the abandoned tests, Scour Tests 2 and 7) to observe the maximum percent variations of ε_{ms} from the maximum scour hole depth ε_m, and the maximum percent variations of r_o, b_{cl}, and b_m from the average scour hole dimensions $\bar{\bar{r}}_o$, $\bar{\bar{b}}_{cl}$, and $\bar{\bar{b}}_m$ respectively.

It was noted that among the observed dimensions, the lowest percent difference was seen for ε_{ms}, and then for r_o. The half-widths b_{cl} and b_m showed the highest percent difference, and the percent differences were very close in value for these dimensions. Except Scour Tests 1 and 6, the percent differences for ε_{ms}, r_o, b_{cl}, and b_m decreased with time, and obtained a constant value if that particular dimension was reached at equilibrium. However, for each dimension there were four percent differences for four sections of the same scour hole at a measurement time. Therefore, only the "maximum percent difference" among the percent differences for four sections has been

reported here. A summary of the maximum percent differences for the observed dimensions for any time during the tests are listed as follows:

- The maximum percent difference for ε_{ms} ranged from 2% (Scour Test 1) to 82% (Scour Test 10);
- The maximum percent difference for r_o ranged from 8% (Scour Test 6) to 92% (Scour Test 1);
- The maximum percent difference for b_{cl} ranged from 11% (Scour Test 6) to 178% (Scour Test 5);
- The maximum percent difference for b_m ranged from 13% (Scour Test 6) to 179% (Scour Test 5).

These results clearly indicate that the section-wise scour hole dimensions varied from the average values for all the cross-sections, and thus also varied among different cross-sections of the scour hole. Therefore, scour hole profiles with time from only one or a couple of cross-sections are unlikely to be a good representation of the overall development of scour hole with time.

4.2.4 What is the Appropriate Characteristic Dimension of the Scour Hole for Assessing Equilibrium?

For assessing the time to reach equilibrium, a graphical approach was used. In this method, the dimensions of the scour hole were first plotted against the logarithm of time as individual graphs. A "plateau" or portion of the curve parallel to the time axis was identified as the final stage of scouring, and a tangent was drawn to this plateau. The co-ordinates of the point of tangency gave the equilibrium scour dimension and time to reach equilibrium. Figure 4.12 gives an illustration of this graphical approach to determine the magnitude of equilibrium dimension and time to equilibrium for the centreline depth of scour for Scour Test 9. For this example, the equilibrium centreline depth was found to be 23.85 mm and time to equilibrium was 264 hours.

Although ten scour tests were conducted, only eight of them were “good tests” because two of the tests were abandoned (Scour Test 2 and 7) due to failure of the samples at the side of the scour hole. A comparison of the time to reach equilibrium determined using the graphical approach using several characteristic dimensions of the scour hole for these good tests is given in Table 4.9.

It is seen that different dimensions came to equilibrium at different times. The dimension that came to equilibrium last was termed the "critical equilibrium dimension". For four scour tests, namely Scour Tests 5, 8, 9 and 10, all the dimensions came to equilibrium. Therefore these scour tests were considered to achieve an overall equilibrium condition. Although it was intended to run all of the tests until equilibrium was reached, during the scour tests it was not possible to plot the development of all the dimensions of the scour hole with time to assess equilibrium. The analysis of the laser data was time consuming and hence preliminary assessment of equilibrium was done based on the volumetric change of the scour hole. This volumetric change was studied without the refraction correction to the laser data. Moreover, near equilibrium, the change in volume of the scour hole was too small to trace compared to other dimensions. Therefore, the detailed analysis of the laser data later revealed that only four of the scour tests had reached equilibrium.

Among the four scour tests that came into equilibrium, for three of the tests (Scour Tests 8, 9 and 10) the critical equilibrium dimension was the section-wise maximum scour depth, ε_{ms}. Also for Scour Test 1, all the dimensions except ε_{ms} reached equilibrium. This was an important observation, since most the previous studies considered either ε_{cl} or ε_m to track scouring progress and to identify the equilibrium condition. But in reality, after the centreline and maximum scour hole depths have reached equilibrium, the sides of the scour hole may still continue to erode. Such a type of erosion is termed here "side slope erosion". From Figure 4.10d, it can be seen that the scour hole for Scour Test 1 was still eroding on the side of the scour hole after 144 h of testing. The scour depth along the lowest depression for this particular section was the section-wise maximum (ε_{ms}). The maximum scour depth for this scour hole reached equilibrium after 120 h, but due to side slope erosion ε_{ms} was still increasing. For this reason, for Scour Test 8, 9, and 10, ε_{ms} was the critical equilibrium dimension.

However, ε_{ms} cannot always be considered as the critical equilibrium dimension. For Scour Test 5, the average half-widths ($\bar{\bar{b}}_{cl}$ and $\bar{\bar{b}}_m$) were the critical equilibrium dimension. This is because, for this particular scour test, side slope erosion affected the half-widths more than the section-wise maximum depths. Further, for different sections of the scour hole ε_{ms} reached to equilibrium at different times during the scouring process (Table 4.10). Therefore, it is important to track the half-widths and the maximum section-wise scour depths for multiple sections of the

scour hole, so that any side slope erosion can be tracked. Tracking of volumetric change of the scour hole is not practical for side slope erosion, since near equilibrium the volumetric change is very small.

The average scour hole radius $\bar{\bar{r}}_o$, and the maximum scour hole depth ε_m came to equilibrium quite early for all tests that reached equilibrium. This contrasts with the development of $\bar{\bar{r}}_o$ in cohesionless soils, where $\bar{\bar{r}}_o$ continues to grow even after the depths reach equilibrium state (Rajaratnam and Beltaos 1977). The reason behind $\bar{\bar{r}}_o$ and ε_m coming early to equilibrium was large chunk removal by mass erosion. When large chunks were removed, $\bar{\bar{r}}_o$ and ε_m rapidly increased. This rapid increase in size would cause a reduction of shear stress along scour hole boundary. When this shear stress reduces below the critical shear stress of the soil, equilibrium conditions are achieved.

4.2.5 Formation of the Equilibrium Shape

The scour holes may obtain the equilibrium shape in dimensionless form before the absolute equilibrium state is achieved. To observe at what time the scour holes started to show similarity to the shape of the scour hole at equilibrium, the scour hole profiles have to be converted into dimensionless form. Mazurek (2001) tested $\varepsilon_{m\infty}$ and $\varepsilon_{cl\infty}$ as scales for the scour hole depths and $r_{o\infty}$, $b_{cl\infty}$, and $b_{m\infty}$ as scales for scour hole radius, where $r_{o\infty}$ = radius of the scour hole from centreline of the jet to the edge of the scour hole at equilibrium; $b_{cl\infty}$ = half-width of the scour hole at equilibrium, or distance from the jet centreline where $\varepsilon=½\varepsilon_{cl\infty}$; and $b_{m\infty}$ = half-width of the scour hole at equilibrium, or distance from the jet centreline where $\varepsilon=½\varepsilon_{m\infty}$. It is not practical to use $r_{o\infty}$ as a scale because defining the scour hole edge accurately is very difficult. Since the soil sample was cut flush with the sample holder during sample preparation, the soil particles near the surface of the soil sample aligned parallel to the soil surface. Such alignment of the soil particles resulted in erosion of the top soil surface around the edge of the scour hole. Therefore, the scour hole edge was difficult to identify. In the scour hole profiles for each cross-section of the scour hole, tangent to the scour hole side was drawn. The point of intersection between the tangent and the initial uneroded soil surface indicated the scour hole edge. This method of determining the scour hole radius was not very precise, hence the scour hole radius was not used as scale for radial distances.

Further, for some asymmetric scour holes, it may not be possible to assess the half-width based on the maximum depth (b_m) of the scour hole. For example, the difficulties of assessing a half-width based on the maximum depth is shown in Figure 4.13a for Scour Test 10. Along the positive side of the jet centreline, the scour hole was shallower than $\varepsilon_m/2$. Therefore, b_m could not be obtained. Also, for the negative side of the jet centreline, there were multiple locations (points A and B) for which b_m could be defined. Half-widths for the centreline depth (b_{cl}) can be measured for both sides of the scour hole. However, for some instances, multiple locations for b_{cl} could be detected for one side of the scour hole. For example, in Section 3 of the Scour Test 1, multiple locations for b_{cl} could be determined (see Figure 4.13b). Judgement was applied for assessing b_{cl} for such instances. In light of the above discussion, $\varepsilon_{cl\infty}$ was used as scale for ε_∞ and $b_{cl\infty}$ was used as scale for r to obtain the dimensionless profiles for this study. The dimensionless scour hole profiles for different sections of the scour hole for all the scour tests at different stages in their development are shown in Appendix D.

A general equation for the dimensionless equilibrium scour hole shape was developed using regression analysis with the equilibrium scour hole profile data for the scour tests that had reached equilibrium (Scour Tests 5, 8, 9, and 10). For each scour hole, scour hole profiles for four sections were extracted. Figure 4.14 shows the dimensionless scour hole profiles for all sections of the scour holes at equilibrium conditions.

Previously, a Gaussian, sine function, or polynomial equations were used in developing a general equation for the equilibrium scour hole, as discussed in Chapter 2. However, the Gaussian equation cannot define the radius of the scour hole as it approaches the soil surface asymptotically. A polynomial equation can show a good fit with the data with normally higher orders of the polynomial, but it can "over fit" the data instead of showing a general trend. Therefore, the sine function was used to produce the general equation for the equilibrium shape. Because the scour holes were made dimensionless using $\varepsilon_{cl\infty}$ as the scale for ε, along the centreline the scour hole depth must be $\varepsilon/\varepsilon_{cl\infty} = -1$. Further, at the depth $\varepsilon/\varepsilon_{cl\infty} = -0.5$, the width of the scour hole is $r/b_{cl\infty}=\pm1$. Hence, there are three data points ((0, -1), (-1, -0.5), and (-1, 0.5)) which the general equation for the dimensionless equilibrium scour hole shape must satisfy. Moreover, the equation has to be symmetric about the centreline to represent the ideal shape. Keeping these constraints in mind, the

best fit sine function was found by linear regression using the least squares method to develop a general equation for the profile of the equilibrium scour hole:

$$\frac{\varepsilon}{\varepsilon_{cl\infty}} = \sin\left(\frac{\pi}{3}\frac{r}{b_{cl\infty}} - \frac{\pi}{2}\right) \quad [4.1]$$

The curve fitting, along with the three constraint points are shown in Figure 4.15. The sine function gave a correlation coefficient $r^2 = 0.78$.

The dimensionless equilibrium profile of an individual scour hole did not necessary follow the general equation for the equilibrium scour hole. Therefore, using any statistical approach to investigate when the dimensionless scour hole profiles started to show similarity with the equilibrium scour hole was not appropriate. Instead, the dimensionless profiles were plotted together for the same section of the same scour hole for different times of scouring in Figure 4.16. Dimensionless profiles were shown starting with the profiles immediately before the similarity was observed, so that one can differentiate between the equilibrium shapes to the shape just before the equilibrium shape. Also, the general equilibrium scour hole shape was shown in Figure 4.16 to observe how the equilibrium profile of a particular section varied from the general equilibrium scour hole shape.

Table 4.11 shows the time to obtain the equilibrium shapes for different scour hole sections resulting from the observations of Figure 4.16. It was observed that different sections of the same scour hole did not necessarily obtain the equilibrium shape at the same time. Therefore, the maximum time required to reach equilibrium among sections of a particular scour hole was considered as the "critical time to equilibrium shape" for that scour hole. This critical time to equilibrium shape (t^*_∞) were compared to the time to equilibrium (t_∞) for the different scour tests. For Scour Test 8, t^*_∞ was only 15% of t_∞; whereas for Scour Test 5, t^*_∞ was 100% of t_∞. For Scour Test 9 and 10, t^*_∞ was 50% and 89% of t_∞ respectively. This indicates, while for some scour tests the equilibrium shapes can be formed very quickly compared to the time to reach equilibrium, for some scour tests the equilibrium shapes are not formed until equilibrium.

4.3 Analysis of Uncertainty

The following section provides estimates of the errors in the measured and calculated quantities used in this study. The procedure described in Topping (1957) was followed for error calculation for most of the quantities, if not otherwise described. During this analysis, the maximum errors were computed and they represent the worst case.

The jet impinging height was constant at 85 mm and was measured with a scale of ±1 mm precision. Thus the error in H was ±1.2%. The jet nozzle diameter was measured along three different cross-sections of the nozzle with slide calipers of ±0.01 mm precision. The average diameter of the jet nozzle measured 7.76 mm with a maximum error of ±0.13 mm from the average. This gives an error in measurement of ±1.7%. Using this error, the error in the derived parameter in nozzle area A_0, can be estimated as ±3.4%. The flowrate through the jet was measured using the manometer, which could be read to ±1 mm. The minimum pressure difference measured with the manometer was 132 mm; which gives a measurement error of ±0.8%. Therefore the error in flow velocity U_0, using Equation 3.19 can be estimated as ±0.4%. Then the error in volumetric flow rate Q, can be estimated as ±3.8% using Equation 3.18.

For the error in the laser measurement, the standard error was calculated as described in Kenney and Keeping (1962). Thirty depth readings were taken for a single point on the soil surface using the laser. The average depth and the standard deviation of the readings were calculated as 287.8 mm and ±0.37 mm respectively. The standard deviation also represents the standard error of the measurements. The probable error is 68% of the standard error, calculated as ±0.25 mm. However, considering the worst case, the standard uncertainty ±0.37 mm was considered as the error in depth measurements. Therefore, the error in depth measurements (for ε_{cl}, ε_m, and ε_{ms}) was ±0.1%.

According to the specifications of the stepper motors and encoders (National Instruments Corporation 2016), the encoder for the traverse system has an angular accuracy of ±3%. The number of steps per revolution was 200, and the step angle was 1.8 degrees. For a single revolution, the linear displacement of the traverse was 2 mm. Therefore, the error for a 2 mm linear displacement is ±0.06 mm. Also, the minimum displacement for the traverse was 2 mm. Hence,

the error in linear displacement was ±3%. However, the measurement of r, b_{cl}, and b_m were dependent on both the depth measurements and the linear measurements, since these parameters were derived from scour hole profiles. Thus the error in r, b_{cl}, and b_m was about ±3.1%.

Though the volume inside the scour holes were not regular shapes, for error calculation a hemispherical depression can be considered. The volume of a hemisphere is equal to two-thirds of the cube of the radius divided by π. Therefore, the volume of the scour hole ξ, is proportional to $r^2\varepsilon_{cl}$; which gives the maximum error in the volume ξ was ±6.3%. The maximum errors for different parameters are summarized in Table 4.12.

Table 4.1: Maximum percent difference between section-wise and average scour hole dimensions for Scour Test 1.

t	ε_{ms} (mm)						r_o (mm)									b_{cl} (mm)										b_m (mm)									
min	S1	S2	S3	S4	ε_m	% Diff.	S1		S2		S3		S4		$\bar{r}_0$	% Diff.	S1		S2		S3		S4		$\bar{b}_{cl}$	% Diff.	S1		S2		S3		S4		$\bar{b}_m$	% Diff.
5	1.70	1.59	1.94	1.82	2.06	23	22	24	32	44	36	20	26	40	31	44	14.50	18.45	14.74	28.01	27.08	12.99	21.21	23.09	20.00	40	15.85	18.09	14.35	12.18	16.56	13.75	15.68	19.60	15.80	24
10	2.53	2.53	2.53	2.53	2.93	14	24	28	18	46	38	20	26	42	30	52	18.88	16.79	11.92	20.29	23.86	11.23	14.58	21.15	17.30	38	18.88	16.79	11.92	20.29	23.86	11.23	14.58	21.15	17.30	38
15	3.37	3.53	3.61	3.44	3.65	7.6	36	32	18	50	40	20	26	42	33	52	23.96	13.87	9.47	29.57	25.82	8.88	11.91	23.58	18.40	61	23.88	13.81	7.37	29.10	23.85	8.05	11.76	23.23	17.60	65
20	3.43	4.26	4.23	4.10	4.54	25	38	32	18	68	40	20	26	42	36	92	28.77	13.79	7.88	36.49	30.42	10.43	11.85	27.77	20.90	74	28.59	13.68	6.01	33.89	27.65	6.80	10.75	23.67	18.90	80
30	3.74	5.70	5.03	4.90	5.77	35	44	34	18	68	58	20	26	48	40	72	29.20	16.71	10.82	44.00	53.33	12.39	13.34	36.46	27.00	97	27.74	16.36	2.98	37.42	46.64	7.07	5.86	31.49	21.90	113
40	4.97	9.92	8.54	7.53	10.18	51	50	34	18	68	72	20	26	52	43	69	35.88	21.61	8.83	48.70	65.85	9.83	11.44	39.60	30.20	118	34.77	20.74		26.83	56.11	1.14	4.46	30.42	24.90	125
50	16.85	16.36	16.36	16.36	16.98	3.7	58	60	36	68	72	44	32	52	53	39	25.31	31.10	12.58	20.03	33.91	21.77	15.60	15.25	21.90	55	25.10	30.43	12.58	20.03	33.91	21.77	15.60	15.25	21.80	55
60	16.85	16.47	16.47	16.47	16.98	3.0	58	60	36	68	74	44	32	52	53	40	25.61	30.94	12.75	19.93	22.31	21.70	15.52	15.41	20.50	51	25.43	30.43	12.75	19.93	22.31	21.70	15.52	15.41	20.40	49
90	16.85	16.47	16.47	16.47	16.98	3.0	58	60	36	68	76	44	40	56	55	39	26.07	31.16	12.87	21.53	22.31	21.70	15.52	16.41	20.90	49	25.88	30.75	12.87	21.53	22.31	21.70	15.52	16.41	20.90	47
120	16.85	16.53	16.53	16.53	16.98	2.6	58	60	36	68	76	44	40	56	55	39	26.03	31.11	13.00	25.81	23.00	21.78	15.48	18.50	21.80	42	25.88	30.76	13.00	25.81	23.00	21.78	15.48	18.50	21.80	41
240	16.85	16.61	16.61	16.61	16.98	2.2	60	60	36	68	76	44	40	90	59	52	25.99	31.20	12.93	54.37	23.86	21.74	15.42	27.99	26.70	104	25.88	30.89	12.93	54.37	23.86	21.74	15.42	27.99	26.60	104
480	16.85	17.01	16.61	16.61	17.60	5.6	60	60	36	68	76	44	40	96	60	60	25.99	31.20	12.93	54.37	23.86	21.74	15.42	47.64	29.10	87	25.88	30.89	12.60	54.20	23.86	21.74	15.42	47.64	29.00	87
960	16.85	17.80	16.61	16.61	19.00	13	60	60	36	68	76	44	40	96	60	60	25.99	31.20	12.93	54.37	23.86	21.74	15.42	77.30	32.90	135	25.88	30.89	11.96	53.88	23.86	21.74	15.42	77.30	32.60	137
1440	16.85	19.93	16.61	16.61	20.00	17	60	60	36	68	76	54	40	108	63	72	25.99	31.20	12.93	54.37	23.17	21.74	15.42	77.38	32.80	136	25.88	30.89	10.73	40.67	23.17	21.74	15.42	77.38	30.70	152
2880	16.85	20.92	16.61	16.61	21.81	24	60	64	36	68	76	54	40	108	63	71	26.03	31.20	14.21	54.72	34.93	22.25	15.95	77.38	34.60	124	25.91	30.89	10.90	53.46	34.93	22.25	15.95	77.38	34.00	128
4320	16.85	21.65	16.61	16.61	21.81	24	60	64	36	68	76	54	40	108	63	71	26.03	31.20	14.21	55.83	34.93	22.25	15.95	77.70	34.80	124	25.91	30.89	10.51	53.98	34.93	22.25	15.95	77.70	34.00	128
5760	16.85	22.15	16.61	16.70	22.80	27	60	64	36	68	76	54	40	108	63	71	26.03	31.20	14.21	55.90	34.93	22.25	15.95	77.70	34.80	124	25.91	30.89	10.24	54.09	34.93	22.25	15.87	77.64	34.00	129
7200	16.85	22.15	16.61	16.84	23.26	29	60	64	36	68	76	54	40	108	63	71	26.03	31.20	14.21	55.90	34.93	22.25	15.95	77.70	34.80	124	25.91	30.89	10.24	54.09	34.93	22.25	15.75	77.55	34.00	128
8640	16.85	22.15	16.61	17.96	23.26	29	60	64	36	68	76	54	40	108	63	71	26.03	31.20	14.21	56.54	34.93	22.25	15.95	78.39	34.90	124	25.91	30.89	10.24	54.38	34.93	22.25	14.80	77.11	33.80	128

Note: S indicates the section of the scour hole.

Table 4.2: Maximum percent difference between section-wise and average scour hole dimensions for Scour Test 3.

t	ε_{ms} (mm)						r_o (mm)									b_{cl} (mm)										b_m (mm)									
min	S1	S2	S3	S4	ε_m	% Diff.	S1		S2		S3		S4		$\bar{r}_0$	% Diff.	S1		S2		S3		S4		$\bar{b}_{cl}$	% Diff.	S1		S2		S3		S4		$\bar{b}_m$	% Diff.
5	3.06	4.11	4.44	3.11	6.03	49	30	32	38	62	74	34	28	48	43	71	15.17	16.35	11.26	43.59	67.19	12.13	11.91	22.96	25.10	168	15.17	16.35	7.69	38.78	61.88	9.06	11.83	22.09	22.90	171
10	4.01	4.11	4.44	3.67	6.03	39	40	36	38	62	74	34	30	48	45	64	33.62	24.81	21.93	41.95	67.01	22.99	19.34	26.87	32.30	107	32.35	21.76	20.20	38.78	61.88	19.11	17.51	26.11	29.70	108
15	5.14	5.05	6.91	5.13	9.20	45	50	38	38	62	82	36	30	52	49	69	28.74	19.25	17.15	35.80	60.92	18.10	15.63	25.58	27.60	120	28.24	19.07	17.14	35.79	58.02	11.69	15.36	23.68	26.10	122
20	6.78	6.48	7.16	6.63	9.20	30	58	42	38	62	82	40	30	54	51	62	31.34	21.78	13.86	33.94	60.12	16.64	13.06	30.91	27.70	117	30.32	21.22	13.83	33.92	56.95	14.82	11.94	30.23	26.70	114
30	9.67	7.88	13.64	8.01	16.23	51	68	46	38	62	104	40	34	54	56	87	58.05	24.69	12.78	35.87	89.29	16.16	13.44	31.22	35.20	154	45.97	19.69	12.62	35.68	75.53	7.13	12.75	29.50	29.90	153
40	9.79	9.56	17.48	8.60	18.44	53	76	52	38	62	104	40	34	54	58	81	58.33	29.04	14.32	35.59	88.01	17.52	17.84	37.01	37.20	137	54.57	25.76	13.03	34.79	68.94	4.00	17.54	36.86	31.90	116
50	9.95	11.91	17.58	9.54	18.68	49	76	52	38	82	104	40	34	66	62	69	59.36	28.03	14.17	67.17	85.59	16.67	18.56	46.47	42.00	104	59.23	25.44	11.23	64.06	69.65	6.00	18.35	45.79	37.50	86
60	9.95	12.49	19.04	9.95	19.31	49	76	52	38	82	104	40	34	66	62	69	59.42	28.96	13.93	66.87	84.95	17.00	18.26	43.98	41.70	104	59.37	28.58	11.52	63.03	63.90	1.00	18.03	43.53	36.10	97
90	12.44	20.39	22.97	12.77	24.15	49	76	52	42	106	104	40	42	80	68	57	59.15	31.58	16.14	86.46	83.16	18.40	21.26	65.68	47.70	81	59.00	29.88	6.64	77.12	67.38	1.00	20.31	63.83	40.60	98
120	12.67	22.05	22.97	13.60	24.15	48	76	52	42	106	104	40	42	80	68	57	59.01	29.33	15.17	85.95	81.98	17.63	20.40	64.02	46.70	84	59.01	29.33	4.85	74.98	67.38	5.62	19.30	62.22	40.30	88
240	14.82	25.30	23.93	17.59	25.60	42	76	54	42	106	104	40	42	86	69	54	58.65	32.59	13.53	84.28	77.84	16.76	18.86	66.70	46.20	83	58.61	32.36	5.48	71.00	66.69	9.59	15.82	63.26	40.40	86
480	18.89	27.89	27.34	21.32	29.41	36	76	56	42	106	104	40	42	86	69	54	57.77	31.38	13.66	79.29	71.32	16.51	18.93	62.12	43.90	81	57.58	30.95	8.08	67.54	62.53	11.42	16.97	59.41	39.30	80
960	23.30	30.38	29.94	26.00	31.11	25	76	56	42	106	104	40	42	86	69	54	56.04	32.96	14.54	78.98	67.43	17.16	17.71	57.92	42.80	84	56.04	32.96	12.08	70.07	60.47	14.68	16.37	55.77	39.80	76
1440	26.29	32.38	31.82	28.73	32.80	20	76	62	42	106	104	40	42	86	70	52	55.56	34.62	16.52	78.82	64.97	20.14	19.08	57.94	43.50	81	54.21	34.49	14.60	71.46	61.13	17.30	17.96	56.82	41.00	74
2880	27.98	32.89	31.91	29.97	33.35	16	76	62	44	106	104	40	50	86	71	49	47.40	39.44	18.07	77.27	63.76	20.25	22.65	57.42	43.30	79	46.86	38.77	15.97	70.76	61.07	18.84	21.52	56.29	41.30	72
4320	28.97	33.27	32.26	30.37	33.57	14	76	62	48	106	104	52	50	86	73	45	46.83	40.98	25.82	76.83	63.43	26.76	33.71	57.33	46.50	65	45.94	40.31	21.74	70.24	60.81	24.43	31.81	56.14	43.90	60
5760	29.38	33.84	32.25	30.58	34.03	14	76	62	48	106	104	52	50	86	73	45	46.13	40.90	25.25	75.75	63.02	27.69	33.10	57.30	46.10	64	45.62	40.51	21.42	70.26	60.81	25.99	31.65	56.23	44.10	60

Table 4.3: Maximum percent difference between section-wise and average scour hole dimensions for Scour Test 4.

t	ε_{ms} (mm)						r_o (mm)										b_{cl} (mm)										b_m (mm)									
min	S1	S2	S3	S4	ε_m	% Diff.	S1		S2		S3		S4		$\bar{\bar{r}}_0$	% Diff.	S1		S2		S3		S4		$\bar{\bar{b}}_{cl}$	% Diff.	S1		S2		S3		S4		$\bar{\bar{b}}_m$	% Diff.
5	6.42	21.84	21.76	11.13	26.67	76	30	68	86	32	24	76	74	36	53	62	13.11	62.45	75.14	14.46	11.90	70.16	68.21	21.95	42.20	78	9.96	58.08	61.20			66	60.84		51.20	81
10	15.48	35.62	36.19	29.70	38.70	60	62	68	88	32	24	76	84	38	59	59	36.42	54.32	63.86	8.28	8.14	68.63	65.10	15.04	40.00	80	34.66	52.13	59.29			63	57.56		53.30	35
15	20.02	38.17	36.29	32.59	38.70	48	62	68	88	32	36	76	84	38	61	47	44.96	52.37	63.97	12.12	14.96	67.68	61.49	18.56	42.00	71	44.93	52.32	57.65	1.13	3.13	63	56.77	6.54	35.70	97
20	20.74	38.36	36.66	32.86	38.76	47	62	68	88	32	36	76	84	38	61	47	46.52	52.26	63.79	13.10	14.73	68.20	61.13	18.18	42.20	69	46.46	52.18	57.54	1.74	3.59	63	56.84	7.48	36.10	95
30	27.93	43.34	38.10	39.20	43.97	37	64	68	88	32	36	76	84	40	61	48	45.98	48.15	61.70	13.53	16.33	66.53	58.15	18.71	41.10	67	45.92	48.06	55.44	5.54	11.30	63	54.96	9.45	36.70	85
40	29.83	43.34	38.10	39.20	43.97	32	64	68	88	32	36	76	84	40	61	48	45.64	46.88	61.24	14.72	17.26	66.11	57.65	20.07	41.20	64	45.55	46.67	55.44	7.35	12.76	63	54.96	12.54	37.30	80
50	30.34	43.40	38.22	39.20	44.12	31	64	68	88	34	40	76	90	44	63	46	45.62	46.60	61.09	16.97	19.29	65.93	57.50	22.79	42.00	60	45.58	46.49	55.43	9.63	14.51	63	54.96	15.37	38.10	75
60	30.53	43.93	38.22	39.39	44.93	32	64	68	88	34	40	76	90	44	63	46	45.62	46.85	61.06	17.80	19.47	65.89	57.47	23.86	42.30	58	45.57	46.70	55.29	9.88	14.51	63	55.04	17.64	38.40	74
90	32.99	43.93	38.36	42.77	44.94	27	64	68	88	42	52	76	90	54	67	37	45.01	44.21	60.47	21.70	24.29	65.61	56.81	28.90	43.40	51	45.00	44.20	55.30	15.20	21.56	64	54.15	22.14	40.20	62
120	33.62	43.93	38.36	43.14	45.00	25	64	68	88	44	52	78	90	54	67	35	45.25	43.98	60.41	24.56	27.72	65.55	56.76	30.64	44.40	48	45.18	43.72	55.30	19.36	24.59	64	54.05	25.59	41.50	54
240	38.09	43.93	38.88	43.65	45.00	15	66	68	88	48	52	78	90	56	68	32	52.32	42.23	59.09	29.98	32.27	64.56	55.99	37.67	46.80	38	51.87	41.60	55.30	26.78	31.20	64	53.96	34.13	44.80	42
480	38.35	44.14	38.97	43.65	45.39	16	68	68	88	48	56	78	90	56	69	30	52.33	41.94	58.79	30.56	38.02	64.38	55.83	38.31	47.50	36	52.00	41.53	55.25	27.53	36.99	64	53.96	34.53	45.70	40
960	39.98	44.14	39.41	43.65	45.40	13	70	68	88	50	56	78	94	66	71	32	55.44	42.29	57.69	31.32	37.77	63.73	55.27	37.46	47.60	34	55.05	41.88	55.25	29.33	37.54	64	53.96	35.24	46.50	37
1440	41.53	44.41	39.73	43.96	45.46	13	76	68	88	50	60	78	94	66	73	31	55.27	42.44	57.21	31.46	42.12	63.49	55.08	37.40	48.10	35	54.56	41.74	55.18	29.71	42.03	63	53.92	35.41	47.00	37
2880	45.22	53.20	49.79	46.60	54.10	16	76	90	88	50	66	78	94	66	76	34	53.83	48.70	55.36	31.26	40.19	61.99	54.07	39.52	48.10	35	53.19	47.80	52.91	26.96	36.02	60	53.67	37.77	46.00	41
4320	46.76	54.14	49.83	46.92	55.34	16	76	90	88	50	66	78	94	66	76	34	53.60	48.56	55.16	31.13	39.76	61.75	53.94	39.15	47.90	35	52.57	46.95	52.67	26.46	35.99	60	53.63	37.80	45.70	42
5760	50.20	59.17	57.36	51.37	59.97	16	76	90	88	50	66	78	94	66	76	34	51.12	45.14	53.80	29.01	36.09	60.03	53.27	38.13	45.80	37	50.84	44.87	50.74	24.58	32.20	52	53.06	37.33	43.30	43
7200	50.51	59.69	57.98	51.89	60.74	17	76	90	88	50	66	78	94	66	76	34	51.11	44.83	53.65	29.16	36.69	59.43	53.20	38.39	45.80	36	50.94	44.70	51.25	24.85	31.82	52	52.99	37.69	43.30	43

Table 4.4: Maximum percent difference between section-wise and average scour hole dimensions for Scour Test 5.

t	ε_{ms} (mm)						r_o (mm)									b_{cl} (mm)										b_m (mm)									
min	S1	S2	S3	S4	ε_m	% Diff.	S1		S2		S3		S4		$\bar{r}_0$	% Diff.	S1		S2		S3		S4		$\bar{b}_{cl}$	% Diff.	S1		S2		S3		S4		$\bar{b}_m$	% Diff.
5	4.37	4.10	4.20	4.12	4.45	7.8	38	50	38	36	40	42	32	40	40	27	13.58	31.21	18.69	19.43	11.92	22.63	14.41	19.97	19.00	65	12.32	29.15	18.61	19.00	11.52	22.18	14.27	19.80	18.40	59
10	7.17	7.30	7.06	7.22	7.38	4.4	52	80	40	36	50	46	40	48	49	63	15.95	47.36	15.36	19.36	17.16	23.80	14.58	24.58	22.30	113	15.07	44.04	14.70	18.44	16.70	23.45	13.94	24.06	21.30	107
15	8.54	8.24	8.24	8.55	8.67	5.0	52	82	40	36	50	46	40	48	49	67	21.75	70.98	14.02	19.76	16.61	21.57	12.89	26.65	25.50	178	21.18	70.58	14.02	19.76	16.61	21.57	12.34	26.21	25.30	179
20	9.81	9.79	9.79	10.07	11.01	11	52	82	40	36	50	46	40	48	49	67	19.40	67.77	15.45	20.17	19.05	21.56	16.62	29.08	26.10	159	19.36	67.75	15.45	20.17	19.05	21.56	16.17	28.73	26.00	160
30	13.49	12.20	15.15	12.35	17.34	30	52	82	68	36	50	92	40	48	59	57	25.12	66.12	50.62	21.42	19.61	71.44	20.17	29.30	38.00	88	21.63	63.83	49.75	21.14	16.01	68.23	19.62	27.67	36.00	90
40	15.52	20.39	23.88	15.44	25.77	40	72	82	76	40	50	92	74	48	67	40	33.51	63.97	65.07	22.79	23.91	72.63	40.44	30.48	44.10	65	33.28	63.93	62.23	18.83	13.46	69.17	40.44	30.48	41.50	68
50	17.83	27.25	26.87	17.42	33.35	48	72	82	78	40	50	92	80	52	68	41	27.33	63.20	64.01	22.70	21.94	71.90	59.83	29.58	45.10	60	26.85	63.04	59.22	14.18	11.96	69.47	59.83	29.58	41.80	71
60	19.29	27.94	29.51	19.02	33.51	43	72	82	78	40	50	92	80	52	68	41	29.75	62.56	63.34	24.00	22.44	72.11	59.04	30.76	45.50	59	29.63	62.47	59.21	17.18	12.88	69.40	59.04	30.76	42.60	70
90	22.10	31.65	31.62	22.31	33.81	35	72	82	78	40	50	92	80	52	68	41	28.48	61.51	62.12	23.45	20.71	71.44	53.91	32.16	44.20	62	27.83	61.33	57.87	16.79	12.70	68.81	49.62	31.54	40.80	69
120	23.27	32.11	31.62	23.87	33.99	32	72	84	82	46	50	92	82	56	71	35	28.23	61.47	61.78	26.79	24.92	71.28	51.49	37.55	45.40	57	27.24	61.09	57.97	20.28	15.62	68.81	47.51	36.16	41.80	65
240	28.98	32.11	32.06	26.52	34.10	22	72	84	82	46	50	92	82	56	71	35	26.73	60.15	59.92	28.32	23.15	70.32	42.07	36.07	43.30	62	24.89	59.05	58.16	24.65	18.51	68.72	41.74	35.74	41.40	66
480	29.61	32.13	32.06	26.85	34.34	22	72	84	82	46	50	94	82	58	71	35	26.75	60.25	60.09	28.20	23.10	70.41	42.13	36.21	43.40	62	24.82	58.98	58.31	24.64	18.58	68.89	41.75	35.90	41.50	66
960	33.69	35.23	36.36	31.86	36.52	13	72	84	82	46	50	94	82	66	72	36	32.42	58.51	58.65	29.19	26.05	69.18	39.27	41.41	44.30	56	31.94	56.84	57.36	27.50	22.64	66.53	38.78	40.74	42.80	56
1440	34.23	35.23	36.36	32.74	36.70	11	72	84	82	46	50	94	82	66	72	36	32.21	58.35	58.52	29.16	26.34	69.09	39.03	42.47	44.40	56	31.43	55.80	57.36	27.52	22.72	66.53	38.29	41.78	42.70	56
2880	34.31	35.28	36.85	33.22	36.88	10	72	84	82	46	50	94	82	66	72	36	32.42	58.50	58.48	29.45	26.23	69.10	39.12	42.60	44.50	55	31.79	54.46	57.35	27.87	22.31	65.87	38.37	41.63	42.50	55
4320	34.31	35.28	36.85	33.22	36.88	10	72	84	82	46	50	94	82	66	72	36	32.50	58.11	58.48	29.45	26.23	69.10	39.12	52.20	45.60	51	31.50	54.99	57.35	27.89	22.52	65.87	38.37	51.09	43.70	51
5760	34.31	35.28	36.85	33.22	36.88	10	72	84	82	46	50	94	82	66	72	36	32.36	57.61	58.48	30.37	26.23	69.10	39.12	52.27	45.70	51	31.42	55.55	57.35	28.36	22.68	65.87	38.37	51.13	43.80	50
7200	34.31	35.28	36.85	33.22	36.88	10	72	84	82	46	50	94	82	66	72	36	32.38	57.49	58.46	30.34	26.19	69.08	39.08	52.22	45.70	51	31.50	53.90	57.35	28.45	22.68	65.87	38.37	51.13	43.70	51
8640	34.31	35.28	36.85	33.22	36.88	10	72	84	82	46	50	94	82	66	72	36	32.32	58.12	58.46	30.56	26.24	69.11	39.08	52.22	45.80	51	31.43	54.58	57.35	28.95	22.68	65.87	38.37	51.28	43.80	50
10080	34.31	35.28	36.85	33.22	36.88	10	72	84	82	46	50	94	82	66	72	36	32.29	58.21	58.46	30.56	26.20	69.09	39.08	52.22	45.80	51	31.38	55.64	57.35	28.95	22.68	65.87	38.37	51.28	43.90	50

Table 4.5: Maximum percent difference between section-wise and average scour hole dimensions for Scour Test 6.

t	ε_{ms} (mm)						r_o (mm)										b_{cl} (mm)										b_m (mm)									
min	S1	S2	S3	S4	ε_m	% Diff.	S1		S2		S3		S4		$\bar{r}_0$	% Diff.	S1		S2		S3		S4		$\bar{b}_{cl}$	% Diff.	S1		S2		S3		S4		$\bar{b}_m$	% Diff.
5	1.39	1.43	1.40	1.32	1.76	25	12	24	20	26	16	20	14	30	20	48	8.34	19.03	6.92	16.42	10.14	13.42	6.48	21.16	12.70	66	7.93	18.46	9.09	18.92	9.60	12.34	6.13	19.55	12.80	53
10	2.04	2.10	2.08	2.14	2.49	18	24	32	28	32	28	28	20	34	28	29	15.55	21.69	10.91	20.80	17.04	12.34	9.99	24.24	16.60	46	15.42	21.61	10.35	20.34	16.78	11.93	9.53	23.47	16.20	45
15	2.60	2.68	2.70	2.73	3.07	15	28	34	36	38	34	34	26	34	33	21	23.68	19.57	21.21	20.47	21.49	15.33	13.78	24.06	19.90	31	23.48	19.52	19.43	20.19	21.20	15.06	13.42	22.90	19.40	31
20	2.83	2.79	3.10	2.85	3.39	18	32	36	44	40	34	34	36	40	37	19	24.25	24.59	20.03	24.33	22.27	17.48	13.49	30.11	22.10	39	23.06	25.17	18.74	23.98	21.14	15.77	13.16	29.43	21.30	38
30	3.25	3.11	3.31	3.14	3.62	14	38	38	44	40	34	36	40	42	39	13	25.77	27.08	19.10	24.71	24.86	20.17	15.64	28.29	23.20	33	25.39	26.42	19.08	24.69	24.21	17.84	15.48	28.09	22.60	32
40	3.48	3.22	3.38	3.23	3.80	15	40	40	44	42	38	38	42	42	41	8	28.25	30.66	21.34	26.51	25.89	23.58	17.83	31.94	25.80	31	27.23	27.44	21.44	26.48	25.20	22.39	17.75	31.86	25.00	29
50	3.71	3.82	3.93	3.53	4.01	12	42	44	44	48	42	44	44	52	45	16	32.11	31.96	27.60	31.86	32.59	27.68	27.47	33.93	30.60	11	29.77	28.02	23.97	29.01	29.14	23.42	27.44	33.77	28.10	20
60	4.11	4.22	4.27	4.25	4.56	10	58	46	44	50	48	52	46	56	50	16	34.38	36.19	33.85	34.97	34.85	28.12	30.88	37.18	33.80	17	32.50	34.09	29.10	33.51	29.83	28.40	28.49	35.58	31.40	13
90	4.10	4.27	4.39	4.25	4.70	13	58	54	54	50	54	56	46	56	54	14	37.64	34.81	37.48	34.35	43.01	30.24	30.13	37.79	35.70	21	37.94	34.64	28.55	35.43	42.00	28.20	29.60	35.88	34.00	23
120	4.33	4.27	4.54	4.25	4.86	13	58	54	54	50	54	56	46	56	54	14	35.43	33.49	37.48	38.05	43.20	31.65	30.13	37.79	35.90	20	31.58	31.10	40.77	35.43	39.53	25.77	29.60	35.88	33.70	24
240	4.47	4.28	4.63	4.30	4.92	13	57	54	54	50	54	70	46	56	55	27	38.31	35.18	44.55	37.64	43.13	56.17	32.67	37.59	40.70	38	29.29	32.84	44.16	35.25	38.92	44.19	32.32	35.33	36.50	21
480	4.92	5.17	5.43	4.95	5.65	13	60	54	54	50	54	70	46	56	56	26	29.71	29.88	40.89	34.16	36.76	46.10	28.40	33.92	35.00	32	29.71	29.88	41.89	33.28	33.75	36.78	28.16	33.82	33.40	25
960	5.78	6.20	5.96	6.47	6.61	13	60	54	54	50	56	70	46	56	56	26	27.77	31.62	38.39	32.53	36.83	39.71	21.06	35.75	33.00	36	26.37	31.35	30.19	30.44	36.01	42.81	16.02	34.04	30.90	48
1440	6.26	6.23	6.52	6.77	7.13	13	60	54	54	50	58	70	46	56	56	25	24.85	32.09	36.02	31.78	36.08	37.31	17.84	36.49	31.60	44	23.74	29.88	30.70	30.47	32.51	29.58	15.36	35.44	28.50	46
2880	7.73	7.49	7.50	8.86	9.37	20	60	54	54	50	58	70	46	56	56	25	27.14	35.99	27.11	31.59	38.21	29.05	22.52	39.98	31.40	28	23.89	34.70	24.52	28.99	35.71	26.58	18.39	38.08	28.90	36
4320	8.44	8.19	8.85	9.38	9.83	17	60	56	54	50	58	74	46	56	57	30	24.92	36.54	24.08	32.80	35.64	26.99	20.90	39.27	30.10	31	23.42	35.43	23.22	32.32	31.84	24.77	17.34	37.36	28.20	39
5760	8.81	8.77	9.29	9.83	10.16	14	60	56	54	50	58	74	46	56	57	30	26.53	36.42	26.96	37.61	36.24	28.19	20.97	39.56	31.60	34	23.05	33.77	24.12	33.26	30.61	25.71	17.74	37.05	28.20	37
7200	9.05	9.26	9.95	10.22	10.99	18	60	56	54	50	58	74	46	56	57	30	27.73	36.68	25.04	39.78	35.63	27.91	20.38	41.42	31.80	36	26.47	35.56	22.97	37.33	31.16	25.65	17.23	39.19	29.40	42
8640	9.30	11.20	10.36	10.77	11.35	18	60	56	54	50	58	74	46	56	57	30	28.00	35.88	24.56	39.20	36.11	28.06	20.65	42.40	31.90	35	26.92	35.11	19.61	33.30	33.93	25.67	16.81	39.57	28.90	42
10080	9.42	11.20	10.36	10.93	11.51	18	60	56	54	50	58	74	46	56	57	30	27.68	36.82	24.54	44.22	35.84	27.82	20.18	42.24	32.40	38	26.61	35.73	19.70	33.59	33.94	25.67	16.64	39.29	28.90	42

Table 4.6: Maximum percent difference between section-wise and average scour hole dimensions for Scour Test 8.

t	ε_{ms} (mm)						r_o (mm)										b_{cl} (mm)										b_m (mm)									
min	S1	S2	S3	S4	ε_m	% Diff.	S1		S2		S3		S4		$\bar{r}_0$	% Diff.	S1		S2		S3		S4		$\bar{b}_{cl}$	% Diff.	S1		S2		S3		S4		$\bar{b}_m$	% Diff.
5	15.61	32.48	24.44	19.81	33.48	53	68	68	124	36	36	74	84	52	68	83	63.27	60.81	120.51	16.74	15.59	69.87	70.35	23.18	55.00	119	60.63	41.27	79.37			64.88	54.38		60.10	32
10	21.05	36.11	31.98	28.26	36.40	42	68	68	124	36	46	78	84	52	70	78	60.96	57.29	116.85	16.73	22.49	67.98	61.68	19.74	53.00	121	58.38	54.87	78.76			55.30	49.77	3.42	50.10	93
15	22.20	37.47	35.66	33.74	38.81	43	68	68	124	36	52	78	84	52	70	77	57.81	54.75	92.50	17.31	21.82	66.01	52.66	18.77	47.70	94	57.81	54.75	78.37	4.52	7.58	53.01	47.52	9.11	39.10	101
20	25.93	37.47	35.66	37.02	38.81	33	68	68	124	36	52	78	84	52	70	77	56.86	51.96	85.61	17.21	20.77	66.27	50.89	20.10	46.20	85	56.80	51.87	78.50	9.41	12.79	53.01	45.99	10.89	39.90	97
30	29.20	39.68	35.99	37.90	40.17	27	68	68	124	36	52	80	84	52	71	76	53.98	50.82	83.01	19.60	22.23	62.23	49.63	23.01	45.60	82	53.91	50.81	75.32	13.66	18.24	53.11	45.74	17.96	41.10	83
40	30.73	39.68	36.07	37.90	40.17	24	68	68	124	38	52	80	84	52	71	75	51.66	49.98	82.28	20.56	24.47	59.49	49.17	24.52	45.30	82	49.84	49.82	75.32	16.49	20.68	53.07	45.74	21.28	41.50	81
50	31.20	39.68	36.07	37.90	40.17	22	68	68	124	38	52	80	84	52	71	75	48.51	50.04	81.89	22.01	25.92	57.79	48.82	25.72	45.10	82	48.29	49.97	75.32	18.38	22.65	53.07	45.74	22.83	42.00	79
60	31.35	39.68	36.07	37.90	40.17	22	68	68	124	38	52	80	84	52	71	75	49.89	49.77	81.79	21.90	25.73	57.22	48.70	27.46	45.30	81	49.10	49.74	75.32	18.38	22.74	53.07	45.74	24.06	42.30	78
90	32.81	39.68	36.07	37.90	40.17	18	68	68	124	40	52	80	84	54	71	74	49.30	49.27	81.27	23.84	29.05	58.65	48.09	30.89	46.30	76	48.01	49.18	75.32	20.46	26.91	53.07	45.74	27.49	43.30	74
120	34.02	39.78	36.12	37.90	40.42	16	68	68	124	40	52	80	84	54	71	74	45.70	49.09	80.92	24.02	29.60	56.48	48.24	31.67	45.70	77	45.65	48.87	75.14	21.71	28.53	53.04	46.10	29.15	43.50	73
240	34.39	39.78	36.12	37.90	40.42	15	68	68	124	42	52	80	98	58	74	68	43.98	48.55	80.66	26.31	31.76	54.83	47.97	34.55	46.10	75	43.27	48.44	75.14	24.25	30.94	53.04	46.10	32.47	44.20	70
480	35.80	39.80	36.12	37.90	40.42	11	68	68	124	42	52	80	98	58	74	68	41.93	48.20	80.26	27.62	31.31	53.56	47.47	35.49	45.70	76	41.52	47.97	75.74	25.85	30.94	53.04	46.10	34.03	44.40	71
960	35.95	39.80	36.67	37.95	40.52	11	68	68	124	44	52	80	98	58	74	68	41.46	47.90	80.01	28.76	31.15	53.14	47.10	35.09	45.60	76	41.46	47.90	75.74	26.75	30.89	52.73	46.07	34.00	44.40	70
1440	35.95	39.80	36.67	37.95	40.52	11	68	68	124	44	52	80	98	58	74	68	41.28	47.99	80.01	29.73	31.15	53.14	47.10	35.09	45.70	75	41.28	47.99	75.74	28.31	30.89	52.73	46.07	34.00	44.60	70
2880	36.81	39.80	37.09	38.21	40.52	9.2	68	68	124	44	52	80	98	60	74	67	41.08	47.54	79.60	29.58	30.94	52.80	46.79	34.77	45.40	75	40.91	47.44	75.74	28.33	30.74	52.48	45.96	33.90	44.40	70
4320	36.93	39.80	37.41	39.03	40.52	8.9	68	68	124	44	52	80	98	60	74	67	41.04	47.64	79.36	29.97	30.84	52.60	46.74	35.08	45.40	75	41.02	47.63	75.74	28.80	30.64	52.30	45.82	34.02	44.50	70
5760	37.14	39.80	37.72	39.03	40.52	8.3	68	68	124	44	52	80	98	60	74	67	40.36	47.43	79.36	29.97	30.85	52.60	46.74	35.14	45.30	75	40.17	47.34	75.74	28.80	30.53	52.12	45.82	34.08	44.30	71
7200	37.14	39.80	37.72	39.03	40.52	8.3	68	68	124	44	52	80	98	60	74	67	40.27	47.34	79.36	29.97	30.85	52.60	46.74	35.14	45.30	75	40.10	47.26	75.74	28.80	30.53	52.12	45.82	34.08	44.30	71
8640	37.35	39.80	37.85	39.03	40.52	7.8	68	68	124	44	52	80	98	60	74	67	39.79	47.19	79.14	29.84	30.72	52.41	46.59	35.37	45.10	75	39.72	47.14	75.74	28.83	30.48	52.04	45.82	34.38	44.30	71
10080	37.42	39.80	38.00	39.03	40.52	7.6	68	68	124	44	52	80	98	60	74	67	40.23	47.46	79.14	29.84	30.72	52.41	46.59	35.37	45.20	75	40.12	47.38	75.74	28.83	30.42	51.96	45.82	34.38	44.30	71
11520	37.42	39.80	38.00	39.03	40.52	7.6	68	68	124	44	52	80	98	60	74	67	39.65	47.24	79.14	29.84	30.72	52.41	46.59	35.37	45.10	75	39.54	47.16	75.74	28.83	30.42	51.96	45.82	34.38	44.20	71
12960	37.42	39.80	38.00	39.03	40.52	7.6	68	68	124	44	52	80	98	60	74	67	39.85	47.14	79.14	29.84	30.72	52.41	46.59	35.37	45.10	75	39.75	47.06	75.74	28.83	30.42	51.96	45.82	34.38	44.20	71
14400	38.02	39.80	38.33	39.03	40.52	6.2	68	68	124	44	52	80	98	60	74	67	39.89	47.29	78.59	29.92	30.46	51.95	46.22	35.02	44.90	75	39.89	47.29	75.74	29.19	30.33	51.78	45.82	34.51	44.30	71
15840	38.02	39.80	38.40	39.03	40.52	6.2	68	68	124	44	52	80	98	60	74	67	40.04	47.17	78.59	30.05	30.77	51.95	46.22	35.02	45.00	75	40.04	47.17	75.74	29.31	30.63	51.74	45.82	34.51	44.40	71
17280	38.02	39.80	38.48	39.16	40.52	6.2	68	68	124	44	52	80	98	60	74	67	39.94	47.05	78.59	30.05	31.07	51.95	46.22	35.18	45.00	75	39.94	47.05	75.74	29.31	30.92	51.70	45.78	34.65	44.40	71
18720	38.02	39.80	38.68	39.16	40.52	6.2	68	68	124	44	52	80	98	60	74	67	39.92	47.22	78.59	30.05	31.07	51.95	46.22	35.28	45.00	75	39.92	47.22	75.74	29.32	30.85	51.58	45.78	34.74	44.40	71
20160	38.09	39.80	38.73	39.19	40.52	6.0	68	68	124	44	52	80	98	60	74	67	40.25	47.24	78.44	30.18	31.09	51.83	46.12	35.43	45.10	74	40.21	47.22	75.74	29.53	30.94	51.56	45.76	34.96	44.50	70

Table 4.7: Maximum percent difference between section-wise and average scour hole dimensions for Scour Test 9.

t	ε_{ms} (mm)						r_o (mm)										b_{cl} (mm)										b_m (mm)									
min	S1	S2	S3	S4	ε_m	% Diff.	S1		S2		S3		S4		$\bar{r}_0$	% Diff.	S1		S2		S3		S4		$\bar{b}_{cl}$	% Diff.	S1		S2		S3		S4		$\bar{b}_m$	% Diff.
5	3.91	15.19	7.59	8.47	16.88	77	42	54	30	76	50	40	40	100	54	85	18.22	37.35	17.46	75.29	47.93	23.32	17.63	98.48	42.00	135	9.06	27.42		71.74	9.34			93.48	42.20	122
10	5.74	19.53	12.08	13.83	21.02	73	44	64	30	76	52	42	40	100	56	79	23.10	43.36	14.21	75.11	47.04	21.25	9.93	98.02	41.50	136	7.86	33.49		69.62	15.04			83.35	41.90	99
15	7.99	23.27	12.88	20.55	26.27	70	46	78	30	76	52	42	40	100	58	72	42.62	49.12	10.59	74.60	45.25	19.54	11.10	95.51	43.50	119	21.65	40.82		64.11	2.85			76.94	41.30	93
20	8.75	24.19	13.80	22.66	29.50	70	46	78	30	76	52	42	40	100	58	72	42.79	50.52	12.37	74.62	45.16	19.50	10.82	95.35	43.90	117	40.70	38.60		61.82	5.21			78.96	45.10	88
30	9.78	29.29	14.79	22.77	30.77	68	46	78	30	76	52	46	40	100	59	71	42.20	60.49	13.13	74.33	44.65	18.00	11.21	94.82	44.90	111	30.11	49.93		60.12	6.61			76.59	44.70	85
40	10.00	29.33	14.79	23.28	30.77	68	46	78	30	76	52	46	40	100	59	71	42.30	60.75	13.58	74.47	44.56	17.86	11.72	94.68	45.00	111	41.11	51.60		60.10	10.05	3.87		77.48	40.70	91
50	12.12	29.63	15.98	23.28	30.78	61	46	78	30	76	52	46	40	100	59	71	42.24	59.31	12.85	74.35	44.22	18.37	11.16	93.95	44.60	111	40.31	43.76		60.24	11.10	3.12		77.56	39.30	97
60	12.52	29.79	15.98	23.80	31.16	60	46	82	30	76	52	46	40	100	59	70	42.37	71.42	13.08	74.33	43.64	29.00	11.52	93.89	47.40	98	34.68	68.28		60.21	14.99	14.85		77.45	45.10	72
90	12.94	29.97	16.24	23.80	31.18	59	46	82	30	78	54	46	40	100	60	68	42.18	70.96	14.75	74.64	44.00	28.03	11.83	93.24	47.50	97	40.77	68.70		60.33	42.76	19.83		77.54	51.70	62
120	13.41	30.14	16.87	27.65	33.77	60	46	82	30	78	54	46	40	100	60	68	42.04	70.55	15.17	74.41	43.84	27.55	24.32	93.16	48.90	91	40.59	68.76		60.44	42.55	20.78		75.98	51.50	60
240	17.89	30.14	18.32	32.87	33.90	47	46	82	30	80	54	46	40	100	60	67	39.85	72.93	14.87	72.89	43.16	24.71	21.17	85.72	46.90	83	38.58	71.69		60.44	42.33	19.28		73.35	50.90	62
480	18.37	30.81	21.75	33.33	34.41	47	46	82	30	80	54	46	40	104	60	73	39.09	72.17	14.20	72.31	42.64	23.09	18.95	83.52	45.70	83	38.50	71.76	3.26	60.69	40.92	17.39		73.50	43.70	68
960	19.34	31.29	22.55	33.33	34.62	44	48	82	30	80	56	46	40	104	61	71	39.06	71.67	14.19	72.69	42.91	21.96	18.81	84.81	45.80	85	38.47	71.14	4.67	60.98	41.89	17.16	4.35	74.54	39.20	90
1440	19.89	31.62	24.70	33.67	34.74	43	48	82	30	80	56	46	40	104	61	71	38.76	71.37	14.81	72.28	42.74	22.67	18.10	84.10	45.60	84	38.36	71.04	6.37	60.96	41.22	17.85	5.42	74.42	39.50	89
2880	20.04	31.62	27.12	33.67	35.05	43	48	82	30	80	56	46	40	104	61	71	38.12	71.67	17.54	72.07	42.59	22.30	18.19	83.31	45.70	82	37.96	71.54	8.06	61.05	40.42	17.31	8.19	74.42	39.90	87
4320	23.19	31.73	27.26	34.10	35.33	34	48	82	30	80	58	46	40	104	61	71	38.61	71.75	17.58	71.91	42.53	24.55	17.75	82.85	45.90	80	37.43	70.67	9.21	61.05	40.51	19.70	8.08	74.29	40.10	85
5760	23.19	31.73	27.41	34.16	35.48	35	48	82	30	80	58	46	40	104	61	71	38.16	71.59	17.75	71.53	42.33	24.39	20.85	81.92	46.10	78	37.42	70.86	11.43	61.05	38.92	20.70	10.18	74.30	40.60	83
7200	23.79	31.75	27.52	34.55	35.64	33	48	82	30	80	58	46	40	104	61	71	38.11	71.35	17.80	71.42	42.38	23.95	20.98	81.91	46.00	78	37.37	70.72	11.75	61.14	40.62	20.87	9.94	74.36	40.80	82
8640	23.81	32.24	28.49	34.79	35.64	33	48	82	30	80	58	46	40	104	61	71	38.17	71.13	17.68	71.21	42.23	23.53	20.51	81.45	45.70	78	37.72	70.78	11.67	61.12	40.44	20.47	11.01	74.49	41.00	82
10080	24.15	31.94	28.70	34.79	35.74	32	48	82	30	82	58	46	40	104	61	70	37.83	72.59	17.87	70.85	42.25	24.55	20.47	81.02	45.90	76	37.38	72.33	12.07	61.04	38.84	21.15	11.37	74.49	41.10	81
11520	23.90	32.34	28.70	34.79	35.98	34	48	82	30	82	58	46	40	106	62	72	37.38	70.68	17.81	71.14	42.26	24.45	20.39	81.58	45.70	79	37.11	70.51	11.98	61.55	38.93	21.15	11.37	74.90	40.90	83
12960	24.47	32.36	28.72	34.79	36.10	32	48	82	30	82	58	46	40	106	62	72	37.64	70.58	17.72	71.75	42.25	24.29	20.28	81.99	45.80	79	37.22	70.15	12.43	61.54	40.56	21.14	11.37	75.22	41.20	83
14400	24.59	32.37	28.72	34.79	36.10	32	48	82	30	82	58	46	40	106	62	72	37.58	70.54	17.72	71.75	42.25	24.26	20.26	81.95	45.80	79	37.00	70.24	12.47	61.54	40.56	21.14	11.37	75.30	41.20	83
15840	24.95	32.62	28.72	35.09	36.57	32	48	82	30	82	58	46	40	108	62	75	37.75	71.10	17.50	71.55	42.18	23.94	20.00	82.15	45.80	80	37.29	70.85	12.52	61.66	40.63	21.14	11.54	75.55	41.40	83
17280	24.96	32.78	28.97	35.09	36.57	32	48	82	30	82	58	46	40	108	62	75	37.70	70.95	17.50	71.55	42.26	23.94	20.00	82.38	45.80	80	37.20	70.68	12.43	61.61	40.61	21.01	11.54	75.57	41.30	83
20160	24.96	32.79	28.97	35.24	36.57	32	48	82	30	82	58	46	40	108	62	75	37.84	70.31	17.49	71.80	42.36	23.92	19.98	82.36	45.80	80	37.30	69.98	12.43	61.98	40.68	21.01	11.43	75.50	41.30	83

Table 4.8: Maximum percent difference between section-wise and average scour hole dimensions for Scour Test 10.

t	ε_{ms} (mm)						r_o (mm)									b_{cl} (mm)										b_m (mm)									
min	S1	S2	S3	S4	ε_m	% Diff.	S1		S2		S3		S4		$\bar{r}_0$	% Diff.	S1		S2		S3		S4		$\bar{b}_{cl}$	% Diff.	S1		S2		S3		S4		$\bar{b}_m$	% Diff.
5	4.43	14.13	17.40	3.25	17.92	82	20	58	76	28	16	58	50	36	43	78	10.47	51.26	73.09	16.10	9.42	55.19	35.42	19.08	33.80	117	6.65	50.26	50.29	40.00		23.77	35.42	19.08	32.20	79
10	5.66	16.49	17.46	6.26	20.87	73	26	60	76	28	24	58	58	36	46	66	11.93	49.78	71.51	12.71	10.39	54.05	50.56	19.03	35.00	104	10.77	47.59	49.44	40.00		14.45	48.68	15.20	32.30	67
15	6.50	17.53	17.61	7.19	21.72	70	28	60	76	28	24	58	58	38	46	64	12.95	49.00	69.93	12.78	10.37	53.05	48.50	18.48	34.40	103	12.57	48.91	49.08	40.00		12.48	47.33	16.63	32.40	62
20	7.14	17.80	21.25	8.57	21.99	68	30	60	76	30	28	58	58	38	47	61	14.38	49.03	70.68	13.36	11.03	53.09	48.30	18.84	34.80	103	13.64	48.60	49.11	40.00		13.28	45.77	16.16	32.40	59
30	8.05	17.84	21.51	10.82	22.29	64	34	60	76	30	28	58	60	38	48	58	15.43	44.66	69.00	13.32	11.53	51.89	47.12	17.76	33.80	104	15.31	44.33	49.27	40.00		13.86	45.08	11.26	31.30	64
40	8.52	18.35	21.51	10.91	22.52	62	34	62	76	32	30	58	60	38	49	56	18.13	46.17	68.37	14.31	11.60	51.86	47.03	18.37	34.50	98	17.53	45.38	49.07	40.00		13.06	45.05	12.54	31.80	61
50	8.87	18.35	21.91	10.91	22.54	61	34	64	76	34	30	58	60	38	49	54	17.21	48.31	68.19	14.30	13.23	51.33	46.25	18.28	34.60	97	17.21	48.30	49.39	40.00		13.50	45.05	13.59	32.40	58
60	9.27	18.62	21.91	11.61	22.80	59	34	64	76	34	30	58	60	38	49	54	18.64	48.20	67.97	15.38	13.98	52.44	46.96	18.38	35.20	93	18.29	47.98	49.82	40.00		9.10	45.08	13.98	32.00	72
120	9.76	18.90	22.51	11.81	23.05	58	34	64	76	34	30	58	60	44	50	52	17.80	48.71	67.92	16.10	14.06	52.06	46.94	18.71	35.30	93	17.80	48.71	49.84	40.00		8.86	45.35	16.21	32.40	73
240	10.27	20.32	22.51	12.54	23.15	56	50	64	78	34	30	58	60	44	52	49	24.81	46.42	67.86	15.69	14.81	51.33	46.71	20.07	36.00	89	24.62	45.62	49.09	40.00		4.07	45.09	16.37	32.10	87
480	11.88	20.64	22.73	12.78	23.42	49	50	64	78	42	30	58	60	44	53	47	23.98	45.81	65.76	19.48	16.59	48.22	45.68	28.26	36.70	79	23.42	45.36	49.03	2.94		6.28	45.05	27.08	28.40	90
960	13.95	20.86	22.78	13.09	23.82	45	50	64	78	42	30	58	60	44	53	47	23.85	45.83	64.58	20.02	16.90	51.01	45.68	28.34	37.00	74	21.32	44.25	49.14	5.29	2.75	9.42	45.08	27.24	25.60	92
1440	14.15	21.13	22.78	14.60	23.98	41	50	64	78	42	30	58	60	44	53	47	23.42	45.44	60.90	19.53	16.44	50.20	45.60	27.75	36.20	68	22.17	44.16	49.04	5.56	5.20	15.48	44.61	26.22	26.60	85
2880	14.25	21.40	22.96	14.84	24.31	41	50	64	78	42	30	58	62	44	54	46	24.79	44.87	60.27	18.63	15.68	48.36	45.15	27.38	35.60	69	23.95	43.99	48.98	6.77	6.73	17.42	44.49	26.05	27.30	79
4320	14.26	21.40	22.96	14.84	24.31	41	50	64	78	42	30	58	62	44	54	46	24.39	45.41	60.27	18.63	16.38	48.44	45.15	27.38	35.80	69	23.00	44.27	48.98	7.49	7.06	18.93	44.49	26.05	27.50	78
5760	15.71	21.58	22.96	14.84	24.31	39	50	64	78	42	30	58	62	44	54	46	24.26	45.04	59.91	22.96	16.48	47.82	45.03	27.15	36.10	66	21.12	43.43	48.91	8.00	8.38	20.12	44.49	26.05	27.60	78
7200	15.64	21.58	23.28	14.84	24.31	39	50	64	78	42	30	58	62	44	54	46	24.99	45.07	59.88	22.94	16.75	49.26	45.02	27.12	36.40	65	21.42	43.57	48.91	9.27	8.14	19.73	44.49	26.05	27.70	77
8640	15.70	21.58	23.28	14.93	24.31	39	50	64	78	42	34	58	62	44	54	44	32.82	45.19	59.82	23.16	20.38	50.11	44.99	27.62	38.00	57	28.54	43.31	48.91	9.62	9.60	20.50	44.45	26.73	29.00	69
10080	15.94	21.61	23.28	15.50	24.31	36	50	64	78	42	34	58	64	44	54	44	32.07	45.08	59.29	23.12	20.59	48.64	44.72	27.19	37.60	58	29.05	43.55	49.11	11.54	10.33	21.13	44.15	26.26	29.40	67
11520	16.10	21.62	23.28	15.50	24.31	36	50	64	78	42	34	58	70	44	55	42	32.18	45.11	59.40	23.18	20.57	48.57	44.71	27.17	37.60	58	28.55	43.76	49.10	11.57	10.54	21.17	44.15	26.27	29.40	67
12960	16.17	21.85	23.28	15.50	24.31	36	50	64	78	42	34	58	70	44	55	42	31.70	45.81	59.14	23.12	20.63	48.01	44.59	27.58	37.60	57	28.94	44.29	48.98	12.00	11.24	23.09	44.15	26.58	29.90	64
14400	16.13	21.88	23.28	15.54	24.31	36	50	64	78	42	34	58	70	44	55	42	31.43	47.77	59.14	23.43	20.70	48.01	44.59	27.58	37.80	56	25.99	44.76	48.97	11.95	12.82	23.09	44.13	26.53	29.80	64
15840	16.15	21.88	23.28	15.54	24.31	36	50	64	78	42	34	58	70	44	55	42	31.74	45.61	59.14	23.43	20.70	48.01	44.59	27.58	37.60	57	27.79	44.13	48.97	11.95	12.82	23.09	44.13	26.53	29.90	64
17280	16.15	21.88	23.28	15.54	24.31	36	50	64	78	42	34	58	70	44	55	42	31.45	45.58	59.11	23.41	20.68	47.94	44.58	27.55	37.50	58	25.89	43.95	48.97	11.95	12.82	23.09	44.13	26.53	29.70	65
18720	16.09	21.88	23.28	15.54	24.31	36	50	64	78	42	34	58	70	44	55	42	30.31	45.37	59.11	23.41	20.68	47.94	44.58	27.56	37.40	58	23.87	43.77	48.97	11.95	12.82	23.09	44.13	26.54		67
20160	16.09	21.88	23.28	15.54	24.31	36	50	64	78	42	34	58	70	44	55	42	31.17	47.09	59.11	23.41	20.68	47.96	44.58	27.74	37.70	57	28.01	44.56	48.97	11.95	12.82	23.44	44.13	26.63	30.10	63
21600	16.12	21.88	23.28	15.54	24.31	36	50	64	78	42	34	58	70	44	55	42	30.43	45.52	59.11	23.41	20.68	47.96	44.58	27.74	37.40	58	26.98	43.88	48.97	11.95	12.82	23.44	44.13	26.63		64
23040	16.13	21.75	23.28	15.54	24.31	36	50	64	78	42	34	58	70	44	55	42	31.98	45.92	58.59	23.54	20.68	47.96	44.58	27.74	37.60	56	29.69	44.27	48.63	12.66	12.82	23.44	44.13	26.63		61

Table 4.9. Time to reach equilibrium for all scour tests for the different characteristic dimensions of the scour hole.

Dimensions	Time to Equilibrium (h)							
	ST1	ST3	ST4	ST5	ST6	ST8	ST9	ST10
$\zeta^{1/3}$	96	-	-	48	144	16	264	168
ε_{cl}	4	-	-	48	-	240	264	216
ε_{m}	120	-	-	48	-	16	264	48
ε_{ms}	-	-	-	48	-	312	288	216
$\bar{\bar{r}}_{o}$	48	-	48	16	72	48	264	192
$\bar{\bar{b}}_{cl}$	48	-	-	72	-	144	216	168
$\bar{\bar{b}}_{m}$	48	-	-	72	-	96	216	216
Longest Time to Equilibrium	-	-	-	72	-	312	288	216

Table 4.10. Time to reach equilibrium for all scour tests for the maximum section-wise scour depths for different sections.

Scour Tests	Time to Equilibrium (h)			
	S1	S2	S3	S4
ST1	0.83	96	4	-
ST3	-	-	-	-
ST4	-	-	-	-
ST5	48	48	48	48
ST6	-	-	-	-
ST8	240	8	312	72
ST9	264	288	288	264
ST10	192	216	120	168

Table 4.11. Critical time to obtain the dimensionless equilibrium shapes from the visual comparison of the dimensionless scour hole profiles.

Scour Tests	Sections	Time to Equilibrium Shape (h)	Longest Time to Equilibrium Shape, t^*_∞ (h)	Time to Equilibrium, t_∞ (h)	t^*_∞/t_∞ (%)
ST5	S1	72	72	72	100
	S2	16			
	S3	24			
	S4	72			
ST8	S1	8	48	312	15
	S2	48			
	S3	24			
	S4	48			
ST9	S1	144	144	288	50
	S2	144			
	S3	96			
	S4	120			
ST10	S1	144	192	216	89
	S2	168			
	S3	168			
	S4	192			

Table 4.12. Maximum errors in measured and derived quantities.

Quantities	Maximum Error (%)
d	±1.7
H	±1.2
Q	±3.8
U_0	±0.4
A_0	±3.4
ε_{cl}	±0.1
ε_m	±0.1
ε_{ms}	±0.1
r	±3.1
b_{cl}	±3.1
b_m	±3.1
ξ	±6.3

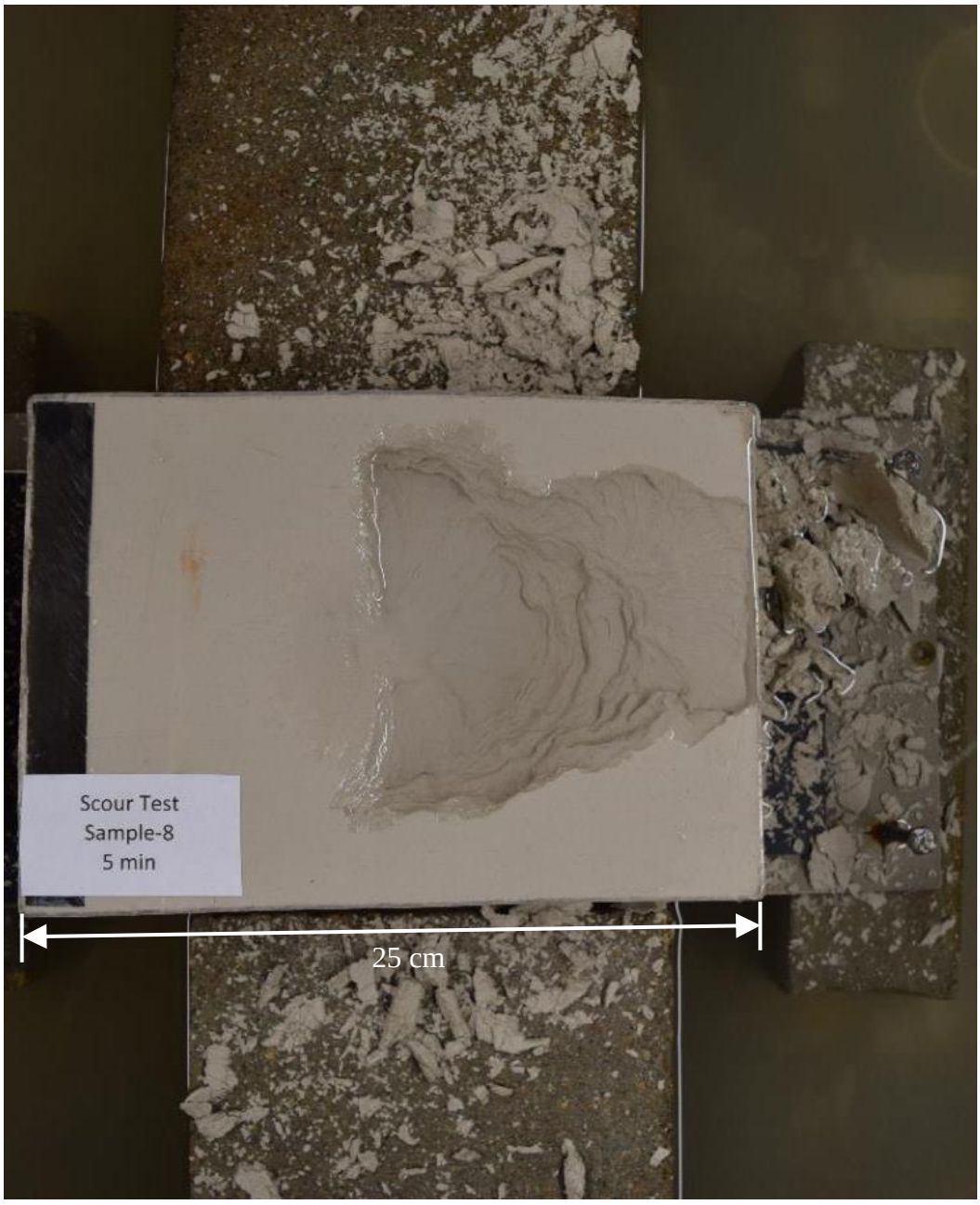

Figure 4.1: Typical soil chunks eroded during Scour Test-8 after 5 min of scouring (M370 clay, U_0=10.69 m/s, d=7.76 mm, H=85 mm, t_d=336 h).

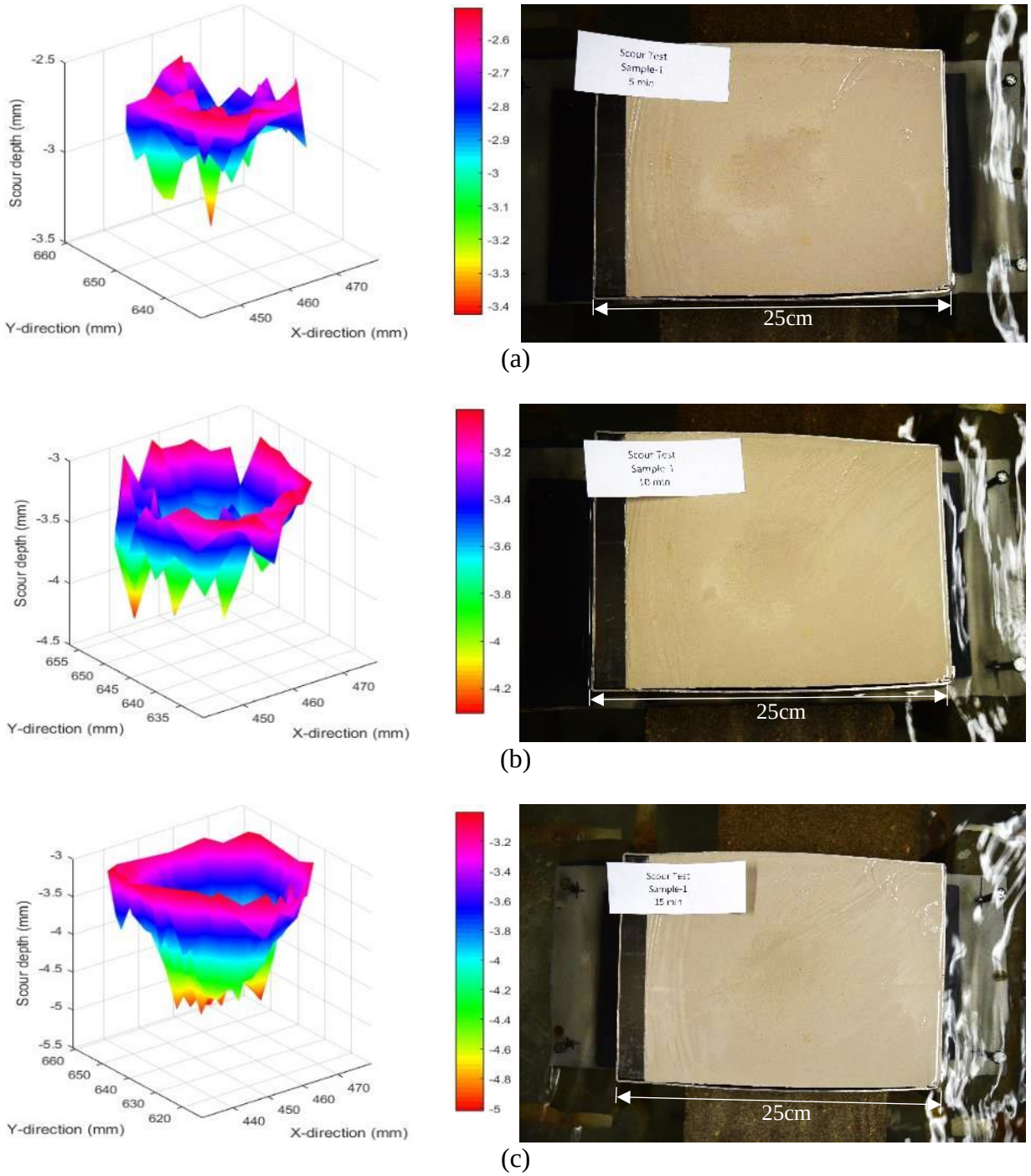

Figure 4.2: Three-dimensional scour hole shape and photo of the sample in plan view for Scour Test 1 (Buffstone clay, U_0=8.6 m/s, d=7.76 mm, H=85 mm, and t_d=144 h) after a test duration of (a) 5 min, (b) 10 min, (c) 15 min, (d) 20 min, (e) 30 min, (f) 40 min, (g) 50 min, (h) 1 h, (i) 1.5 h, (j) 2 h, (k) 4 h, (l) 8 h, (m) 16 h, (n) 24 h, (o) 48 h, (p) 72 h, (q) 96 h, (r) 120 h, and (s) 144 h.

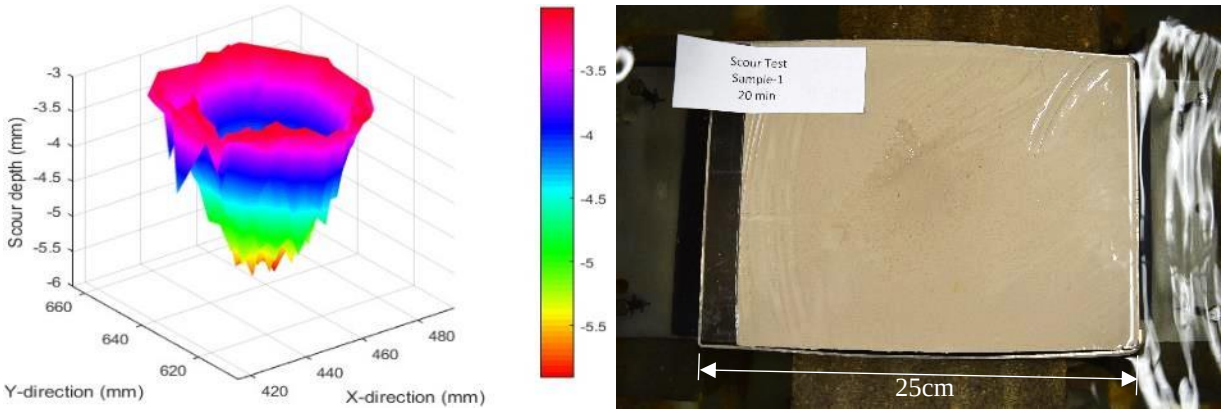

(d)

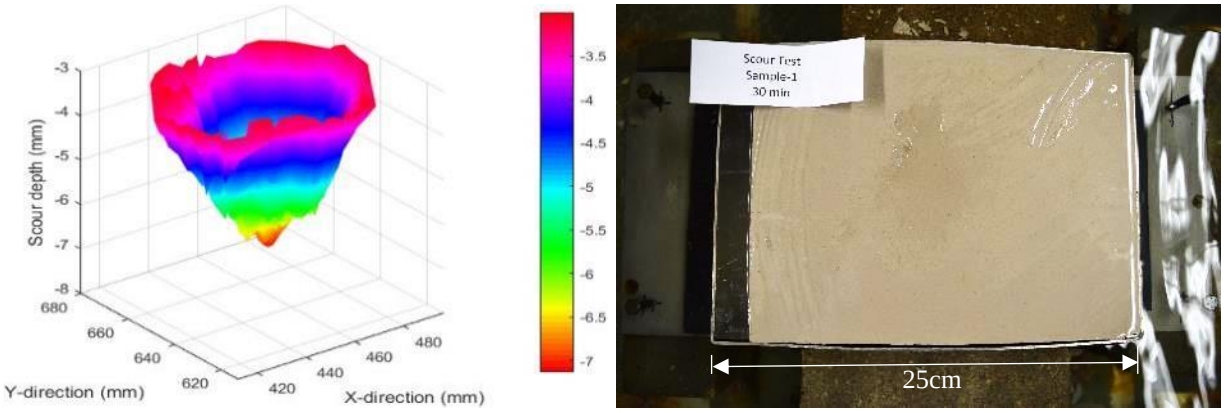

(e)

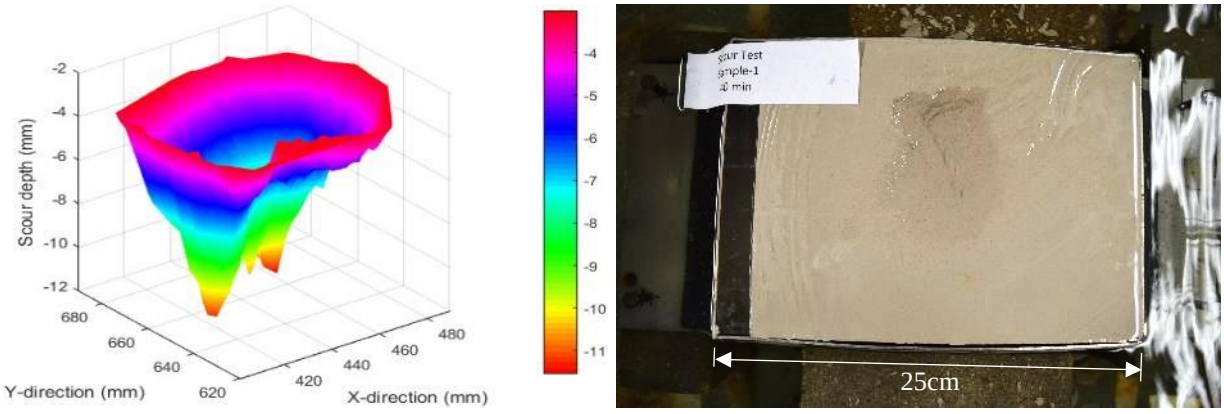

(f)

Figure 4.2: cont'd.

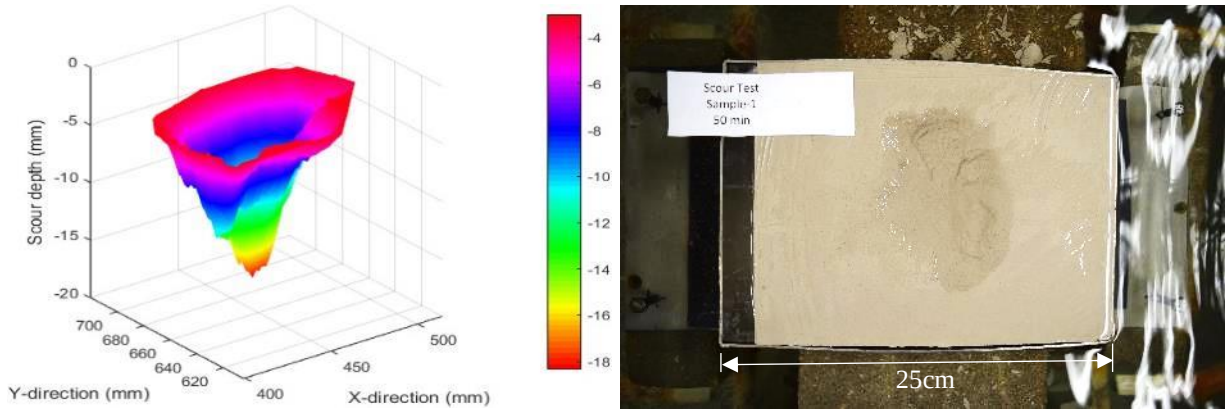

(g)

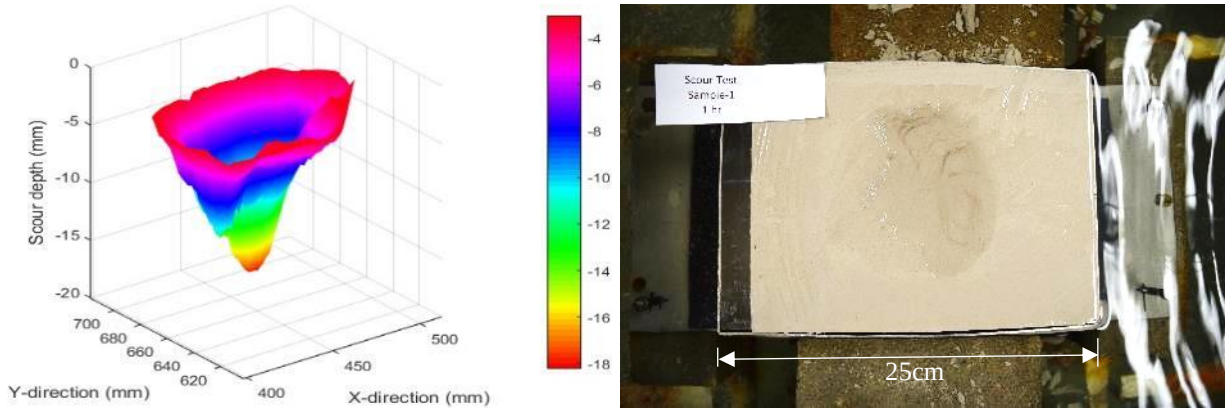

(h)

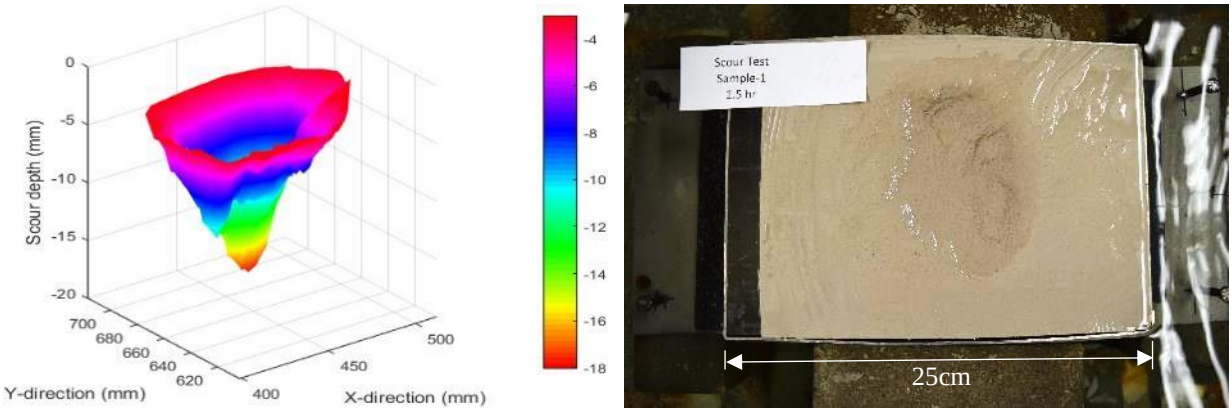

(i)

Figure 4.2: cont'd.

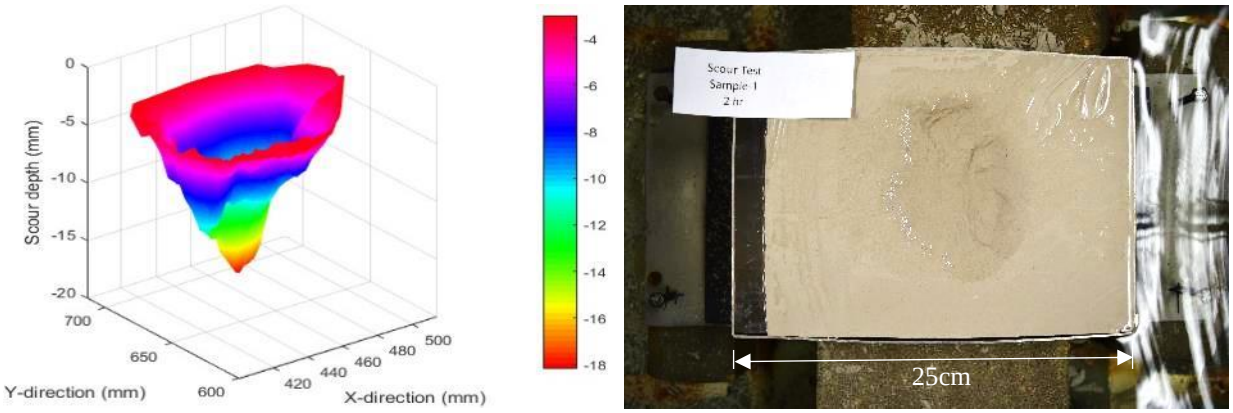

(j)

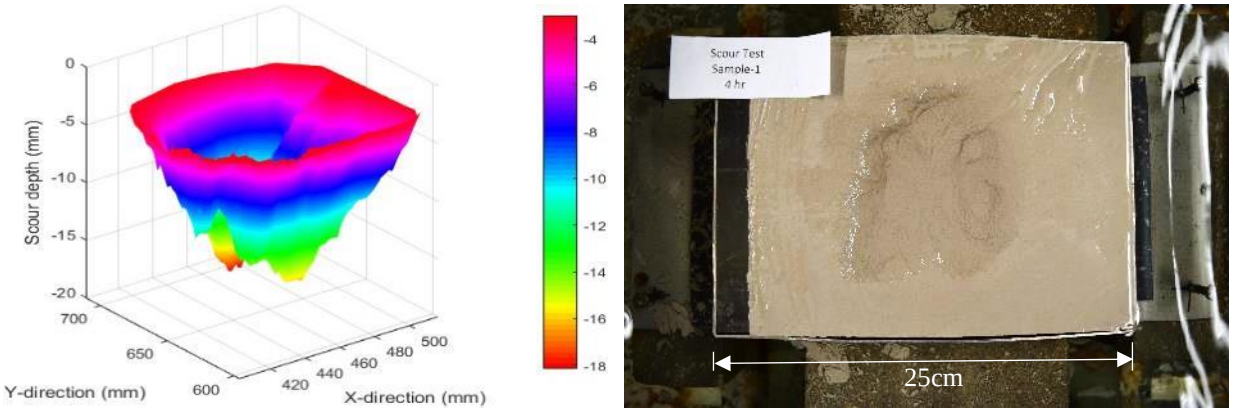

(k)

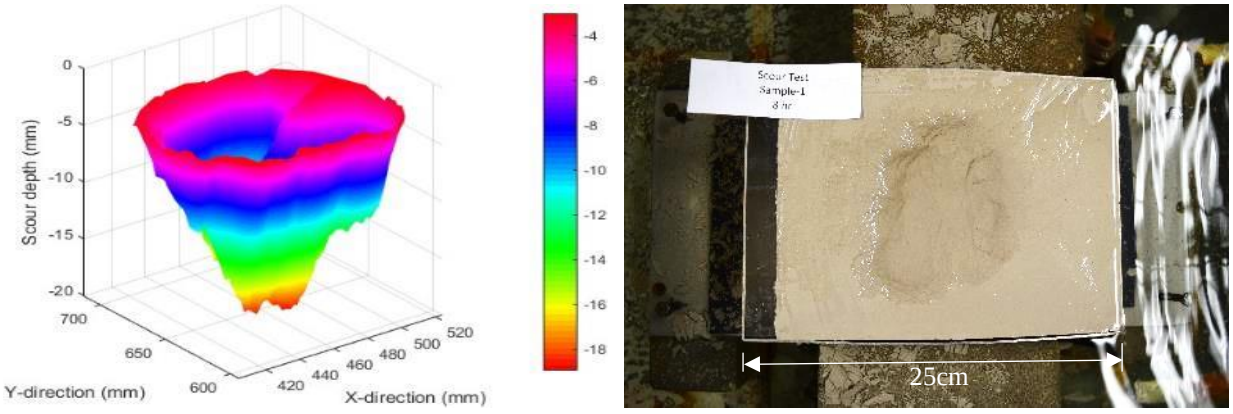

(l)

Figure 4.2: cont'd.

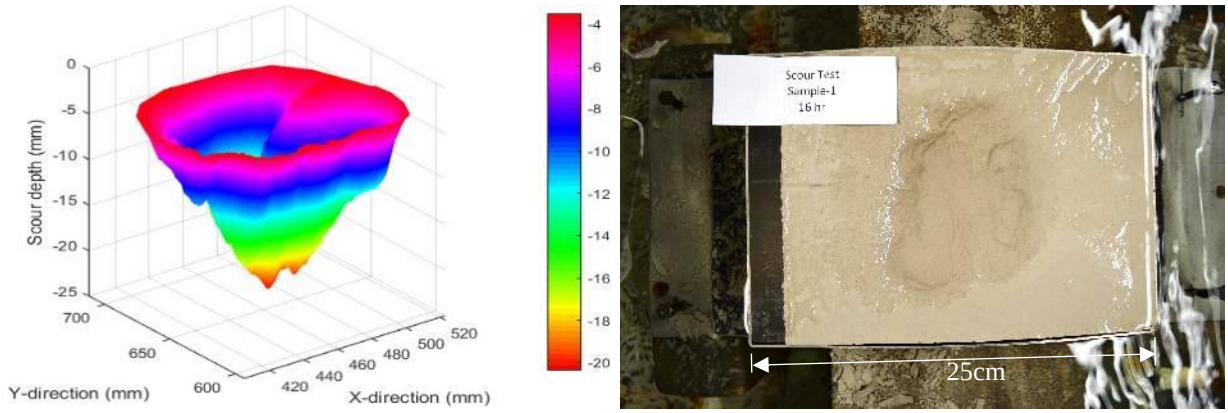

(m)

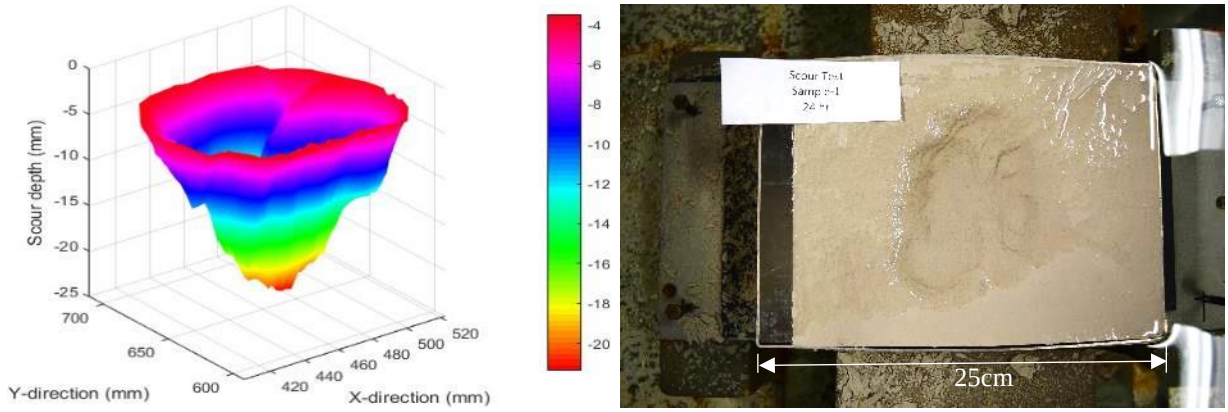

(n)

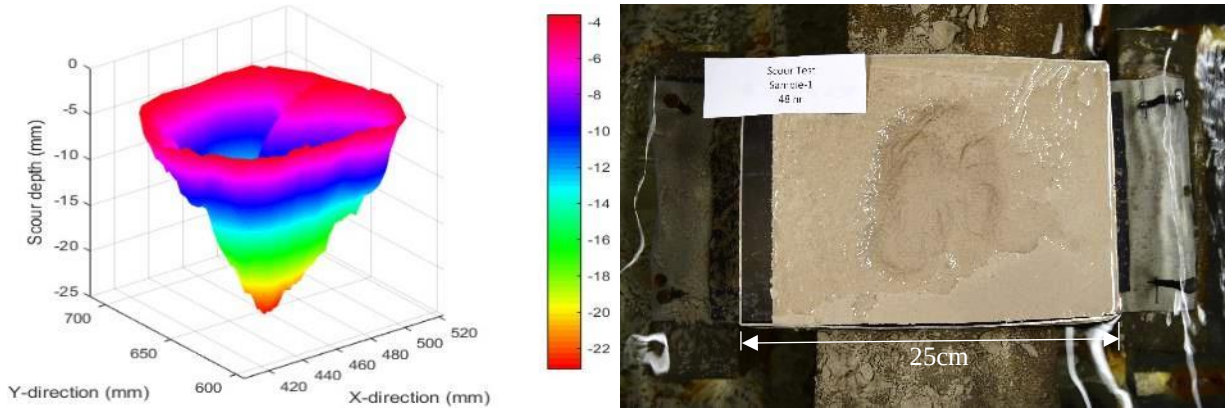

(o)

Figure 4.2: cont'd.

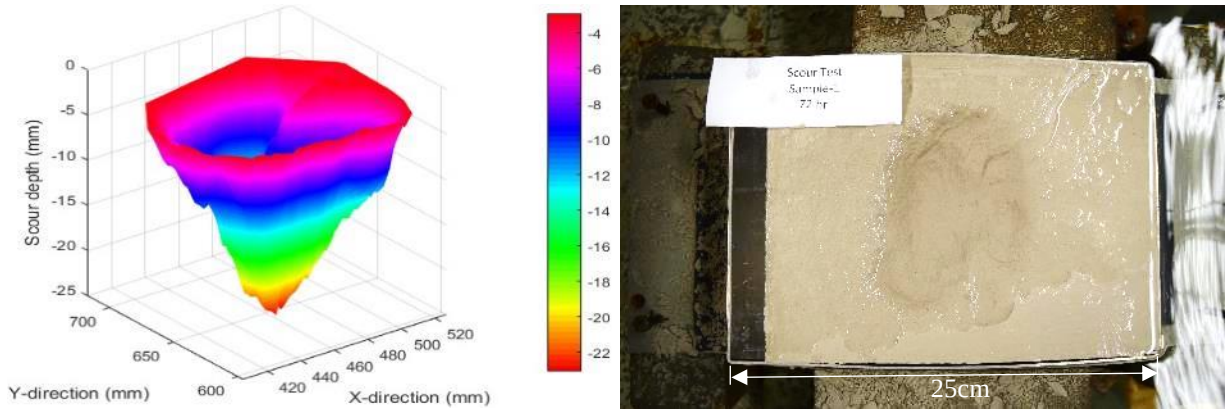

(p)

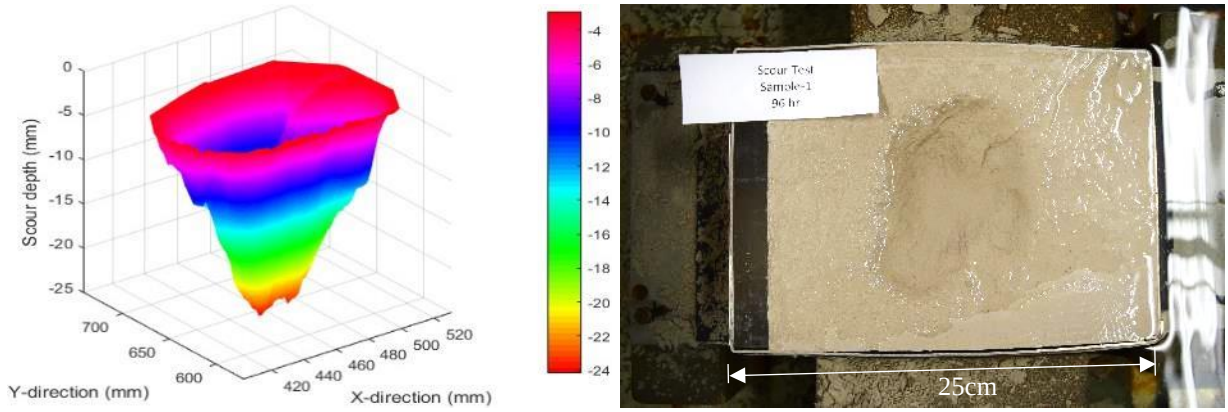

(q)

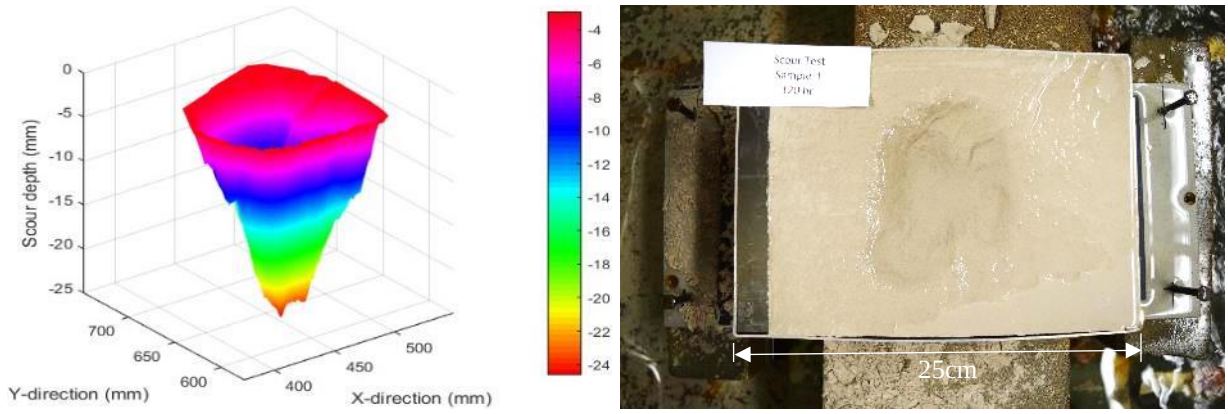

(r)

Figure 4.2: cont'd.

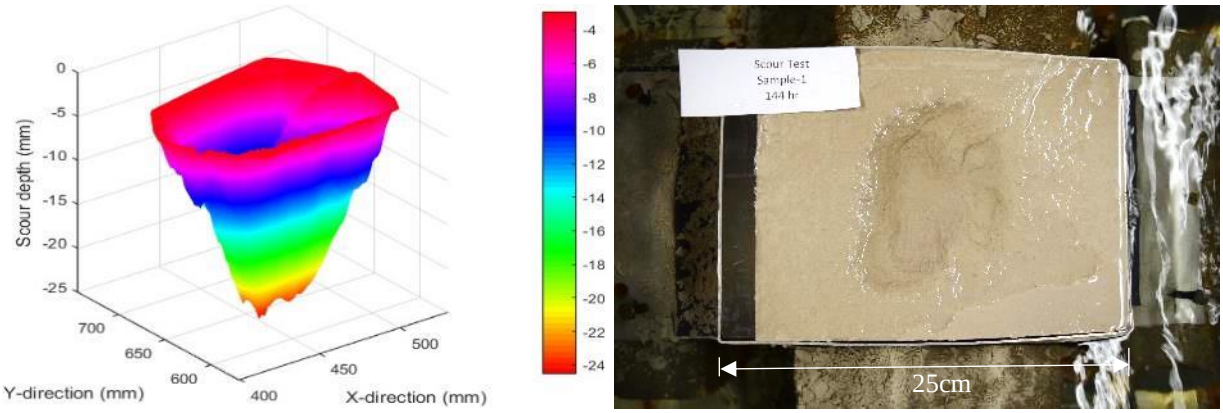

(s)

Figure 4.2: cont'd.

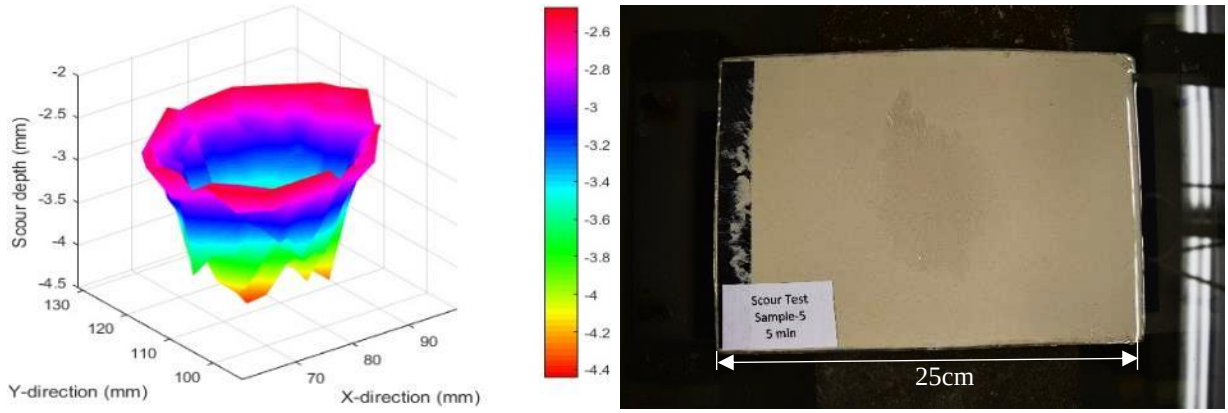

(a)

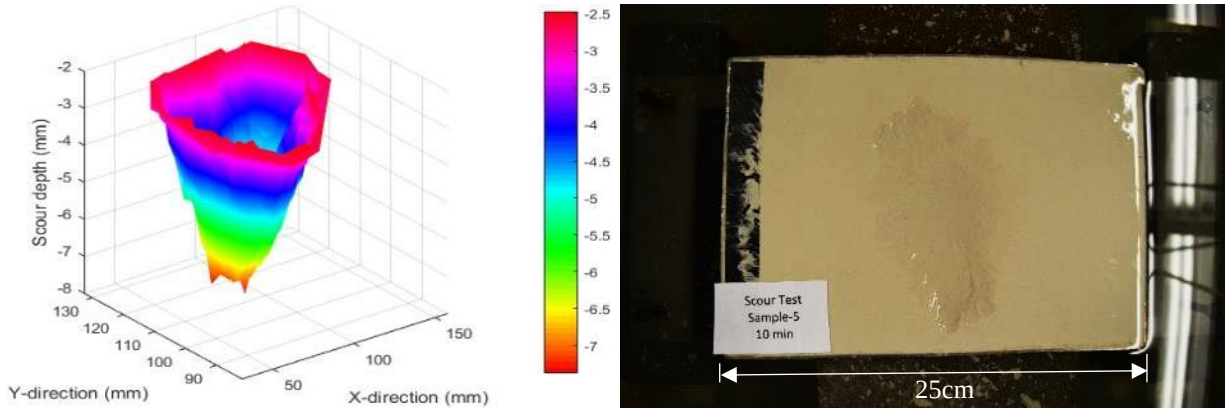

(b)

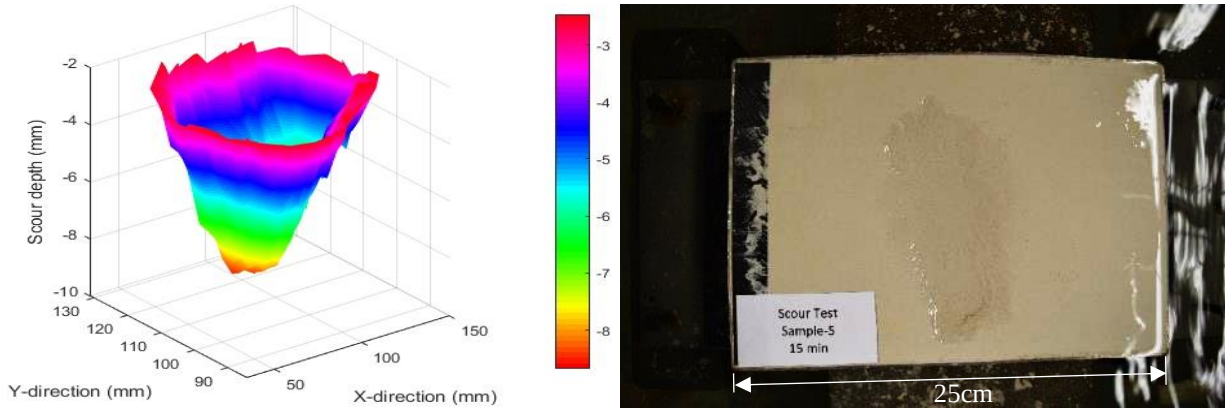

(c)

Figure 4.3: Three-dimensional scour hole shape and photo of the sample in plan view for Scour Test 5 (P300 clay, U_0=8.3 m/s, d=7.76 mm, H=85 mm, and t_d=168 h) after a test duration of (a) 5 min, (b) 10 min, (c) 15 min, (d) 20 min, (e) 30 min, (f) 40 min, (g) 50 min, (h) 1 h, (i) 1.5 h, (j) 2 h, (k) 4 h, (l) 8 h, (m) 16 h, (n) 24 h, (o) 48 h, (p) 72 h, (q) 96 h, (r) 120 h, (s) 144 h, and (t) 168 h.

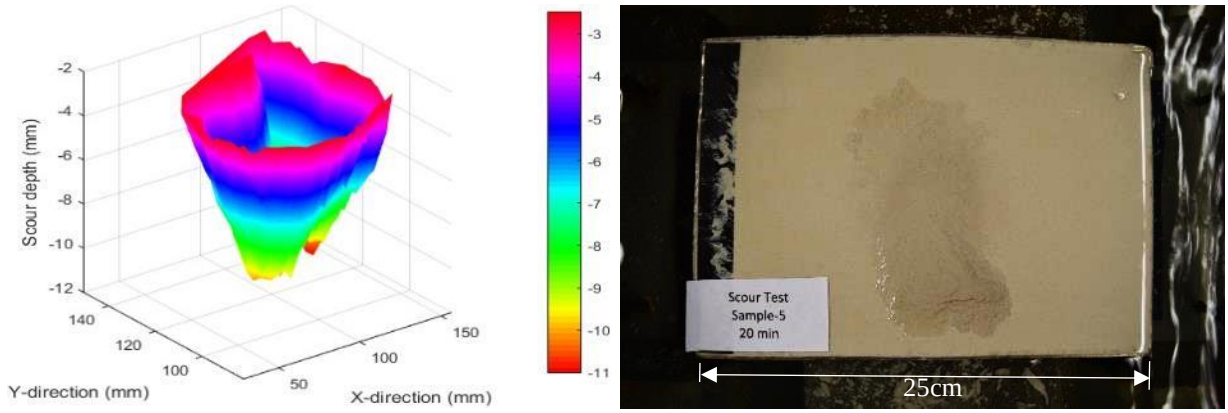

(d)

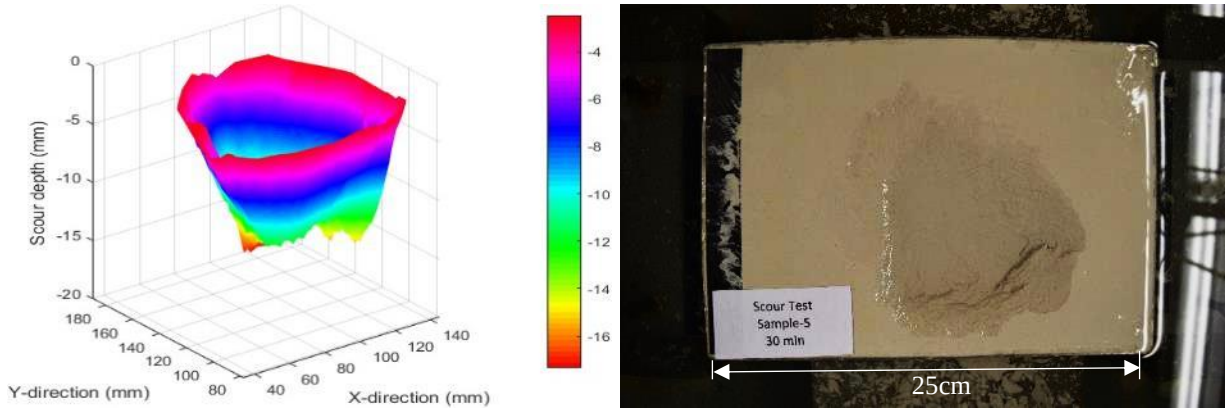

(e)

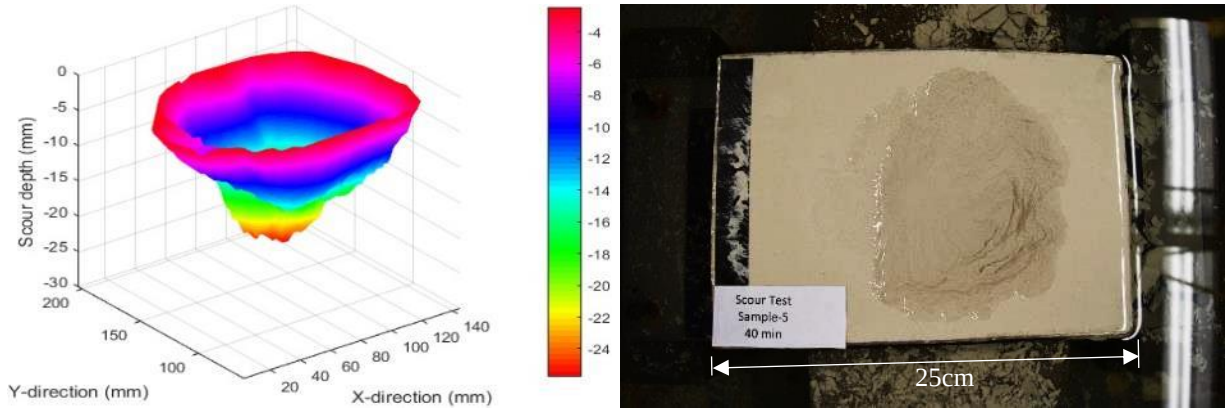

(f)

Figure 4.3: cont'd.

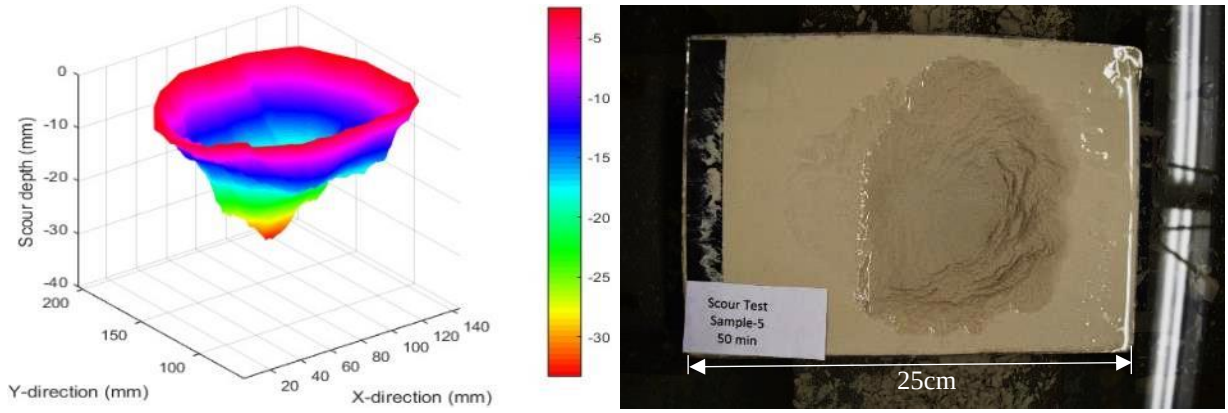

(g)

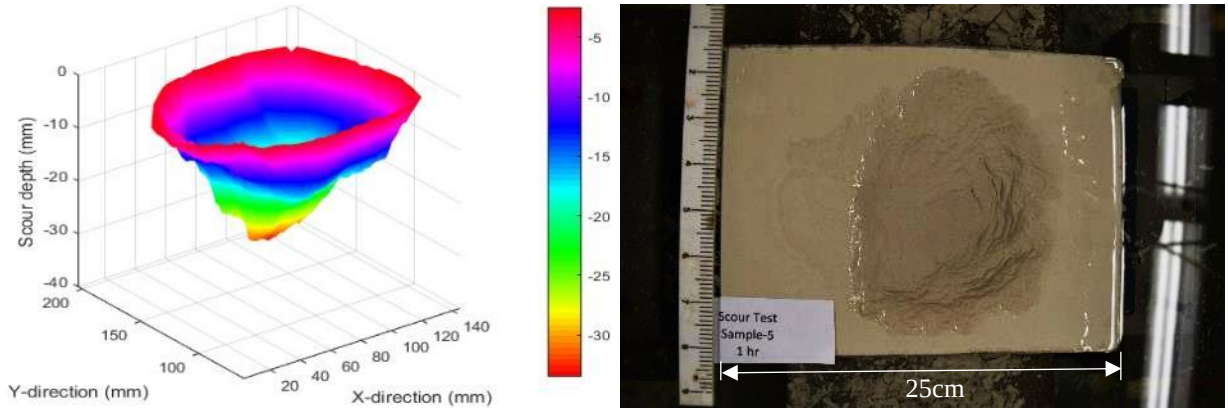

(h)

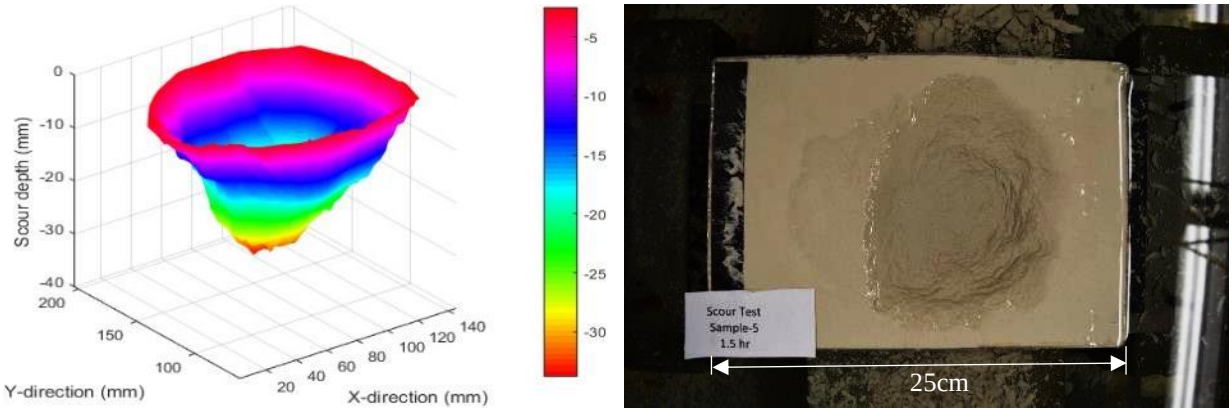

(i)

Figure 4.3: cont'd.

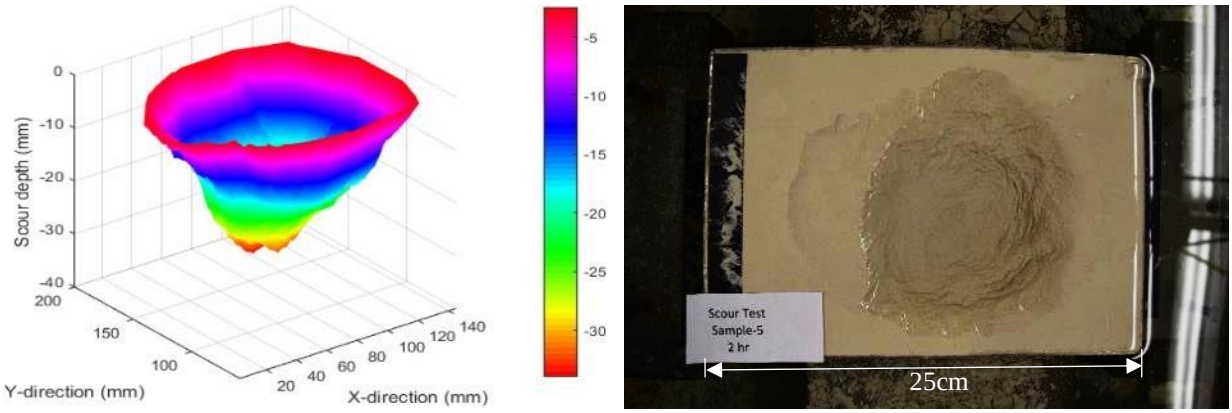

(j)

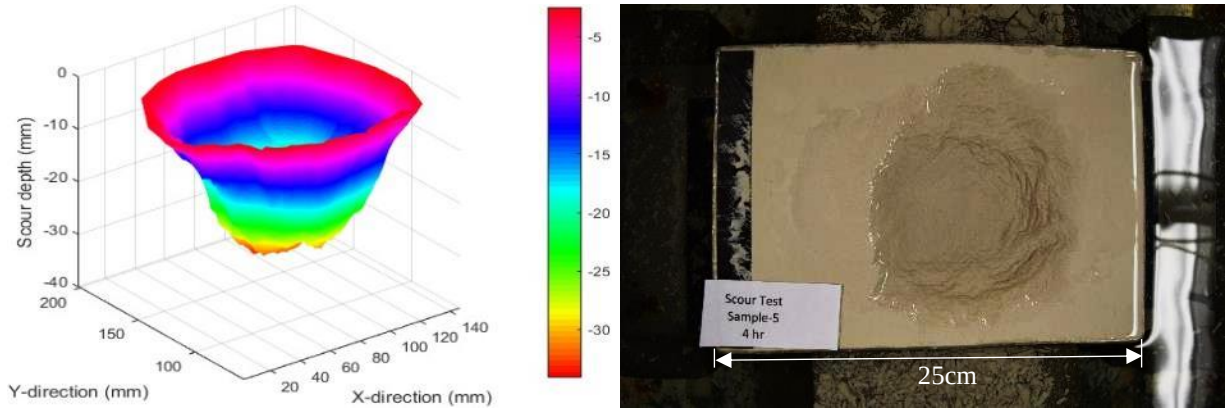

(k)

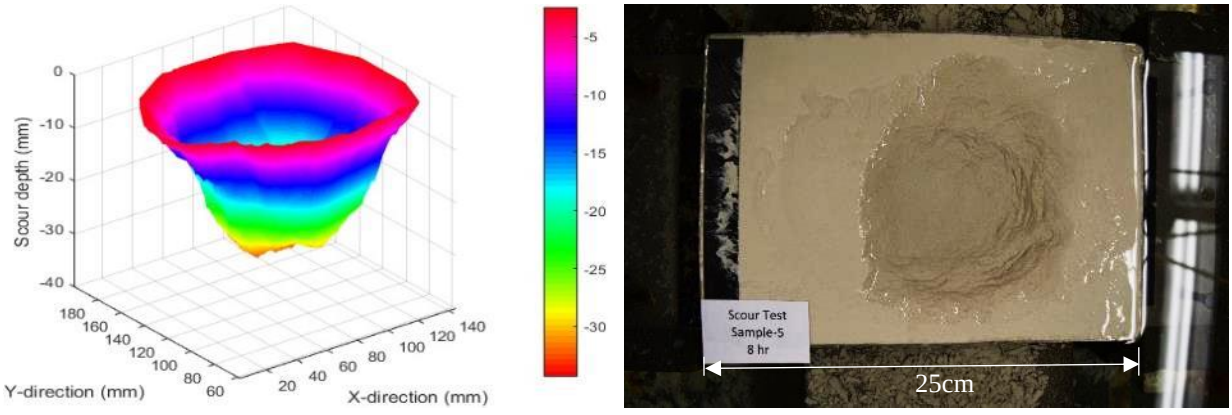

(l)

Figure 4.3: cont'd.

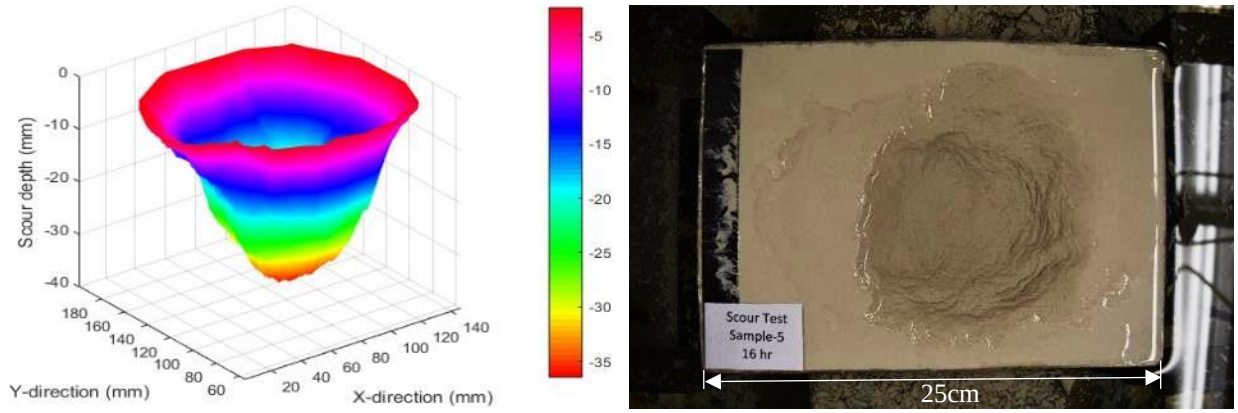

(m)

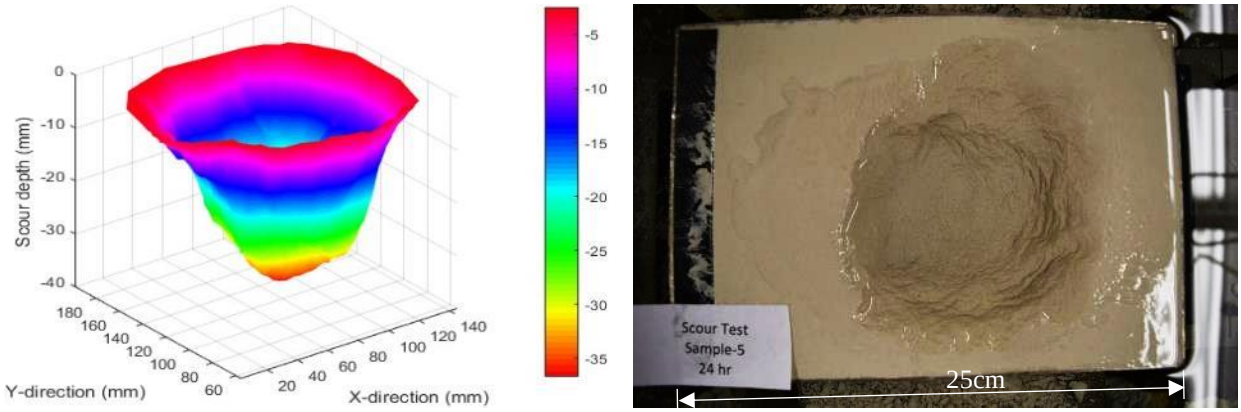

(n)

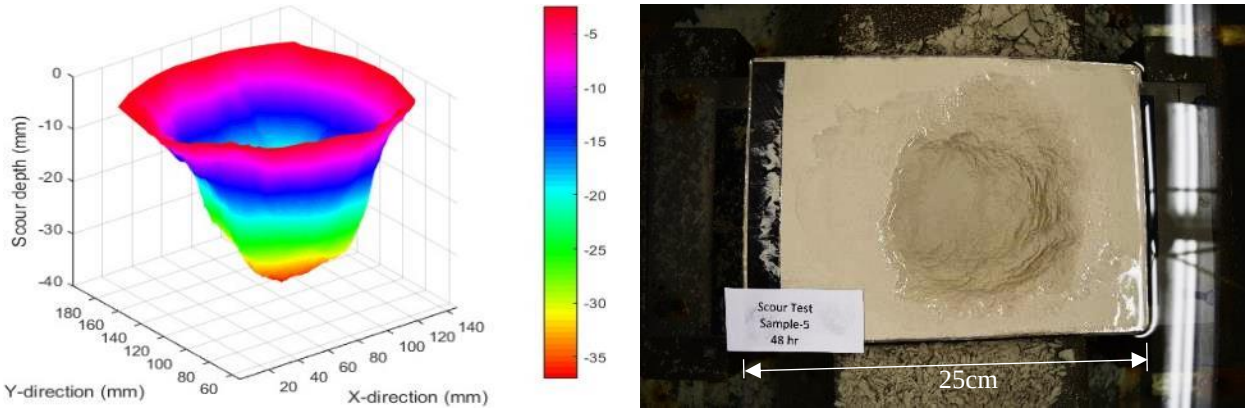

(o)

Figure 4.3: cont'd.

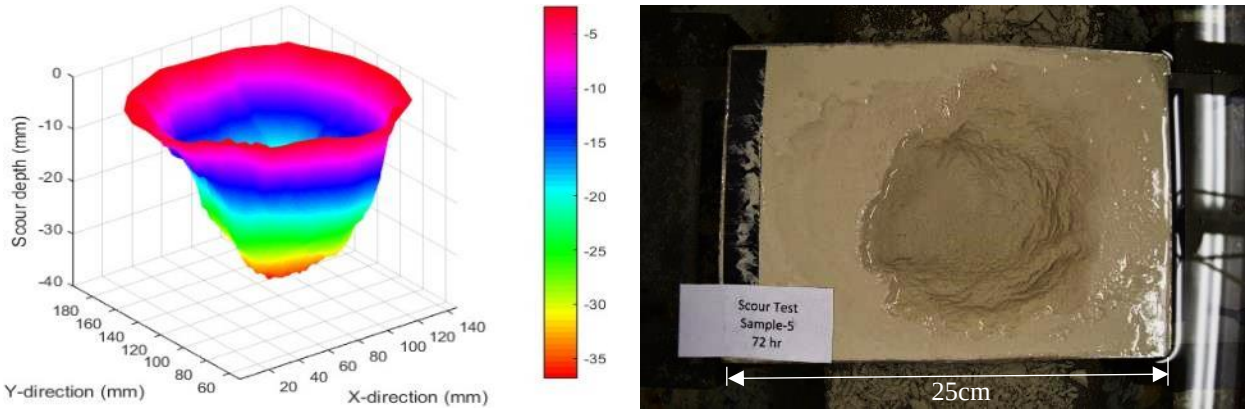

(p)

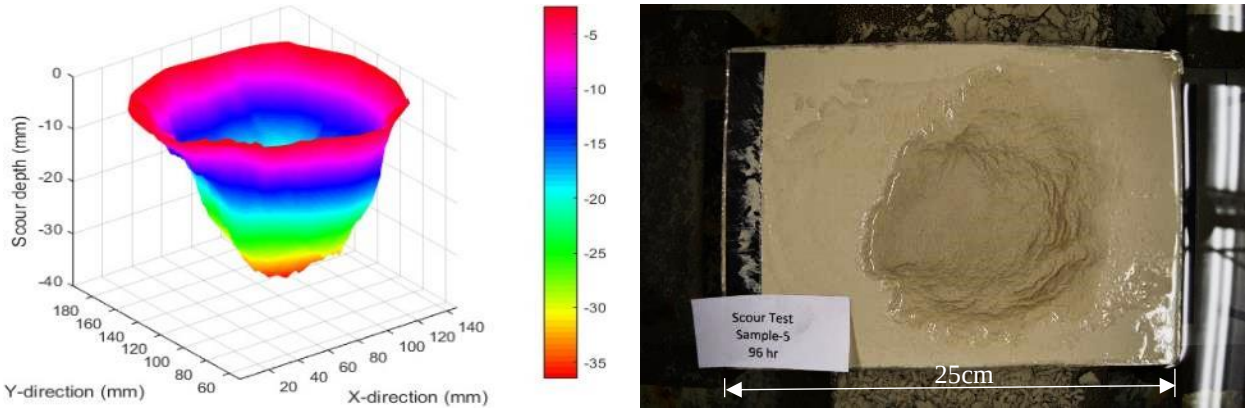

(q)

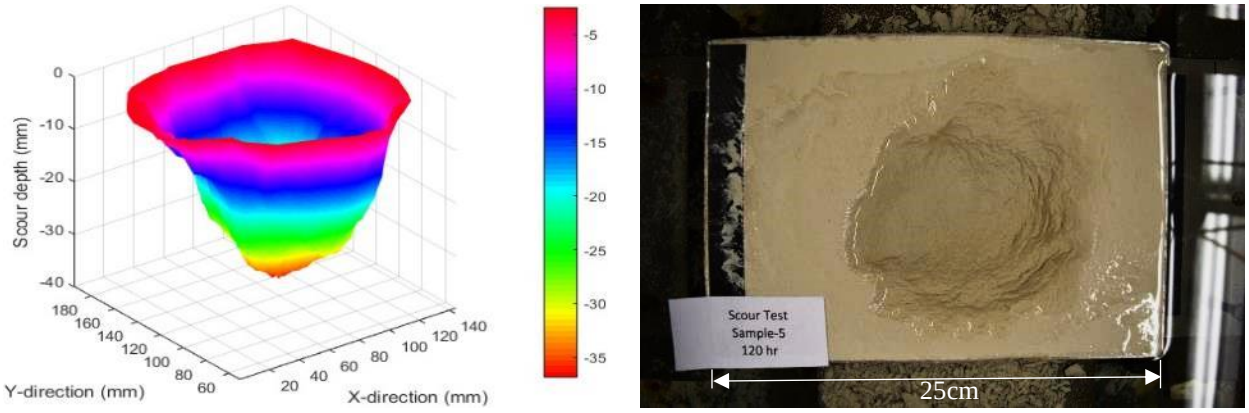

(r)

Figure 4.3: cont'd.

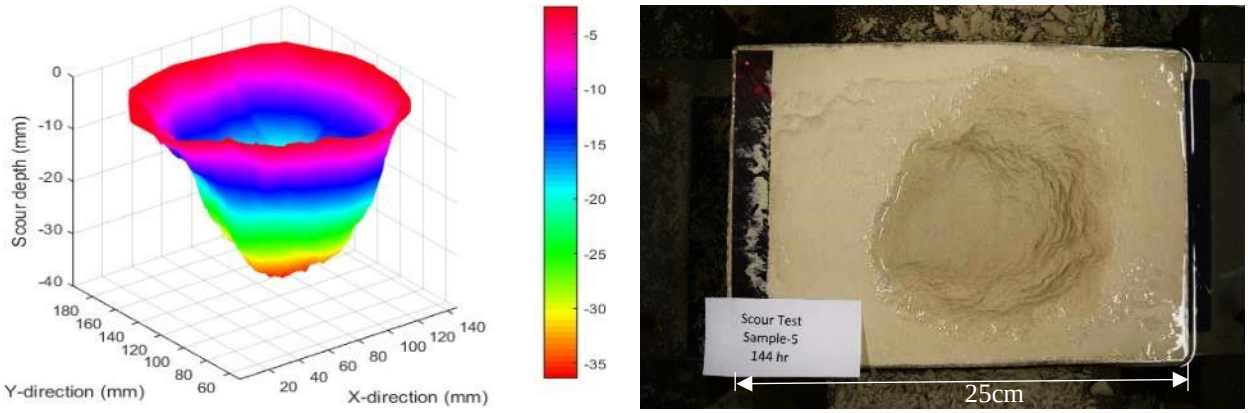

(s)

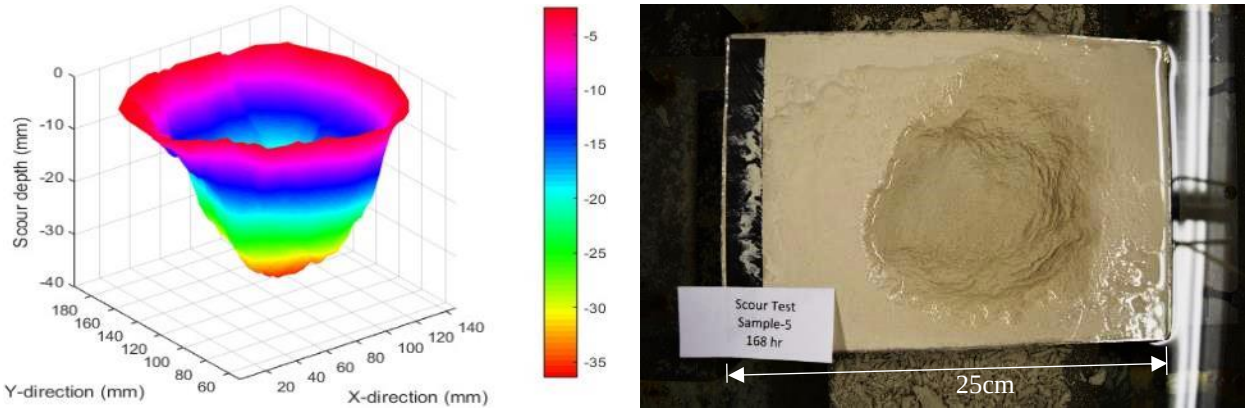

(t)

Figure 4.3: cont'd.

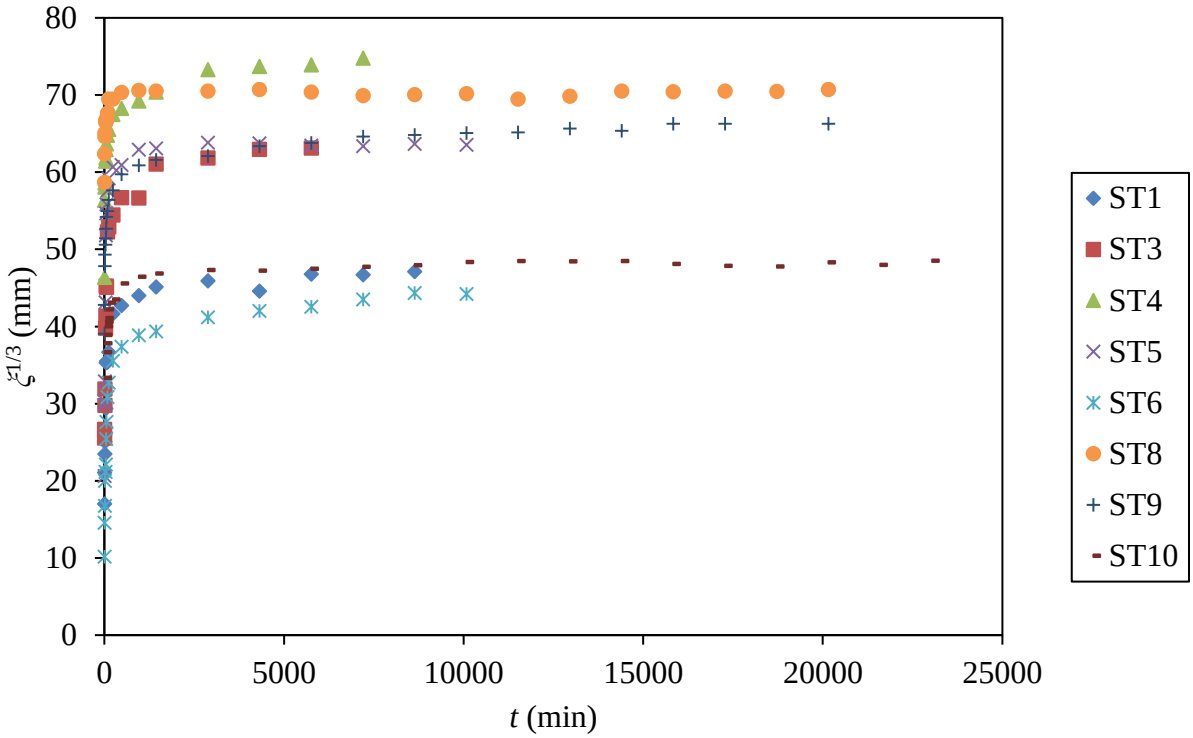

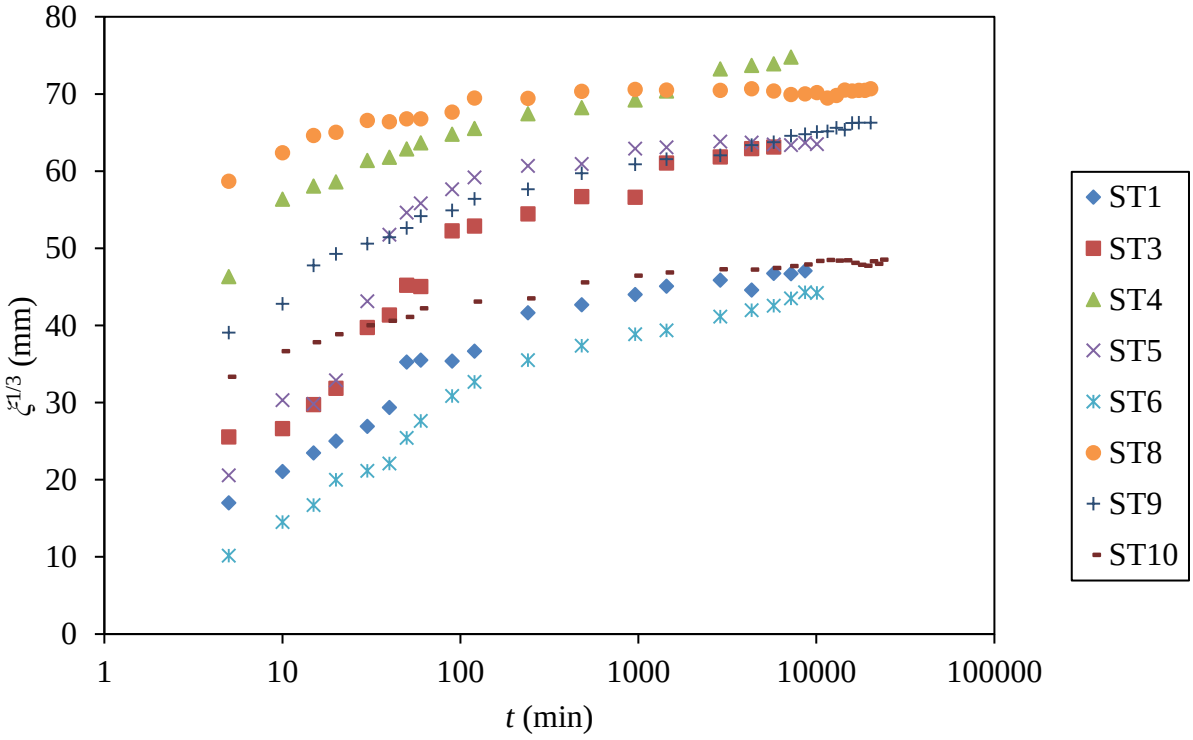

(b)

Figure 4.4: Development of the cube root of scour hole volume ($\xi^{1/3}$) (a) with time and (b) with the logarithm of time.

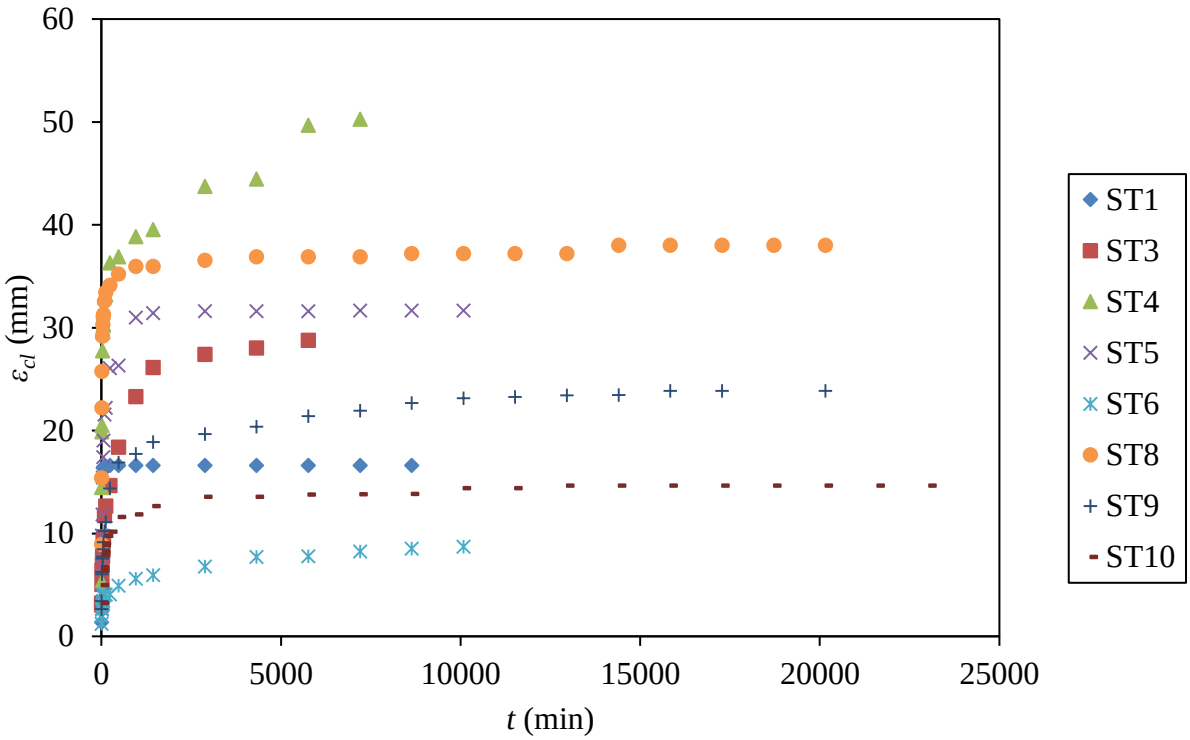

(a)

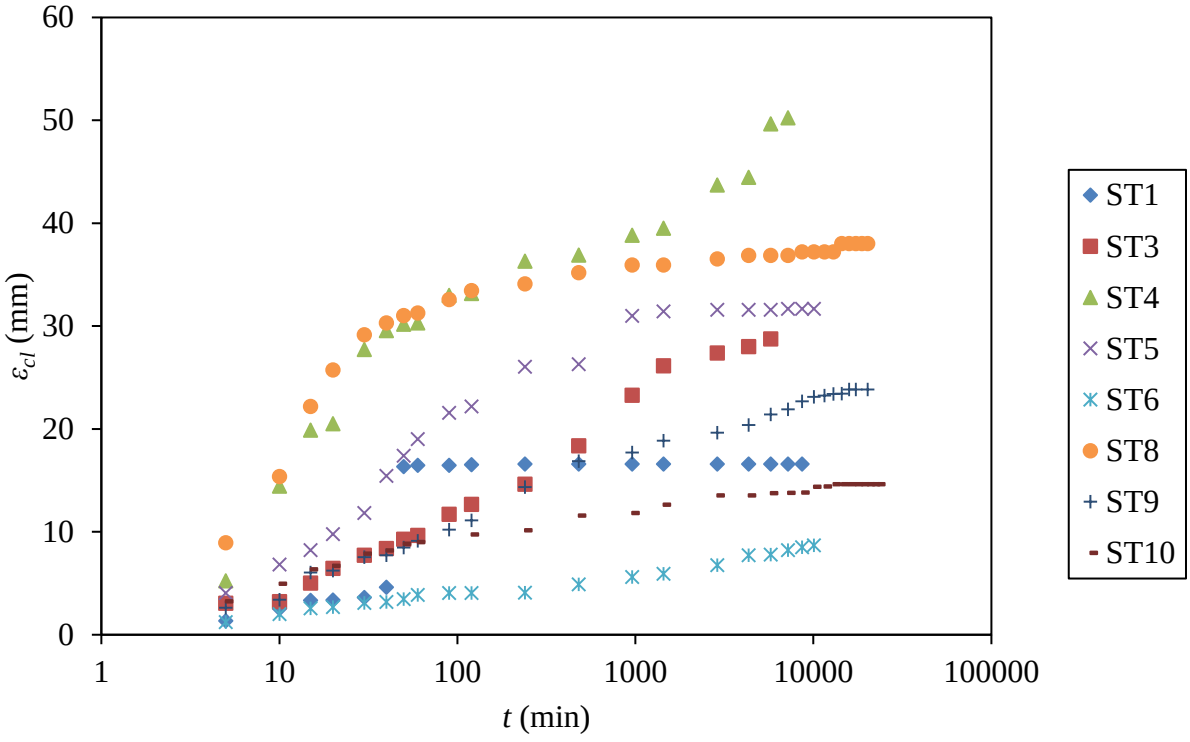

(b)

Figure 4.5: Development of the centreline scour hole depth (ε_{cl}) (a) with time and (b) with the logarithm of time.

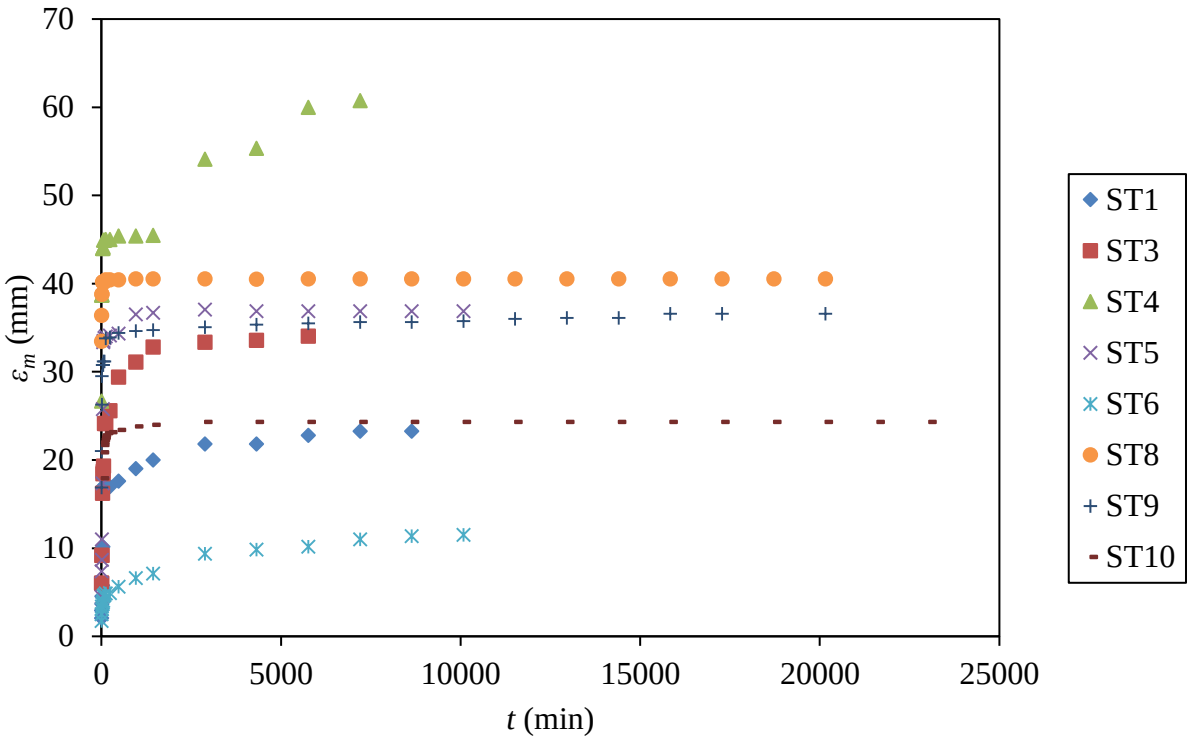

(a)

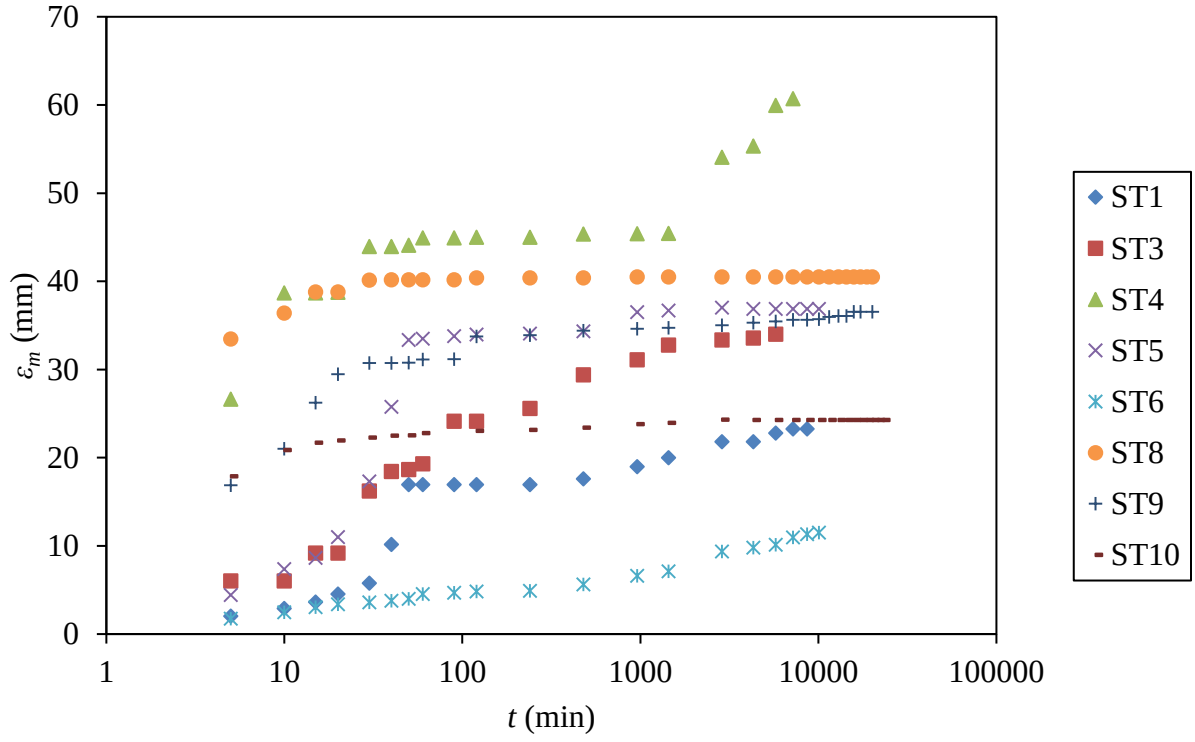

(b)

Figure 4.6: Development of the maximum scour hole depth (ε_m) (a) with time and (b) with the logarithm of time.

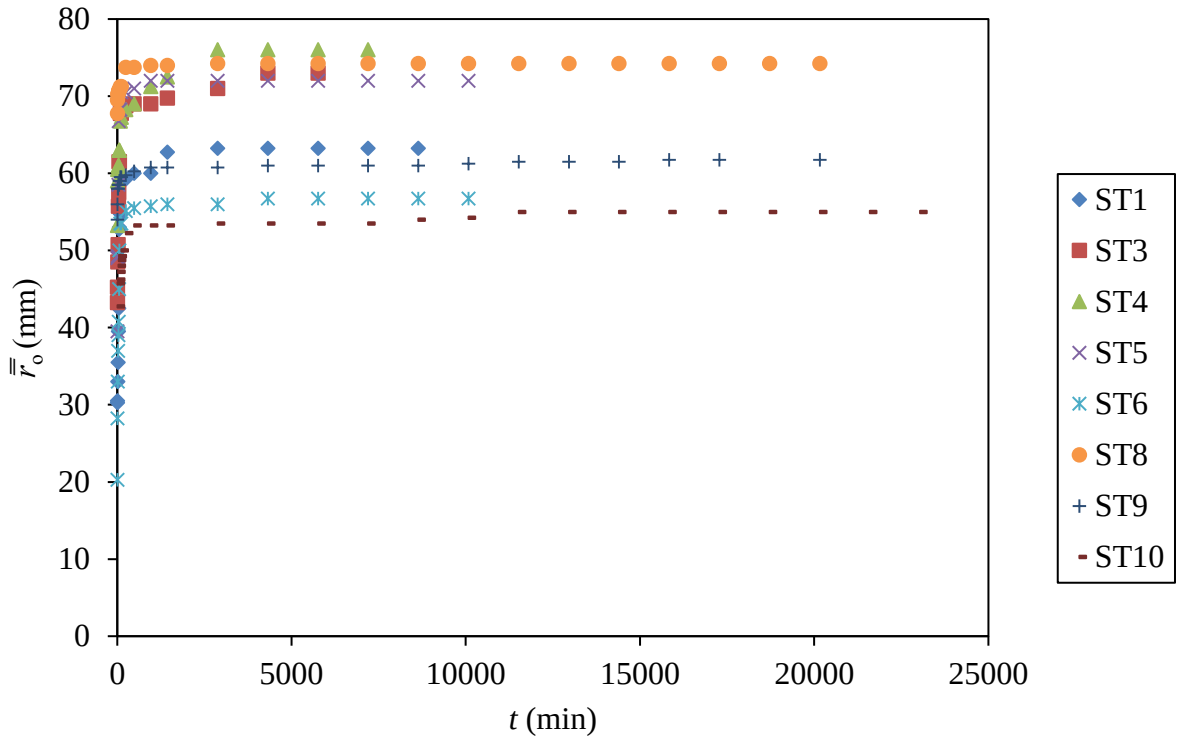

(a)

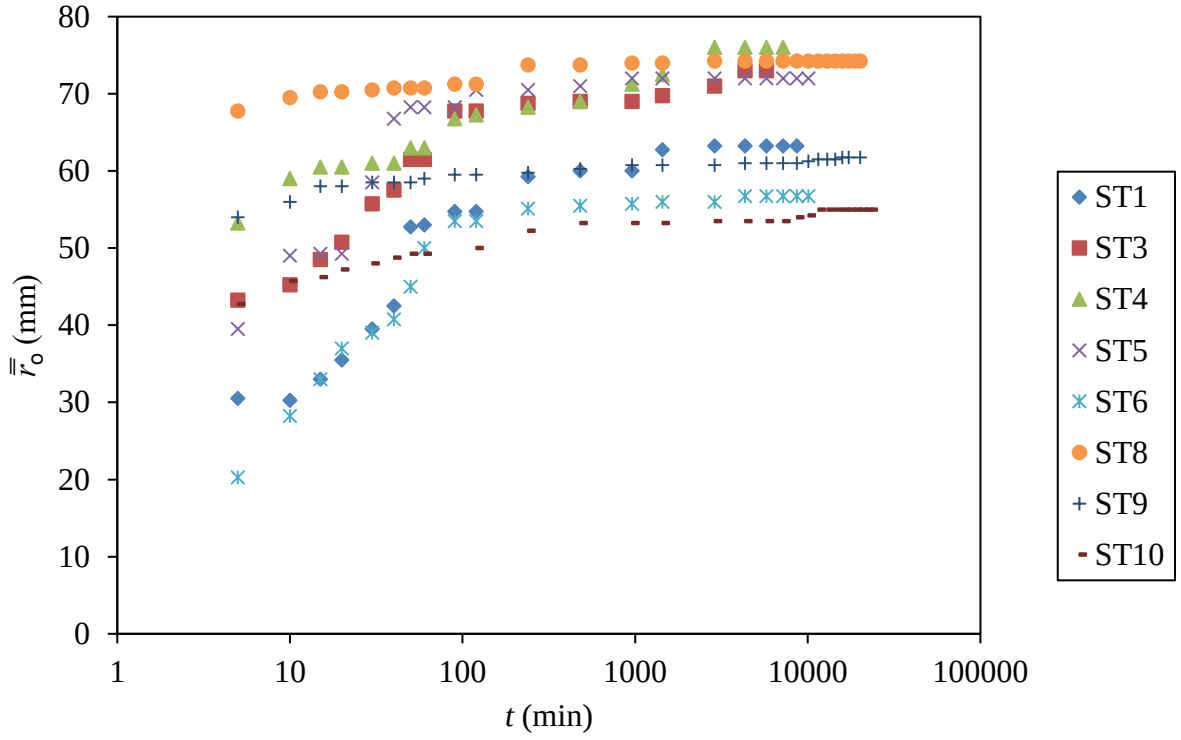

(b)

Figure 4.7: Development of the average scour hole radius ($\overline{\overline{r_o}}$) (a) with time and (b) with the logarithm of time.

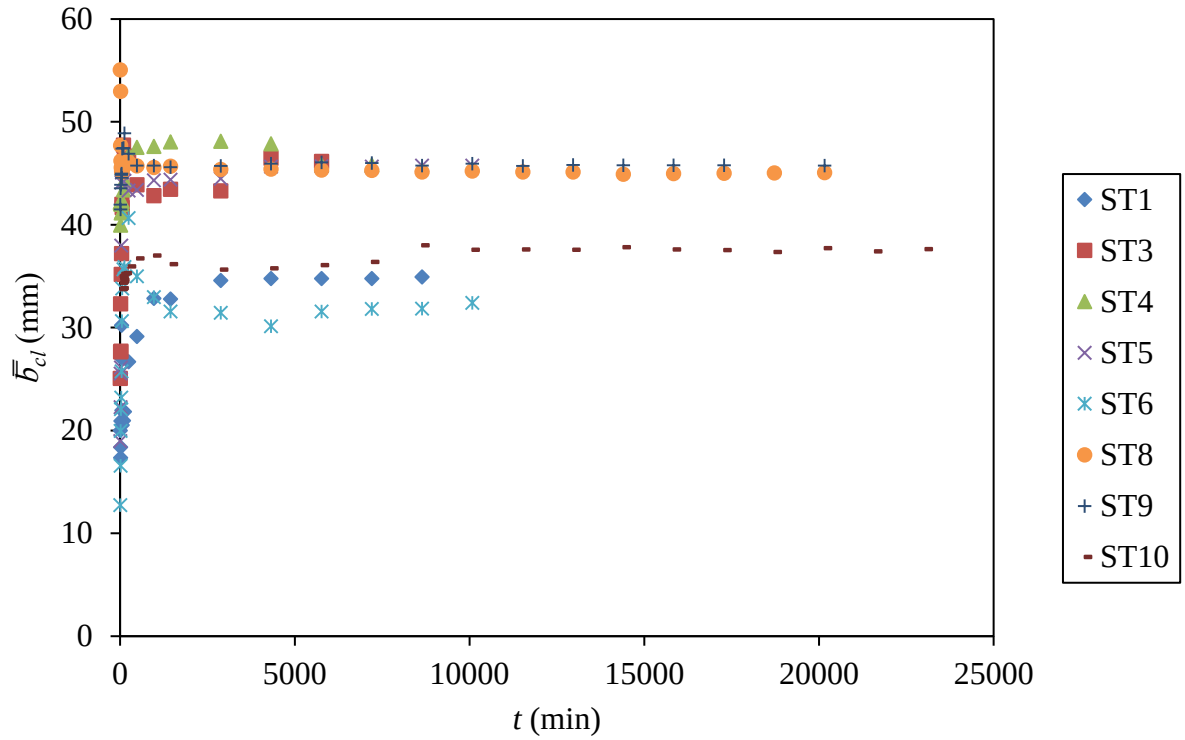

(a)

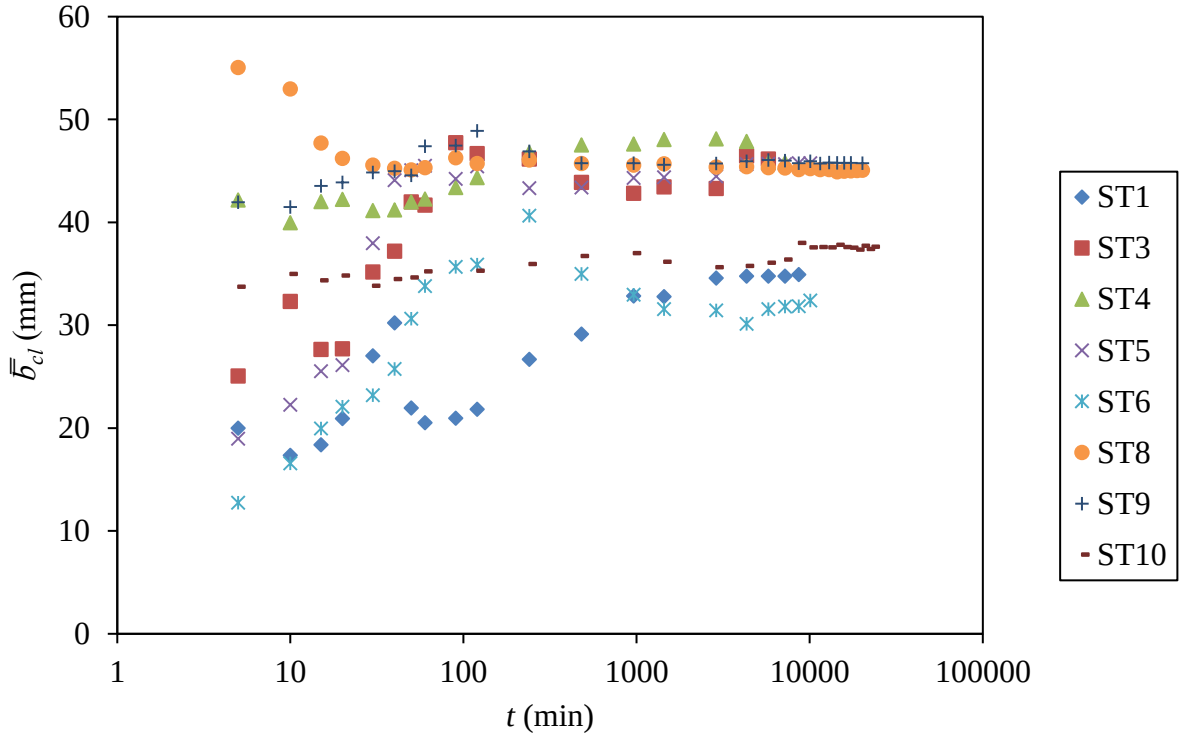

(b)

Figure 4.8: Development of the average scour hole half-width based on the centreline scour depth ($\bar{b}_{cl}$) (a) with time and (b) with the logarithm of time.

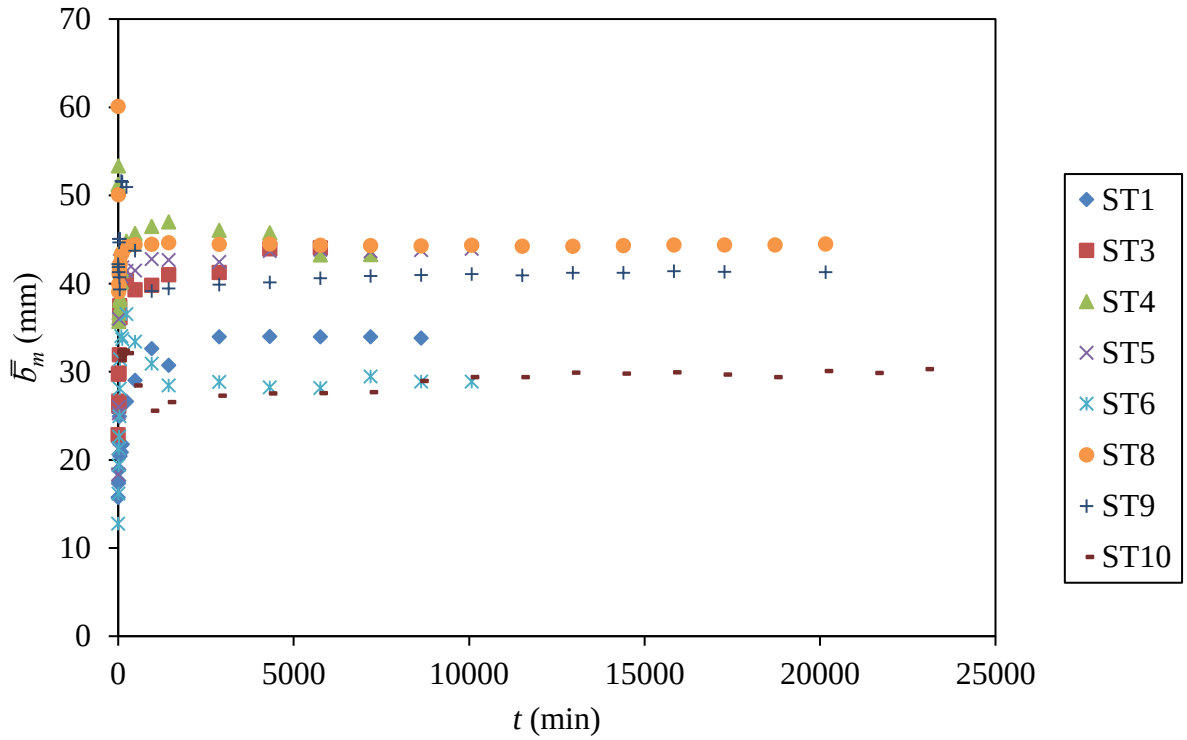

(a)

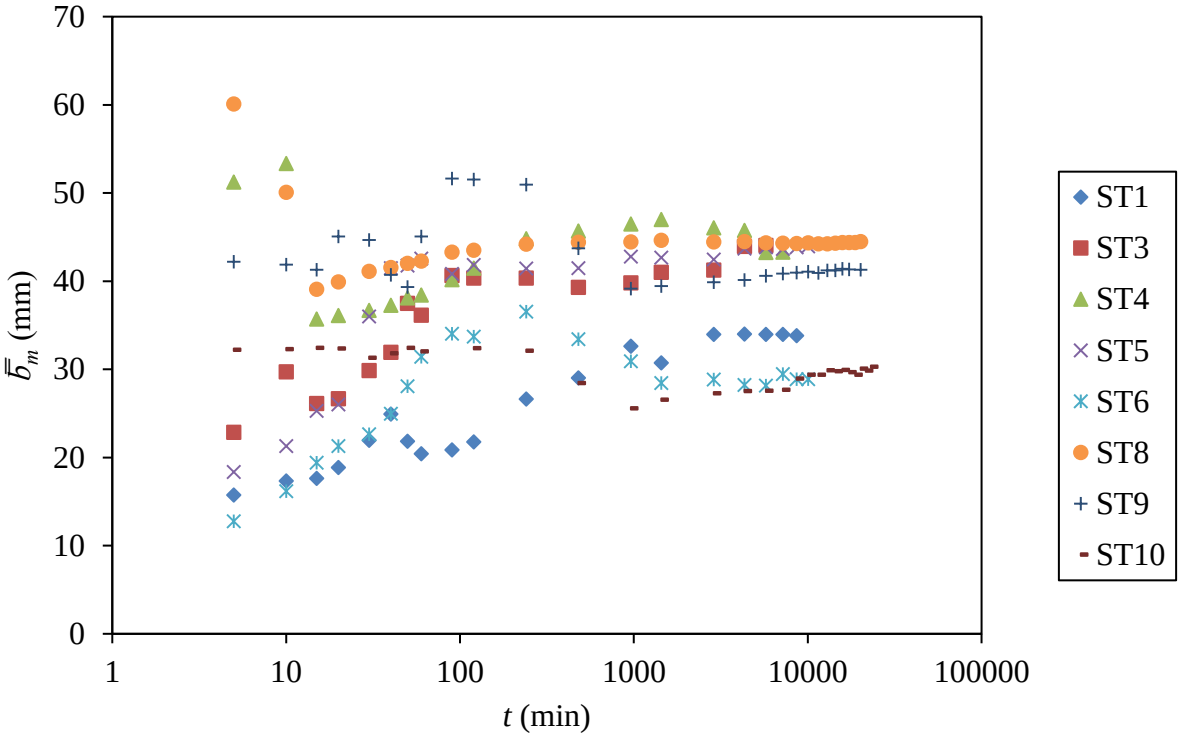

(b)

Figure 4.9: Development of the average scour hole half-width based on the maximum scour depth ($\bar{b}_m$) (a) with time and (b) with the logarithm of time.

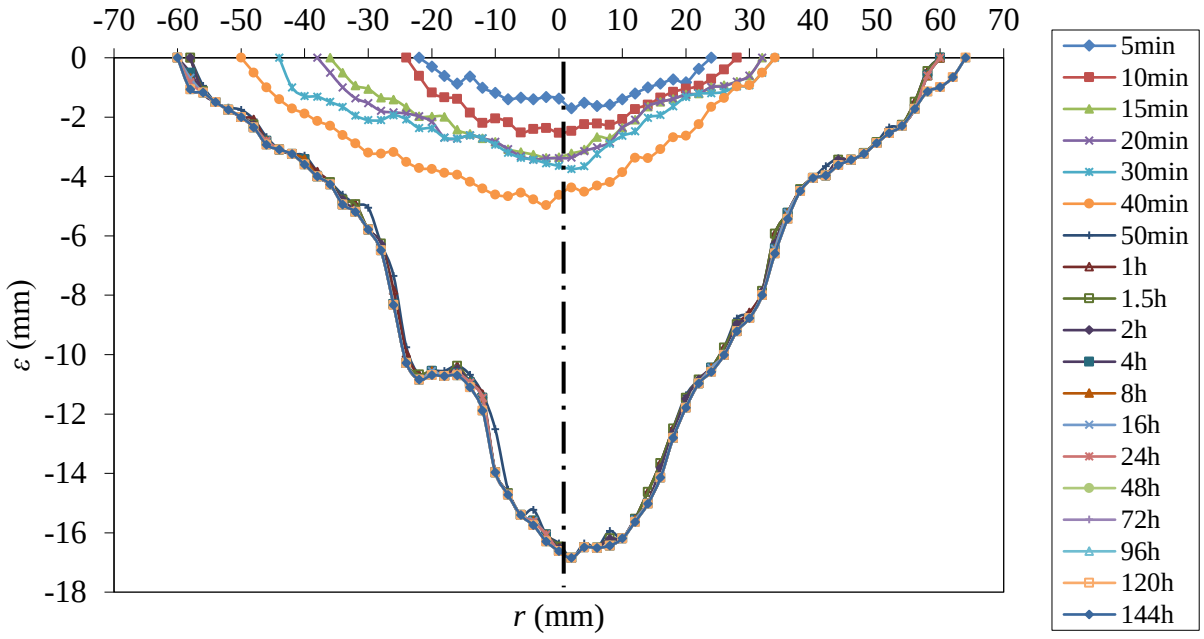

(a)

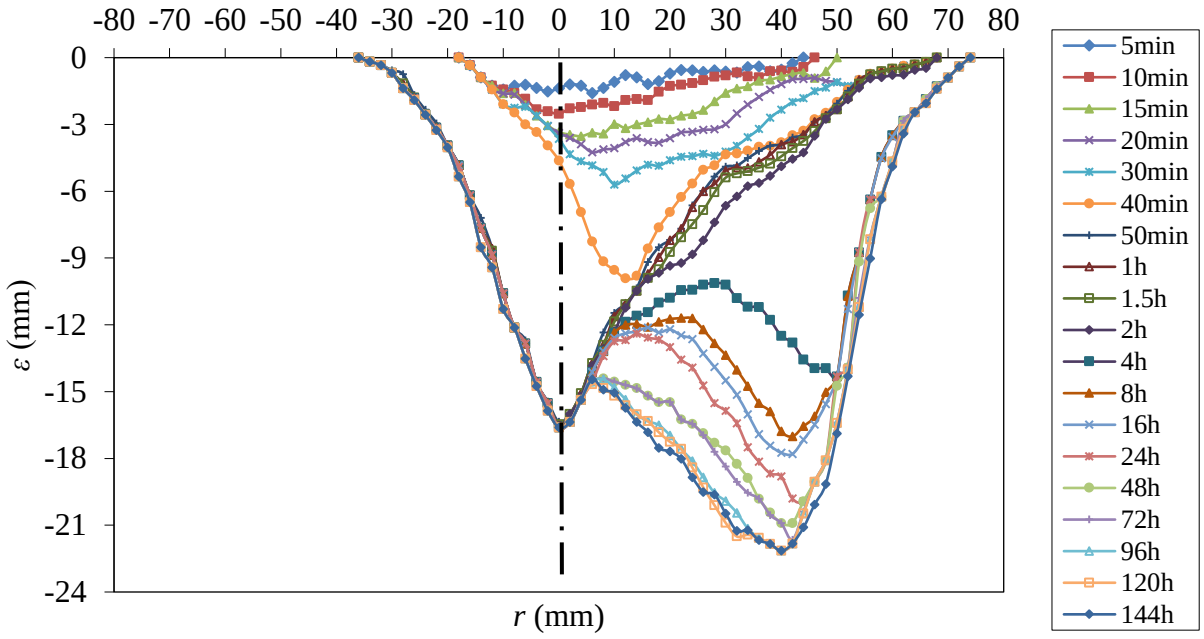

(b)

Figure 4.10: Scour hole profiles with time for Scour Test 1 for four different sections (a) Section 1, (b) Section 2, (c) Section 3, and (d) Section 4.

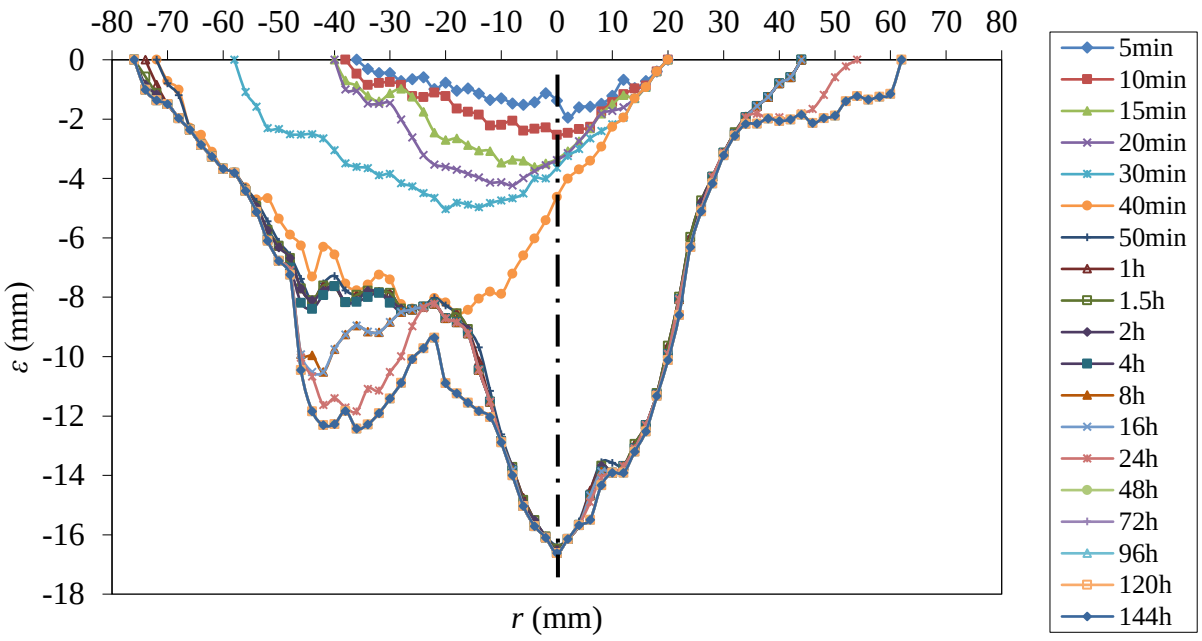

(c)

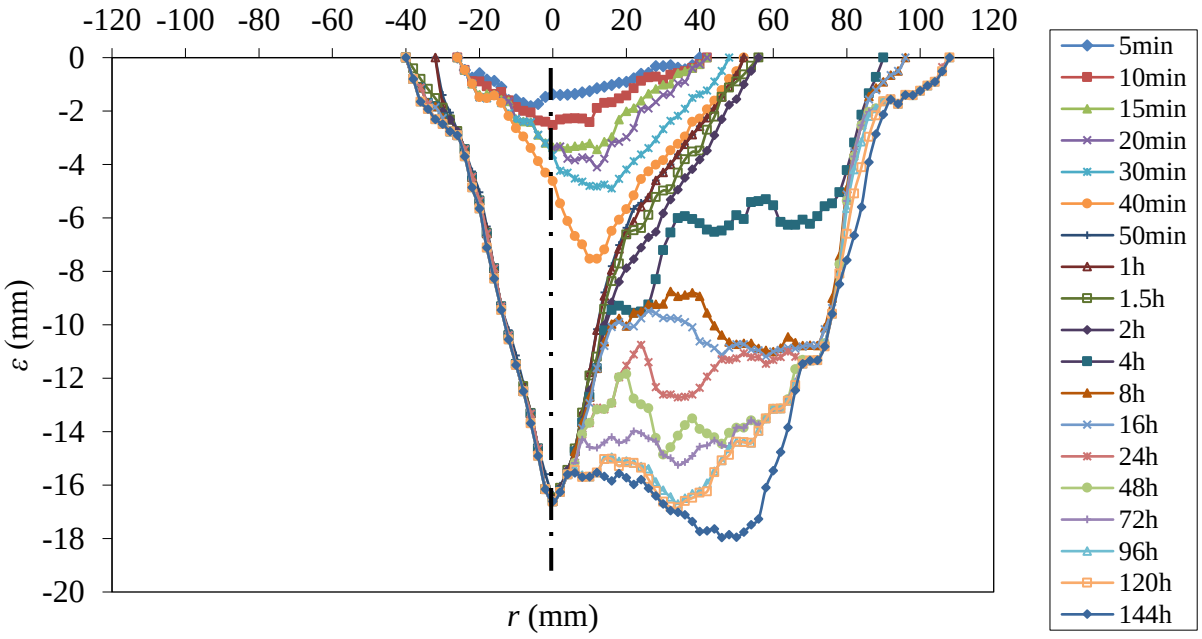

(d)

Figure 4.10: cont'd.

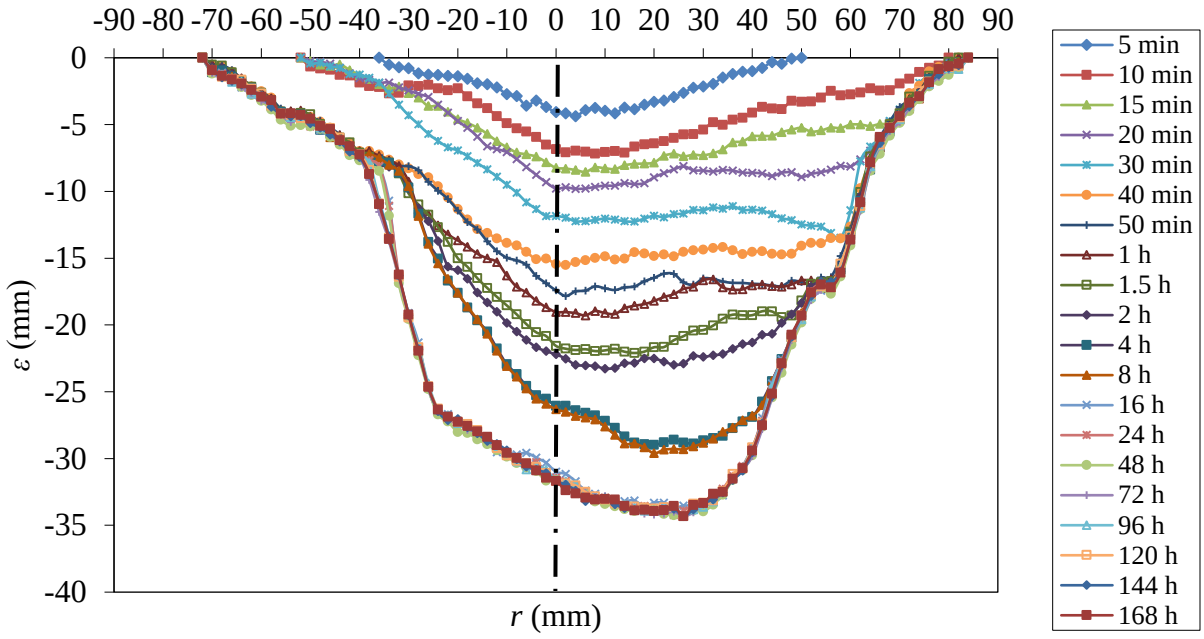

(a)

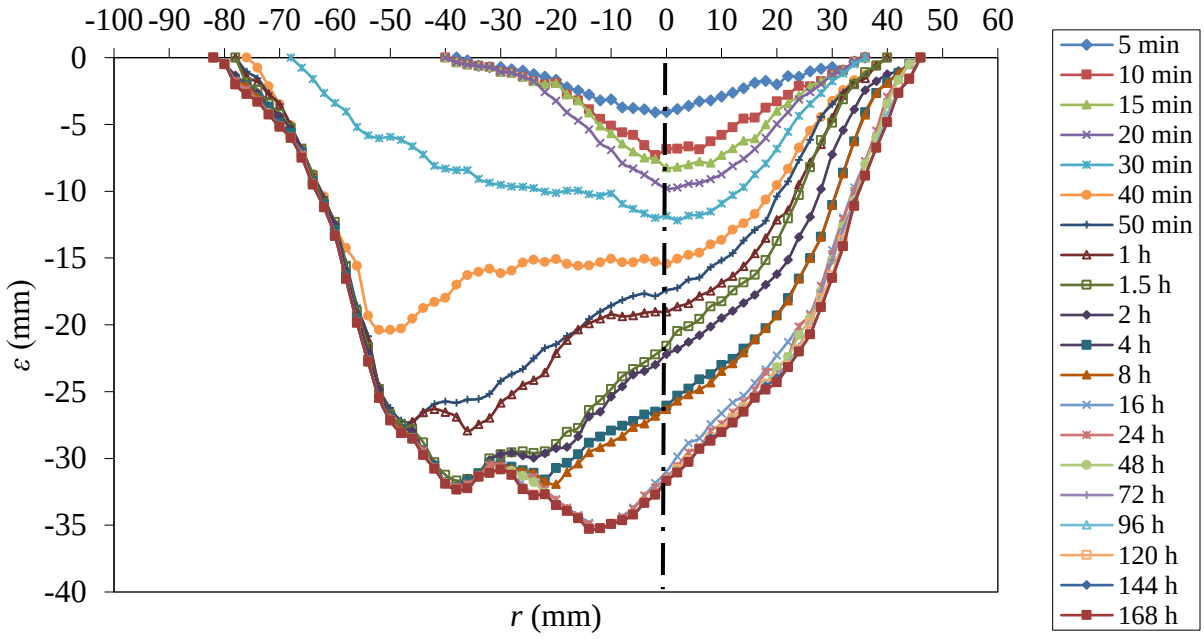

(b)

Figure 4.11: Scour hole profiles with time for Scour Test 5 for four different sections (a) Section 1, (b) Section 2, (c) Section 3, and (d) Section 4.

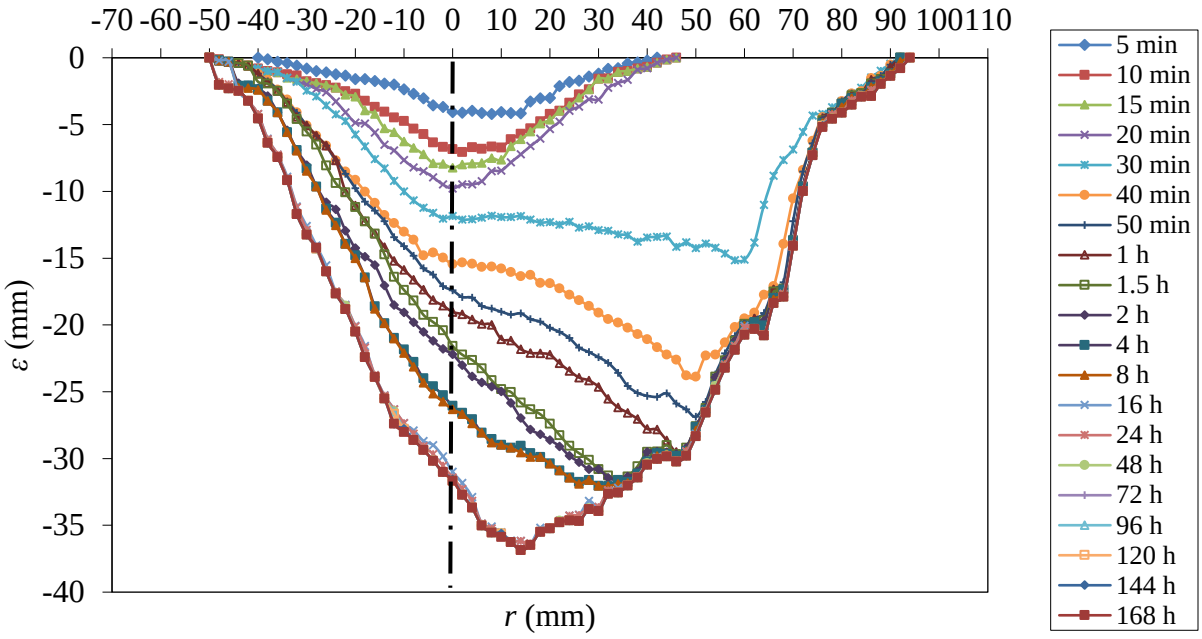

(c)

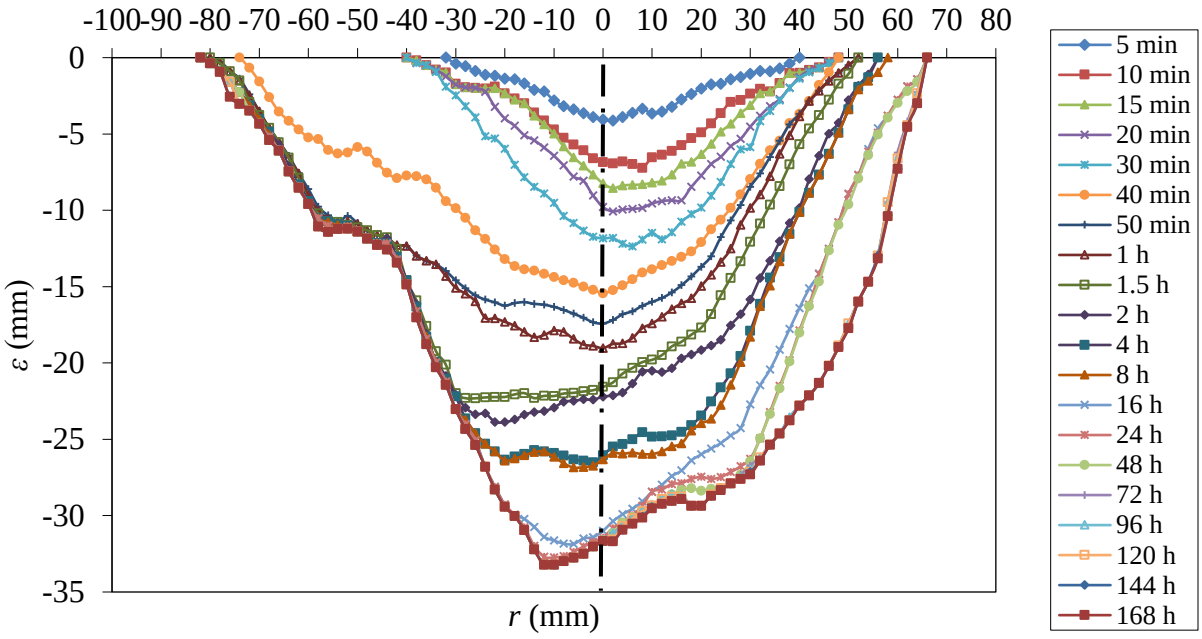

(d)

Figure 4.11: cont'd.

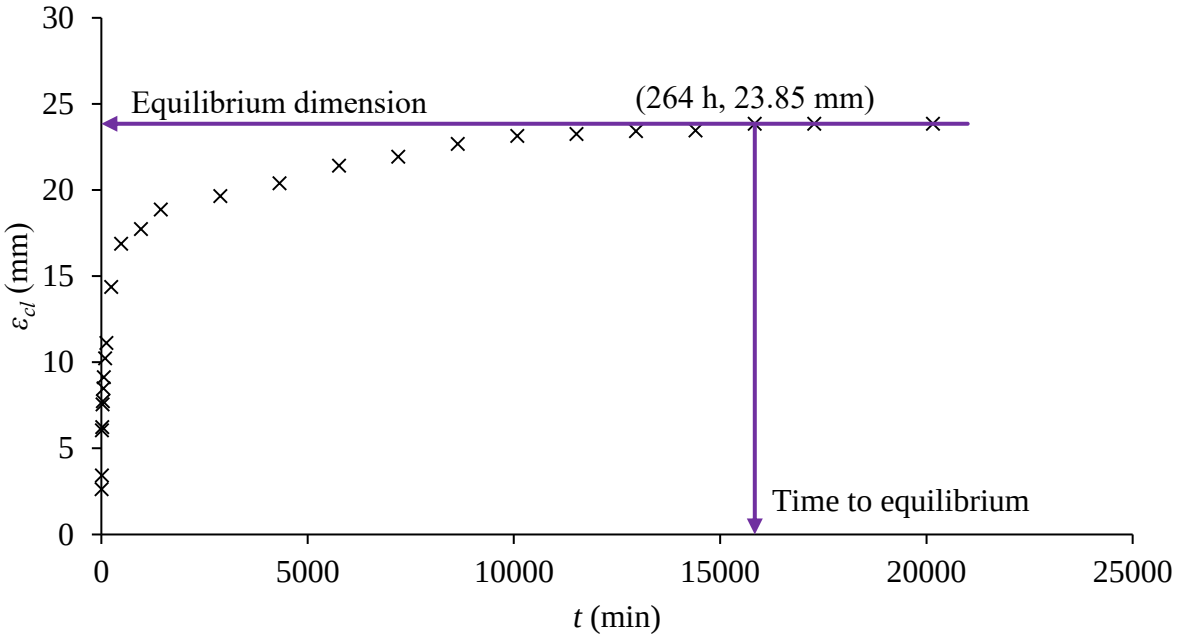

(a)

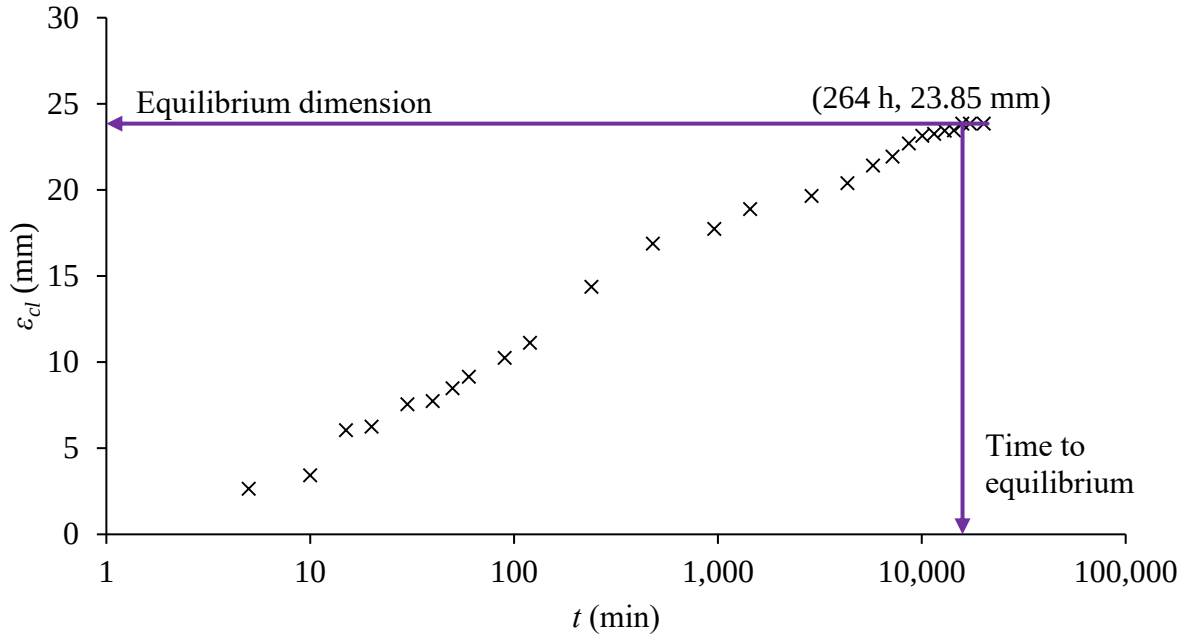

(b)

Figure 4.12: Assessing $\varepsilon_{cl\infty}$ and t_{∞} by graphical approach for Scour Test 9 using (a) arithmetic plot, and (b) logarithmic plot.

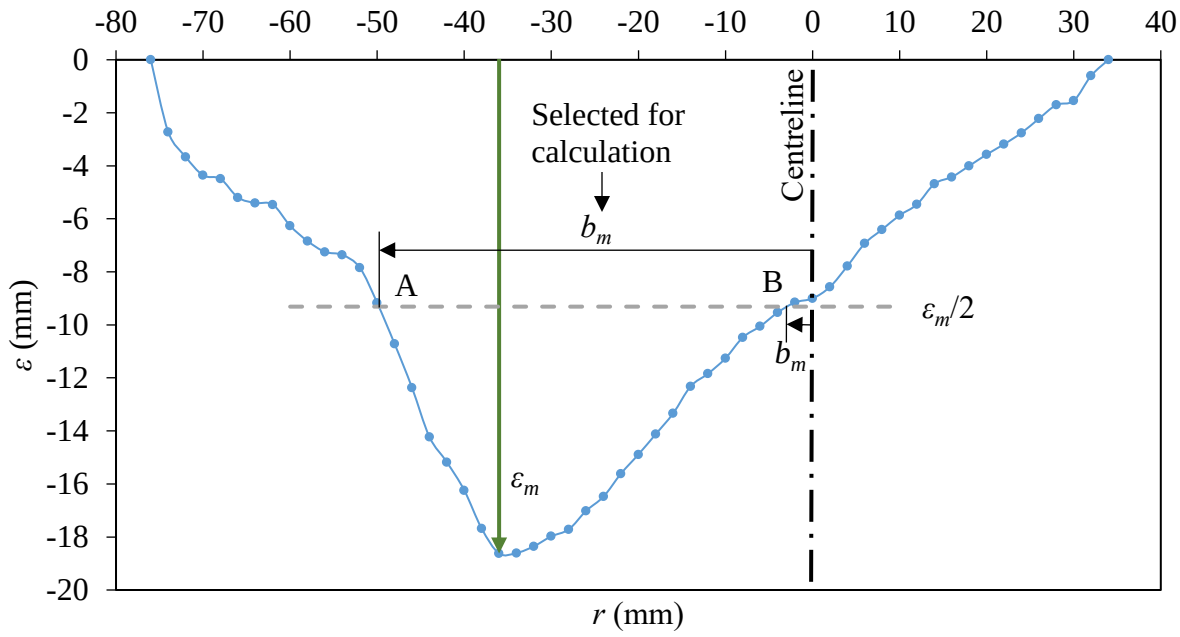

(a)

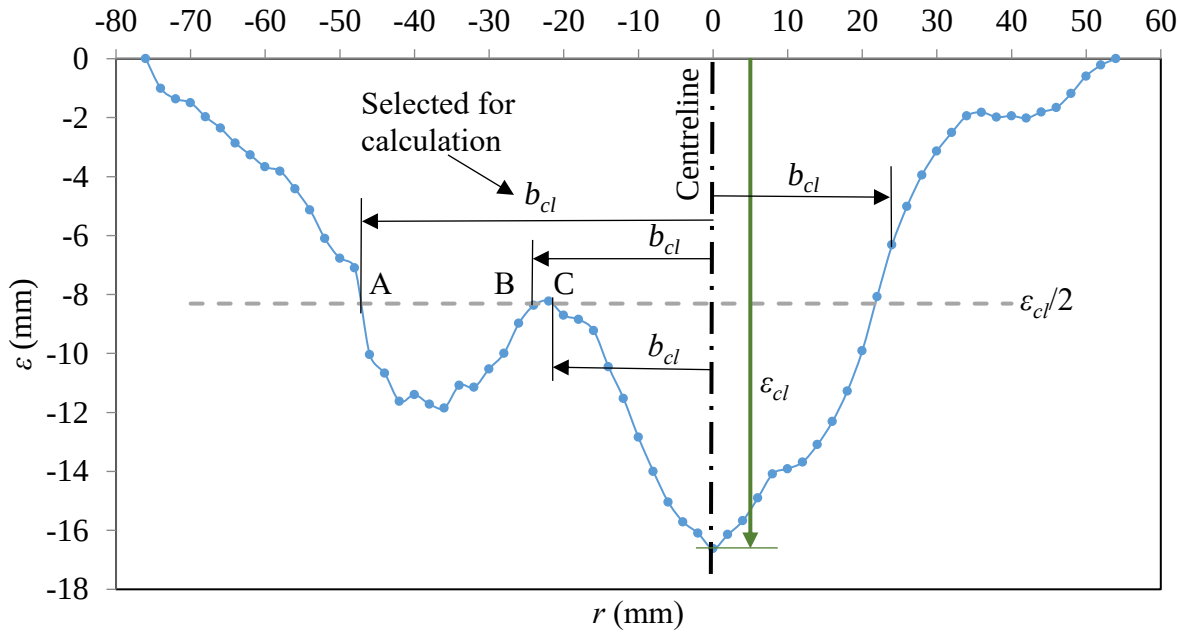

(b)

Figure 4.13: Determining half-widths (a) b_m for Section 2 of Scour Test 10 after 1 hours testing, (b) b_{cl} for Section 3 of Scour Test 1 after 24 hours testing.

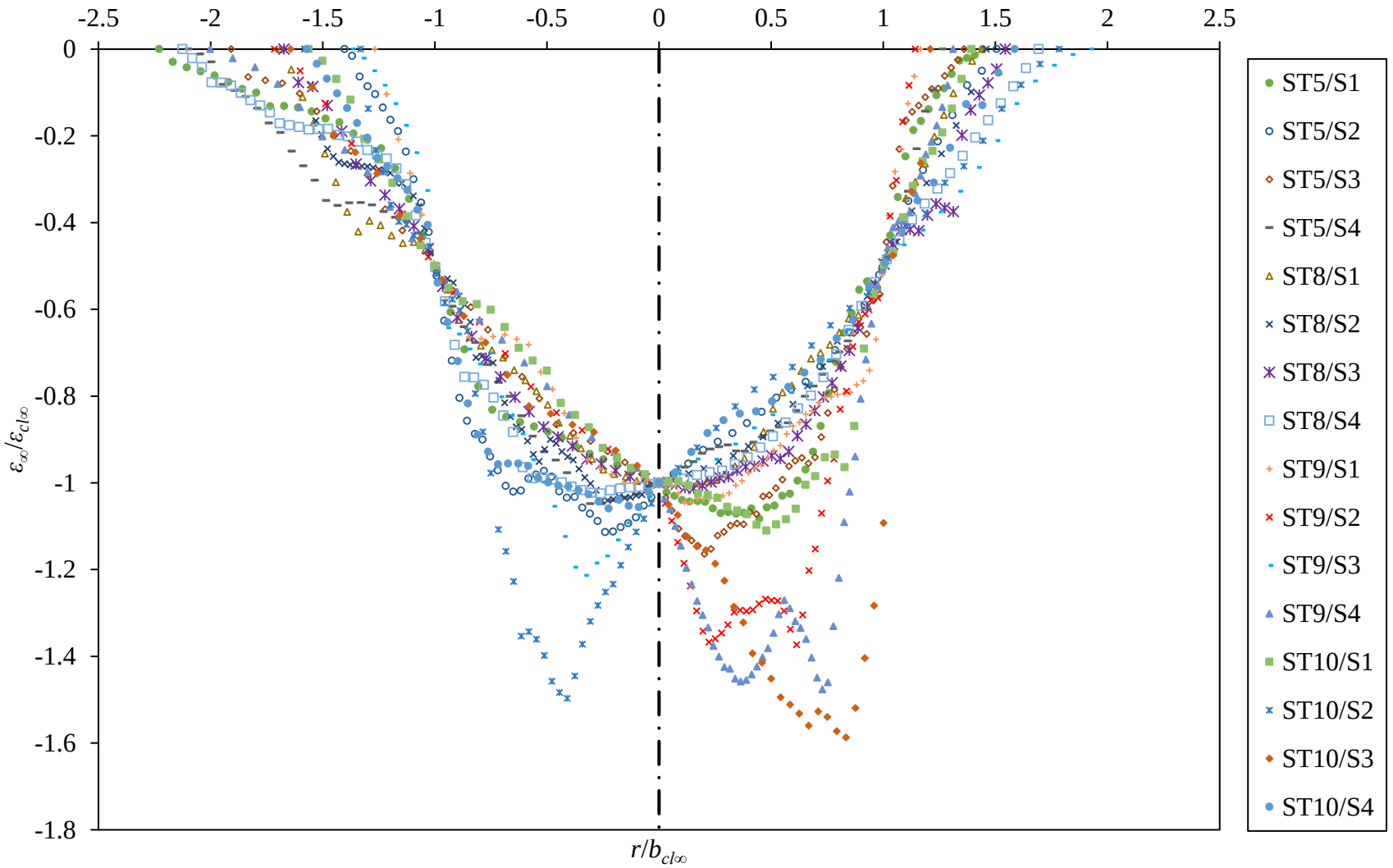

Figure 4.14. Dimensionless scour hole profiles for equilibrium scour holes.

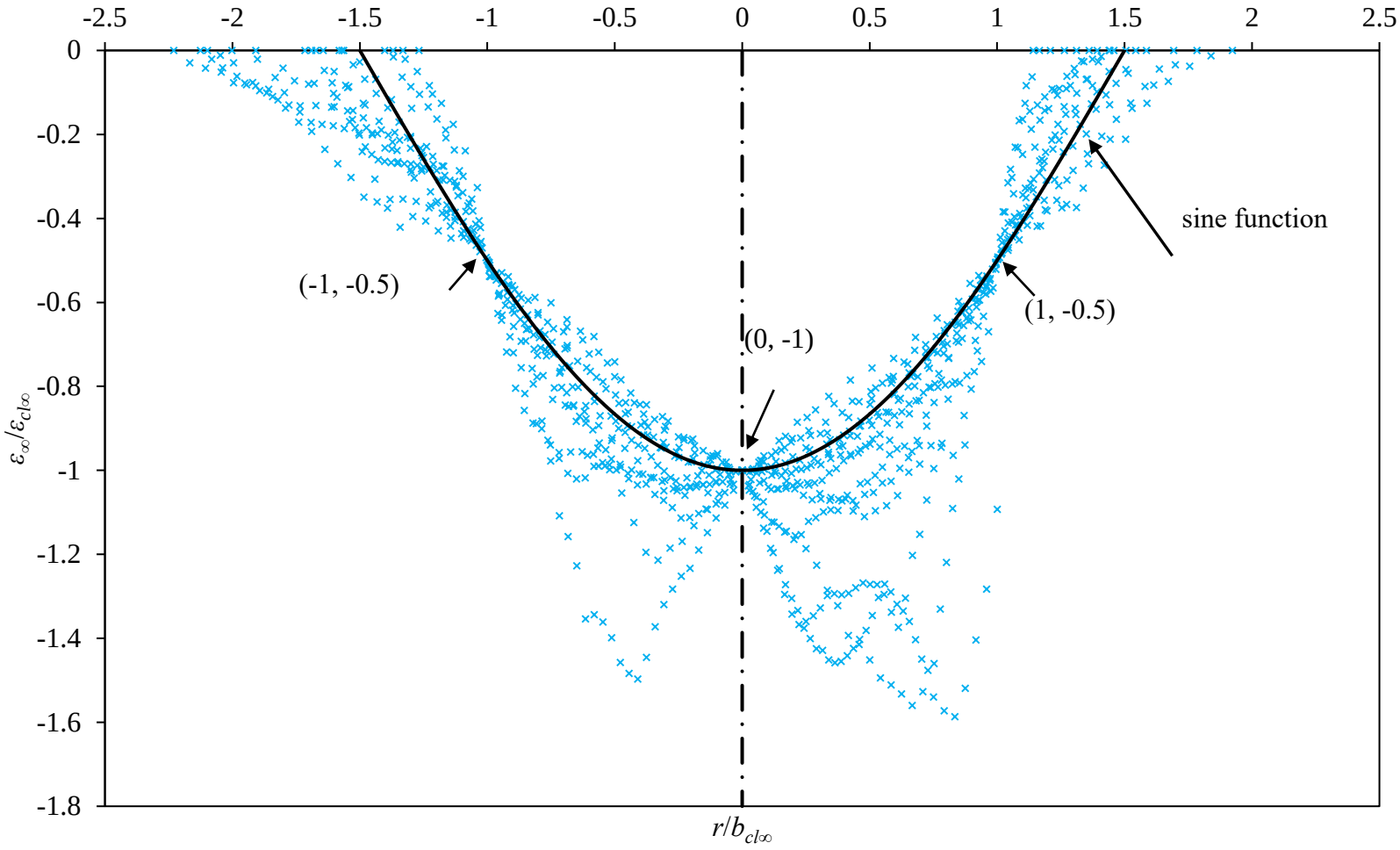

Figure 4.15: Curve fitting of the sine function to the dimensionless scour hole profiles at equilibrium condition

.

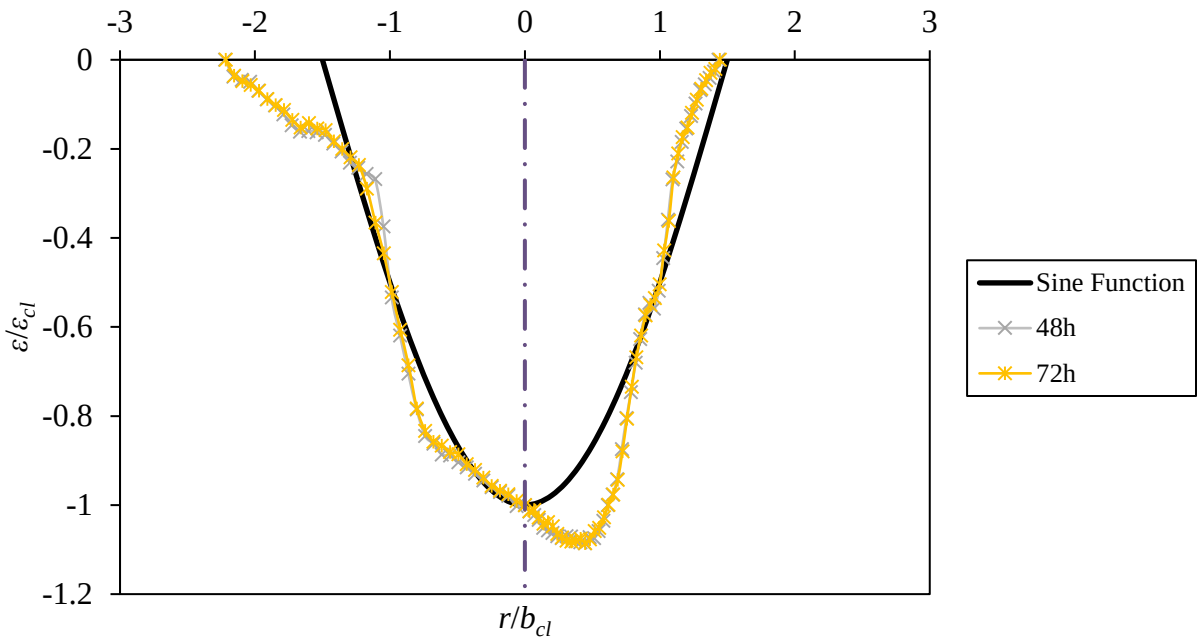

(a)

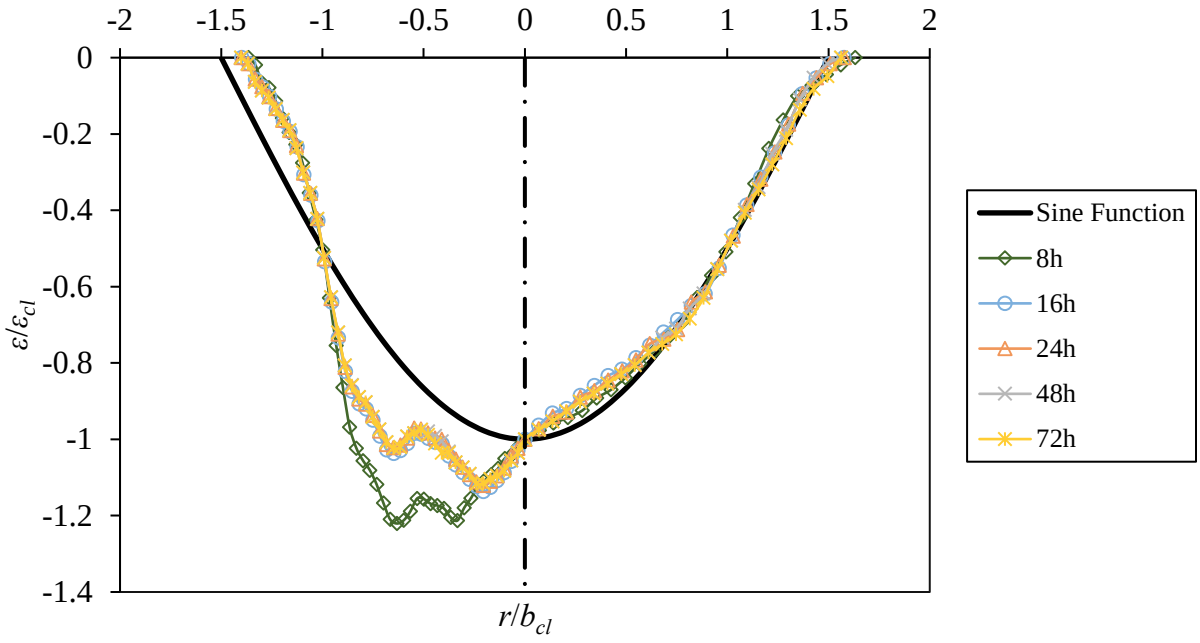

(b)

Figure 4.16: Investigating the similarities of the dimensionless scour hole profiles to the equilibrium scour hole shapes. Profiles starting immediately before the similarity to the equilibrium and the general scour hole shape are shown for (a) ST5/S1, (b) ST5/S2, (c) ST5/S3, (d) ST5/S4, (e) ST8/S1, (f) ST8/S2, (g) ST8/S3, (h) ST8/S4, (i) ST9/S1, (j) ST9/S2, (k) ST9/S3, (l) ST9/S4, (m) ST10/S1, (n) ST10/S2, (o) ST10/S3, and (p) ST10/S4.

Note: ST represents Scour Test and S represents cross-section of the scour hole.

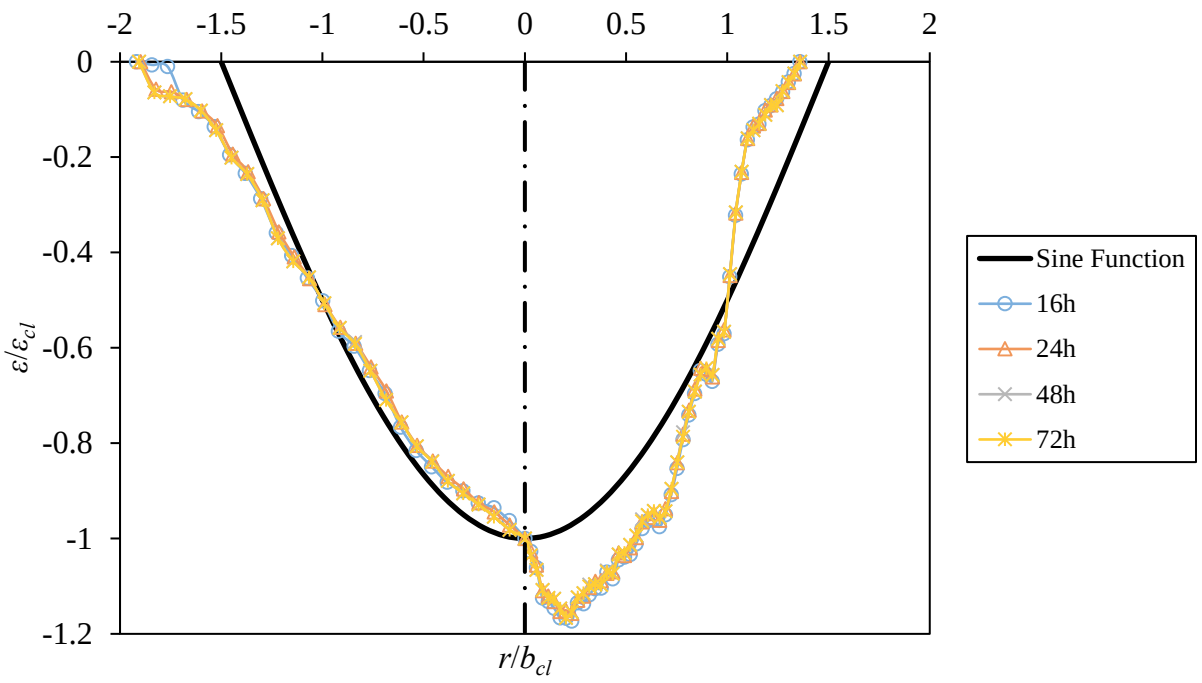

(c)

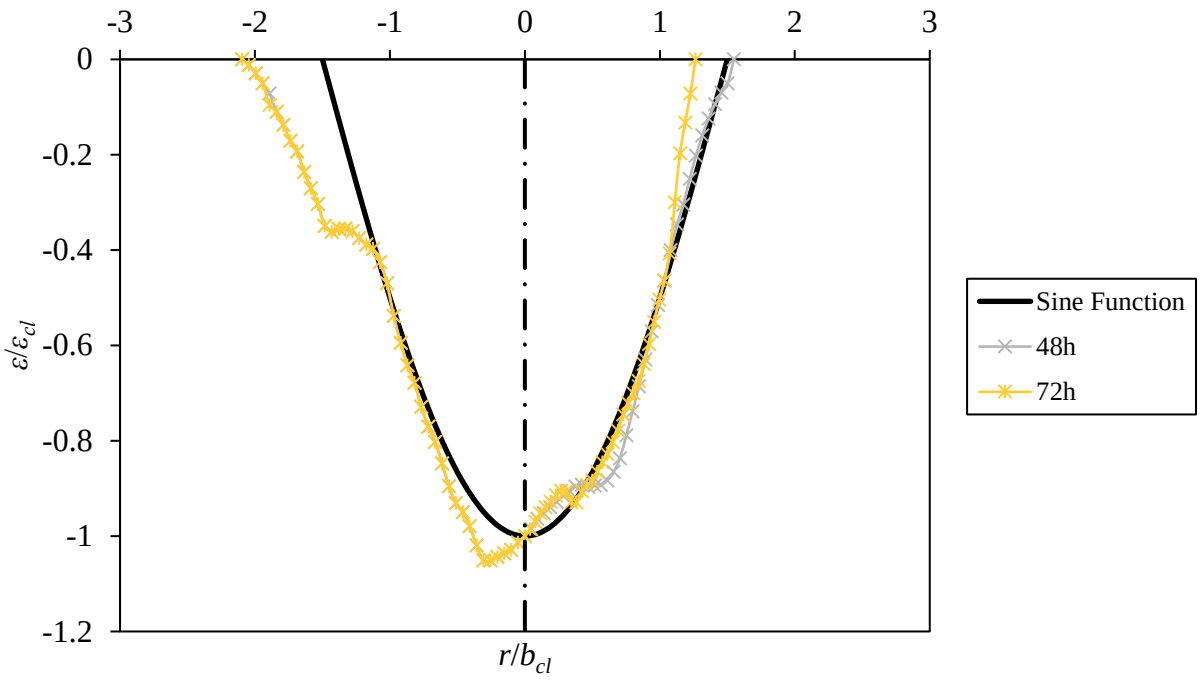

(d)

Figure 4.16: cont'd.

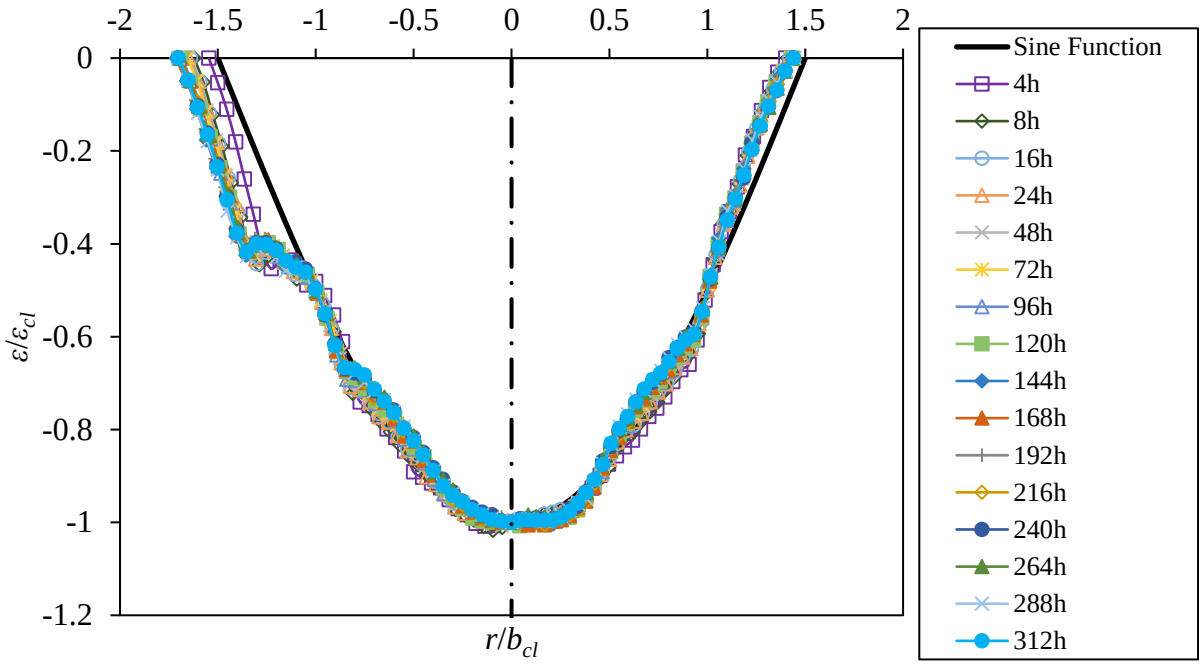

(e)

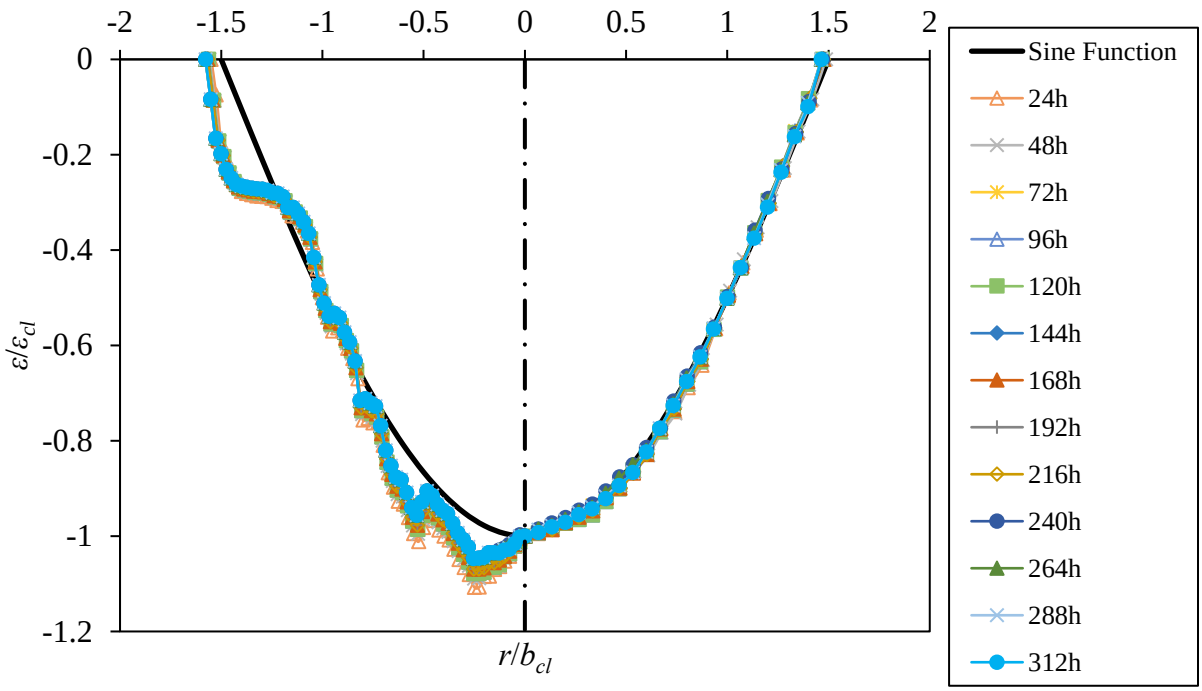

(f)

Figure 4.16: cont'd.

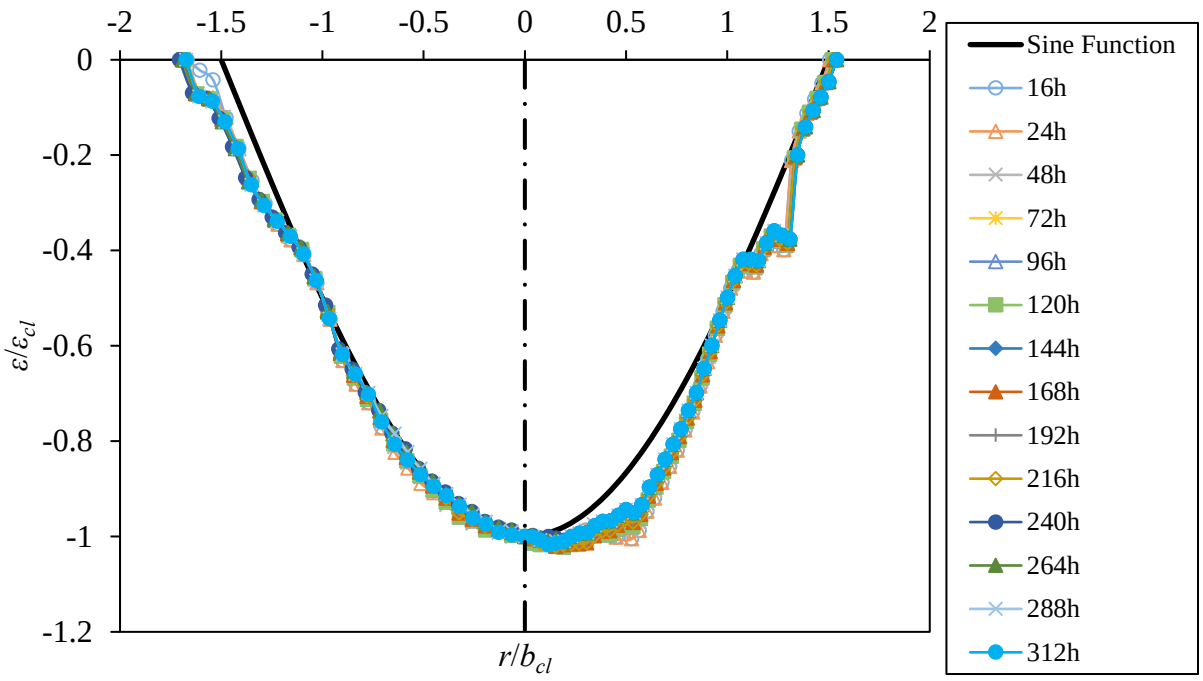

(g)

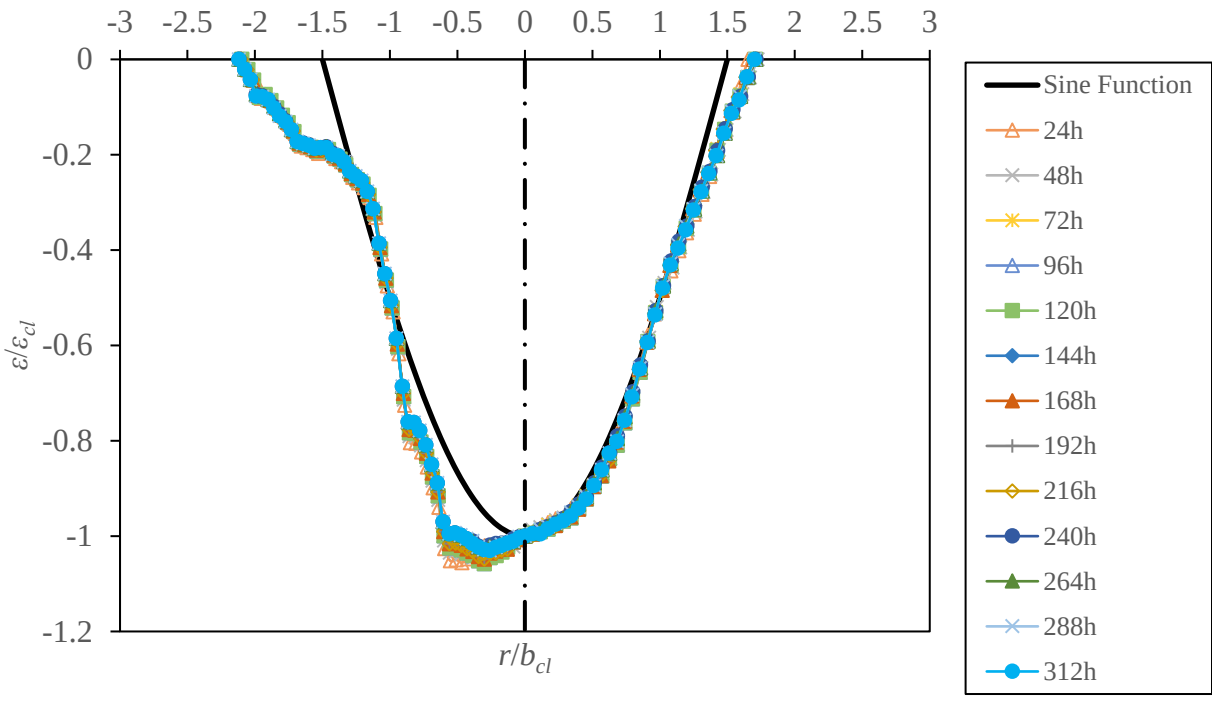

(h)

Figure 4.16: cont'd.

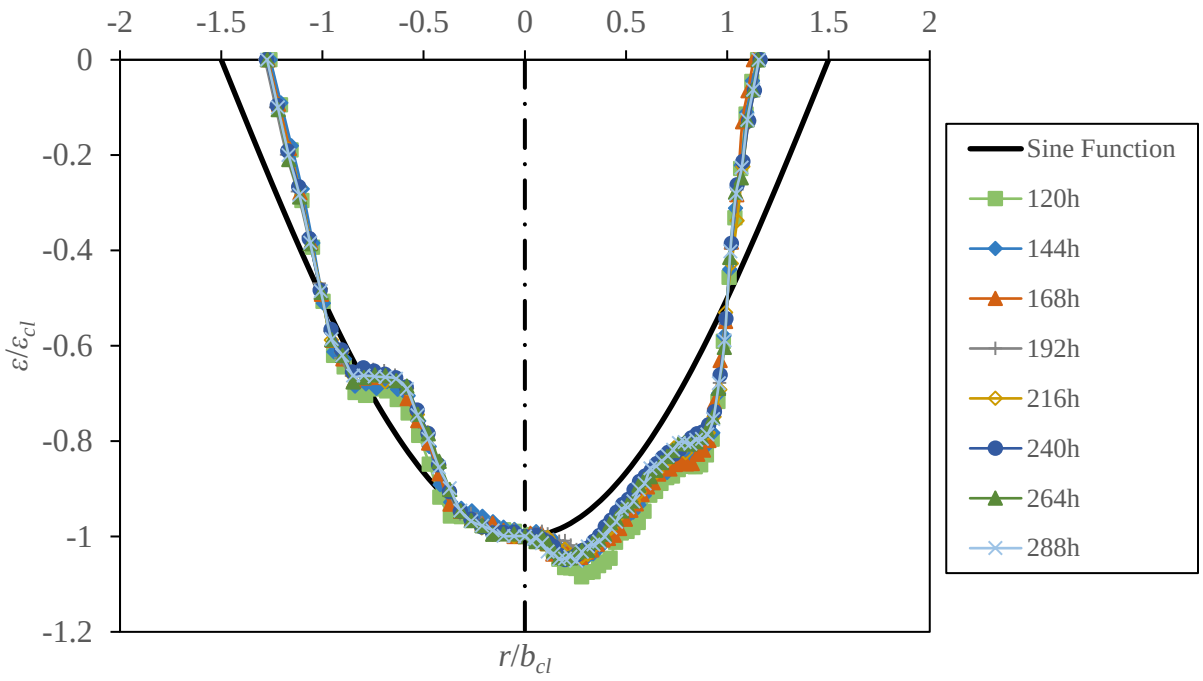

(i)

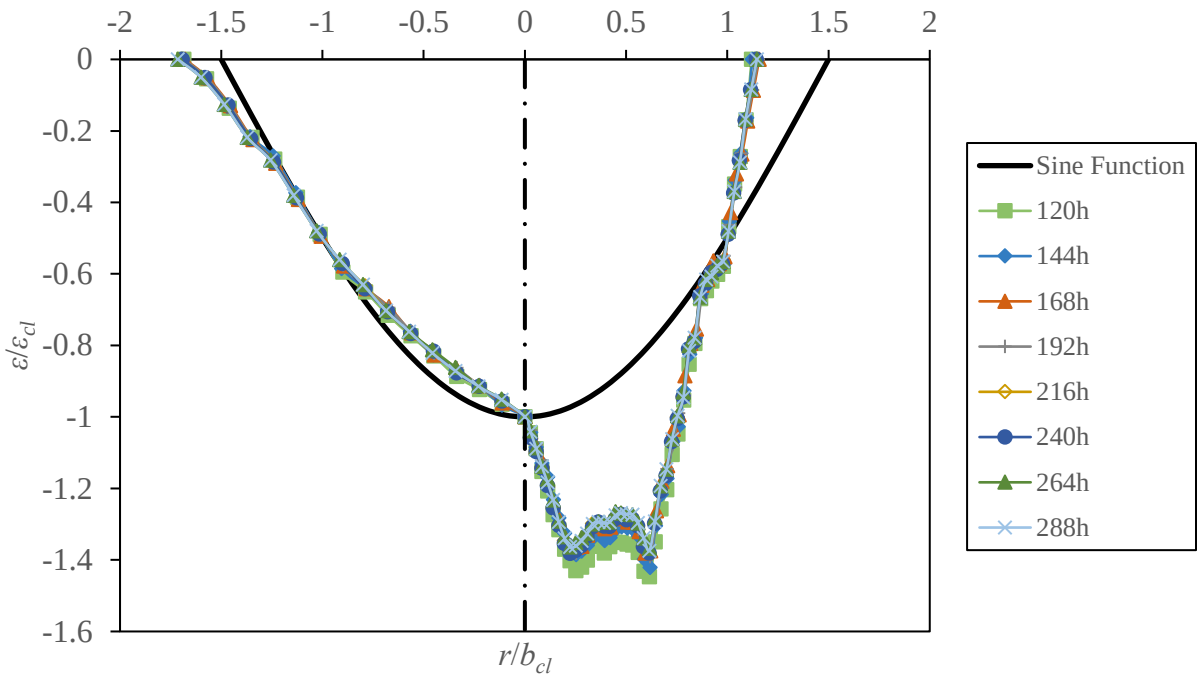

(j)

Figure 4.16: cont'd.

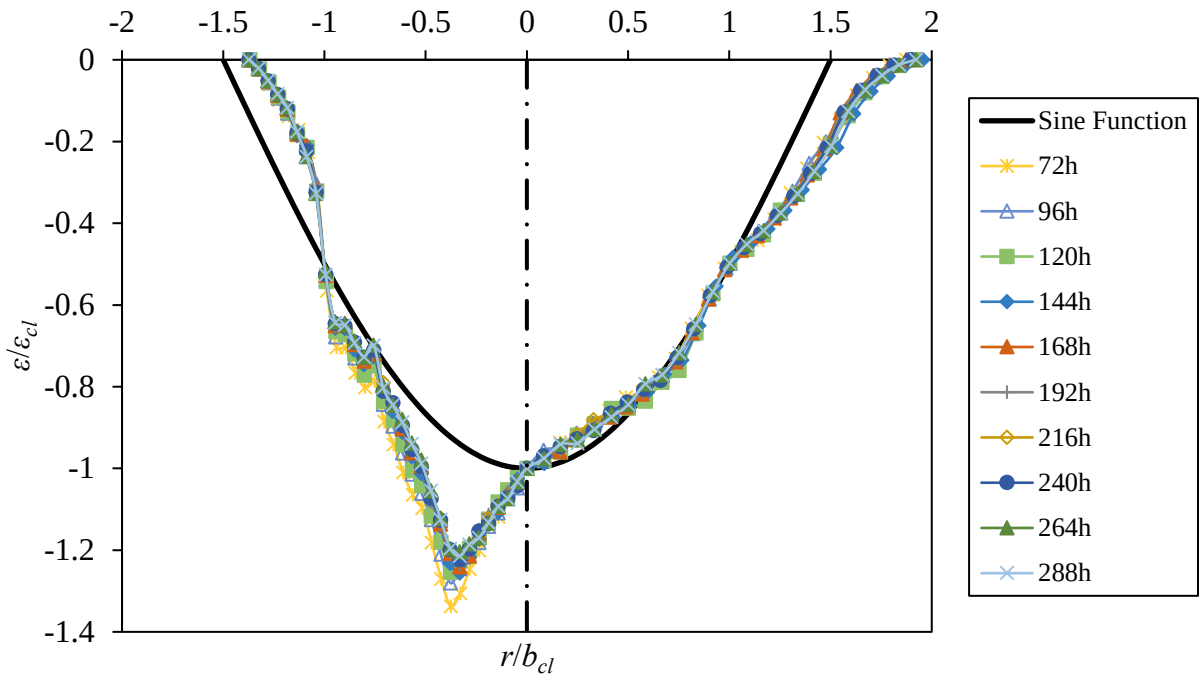

(k)

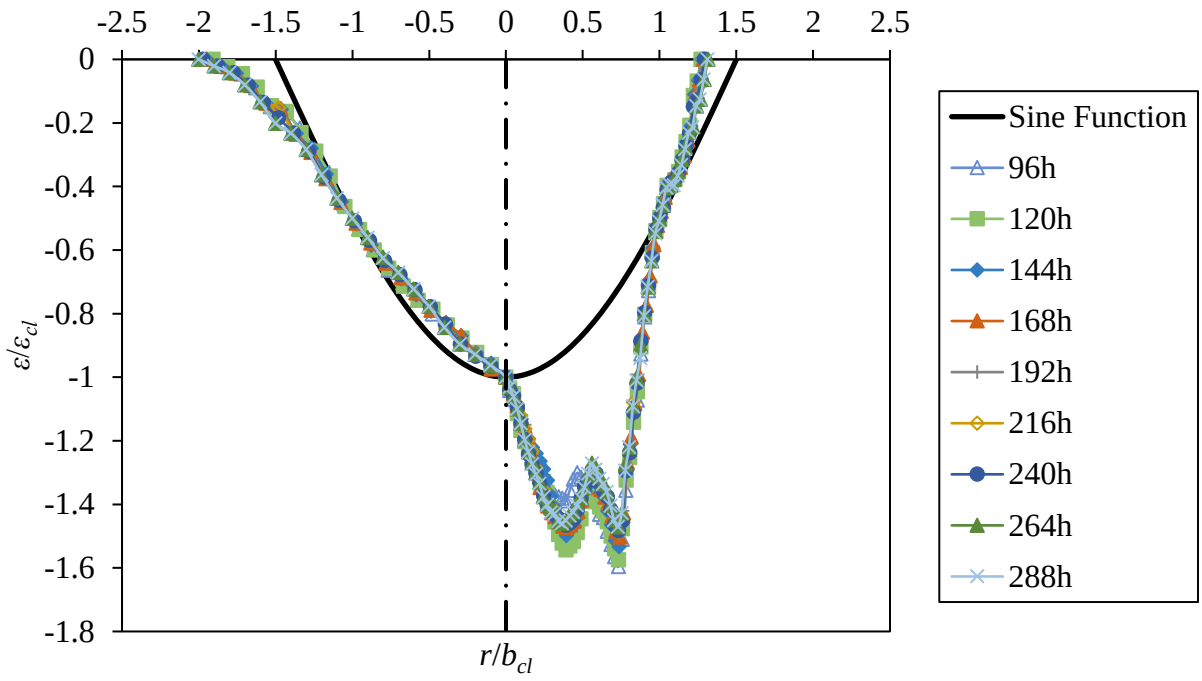

(l)

Figure 4.16: cont'd.

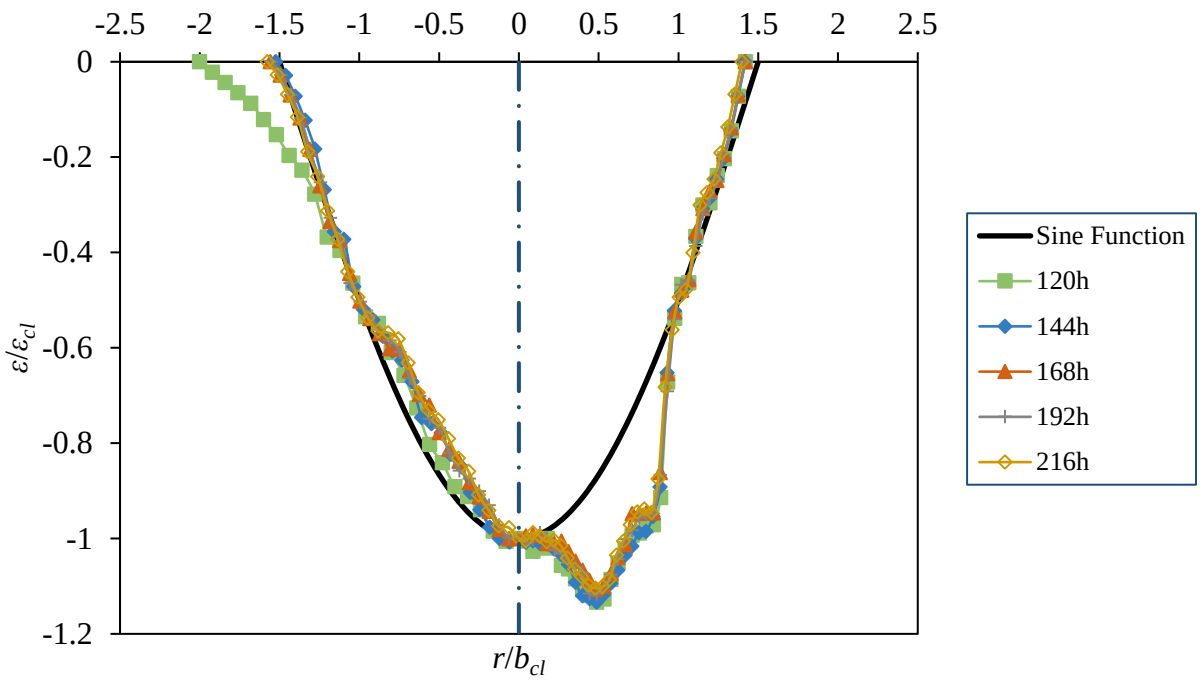

(m)

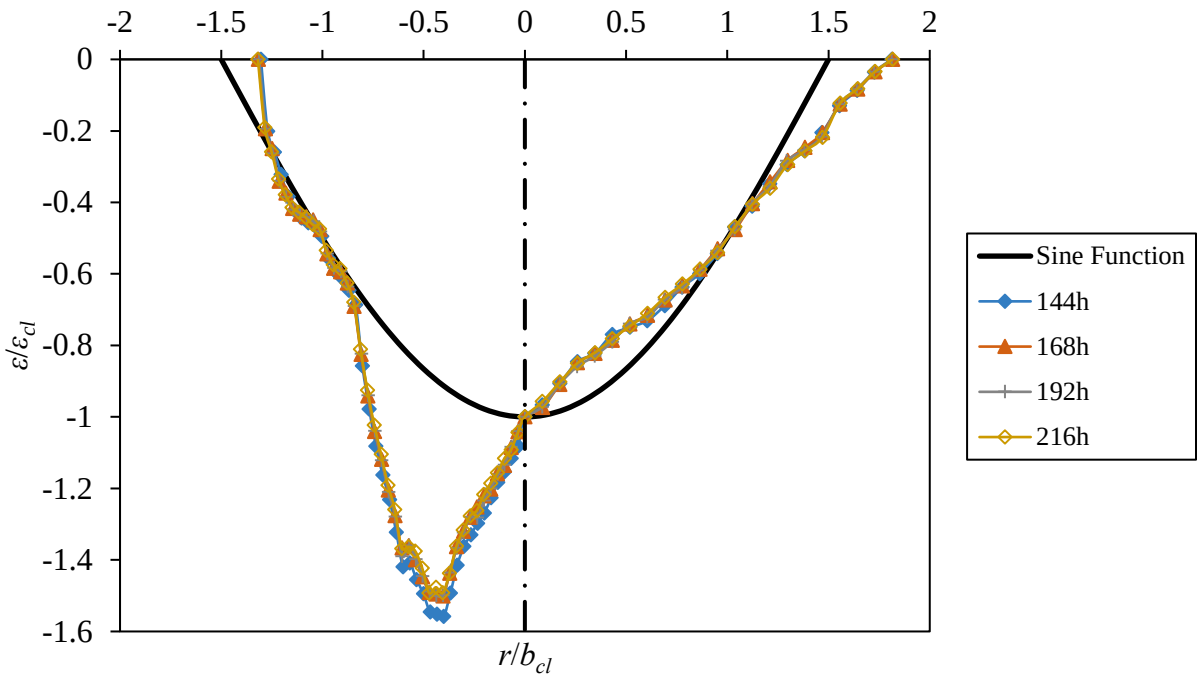

(n)

Figure 4.16: cont'd.

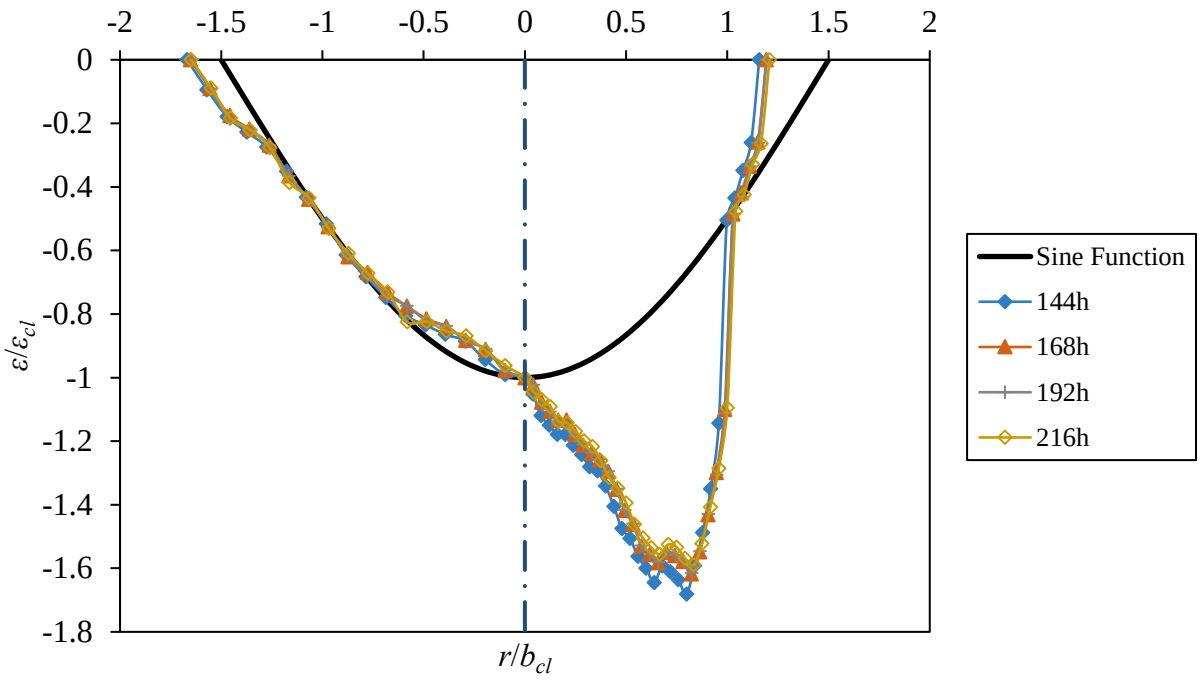

(o)

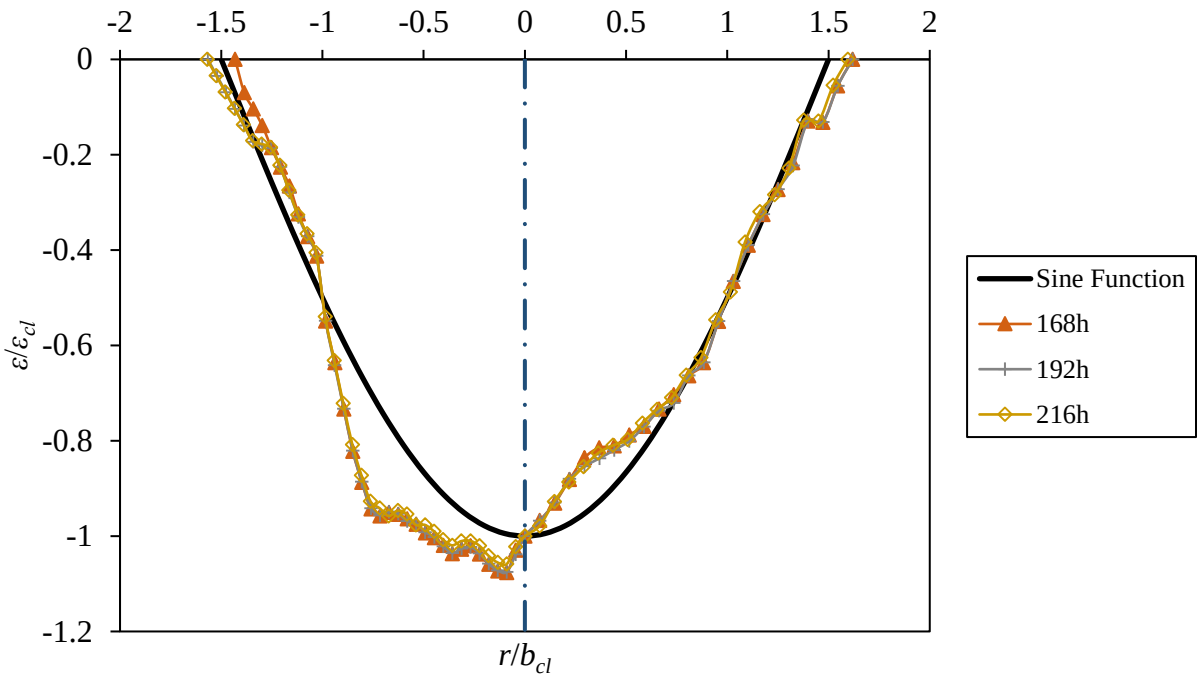

(p)

Figure 4.16: cont'd

CHAPTER 5. SUMMARY, CONCLUSIONS AND RECOMMENDATIONS

5.1 Summary and Conclusions

The first objective of this research was to observe the development of scour hole shape with time. The following observations were made corresponding to this objective:

- Mass erosion in the form of individual soil chunk removal was the dominant form of erosion throughout the scouring process. Soil chunks removed earlier in a test were larger in size and irregular in shape compared to the chunks removed later on a test. The dimensions of the smaller chunks ranged between 1-3 mm, while the dimensions of the bigger chunks ranged between 1-2 cm.

- In accordance with previous studies of erosion of cohesive soils with vertical circular impinging jets (Dunn 1959; Moore and Masch 1962; Mazurek *et al.* 2001), the initial scour was observed to occur at locations other than the jet centreline. However, this location could not be traced because the first measurement of the scour hole was made after 5 minutes of testing.

- During very early stage of testing, multiple depressions on the soil sample were observed instead of a distinct scour hole. However, as the scouring progressed with time, a distinct scour hole was identified, usually after 5 to 10 minutes of testing.

- Significant changes of the scour hole shape occurred during the early stage of the experiment, because the erosion rate was higher and the removed soil chunks were larger in size at that stage. Later in the scouring process, the eroded soil chunks were smaller. Therefore, as the scour hole grew with time, it took a more regular shape, more symmetrical with respect to the centreline or maximum scour depth.

- As reported by previous researchers (Moore and Masch 1962; Mazurek *et al* 2001; Mazurek 2001), for a significant portion of the scouring, the centreline and maximum scour depth was observed to increase linearly with the logarithm of time. However, this logarithmic relationship was not observed in case of the average radius and half-widths of the scour hole.

- For the majority of the tests (five for half-widths about the jet centreline and eight for half-widths about the maximum scour depth) the half-widths decreased with time. This happened because with time the scour hole shape changed from a wide and shallow scour hole to a narrow and deep scour hole.

- Temporary ceasing of the growth of some scour hole dimensions were observed as plateaus in the time development plots. This resulted due to large chunk removal by mass erosion. The centreline and maximum scour depths and scour hole radius were observed to form plateaus in the time development plots, but the half-widths did not exhibit this behavior.

- The section-wise maximum scour hole depths and the maximum scour hole depths did not coincide with the centreline scour depth at any time during the scour tests.

- Scour hole dimensions for any particular cross-section varied from the average dimensions of the scour hole. Therefore, scour hole profiles with time from only one or a couple of cross-sections cannot clearly show the development of scour hole with time. Among the section-wise maximum scour depths, scour hole radius and half-widths, the section-wise maximum scour depths showed less variability from the maximum scour depth. The half-widths showed the highest variability from the average half-widths. However, except Scour Test 1 and 6, the variability of the section-wise scour hole dimensions from the average for the whole scour hole decreased overall with time.

The second objective of this research was to identify the characteristic dimension of the scour hole to decide on whether a scour hole has reached the equilibrium condition. This characteristic dimension was termed the "critical equilibrium dimension". The considered characteristic dimensions to assess the critical equilibrium dimension were the average, maximum, section-wise maximum, and centreline scour hole depths; average radius; and average half-widths about the jet centreline and about the maximum scour depth. For four scour tests, Scour Test 5, 8, 9 and 10, all the dimensions came to equilibrium. Therefore these scour tests were considered to achieve an overall equilibrium condition. For three of the tests, Scour Tests 8, 9 and 10, the critical equilibrium dimension was the section-wise maximum scour depth. For Scour Test 5, the average

half-widths based on the centreline and maximum scour depths were the critical equilibrium dimensions.

Previously in most studies, either the centreline or maximum scour depths were used to track equilibrium scour. This study showed that the section-wise maximum scour depth and the half-widths were still growing while the centreline and maximum equilibrium depth were already at equilibrium. This happened because the sides of the scour hole were eroding after the centreline and maximum scour depth ceased growing. Therefore, both the section-wise maximum scour depth and average half-widths should be tracked for multiple sections of the scour hole, because the maximum scour depths for different sections of the scour hole ceased growing at different times of the scouring process.

The third objective of this study was to compare the dimensionless scour hole profiles during scour to the dimensionless equilibrium scour hole profile to find at what time in the scouring process any similarity in the scour hole shape starts to be present. Using data from the scour tests those reached to equilibrium (Scour Test 5, 8, 9 and 10), dimensionless scour hole profiles were developed. For the dimensionless scour hole profile, the centreline equilibrium scour depth was used to scale the scour hole depth, and the half-width about the jet centreline at equilibrium was used to scale the radial distance from jet centreline. From the dimensionless equilibrium scour hole profiles, a sine function was found by curve fitting as a general equation of the equilibrium scour hole. For the curve fitting, linear regression by least square method was used. The sine function curve fitting gave a correlation coefficient r^2=0.78.

The general equation did not necessarily represent any particular scour hole profile at equilibrium. Therefore, the scour hole profiles with time were compared visually with both the equilibrium scour hole profiles and the general equation. The time at which the scour hole profile started to show similarity with the equilibrium scour hole profile was termed as the "time to equilibrium shape" for that scour hole. This time to equilibrium shape (t^*_∞) was compared to the time to equilibrium (t_∞) for different scour tests. For Scour Tests 5, 8, 9, and 10, t^*_∞ was found to be 100%, 15%, 50%, and 89% of t_∞ respectively. This indicates, while for some scour tests, the equilibrium shapes were formed very quickly compared to the time to reach equilibrium, for some scour tests the equilibrium shapes were not formed until equilibrium.

5.2 Contributions of Work

The main contributions of this work are as follows:

- It includes the first study of the time development of the scour hole shape in cohesive soils by a submerged vertical circular impinging jet, and provides several important observations.

- It shows that tracking only the centreline or maximum scour depths with time is not appropriate to decide on the equilibrium state of the scour hole, as practiced in the previous studies. Rather, scour hole dimensions for multiple sections of the scour hole should be tracked with time.

- It shows that the shape of the scour hole can show similarity to the equilibrium scour hole shape before the equilibrium state is reached. However, the time of scouring to achieve that similarity varies from test to test, and some scour holes may not exhibit such behavior. Therefore, modeling of the earlier stage of scouring using the dimensionless equilibrium scour hole shape may not be appropriate.

- A general equation for the equilibrium scour hole shape was developed.

5.3 Recommendations

The following are recommendations for future work:

- The LASER optical profiler used in this study could measure the elevation of one single point on the soil surface at a time. To obtain the three-dimensional eroded soil surface, the profiler was moved over a 2 mm by 2 mm grid using a traverse system. The measurement time for each data point was slightly over 2 seconds. Therefore, it would take about 1.5 hours for the profiler to scan a soil surface area of 10 cm by 10 cm. The duration of this measurement was long enough for the sample to dry and shrink during measurement. To overcome this, the sample was kept submerged, and the collected data needed the correction for refraction. Further, during analysis, the continuous soil surface was found by linear interpolation of the data points on the 2 mm by 2 mm grid, which induced some errors in the surface. The problems of using a single point measurement profiler can be overcome by using a three-dimensional

LASER scanner- the Accuprofile 820 LASER Scanner by Acuity Laser, scanCONTROL by Micro-Epsilon, and Ultra-High Speed In-line Profilometer LJ-V series by KEYENCE to name a few. These scanners can take elevation measurement of points along a line instead of a single point. Therefore, the measurement is very quick, will take only few minutes for a big scour hole and will provide better resolution than a 2 mm by 2 mm grid.

- The percentage of clay in the tested soil samples was ranged from 48.7% to 51.7%. Manufactured soil samples with a wider range of clay percentage are difficult to find. However, soil samples can be prepared in the laboratory using powdered pottery clay and fine sand to obtain desired amount of clay content in the sample. Therefore, variability in the scour hole shape for samples with different clay percentage can be studied.

- The developed general equation for the dimensionless scour hole shape at equilibrium can be used to make physical and computational fluid dynamics models of the scour hole. Thus the turbulence of jet inside the scour hole and the stress distribution on the scour hole surface at equilibrium can be studied. This will help to understand how the scour hole itself affects the jet and thus affects the induced stress.

REFERENCES

Abramovich, G.N. (1963). The Theory of Turbulent Jets. MIT Press, Cambridge, Massachusetts, USA.

Aderibigbe, O. (1996). Contributions to Erosion by Jets. Ph.D. Thesis. Department of Civil Engineering. University of Alberta, Edmonton, Alberta.

Aderibigbe, O., and Rajaratnam, N. (1996). Erosion of Loose Beds by Submerged Circular Impinging Vertical Turbulent Jets. Journal of Hydraulic Research, IAHR, 34(1), 19–33.

Ahmed, F., & Rajaratnam, N. (1998). Flow Around Bridge Piers. Journal of Hydraulic Engineering, ASCE, 124(3), 288–300.

Albertson, M.L., Dai, Y.B., Jensen, R.A., and Rouse, H.M. (1950). Diffusion of Submerged Jets. Transactions of the ASCE, 115(1), 639–664.

Anderson, C. (1975). Chapter II. Sediment Transportation Mechanics; Section C, Erosion of Sediment- Local Scour. Sedimentation Engineering, Manual No. 54. Vanony, Vito A. (Ed.), ASCE, USA.

Annandale, G. W. (2006). Scour Technology: Mechanics and Engineering Practice. New York: McGraw Hill, 430 p.

Ansari, S. A. (1999). Influence of Cohesion on Local Scour. PhD. Thesis. Department of Civil Engineering, University of Roorkee, Roorkee, India.

Ansari, S.A. (2004). Discussion of "Hydraulics of Submerged Jet Subject to Change in Cohesive Bed Geometry" by Subhasish Dey and Bernhard Westrich. Journal of Hydraulic Engineering, 130(6), 590–592.

Ansari, S.A., Kothyari, U.C., and Raju, K.G.R. (2003). Influence of Cohesion on Scour under Submerged Circular Vertical Jets. Journal of Hydraulic Engineering, ASCE, 129(12), 1014-1019.

Arulanandan, K., Krone, R.B., and Loganathan, P. (1975). Pore and Eroding Fluid Influences on Surface Erosion on Soil. Journal of the Geotechnical Engineering Division, ASCE, 101(1), 51–66.

Ashforth-Frost, S., and Jambunathan, K. (1996). Effect of Nozzle Geometry and Semi-Confinement on the Potential Core of a Turbulent Axisymmetric Free Jet. International Communications in Heat and Mass Transfer, Elsevier, 23(2), 155–162.

ASME (American Society of Mechanical Engineers). (1990). Measurement of Fluid Flow in Pipes Using Orifice, Nozzle, and Venturi. ASME, New York. (ASME MFC-3M-1990).

ASTM (American Society of Testing and Materials) D2216-10(2010), Standard Test Methods for Laboratory Determination of Water (Moisture) Content of Soil and Rock by Mass, ASTM International, West Conshohocken, PA.

ASTM D421-85(2007), Standard Practice for Dry Preparation of Soil Samples for Particle-Size Analysis and Determination of Soil Constants, ASTM International, West Conshohocken, PA.

ASTM D422-63(2007)e2, Standard Test Method for Particle-Size Analysis of Soils, ASTM International, West Conshohocken, PA. 14

ASTM D4318-10(2010)e1, Standard Test Methods for Liquid Limit, Plastic Limit, and Plasticity Index of Soils, ASTM International, West Conshohocken, PA.

ASTM D5852-00(2007)e1, Standard Test Method for Erodibility Determination of Soil in the Field or in the Laboratory by the Jet Index Method, ASTM International, West Conshohocken, PA.

ASTM D7263-09(2009), Standard Test Methods for Laboratory Determination of Density (Unit Weight) of Soil Specimens, ASTM International, West Conshohocken, PA.

ASTM D854-14(2014), Standard Test Methods for Specific Gravity of Soil Solids by Water Pycnometer, ASTM International, West Conshohocken, PA.

Beltaos, S. (1974). Turbulent Impinging Jets. Ph.D. Thesis, Department of Civil Engineering, University of Alberta, Edmonton.

Beltaos, S., and Rajaratnam, N. (1974). Impinging Circular Turbulent Jets. Journal of the Hydraulics Division, ASCE, 100(10), 1313–1328.

Beltaos, S., and Rajaratnam, N. (1977). Impingement of Axisymmetric Developing Jets. Journal of Hydraulic Research, IAHR, 15(4), 311–326.

Blaisdell, F.W., Anderson, C.L., and Hebaus, G.G. (1981). Ultimate Dimensions of Local Scour. Journal of the Hydraulics Division, ASCE, 107(3), 327–337.

Bradshaw, P., and Love, E. (1961). The Normal Impingement of a Circular Air Jet on a Flat Surface. R& M No. 3205, Aeronautical Research Council, UK.

Breusers, H.N.C. (1967). Time Scale of Two-Dimensional Local Scour. 12th IAHR Congress. Fort Collins, Colorado, 275-282.

Cardoso, A.H., and Bettess, R. (1999). Effects of Time and Channel Geometry on Scour at Bridge Abutments. Journal of Hydraulic Engineering, ASCE, 125(4), 388–399.

Chabert, J., Engeldinger, P. (1956). Etude Des Affouillements Autour Des Piles De Ponts. Serie A. Laboratoire National d'Hydraulique, 6, Qui Watier, Chatou, France (in French).

Chreties, C., Simarro, G., Teixeira, L. (2008). New Experimental Method to Find Equilibrium Scour at Bridge Piers. Journal of Hydraulic Engineering, ASCE, 134(10), 1491–1495.

Coleman, S.E., Lauchlan, C.S., and Melville, B.W. (2003). Clear-Water Scour Development at Bridge Abutments. Journal of Hydraulic Research, IAHR, 41(5), 521–531.

Corrsin, S. (1943). Investigation of Flow in an Axially Symmetrical Heated Jet of Air. NACA Wartime Report (Vol. W-94, p. 43), NACA, Washington, USA.

Cossette, D., Mazurek, K.A., and Rennie, C.D. (2012). Critical Shear Stress from Varied Method of Analysis of a Submerged Circular Turbulent Impinging Jet Test for Determining Erosion Resistance of Cohesive Soils. In 6th International Conference on Scour and Erosion, Paris, 11-18.

Doddiah, D. Albertson, M.L., and Thomas, R. (1953). Scour from Jets. Fifth IAHR Congress Minneapolis, USA, 161–169.

Dunn, I. S. (1959). Tractive Resistance of Cohesive Channels. Journal of the Soil Mechanics and Foundations Division, ASCE, 85, 1–24.

Ettema, R. (1980). Scour at Bridge Piers. Report No. 216, School of Engineering, University of Auckland, Auckland, New Zealand.

Excelforum.com. (2005). Linear Interpolation Function in Excel. Available from http://www.excelforum.com/excel-formulas-and-functions/466389-linear-interpolation-function-in-excel.html [accessed 12 June 2016].

Fael, C.M.S., Simarro, G., Martín, J.P., and Cardoso, A.H. (2006). Local Scour at Vertical-Wall Abutments under Clear-Water Flow Conditions. Water Resources Research, AGU, 42(10), 1–12.

Fellouah, H., and Pollard, A. (2009). The Velocity Spectra and Turbulence Length Scale Distributions in the Near to Intermediate Regions of a Round Free Turbulent Jet. Physics of Fluids, American Institute of Physics, 21(11), 1–9.

Fellouah, H., Ball, C.G., and Pollard, A. (2009). Reynolds Number Effects within the Development Region of a Turbulent Round Free Jet. International Journal of Heat and Mass Transfer, Elsevier, 52(17-18), 3943–3954.

Franzetti, S., Larcan, E., and Mignosa, P. (1982). Influence of Tests Duration on the Evaluation of Ultimate Scour around Circular Piers. International Conference on the Hydraulic Modelling of Civil Engineering Structures. Coventry, England, 381-396.

George, W. (1989). The Self-Preservation of Turbulent Flows and Its Relation to Initial Conditions and Coherent Structures. In W. George & A. Roger (Eds.), Advances in Turbulence (pp. 39–73). Buffalo, NY: Hemisphere Phublishing Corporation.

Ghaneeizad, S.M., Atkinson, J.F., and Bennett, S.J. (2014). Effect of Flow Confinement on The

Hydrodynamics of Circular Impinging Jets: Implications for Erosion Assessment. Environmental Fluid Mechanics, Springer, 15(1), 1–25.

Ghaneeizad, S.M., Karamigolbaghi, M., Atkinson, J.F., and Bennett, S.J. (2015). Hydrodynamics of Confined Impinging Jets and the Assessment of Soil Erodibility. In World Environmental and Water Resources Congress 2015,1742–1751.

Gill, M.A. (1972). Erosion of Sand Beds Around Spur Dikes. Journal of the Hydraulics Division, ASCE, 98(9), 1587–1602.

Glauert, M.B. (1956). The Wall Jet. Journal of Fluid Mechanics, Cambridge University Press, 1(06), 625–643.

Grabowski, R.C., Droppo, I.G., and Wharton, G. (2011). Erodibility of Cohesive Sediment: The Importance of Sediment Properties. Earth-Science Reviews, Elsevier, 105(3), 101–120.

Grimaldi, C. (2005). Non-Conventional Countermeasures Against Local Scouring at Bridge Piers. Ph.D. Thesis. Hydraulic Engineering for Environment and Territory, University of Calabria, Cosenza, Italy.

Haehnel, R.B., Cushman-Roisin, B., and Dade, W.B. (2006). Cratering by a Subsonic Jet Impinging on a Bed of Loose Particles. Earth and Space 2006 - 10th Biennial International Conference on Engineering, Construction, and Operations in Challenging Environments. League City/Houston, Texas, United States, 1-8.

Haehnel, R.B., Dade, W.B., and Cushman-Roisin, B. (2008). Crater Evolution due to a Jet Impinging on a Bed of Loose Particles. Proceeding of Earth and Space 2008, 1-10.

Hanson, G. J. (1990). Surface Erodibility of Earthen Channels at High Stresses. Part II-Developing an in situ testing device. Transactions of the ASAE, 33(1), 132–137

Hanson, G.J. (1991). Development of A Jet Index to Characterize Erosion Resistance of Soils in Earthen Spillways. Transactions of the ASABE, 34(5), 2015–2020.

Hanson, G.J., and Cook, K.R. (1997). Development of Excess Shear Stress Parameters for Circular Jet Testing. ASAE Paper No. 972227, 21p.

Hanson, G.J., and Cook, K.R. (2004). Apparatus, Test Procedures, and Analytical Methods to Measure Soil Erodibility in Situ. Applied Engineering in Agriculture, ASABE, 20(4), 455-462.

Hanson, G.J., Robinson, K.M., and Temple, D.M. (1990). Pressure and Stress Distributions Due to a Submerged Impinging Jet. In Hydraulic Engineering - Proceedings of the 1990 National Conference, San Diego, CA, USA, 525–530.

Hashiehbaf, A., Baramade, A., Agrawal, A., and Romano, G.P. (2015). Experimental Investigation on an Axisymmetric Turbulent Jet Impinging on a Concave Surface. International Journal of Heat and Fluid Flow, Elsevier, 53, 167–182.

Hinze, J.O., and Zijnen, B.G.V.D.H. (1949). Transfer of Heat and Matter in the Turbulent Mixing Zone of an Axially Symmetrical Jet. Applied Scientific Research, Springer, 1(1), 435–461.

Hollick, M. (1976). Towards a Routine Test for the Assessment of the Critical Tractive Forces of Cohesive Soils. Transactions of the ASAE, 19(6), 1076–1081.

Hussein, H.J., Capp, S.P., and George, W.K. (1994). Velocity Measurements in a High Reynolds Number, Momentum Conserving, Axisymmetric, Turbulent Jet. Journal of Fluid Mechanics, Cambridge University Press, 258(1), 31–75.

Jones, J.S., and Sheppard, D.M. (2000). Scour at Wide Bridge Piers. Proceedings of the Joint Conference on Water Resources Engineering and Water Resources Planning and Management, ASCE, Minneapolis, Minnesota, 1-10.

Kenney, J.F. and Keeping, E.S. (1962). Mathematics of Statistics, Pt. 1, 3rd ed. Princeton, NJ: Van Nostrand, 348p.

Kobus, H., Leister, P., and Westrich, B. (1979). Flow Field and Scouring Effects of Steady and Pulsating Jets Impinging on a Movable Bed. Journal of Hydraulic Research, IAHR, 17(3), 175-192.

Kohli, A., and Hager, W.H. (2001). Building Scour in Floodplains. Proceedings of the ICE - Water and Maritime Engineering, 148(2), 61–80.

Kristiawan, M., Sodjavi, K., Montagné, B., Meslem, A., and Sobolik, V. (2015). Mass Transfer and Shear Rate on a Wall Normal to an Impinging Circular Jet. Chemical Engineering Science, 132, 32–45.

Lança, R., Fael, C., & Cardoso, A. (2010). Assessing Equilibrium Clear Water Scour Around Single Cylindrical Piers. Proceedings of International Conference on Fluvial Hydraulics River Flow 2010, A. Dittrich et al., eds.,International Association For Hydro-Environment Engineering and Research, 1207-1213.

Lauchlan, C.S. (1999). Countermeasures for Pier Scour. Ph.D. Thesis. University of Auckland, Auckland, New Zealand.

Laursen, E. M. (1952). Observations on the Nature of Scour. Proceedings of the 5th Hydraulic Conference, Bulletin 34, University of Iowa, Iowa City, Iowa, 179–197.

Lee, J.H.W., and Chu, V.H. (2003). Turbulent Jets and Plumes: a Lagrangian Approach. Kluwer Academic Publishers, Norwell, Massachusetts, USA, 390 p.

Mazurek, K.A. (2001). Scour of Clay by Jets. Ph.D. Thesis, Department of Civil Engineering, University of Alberta, Edmonton, Alberta.

Mazurek, K.A. (2003). Discussion of "Influence of Cohesion on Scour under Submerged Circular Vertical Jets" by Sarfaraz A. Ansari, Umesh C. Kothyari, and Kittur G. Ranga Raju. Journal

of Hydraulic Engineering, 131(8), 737–738.

Mazurek, K.A. (2010). Erodibility of A Cohesive Soil Using a Submerged Circular Turbulent Impinging Jet Test. In 2nd Joint Federal Interagency Conference, USGS, Las Vegas, NV, USA, 10p.

Mazurek, K.A., and Gheisi, A. (2009). Assessment of the Erodibility of a Cohesive Soil using a Submerged Circular Turbulent Impinging Jet. In 33rd IAHR Congress: Water Engineering for a Sustainable Environment, Vancouver, Canada.

Mazurek, K.A., Rajaratnam, N., and Sego, D.C. (2001). Scour of Cohesive Soil by Submerged Circular Turbulent Impinging Jets. Journal of Hydraulic Engineering, 127(7), 598–606.

Mazurek, K.A., Rajaratnam, N., and Sego, D.C. (2006). Time Development of Scour in a Cohesive Material due to a Submerged Circular Turbulent Impinging Jet. In ICSE-3, 3rd International Conference on Scour and Erosion. Amsterdam, The Netherlands.

Melville, B. W., Chiew, Y.M. (1999). Time Scale for Local Scour at Bridge Piers. Journal of Hydraulic Engineering, 125(1), 59–65.

Moore, W.L., and Masch, F.D. (1962). Experiments on the Scour Resistance of Cohesive Sediments. Journal of Geophysical Research, 67(4), 1437–1446.

National Instruments Corporation. Specifications for Stepper Motors and Encoders. Available from http://www.ni.com/datasheet/pdf/en/ds-311 [accessed 12 June 2016].

Oliveto, G., and Hager, W.H. (2002). Temporal Evolution of Clear-Water Pier and Abutment Scour. Journal of Hydraulic Engineering, 128(9), 811–820.

Phares, D.J., Smedley, G.T., and Flagan, R.C. (2000). The Wall Shear Stress Produced by the Normal Impingement of a Jet on a Flat Surface. Journal of Fluid Mechanics, Cambridge University Press, 418, 351–375.

Pope, S.B. (2000). Turbulent Flows. Cambridge University Press, Cambridge, 771p.

Poreh, M., and Hefez, E. (1967). Initial Scour and Sediment Motion due to an Impinging Jet. In International Association for Hydraulic Research. Fort Collins, Colorado, 8p.

Poreh, M., Tsuei, Y.G., and Cermak, J.E. (1967). Investigation of a Turbulent Radial Wall Jet. Journal of Applied Mechanics, 34(2), 457–463.

Radice, A., Franzetti, S., and Ballio, F. (2002). Local Scour at Bridge Abutments. In River Flow 2002, International Conference on Fluvial Hydraulics, International Association for Hydro-Environment Engineering and Research.

Rajaratnam, N. (1976). Turbulent Jets. Elsevier, New York, 304 p.

Rajaratnam, N. (1981). Erosion by Plane Turbulent Jets. Journal of Hydraulic Research, IAHR,

19(4), 339–358.

Rajaratnam, N. (1982). Erosion by Submerged Circular Jets. Journal of the Hydraulics Division, ASCE, 108(2), 262–267.

Rajaratnam, N., and Beltaos, S. (1977). Erosion by Impinging Circular Turbulent Jets. Journal of the Hydraulics Division, ASCE, 103(10), 1313–1328.

Rajaratnam, N., and Berry, B. (1977). Erosion by Circular Turbulent Wall Jets. Journal of Hydraulic Research, IAHR, 15(3), 277–289.

Rajaratnam, N., and Flint-Petersen, L. (1989). Low Reynolds Number Circular Turbulent Jets. In ICE Proceedings, Ice Virtual Library, 87, 299–305.

Rajaratnam, N., and Mazurek, K.A. (2003). Erosion of Sand by Circular Impinging Water Jets with Small Tailwater, Journal of Hydraulic Engineering, ASCE, 129(3), 225–229.

Rajaratnam, N., Johnston, G.A., and Barber, M.A. (1993). Energy Dissipation by Jet Diffusion in Stormwater Drop Shafts. Canadian Journal of Civil Engineering, NRC Research Press, 20(3), 374–379.

Rajaratnam, N., Zhu, D.Z., and Rai, S.P. (2010). Turbulence Measurements in the Impinging Region of a Circular Jet. Canadian Journal of Civil Engineering, NRC Research Press, 37(5), 782–786.

Rouse, H. (1939). Criteria for Similarity in the Transportation of Sediment. In 1st Hydraulic Conference, Bulletin 20, State University of Iowa.

Rouse, H. (1965). Engineering Hydraulics: Sediment Transportation. New York: John Wiley and Sons.

Sarma, K.V.N. (1967). Existence of Limiting Scour Depth. Journal of the Institution of Engineers (India), 48(1), 84–92.

Sarma, K.V.N., and Sivasankar, R. (1967). Scour Under Vertical Circular Jets. Journal of the Institution of Engineers (India), 48(3), 568–579.

Sheppard, D. M., Odeh, M., & Glasser, T. (2004). Large Scale Clear-Water Local Pier Scour Experiments. Journal of Hydraulic Engineering, ASCE, 130(10), 957–963.

Simarro, G., and Martín, J.P. (2004). Exponential Expression for Time Evolution in Local Scour. Journal of Hydraulic Research, IAHR, 42(6), 663-665.

Simarro, G., Fael, C.M.S., and Cardoso, A.H. (2011). Estimating Equilibrium Scour Depth at Cylindrical Piers in Experimental Studies. Journal of Hydraulic Engineering, ASCE, 137(9), 1089–1093.

Stein, O.R. (1990). Mechanics of Headcut Migration in Rills. Ph.D. Thesis. Colorado State

University. Fort Collins, Colorado, USA.

Stein, O.R., and Julien, P.Y. (1994). Sediment Concentration Below Free Overfall. Journal of Hydraulic Engineering, ASCE, 120(9), 1043-1059.

Stein, O.R., Julien, P.Y., & Alonso, C.V. (1993). Mechanics of Jet Scour Downstream of a Headcut. Journal of Hydraulic Research, IAHR, 31(6), 723–738.

Topping, J. (1957). Errors of Observation and their Treatment. The Institute of Physics: London, England.

Uddin, M., and Pollard, A. (2007). Self-Similarity of Coflowing Jets: The Virtual Origin. Physics of Fluids, American Institute of Physics, 19(6), 2–6.

Walder, J.S. (2015). Dimensionless Erosion Laws for Cohesive Sediment. Journal of Hydraulic Engineering, ASCE, 10.1061/(ASCE)HY.1943-7900.0001068 , 04015047.

Weidner, K. (2012). Evaluation of the Jet Test Method for Determining the Erosional Properties of Cohesive Soils; A Numerical Approach. M.Sc. Thesis, Department of Civil Engineering, Virginia Polytechnic Institute and State University, Blacksburg, Virginia, USA.

Weidner, K.L., Petrie, J., Diplas, P., Nam, S., Gutierrez, M., and Ellenberg, M. (2012). Numerical Simulation of Jet Test and Associated Soil Erosion. 6th International Conference on Scour and Erosion (ICSE6, Paris, France, 609–616.

Westrich, B., and Kobus, H. (1973). Erosion of a Uniform Sand Bed by Continuous and Pulsating Jets. In International Association for Hydraulic Research Congress (Vol. 1, p. 8). Istanbul, Turkey.

Wygnanski, I., and Fiedler, H. (2006). Some Measurements in the Self-Preserving Jet. Journal of Fluid Mechanics, Cambridge University Press, 38(03), 577.

Xu, G., and Antonia, R. a. (2002). Effect of Initial Conditions on The Temperature Field of a Turbulent Round Free Jet. International Communications in Heat and Mass Transfer, Elsevier, 29(8), 1057–1068.

Zaghloul, N.A. (1983). Local Scour Around Spur-Dikes. Journal of Hydrology, Elsevier, 60, 123-140.

APPENDIX A: Codes used for Data Processing

A-1. Python Code for Refraction Correction and Elevation Recalculation of Sample Surface Points

```
# Refraction correction and elevation.py
# Created on: 2016-06-18 01:47:09.00000
#   (generated by ArcGIS/ModelBuilder)
# Usage: Refraction correction and elevation <Scour_Data_Text_Input> <Water_Level>
<Corner1__Same_for_all_> <Output_Point_Shape_File>
# Description:
# Converts scour hole profile text data into shape files and corrects for refraction. After the
shapes are created, manually the files are corrected if error is present.

# Set the necessary product code
# import arcinfo

# Import arcpy module
import arcpy

# Script arguments
Scour_Data_Text_Input = arcpy.GetParameterAsText(0)
Water_Level = arcpy.GetParameterAsText(1)
Corner1__Same_for_all_ = arcpy.GetParameterAsText(2)
Output_Point_Shape_File = arcpy.GetParameterAsText(3)

# Local variables:
apparent_d = Output_Point_Shape_File
PointFile__5_ = apparent_d
actual_d = apparent_d
PointFile__3_ = actual_d
actual_h = actual_d
PointFile__2_ = actual_h
height = PointFile__2_
```

```
Output_Point_File = height
Intermediate_File = Scour_Data_Text_Input

# Process: Make XY Event Layer
arcpy.MakeXYEventLayer_management(Scour_Data_Text_Input, "X Position (mm)", "Y Position (mm)", Intermediate_File, "PROJCS['Laser Data',GEOGCS['GCS_WGS_1984',DATUM['D_WGS_1984',SPHEROID['WGS_1984',6378137.0,298.257223563]],PRIMEM['Greenwich',0.0],UNIT['Degree',0.0174532925199433]],PROJECTION['Transverse_Mercator'],PARAMETER['False_Easting',0.0],PARAMETER['False_Northing',0.0],PARAMETER['Central_Meridian',0.0],PARAMETER['Scale_Factor',1.0],PARAMETER['Latitude_Of_Origin',0.0],UNIT['Millimeter',0.001]];-5623113000 -10002065800 450266.946591223;-100000 10000;-100000 10000;1;0.001;0.001;IsHighPrecision", "Laser Position (mm)")

# Process: Feature To Point
arcpy.FeatureToPoint_management(Intermediate_File, Output_Point_Shape_File, "CENTROID")

# Process: Add Field
arcpy.AddField_management(Output_Point_Shape_File, "apparent_d", "DOUBLE", "", "", "", "", "NULLABLE", "NON_REQUIRED", "")

# Process: Calculate Field
arcpy.CalculateField_management(apparent_d, "apparent_d", "[Laser_Posi]-%Water Level%", "VB", "")

# Process: Add Field (2)
arcpy.AddField_management(apparent_d, "actual_d", "DOUBLE", "", "", "", "", "NULLABLE", "NON_REQUIRED", "")
# Process: Calculate Field (2)
arcpy.CalculateField_management(actual_d, "actual_d", "[apparent_d]*1.33", "VB", "")
```

```
# Process: Add Field (3)
arcpy.AddField_management(actual_d, "actual_h", "DOUBLE", "", "", "", "", "NULLABLE",
"NON_REQUIRED", "")

# Process: Calculate Field (3)
arcpy.CalculateField_management(actual_h, "actual_h", "%Water Level%+ [actual_d]", "VB",
"")

# Process: Add Field (4)
arcpy.AddField_management(PointFile__2_, "height", "DOUBLE", "", "", "", "",
"NULLABLE", "NON_REQUIRED", "")

# Process: Calculate Field (4)
arcpy.CalculateField_management(height, "height", "%Corner1 (Same for all)%+105-
[actual_h]", "VB", "")
```

A-2. Visual Basic Code for Calculating Half-widths of Scour hole in MS Excel (adapted from Excelforum.com 2005)

```
Function HalfWidth(xVal As Double, _
   xRange As Variant, _
   yRange As Variant, _
   Optional isSorted As Long = 1) As Double
   Dim yVal As Double
   Dim xBelow As Double, xAbove As Double
   Dim yBelow As Double, yAbove As Double
   Dim testVal As Double
   Dim High As Long, Med As Long, Low As Long

   Low = 1
   High = xRange.Cells.Count

   If isSorted <> 0 Then
      Rem binary search sorted range
      Do
         Med = Int((Low + High) \ 2)
         If (xRange.Cells(Med).Value) < (xVal) Then
            Low = Med
         Else
            High = Med
         End If
      Loop Until Abs(High - Low) <= 1
   Else
      Rem search every entry
      xBelow = -1E+205
      xAbove = 1E+205

      For Med = 1 To xRange.Cells.Count
```

```
        testVal = xRange.Cells(Med)
        If testVal < xVal Then
            If Abs(xVal - testVal) < Abs(xVal - xBelow) Then
                Low = Med
                xBelow = testVal
            End If
        Else
            If Abs(xVal - testVal) < Abs(xVal - xAbove) Then
                High = Med
                xAbove = testVal
            End If
        End If
    Next Med
End If

xBelow = xRange.Cells(Low): xAbove = xRange.Cells(High)
yBelow = yRange.Cells(Low): yAbove = yRange.Cells(High)

HalfWidth = yBelow + (xVal - xBelow) * (yAbove - yBelow) / (xAbove - xBelow)
```

APPENDIX B: Three Dimensional Plots of the Scour Holes with Time

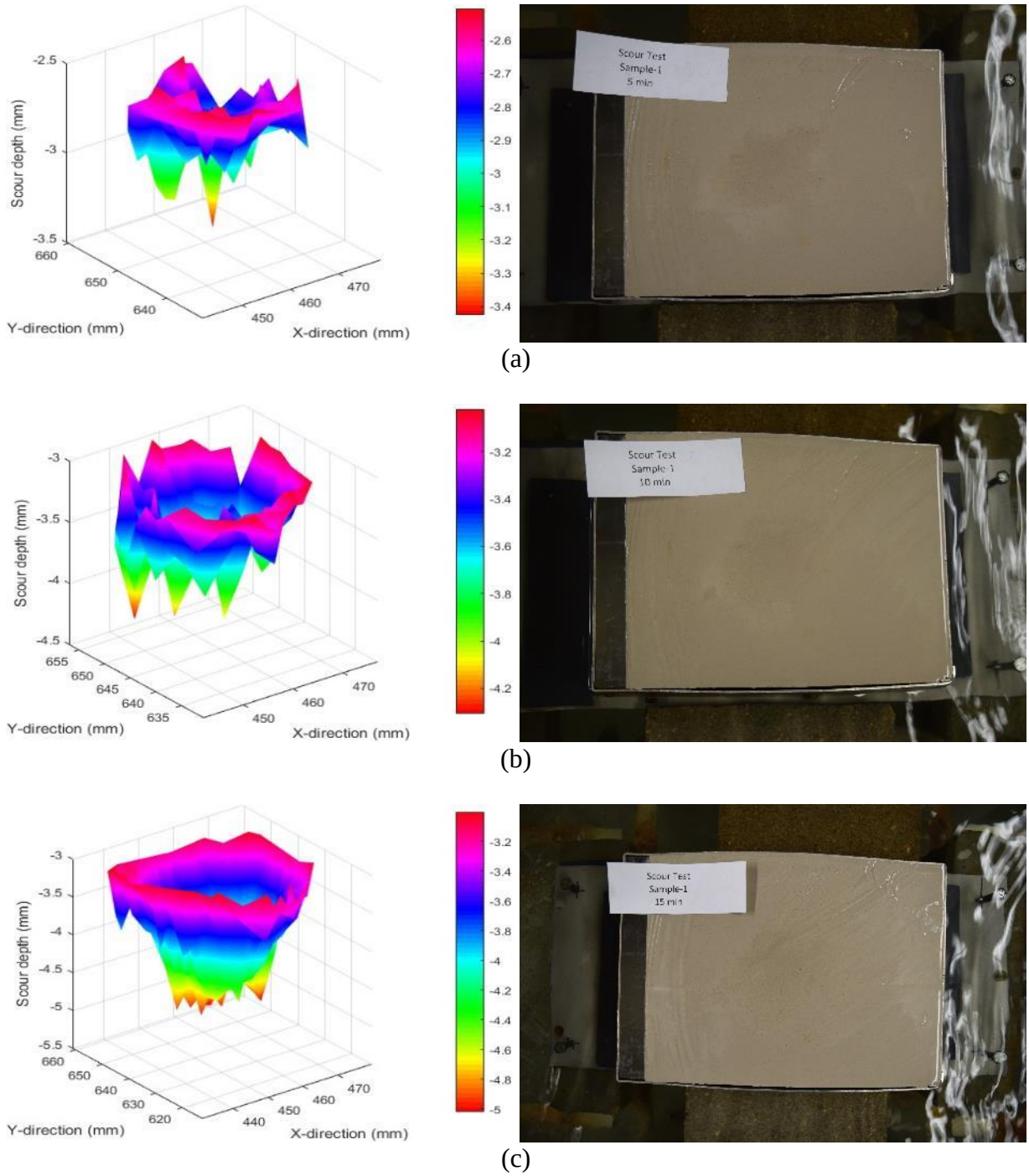

Figure B-1: Three-dimensional scour hole shape and photo of the sample in plan view for Scour Test 1 (Buffstone clay, U_0=8.6 m/s, d=7.76 mm, H=85 mm, and t_d=144 h) after a test duration of (a) 5 min, (b) 10 min, (c) 15 min, (d) 20 min, (e) 30 min, (f) 40 min, (g) 50 min, (h) 1 h, (i) 1.5 h, (j) 2 h, (k) 4 h, (l) 8 h, (m) 16 h, (n) 24 h, (o) 48 h, (p) 72 h, (q) 96 h, (r) 120 h, and (s) 144 h.

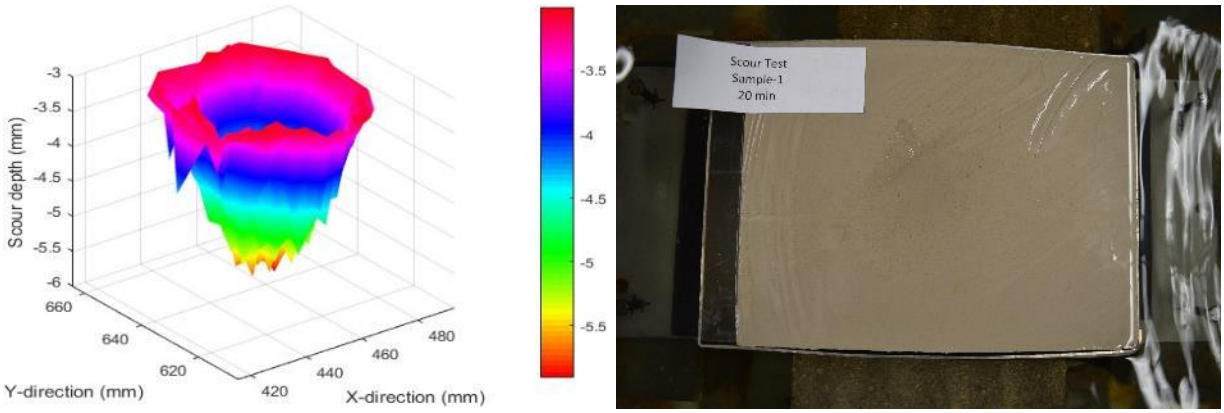

(d)

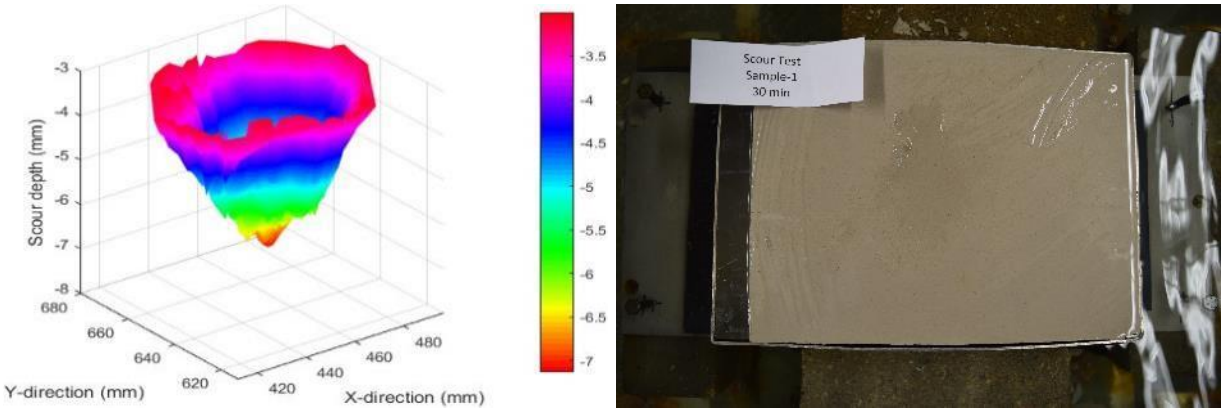

(e)

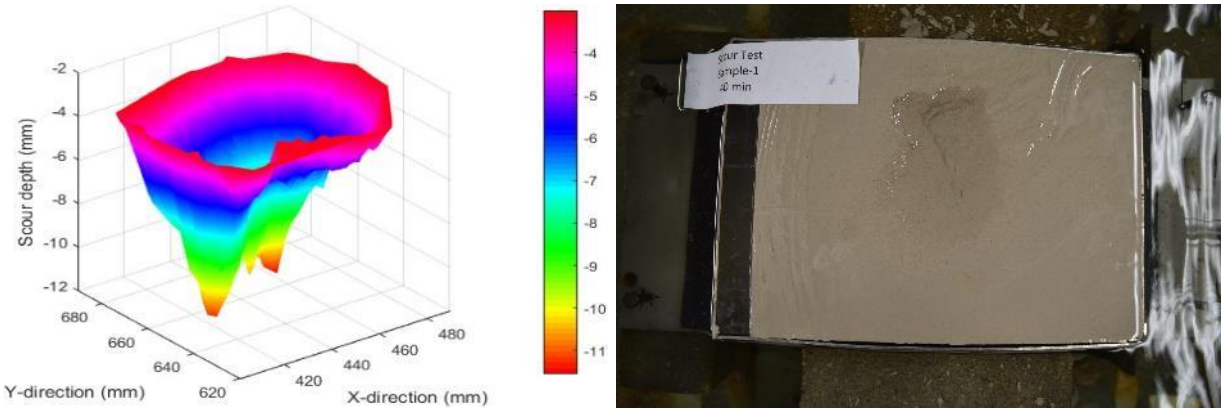

(f)

Figure B-1: cont'd.

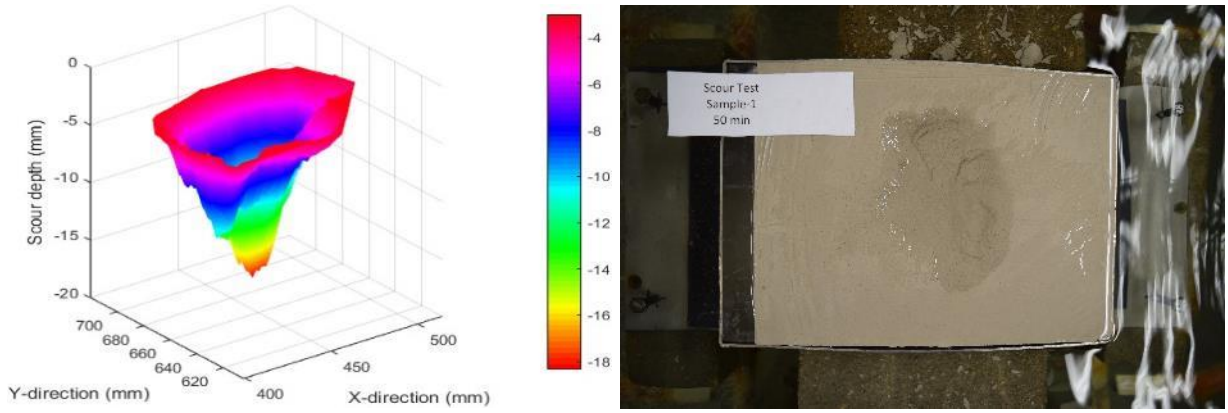

(g)

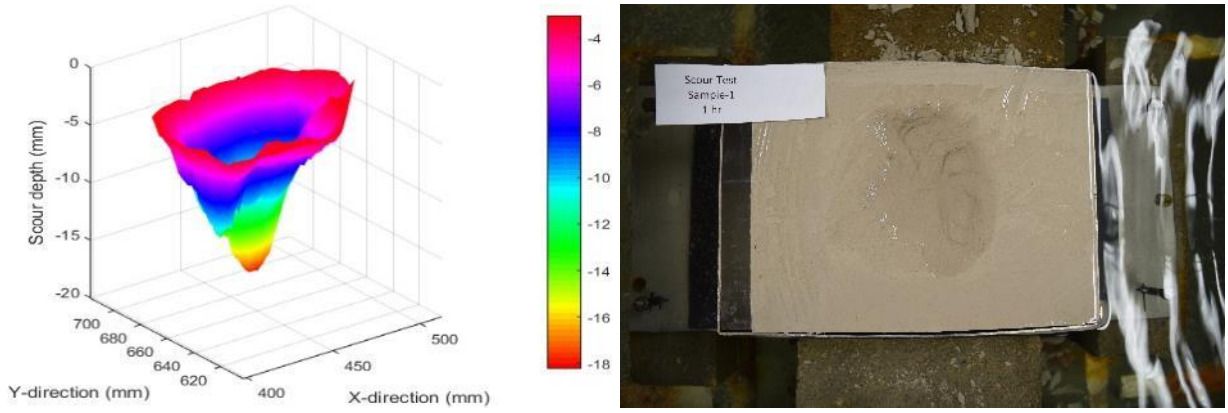

(h)

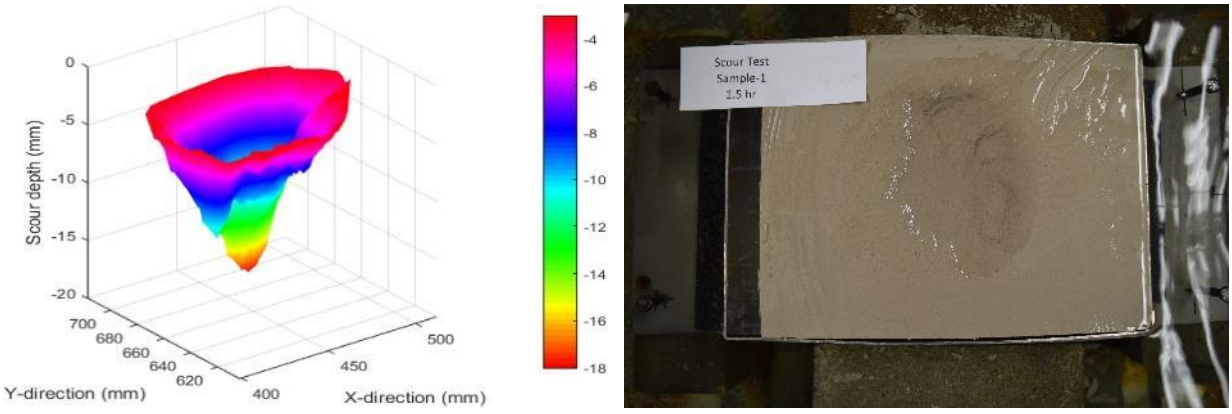

(i)

Figure B-1: cont'd.

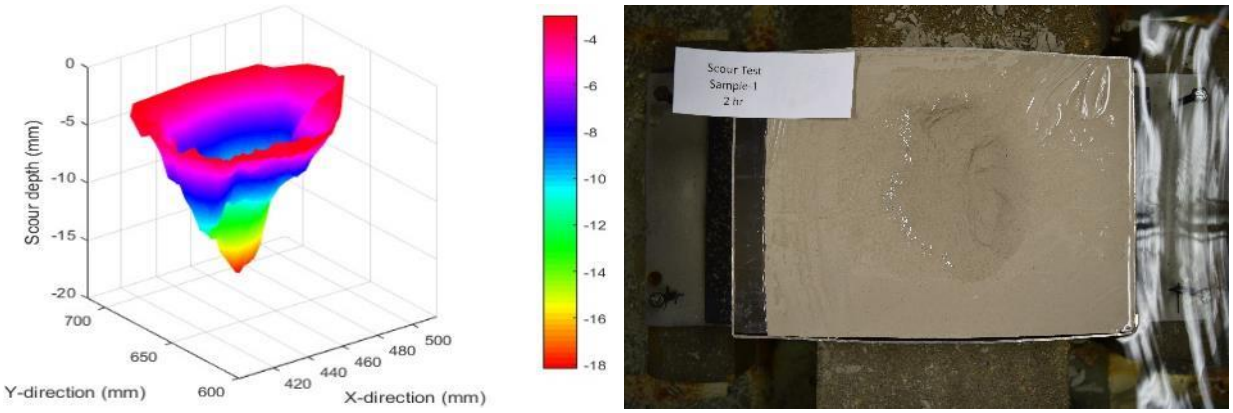

(j)

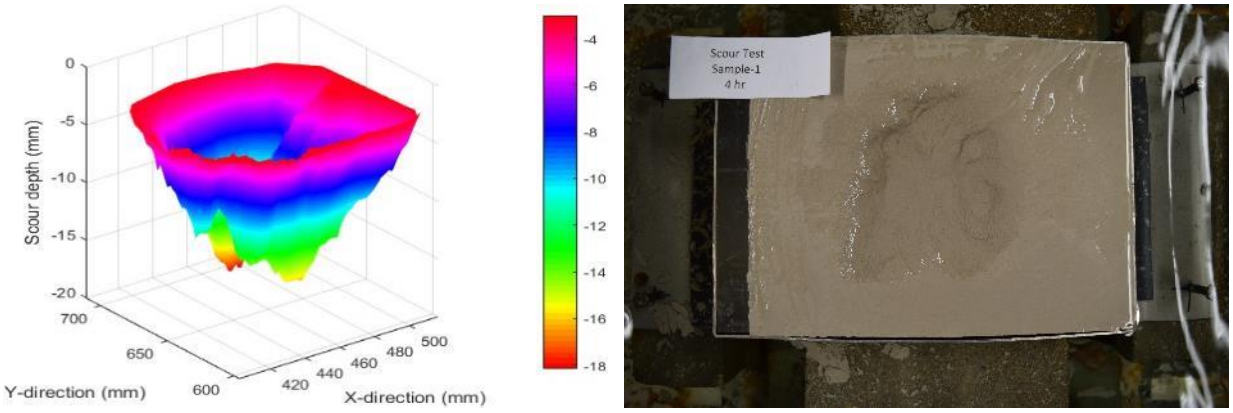

(k)

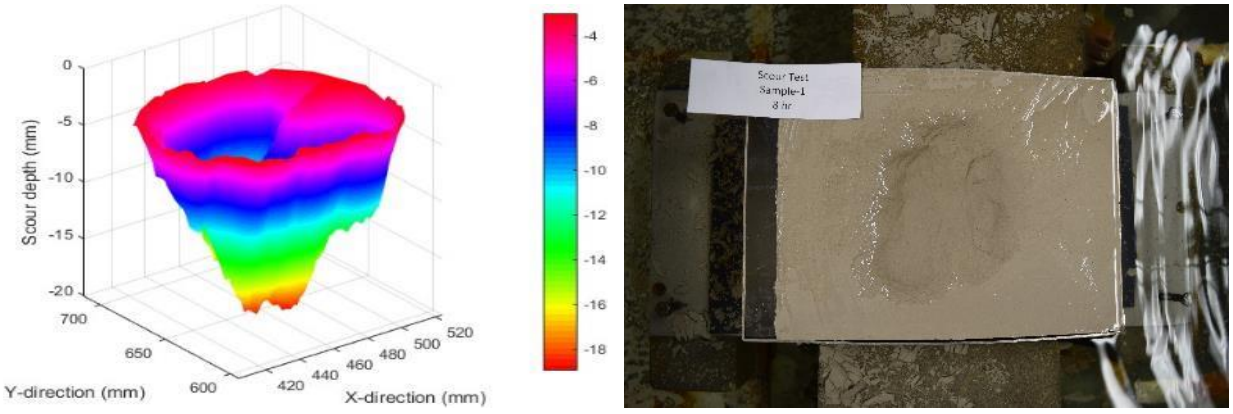

(l)

Figure B-1: cont'd.

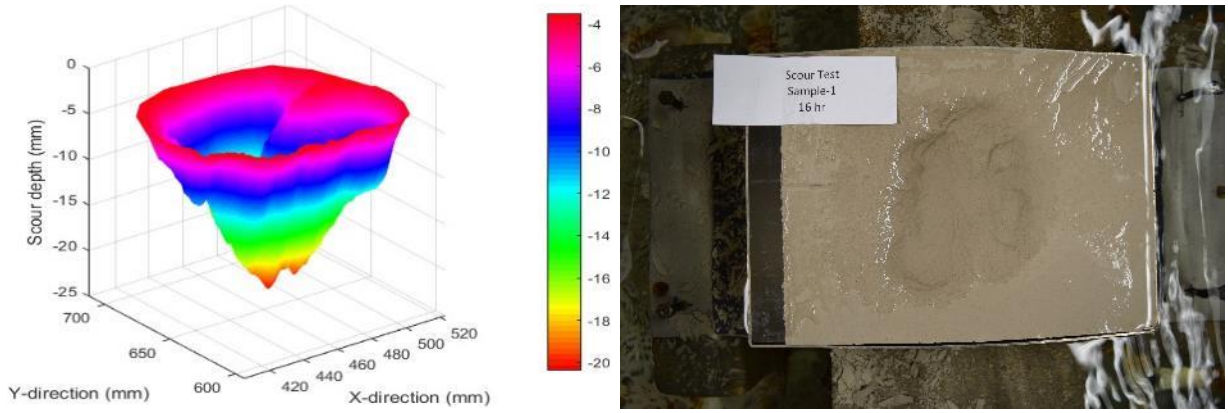

(m)

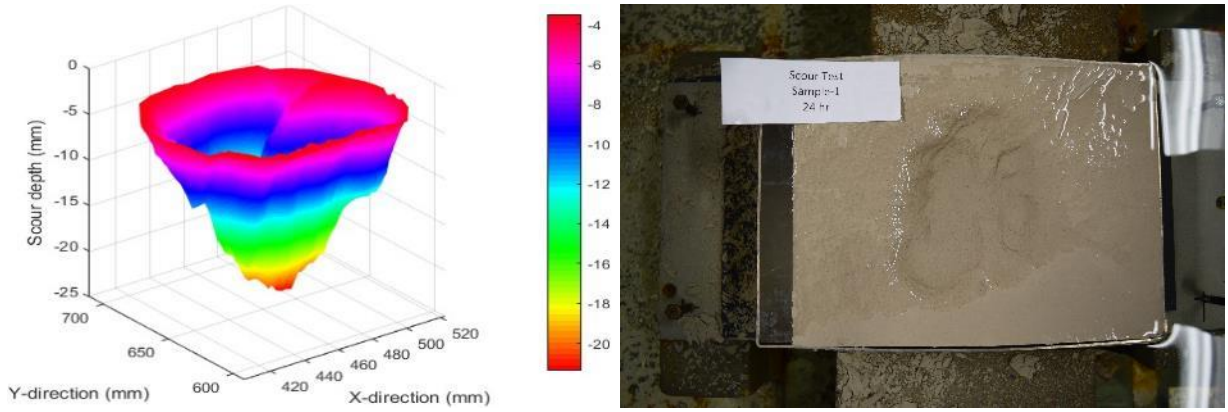

(n)

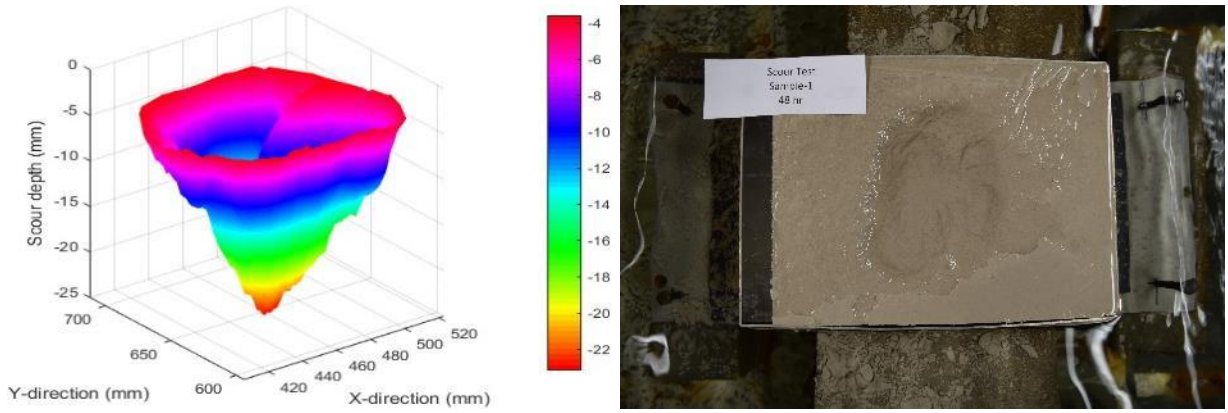

(o)

Figure B-1: cont'd.

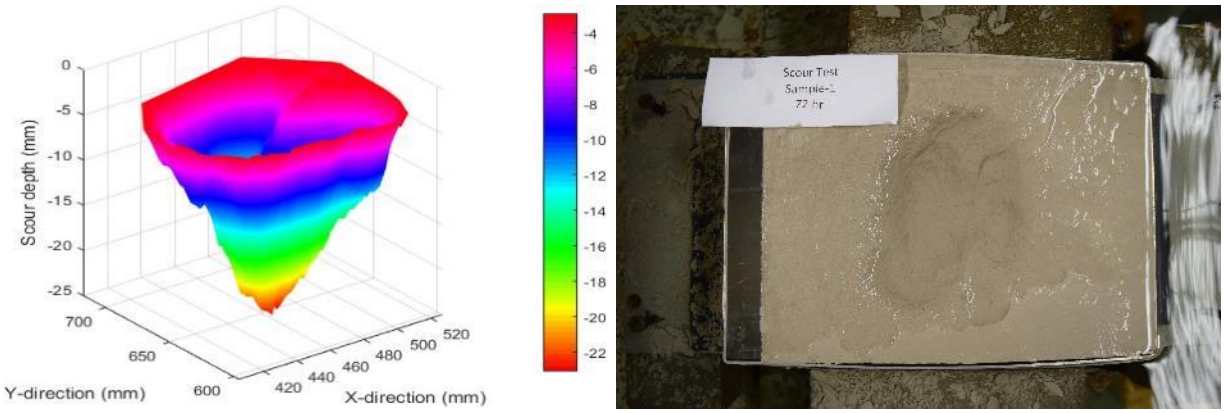

(p)

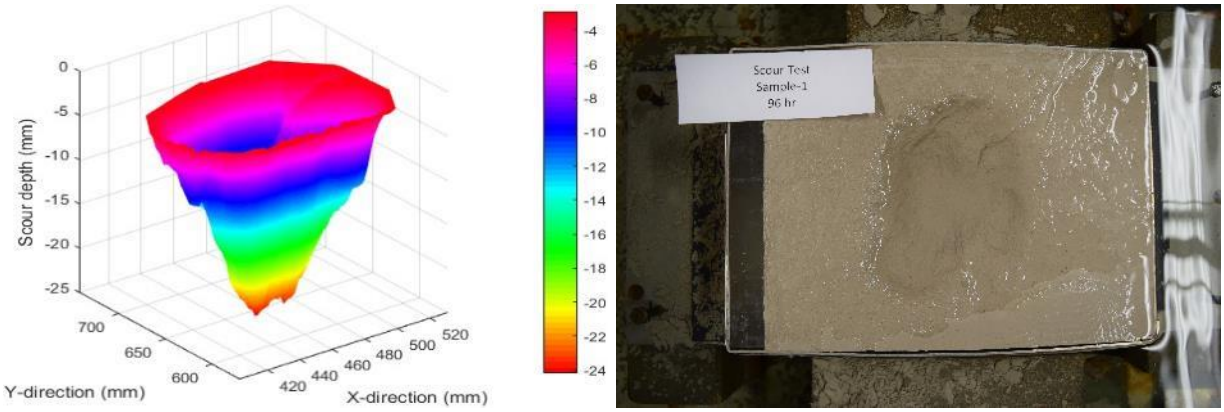

(q)

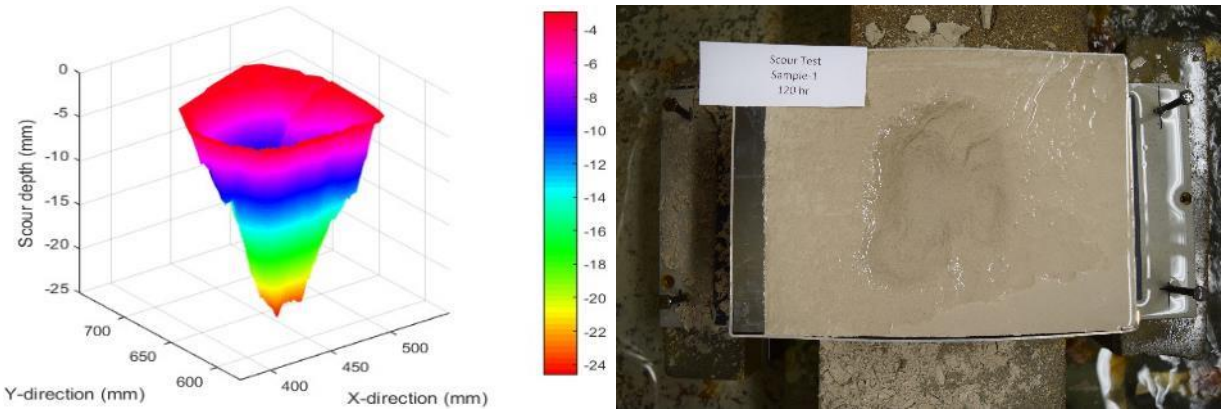

(r)

Figure B-1: cont'd.

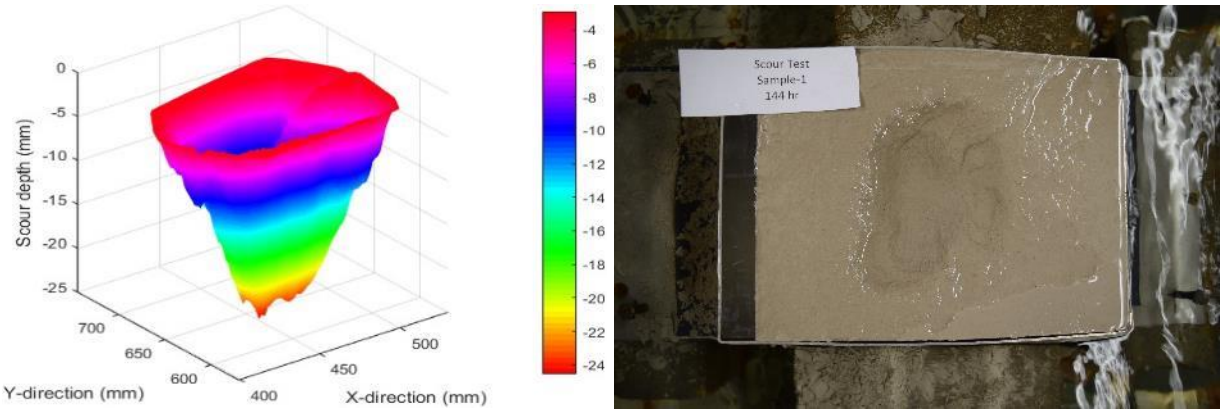

(s)

Figure B-1: cont'd.

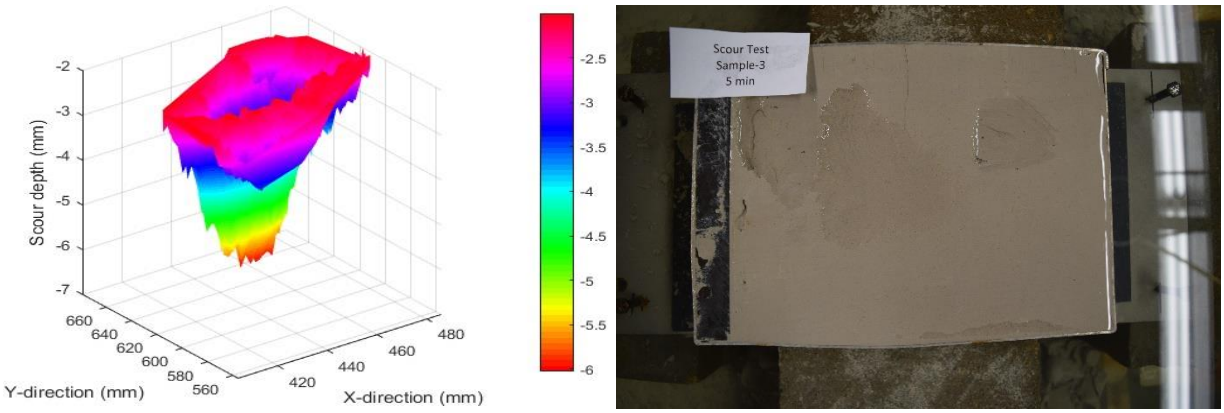

(a)

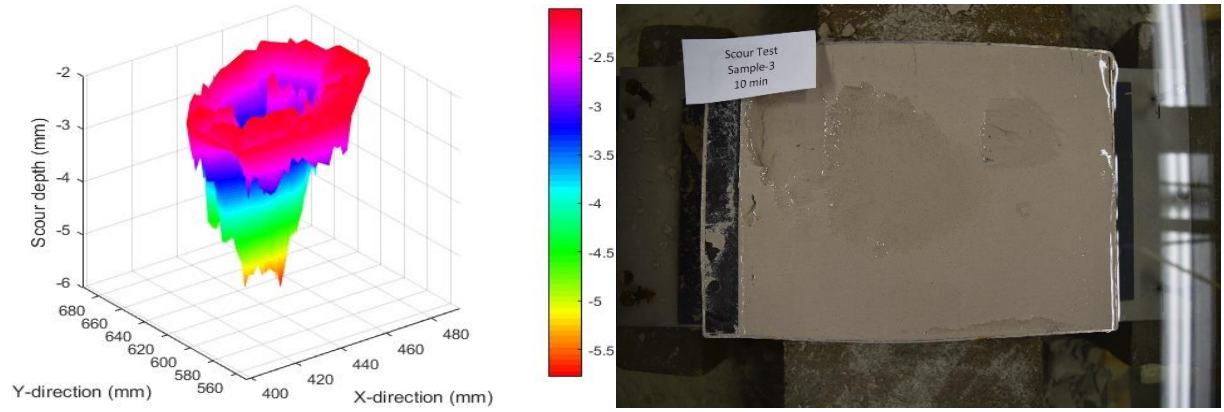

(b)

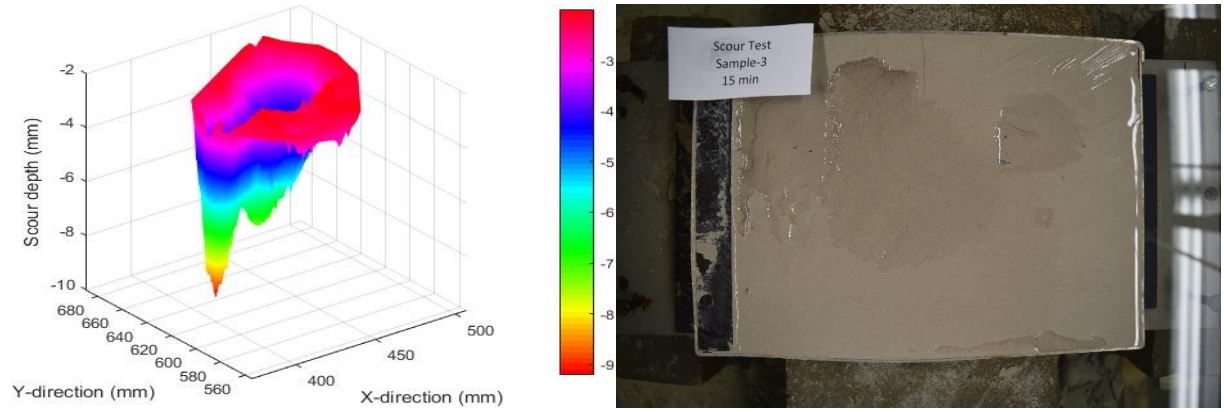

(c)

Figure B-2: Three-dimensional scour hole shape and photo of the sample in plan view for Scour Test 3 (Buffstone clay, U_0=10.0 m/s, d=7.76 mm, H=85 mm, and t_d=96 h) after a test duration of (a) 5 min, (b) 10 min, (c) 15 min, (d) 20 min, (e) 30 min, (f) 40 min, (g) 50 min, (h) 1 h, (i) 1.5 h, (j) 2 h, (k) 4 h, (l) 8 h, (m) 16 h, (n) 24 h, (o) 48 h, (p) 72 h, and (q) 96 h.

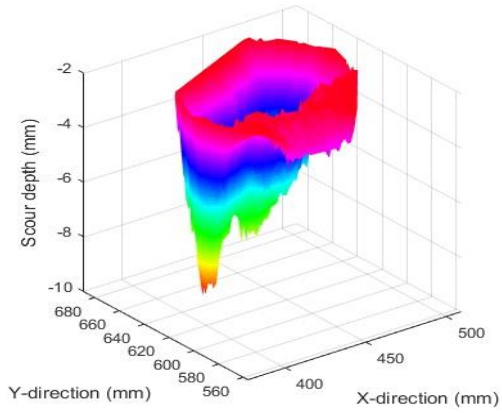

(d)

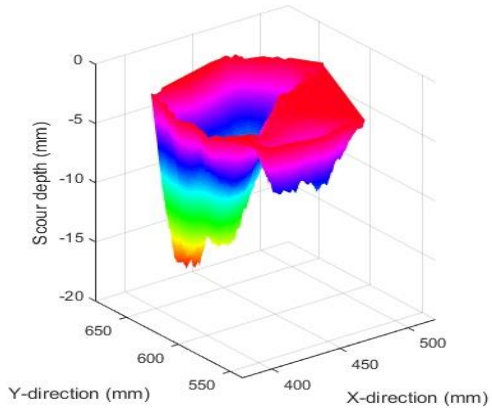

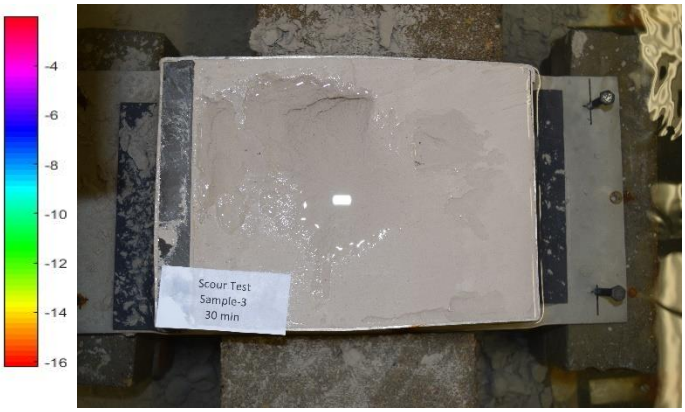

(e)

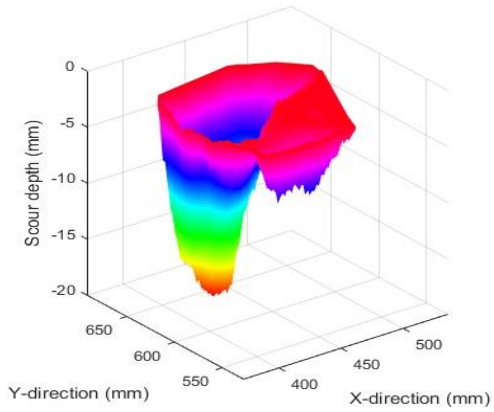

(f)

Figure B-2: cont'd.

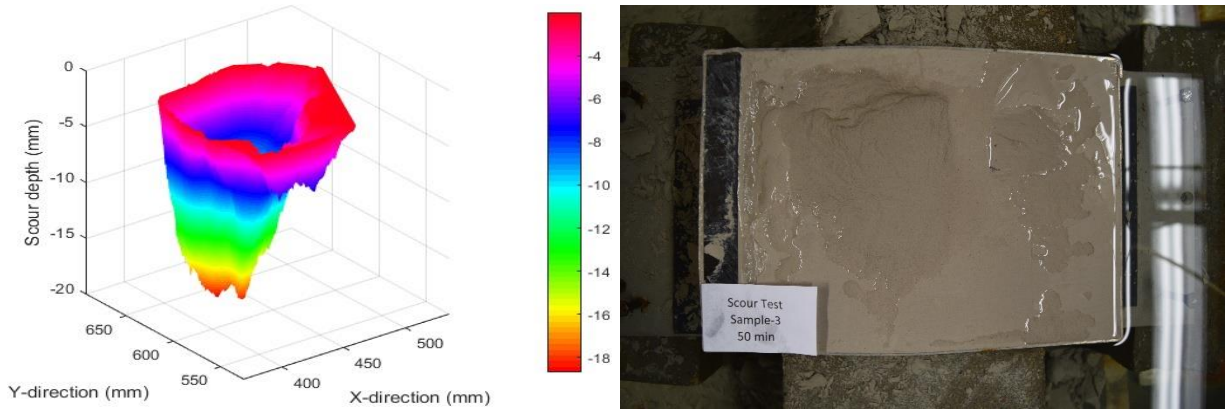

(g)

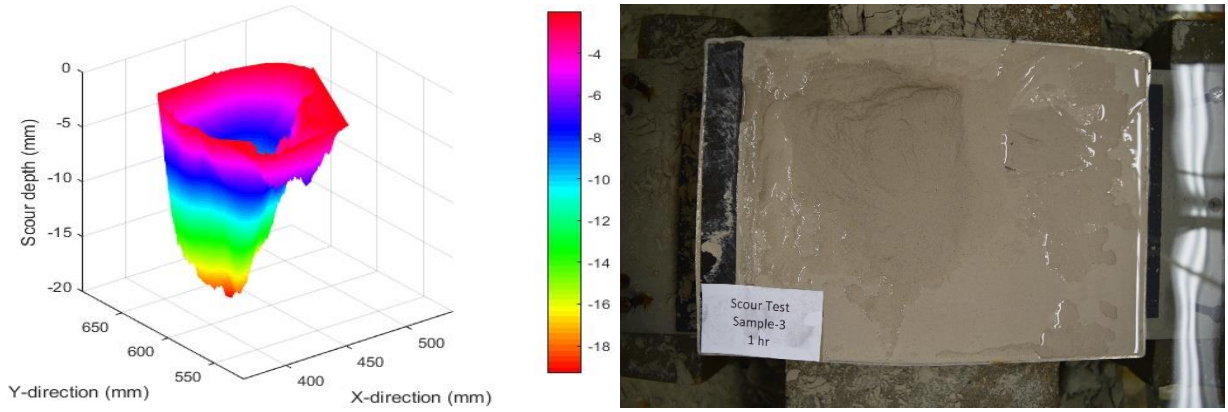

(h)

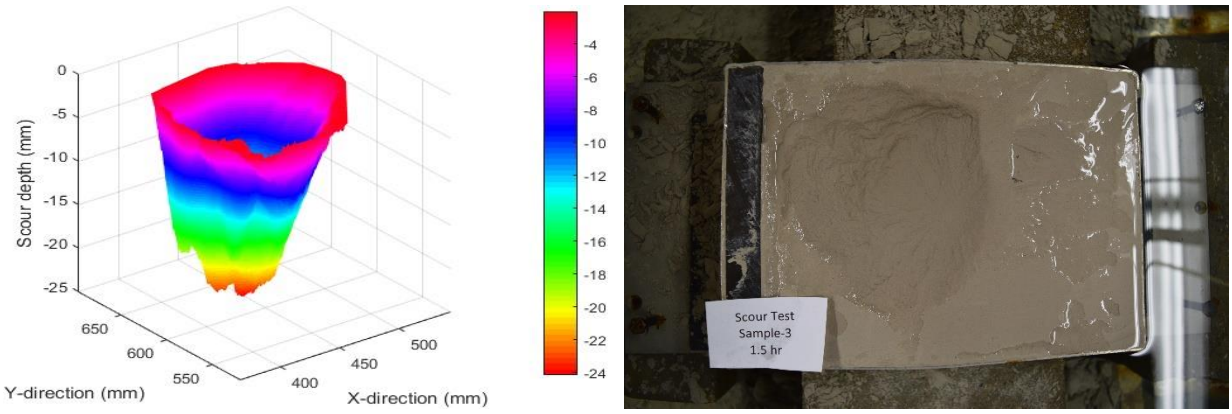

(i)

Figure B-2: cont'd.

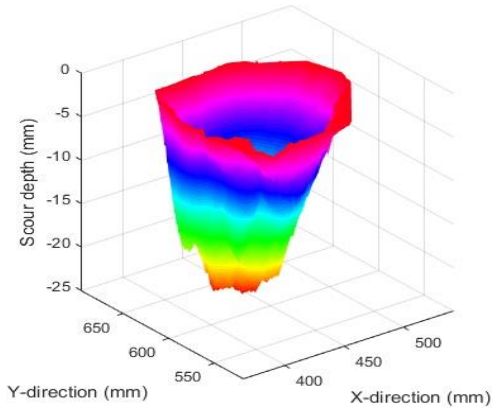

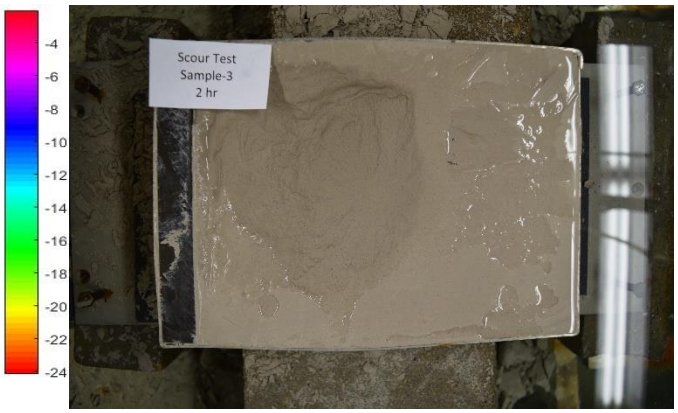

(j)

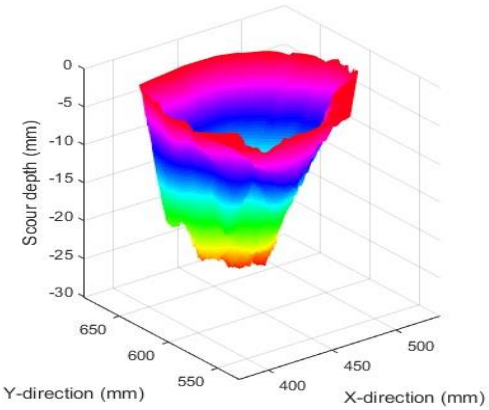

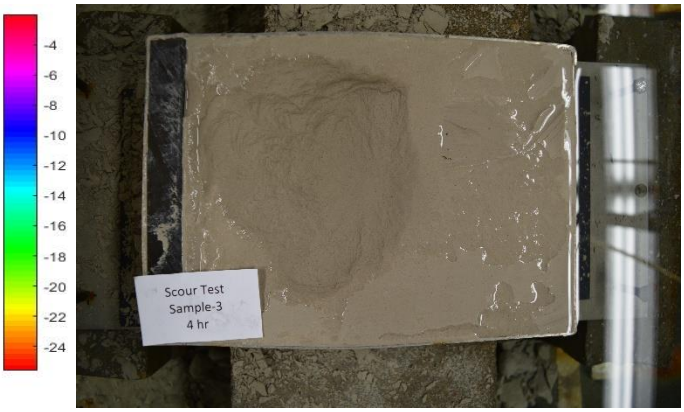

(k)

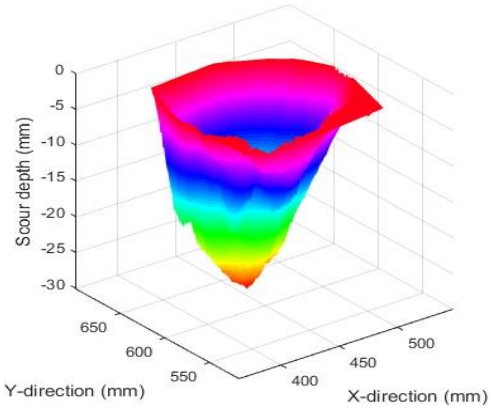

(l)

Figure B-2: cont'd.

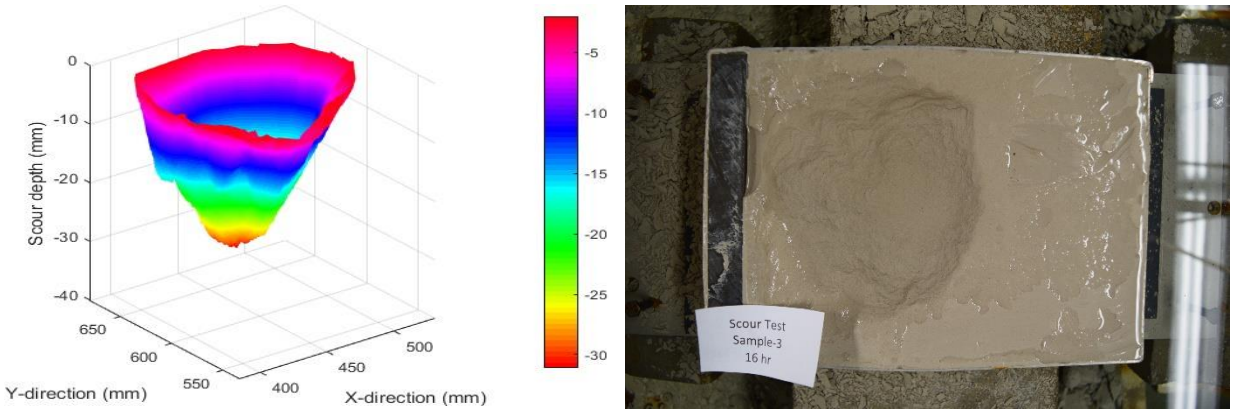

(m)

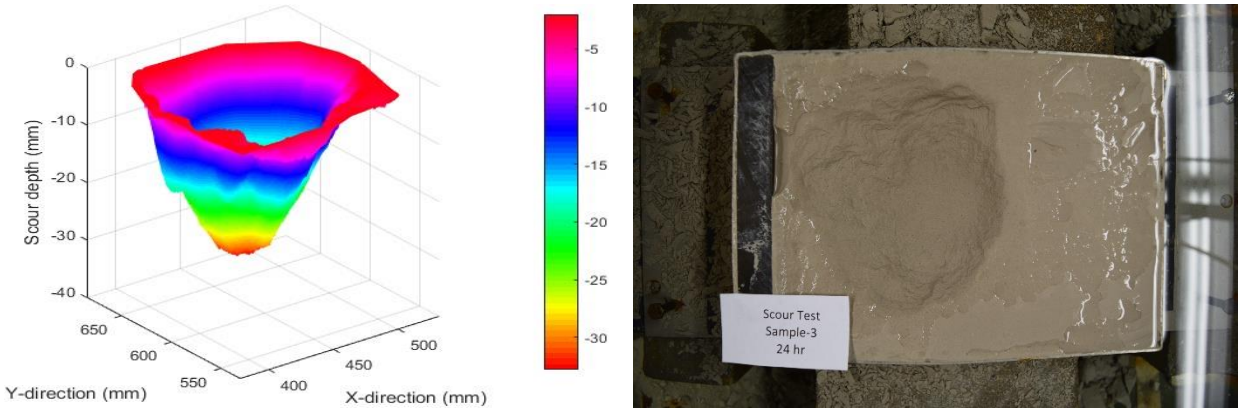

(n)

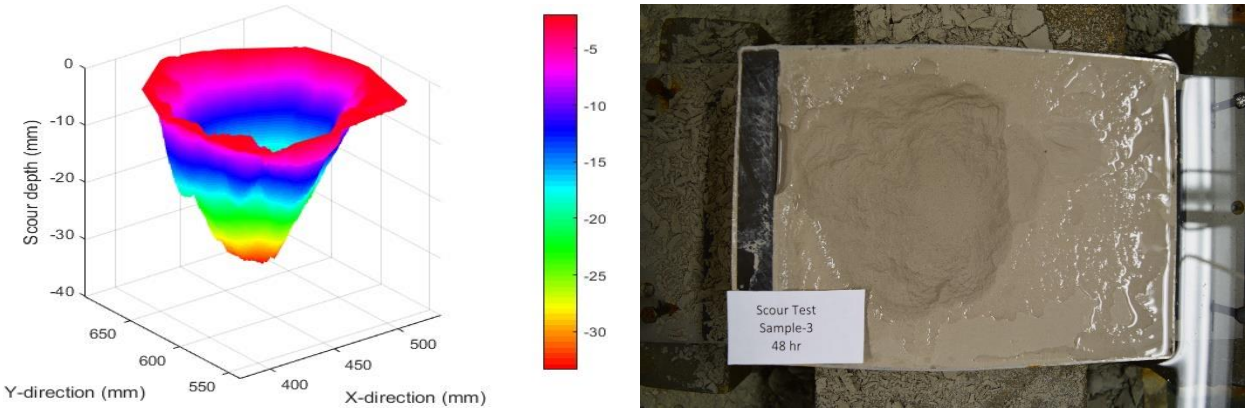

(o)

Figure B-2: cont'd.

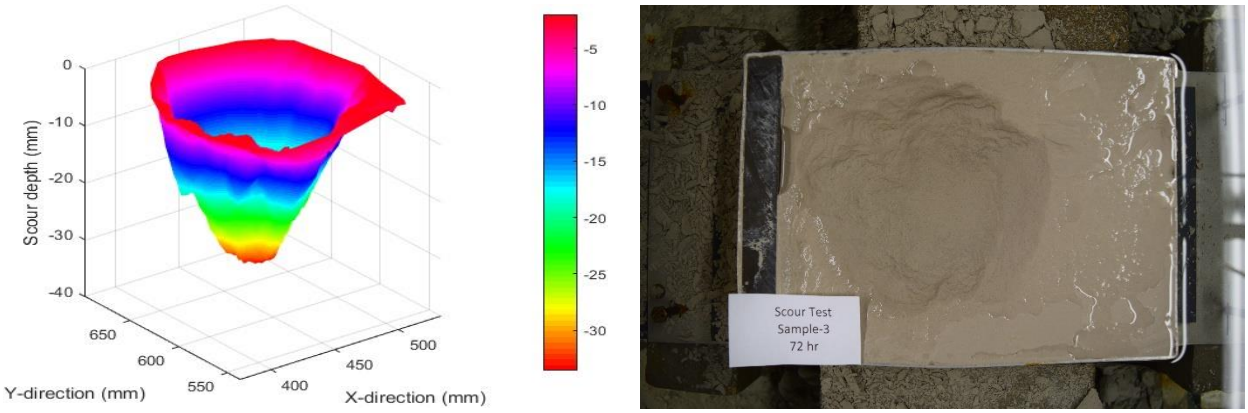

(p)

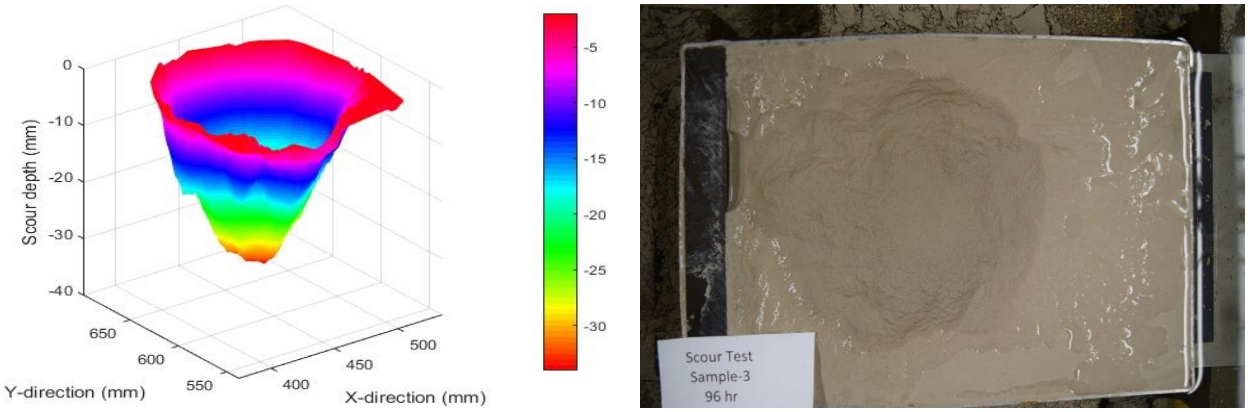

(q)

Figure B-2: cont'd.

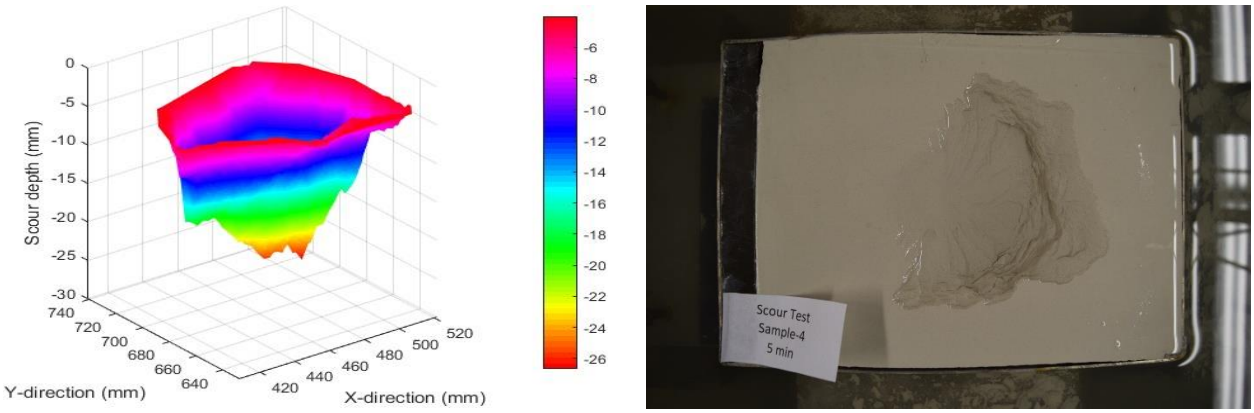

(a)

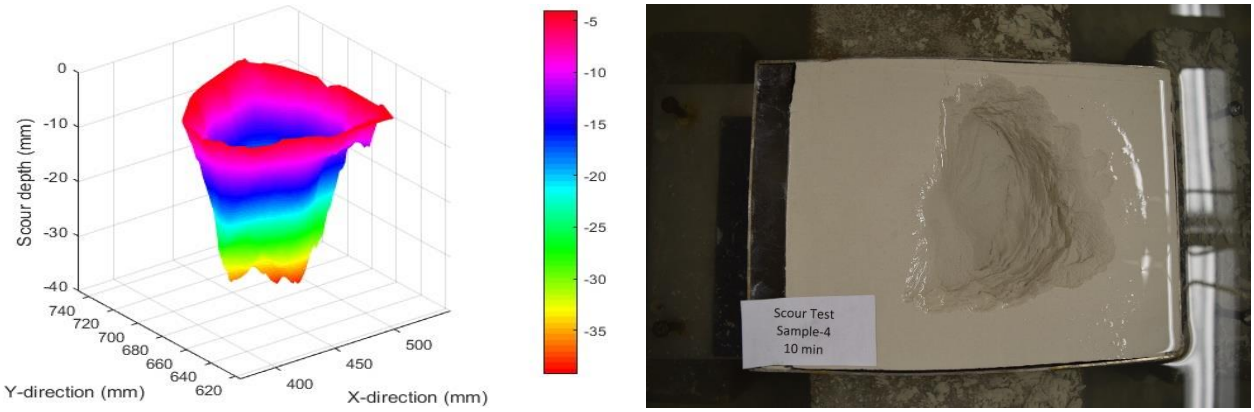

(b)

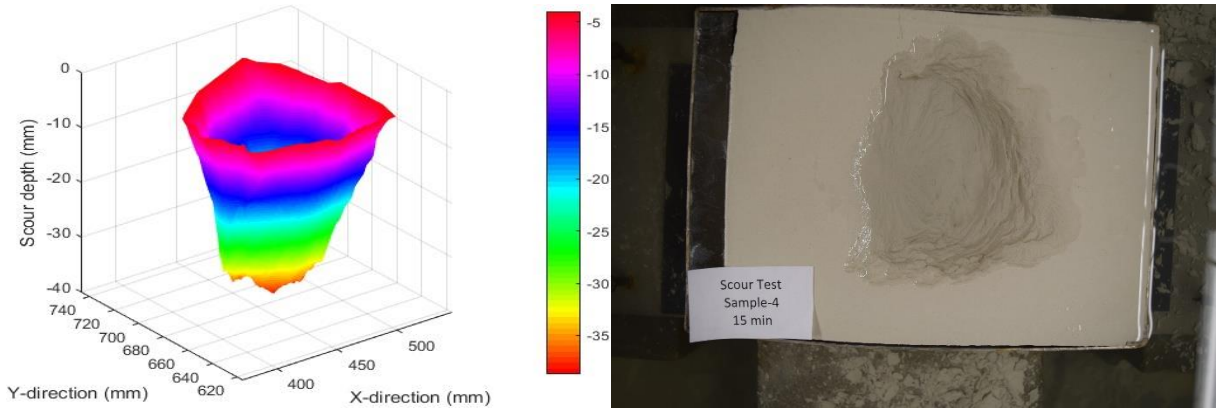

(c)

Figure B-3: Three-dimensional scour hole shape and photo of the sample in plan view for Scour Test 4 (P300 clay, U_0=10.1 m/s, d=7.76 mm, H=85 mm, and t_d=120 h) after a test duration of (a) 5 min, (b) 10 min, (c) 15 min, (d) 20 min, (e) 30 min, (f) 40 min, (g) 50 min, (h) 1 h, (i) 1.5 h, (j) 2 h, (k) 4 h, (l) 8 h, (m) 16 h, (n) 24 h, (o) 48 h, (p) 72 h, (q) 96 h, and (r) 120 h.

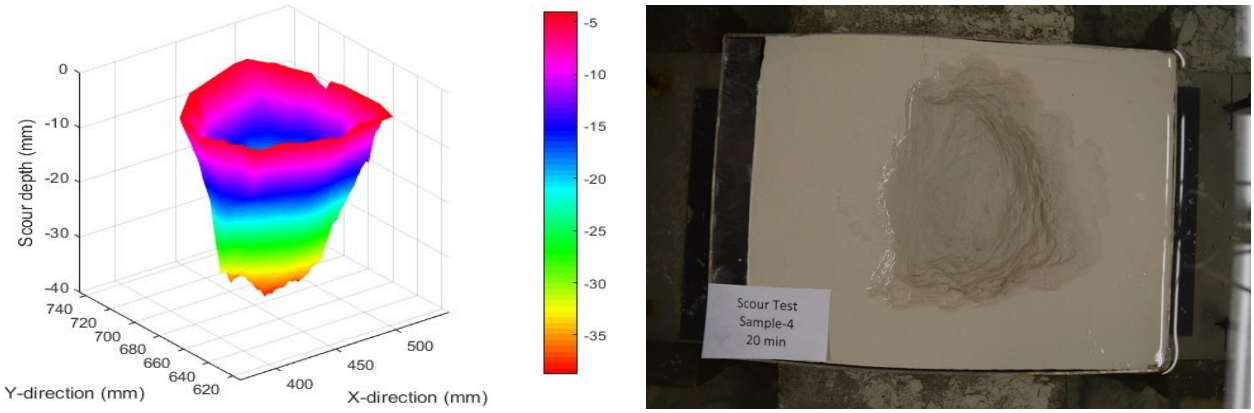

(d)

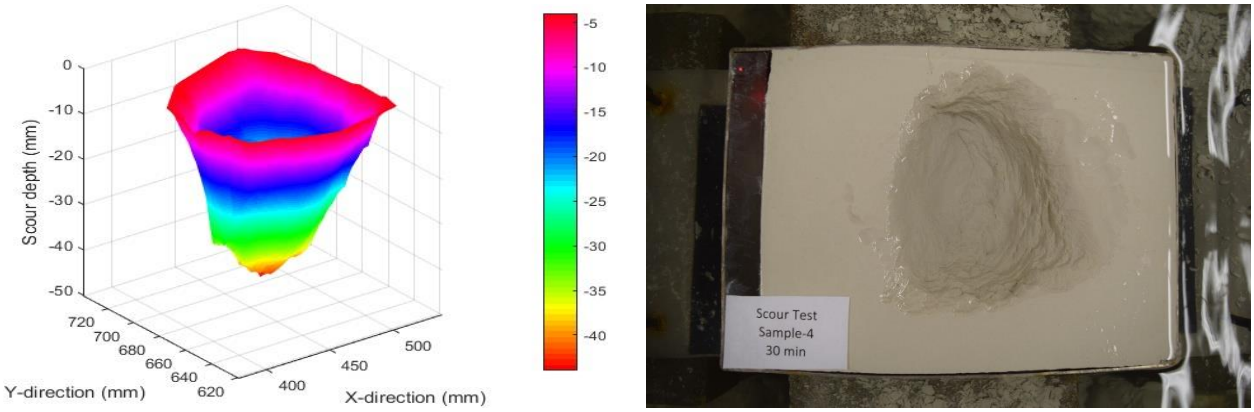

(e)

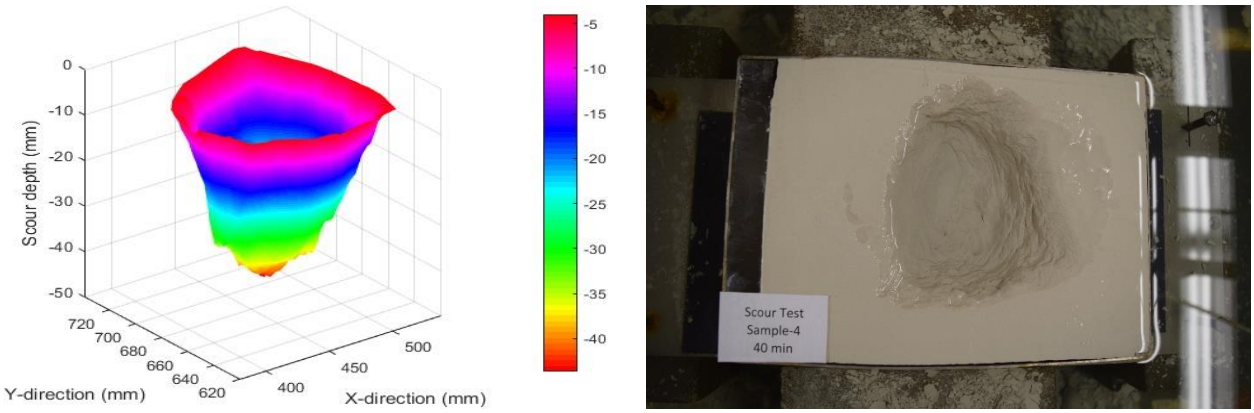

(f)

Figure B-3: cont'd.

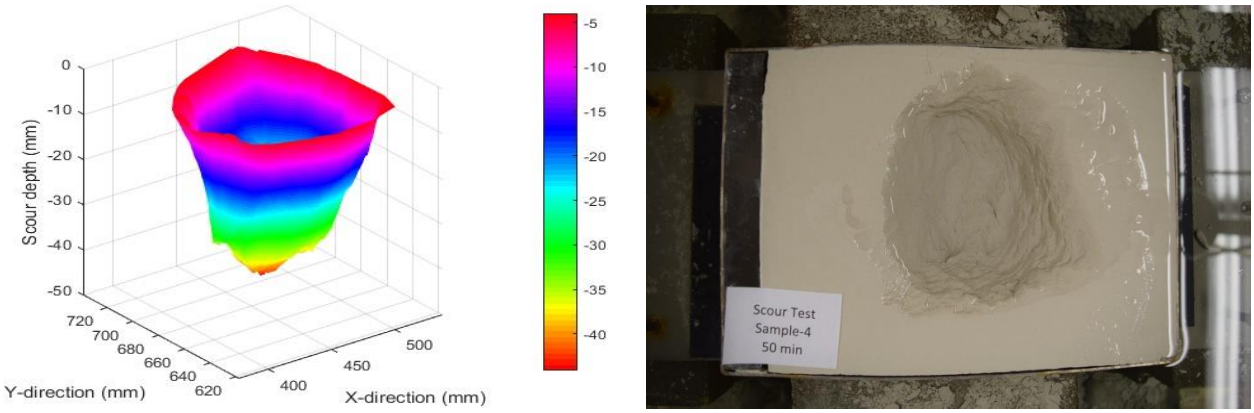

(g)

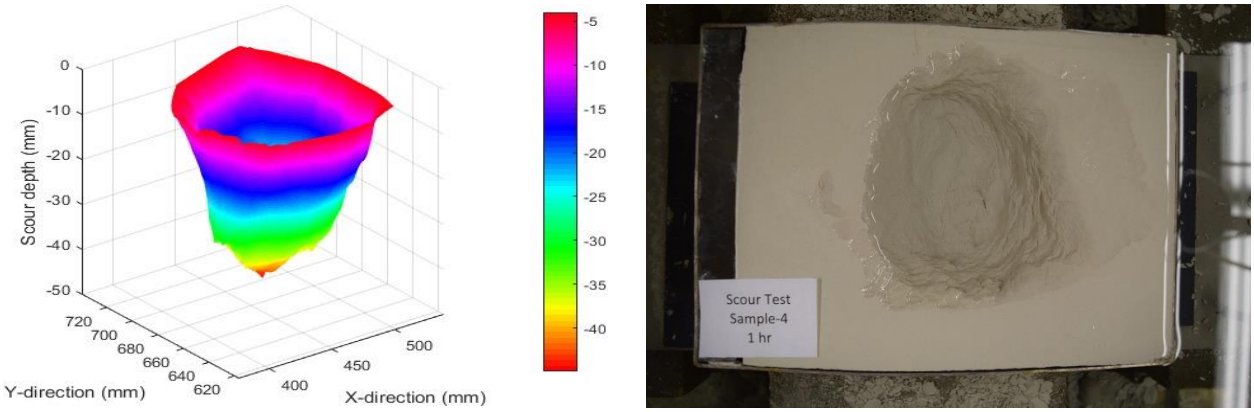

(h)

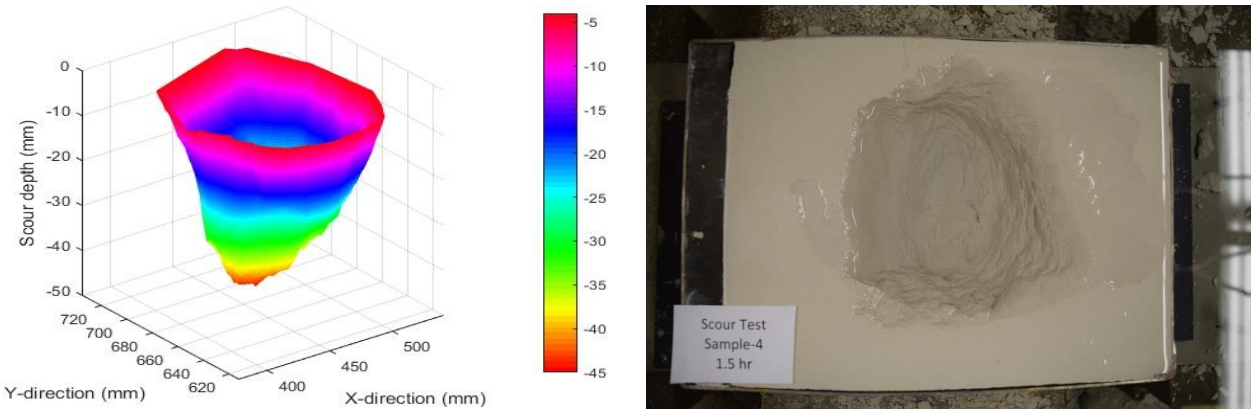

(i)

Figure B-3: cont'd.

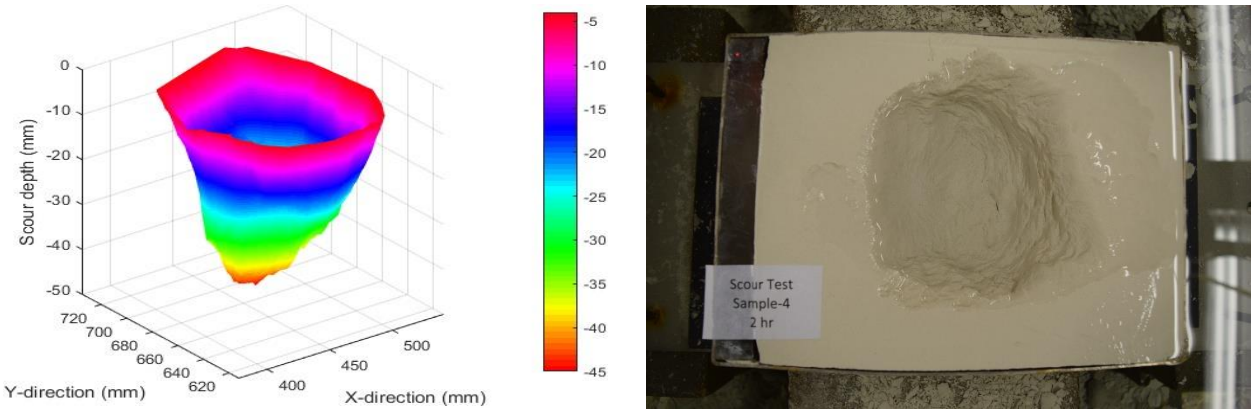

(j)

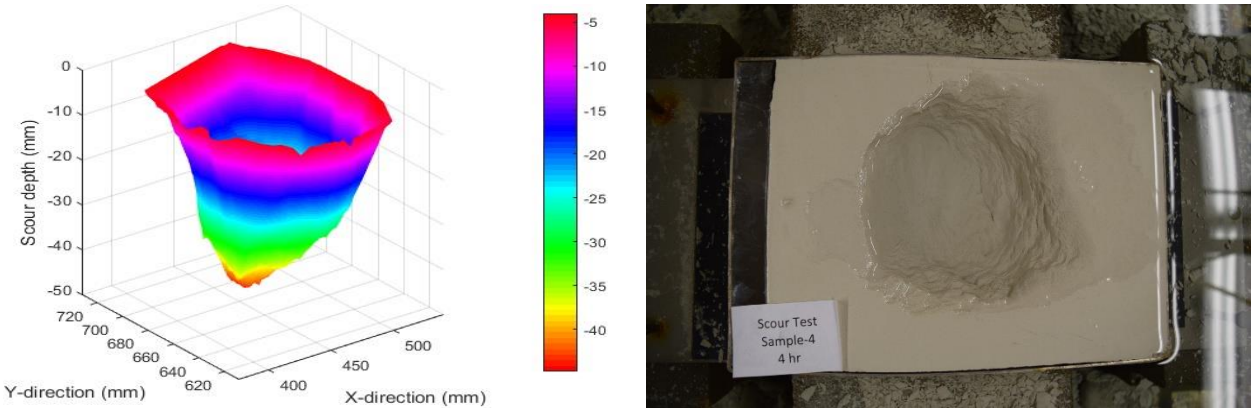

(k)

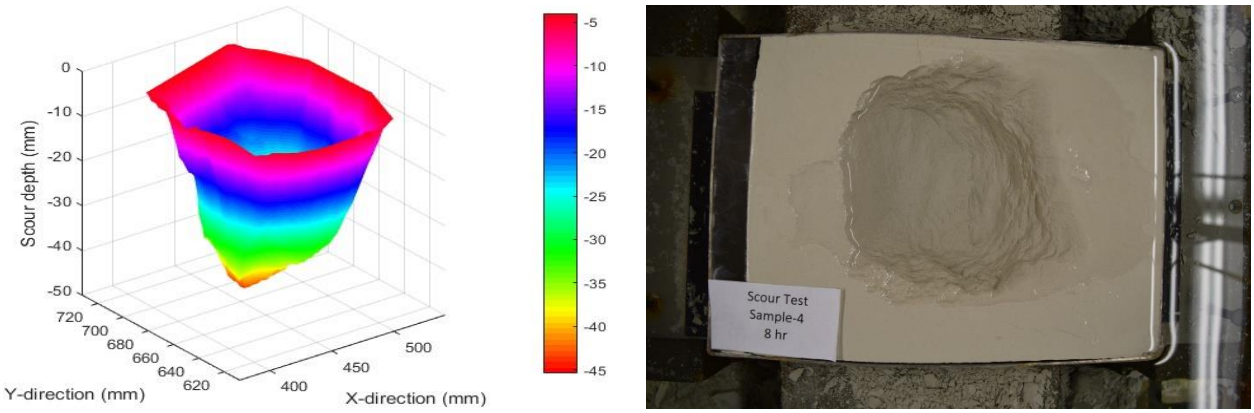

(l)

Figure B-3: cont'd.

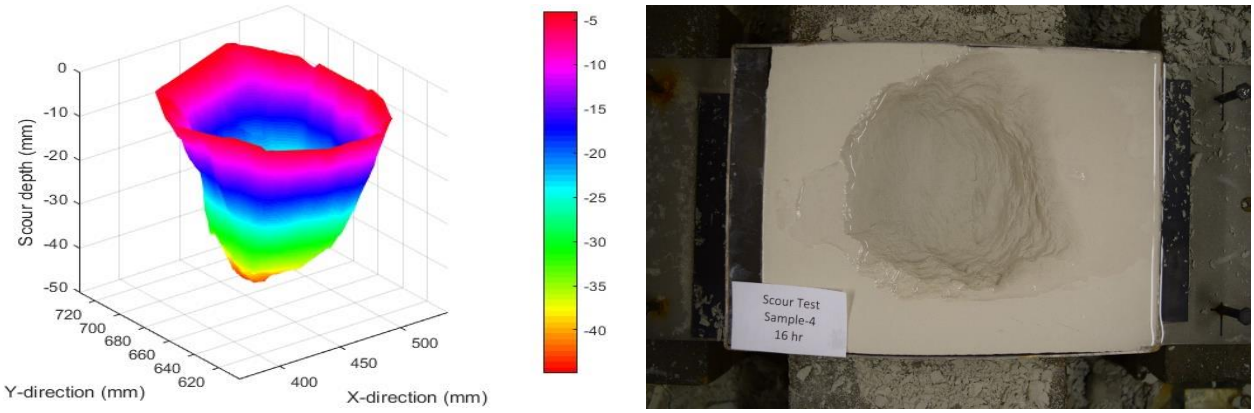

(m)

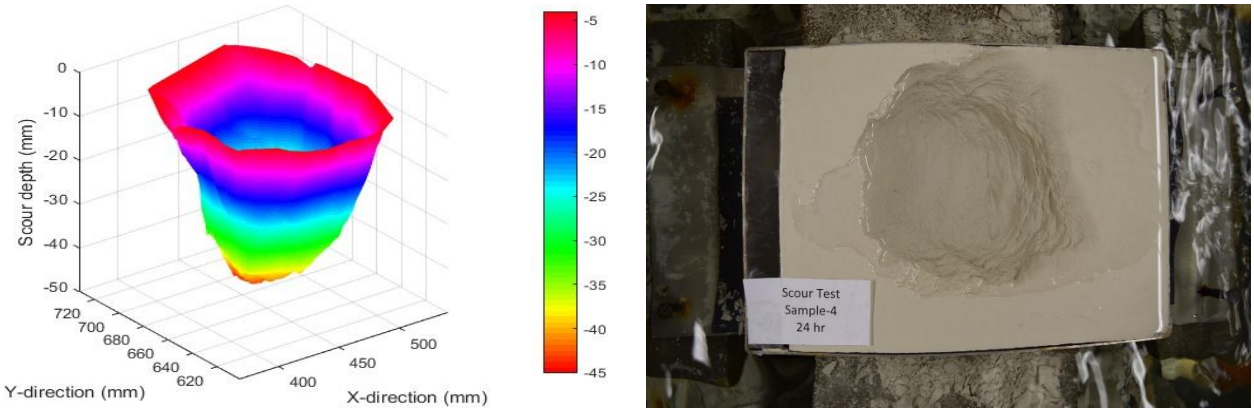

(n)

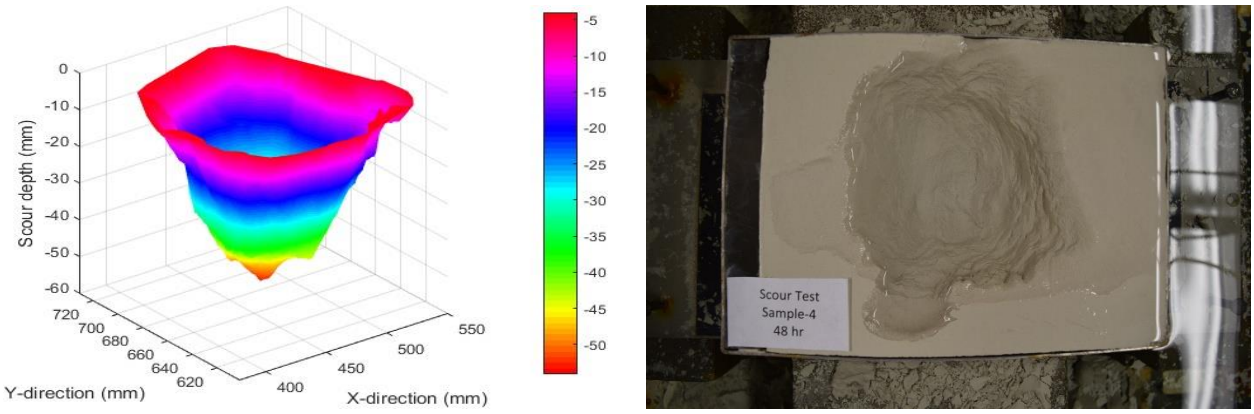

(o)

Figure B-3: cont'd.

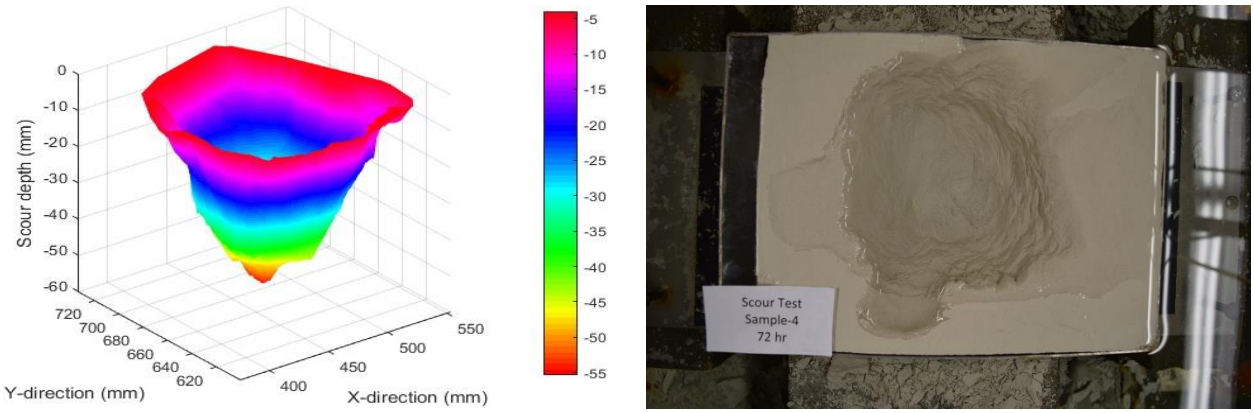

(p)

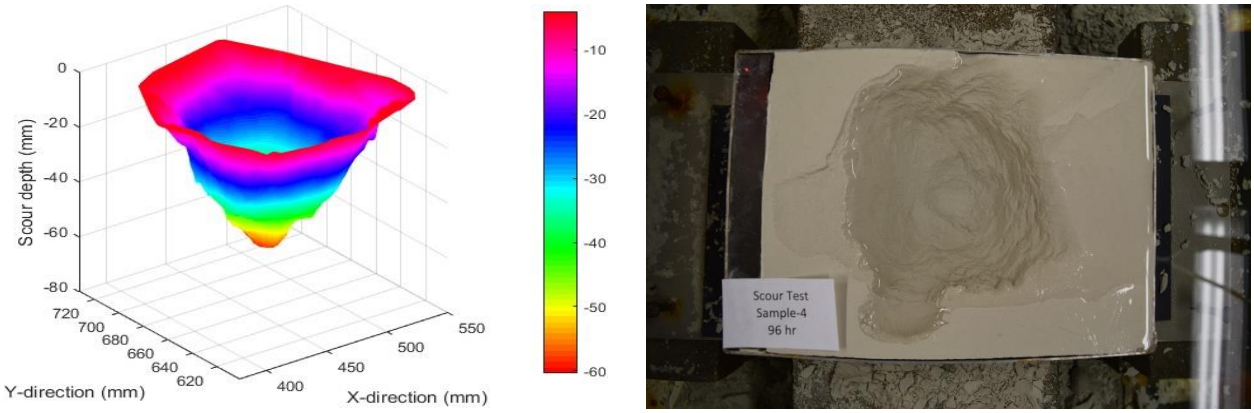

(q)

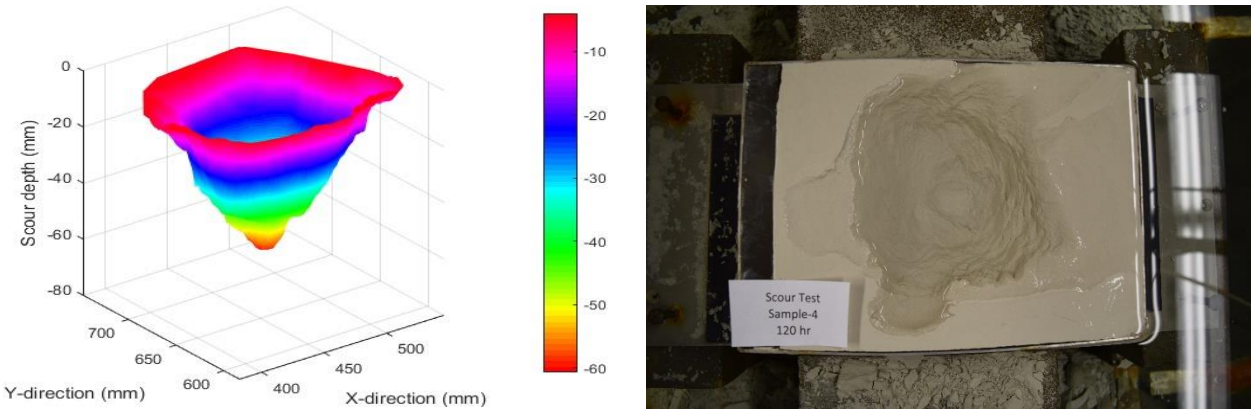

(r)

Figure B-3: cont'd.

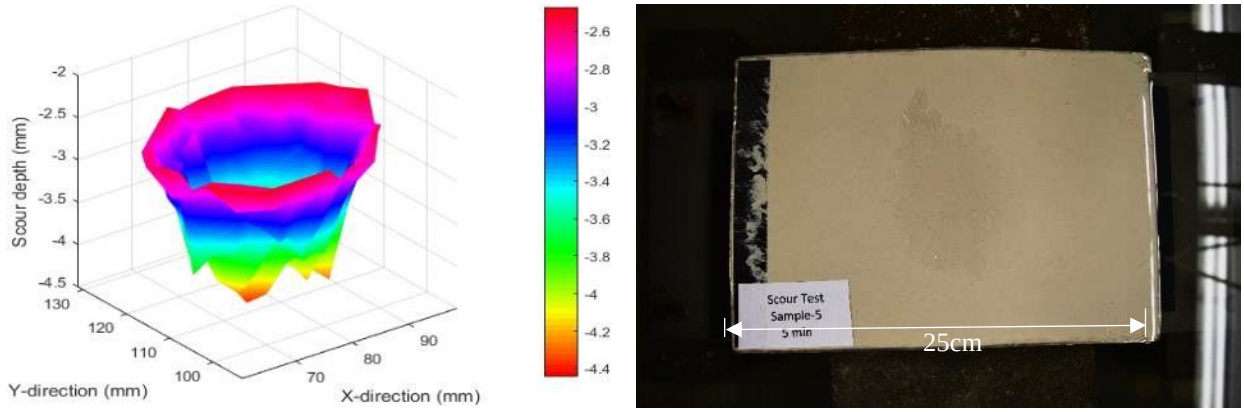

(a)

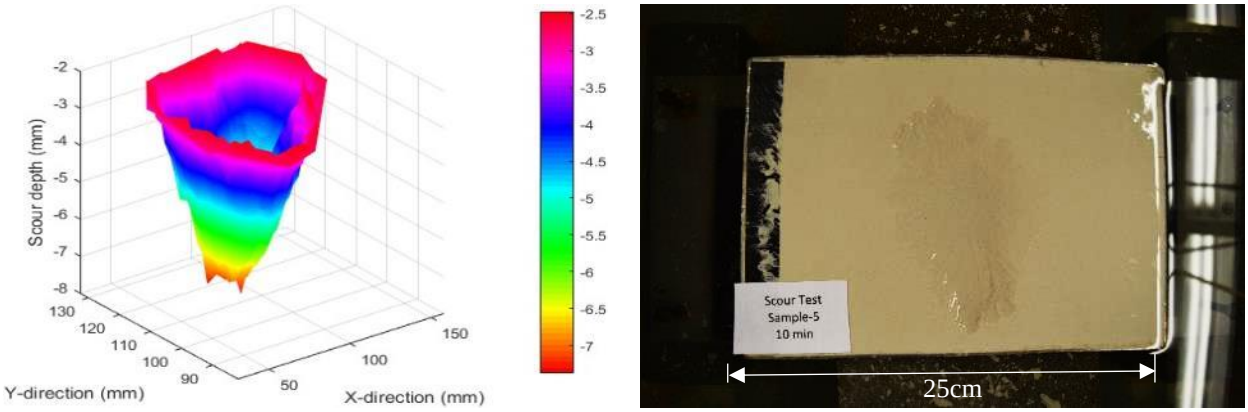

(b)

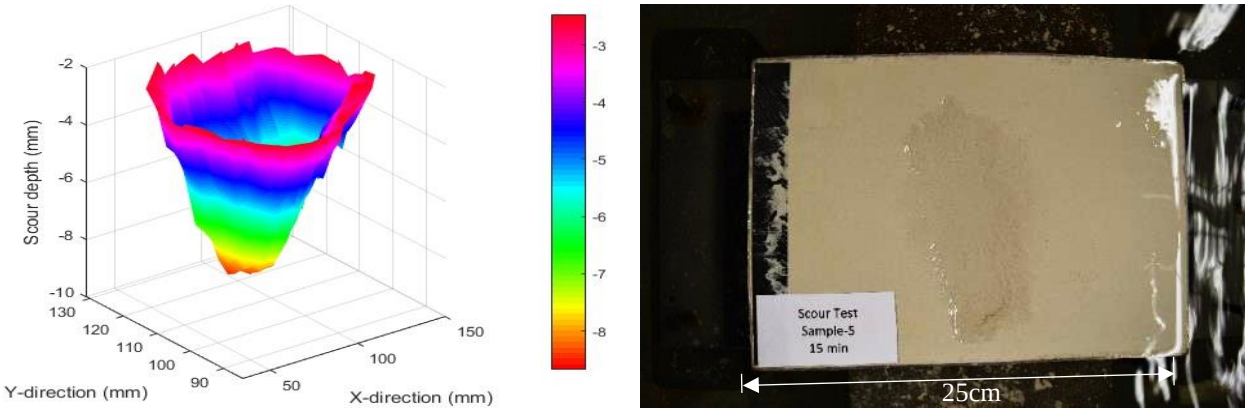

(c)

Figure B-4: Three-dimensional scour hole shape and photo of the sample in plan view for Scour Test 5 (P300 clay, U_0=8.3 m/s, d=7.76 mm, H=85 mm, and t_d=168 h) after a test duration of (a) 5 min, (b) 10 min, (c) 15 min, (d) 20 min, (e) 30 min, (f) 40 min, (g) 50 min, (h) 1 h, (i) 1.5 h, (j) 2 h, (k) 4 h, (l) 8 h, (m) 16 h, (n) 24 h, (o) 48 h, (p) 72 h, (q) 96 h, (r) 120 h, (s) 144 h, and (t) 168 h.

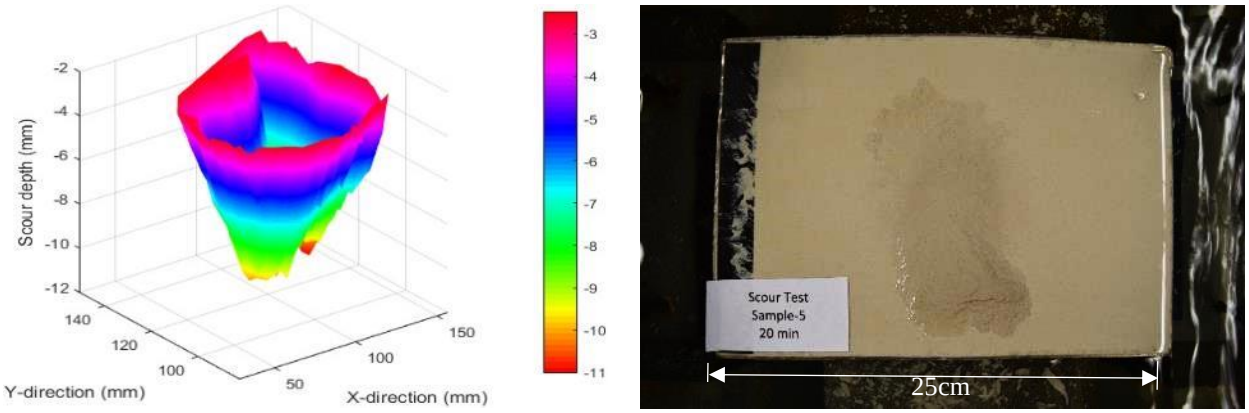

(d)

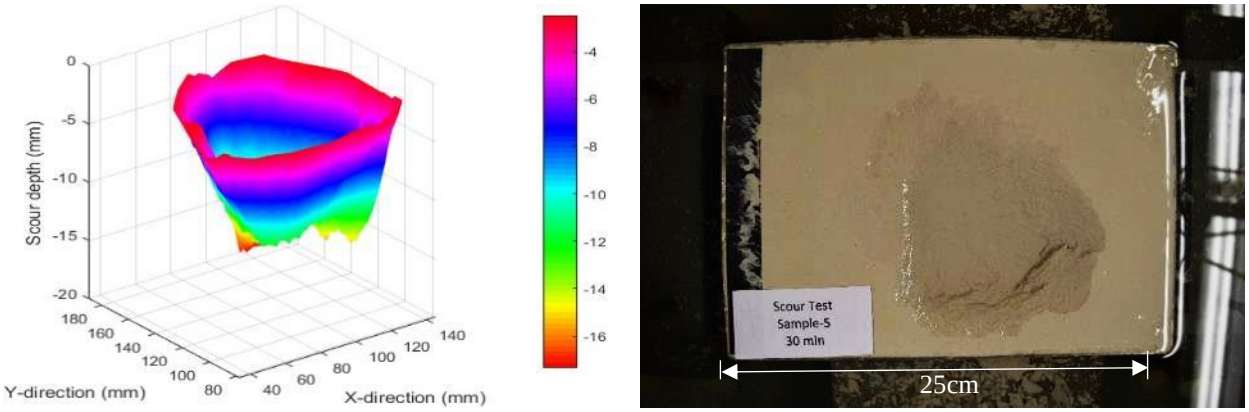

(e)

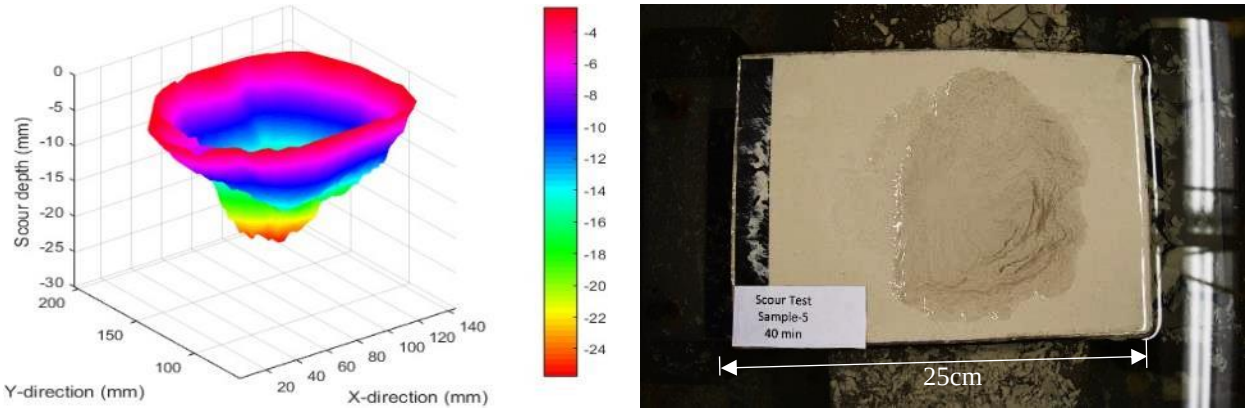

(f)

Figure B-4: cont'd.

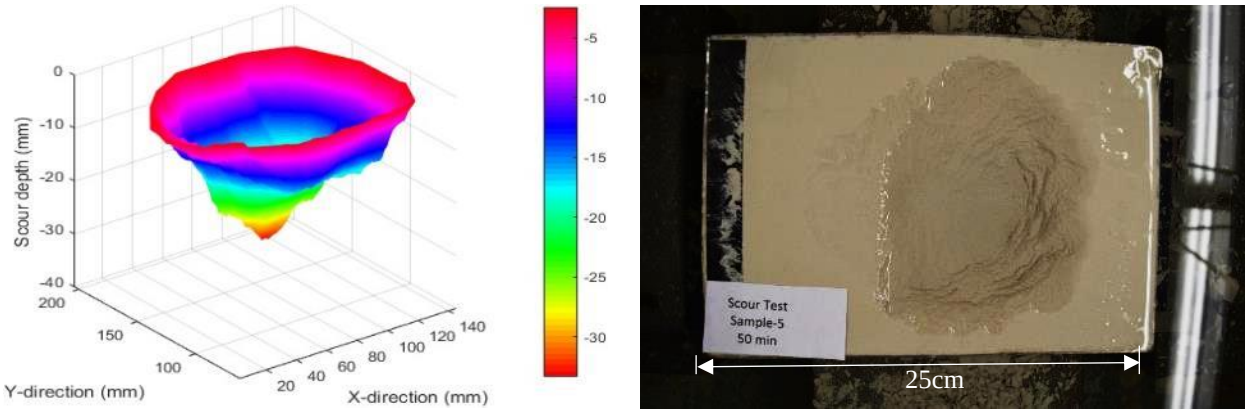

(g)

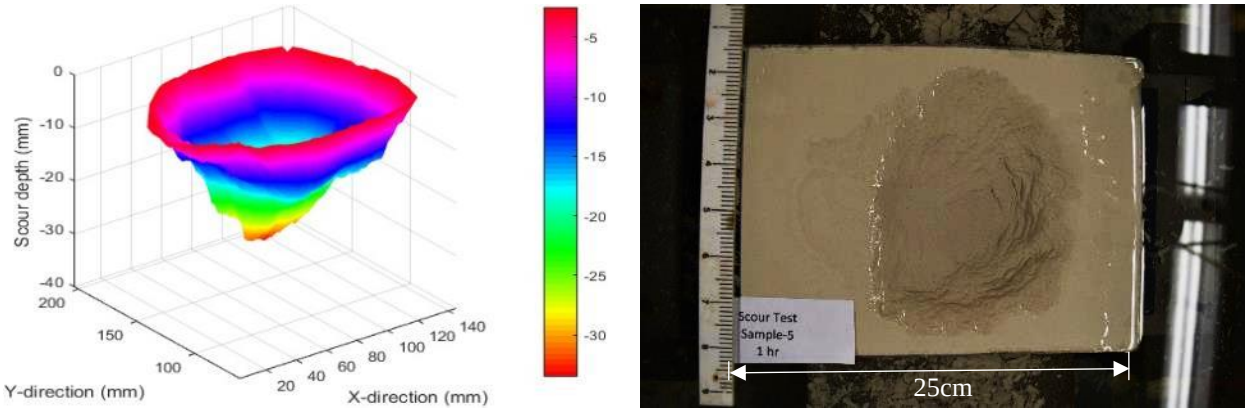

(h)

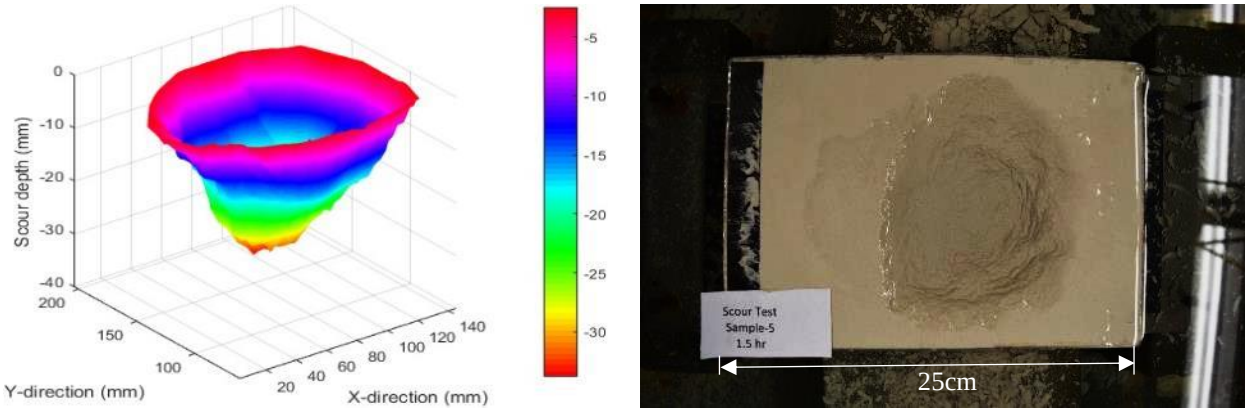

(i)

Figure B-4: cont'd.

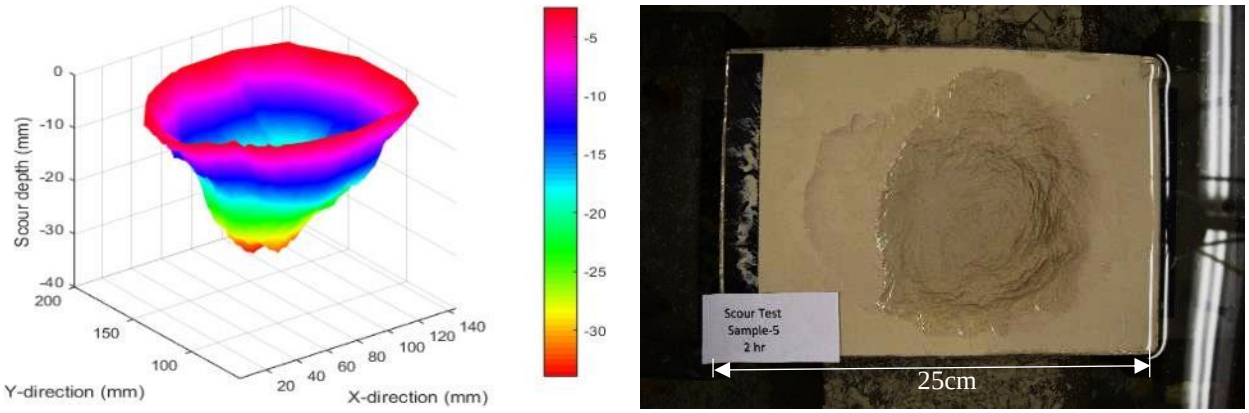

(j)

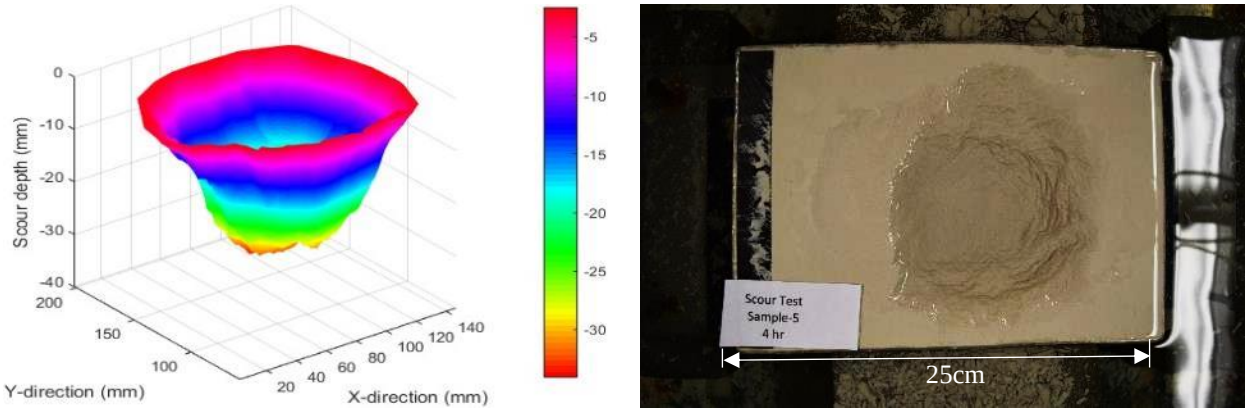

(k)

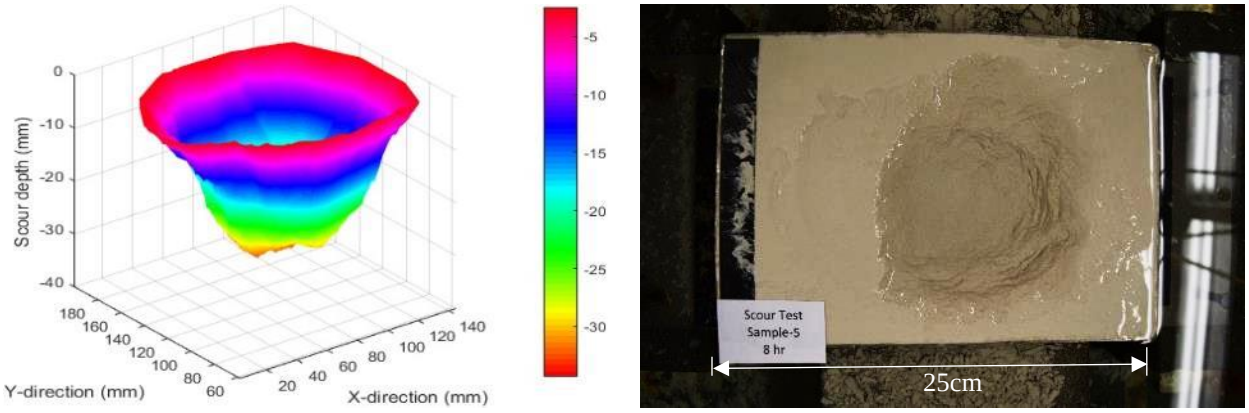

(l)

Figure B-4: cont'd.

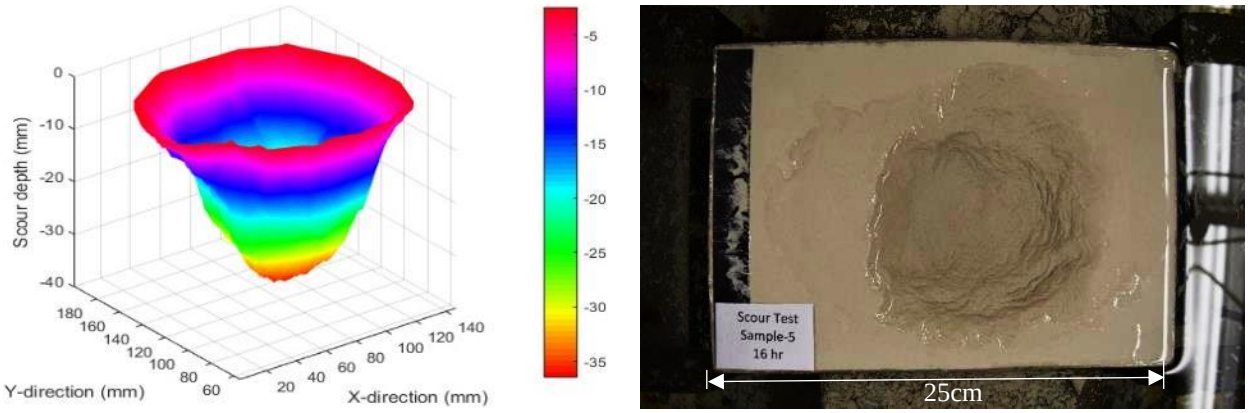

(m)

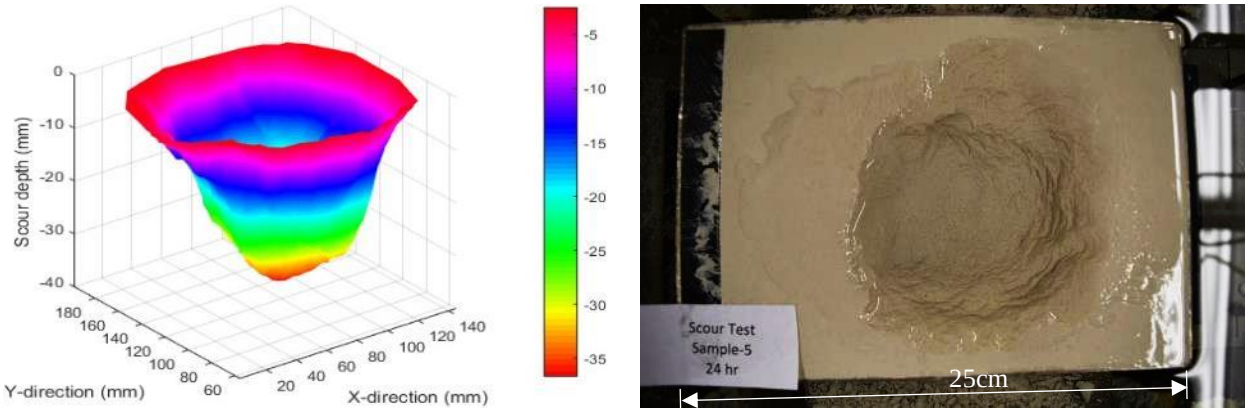

(n)

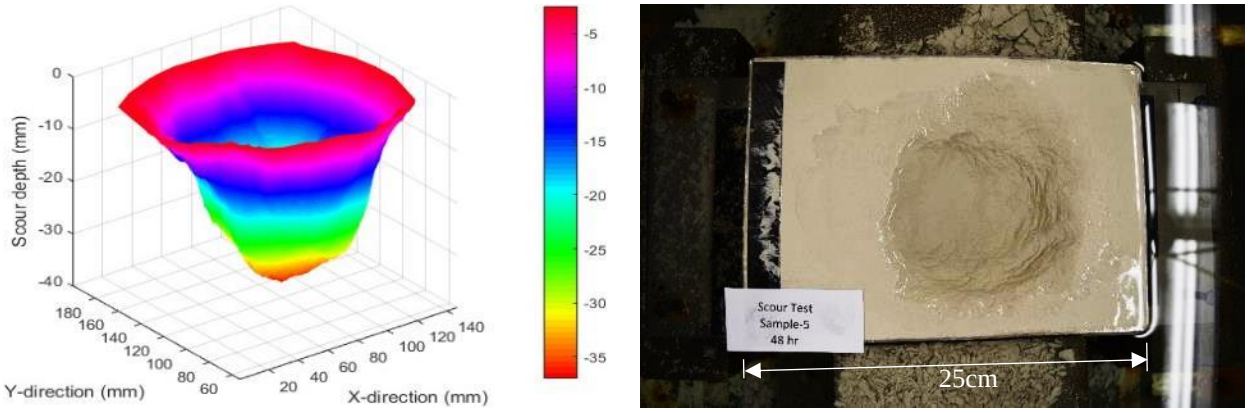

(o)

Figure B-4: cont'd.

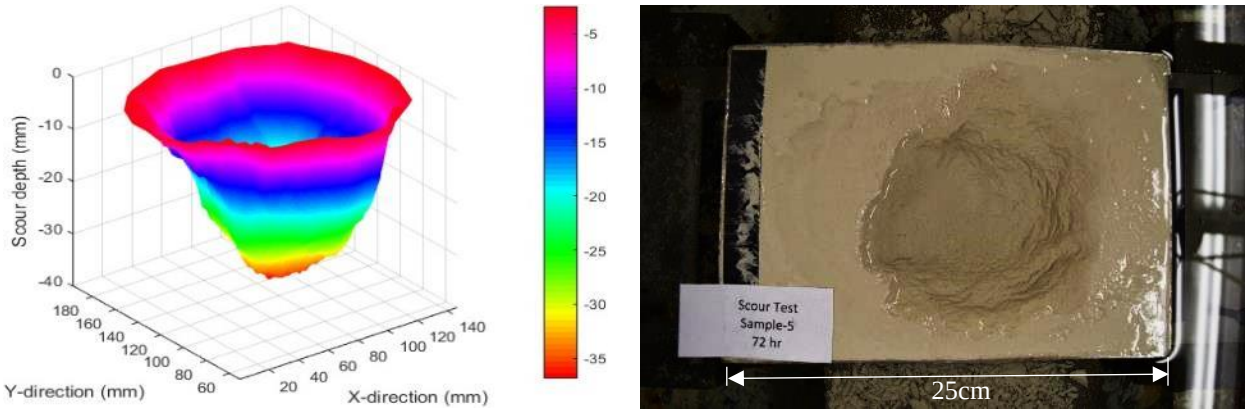

(p)

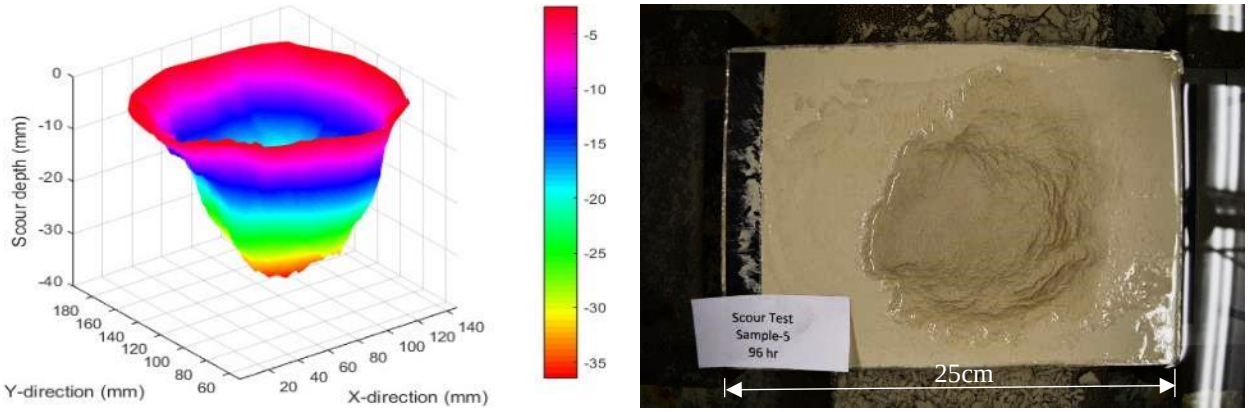

(q)

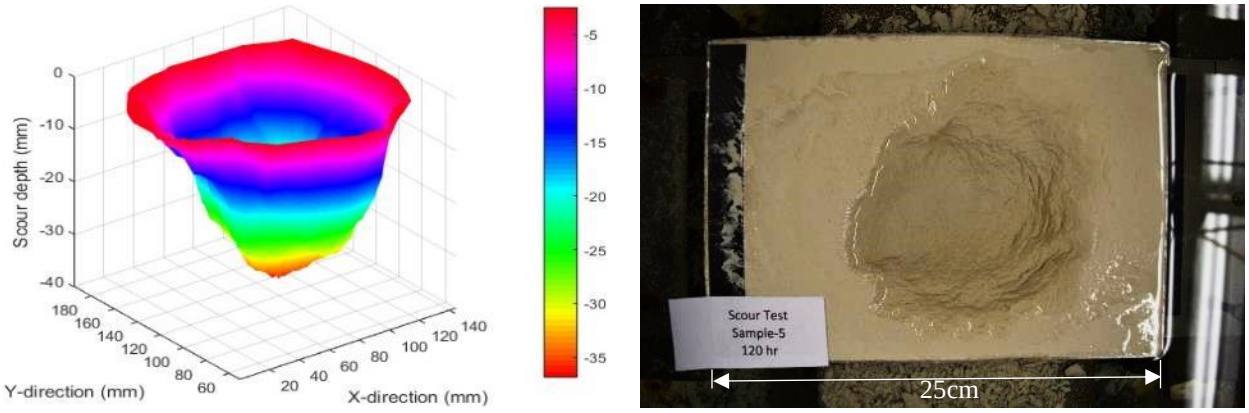

(r)

Figure B-4: cont'd.

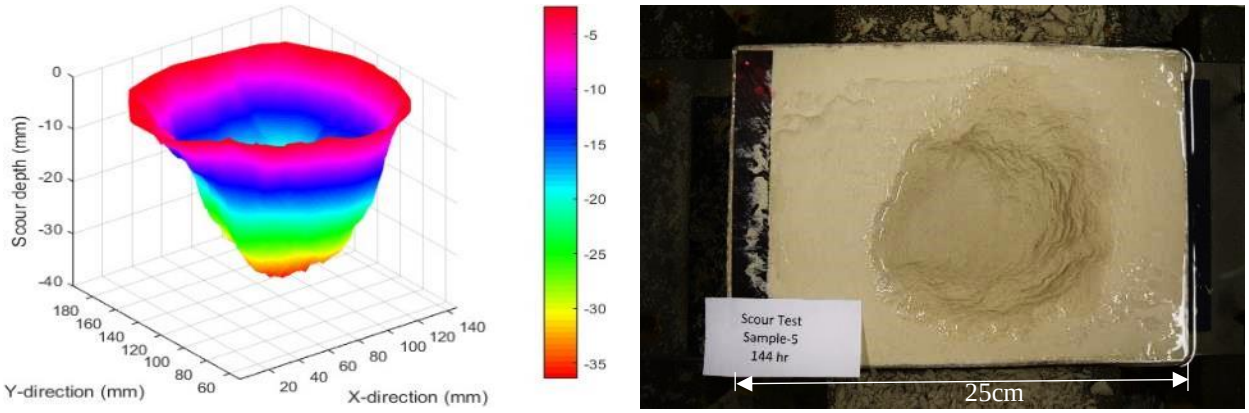

(s)

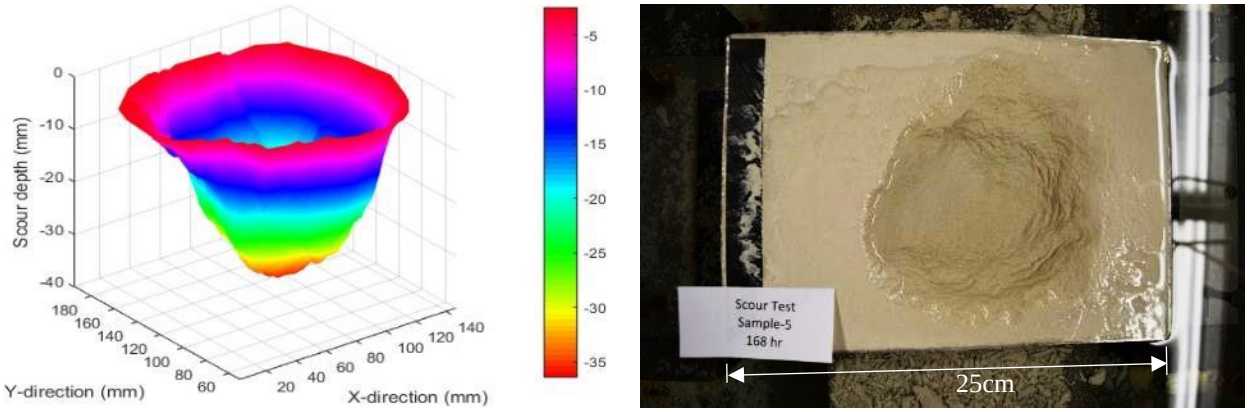

(t)

Figure B-4: cont'd.

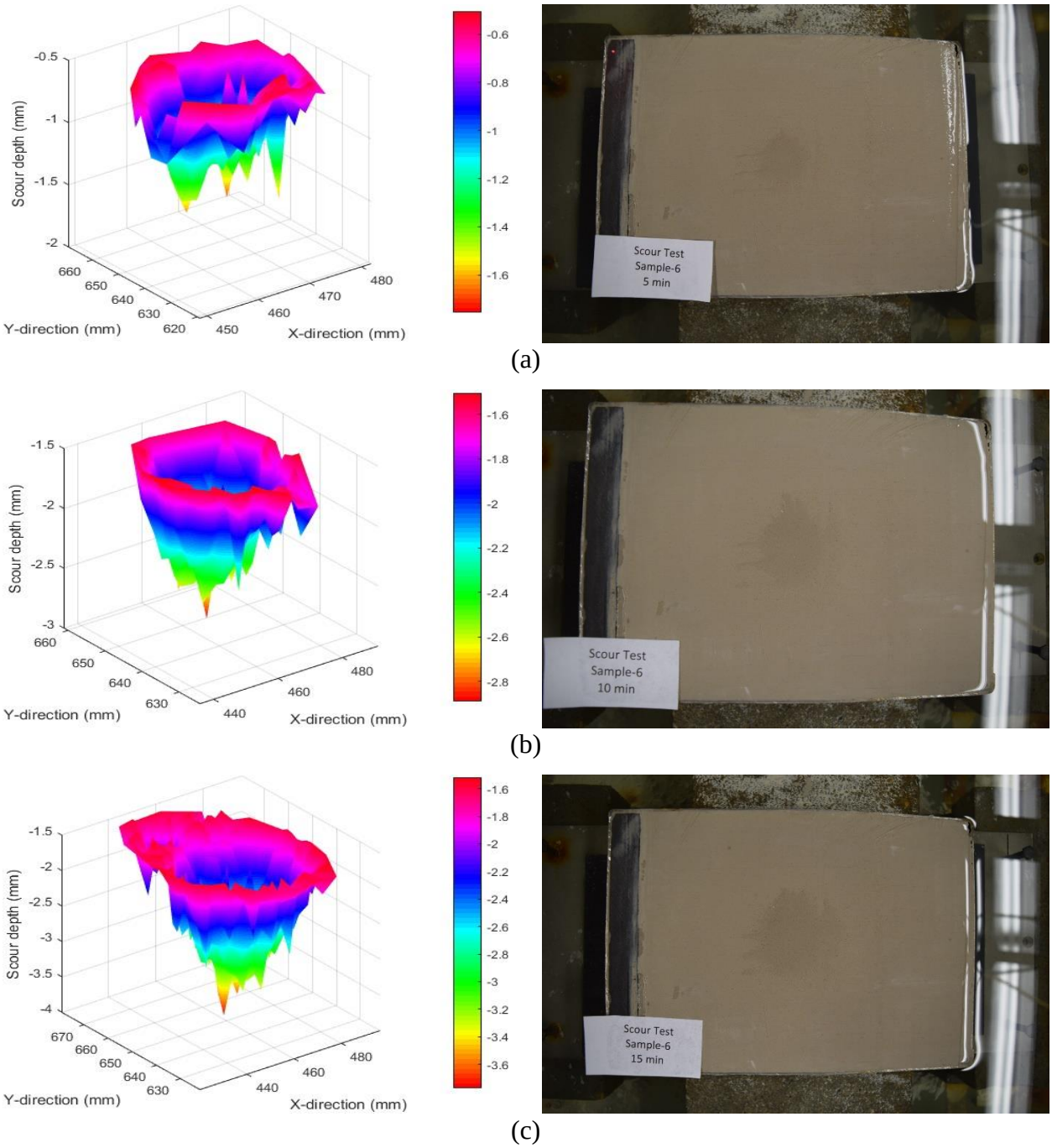

Figure B-5: Three-dimensional scour hole shape and photo of the sample in plan view for Scour Test 6 (Buffstone clay, U_0=6.6 m/s, d=7.76 mm, H=85 mm, and t_d=168 h) after a test duration of (a) 5 min, (b) 10 min, (c) 15 min, (d) 20 min, (e) 30 min, (f) 40 min, (g) 50 min, (h) 1 h, (i) 1.5 h, (j) 2 h, (k) 4 h, (l) 8 h, (m) 16 h, (n) 24 h, (o) 48 h, (p) 72 h, (q) 96 h, (r) 120 h, (s) 144 h, and (t) 168 h.

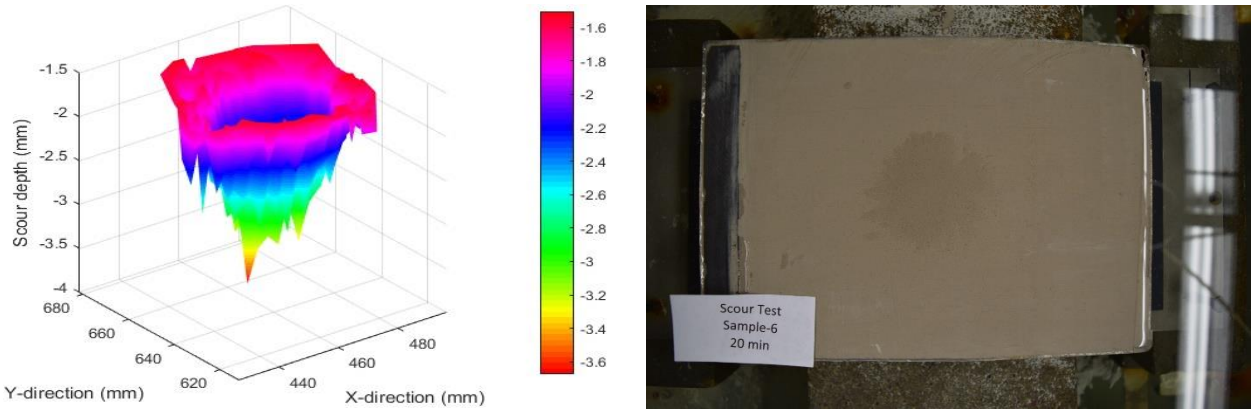

(d)

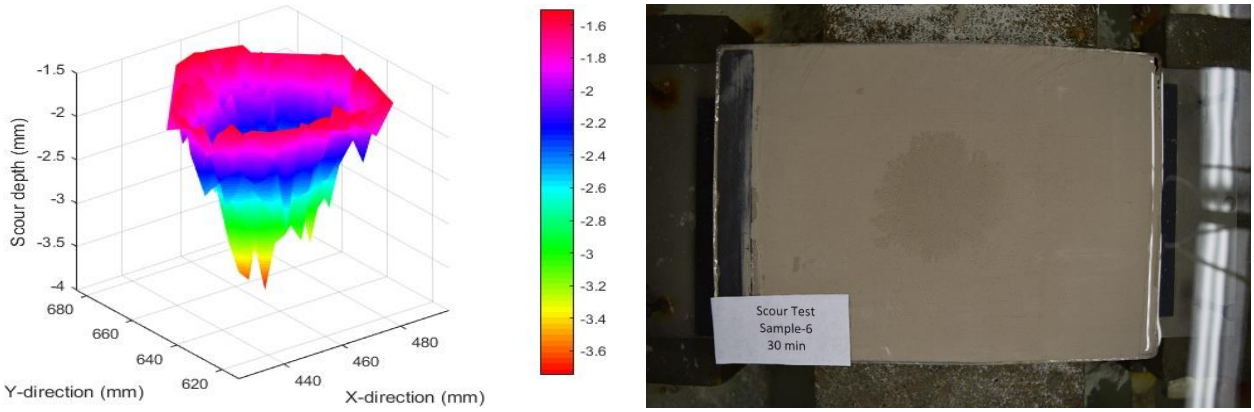

(e)

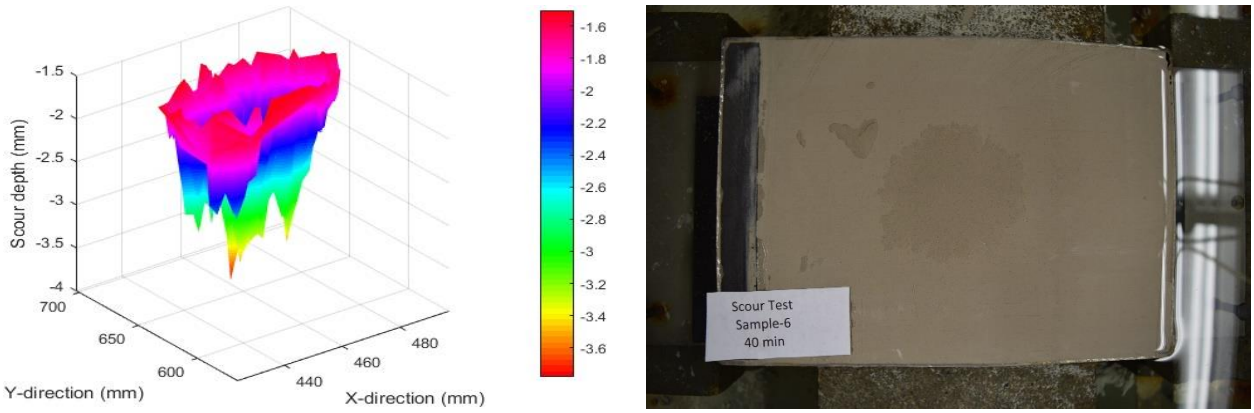

(f)

Figure B-5: cont'd.

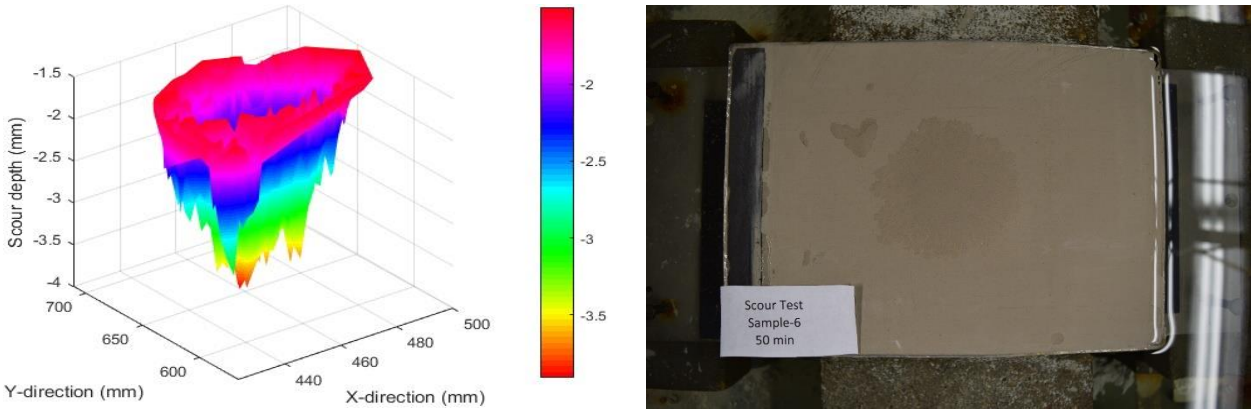

(g)

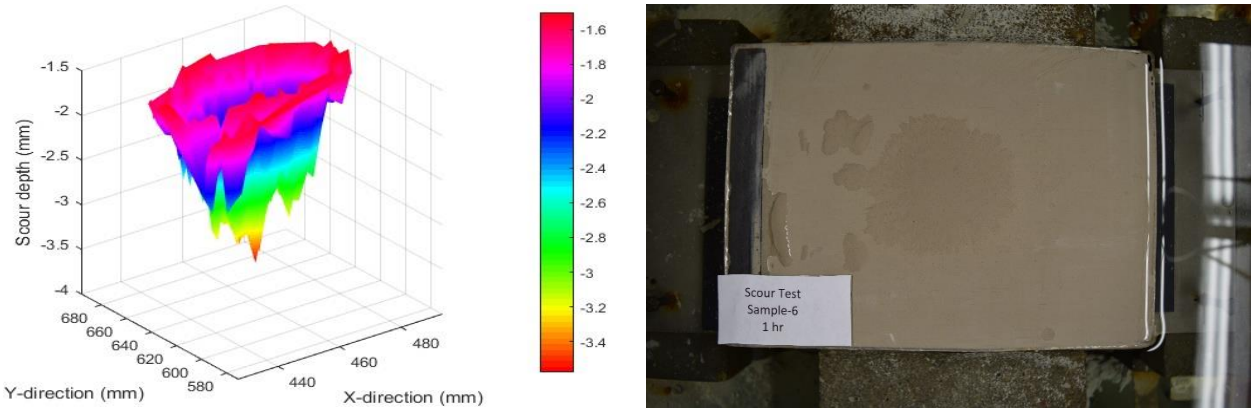

(h)

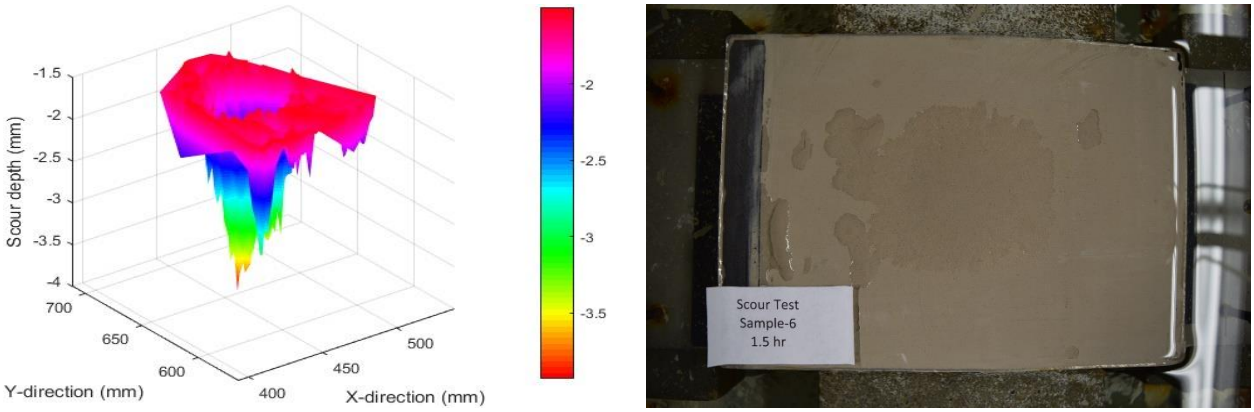

(i)

Figure B-5: cont'd.

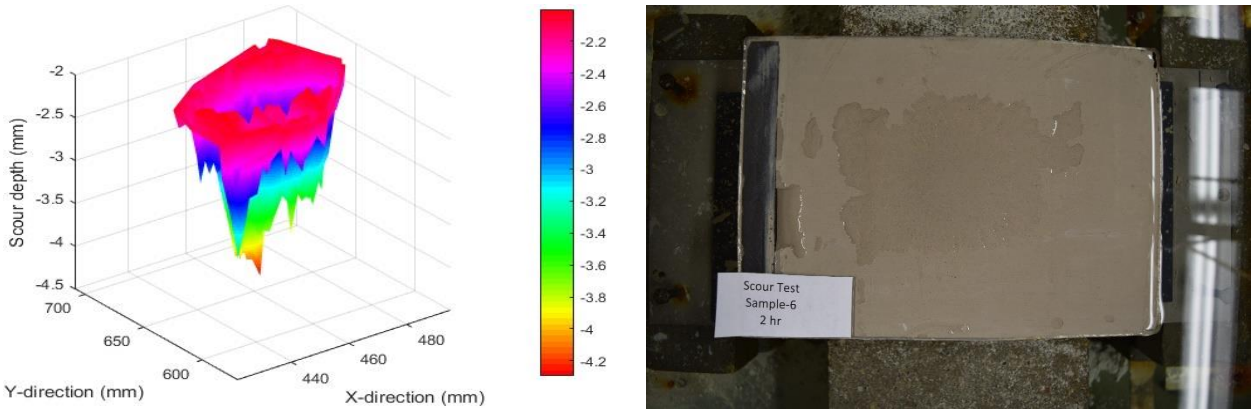

(j)

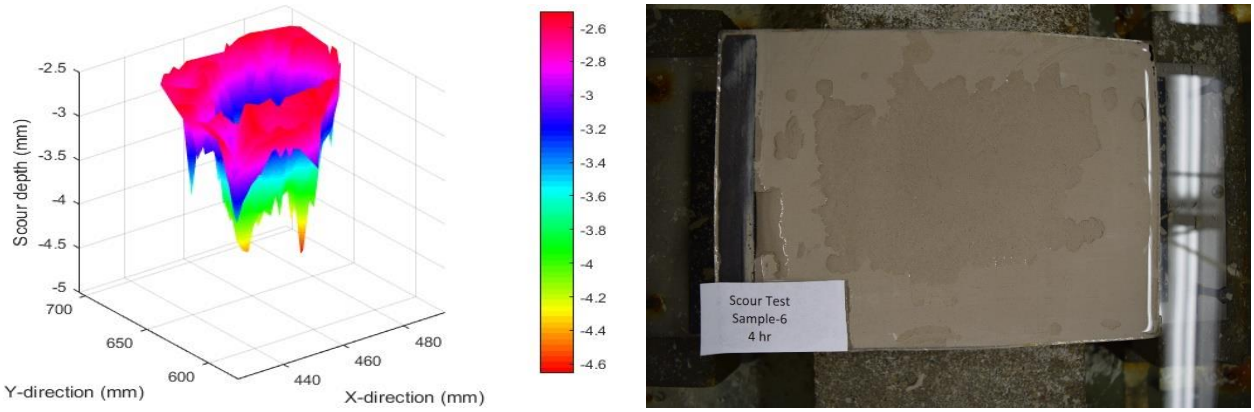

(k)

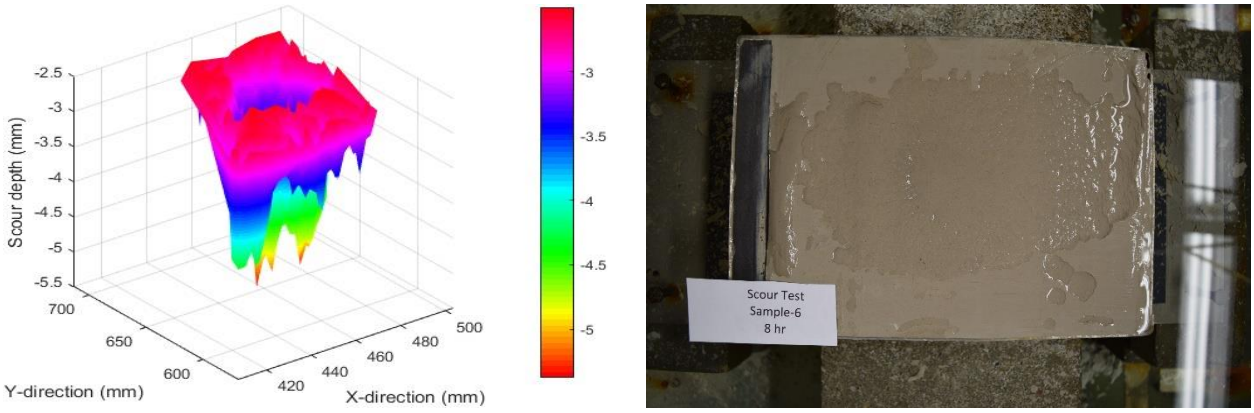

(l)

Figure B-5: cont'd.

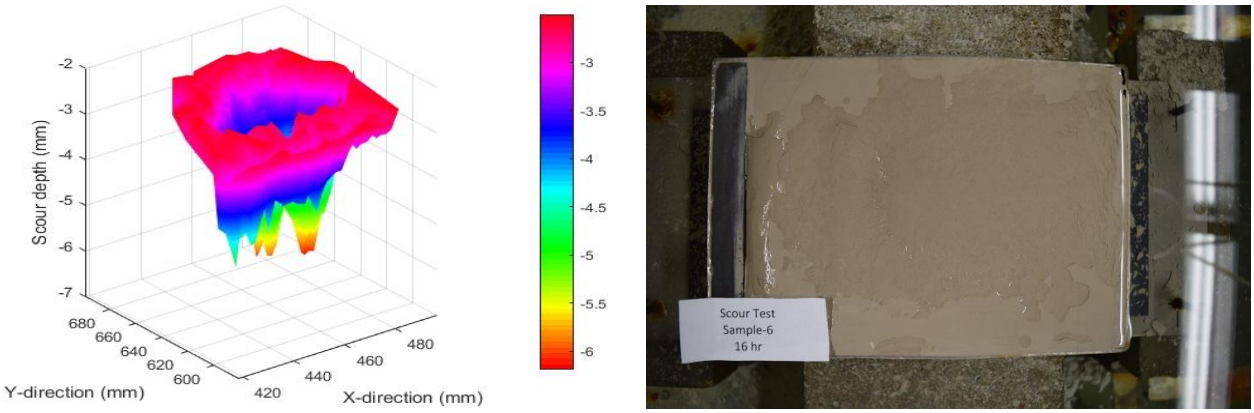

(m)

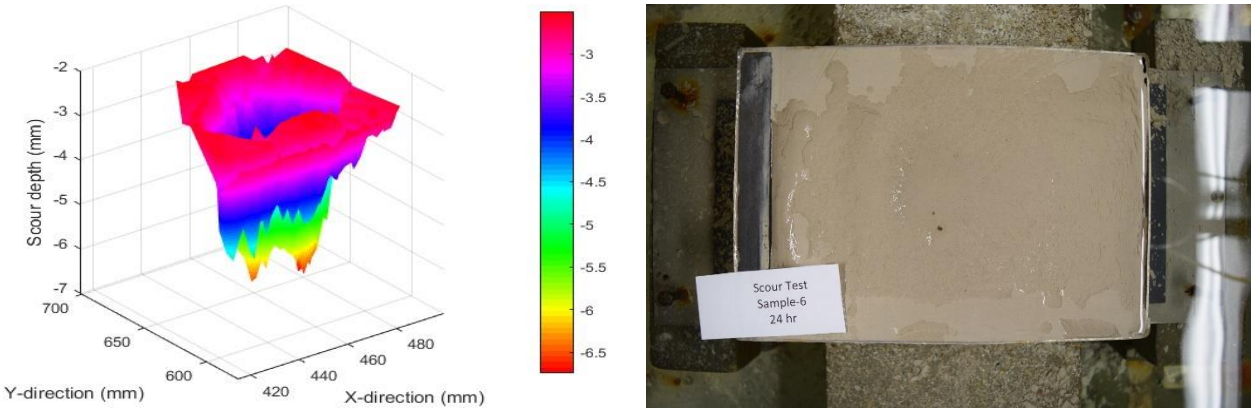

(n)

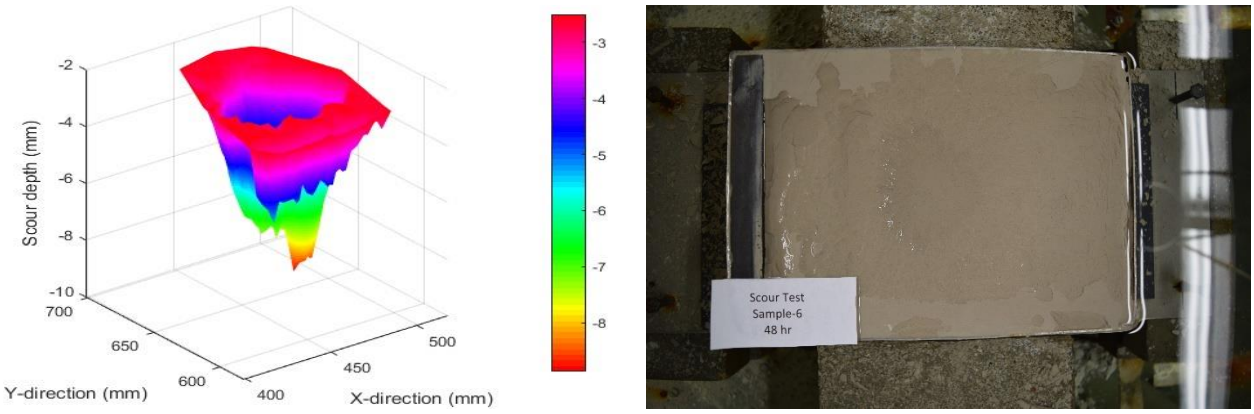

(o)

Figure B-5: cont'd.

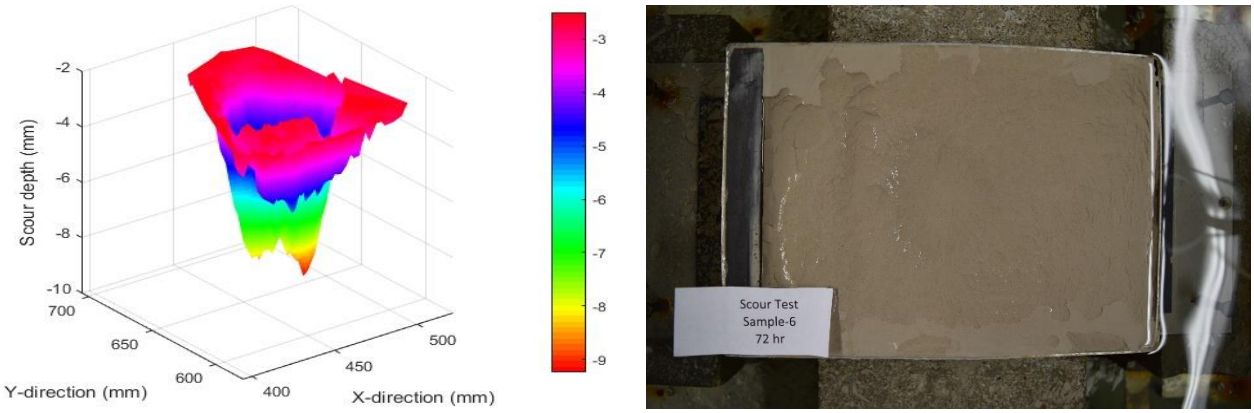

(p)

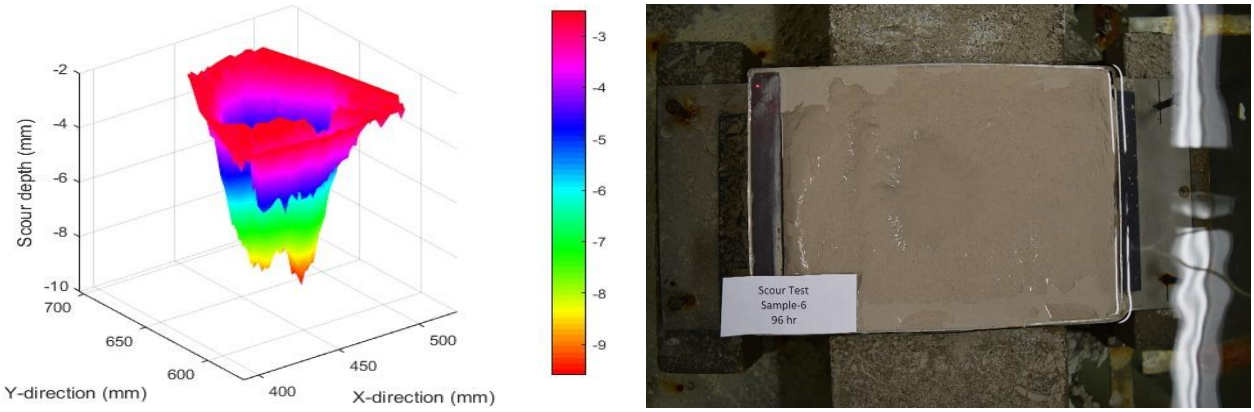

(q)

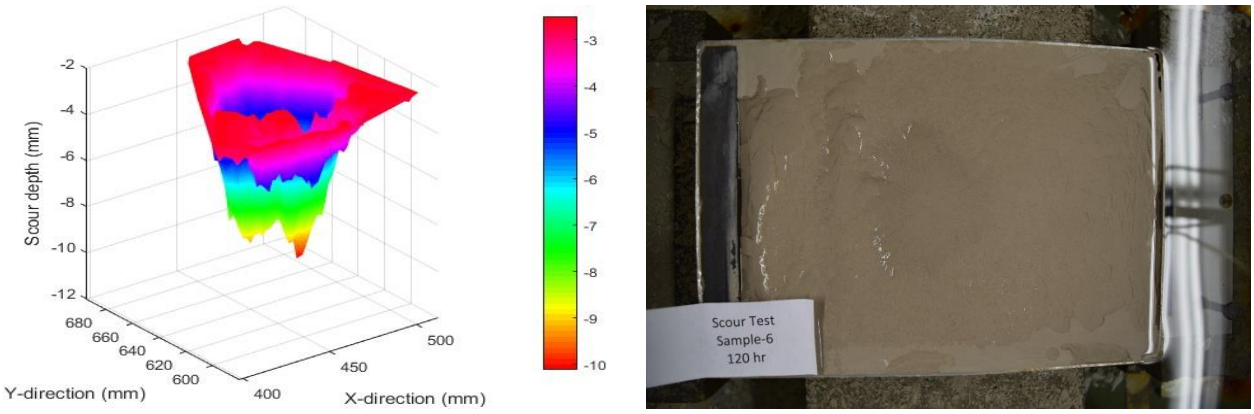

(r)

Figure B-5: cont'd.

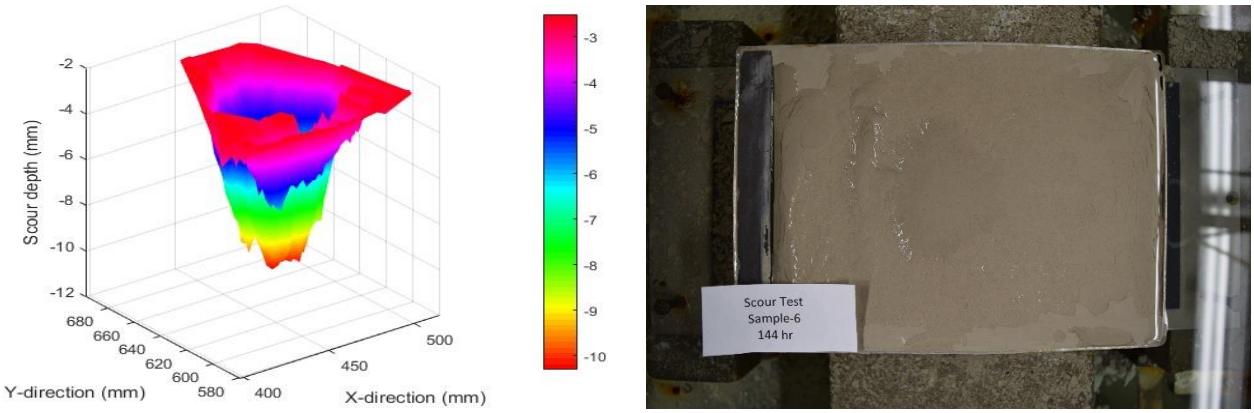

(s)

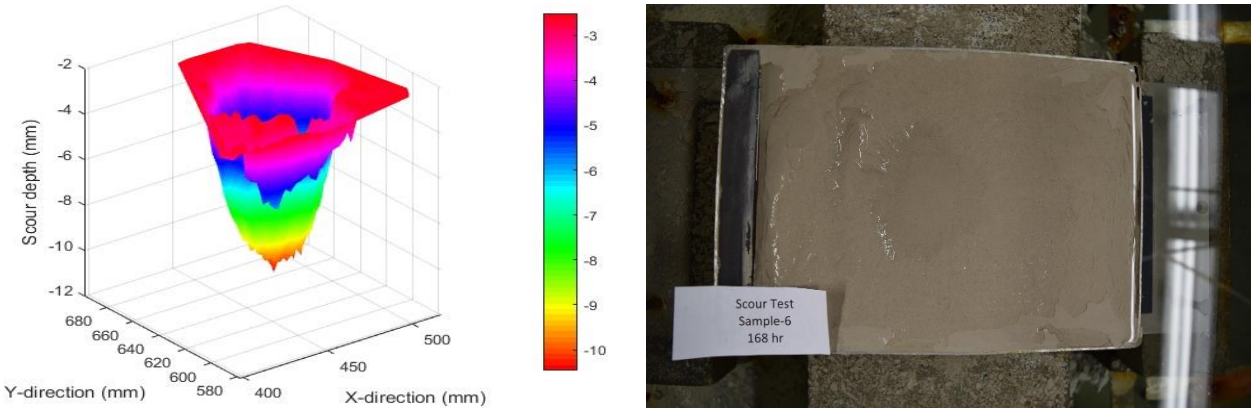

(t)

Figure B-5: cont'd.

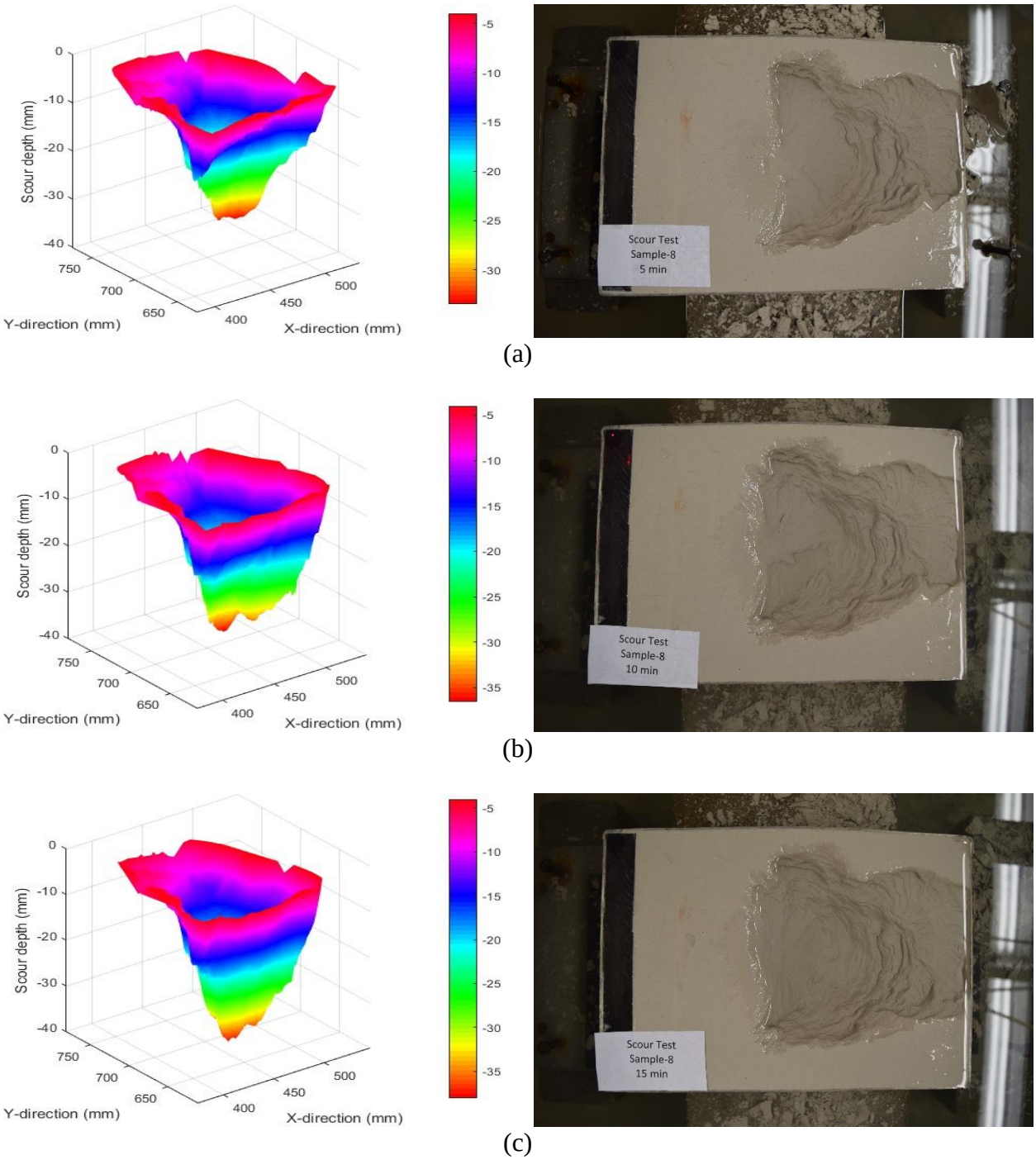

Figure B-6: Three-dimensional scour hole shape and photo of the sample in plan view for Scour Test 8 (M370 clay, U_0=9.9 m/s, d=7.76 mm, H=85 mm, and t_d=336 h) after a test duration of (a) 5 min, (b) 10 min, (c) 15 min, (d) 20 min, (e) 30 min, (f) 40 min, (g) 50 min, (h) 1 h, (i) 1.5 h, (j) 2 h, (k) 4 h, (l) 8 h, (m) 16 h, (n) 24 h, (o) 48 h, (p) 72 h, (q) 96 h, (r) 120 h, (s) 144 h, (t) 168 h, (u) 192 h, (v) 216 h, (w) 240 h, (x) 264 h, (y) 288 h, (z) 312 h, and (aa) 336 h.

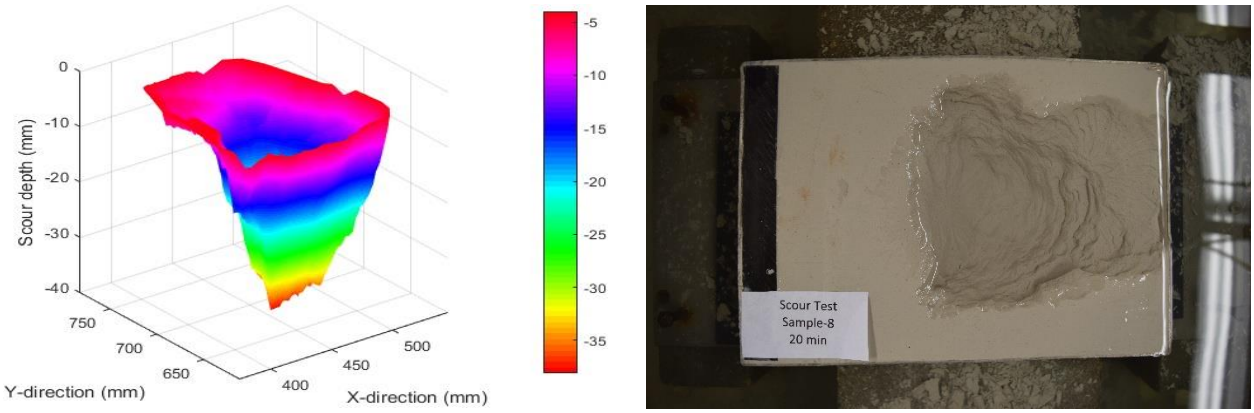

(d)

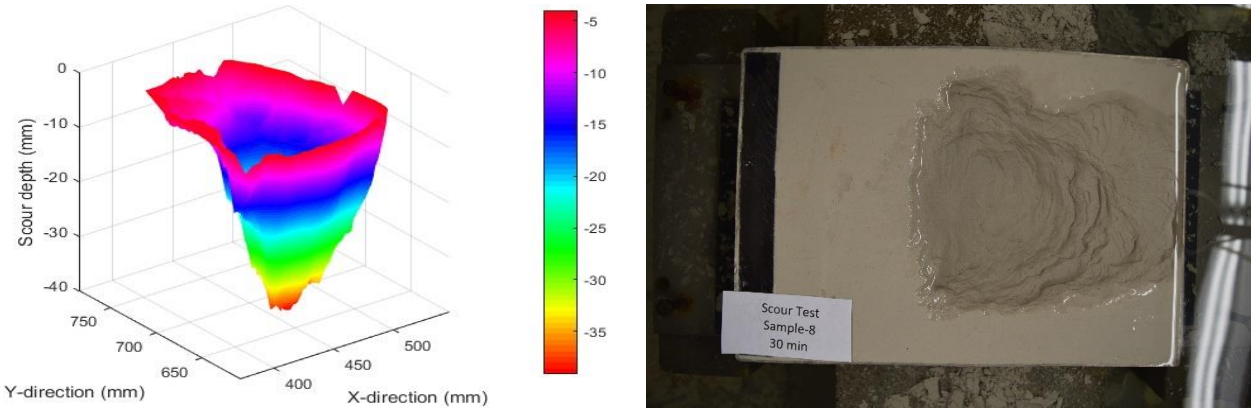

(e)

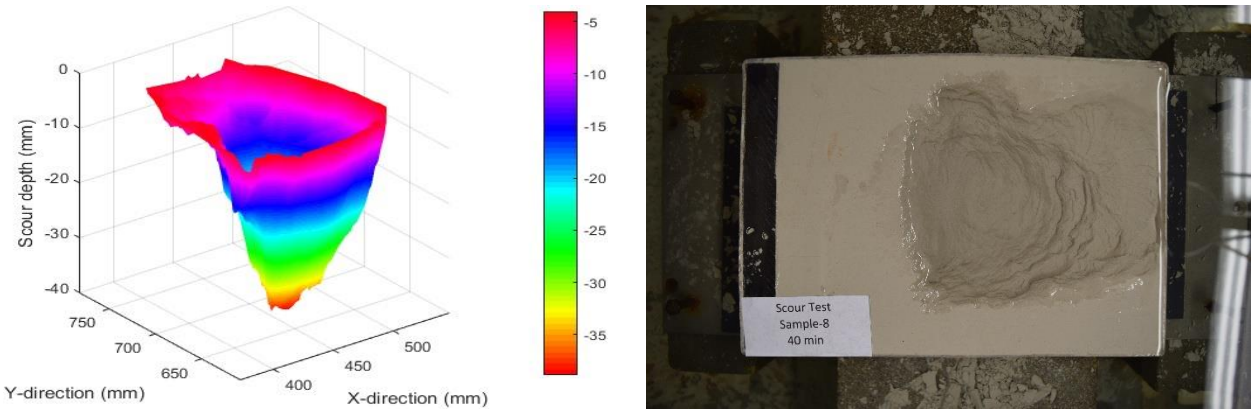

(f)

Figure B-6: cont'd.

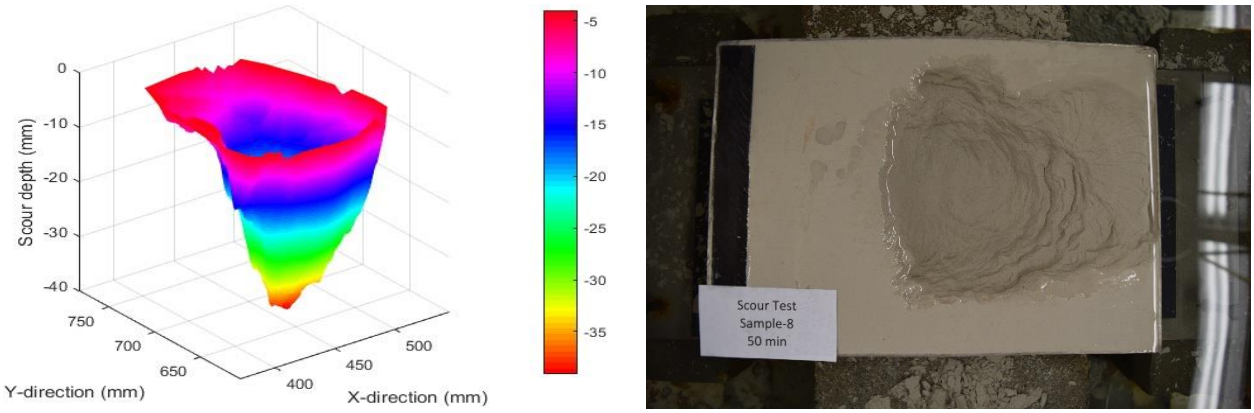

(g)

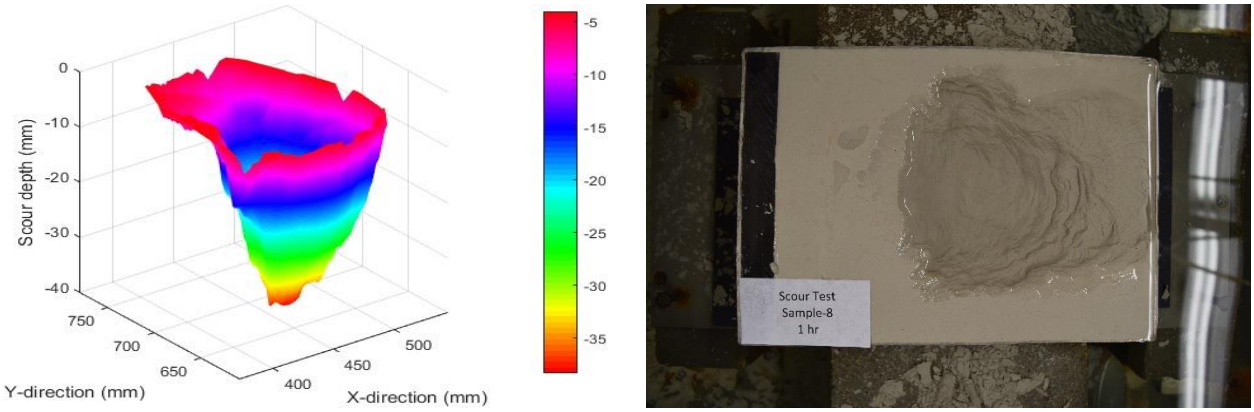

(h)

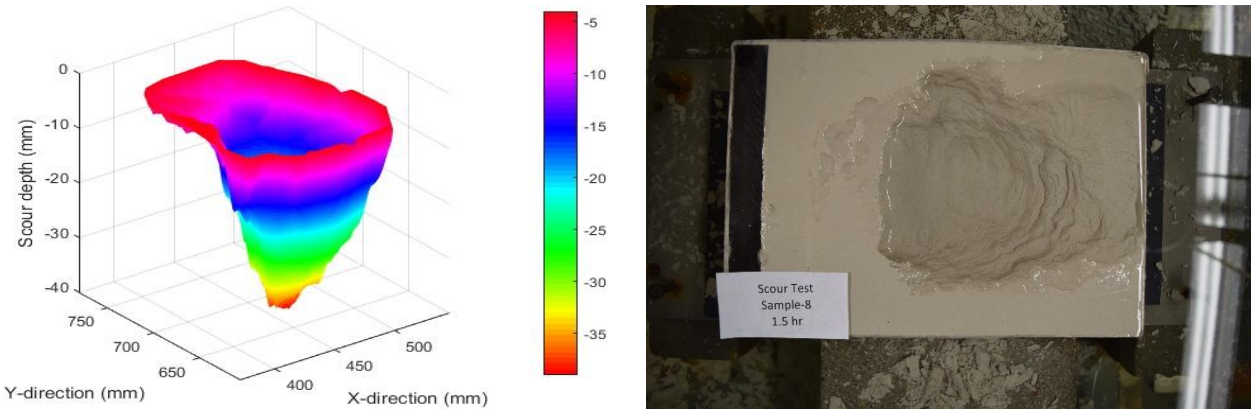

(i)

Figure B-6: cont'd.

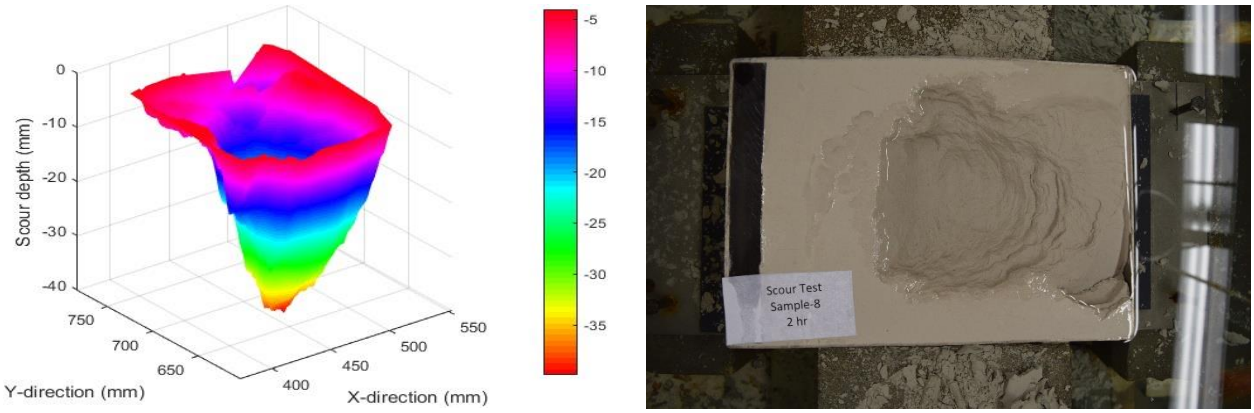

(j)

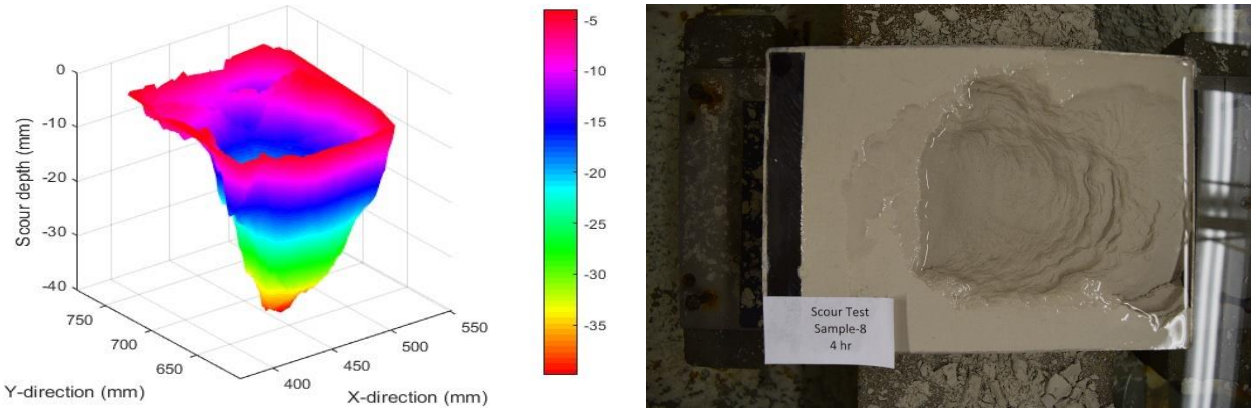

(k)

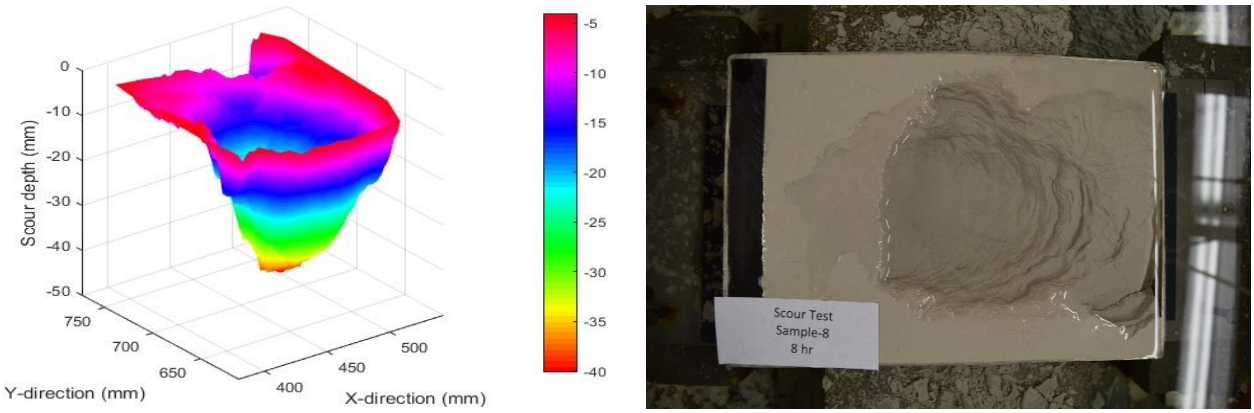

(l)

Figure B-6: cont'd.

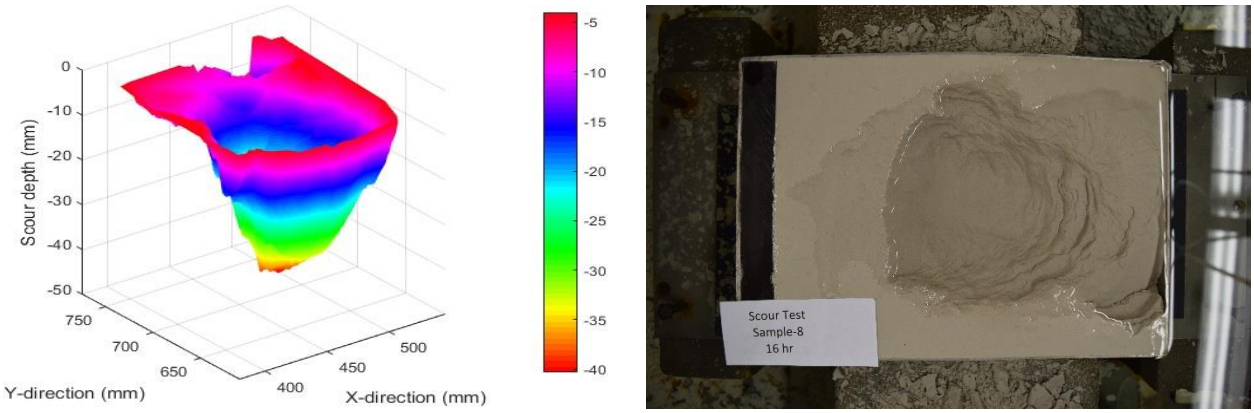

(m)

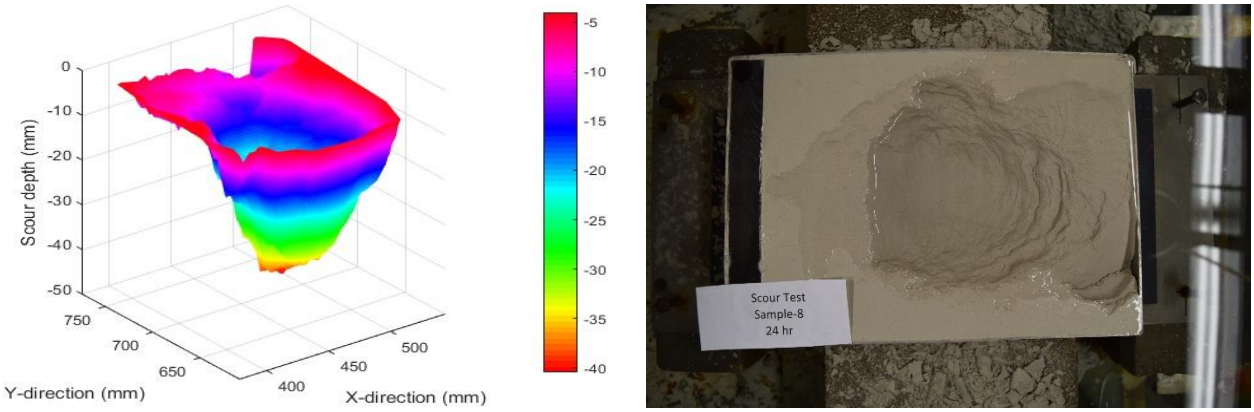

(n)

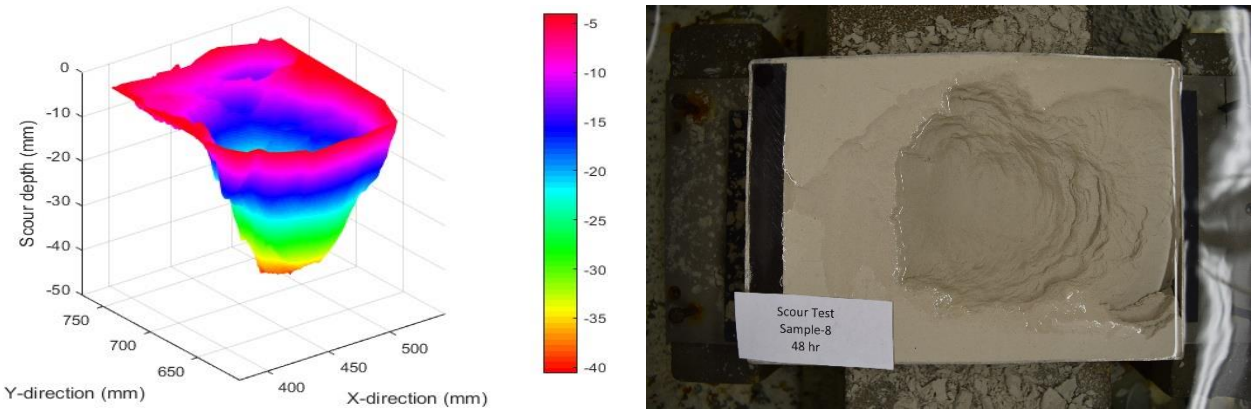

(o)

Figure B-6: cont'd.

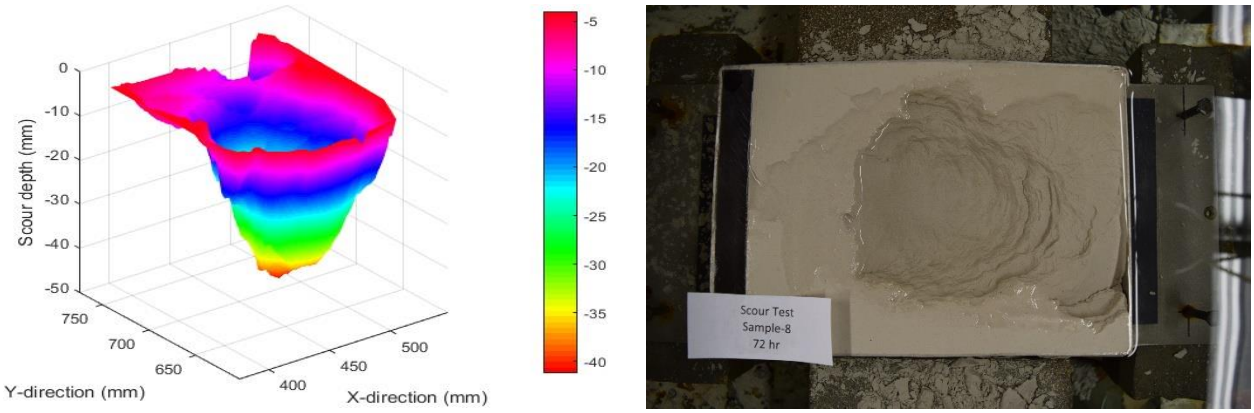

(p)

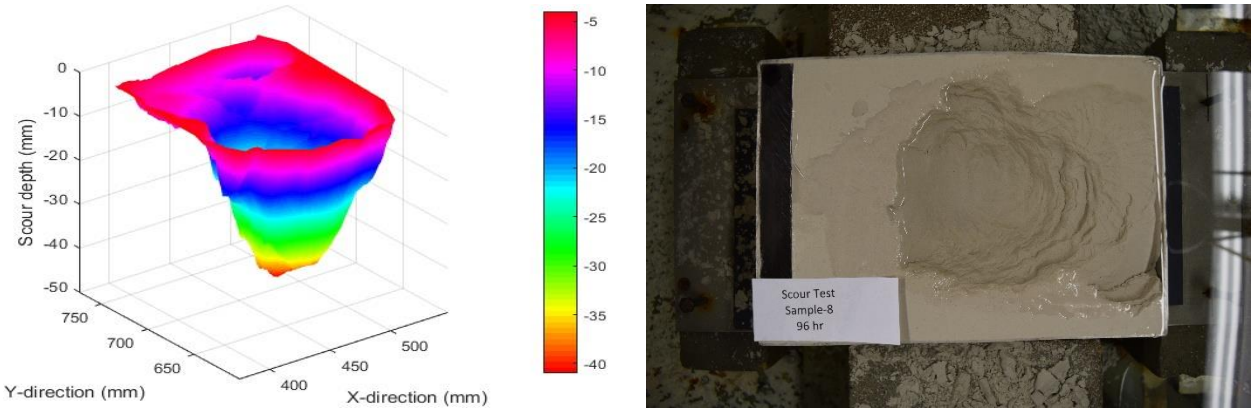

(q)

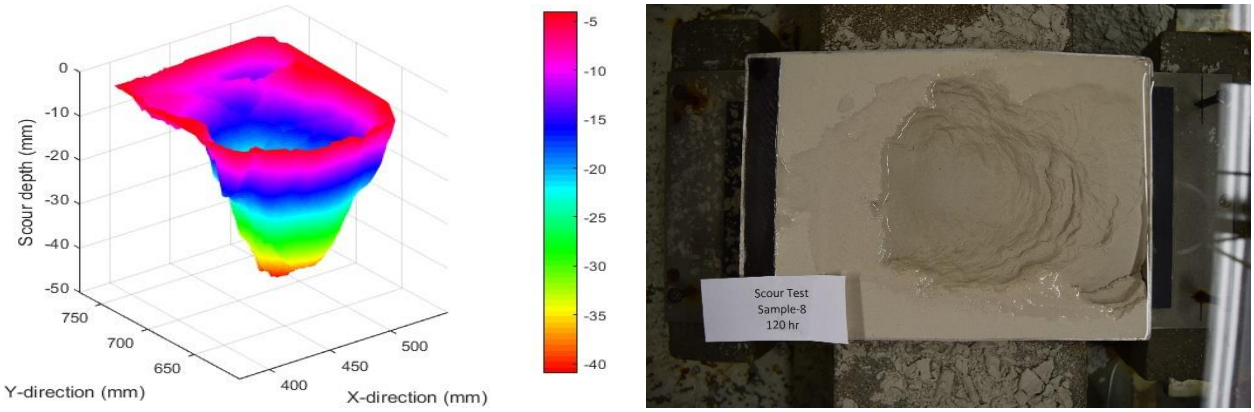

(r)

Figure B-6: cont'd.

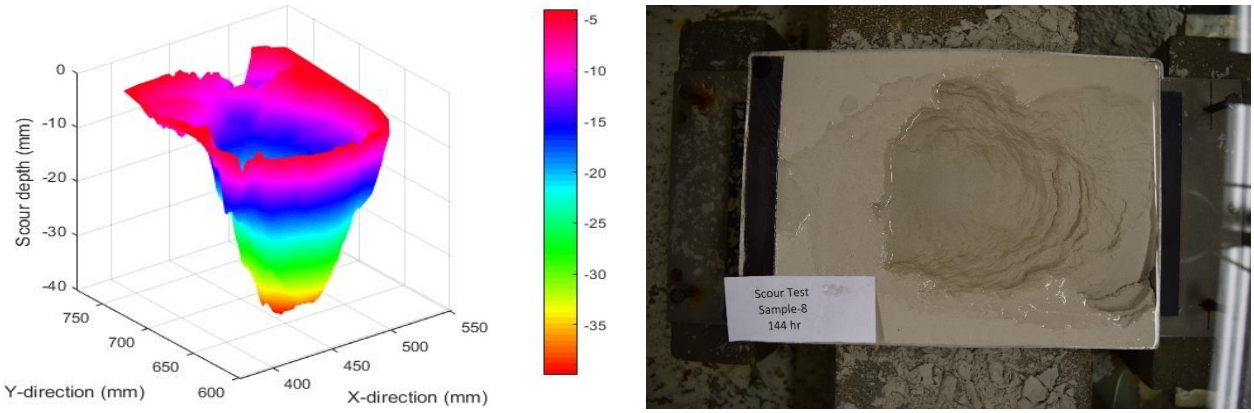

(s)

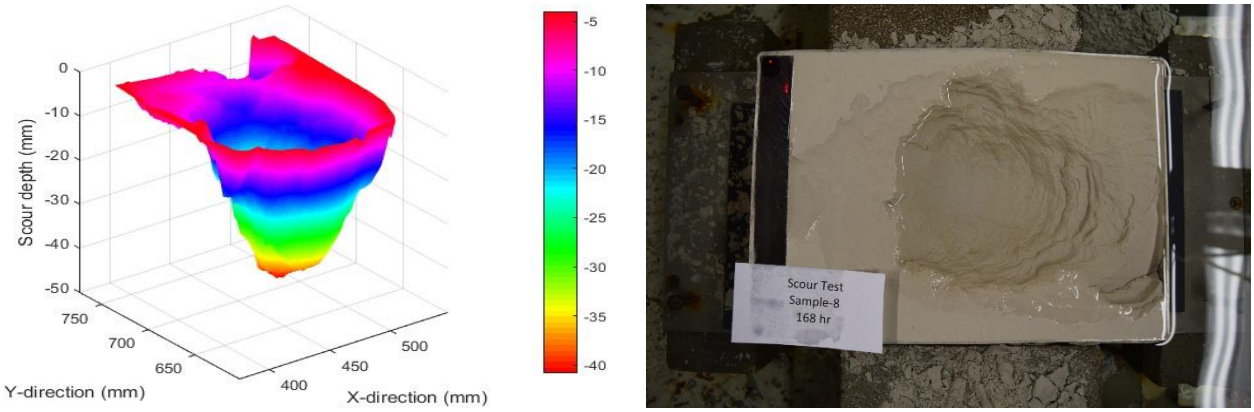

(t)

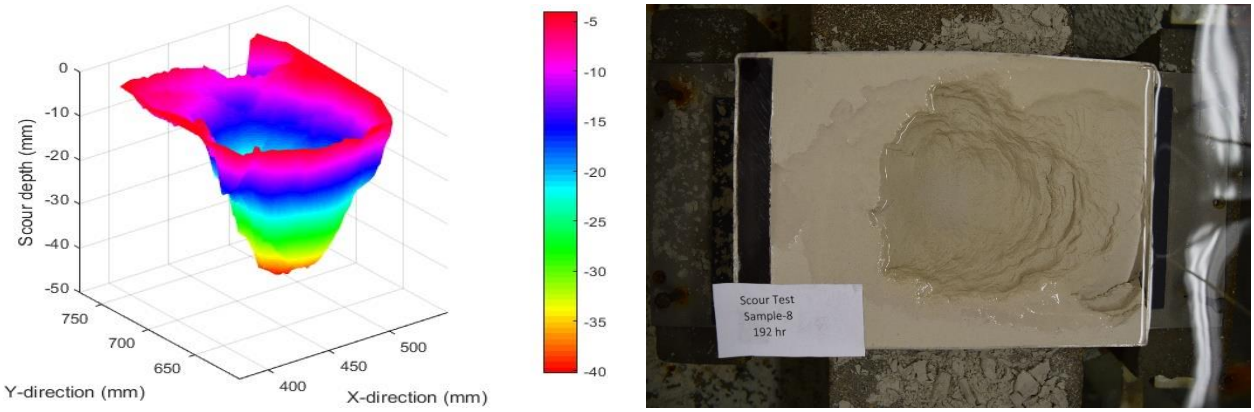

(u)

Figure B-6: cont'd.

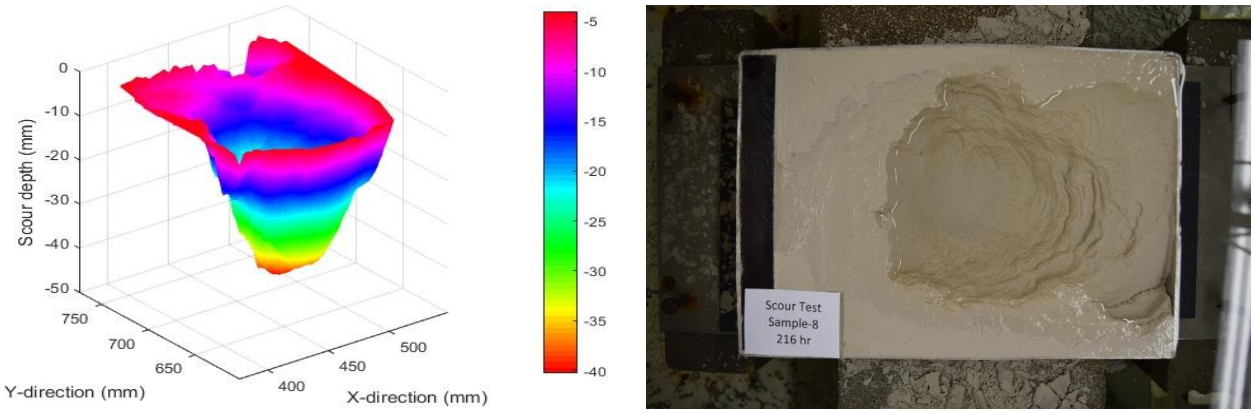

(v)

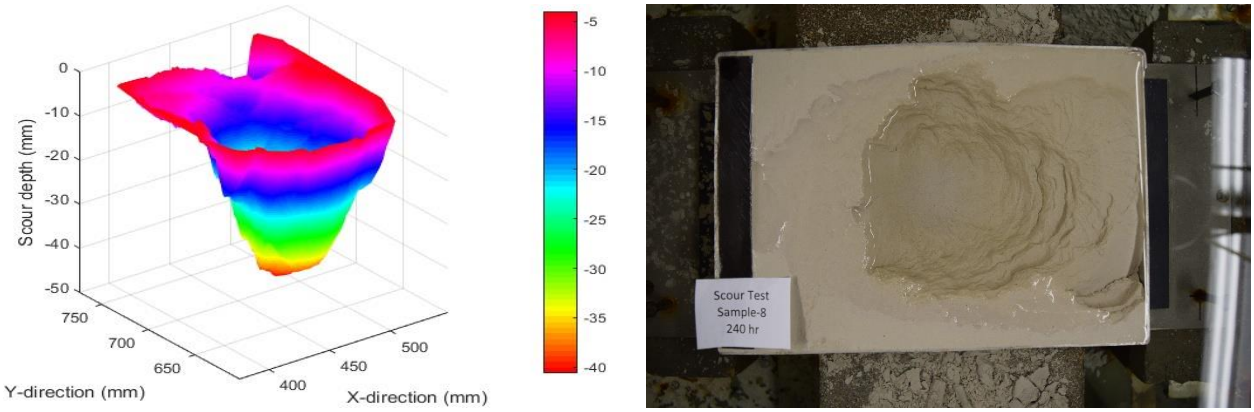

(w)

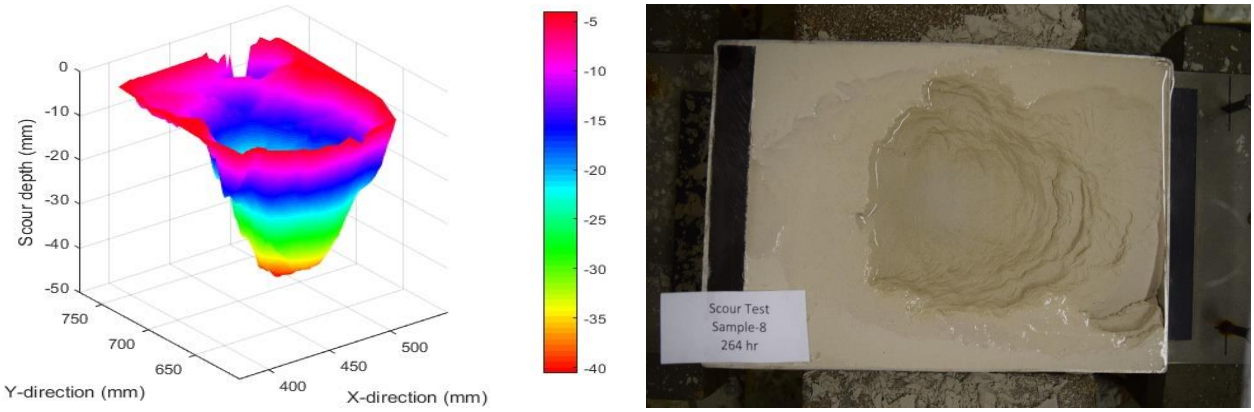

(x)

Figure B-6: cont'd.

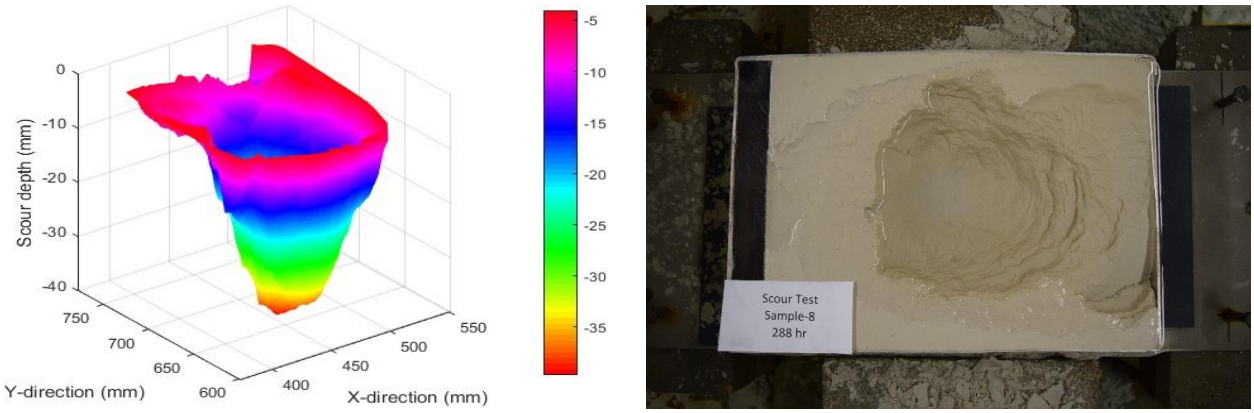

(y)

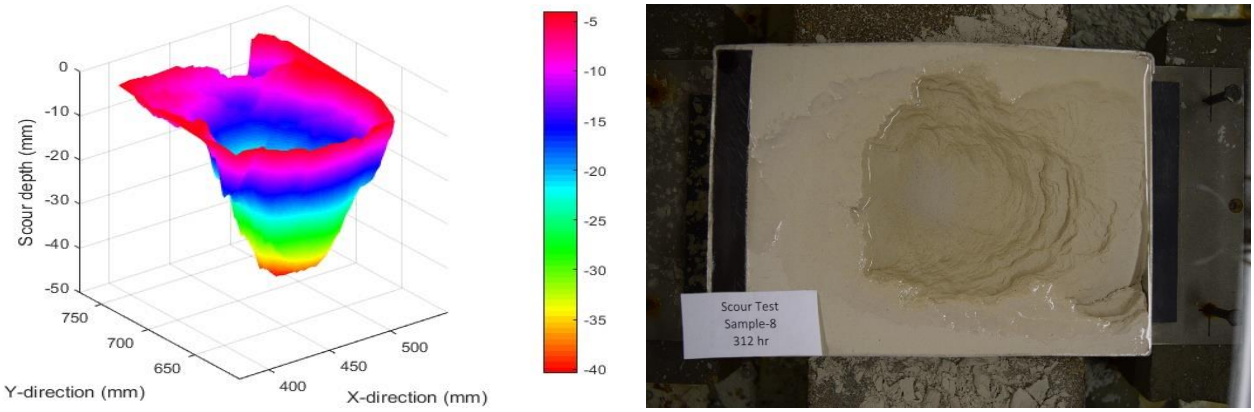

(z)

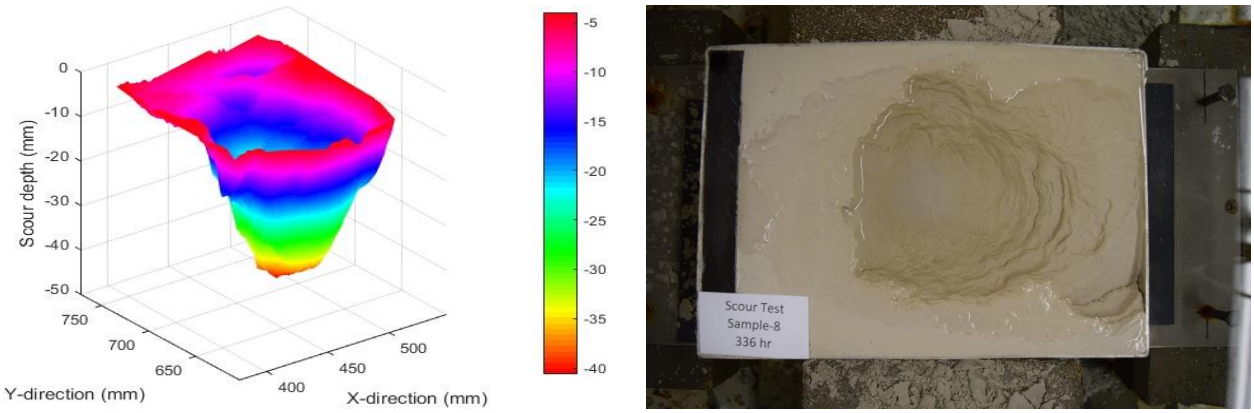

(aa)

Figure B-6: cont'd.

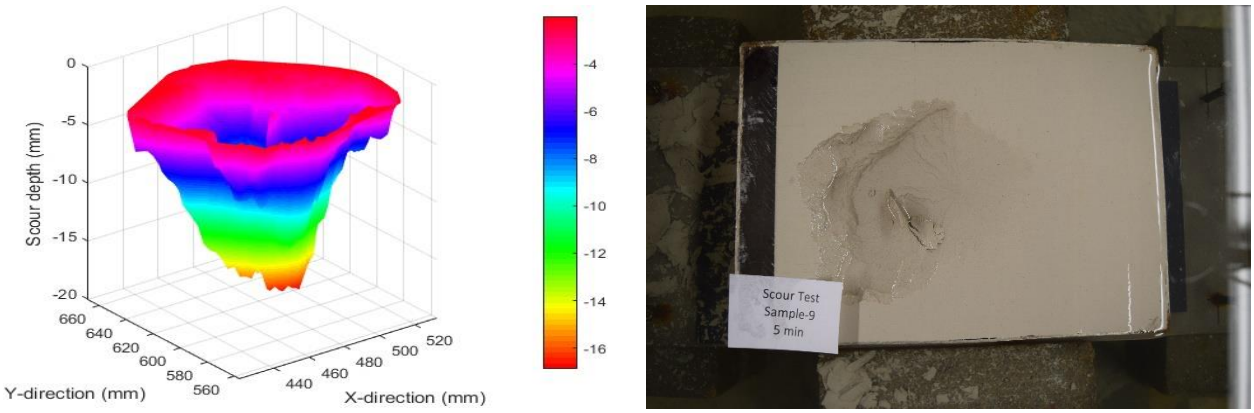

(a)

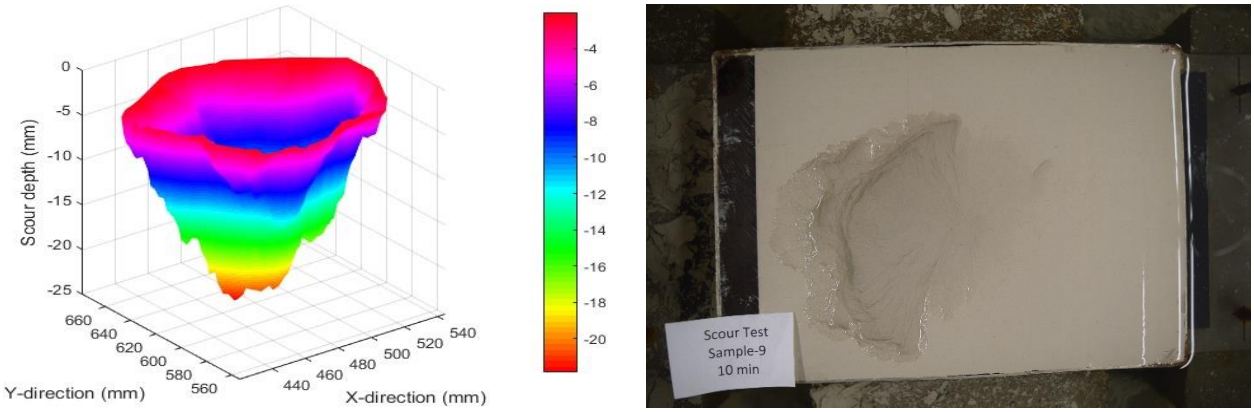

(b)

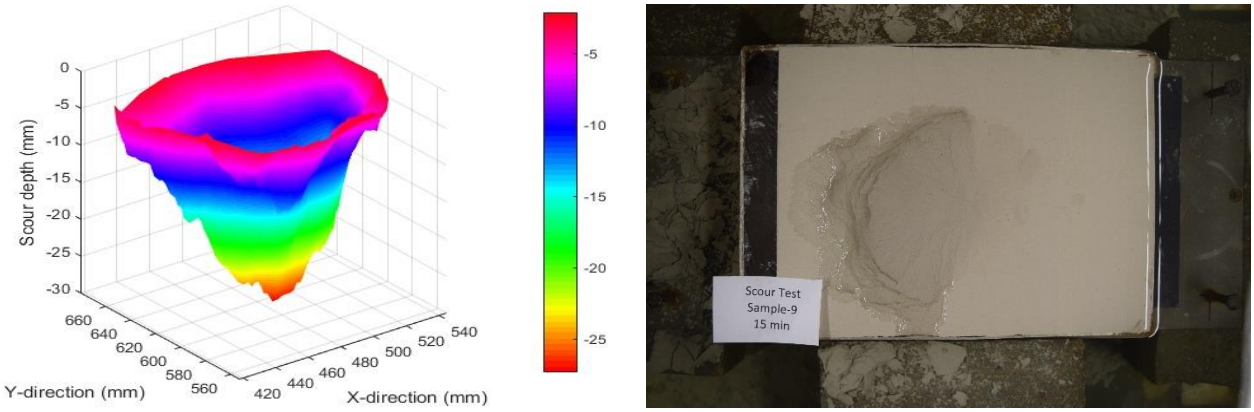

(c)

Figure B-7: Three-dimensional scour hole shape and photo of the sample in plan view for Scour Test 9 (M370 clay, U_0=8.4 m/s, d=7.76 mm, H=85 mm, and t_d=336 h) after a test duration of (a) 5 min, (b) 10 min, (c) 15 min, (d) 20 min, (e) 30 min, (f) 40 min, (g) 50 min, (h) 1 h, (i) 1.5 h, (j) 2 h, (k) 4 h, (l) 8 h, (m) 16 h, (n) 24 h, (o) 48 h, (p) 72 h, (q) 96 h, (r) 120 h, (s) 144 h, (t) 168 h, (u) 192 h, (v) 216 h, (w) 240 h, (x) 264 h, (y) 288 h, and (z) 336 h.

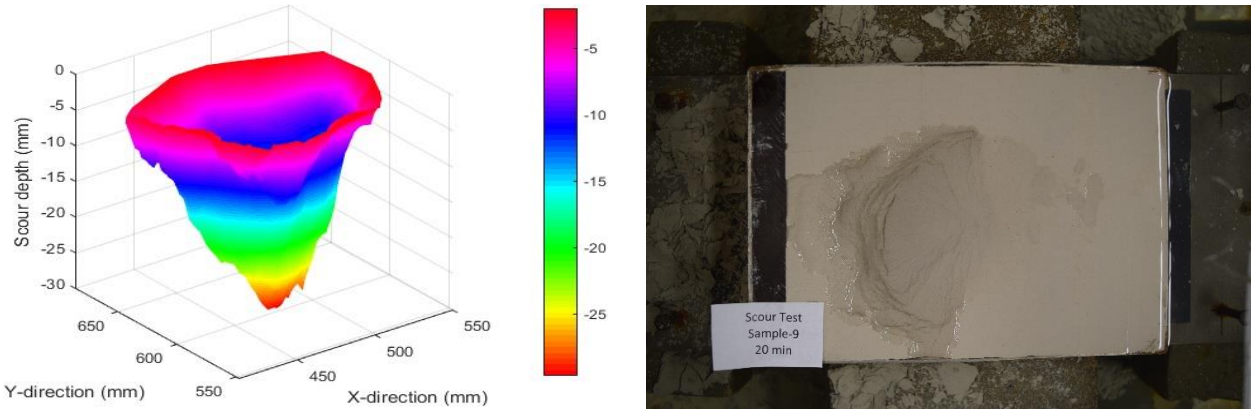

(d)

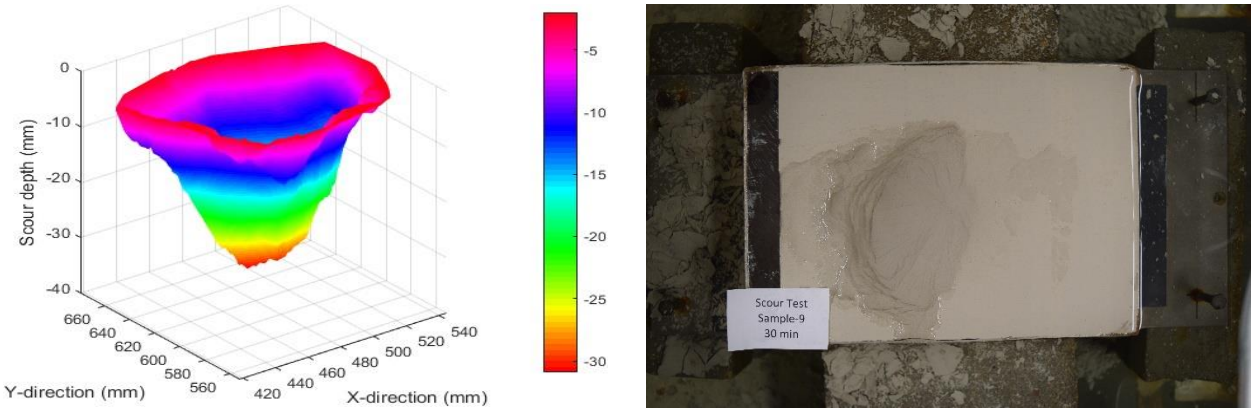

(e)

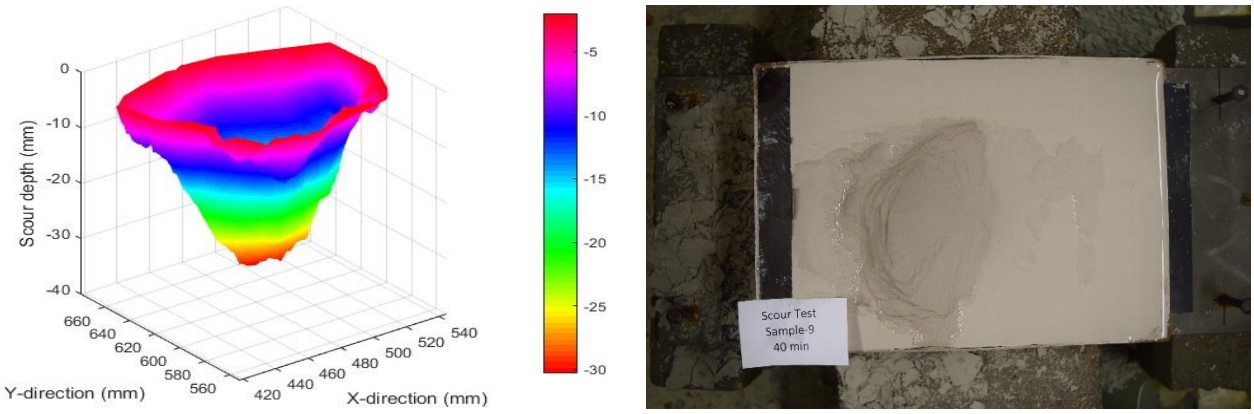

(f)

Figure B-7: cont'd.

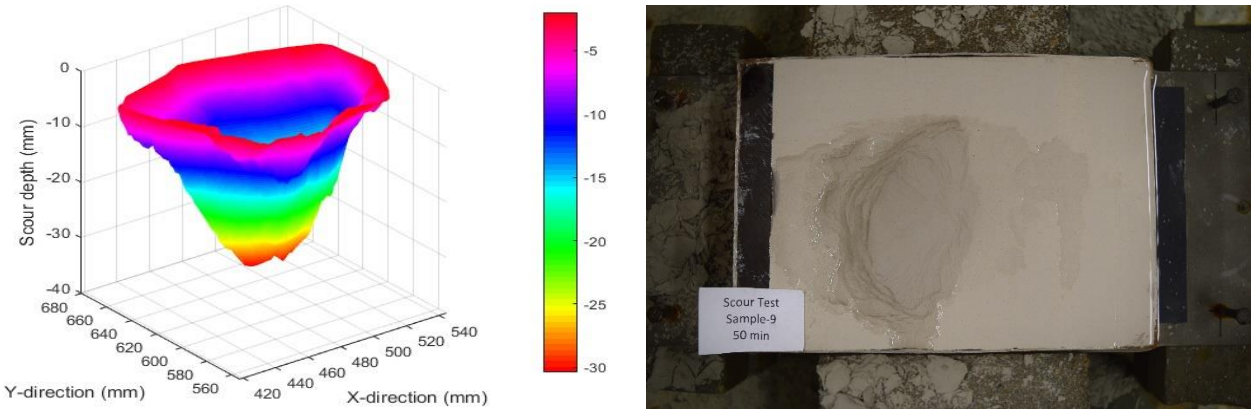

(g)

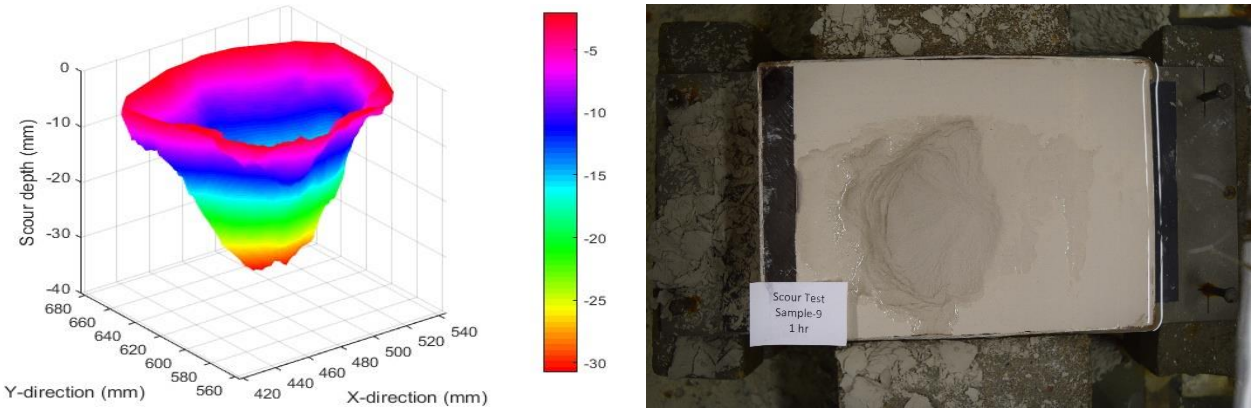

(h)

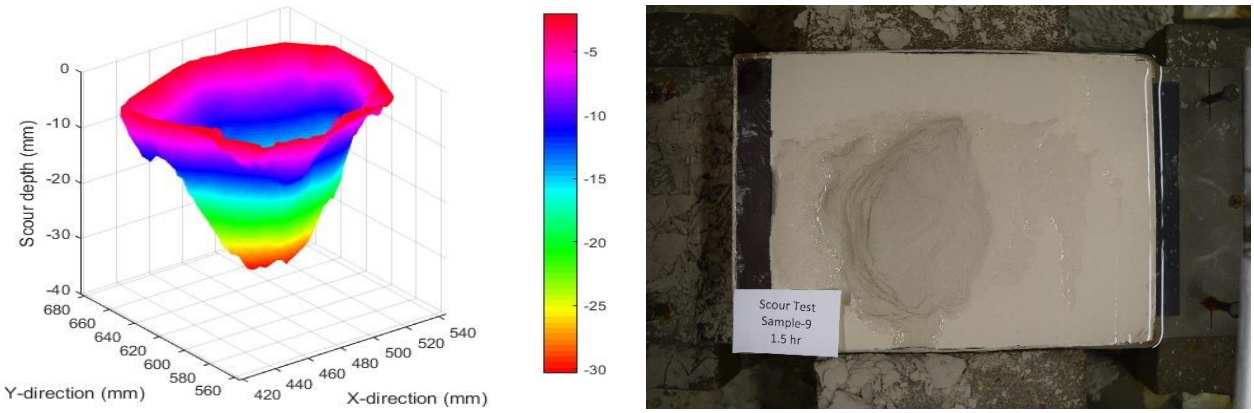

(i)

Figure B-7: cont'd.

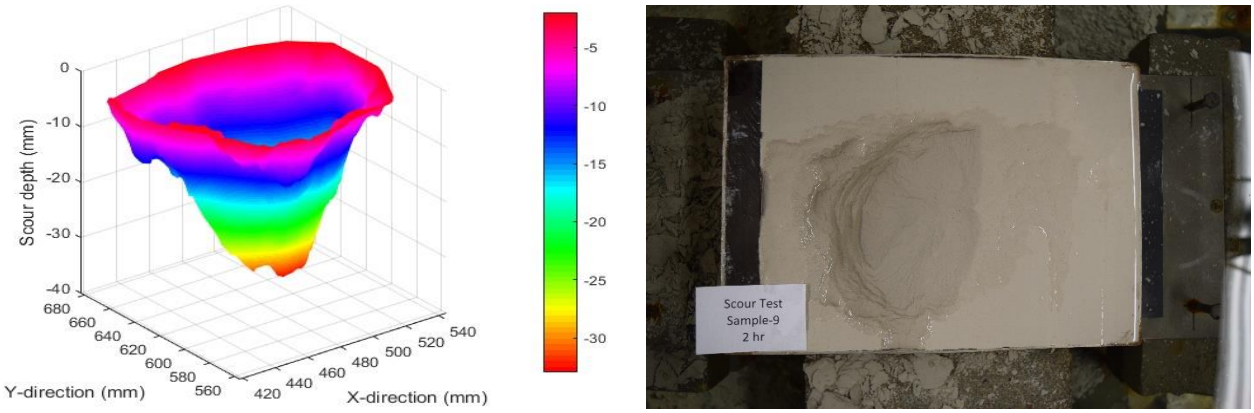

(j)

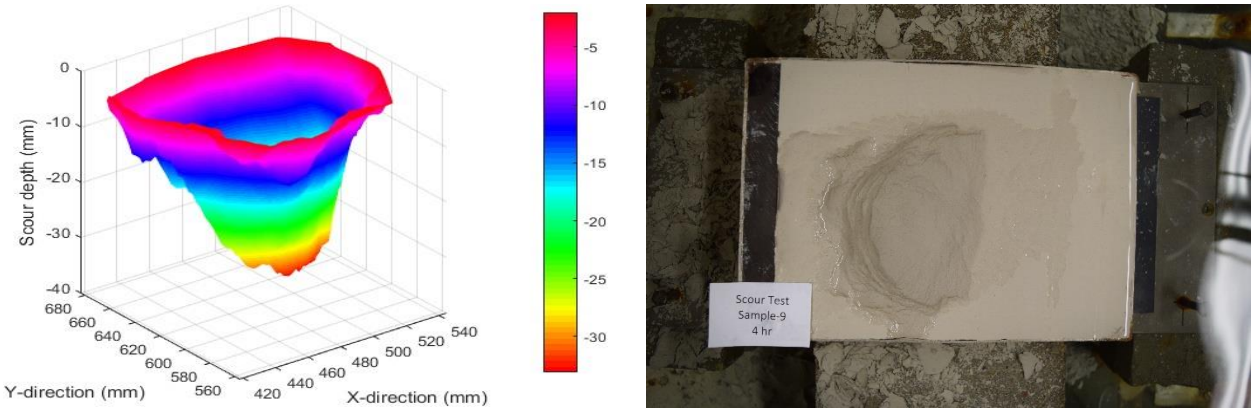

(k)

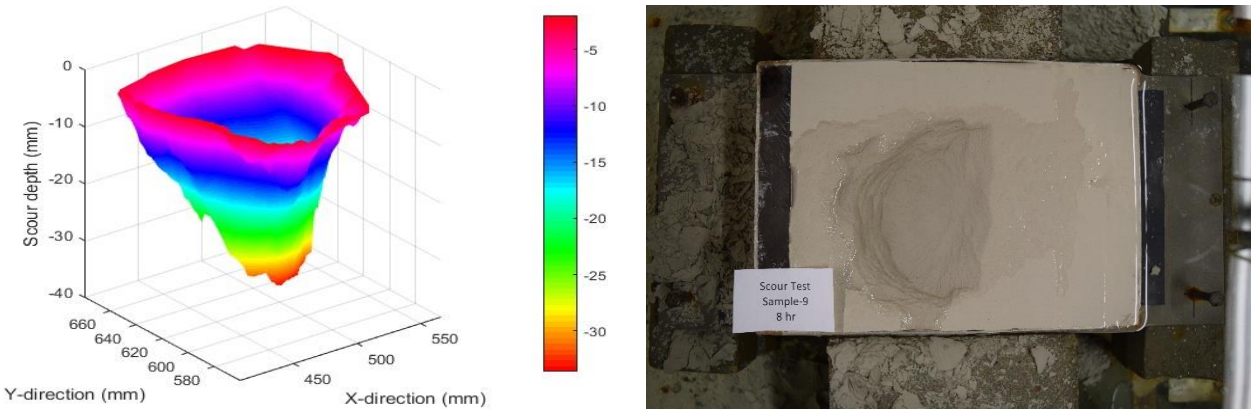

(l)

Figure B-7: cont'd.

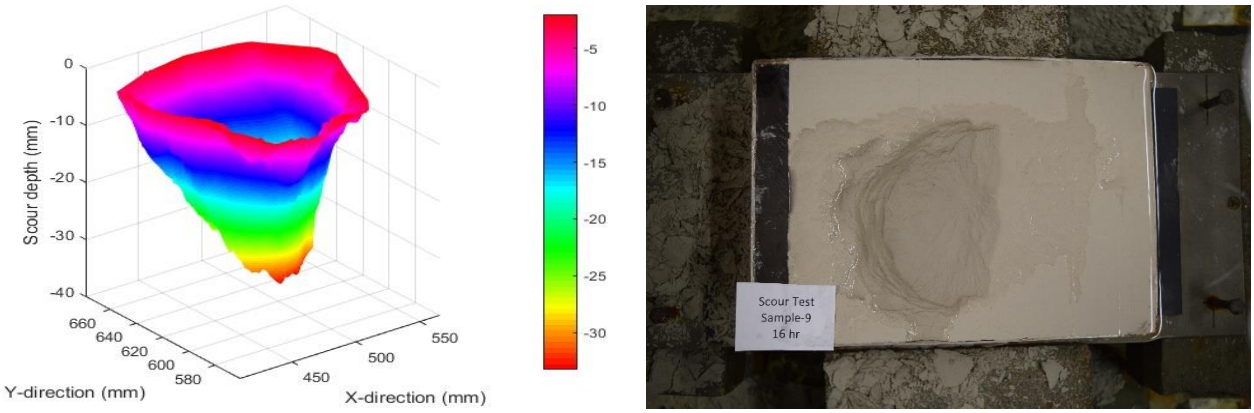

(m)

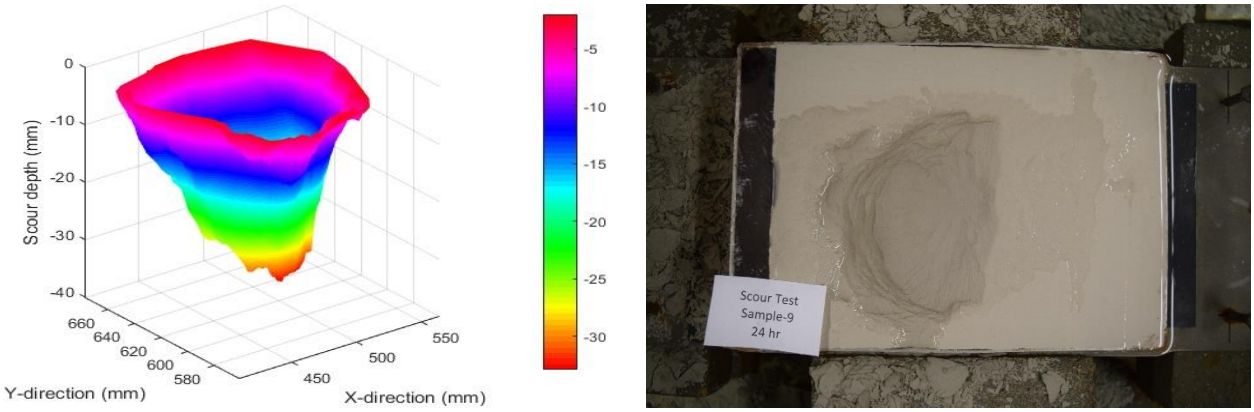

(n)

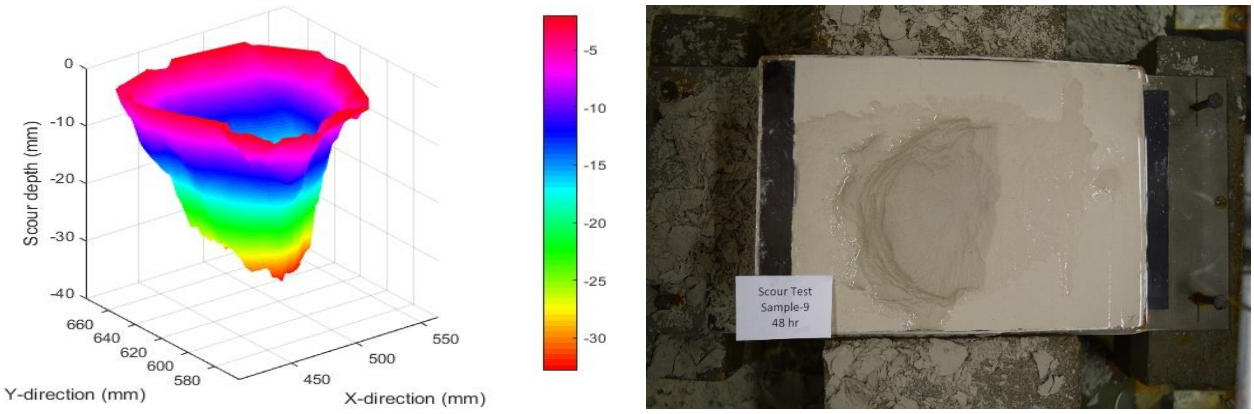

(o)

Figure B-7: cont'd.

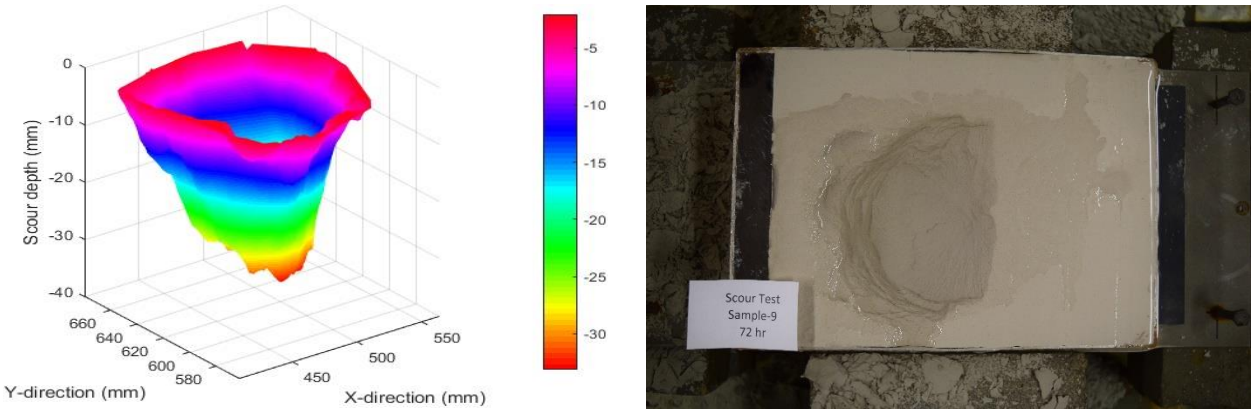

(p)

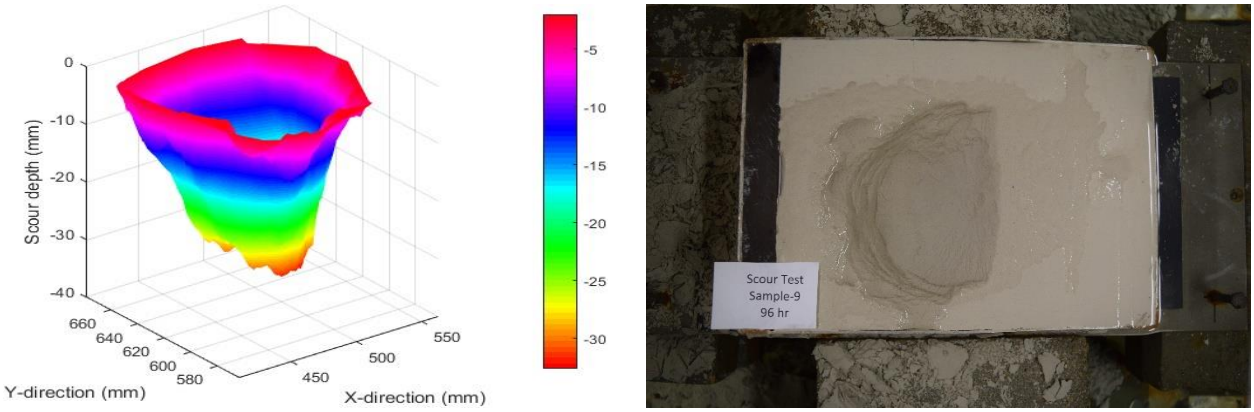

(q)

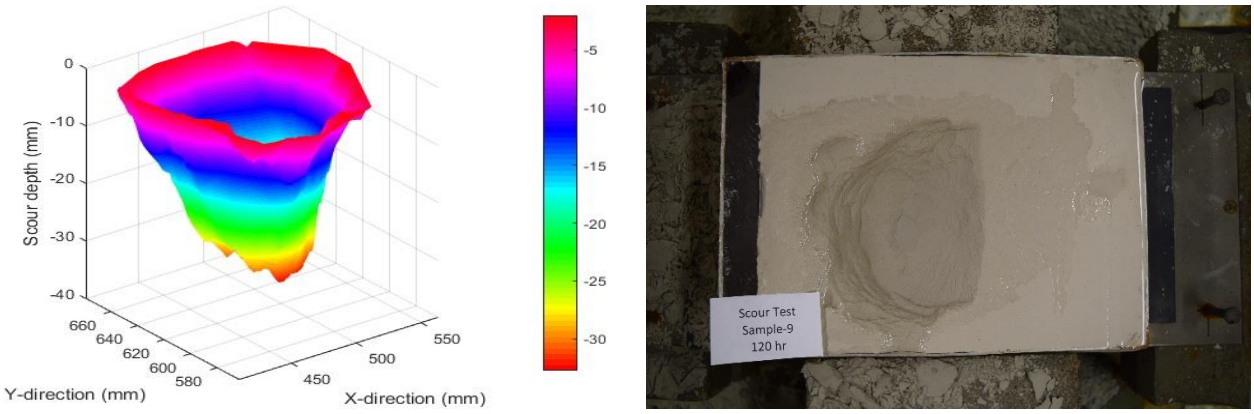

(r)

Figure B-7: cont'd.

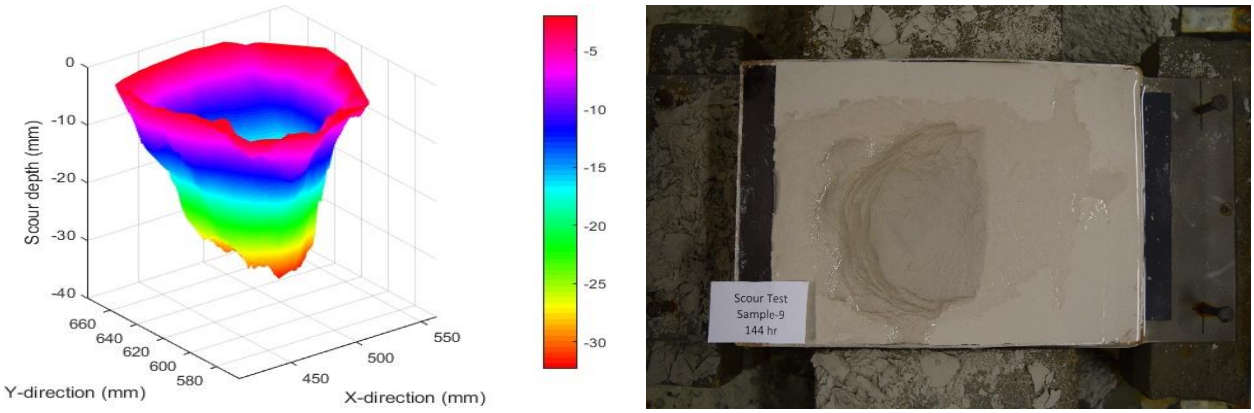

(s)

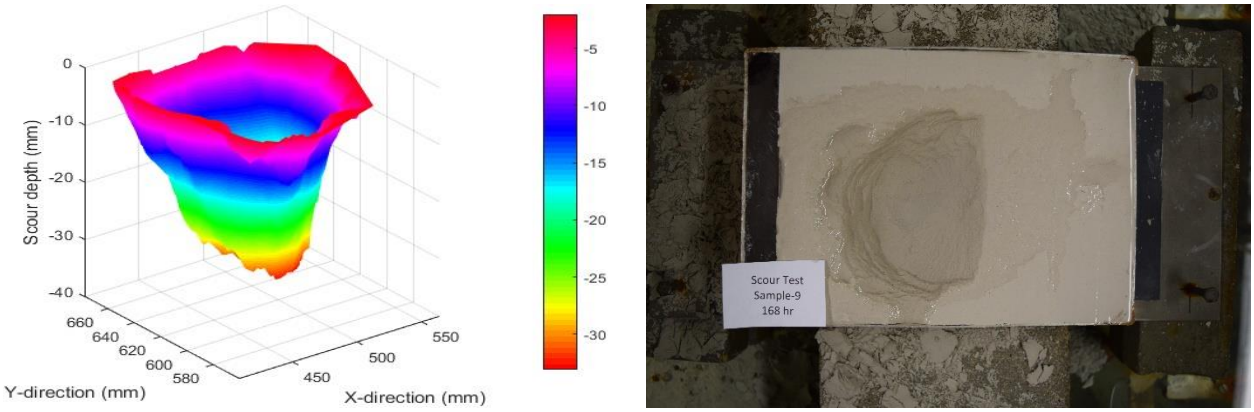

(t)

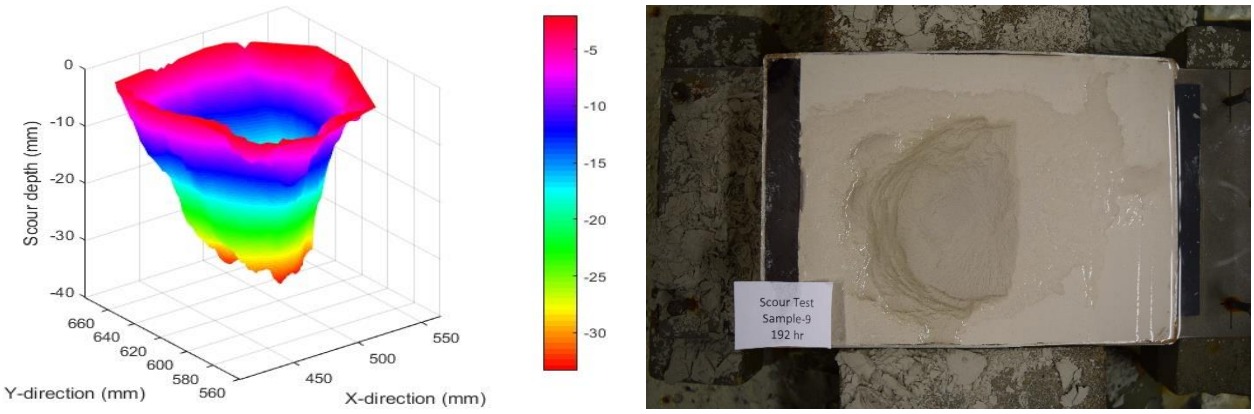

(u)

Figure B-7: cont'd.

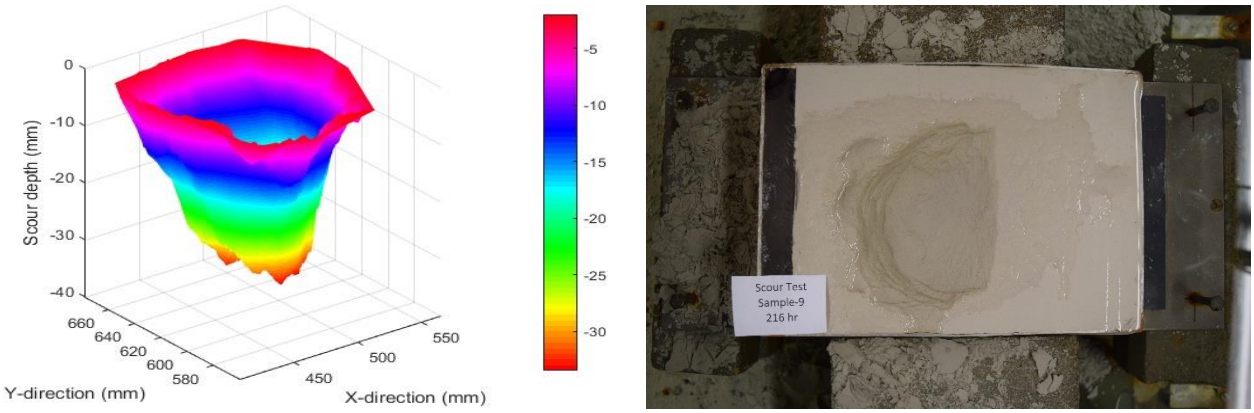

(v)

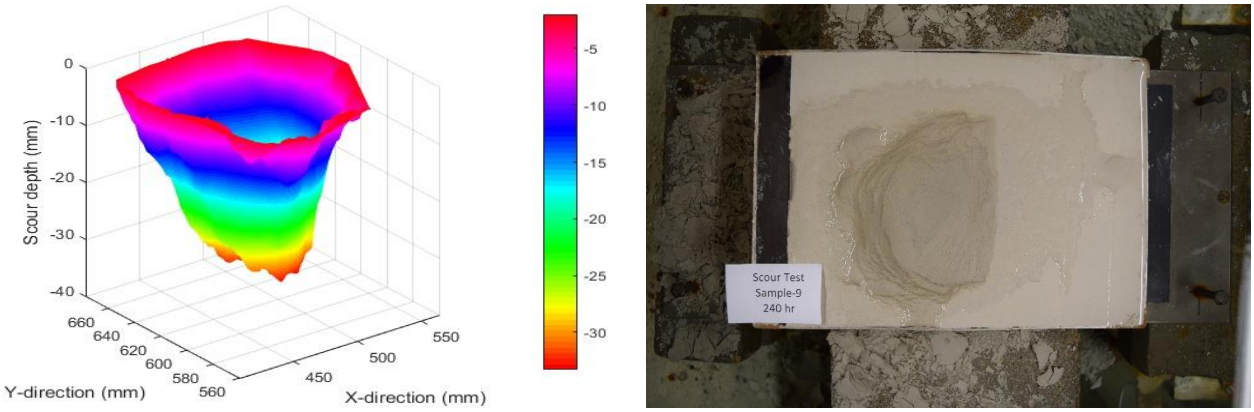

(w)

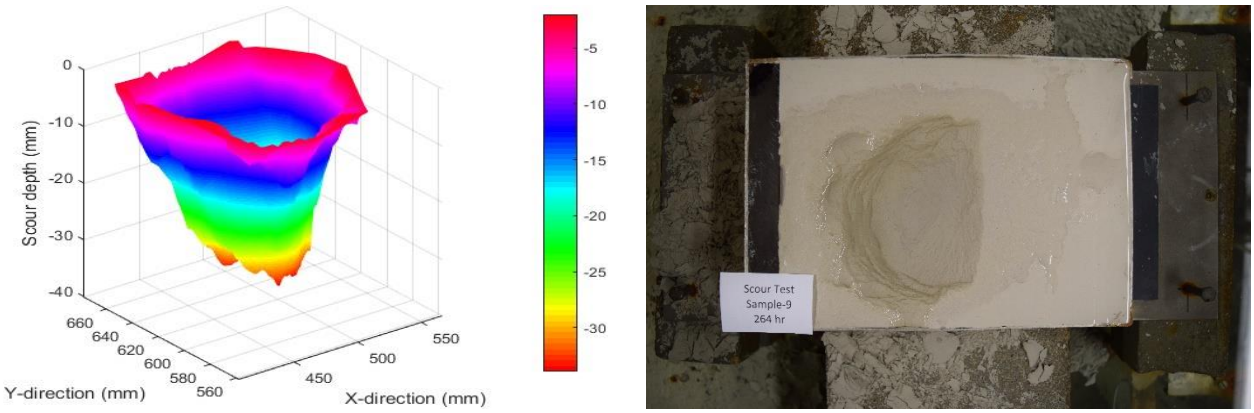

(x)

Figure B-7: cont'd.

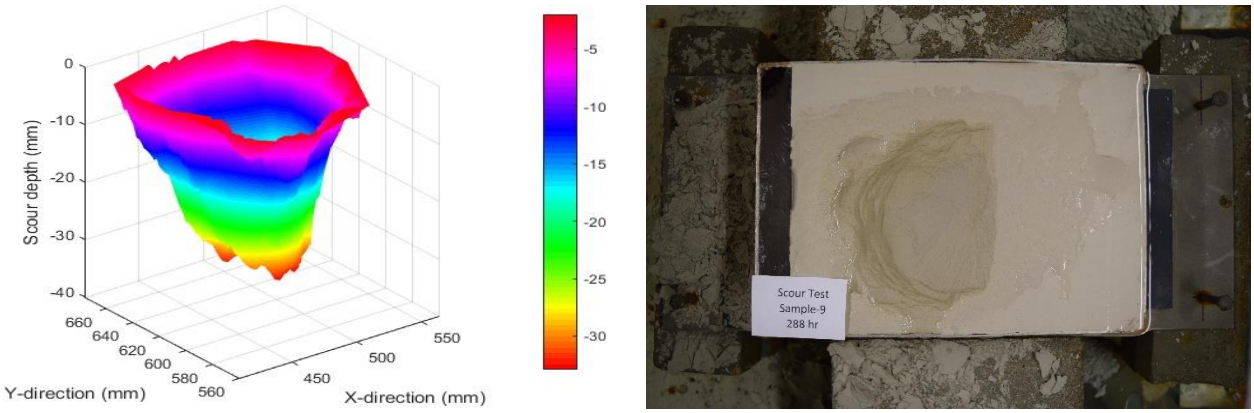

(y)

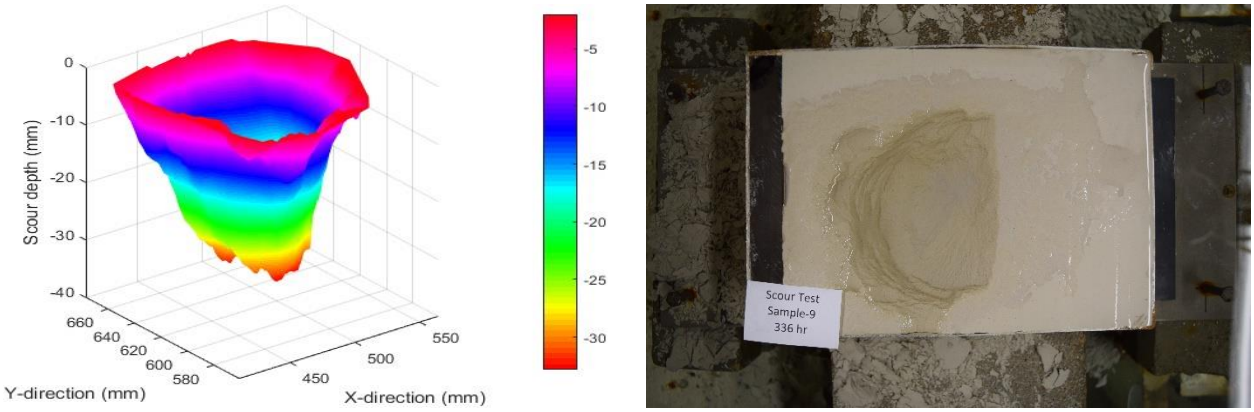

(z)

Figure B-7: cont'd.

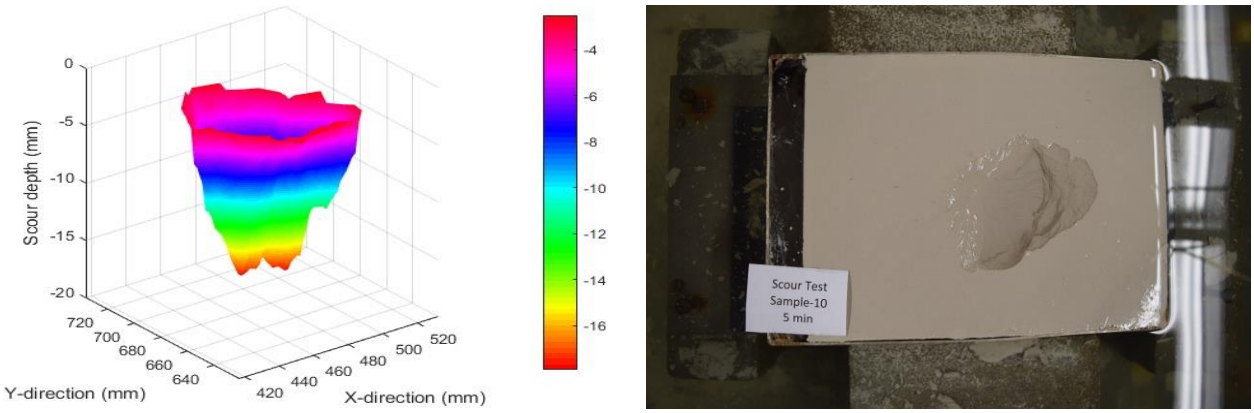

(a)

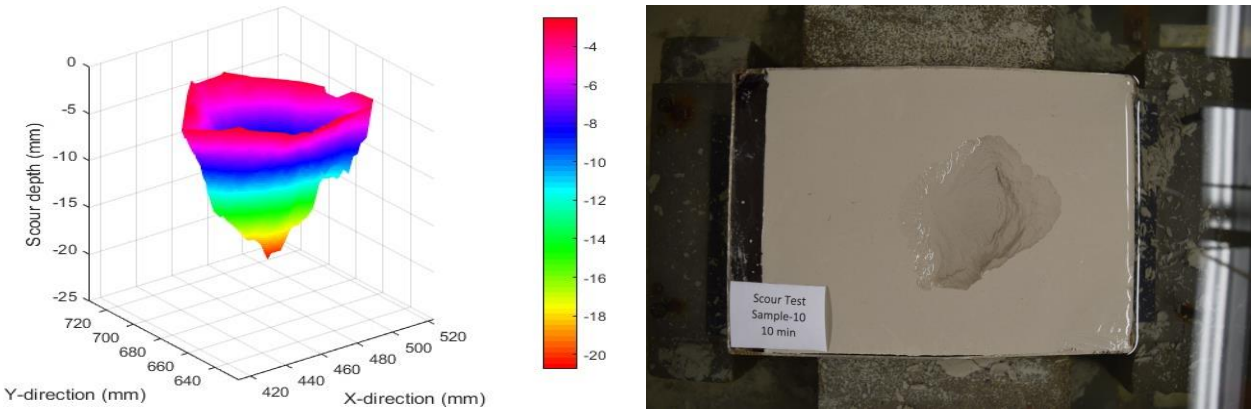

(b)

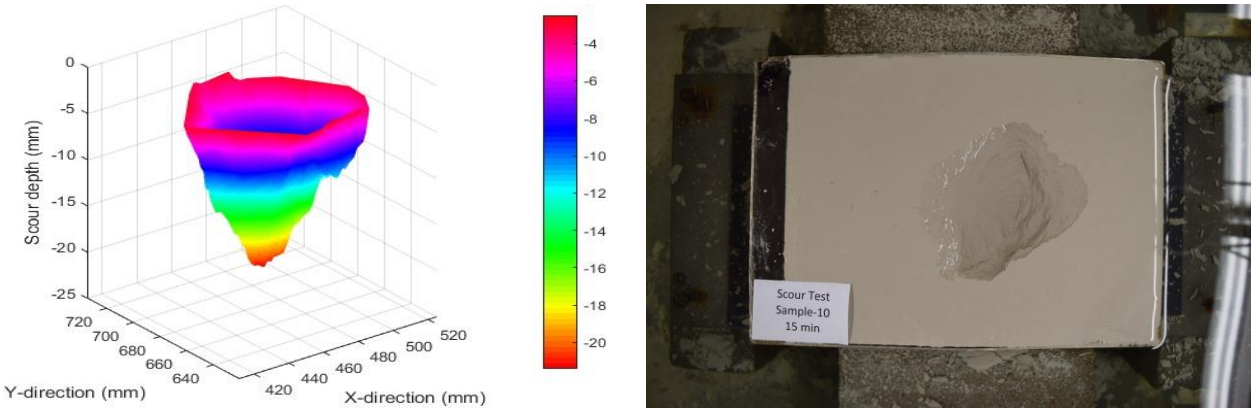

(c)

Figure B-8: Three-dimensional scour hole shape and photo of the sample in plan view for Scour Test 10 (M370 clay, U_0=6.5 m/s, d=7.76 mm, H=85 mm, and t_d=384 h) after a test duration of (a) 5 min, (b) 10 min, (c) 15 min, (d) 20 min, (e) 30 min, (f) 40 min, (g) 50 min, (h) 1 h, (i) 2 h, (j) 4 h, (k) 8 h, (l) 16 h, (m) 24 h, (n) 48 h, (o) 72 h, (p) 96 h, (q) 120 h, (r) 144 h, (s) 168 h, (t) 192 h, (u) 216 h, (v) 240 h, (w) 264 h, (x) 288 h, (y) 312 h, (z) 336 h, (aa) 360 h, and (ab) 384 h.

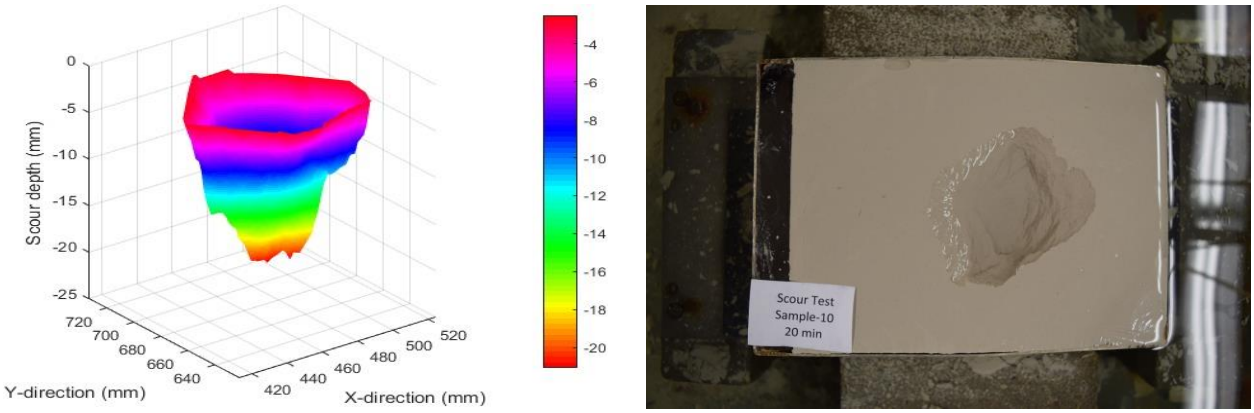

(d)

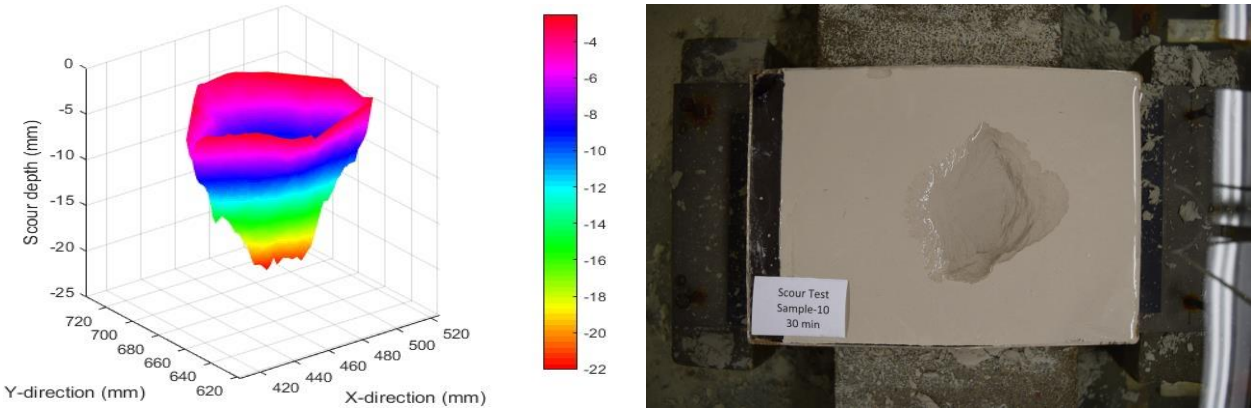

(e)

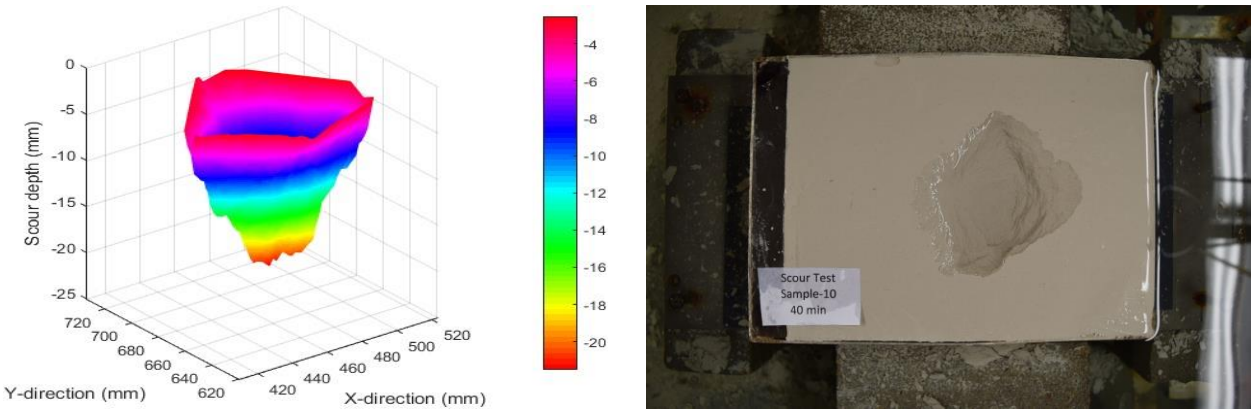

(f)

Figure B-8. cont'd.

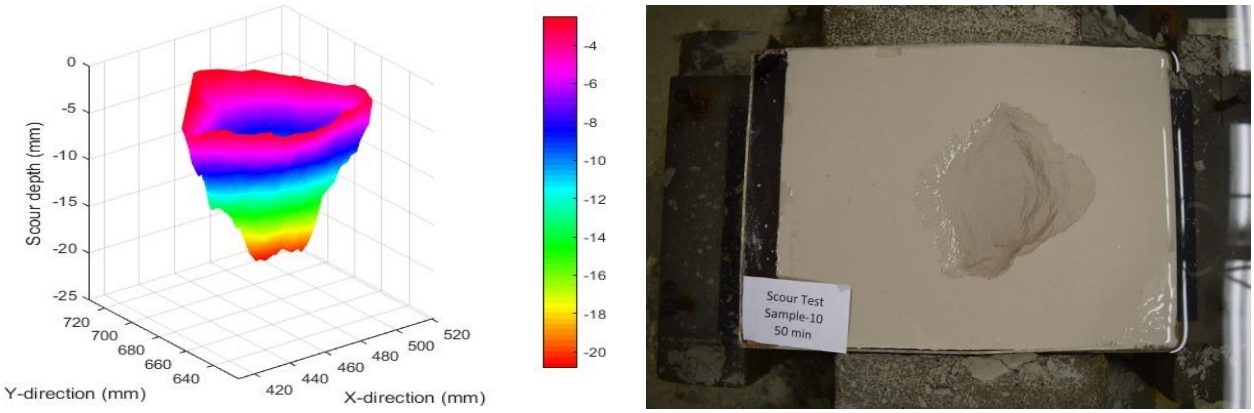

(g)

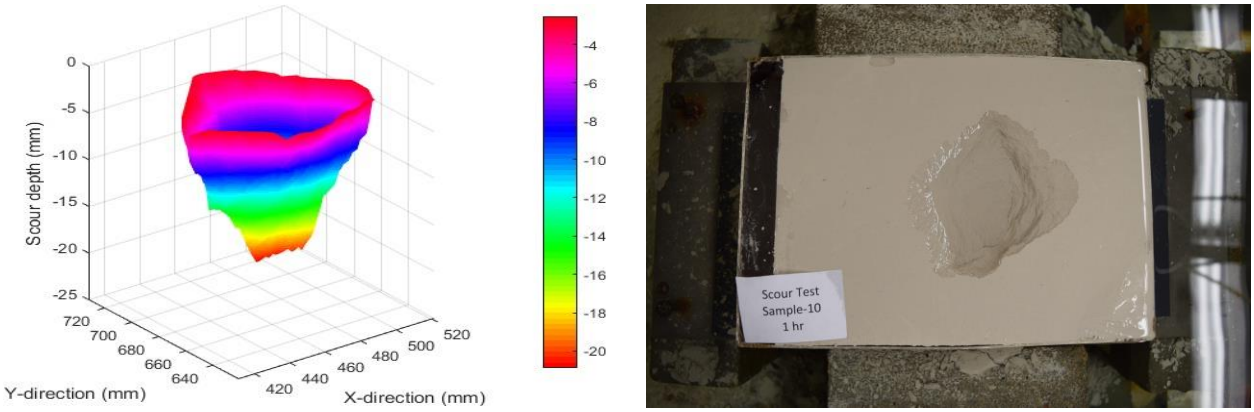

(h)

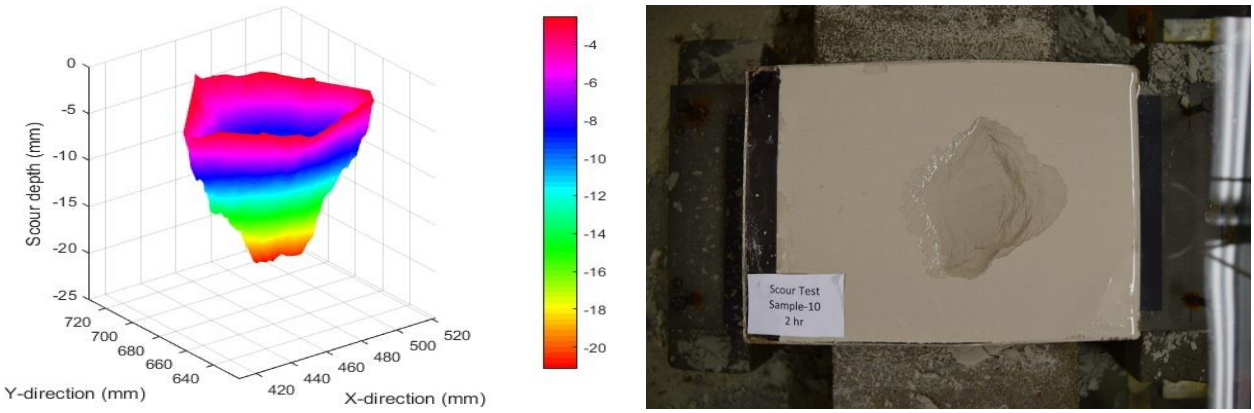

(i)

Figure B-8. cont'd.

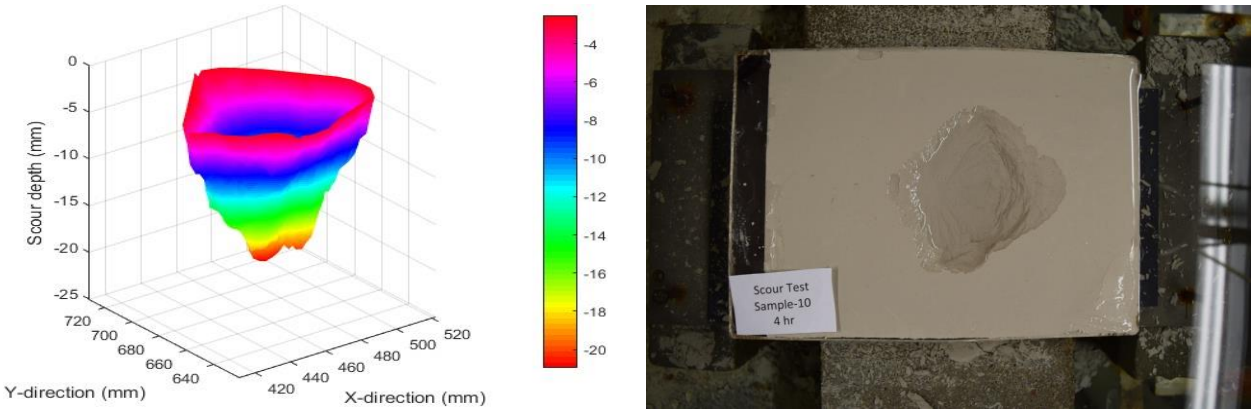

(j)

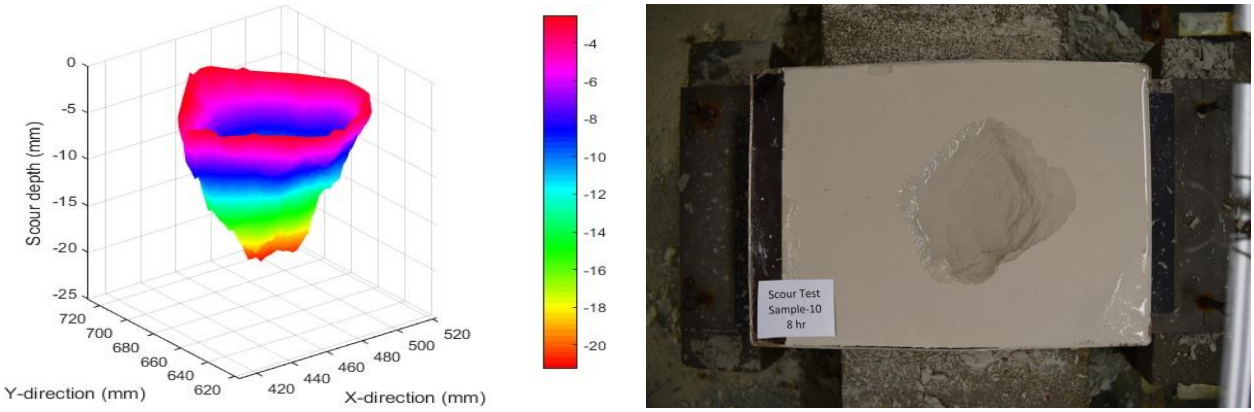

(k)

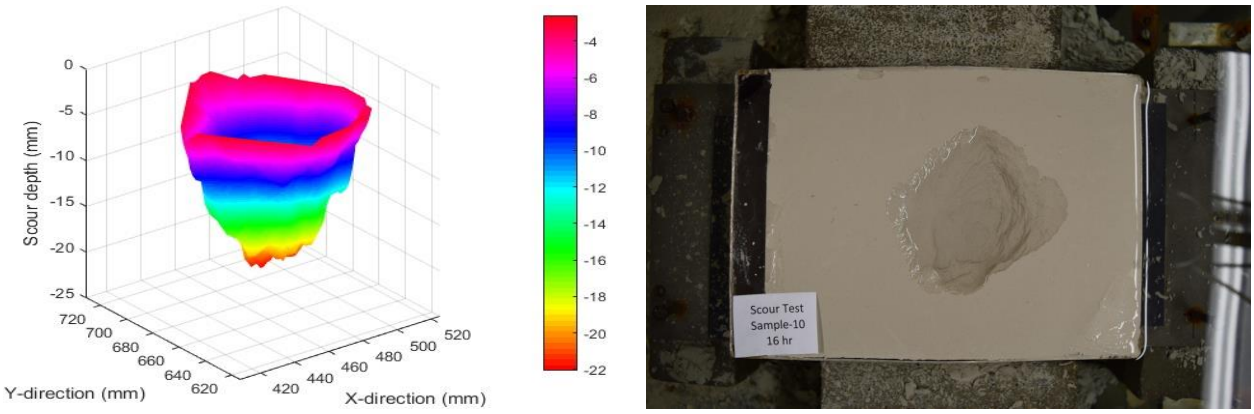

(l)

Figure B-8. cont'd.

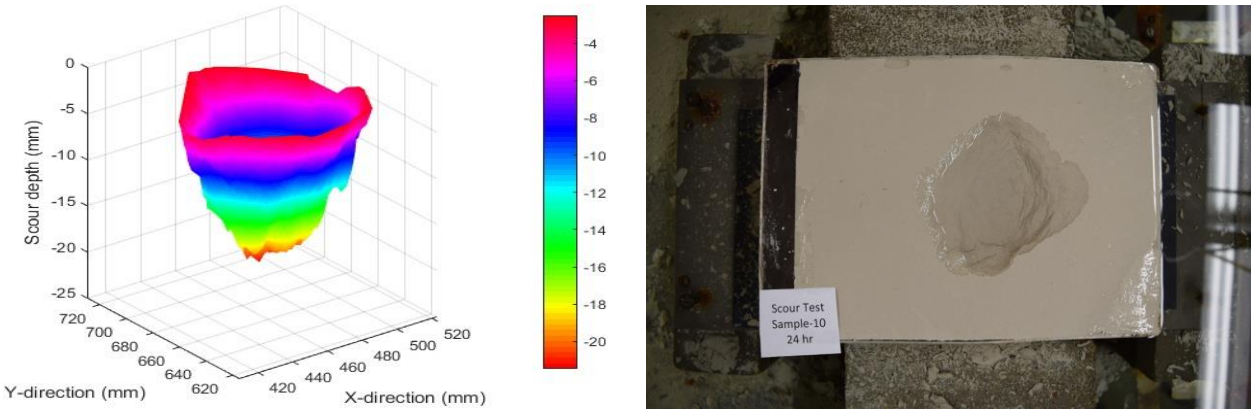

(m)

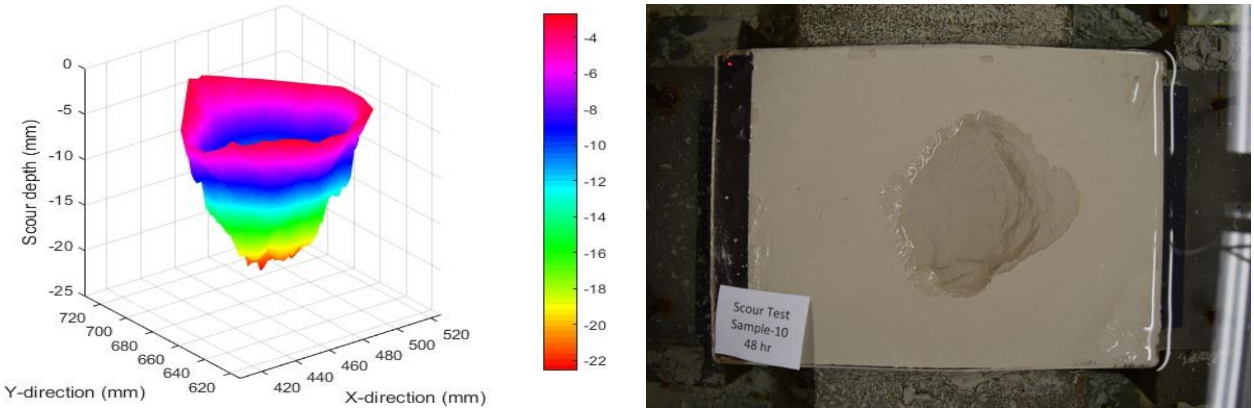

(n)

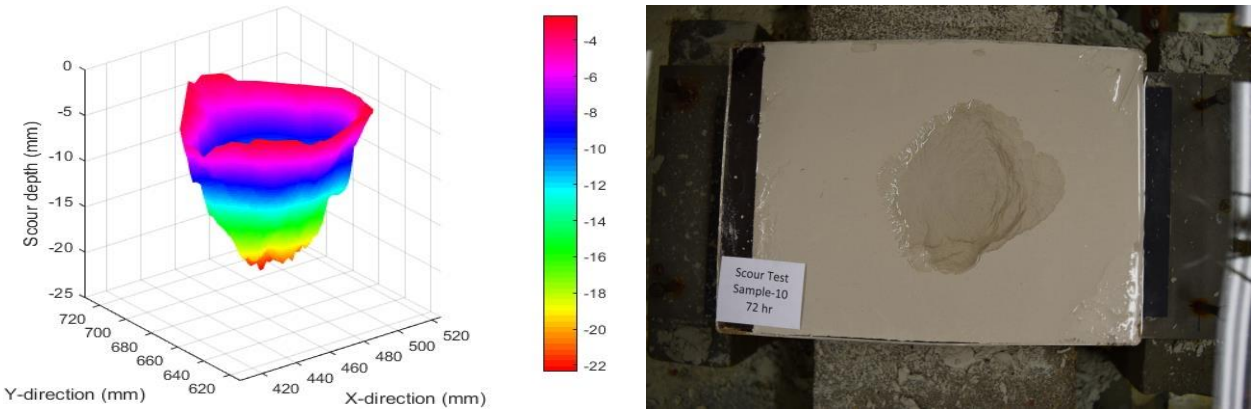

(o)

Figure B-8. cont'd.

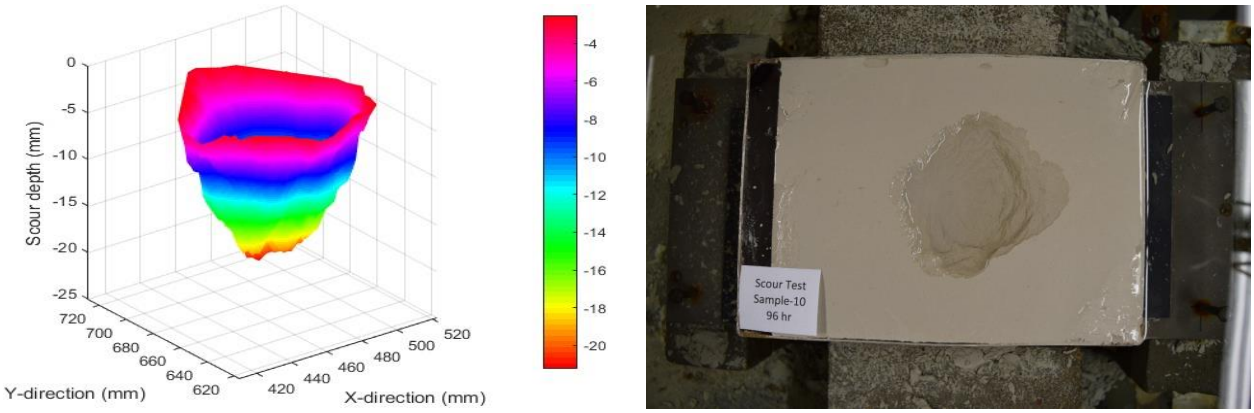

(p)

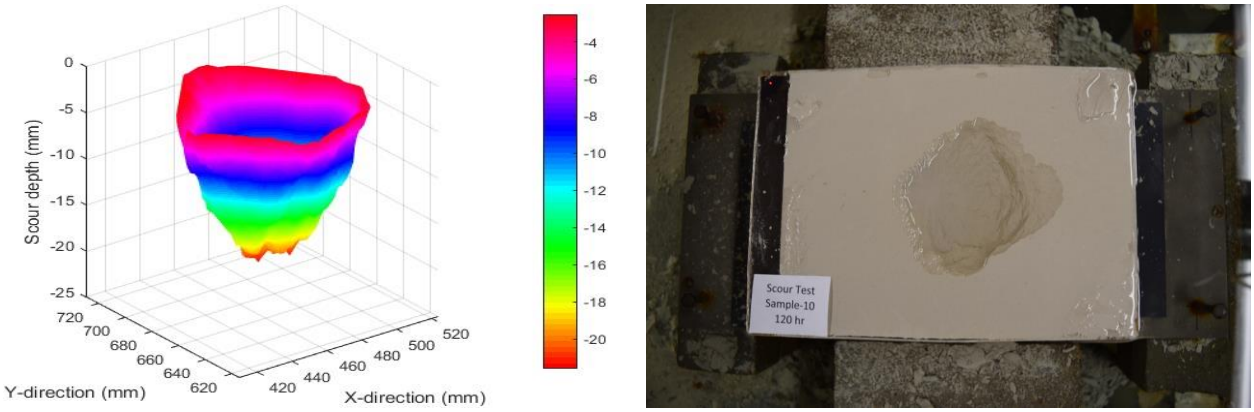

(q)

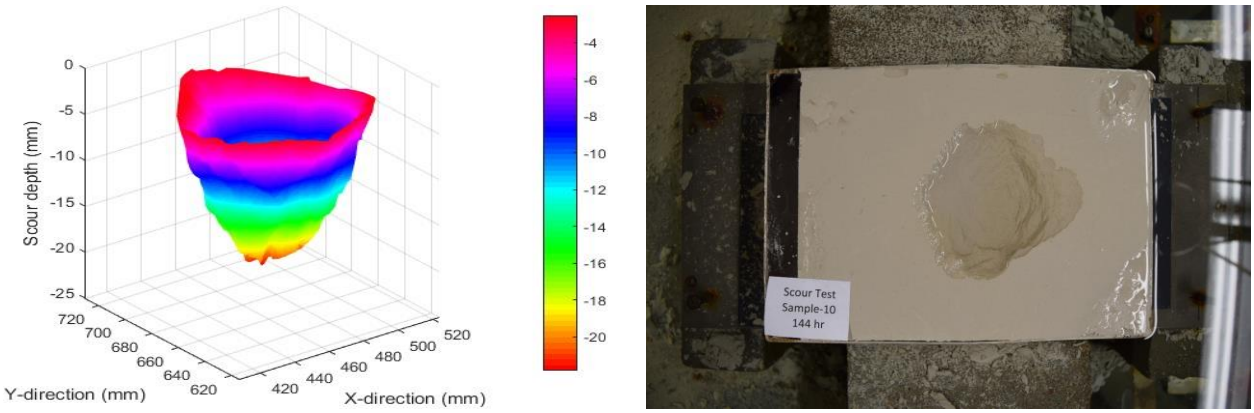

(r)

Figure B-8. cont'd.

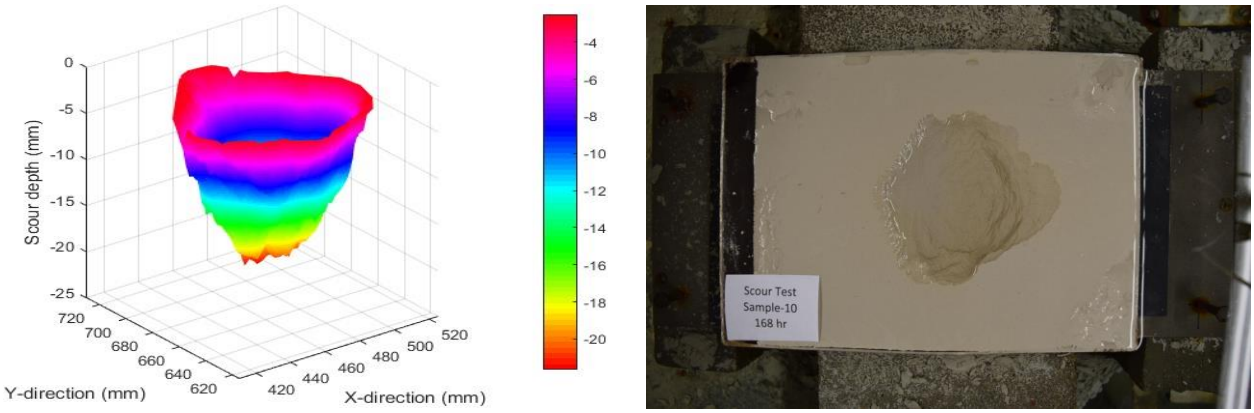

(s)

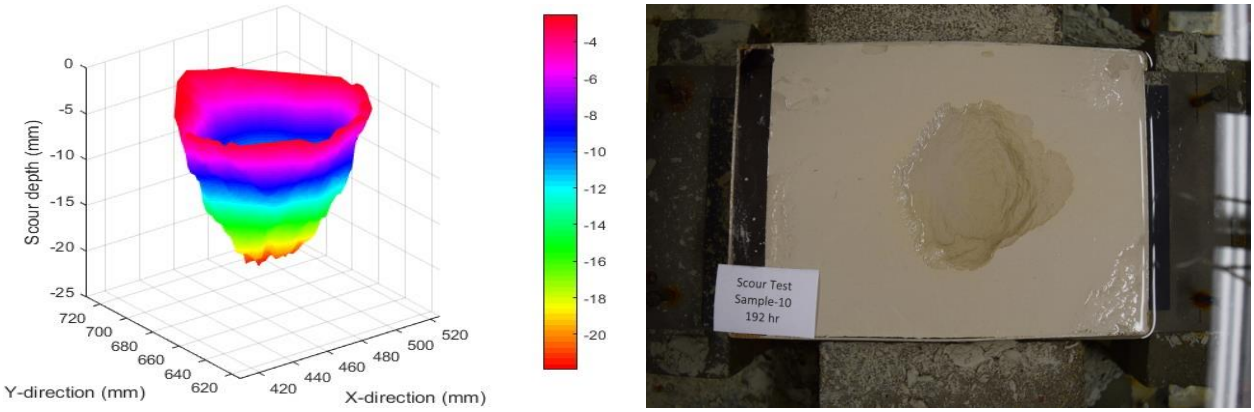

(t)

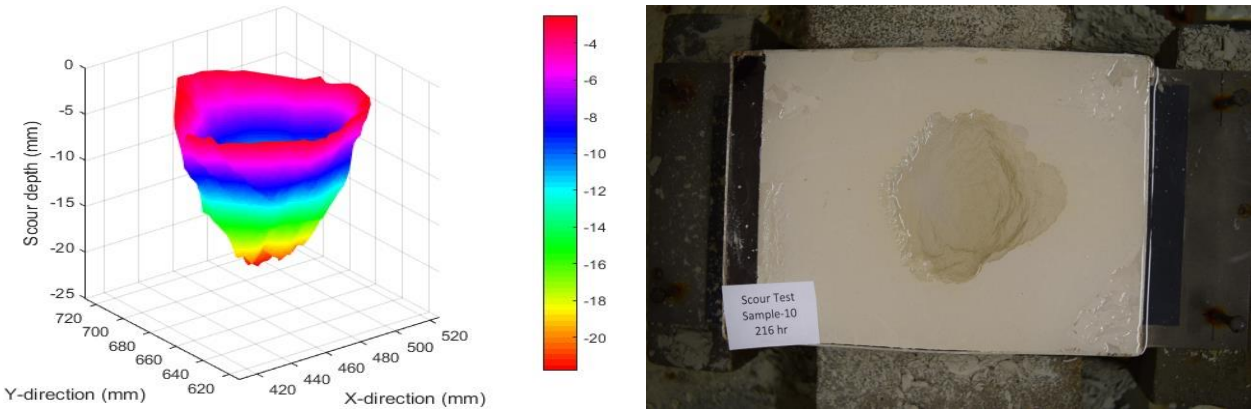

(u)

Figure B-8. cont'd.

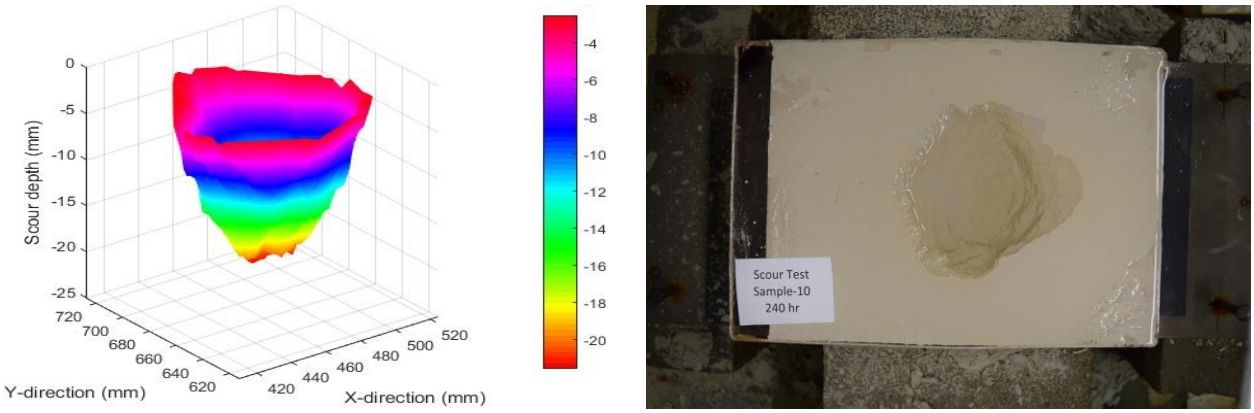

(v)

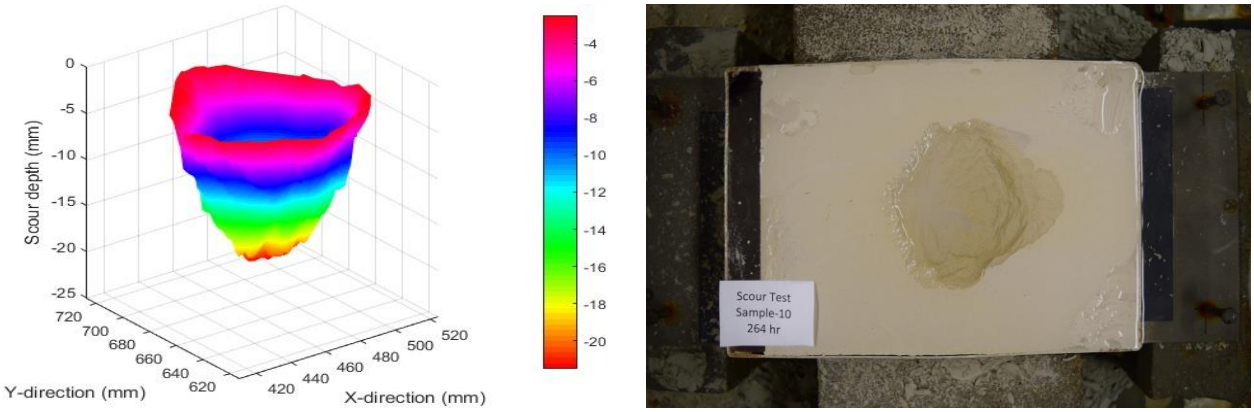

(w)

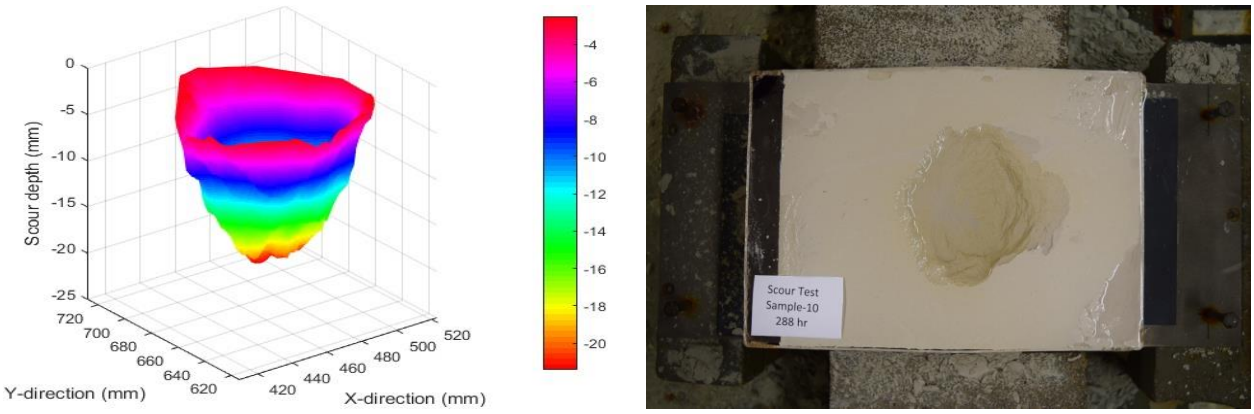

(x)

Figure B-8. cont'd.

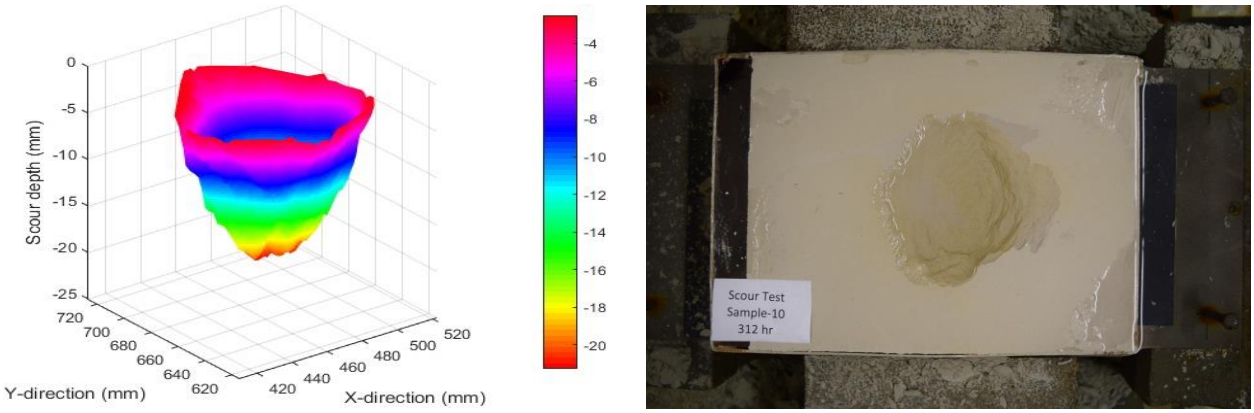

(y)

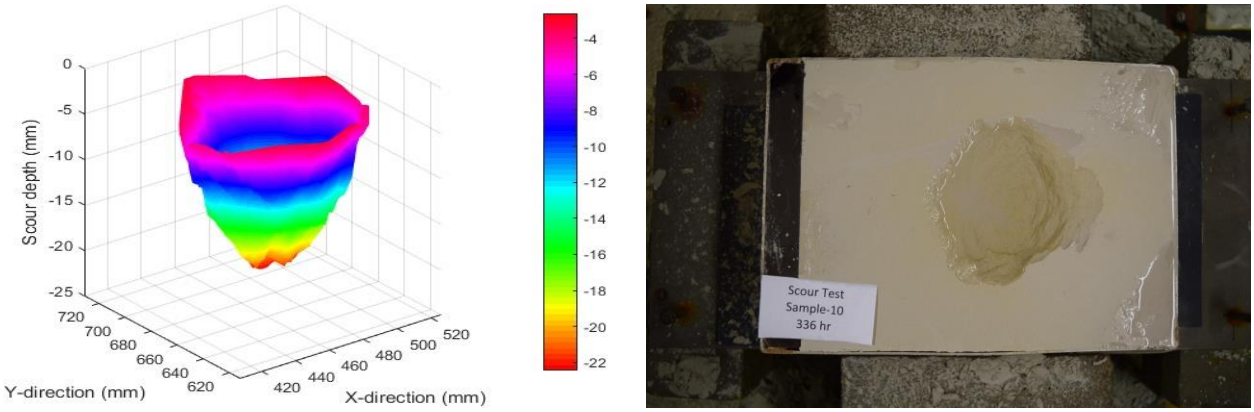

(z)

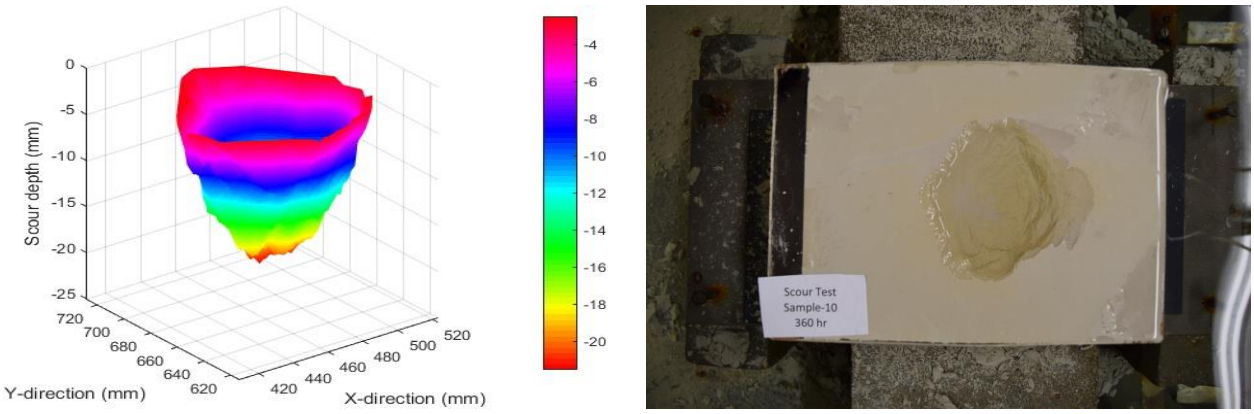

(aa)

Figure B-8. cont'd.

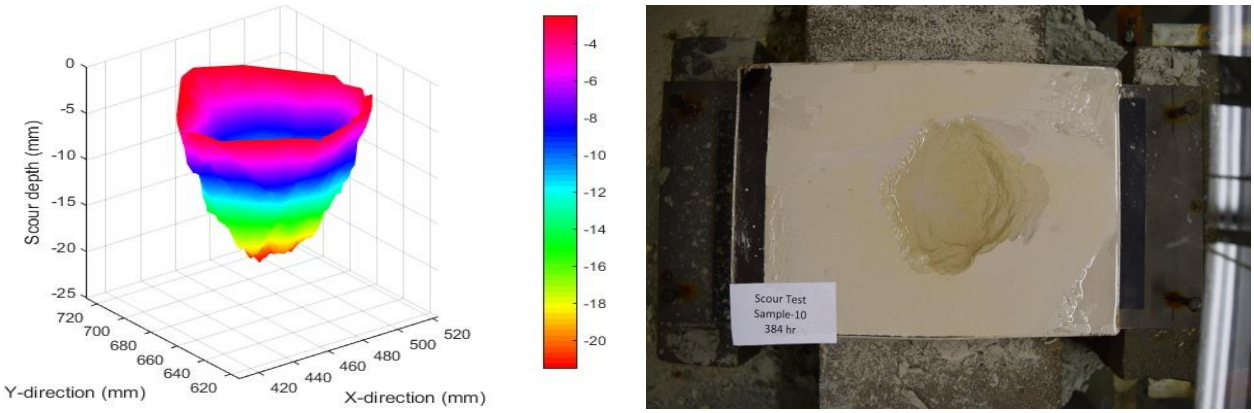

(ab)

Figure B-8. cont'd.

APPENDIX C: Scour Hole Profiles with Time for Different Cross-sections

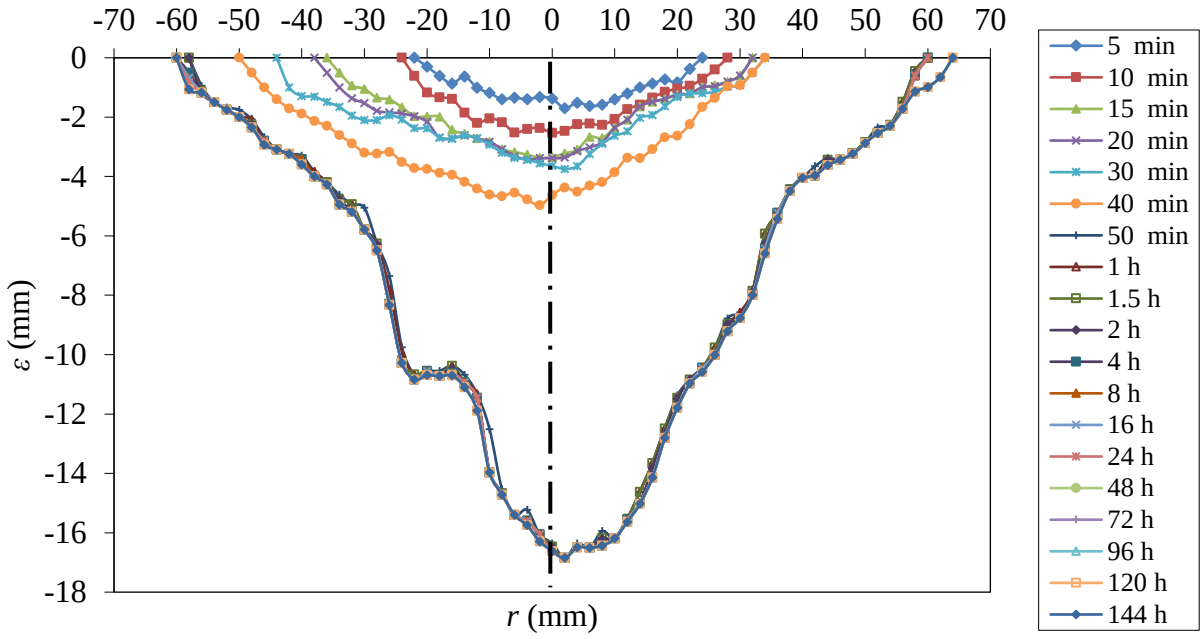

(a)

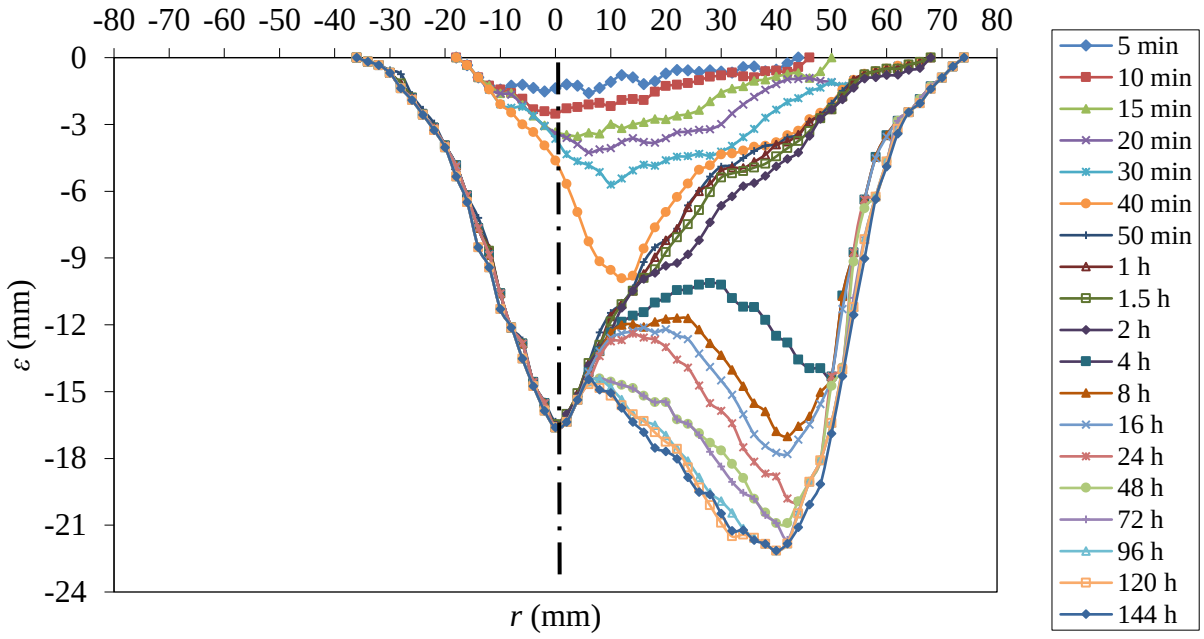

(b)

Figure C-1: Scour hole profiles with time for Scour Test 1 for four different sections (a) Section 1, (b) Section 2, (c) Section 3, and (d) Section 4.

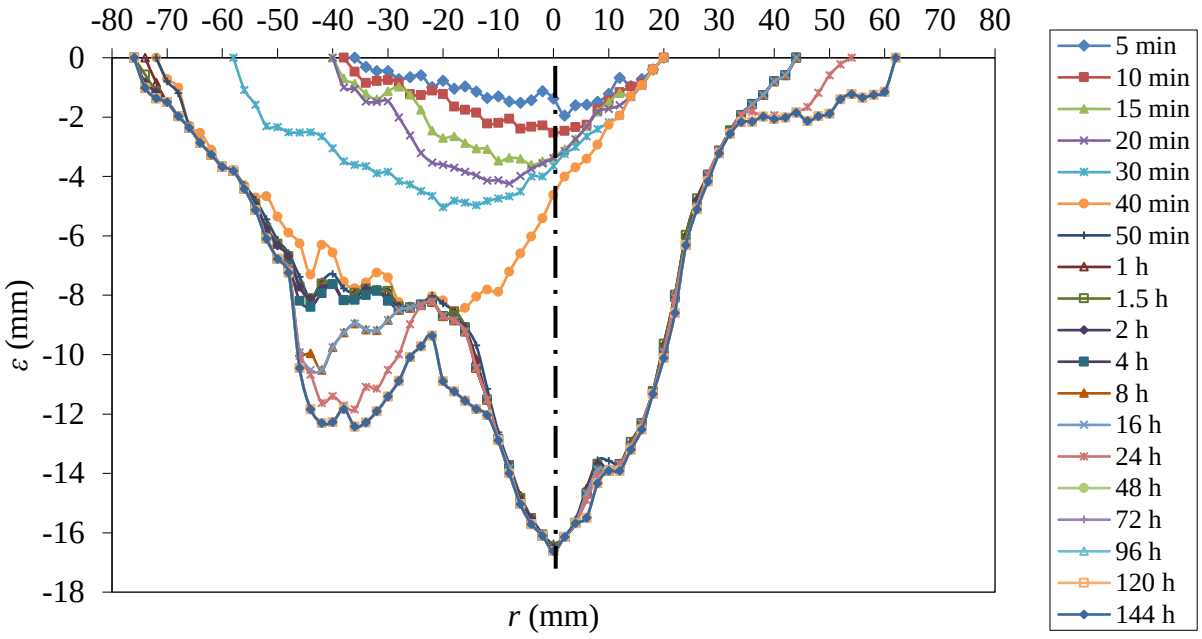

(c)

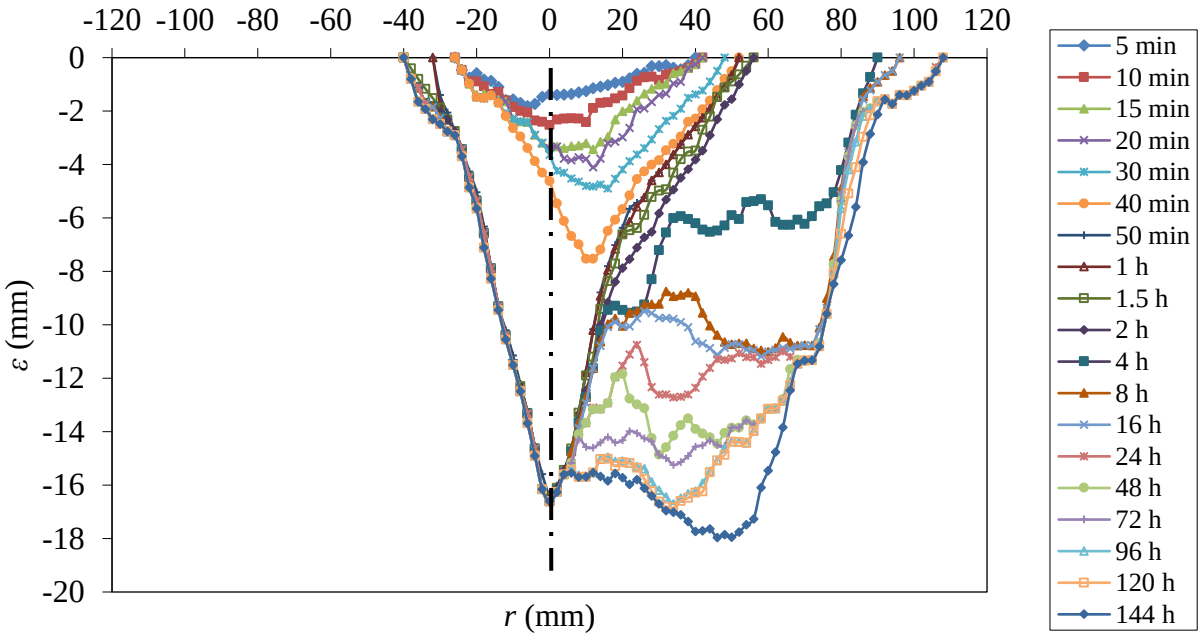

(d)

Figure C-1: cont'd.

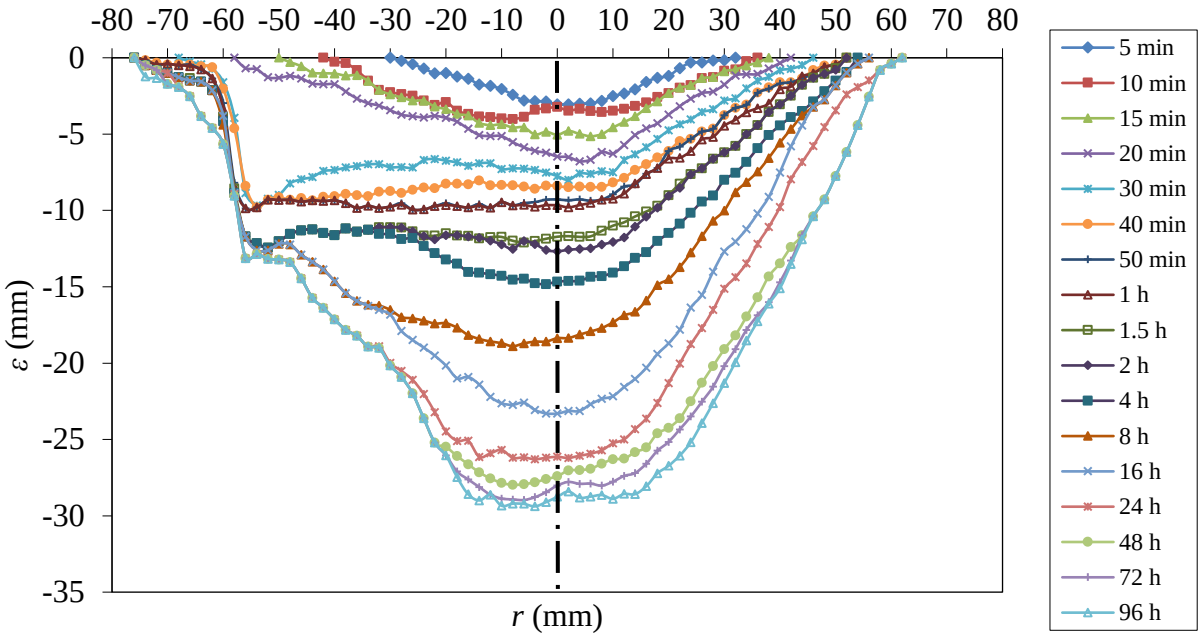

(a)

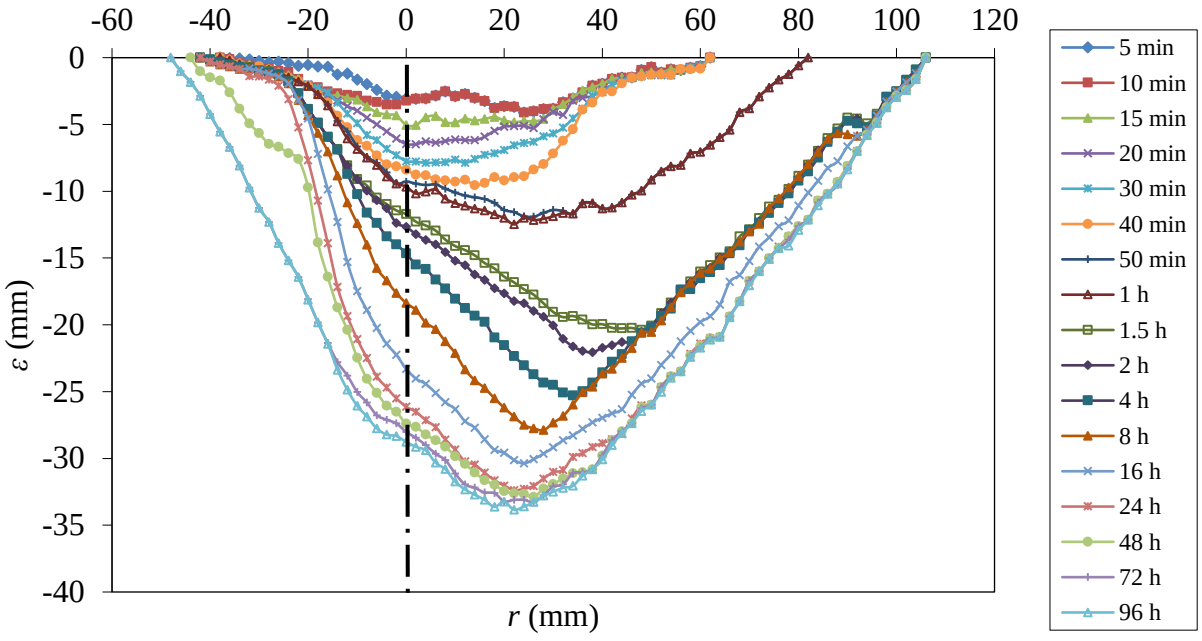

(b)

Figure C-2: Scour hole profiles with time for Scour Test 3 for four different sections (a) Section 1, (b) Section 2, (c) Section 3, and (d) Section 4.

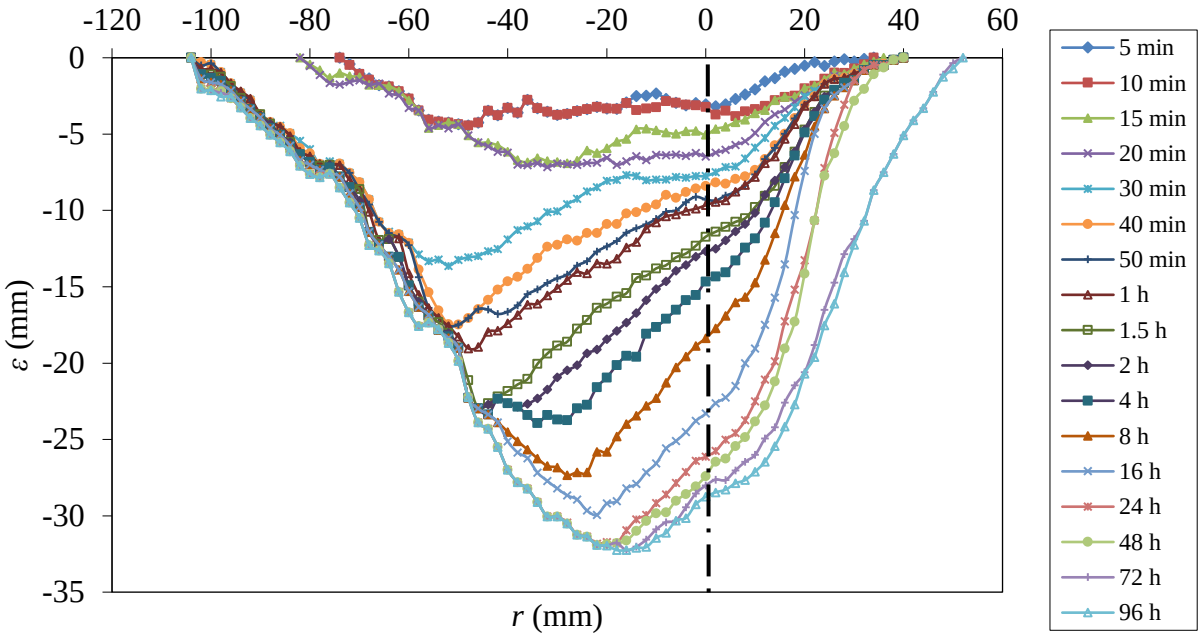

(c)

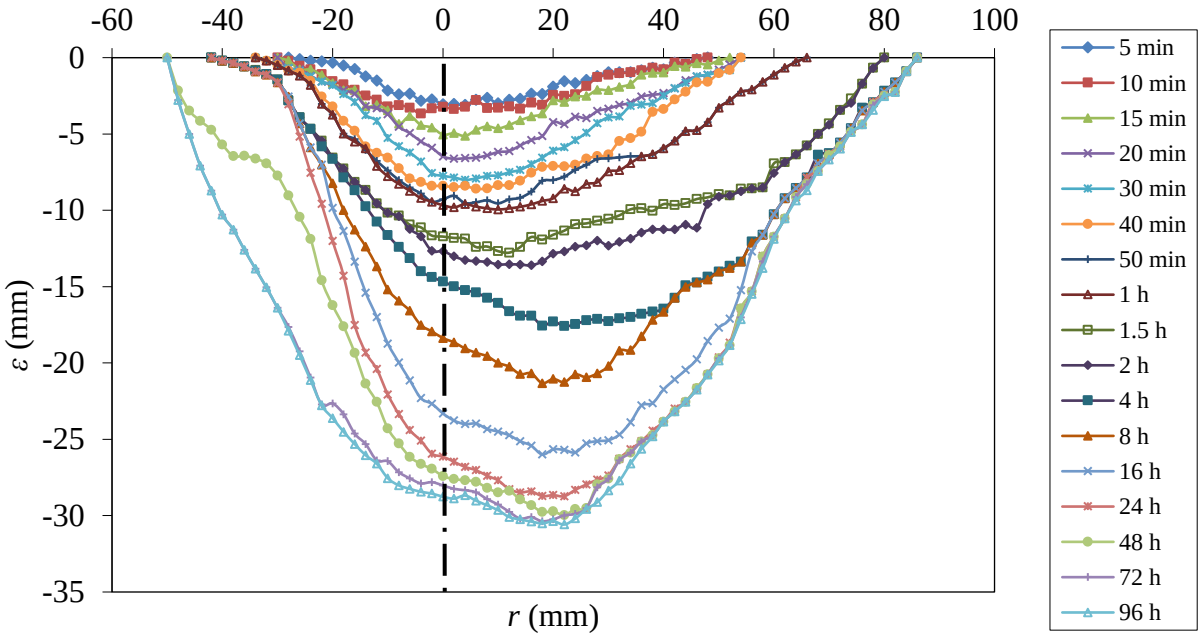

(d)

Figure C-2: cont'd.

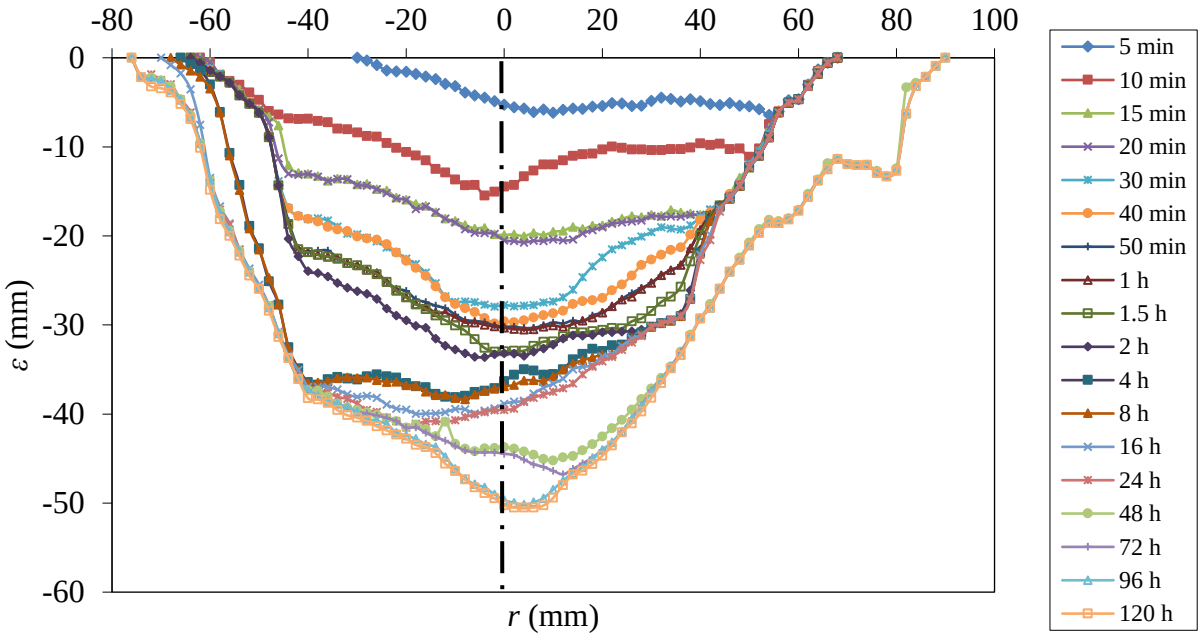

(a)

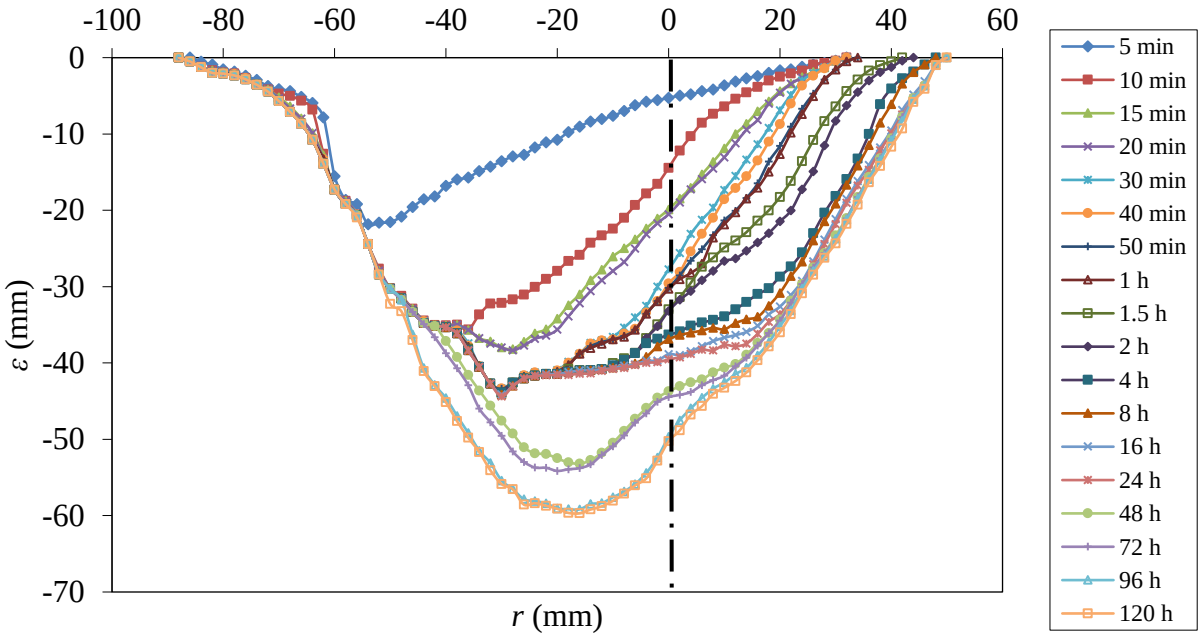

(b)

Figure C-3: Scour hole profiles with time for Scour Test 4 for four different sections (a) Section 1, (b) Section 2, (c) Section 3, and (d) Section 4.

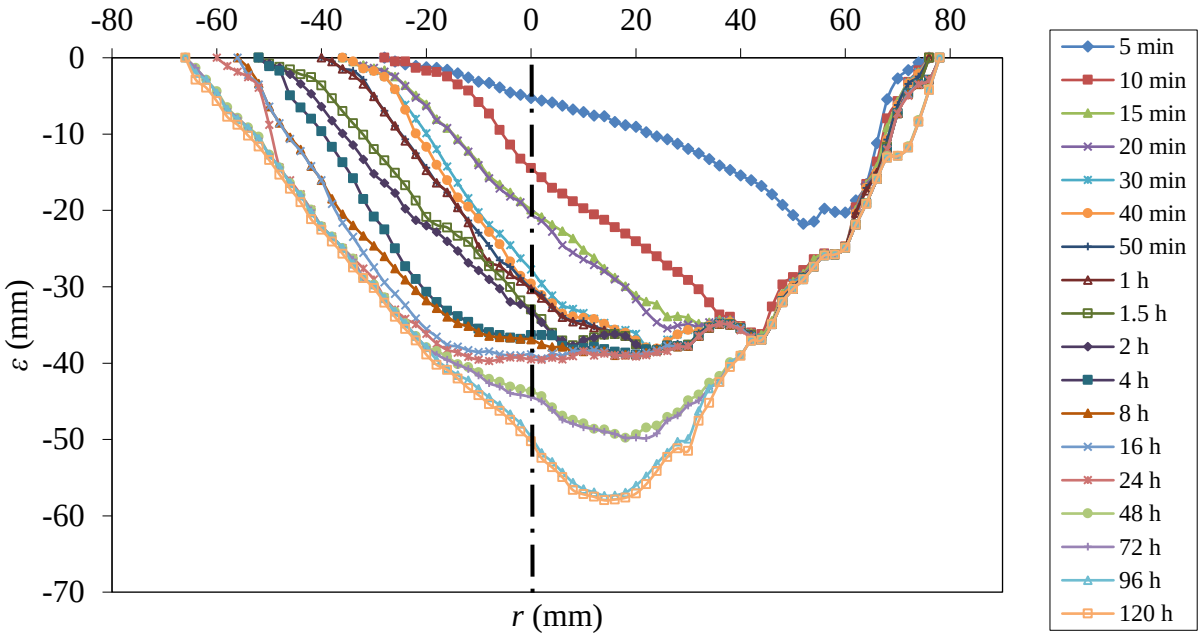

(c)

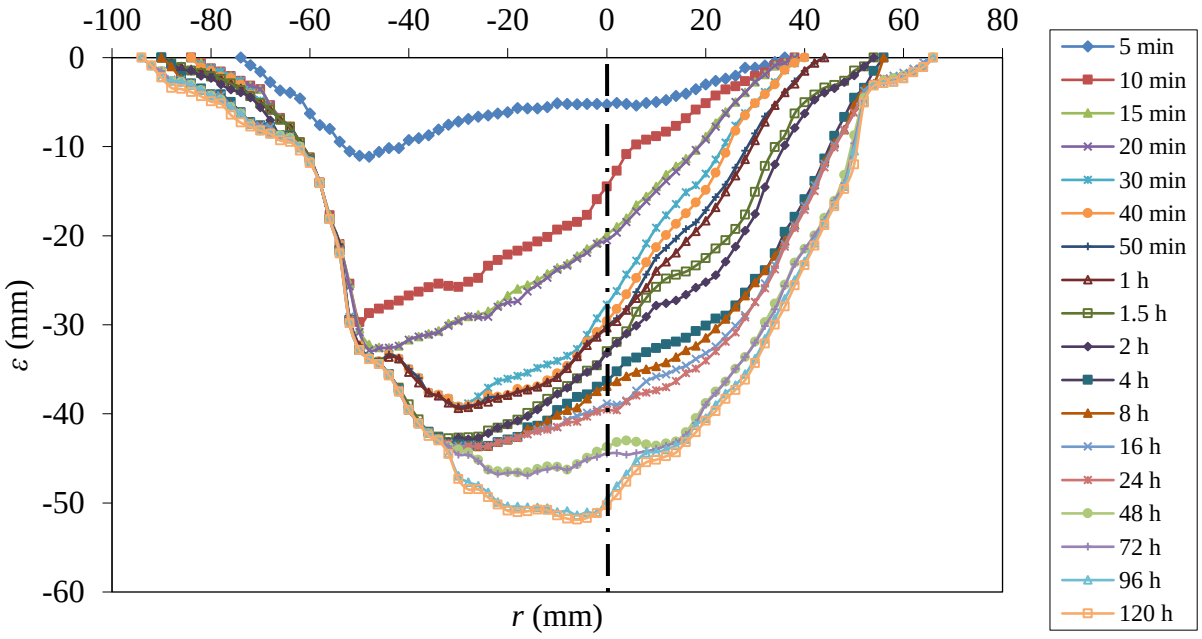

(d)

Figure C-3: cont'd.

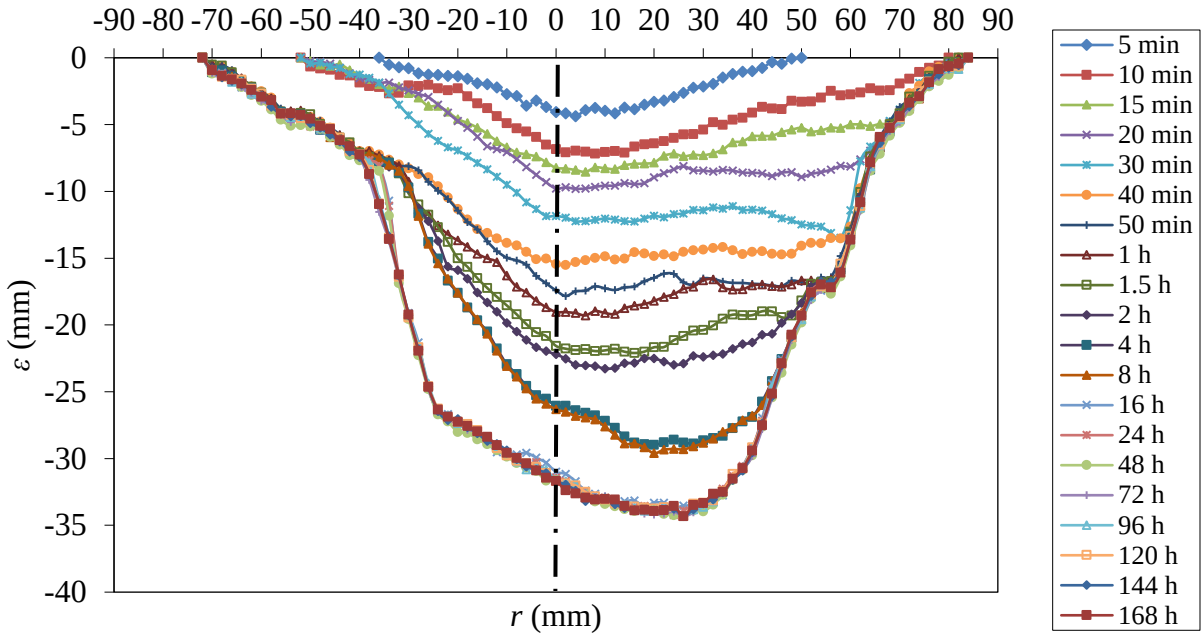

(a)

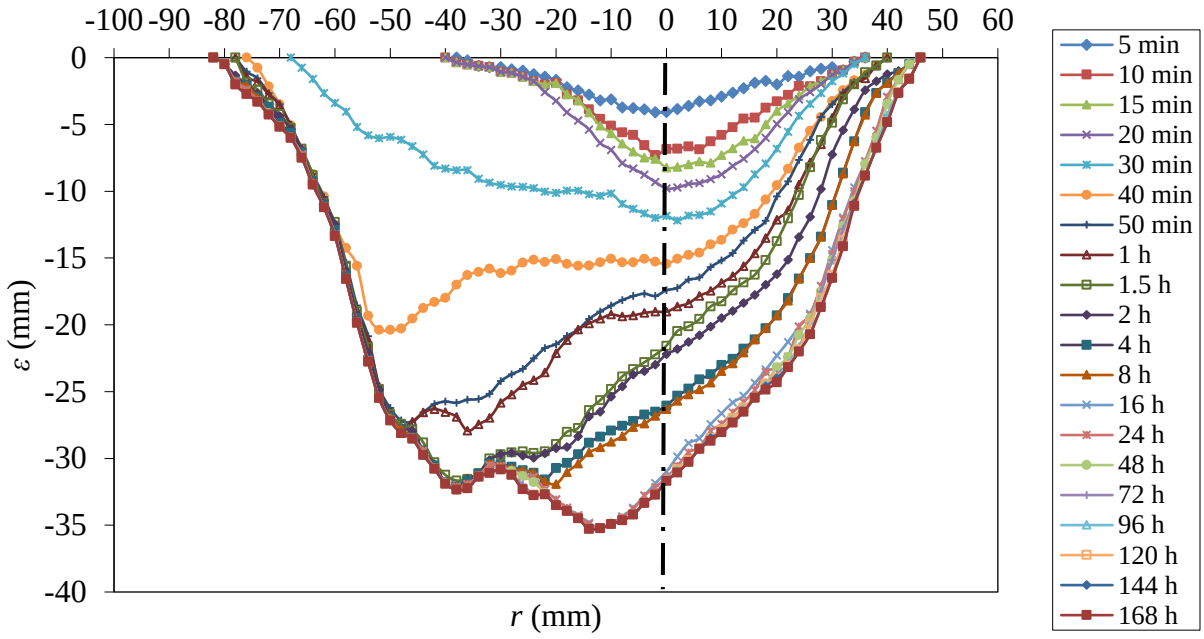

(b)

Figure C-4: Scour hole profiles with time for Scour Test 5 for four different sections (a) Section 1, (b) Section 2, (c) Section 3, and (d) Section 4.

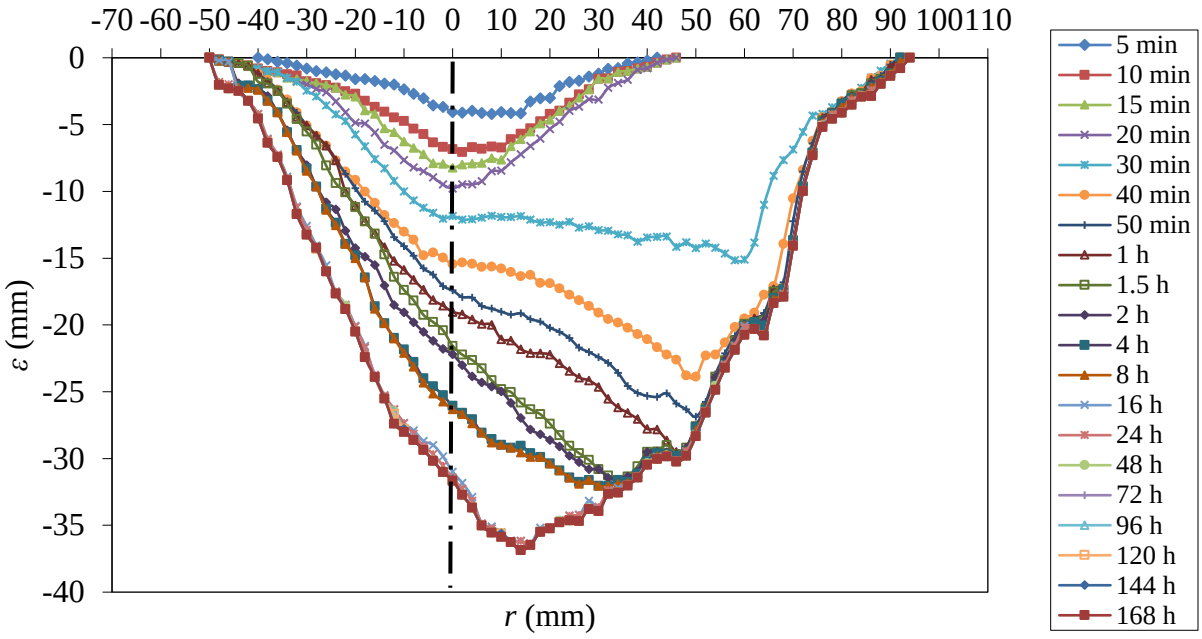

(c)

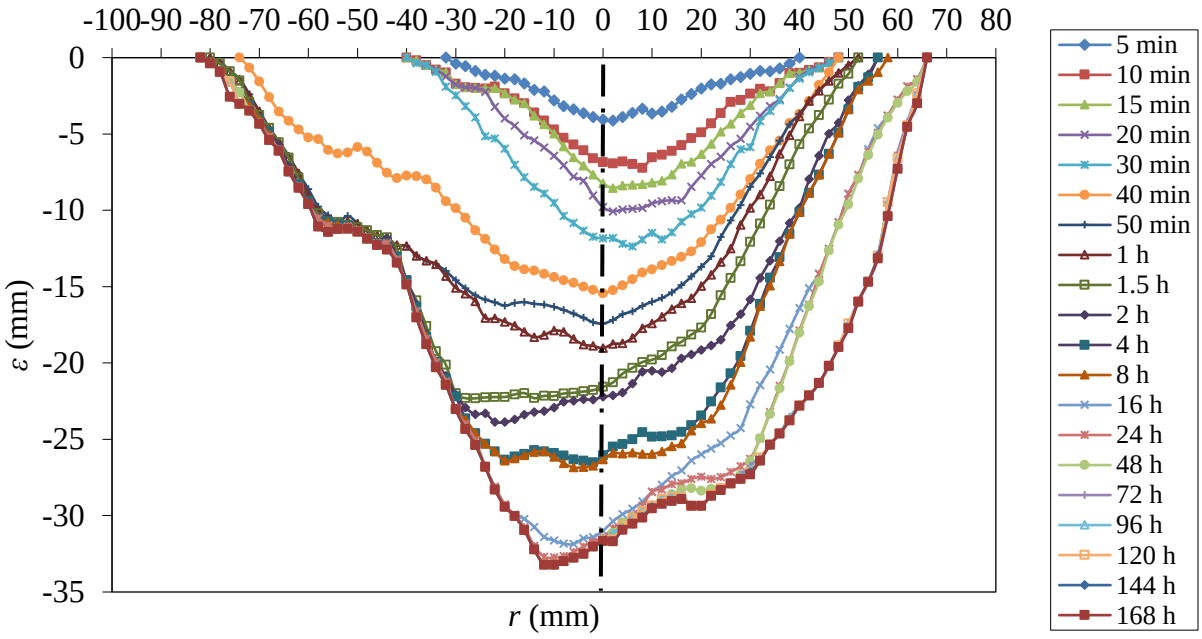

(d)

Figure C-4: cont'd.

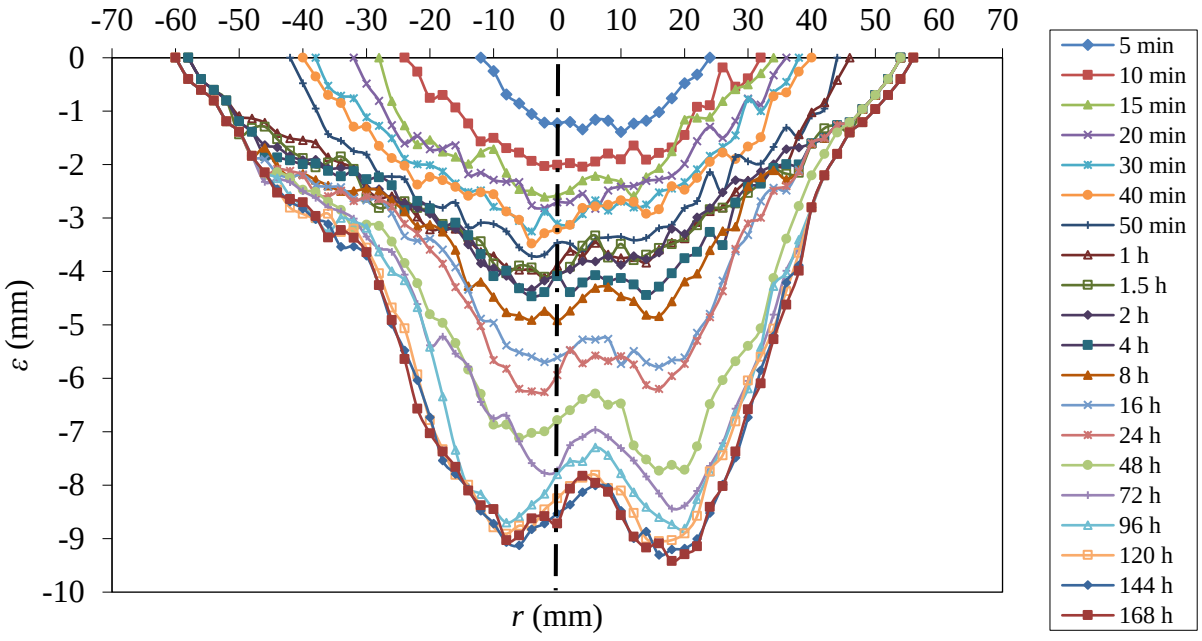

(a)

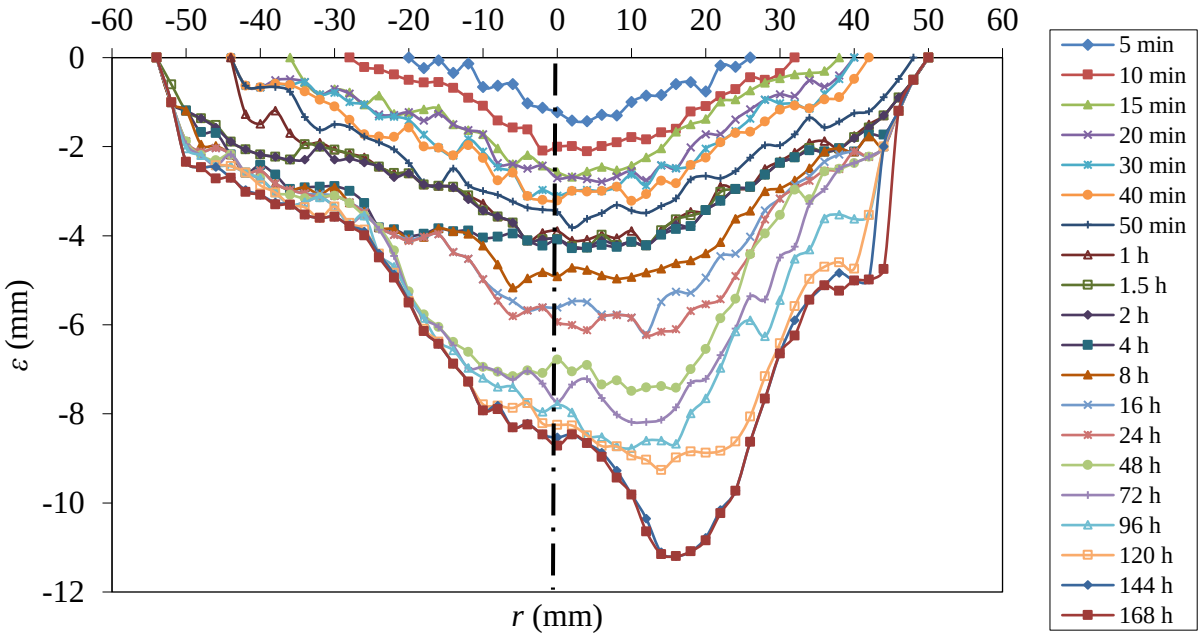

(b)

Figure C-5: Scour hole profiles with time for Scour Test 6 for four different sections (a) Section 1, (b) Section 2, (c) Section 3, and (d) Section 4.

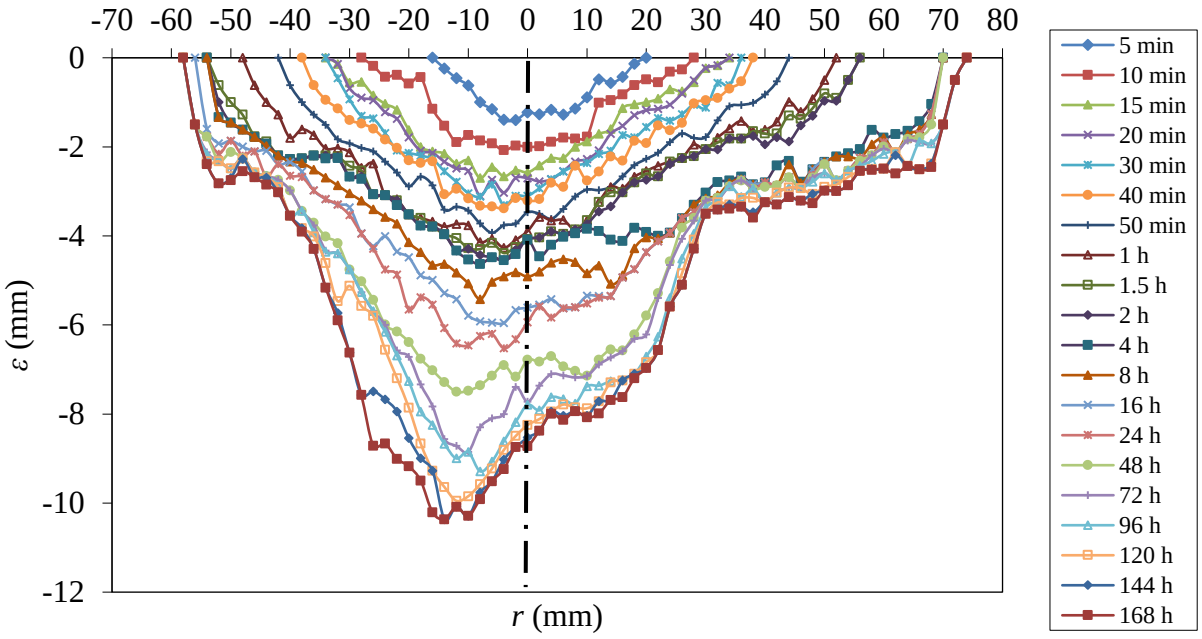

(c)

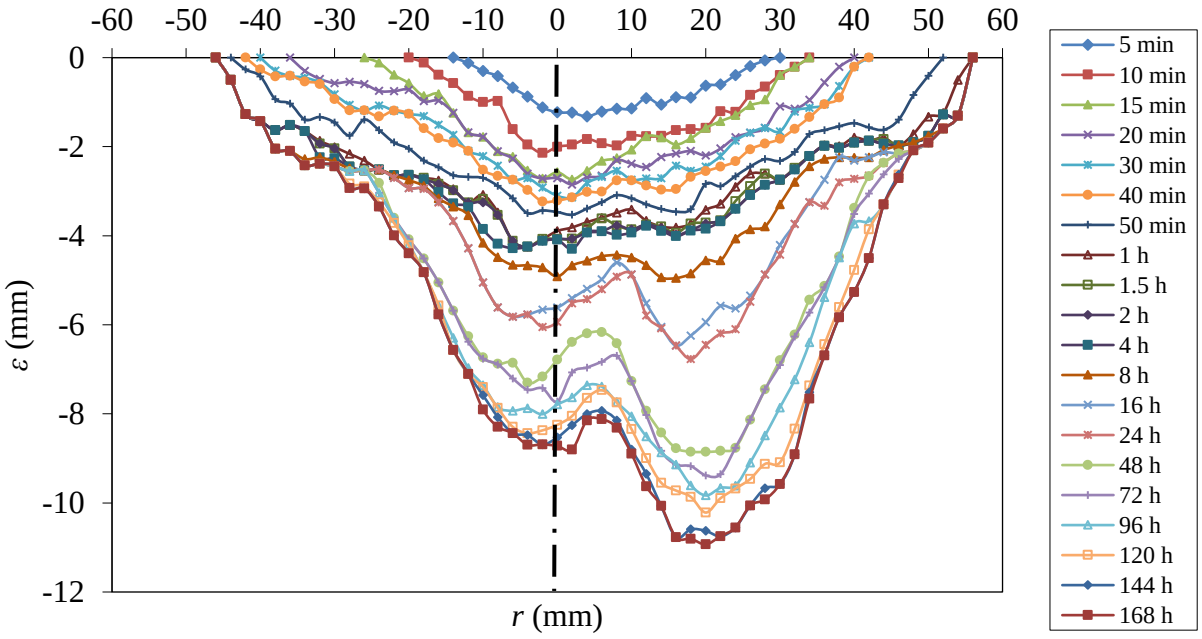

(d)

Figure C-5: cont'd.

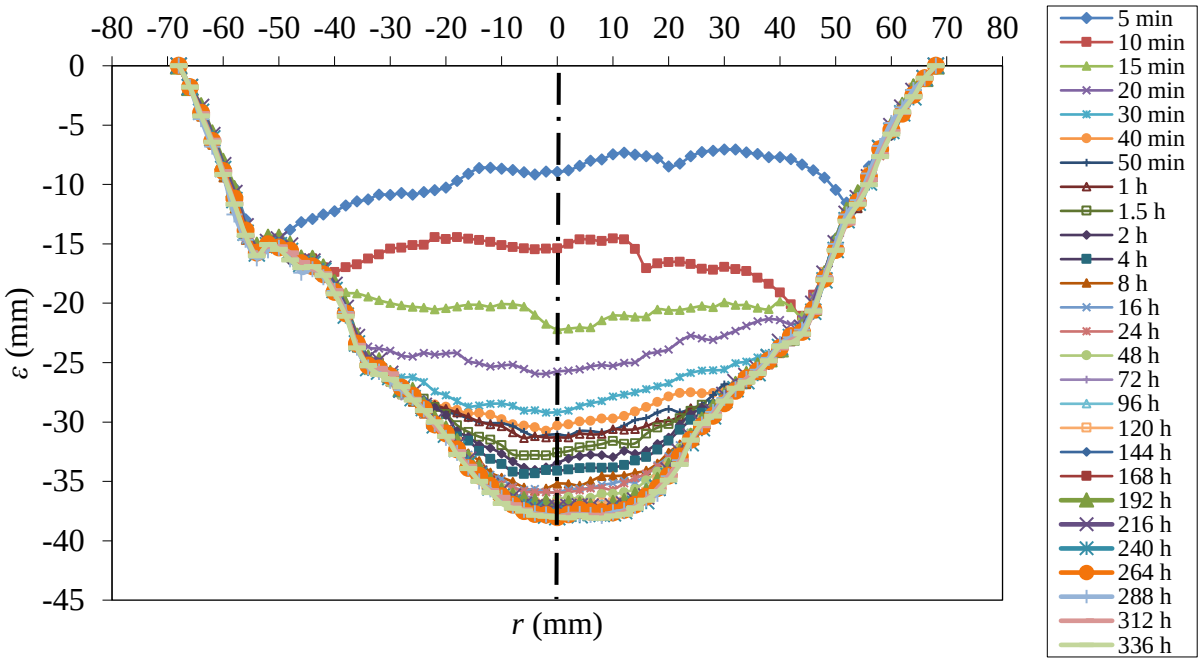

(a)

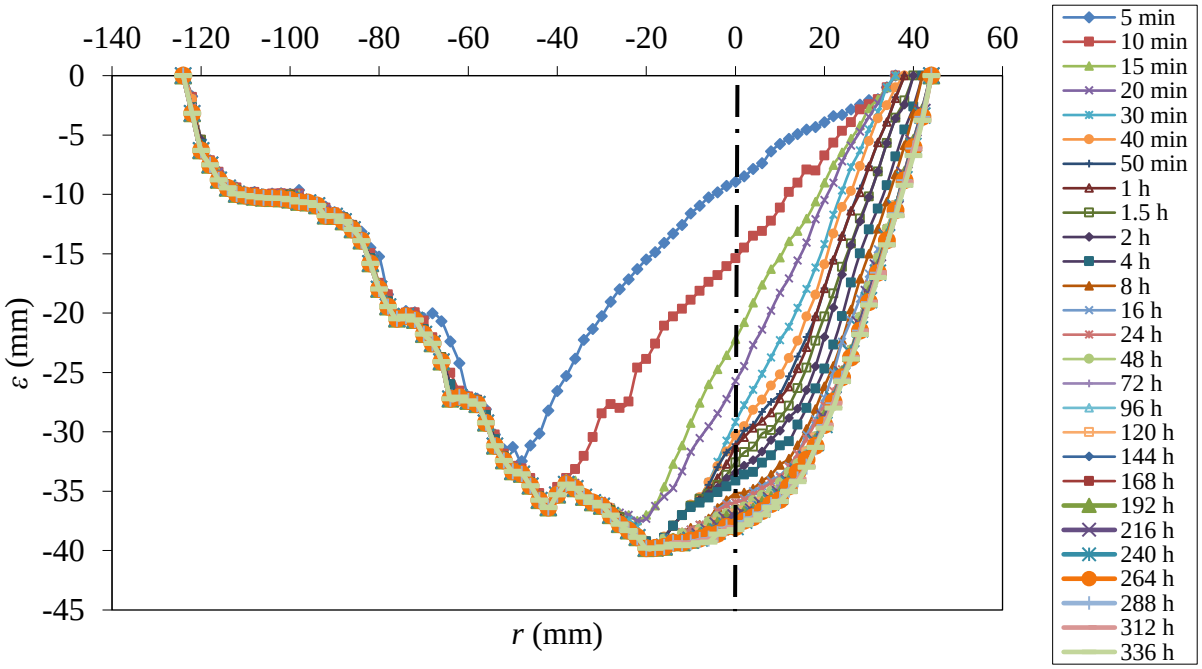

(b)

Figure C-6: Scour hole profiles with time for Scour Test 8 for four different sections (a) Section 1, (b) Section 2, (c) Section 3, and (d) Section 4.

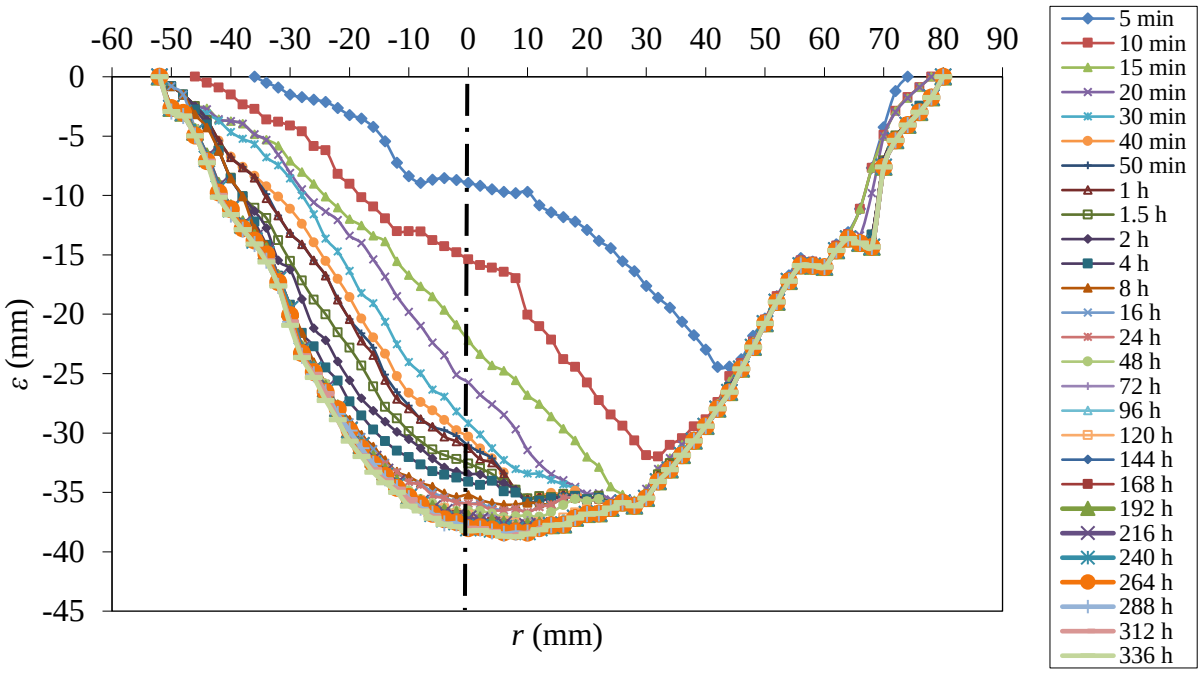

(c)

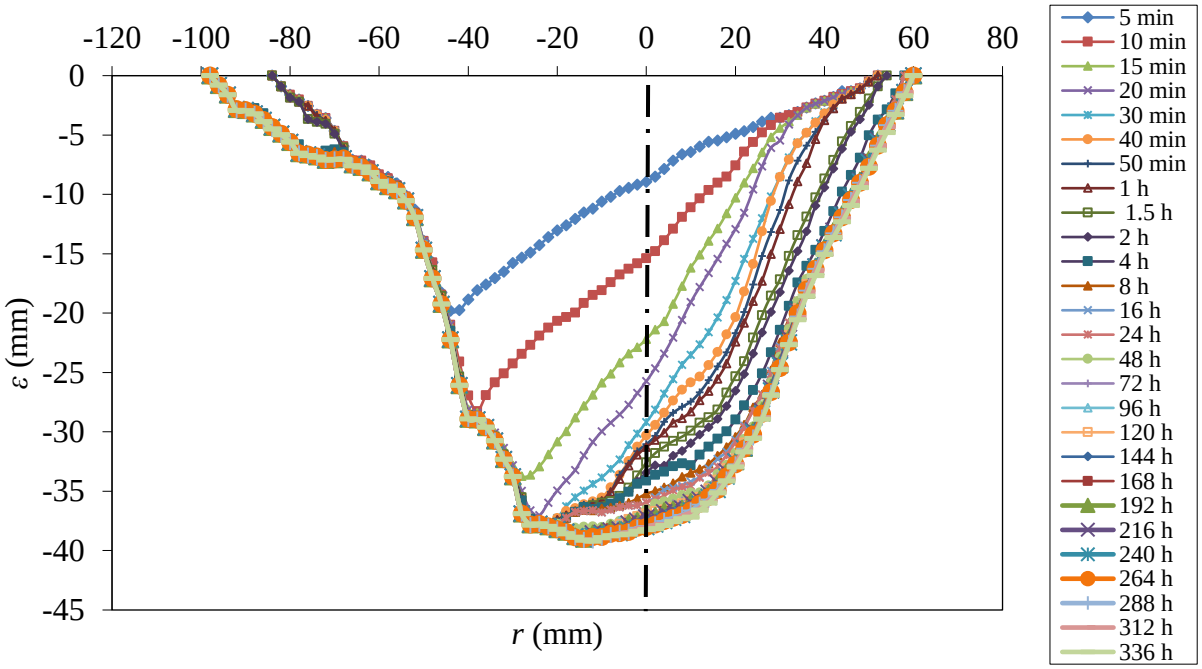

(d)

Figure C-6: cont'd.

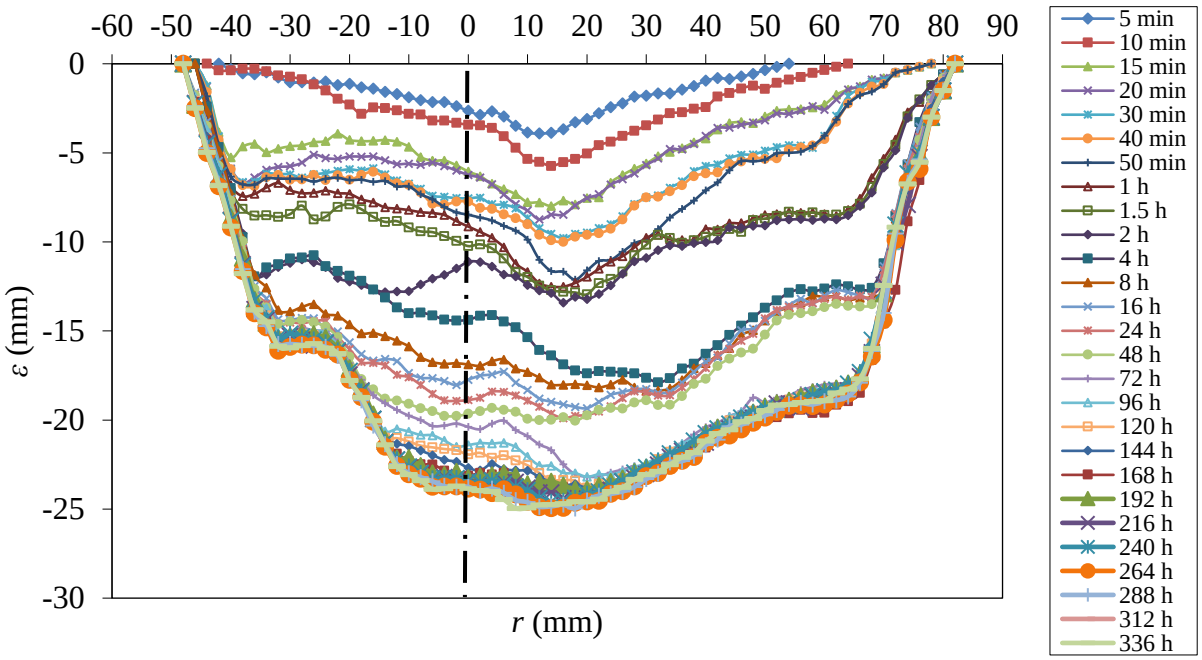

(a)

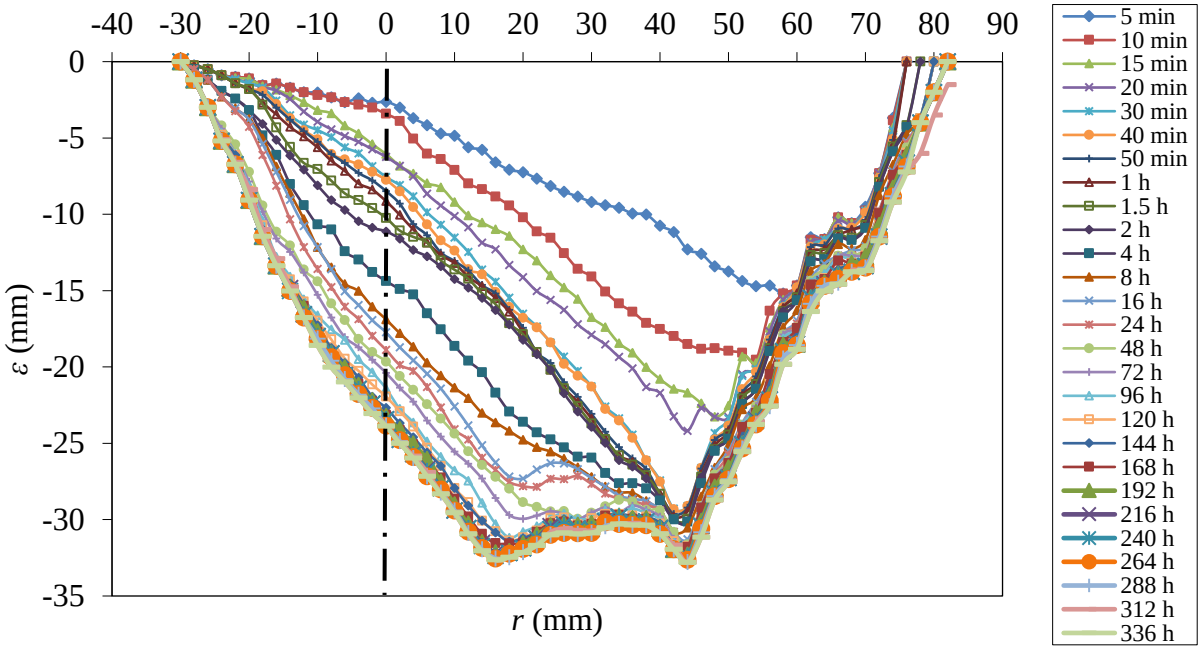

(b)

Figure C-7: Scour hole profiles with time for Scour Test 9 for four different sections (a) Section 1, (b) Section 2, (c) Section 3, and (d) Section 4.

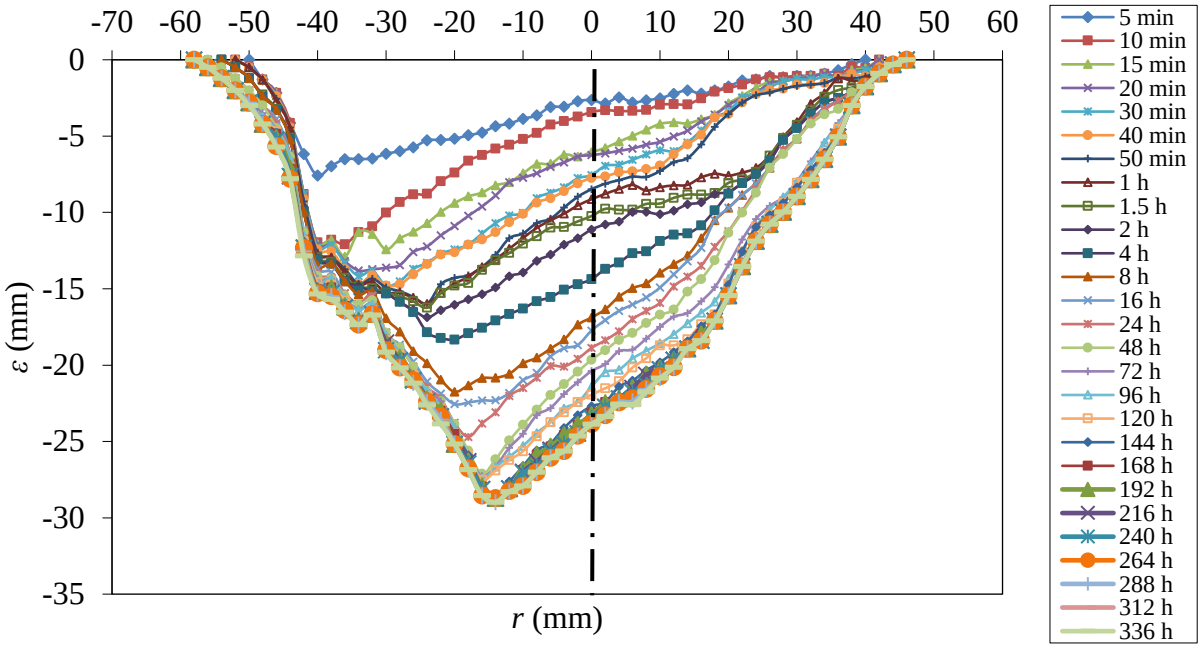

(c)

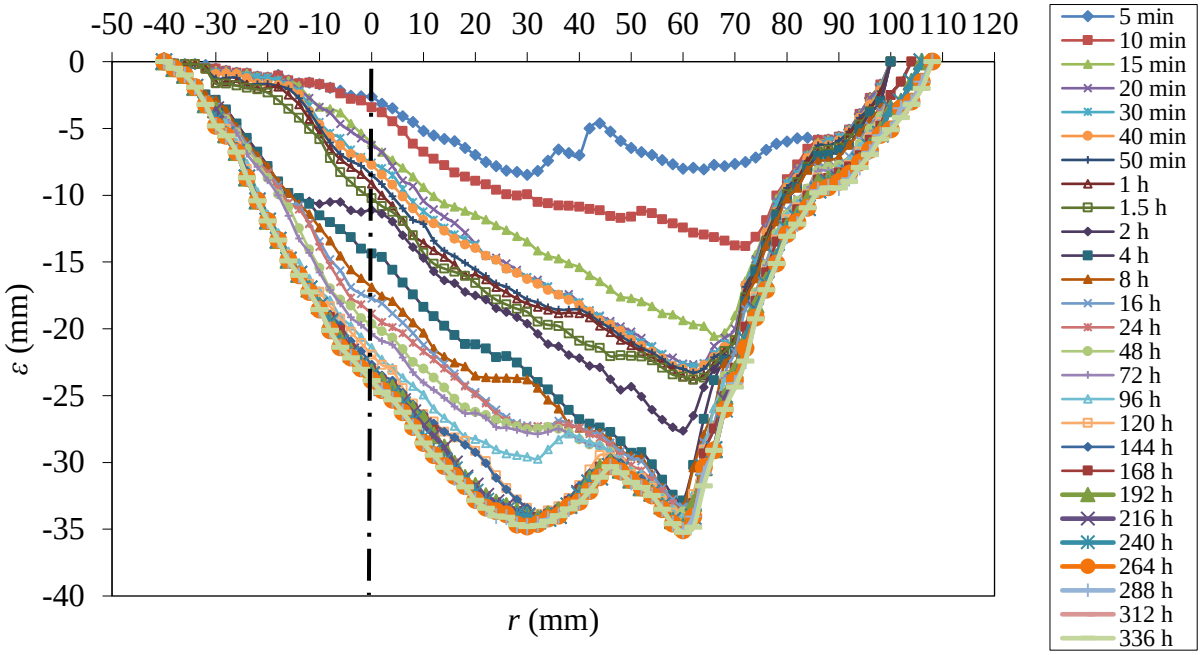

(d)

Figure C-7: cont'd.

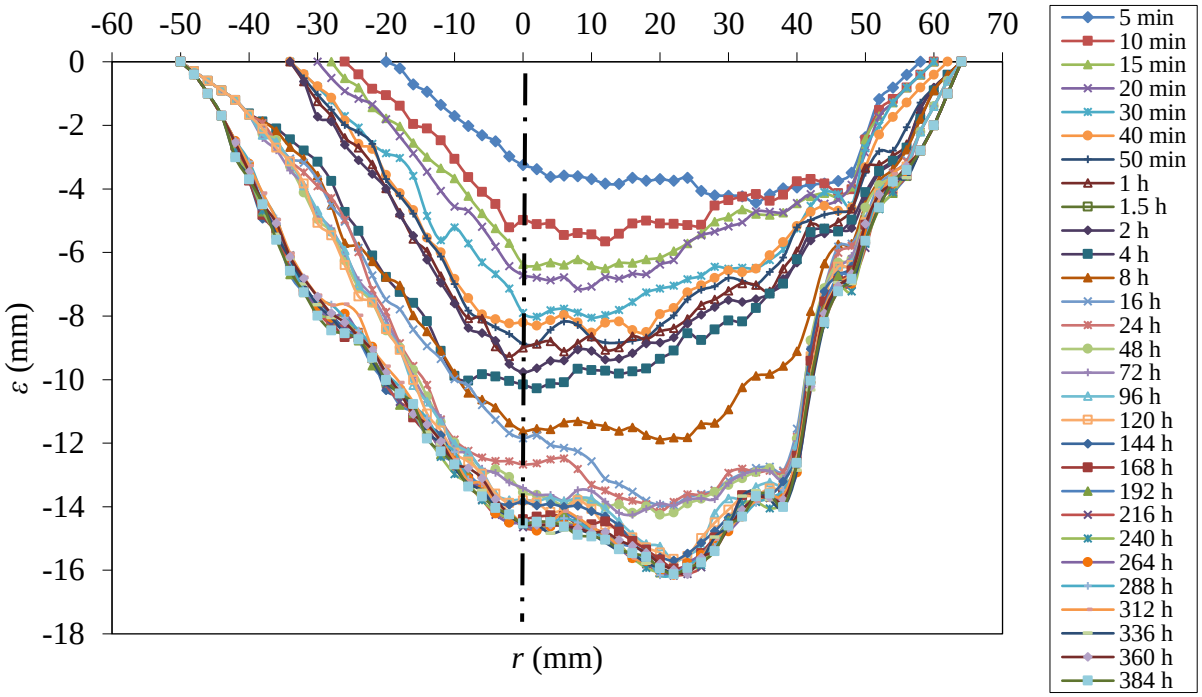

(a)

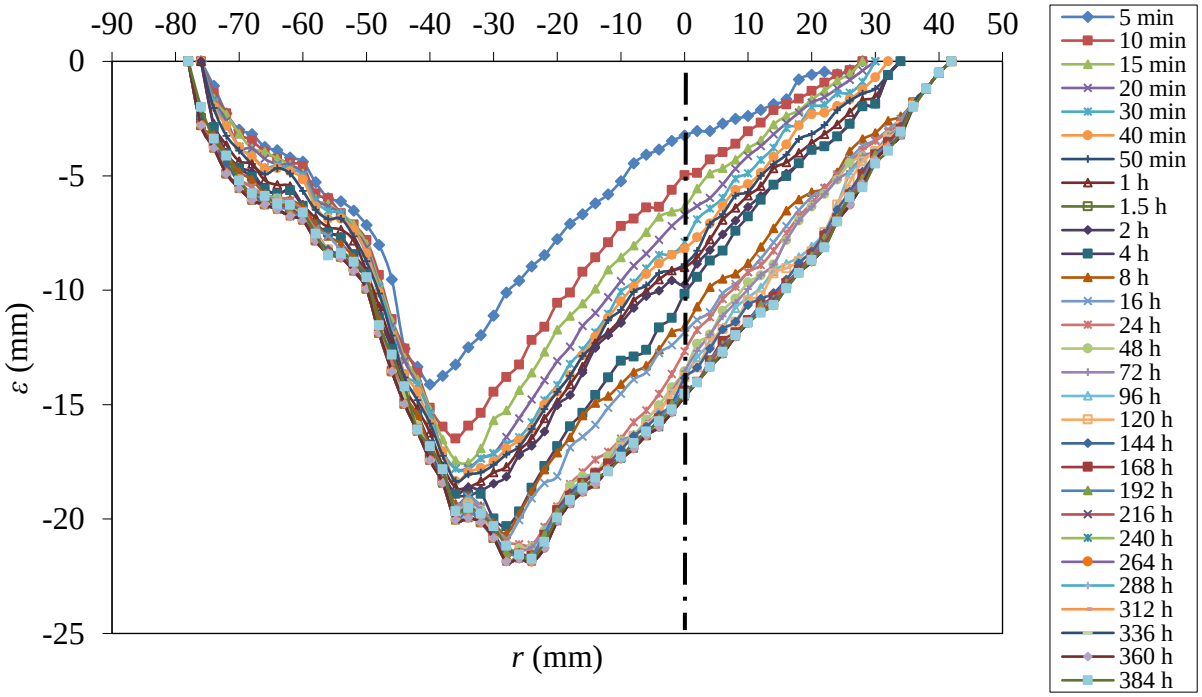

(b)

Figure C-8: Scour hole profiles with time for Scour Test 10 for four different sections (a) Section 1, (b) Section 2, (c) Section 3, and (d) Section 4.

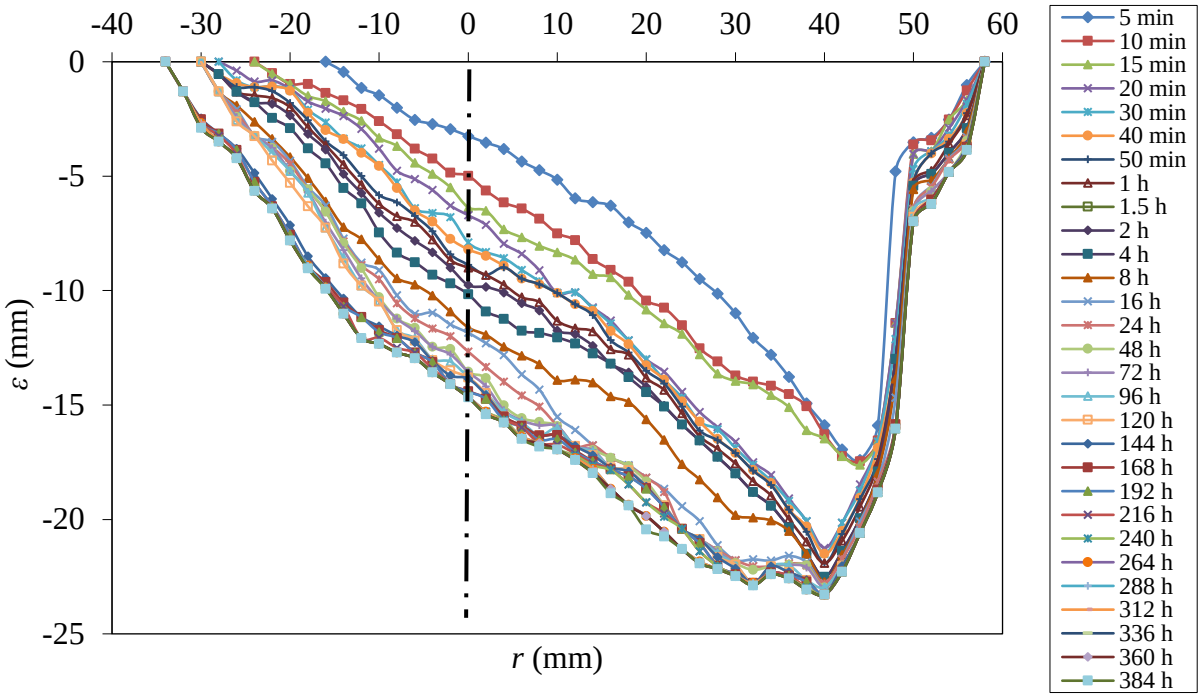

(c)

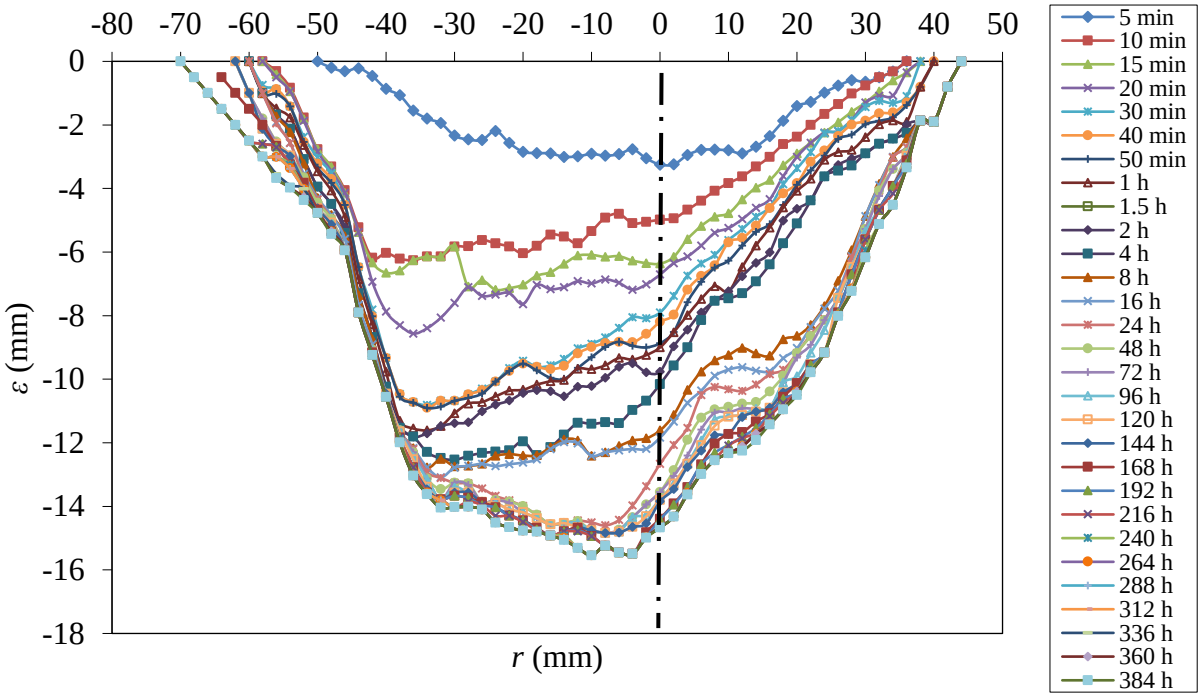

(d)

Figure C-8: cont'd.

APPENDIX D: Dimensionless Scour Hole Profiles with Time for Different Cross-sections

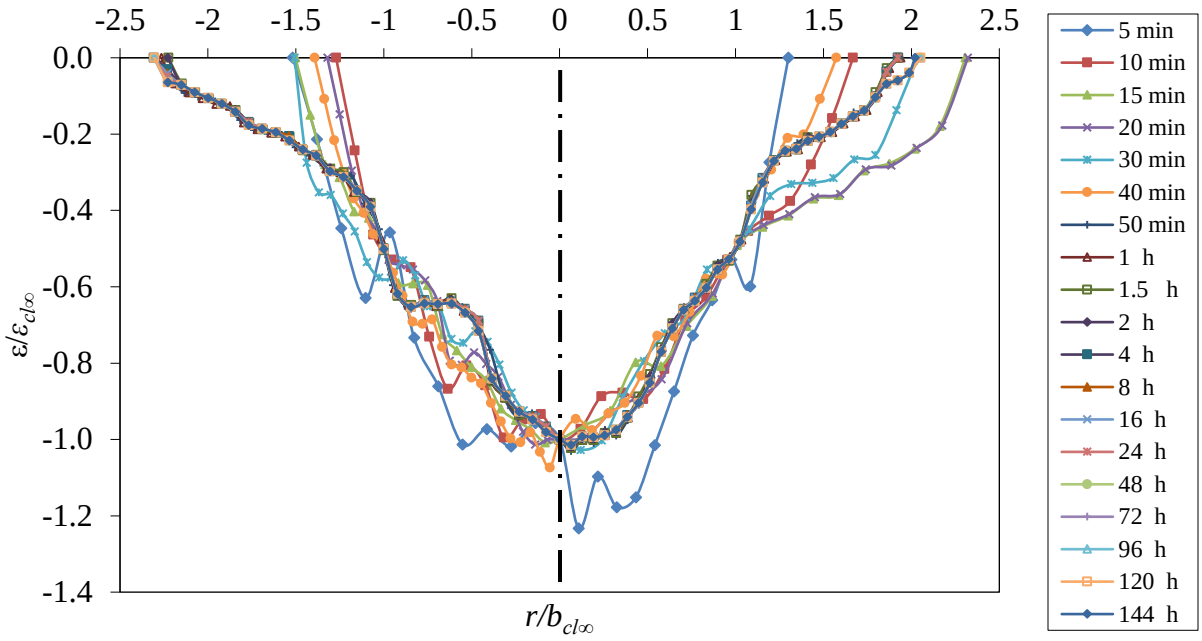

(a)

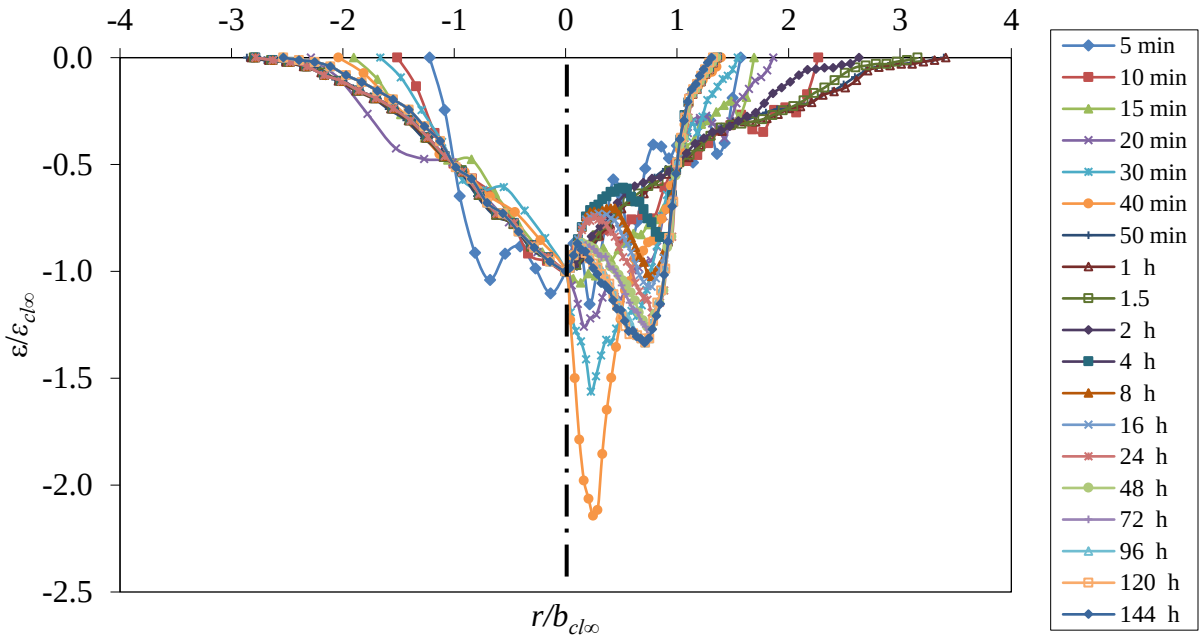

(b)

Figure D-1: Dimensionless Scour hole profiles with time for Scour Test 1 for four different sections (a) Section 1, (b) Section 2, (c) Section 3, and (d) Section 4.

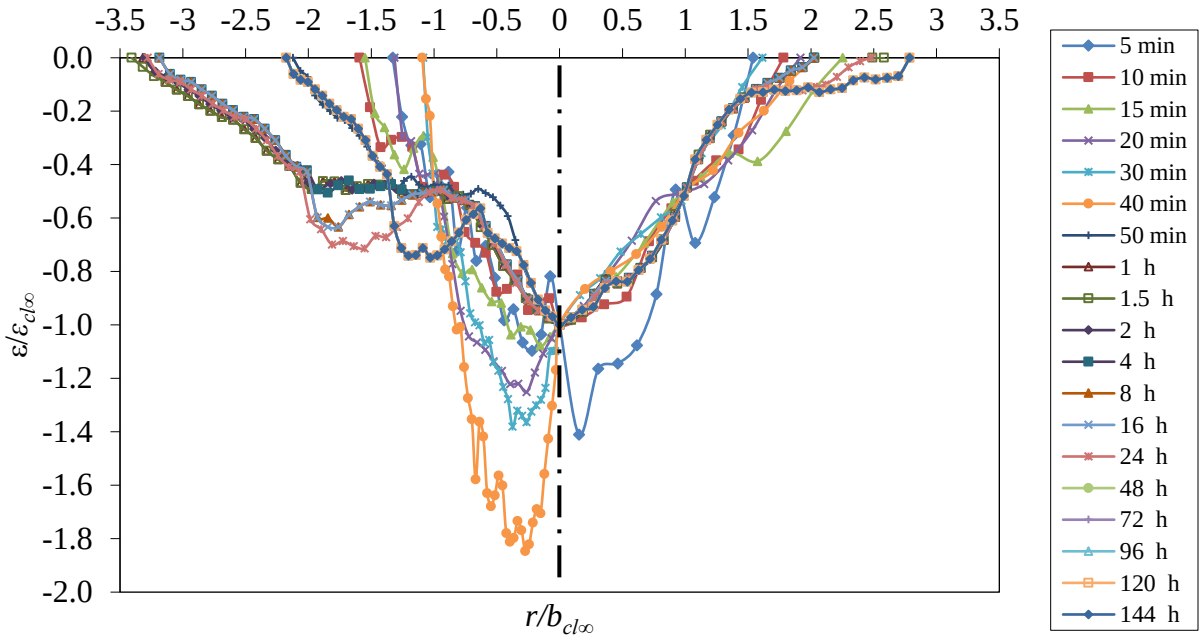

(c)

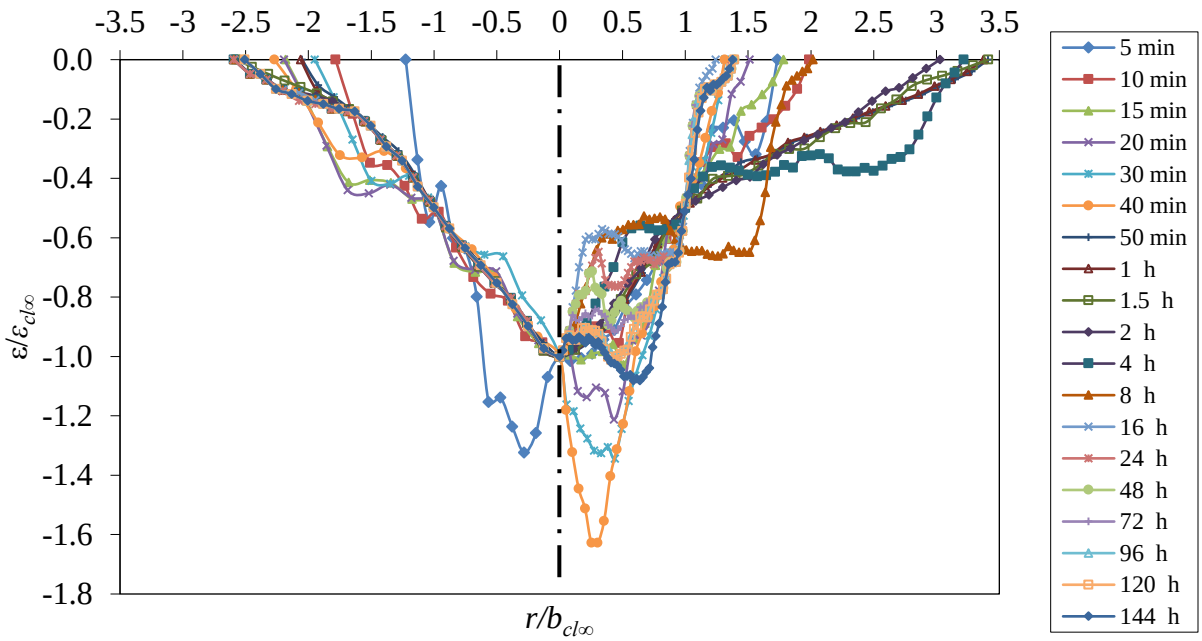

(d)

Figure D-1: cont'd.

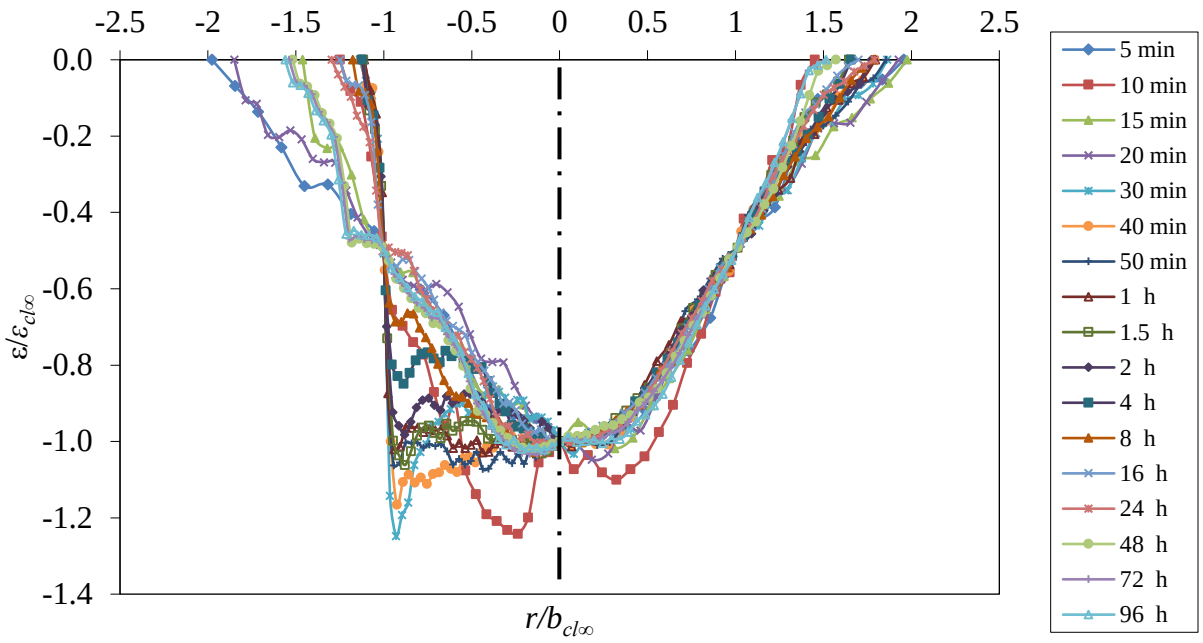

(a)

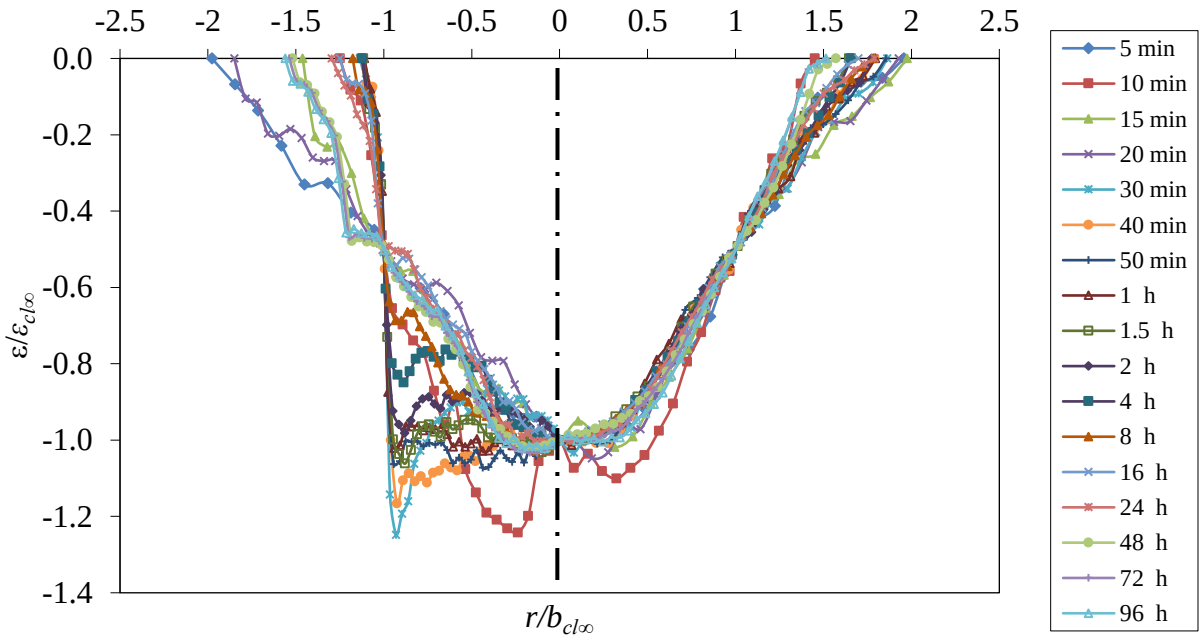

(b)

Figure D-2: Dimensionless Scour hole profiles with time for Scour Test 3 for four different sections (a) Section 1, (b) Section 2, (c) Section 3, and (d) Section 4.

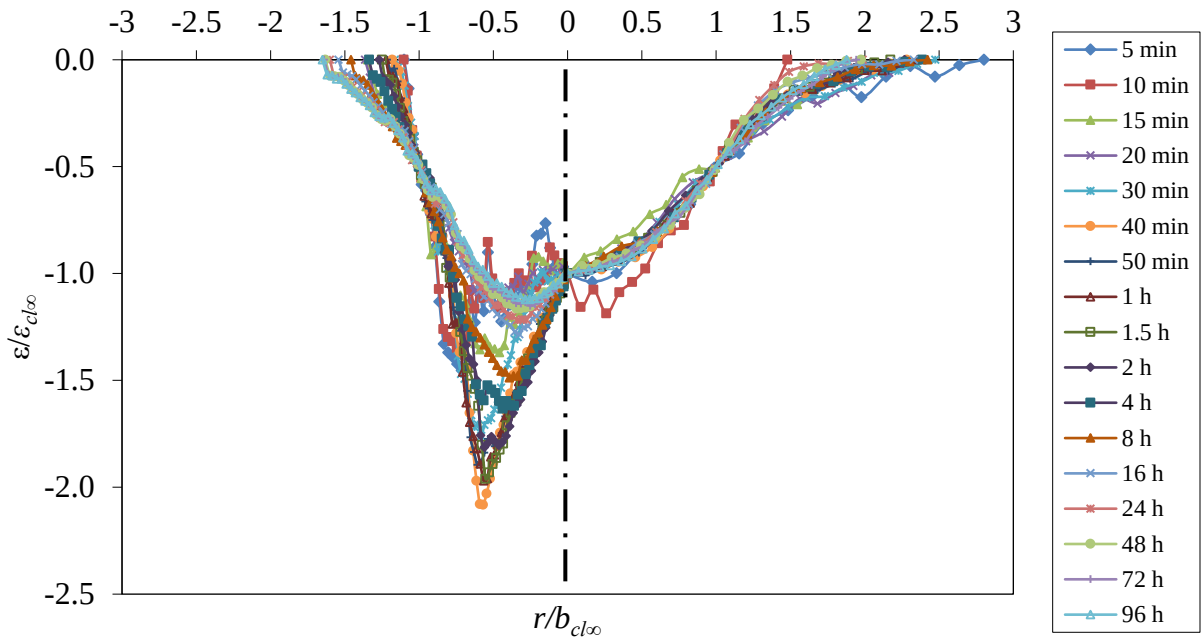

(c)

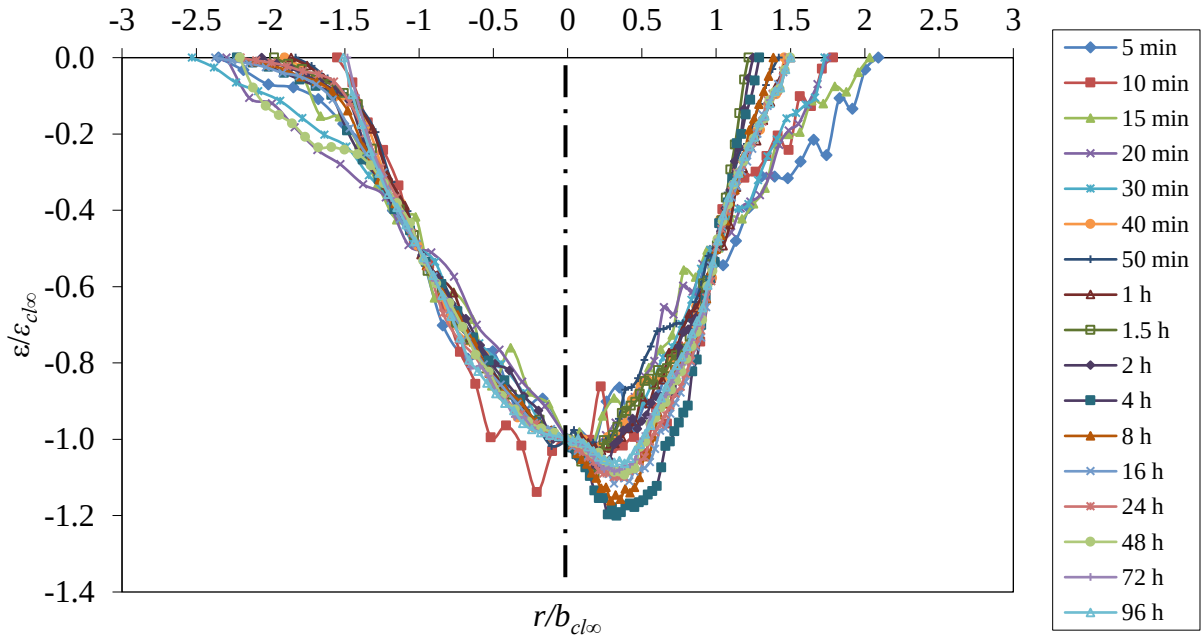

(d)

Figurer D-2: cont'd.

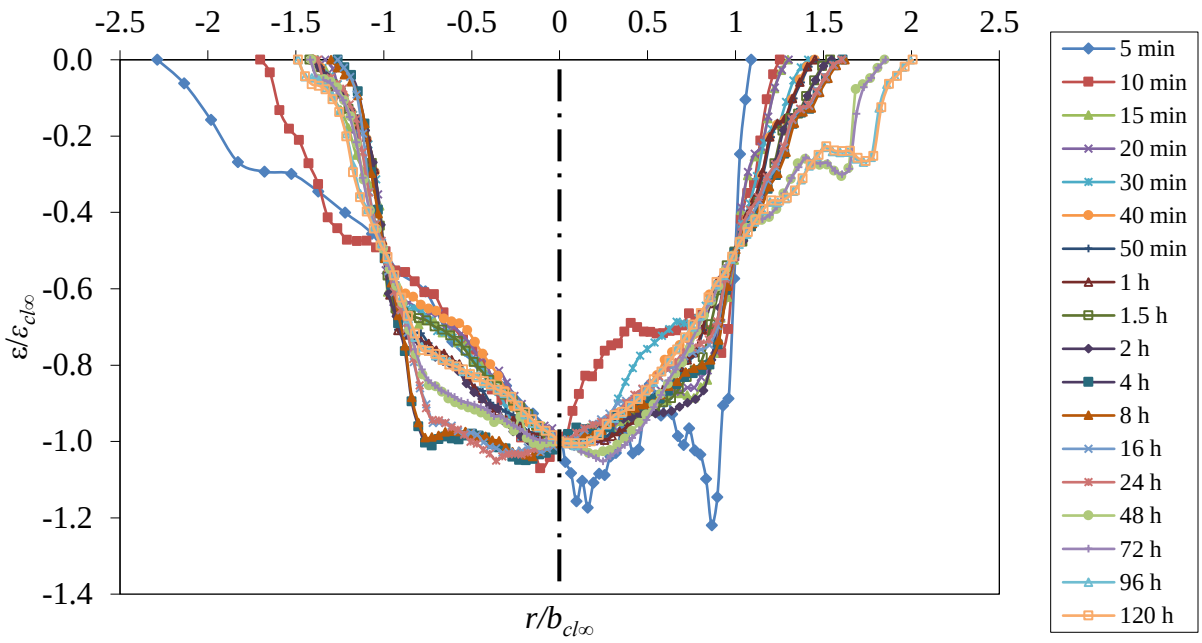

(a)

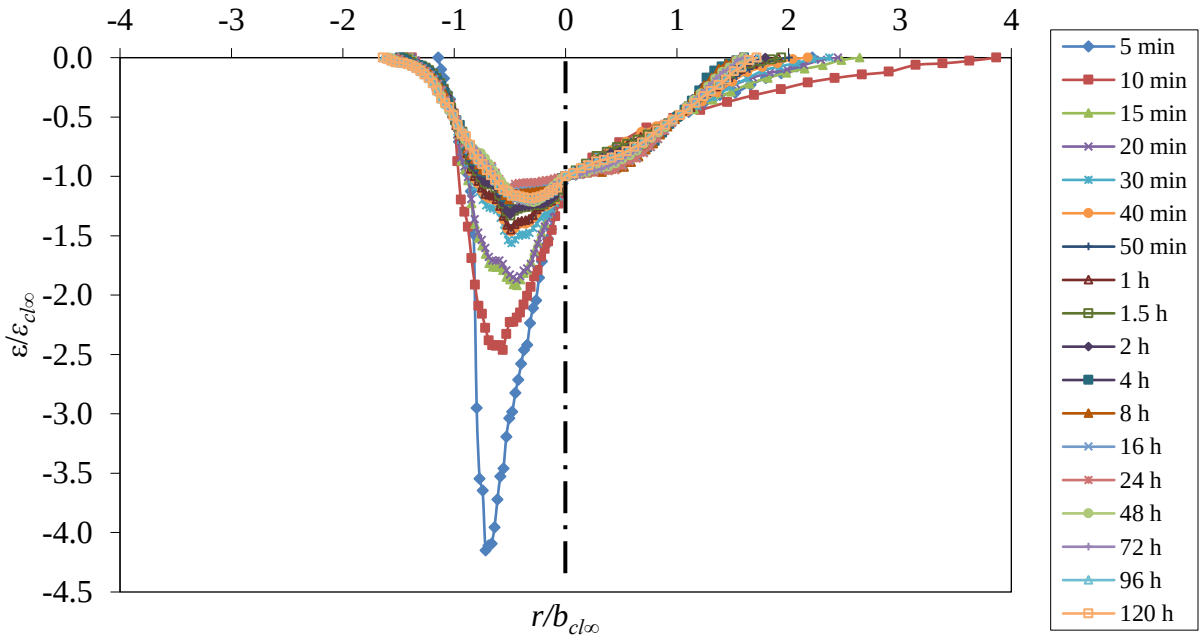

(b)

Figure D-3: Dimensionless Scour hole profiles with time for Scour Test 4 for four different sections (a) Section 1, (b) Section 2, (c) Section 3, and (d) Section 4.

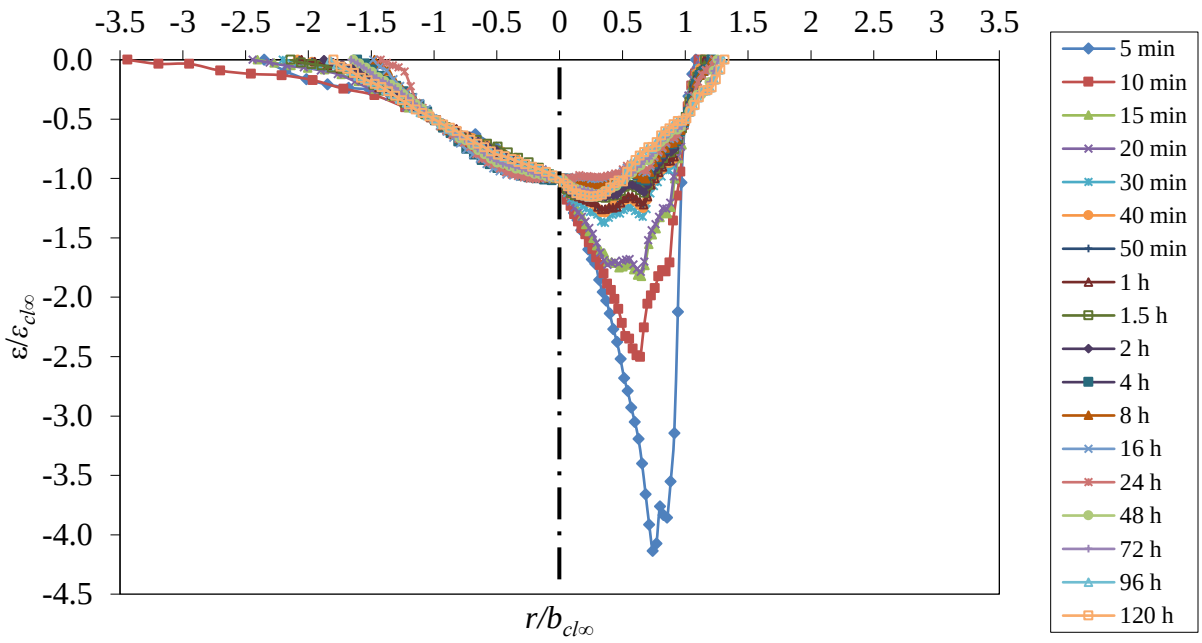

(c)

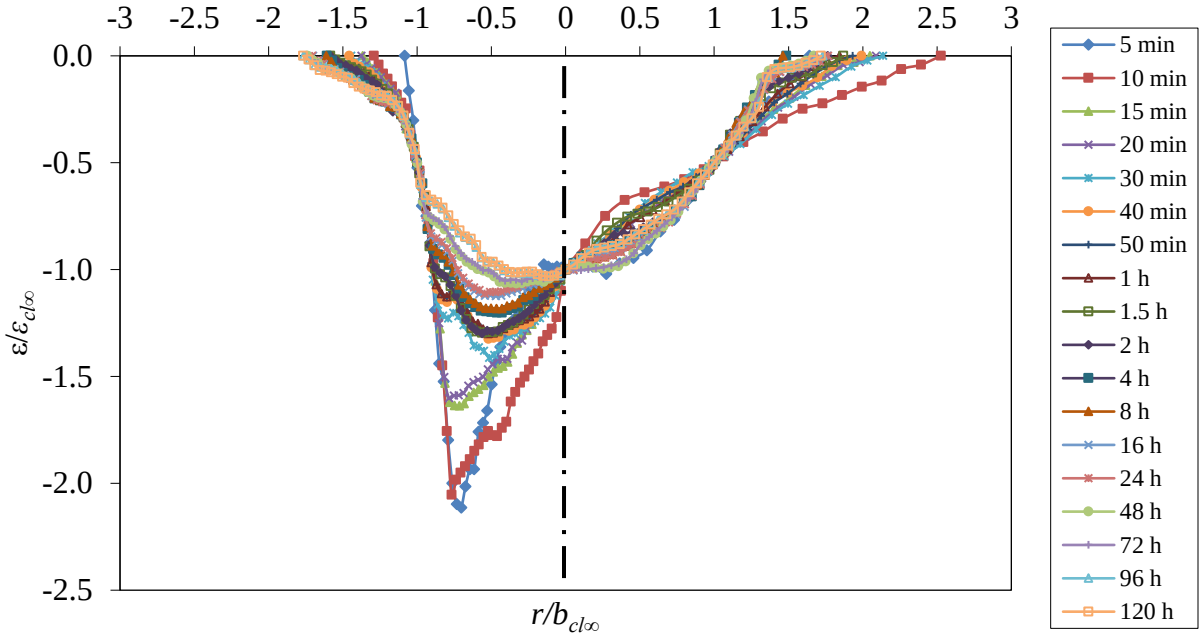

(d)

Figure D-3: cont'd.

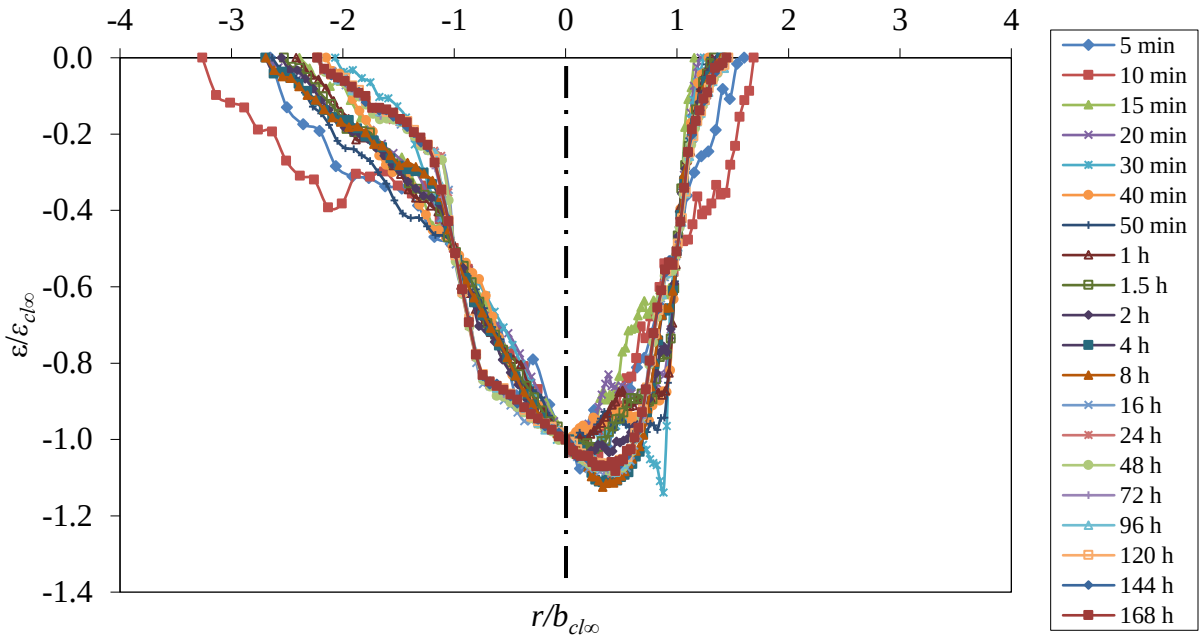

(a)

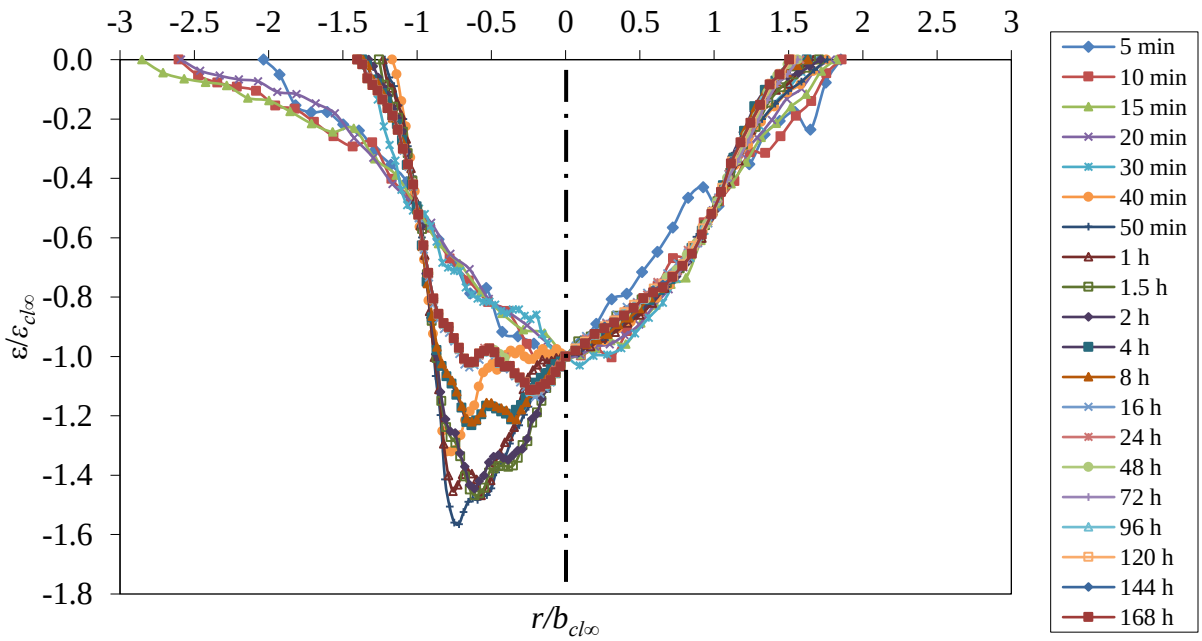

(b)

Figure D-4: Dimensionless Scour hole profiles with time for Scour Test 5 for four different sections (a) Section 1, (b) Section 2, (c) Section 3, and (d) Section 4.

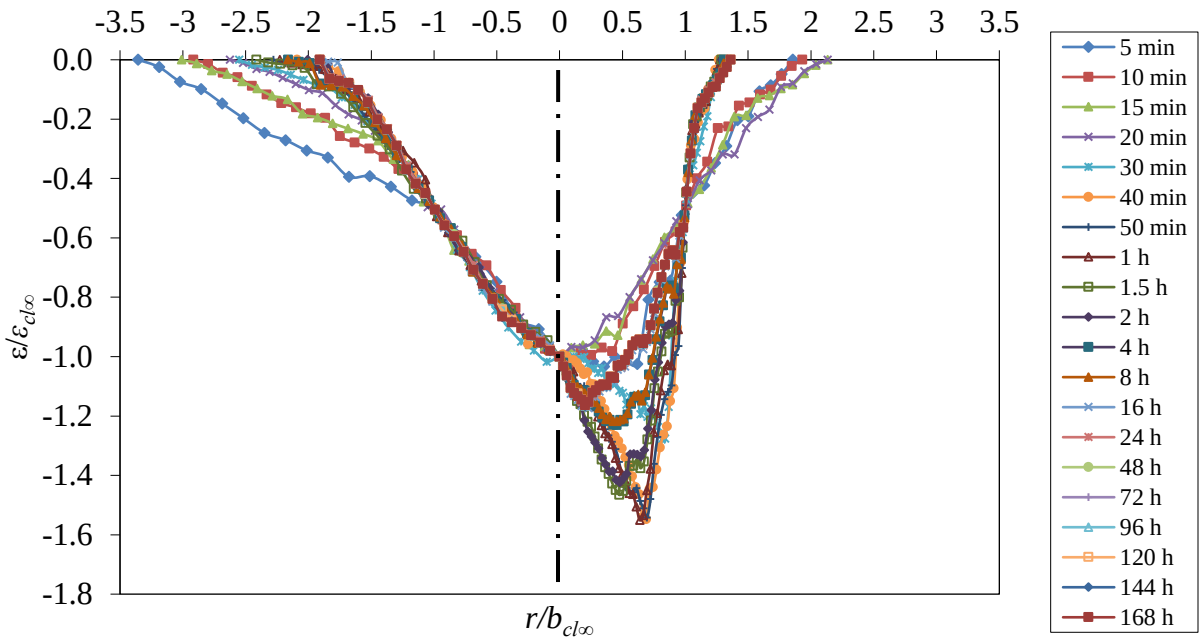

(c)

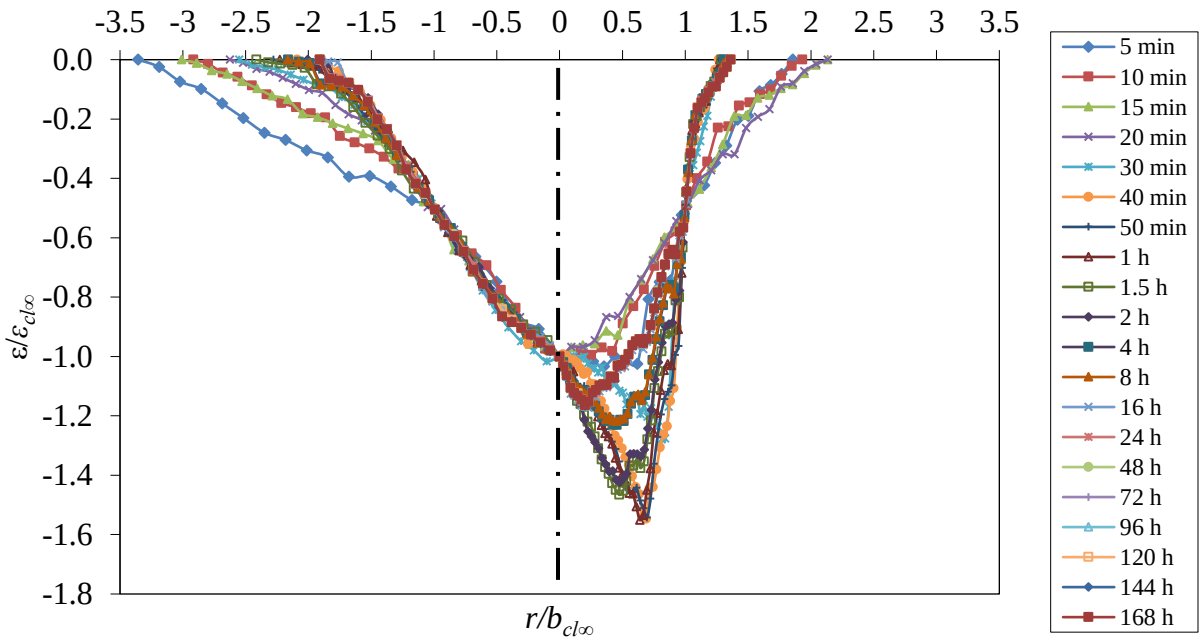

(d)

Figure D-4: cont'd.

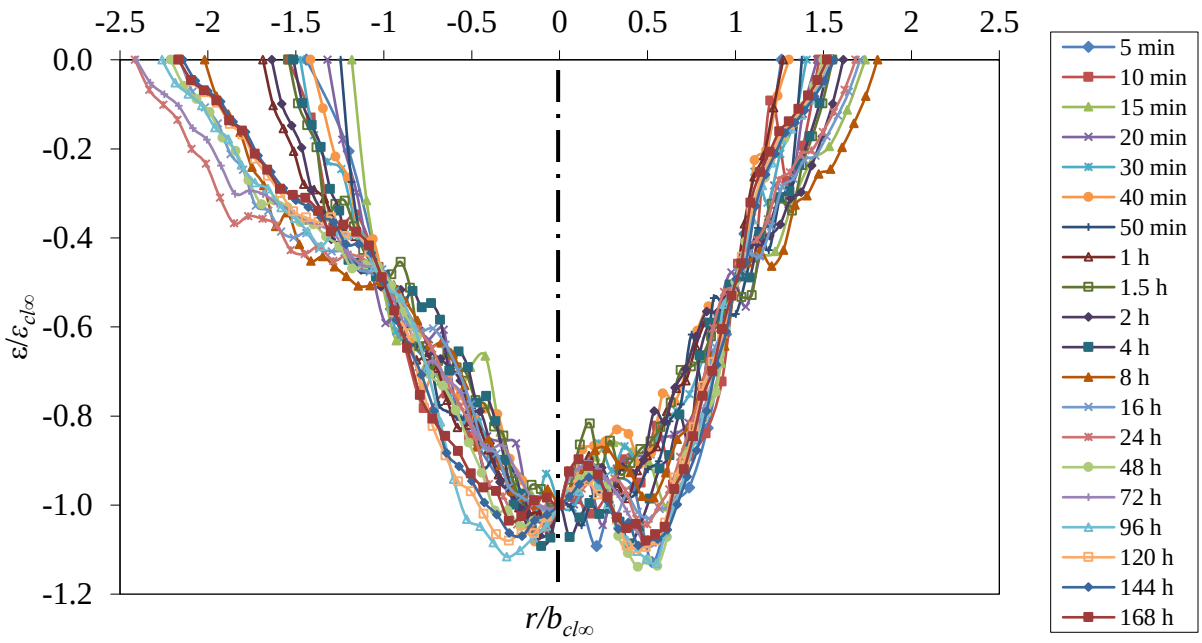

(a)

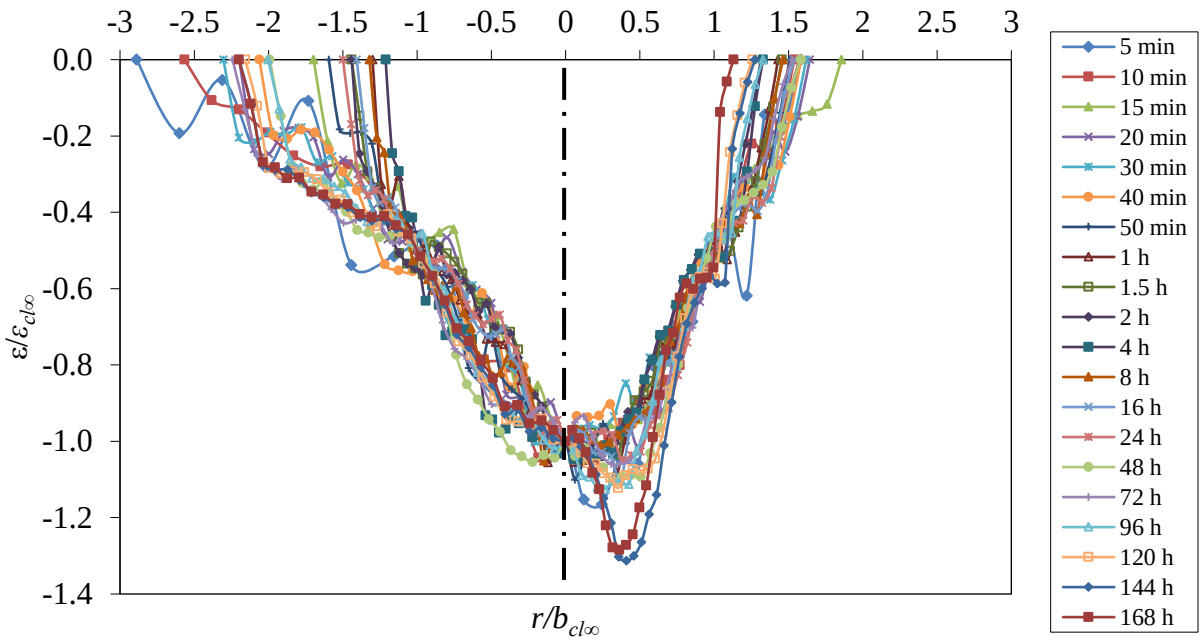

(b)

Figure D-5: Dimensionless Scour hole profiles with time for Scour Test 6 for four different sections (a) Section 1, (b) Section 2, (c) Section 3, and (d) Section 4.

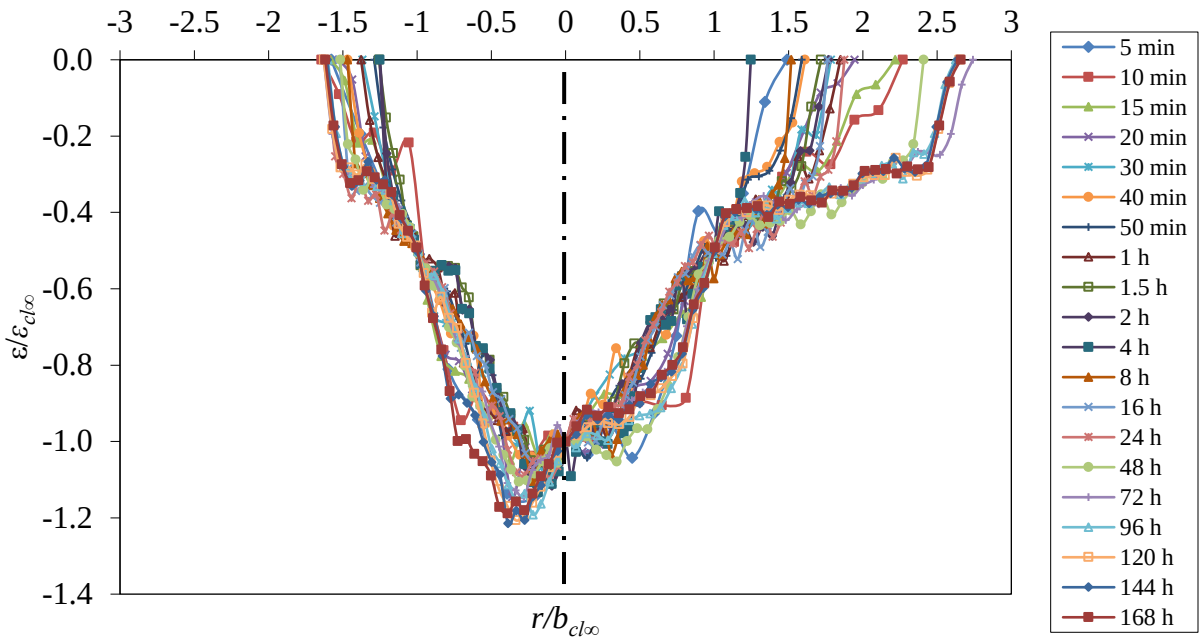

(c)

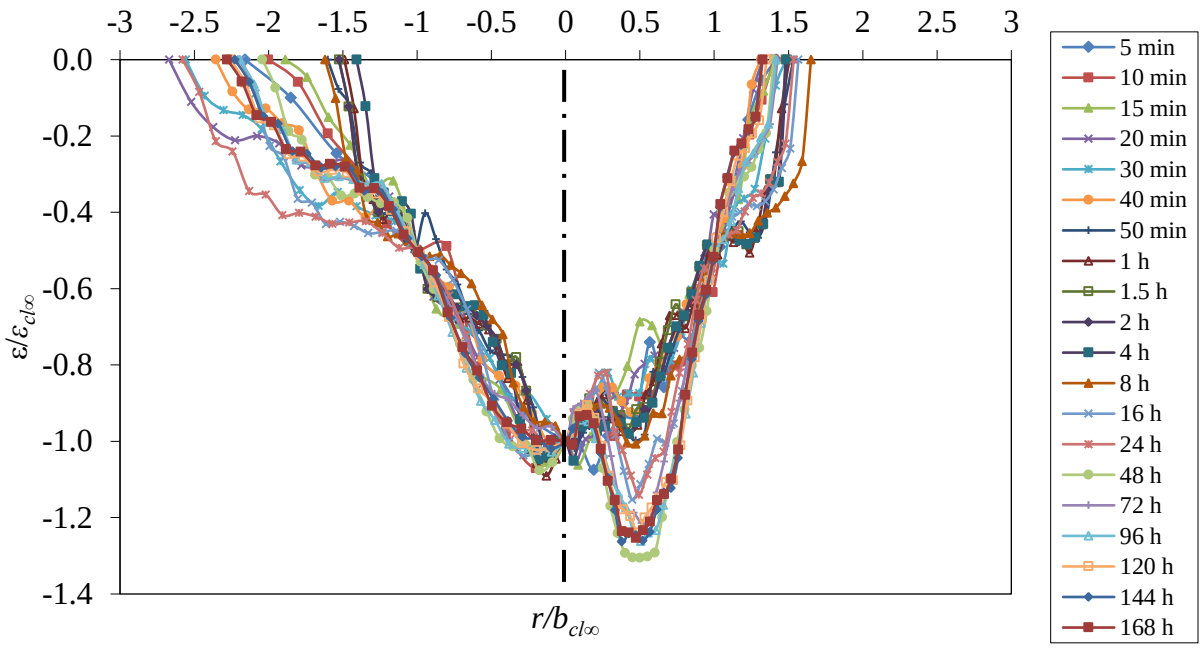

(d)

Figure D-5: cont'd.

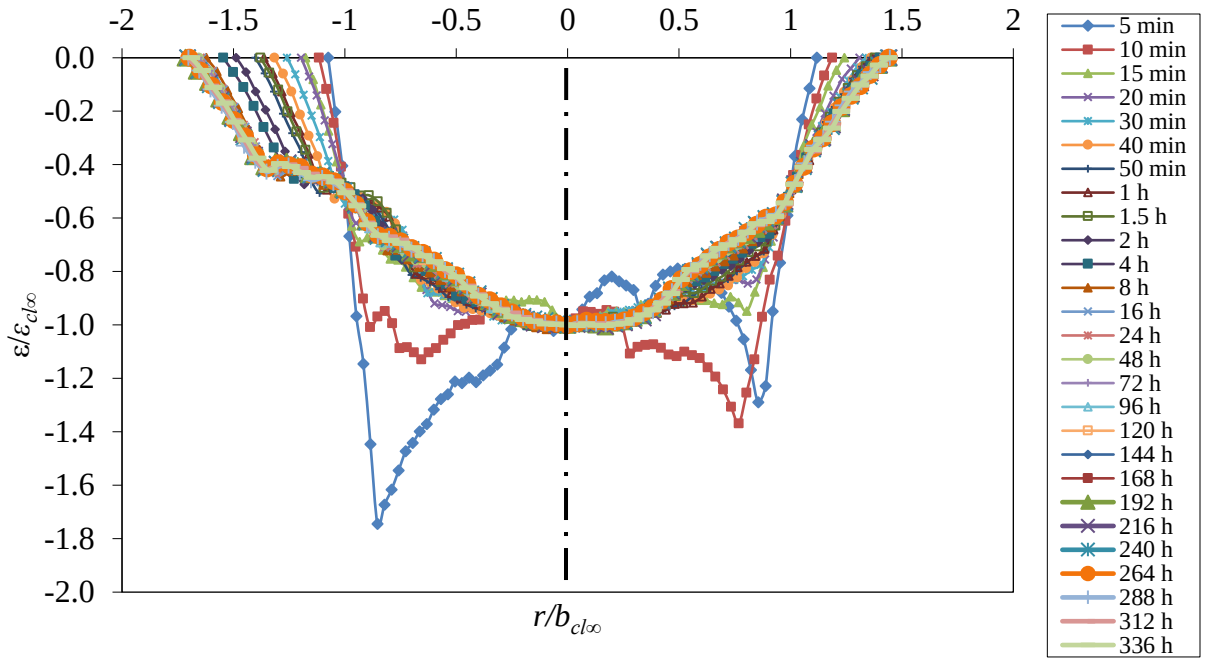

(a)

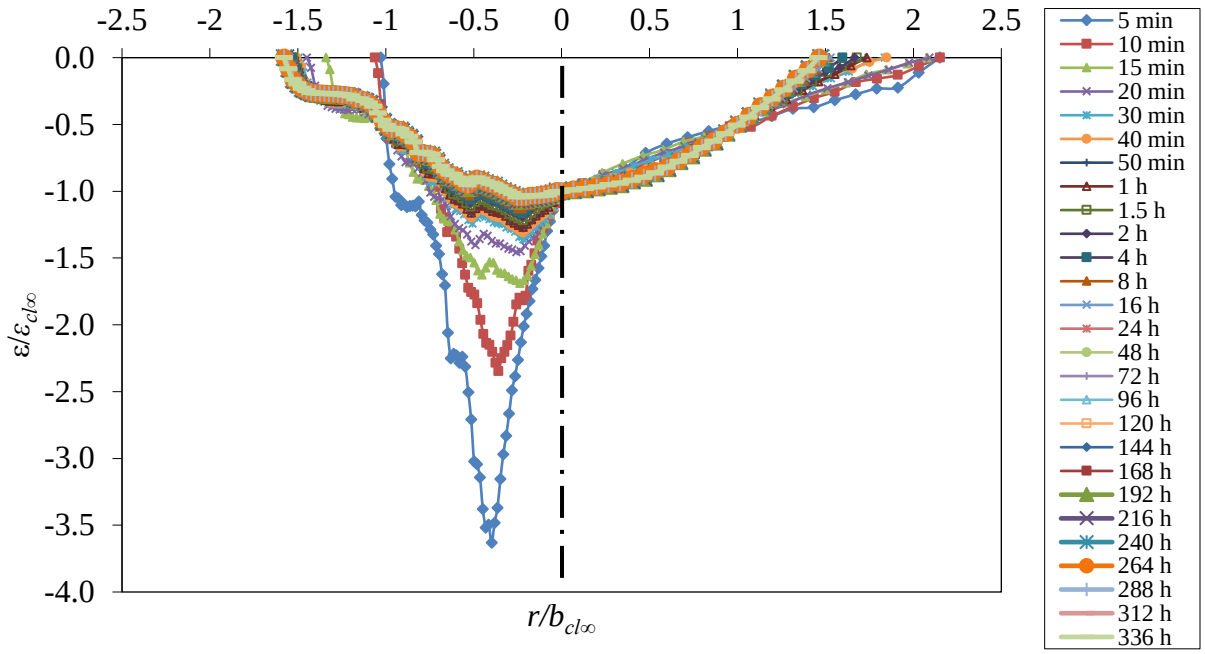

(b)

Figure D-6: Dimensionless Scour hole profiles with time for Scour Test 8 for four different sections (a) Section 1, (b) Section 2, (c) Section 3, and (d) Section 4.

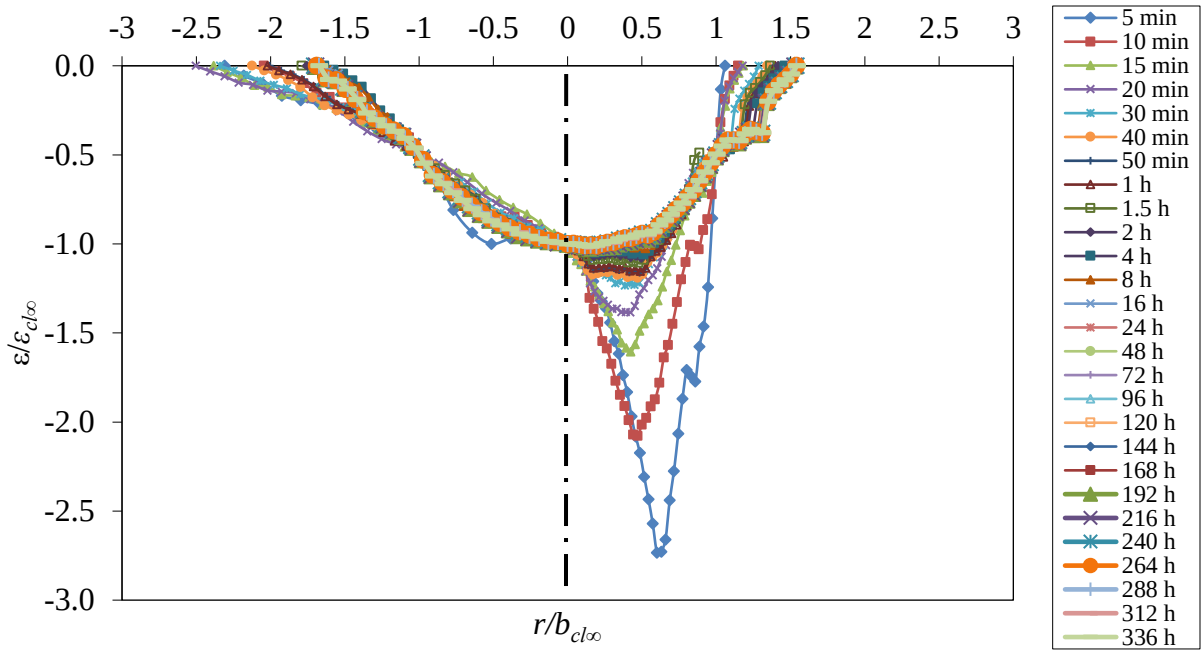

(c)

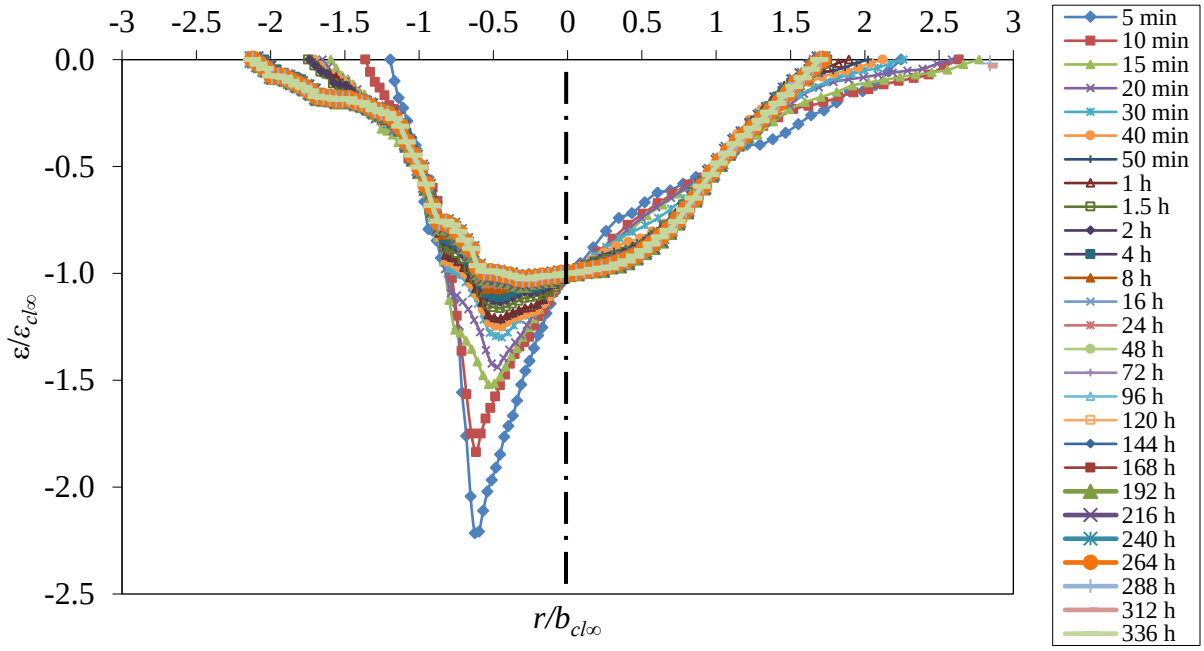

(d)

Figure D-6: cont'd.

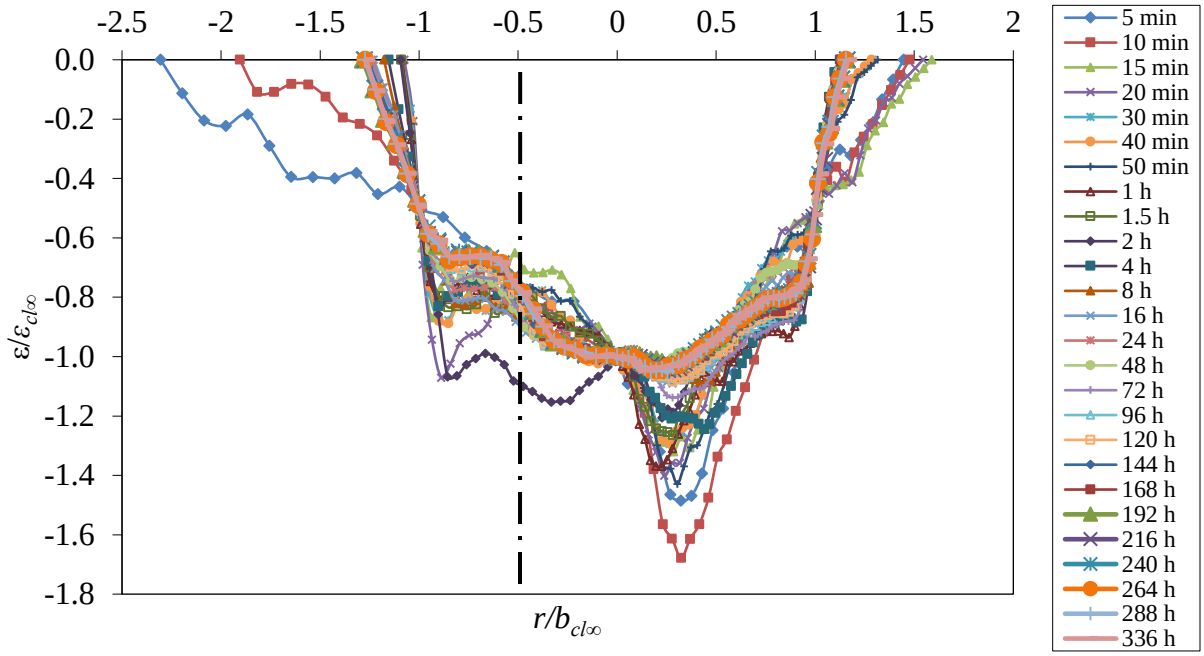

(a)

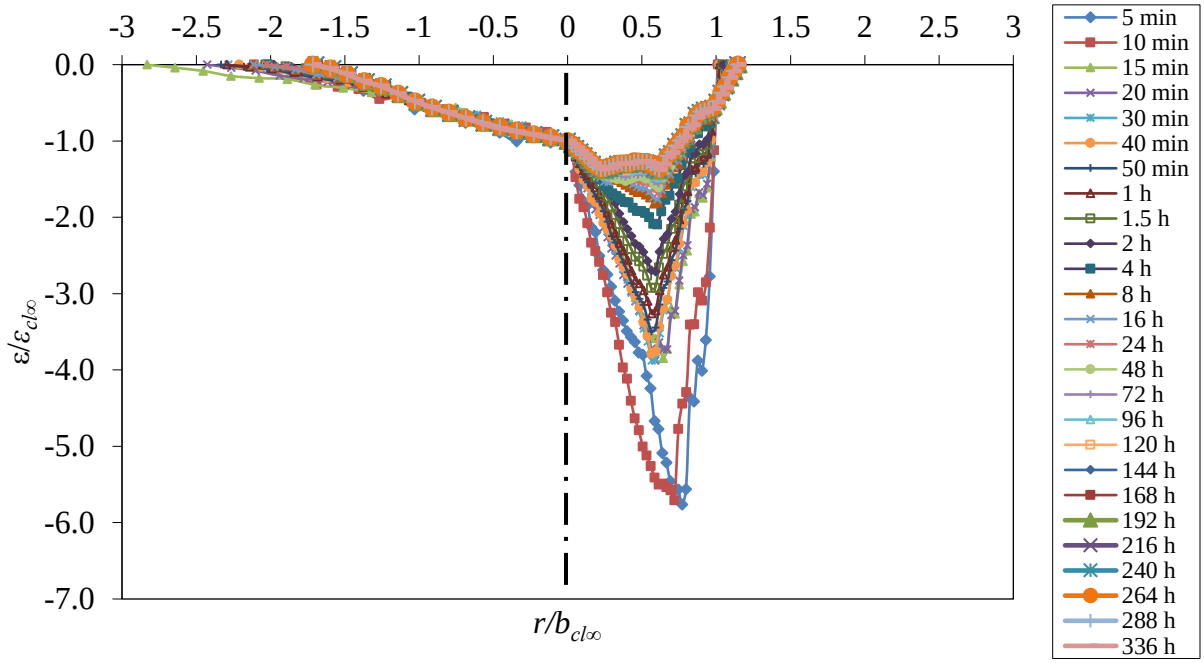

(b)

Figure D-7: Dimensionless Scour hole profiles with time for Scour Test 1 for four different sections (a) Section 1, (b) Section 2, (c) Section 3, and (d) Section 4.

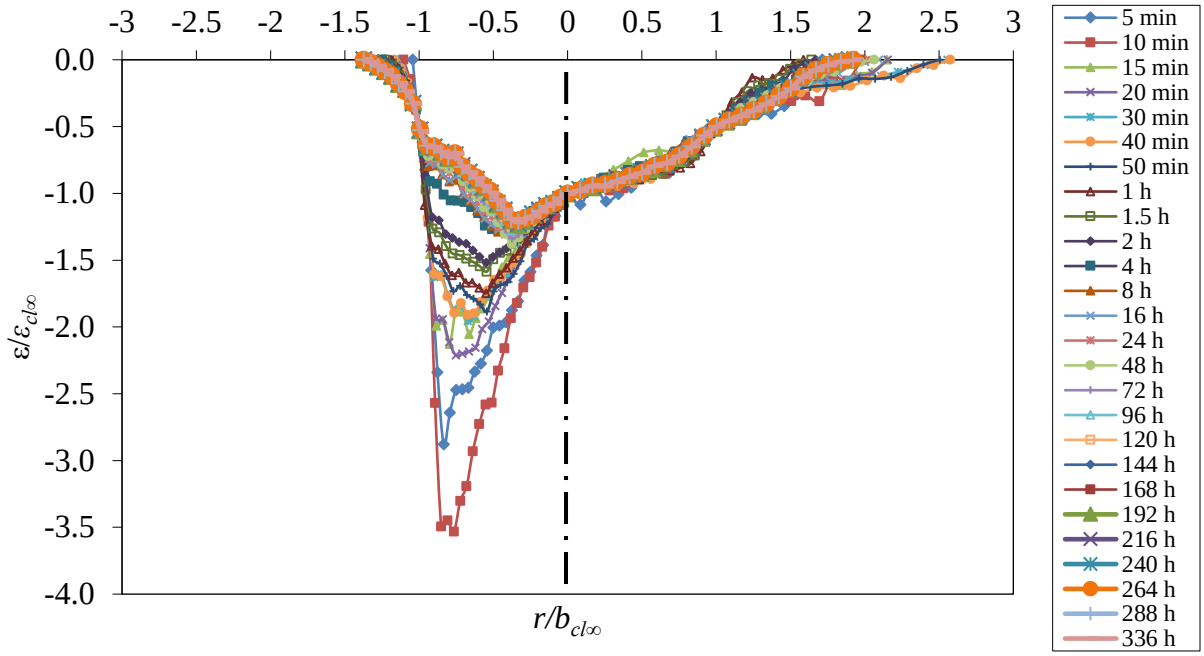

(a)

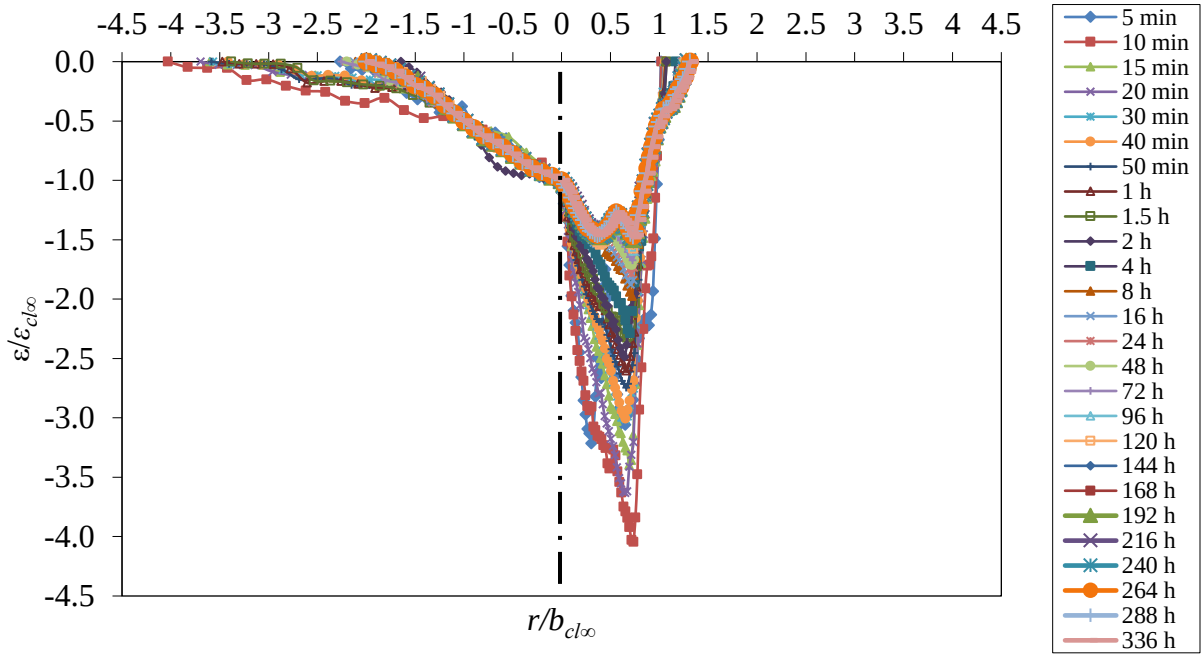

(b)

Figure D-7: cont'd.

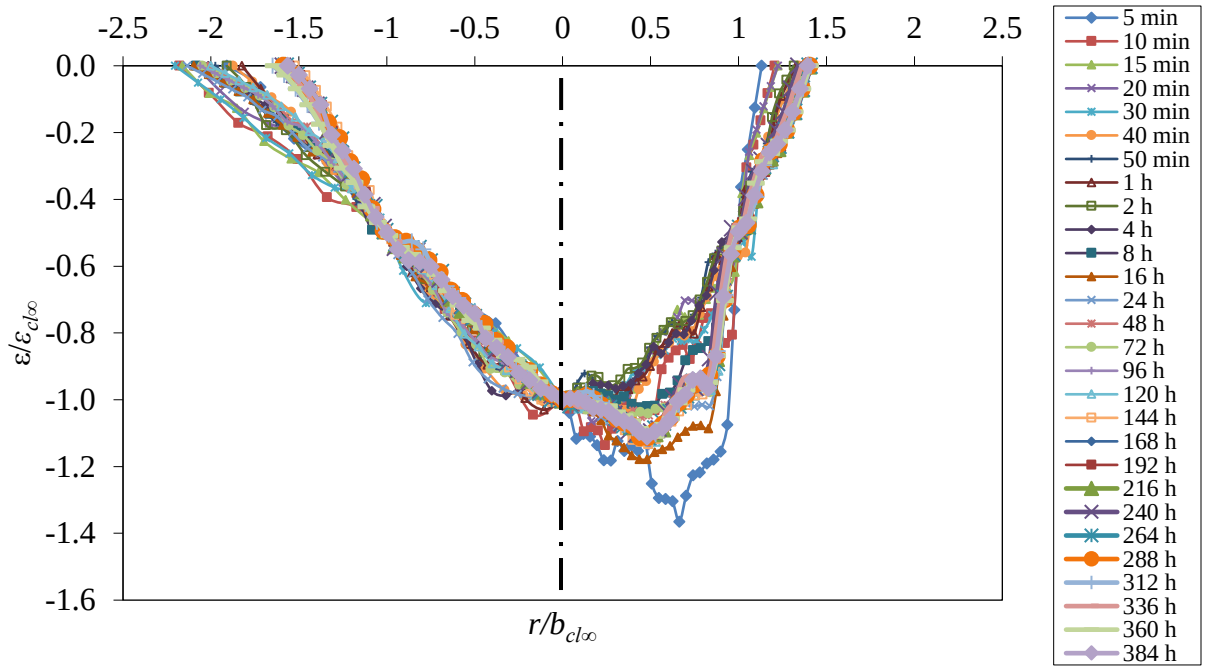

(a)

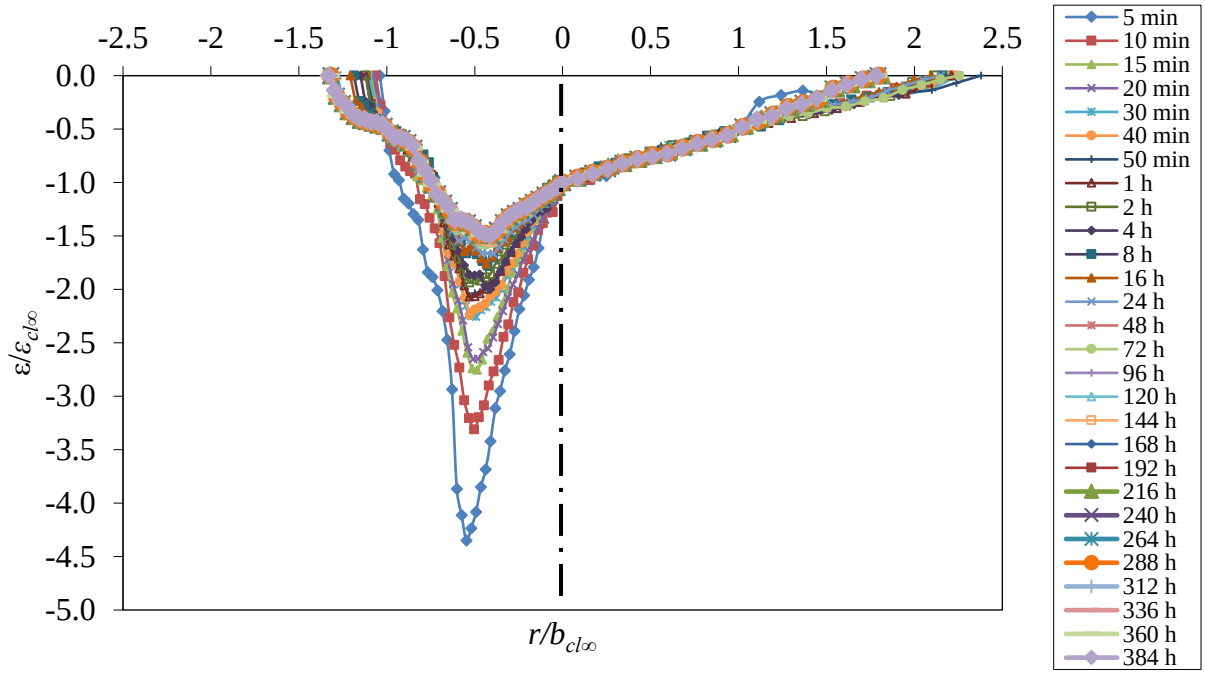

(b)

Figure D-8: Dimensionless Scour hole profiles with time for Scour Test 10 for four different sections (a) Section 1, (b) Section 2, (c) Section 3, and (d) Section 4.

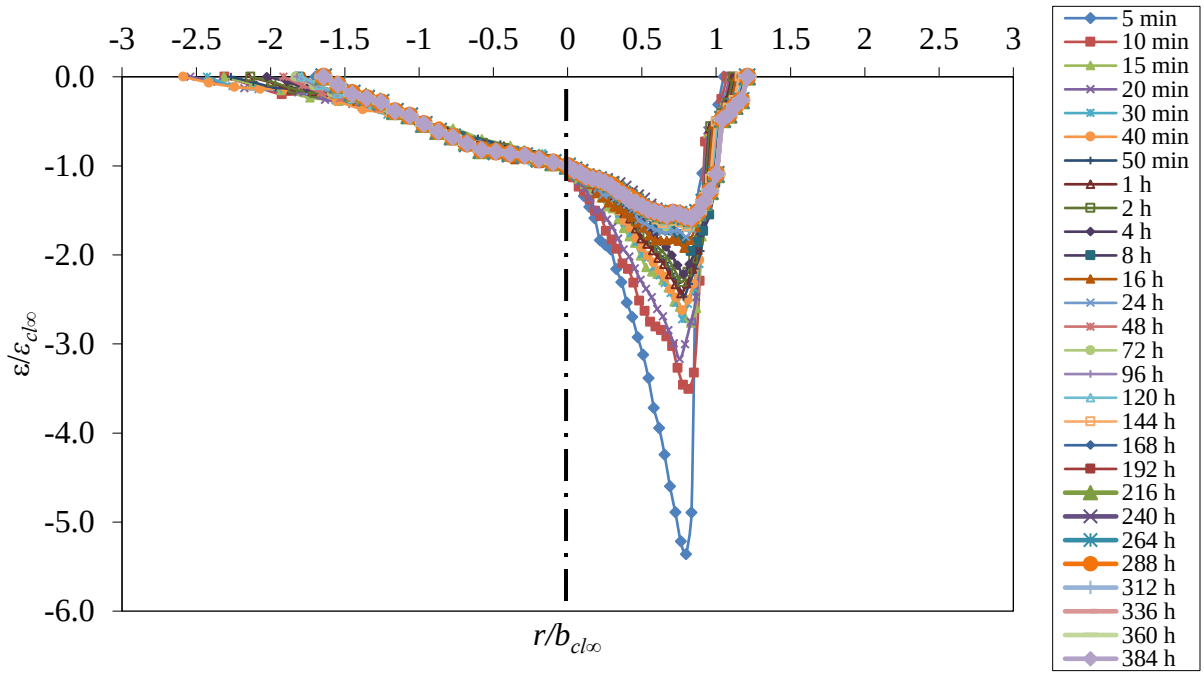

(c)

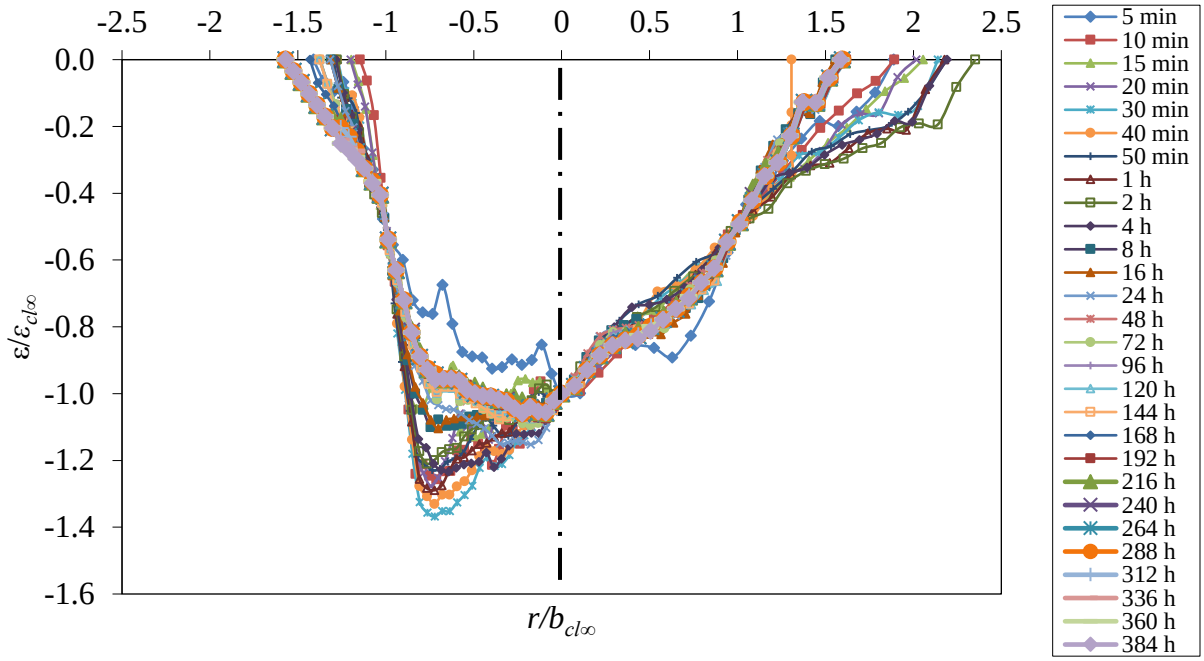

(d)

Figure D-8: cont'd.